THE FOURTH IAEA SYMPOSIUM ON

NEUTRON INELASTIC SCATTERING

VOL. II

PROCEEDINGS OF A SYMPOSIUM, COPENHAGEN, 20-25 MAY 1968

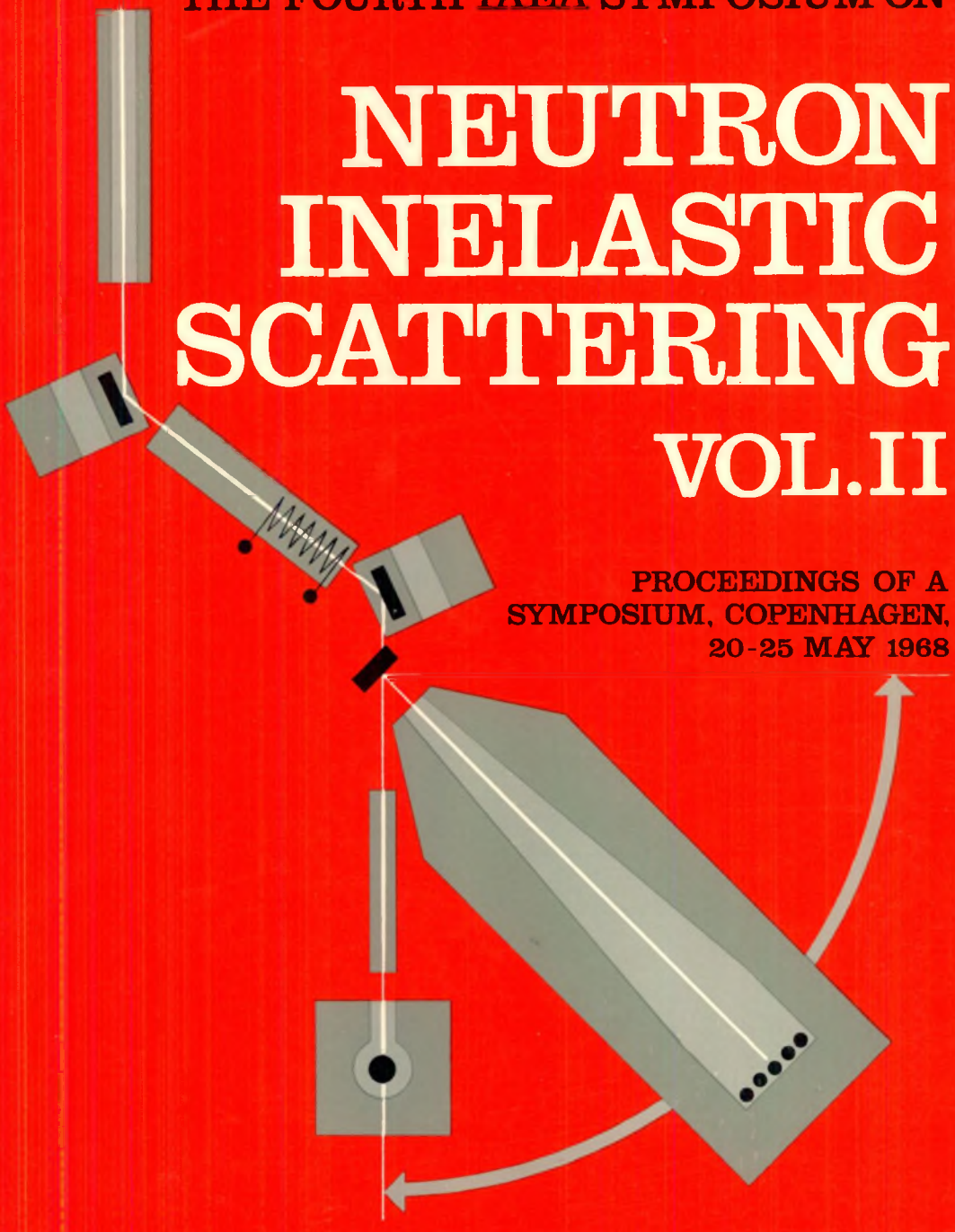

INTERNATIONAL ATOMIC ENERGY AGENCY, VIENNA, 1968

NEUTRON INELASTIC SCATTERING, VOLUME II

ERRATA

Contents page

In title of C.G. Windsor's paper:
For Heisenberg parameters read Heisenberg paramagnets.

Page 205

The footnote marked † refers to N.A. Lurie.

Page 299

Delete the asterisk after the first author's name.

Page 447

For Lingård, P.-A. read Lindgård, P.-A.

Page 454

For Grünberg, B. read Grinberg, B.

NEUTRON INELASTIC SCATTERING
VOL. II

The following States are Members of the International Atomic Energy Agency:

AFGHANISTAN
ALBANIA
ALGERIA
ARGENTINA
AUSTRALIA
AUSTRIA
BELGIUM
BOLIVIA
BRAZIL
BULGARIA
BURMA
BYELORUSSIAN SOVIET SOCIALIST REPUBLIC
CAMBODIA
CAMEROON
CANADA
CEYLON
CHILE
CHINA
COLOMBIA
CONGO, DEMOCRATIC REPUBLIC OF
COSTA RICA
CUBA
CYPRUS
CZECHOSLOVAK SOCIALIST REPUBLIC
DENMARK
DOMINICAN REPUBLIC
ECUADOR
EL SALVADOR
ETHIOPIA
FINLAND
FRANCE
GABON
GERMANY, FEDERAL REPUBLIC OF
GHANA
GREECE
GUATEMALA
HAITI
HOLY SEE
HUNGARY
ICELAND
INDIA
INDONESIA
IRAN
IRAQ
ISRAEL
ITALY
IVORY COAST
JAMAICA
JAPAN
JORDAN
KENYA
KOREA, REPUBLIC OF
KUWAIT
LEBANON
LIBERIA
LIBYA
LUXEMBOURG
MADAGASCAR
MALI
MEXICO
MONACO
MOROCCO
NETHERLANDS
NEW ZEALAND
NICARAGUA
NIGERIA
NORWAY
PAKISTAN
PANAMA
PARAGUAY
PERU
PHILIPPINES
POLAND
PORTUGAL
ROMANIA
SAUDI ARABIA
SENEGAL
SIERRA LEONE
SINGAPORE
SOUTH AFRICA
SPAIN
SUDAN
SWEDEN
SWITZERLAND
SYRIAN ARAB REPUBLIC
THAILAND
TUNISIA
TURKEY
UGANDA
UKRAINIAN SOVIET SOCIALIST REPUBLIC
UNION OF SOVIET SOCIALIST REPUBLICS
UNITED ARAB REPUBLIC
UNITED KINGDOM OF GREAT BRITAIN AND NORTHERN IRELAND
UNITED STATES OF AMERICA
URUGUAY
VENEZUELA
VIET-NAM
YUGOSLAVIA

The Agency's Statute was approved on 23 October 1956 by the Conference on the Statute of the IAEA held at United Nations Headquarters, New York; it entered into force on 29 July 1957. The Headquarters of the Agency are situated in Vienna. Its principal objective is "to accelerate and enlarge the contribution of atomic energy to peace, health and prosperity throughout the world".

Printed by the IAEA in Austria

September 1968

PROCEEDINGS SERIES

NEUTRON INELASTIC SCATTERING

PROCEEDINGS OF A SYMPOSIUM ON
NEUTRON INELASTIC SCATTERING
HELD BY THE
INTERNATIONAL ATOMIC ENERGY AGENCY
IN COPENHAGEN, 20-25 MAY, 1968

In two volumes

VOL. II

INTERNATIONAL ATOMIC ENERGY AGENCY
VIENNA, 1968

NEUTRON INELASTIC SCATTERING
(Proceedings Series)

ABSTRACT. Proceedings of a Symposium convened by the IAEA and held in Copenhagen, 20-25 May 1968. The meeting was attended by 167 participants from 29 Member States and 4 international organizations. These are the fourth IAEA Symposium Proceedings to have neutron inelastic scattering as their main theme, the previous ones being Inelastic Scattering of Neutrons in Solids and Liquids (Vienna), IAEA (1961), Inelastic Scattering of Neutrons in Solids and Liquids (Chalk River), IAEA (1963), and Inelastic Scattering of Neutrons (Bombay), IAEA (1965).

Contents: Dynamics of solids, including: lattice vibrations and local modes (6 papers), lattice dynamics in metals (7 papers), lattice dynamics of metals and alloys (13 papers), lattice dynamics of non-metals (11 papers) and review paper; Dynamics of liquids, including: coherent neutron scattering on liquids (5 papers), neutron scattering on hydrogenous liquids (14 papers) and 2 review papers; Magnetic systems (13 papers and review paper); Molecular dynamics (9 papers); Experimental methods (17 papers); and Summary.

Each paper is in its original language (93 English, 2 French, 4 Russian) and is preceded by an abstract in English with one in the original language where this is not English. Discussions are in English.

(Vol.II: 457 pp., 16×24 cm, paper-bound, 228 figures)
(1968) Price: US $11.00; £4.11.8

NEUTRON INELASTIC SCATTERING
IAEA, VIENNA, 1968
STI/PUB/187

FOREWORD

Three and a half years have passed since the IAEA held its third Symposium on Neutron Inelastic Scattering in Bombay, India. During this period, studies of the dynamics of liquids, solids and magnetic systems by inelastic scattering of neutrons have resulted in the maturing of the theoretical aspects, and in more sophisticated interpretation of experimental data. From the many laboratories where neutron scattering research was recently introduced, the first results have now been obtained. This situation was reflected in the very large number of abstracts submitted to the selection committee that prepared the program for the Fourth Symposium held in Copenhagen from 20 to 25 May 1968. In the event, 99 papers from 21 countries and two international organizations were selected for presentation. Because of this large number of contributions, 53 papers were summarized by seven rapporteurs. These papers were discussed in groups and the discussion is included in these Proceedings after the full texts of the contributions; the rapporteurs' texts, however, have not been included.

Although the meeting concentrated on experimental results and their interpretation, it was realized that experimental methods and techniques have been greatly improved during the last few years. Consequently, a Special Session was organized, devoted entirely to this topic. Several of the new experimental techniques are arousing interest.

Three prominent experts were invited to present review papers covering the advances of recent years. In addition, two invited papers on competitive, non-neutron techniques for dynamics studies were included in the program, thereby establishing a connection between neutron inelastic scattering and nuclear magnetic resonance, optical and other techniques for investigating the dynamics of solids and liquids.

The Symposium was held at the kind invitation of the Danish Government. Gratitude is also expressed to the authors of the papers, the rapporteurs, the chairmen of sessions and the discussion participants for their contributions to the success of the Symposium.

CONTENTS OF VOL. II

MAGNETIC SYSTEMS

MOLECULAR DYNAMICS

EXPERIMENTAL METHODS

MAGNETIC SYSTEMS

(Session C)

Chairmen : A.G.SJOLANDER
R.D.LOWDE

NEUTRON SPIN SCATTERING BY SPIN WAVES IN METALS

H. BJERRUM MØLLER
RISØ RESEARCH ESTABLISHMENT,
ROSKILDE, DENMARK

Abstract

NEUTRON SPIN SCATTERING BY SPIN WAVES IN METALS. This paper reviews neutron scattering studies of spin waves in magnetic metals. In the rare earth metals such studies have given rather detailed information on the indirect exchange interaction and its relation to the electronic structure. Measurements on the iron group metals have so far given much less information and no effects which show unambiguously the itinerant character of the magnetic electrons have been observed, probably because spin-wave studies in iron group metals have only been possible for rather low wavevectors of the spin waves.

1. INTRODUCTION

The metallic magnetic elements may be divided into two groups; the rare earth metals and the 3d transition metals. The magnetic moment on a rare earth ion is due to the unfilled 4f shell, which is well shielded from its environment by the 5s and 5p orbitals. The orbital angular momentum of the 4f electrons is therefore not significantly quenched in the metal so that L, S and J are good quantum numbers and the ground state of the ion is determined by Hund's rules. The direct exchange between the localized moments on the ions is negligible, but they are coupled through the medium of the conduction electrons by the indirect exchange interaction [1] which may be written in the form

$$H = -\sum_{i>j} J(\vec{R}_i - \vec{R}_j)\vec{J}_i \cdot \vec{J}_j \qquad (1)$$

This interaction is long range and oscillatory and, together with the strong anisotropy forces, which are a consequence of the anisotropic charge distribution in the 4f shell, lead to the complex magnetic structures illustrated in Fig. 1.

The situation in the 3d transition metals is much less clear. The orbital moment on the 3d electrons is essentially completely quenched and Fermi surface experiments [2] have made it clear that these electrons must be considered as conduction electrons contributing to the transport properties and being effectively delocalized. On the other hand, the simple independent particle model, which is used to describe non-magnetic metals, must clearly be supplemented with a realistic treatment of the electron interactions which give rise to the magnetic state. These interactions may be taken into account in a reasonable way for Ni [3], but in Fe, for which the moments appear to be much more effectively localized, a satisfactory treatment has not yet been given. A Heisenberg Hamiltonian of the form of Eq. (1) is frequently used to describe the exchange interaction between the non-integral moments distributed around the transition

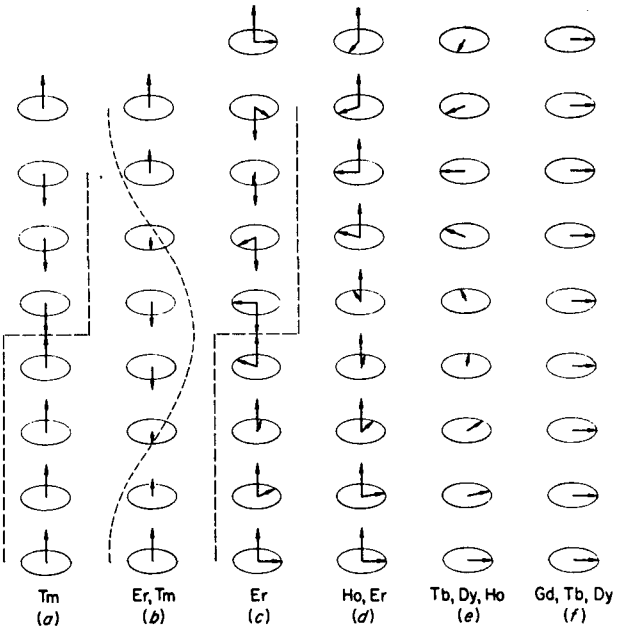

FIG.1. Magnetic structure of heavy rare earth metals (after KOEHLER, W.C., J. appl. Phys. 36 (1965) 1078).

metal ions, although there appears to be little justification for this procedure from a fundamental viewpoint.

In both groups an understanding of the magnetic properties depends on a detailed knowledge of the exchange interactions and these can best be determined from a study of the magnetic excitations or spin waves. In the rare earth metals these may be thought of as a precession of the moment about the local direction of magnetic ordering, in such a way that a constant phase relation is maintained between the magnetization vectors on the different ions. In the extreme form of the ferromagnetic band model on the other hand the energy bands of up and down spin are split by the exchange interaction as shown in Fig. 2a. The ordered moment of the system may then be reduced by single-particle excitations, in which a single electron changes its $\vec{k}$ vector and spin, or by collective excitations, which may be approximated as a linear combination of single-particle excitations, and which are the spin waves of the band model [4]. The allowed values of E and $\vec{q}$ for the single-particle and collective excitations are shown schematically in Fig. 2b. The interactions in the system may complicate this simple model substantially, but it seems that collective spin-wave excitations will exist for any reasonable model, and they are, of course, observed in practice.

Inelastic neutron scattering, in which a neutron interchanges energy and momentum with a spin-wave quantum, or magnon, provides the most powerful technique for the study of magnon-dispersion relations in solids, and it is the purpose of this paper to review the information which has thereby been obtained on the magnetic interactions in metals. After a brief discussion of the experimental technique, the existing experimental results on the rare earth and 3d transition metals are reviewed and

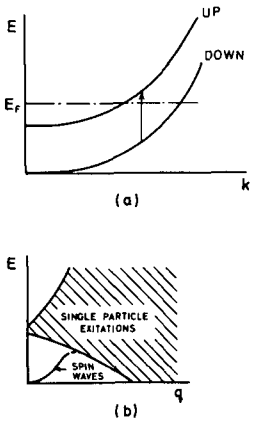

FIG.2. (a) Ferromagnetic band model. The energy bands of up and down spins are split by the exchange interaction. Both bands are filled to the same level E_F. (b) Diagram showing the allowed values of E and q for single-particle excitations and collective excitations (spin waves).

discussed, and some suggestions for further work in this field are proposed.

2. EXPERIMENTAL TECHNIQUES

The inelastic scattering of neutrons resulting from the creation of a single spin-wave quantum (magnon) is subject to the conservation conditions for energy and momentum

$$\vec{\kappa} = \vec{k}_1 - \vec{k}_2 = \vec{\tau} - \vec{q} \tag{2}$$

$$E = E_1 - E_2 = \epsilon(\vec{q}) \tag{3}$$

where $\vec{k}_1$ and $\vec{k}_2$ are initial and final neutron wavevectors and E_1 and E_2 are the associated energies. $\vec{q}$ is the wavevector of the magnon and $\epsilon(\vec{q})$ is its energy. $\vec{\tau}$ is a reciprocal lattice vector, $\vec{\kappa}$ is the neutron scattering vector and E is the energy transfer.

The most direct method of measuring the dispersion relation $\epsilon(\vec{q})$ is therefore by direct energy analysis of the scattered neutrons, by a triple-axis spectrometer or by a time-of-flight method. The natural variables of such an experiment are $\vec{q}$ and E. With the triple-axis spectrometer it is possible to vary one of these variables, while the other is kept constant (constant-$\vec{q}$ method and constant-E method [5]). The positions of the neutron groups observed in such scans determine the dispersion relation $\epsilon(\vec{q})$, and the width of the neutron groups gives the magnon lifetimes, provided that the instrumental resolution can be extracted. Any disturbance from phonon scattering can generally be eliminated by an appropriate choice of the relative directions of the polarization vectors and $\vec{\kappa}$. The identification of the magnon peaks can also be accomplished by application of a magnetic field [6].

In contrast to phonon scattering experiments, it is necessary to use small $\vec{\kappa}$ vectors in magnon scattering because the scattered intensity de-

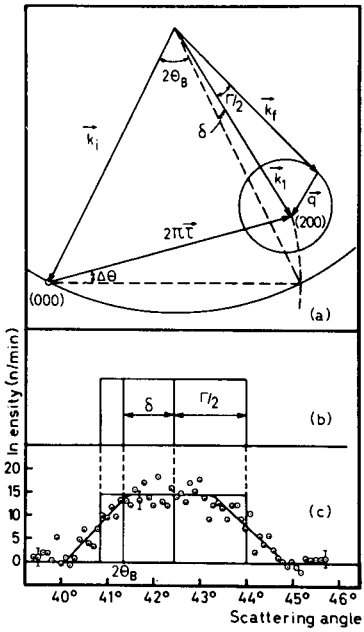

FIG. 3. (a) Representation in $\vec{k}$ space of inelastic neutron-magnon scattering in the (001) plane (not to scale). (b) Expected angular distribution, of scattered neutrons for ideal resolution in the (001) plane and poor resolution perpendicular to it. (c) Observed angular distribution, corrected for background, for non-ideal resolution in the (001) plane and poor resolution perpendicular to it (after Ref. [8]).

creases strongly with increasing $\vec{\kappa}$, due to the magnetic form factor. As pointed out by Lowde [7], this limits the energy transfer for given incoming neutron energy, and this restriction becomes very severe for the measurements of high magnon energies where neutrons of high energy must be used because of this limitation.

Another method which does not require energy analysis of the scattered neutrons is the diffraction method, illustrated in Fig. 3. It consists of missetting the crystal by an angle $\Delta\theta$ from a Bragg reflection, and measuring the width Γ of the peak in the scattered neutron intensity as a function of scattering angle, which is due to excitation of magnons. It follows from Eqs (2) and (3) that magnon scattering is only possible for $\vec{q}$ vectors lying on a surface (the scattering surface) around the reciprocal lattice point. If the dispersion relation is quadratic and isotropic, the scattering surface can be shown to be a sphere, the size of which depends on the missetting in such a way that a plot of $\sin^2(\Gamma/2)$ versus k_i^2/k_1^2 gives a straight line, from which the constant D in the dispersion relation $\epsilon(\vec{q}) = Dq^2$ may be determined [8]. It is also possible by successive approximations to deduce the dispersion relations from the measurements of the width Γ as a function of the misset angle $\Delta\theta$, and higher order terms in the power expansion of the dispersion relation $\epsilon(\vec{q})$ may thus be determined [9]. By use of polarized neutrons it is possible to distinguish unambiguously the spin-wave scattering from other scattering contributions [10] (see Fig. 4).

Since the diffraction method measures only the cut-off of the scattering in the horizontal plane (the scattering plane), very coarse vertical colli-

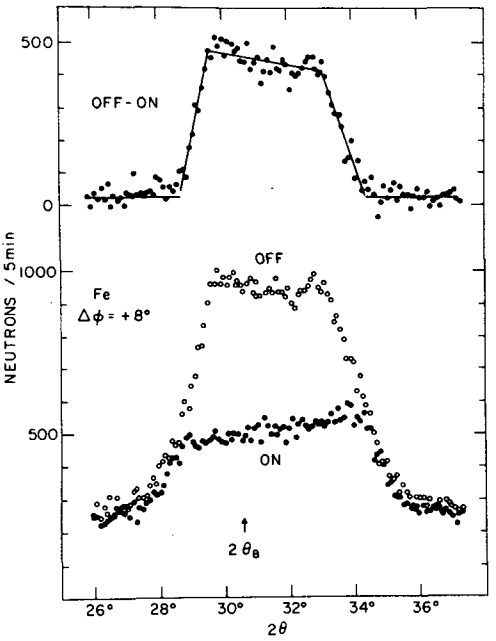

FIG.4. Observed angular distributions of scattered neutrons with magnetic field applied in the direction of the scattering vector and no field applied, for incoming neutrons polarized in the direction of the scattering vector. The difference between these two measurements contains the magnon contribution only (after Ref. [10]).

mations can be used, so that the whole scattering surface is used to determine a single $\vec{q}$ value at the tangential position. The diffraction method therefore gives higher intensities than the triple-axis spectrometer method. It may also be more accurate for very small $\vec{q}$ vectors, since the relatively poor vertical collimation in the triple-axis spectrometer gives an uncertainty in the determination of $\vec{q}$.

The small-angle scattering method is a special case of the diffraction method for which $\vec{\tau} = 0$. For a quadratic dispersion relation $\epsilon(\vec{q}) = Dq^2$, it can be shown that magnon scattering gives a rectangular distribution of scattered neutrons as a function of scattering angle around the direct beam. If the neutron energy is written as dk^2, the cut-off angle can be shown to be $\theta_c = d/D$, which is independent of the neutron energy. The whole reactor spectrum can therefore be used and, since $\vec{\tau} = 0$, the orientation of the sample is unimportant so that a polycrystalline sample can be used. If the difference of the scattered intensity with the specimen magnetized horizontally and vertically in the plane perpendicular to the beam is measured, then background effects subtract out to a high order of accuracy [11]. Magnon lifetimes may also be deduced from measurements of small-angle scattering [12] by measuring the width of the cut-off edge. For a quadratic dispersion law, this width, corrected for instrumental resolution, reflects an uncertainty in D due to a finite magnon lifetime. For a non-quadratic dispersion relation, a numerical method must be employed to calculate the angular distributions arising from scattering of a beam containing the complete thermal spectrum [13].

3. RARE EARTH METALS

Many of the rare earth metals have undesirably high capture cross-sections for thermal neutrons, and inelastic neutron scattering measurements are difficult if not impossible. However, Tb, Ho and Er are relatively favourable in this respect and have the additional advantage of a large magnetic moment, so that the magnetic scattering cross-section is large. Measurements of the magnon dispersion relations have therefore been performed on Tb [14] and Er [15] and an alloy of Tb-10% Ho [16,17]. The experimental dispersion relations are shown in Figs 5, 6, and 7. These measurements represent three different magnetic structures, namely the ferromagnetic structure (Tb at 90°K and Tb-10% Ho at 110°K), the spiral structure (Tb-10% Ho at 200°K) and the cone structure (Er at 4.2°K).

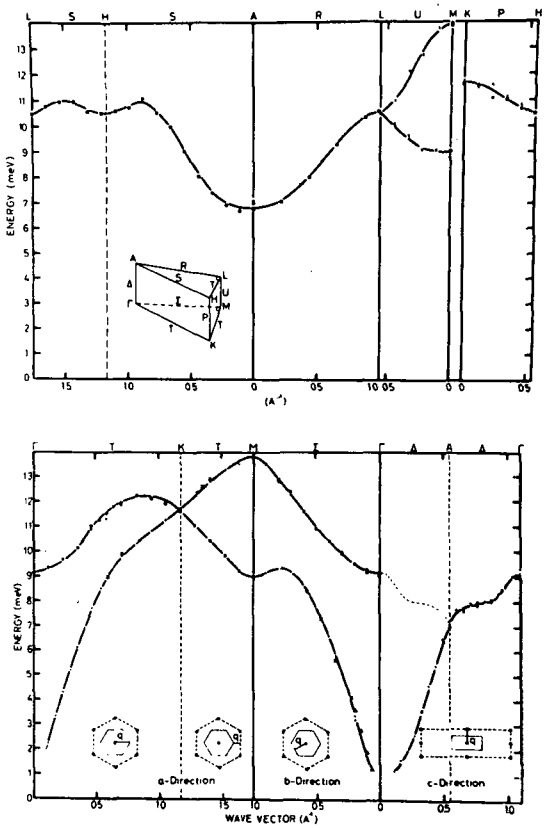

FIG. 5. Experimental magnon dispersion relations in Tb along symmetry lines in the Brillouin zone at 90° K (after Ref. [17]).

Since the magnon energies are low, it has been possible to measure the magnon dispersion relations throughout the entire zone. In the case of Tb at 90° (Fig. 5) the magnon dispersion relations have been measured along all symmetry lines of the zone, and an analytical interpolation scheme

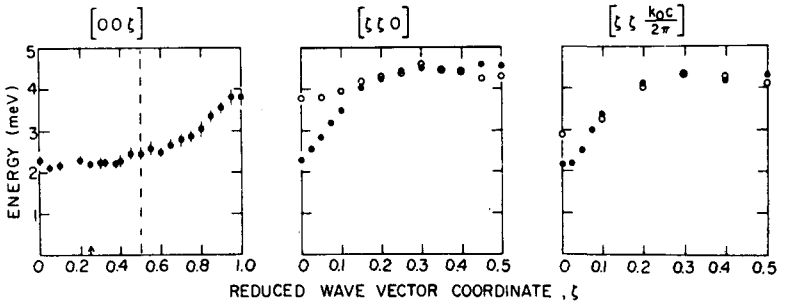

FIG. 6. Experimental magnon dispersion relations in Er at 4.2°K. The wavevector co-ordinates are measured from the nuclear reciprocal lattice points (after Ref. [15]).

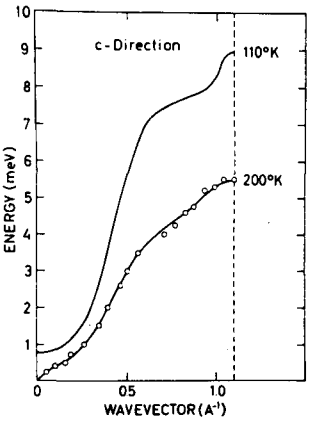

FIG. 7. Experimental magnon dispersion relations in Tb-10% Ho in the ferromagnetic and spiral phases. The full line for the ferromagnetic phase is derived principally from the experimental points of Fig. 14. The full line for the spiral phase is a weighted least-squares fit of the experimental points to Eq. (8). The resulting interplanar exchange parameters are given in Table I (after Ref. [17]).

has been developed to obtain magnon energies throughout the zone from these results [18]. The lattice structure is hcp so the dispersion relation consists of two branches, an acoustic and an optical one.

All the inelastic neutron scattering measurements on the rare earth metals were performed with triple-axis spectrometers. The scattering cross-sections for one-magnon creation have the form

$$\frac{d^2\sigma}{d\Omega dE} \sim \sum_{\vec{\tau}} (1 + e_m^2)\, \delta(\vec{\kappa} - \vec{\tau} - \vec{q})\, \delta(E - \epsilon(\vec{q})) \tag{4}$$

for the ferromagnetic structure and

$$\frac{d^2\sigma}{d\Omega dE} \sim \sum_{\vec{\tau}} \Big\{ (1 + e_Q^2) \Big[f_1(\vec{q})\, \delta(\vec{\kappa} - \vec{\tau} - \vec{q} - \vec{Q}) + f_2(\vec{q})\, \delta(\vec{\kappa} - \vec{\tau} - \vec{q} + \vec{Q}) \Big] + 4(1 - e_Q^2) f_3(\vec{q}) \delta(\vec{\kappa} - \vec{\tau} - \vec{q}) \Big\} \delta(E - \epsilon(\vec{q})) \tag{5}$$

for the cone structure and the spiral structure with wavevector $\vec{Q}$[19]. Here e_m and e_Q are the components of the unit scattering vector in the direction of the magnetization and spiral wavevector respectively.

From (5) it is seen that the spiral and cone structures give rise to three peaks in a constant-E scan, separated by an interval $\vec{Q}$. If a multi-domain sample is used, two sets of three neutron peaks will be seen in the case of the cone structure because the dispersion curve is non-symmetric. The peaks have different weight factors $f_1(\vec{q})$, $f_2(\vec{q})$ and $f_3(\vec{q})$. For the spiral structure $f_1 = f_2 = f_3^{-1}$. For the measurements of the spiral dispersion relation (Fig. 6) a scan with $\vec{\kappa}$ along $\vec{Q}$ was used so that the centre peak was eliminated and the resolution of the remaining two was possible. In the case of a cone with small cone angle (as Er) $f_1(\vec{q})$ is very much larger than $f_2(\vec{q})$ and $f_3(\vec{q})$ so in a multi-domain sample only two of the six modes are observable, but the splitting in energy between these two is small and difficult to resolve in the case of Er [15].

The fact that most of the rare earth metals have a markedly non-spherical 4f charge distribution gives rise to an anisotropic crystal field which acts on the localized moments. This field is large in the rare earth metals and has to be included in the Hamiltonian, which may then be written

$$H = -\sum_{i>j} J(\vec{R}_i - \vec{R}_j)\vec{J}_i\vec{J}_j + \sum_i \left\{ BJ_{zi}^2 - \tfrac{1}{2}G\left[(J_{xi} + iJ_{yi})^6 + (J_{xi} - iJ_{yi})^6 \right] \right\} \qquad (6)$$

where $J(\vec{R}_i - \vec{R}_j)$ represents the indirect exchange interaction between ions at $\vec{R}_i$ and $\vec{R}_j$, and B and G are single-ion anisotropy parameters describing the two-fold and six-fold anisotropy respectively.

The non-spherical distribution of the 4f electrons also introduces an anisotropy in the exchange interaction. This anisotropy is, however, not expected to be large [20] and should not have much influence on the magnon energies [21]. Anisotropy in the exchange should manifest itself by removing the degeneracies in the magnon spectrum over the hexagonal face of the zone and along the line KH [22]. The fact that such degeneracies are observed in the experimental magnon dispersion relations indicates that any anisotropy of the exchange is small so far as effects on the magnons are concerned.

The dispersion relations for magnons propagating in the c-direction can be regarded as a single acoustic branch extending twice as far as the first Brillouin zone if the points of the optical branch are shifted from $\vec{q}$ to $(2\pi/c)-\vec{q}$. If this is done, the dispersion relation for this direction is particularly simple. An approximate diagonalization of the Hamiltonian then gives

$$\epsilon(\vec{q}) = J\left[(J(0)-J(\vec{q}))^2 + 2(B + 21GJ^4)(J(0)-J(\vec{q})) + 72GJ^4(B+3GJ^4) \right]^{\frac{1}{2}} \qquad (7)$$

in the ferromagnetic phase [21, 23]

$$\epsilon(\vec{q}) = J\left\{ \left[J(\vec{Q}) - \tfrac{1}{2}J(\vec{Q}+\vec{q}) - \tfrac{1}{2}J(\vec{Q}-\vec{q}) \right]\left[J(\vec{Q}) - J(\vec{q}) + 2B \right] \right\}^{\frac{1}{2}} \qquad (8)$$

in the spiral phase [24], and

$$\epsilon(\vec{q}) = \tfrac{1}{2}J\cos\theta\left[J(\vec{Q}+\vec{q})-J(\vec{Q}-\vec{q})\right] + J\left\{\left[J(\vec{Q})-\tfrac{1}{2}(J(\vec{Q}+\vec{q})+J(\vec{Q}-\vec{q}))\right]\right.$$
$$\left.\times\left[J(\vec{Q})-\tfrac{1}{2}\cos^2\theta\,(J(\vec{Q}+\vec{q})+J(\vec{Q}-\vec{q}))-\sin^2\theta\,(J(\vec{q})-2B)\right]\right\}^{\frac{1}{2}} \qquad (9)$$

for the cone structure [25] with cone angle θ. For small cone angle this expression may be approximated by [15]

$$\epsilon(\vec{q}\,') = J\left[J(0)-J(\vec{q}\,')+B\cos^2\theta\right] \qquad (10)$$

which is the expression that was used to analyse the Er results. In Eq. (10) $\vec{q}\,' = \vec{Q}-\vec{q}$ is defined with respect to the laboratory co-ordinate system. Later results [26] on Er with improved resolution indicate, however, that the anisotropy is so large that the approximations leading to Eq. (10) may not be really valid.

It has been assumed in Eqs (8) and (9) that the six-fold anisotropy is negligible in the spiral and cone phases.

For other directions in the crystal the expressions for the dispersion relations are more complicated and contain two Fourier transformed exchange parameters

$$J(\vec{q}) = \sum_{\vec{R}_j} J(\vec{R}_j)e^{i\vec{q}\cdot\vec{R}_j} \qquad (11)$$

$$J'(\vec{q}) = \sum_{\vec{R}'_j} J(\vec{R}'_j)e^{i\vec{q}\cdot\vec{R}'_j} \qquad (12)$$

where unprimed vectors lie between ions in the same sub-lattice and primed vectors between ions in different sub-lattices [14, 21].

From expressions (7), (8) and (9) it is possible to obtain the Fourier transformed exchange parameters $J(0)-J(\vec{q})$ from the measured dispersion relation, if the anisotropy constants are known. From the $\vec{q}$ dependence of the neutron group intensities [21] in Tb-10% Ho at 110°K a value of B was deduced which is about 70% of that found from torque measurements for pure Tb [27]. On the other hand, the value of G deduced from the energy gap at $\vec{q} = 0$ is about a factor of six greater than that found by analysis of the magnetostriction data [27]. In interpreting the results for Tb and Tb-10% Ho, the anisotropy constants derived from the neutron measurements [21] at 110°K have been used, but scaled with temperature according to the macroscopic measurements [27]. Fortunately, the values of $J(\vec{q})$ deduced from the magnon dispersion relations are rather insensitive to variations in the anisotropy constants. In the case of Er the energy gap for $\vec{q}\,' = 0$ gives the two-fold anisotropy. It was found to be much larger than that derived from susceptibility measurements, suggesting that higher-order terms in the axial anisotropy are required. The presence of such terms are also necessary to stabilize the cone structure [25].

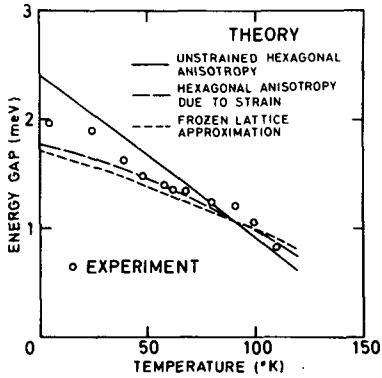

FIG. 8. Temperature dependence of the energy gap for $\vec{q}=0$ in Tb-10% Ho compared with the predictions of three different models (after Ref. [28]).

Since the energy gap at q = 0 depends only on the anisotropy constants, their temperature dependence can be studied by measuring the energy gap as a function of temperature. The results of such measurements [28] are shown in Fig. 8 compared with the predictions in three different models [25]. The solid line gives the energy gap resulting from single-ion crystal field anisotropy of the form assumed in the Hamiltonian of Eq. (6), whereas the other two curves take into account anisotropy resulting from magnetostriction.

The Fourier transformed exchange parameters $J(0) - J(\vec{q})$ found from the experimental measurements (Figs 5 and 7) using Eqs (7) and (8) are shown in Fig. 9 for Tb in the ferromagnetic phase (90°K) and in Fig. 10 for Tb-10% Ho in the ferromagnetic phase (110°K) and in the spiral phase (200°K).

From Eq. (11) we get for the c-direction

$$J(0)-J^c(\vec{q}) = 2\sum_{m=1}^{\infty} J_m^c(1-\cos\tfrac{1}{2}mcq) \quad \left(-\frac{2\pi}{c} \leqq q \leqq \frac{2\pi}{c}\right) \tag{13}$$

where J_m^c are the interplanar exchange parameters, between planes of atoms perpendicular to the c-axis. For other symmetry directions the Fourier transformed exchange parameters can be expressed in terms of interplanar exchange parameters for the same sub-lattice and between the two sub-lattices [14].

The interplanar exchange parameters obtained from Eq. (13) and the similar expressions for other symmetry directions are given in Table I for Tb at 90°K, Tb-10% Ho at 200°K and Er at 4.2°K. The number of interplanar exchange parameters determined is the minimum necessary to fit the data within the experimental accuracy.

It is seen that the exchange interaction is long range (reaches at least 5 planes away) and oscillatory (some interplanar exchange constants are negative), as expected from an indirect exchange interaction. The oscillatory long-range nature of the interaction is also seen from 'interlinear' exchange parameters [18, 29] and 'interatomic' exchange parameters [18, 30] calculated from the experimental measurements on Tb at 90°K.

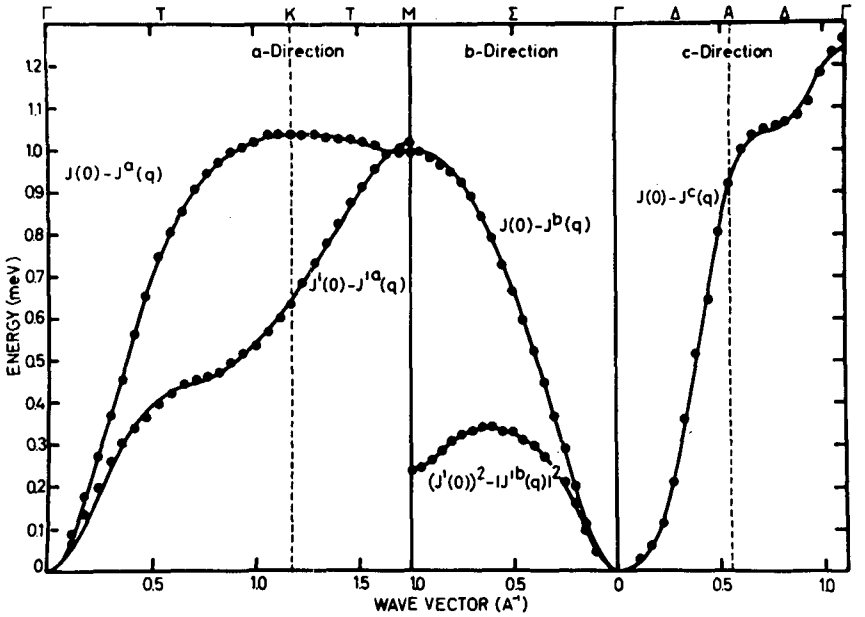

FIG.9. Fourier transformed exchange parameters for Tb at 90°K. The points are derived from Fig.5 using Eq. (7) and similar equations for the a- and b-directions. The solid curve represents a weighted least-squares fit of Eq. (13) and similar equations for the a- and b-directions to the points. The resulting interplanar exchange parameters are given in Table I (after Ref. [17]).

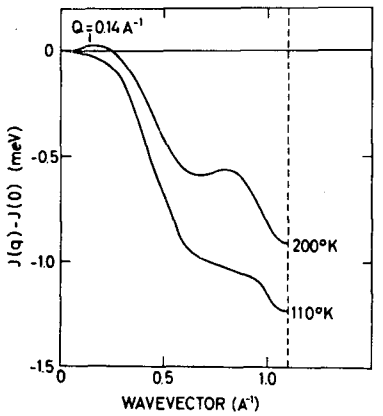

FIG.10. Fourier transformed exchange parameters for Tb-10% Ho deduced from Fig.7 using Eqs (7) and (8). The resulting interplanar exchange parameters are given in Table I (after Ref. [17]).

In the absence of six-fold anisotropy the spiral (and cone) can be shown to be stable with wavevector $\vec{Q}$ if $J(\vec{q})$ has an absolute maximum for $\vec{q} = \vec{Q}$ [24]. The six-fold anisotropy will, of course, tend to prevent the formation of a spiral structure by keeping the spins in the preferred directions. It is seen that such a maximum of $J(\vec{q})$ exists for Tb-10% Ho in the spiral phase at the right $\vec{q}$ value, whereas it is absent in all measurements in the ferromagnetic phase of Tb and Tb-10% Ho. The

TABLE I. INTERPLANAR EXCHANGE PARAMETERS
All are given in meV except the J' for the b-direction, which are in $(meV)^2$.

	Tb 90°K [14]			Tb-10% Ho 200°K	Er [15] 4.2°K
	a-direction	b-direction	c-direction	c-direction	c-direction
J_1	0.200	0.240	0.305	0.212	0.086
J_2	0.120	0.040	0.075	0.017	-0.036
J_3	0.045	0.010	0.005	0.003	0.018
J_4	0.020	0.005	-0.035	-0.043	-0.014
J_5	0.005			0.004	
J_1'	0.195	0.050			
J_2'	-0.005	0.050			
J_3'	0.050	0.010			
J_4'	0.015	0.010			
J_5'	0.010				

strong change in $J(\vec{q})$ at the transition from the ferromagnetic structure to the spiral structure is believed to be a result of the transition rather than the driving mechanism for the transition [25].

In the indirect exchange interaction $J(\vec{q})$ is directly related to the conduction electron energy band structure and is given by an expression of the form [31]

$$J(\vec{q}) = \sum_{n,n',\vec{k}} \frac{I_{nn'}(\vec{k}, \vec{k}+\vec{q})\,[f(\epsilon_n(\vec{k})) - f(\epsilon_{n'}(\vec{k}+\vec{q}))]}{\epsilon_{n'}(\vec{k}+\vec{q}) - \epsilon_n(\vec{k})} \tag{14}$$

in the periodic zone scheme. Here $\epsilon_n(\vec{k})$ is the energy of a Bloch state of wavevector $\vec{k}$ in band n, $I_{nn'}(\vec{k}, \vec{k}+\vec{q})$ is a slowly varying function and $f(\epsilon)$ is the Fermi-Dirac distribution.

The peaks in $J(\vec{q})$ in the spiral phase at position $\vec{q} = \vec{Q}$ and $\vec{q} = \vec{\tau} - \vec{Q}$, where $\vec{\tau}$ is the (001) reciprocal lattice vector, probably reflect the contribution of a large number of small energy denominators in expression (14) for $J(\vec{q})$ at $\vec{q}$ values corresponding to the separation between flat regions of the Fermi surface [32-34]. The former of these peaks is responsible for the stability of the spiral structure. The abrupt flattening of those peaks at the ferromagnetic transition is ascribed to the splitting of the different spin bands by the ferromagnetic exchange interaction [17].

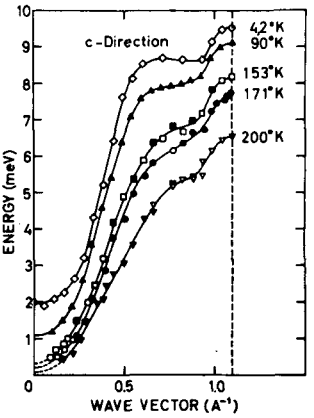

FIG.11. Temperature dependence of magnon energies in the c-direction in the ferromagnetic phase of Tb (after Ref. [17]).

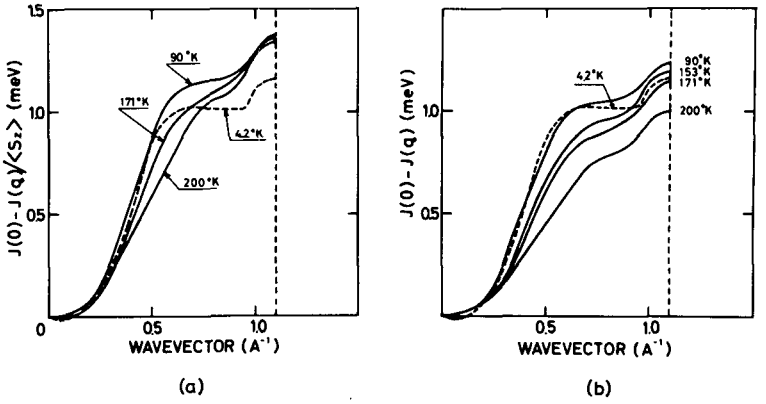

FIG.12. (a) Temperature dependence of the Fourier transformed exchange parameters in the c-direction in the ferromagnetic phase of Tb. (b) J(O) - J(q) divided by the ordered moment in the ferromagnetic phase of Tb (after Ref. [17]).

The magnon energies in the c-direction in Tb have been studied as a function of temperature [17]. The results are shown in Fig. 11 for five temperatures in the ferromagnetic phase of Tb. The magnon energies are seen to decrease with increasing temperature due to magnon-magnon interaction. It is useful to distinguish between those interactions originating in the exchange terms and those from the crystal field terms in the Hamiltonian, referring to the corresponding effects as exchange renormalization and crystal field renormalization, respectively. It can be shown [35] that the effect of crystal field renormalization on the magnon energy is to introduce a temperature dependence of the crystal field anisotropy parameters similar to that observed in macroscopic measurements [27]. The effect of exchange renormalization can therefore be found by comparing the Fourier transformed exchange parameters obtained from the experimental dispersion relation, using the appropriate anisotropy constants. The results of such an analysis are shown in Fig. 12, and it may be seen that

the exchange forces at higher temperatures scale generally as the ordered moment, in accord with the random phase approximation [36], although the detailed dependence on q also changes somewhat. From Eq. (14), it is clear that the temperature affects $J(\vec{q})$ both through the change in energy of the conduction electron states consequent on magnetization changes, and also through the temperature dependence of the Fermi functions. It seems likely that the former effect is responsible for the overall changes of $J(\vec{q})$ with temperature, while the latter produces the sharpening with increasing temperature of the Kohn-type kink in the dispersion curves at large q.

The magnon lifetimes in the ferromagnetic phase of Tb-10% Ho have been studied [16] by measuring the neutron group widths. The widths for the alloy, shown in Fig. 13, are within the experimental error the same as those for pure Tb, where the latter have been measured at small and large $\vec{q}$. Since these widths are furthermore not observably temperature dependent, the principal mechanism limiting the magnon lifetime is probably absorption by the conduction electrons [37]. This process involves a spin flip by the electron, and the absorption may therefore decrease rapidly at critical wavevectors determined by the separation of the Fermi surfaces of different spins. For the free-electron model, the width well above the critical $\vec{q}$ is given by [37]

$$\Delta\epsilon(\vec{q}) = c\epsilon(\vec{q})/q \tag{15}$$

where c is a constant. This function, fitted at $q = 0.72\ \text{Å}^{-1}$ is shown in Fig. 13. The widths fall rather abruptly at about $q = 0.35\ \text{Å}^{-1}$ and this may

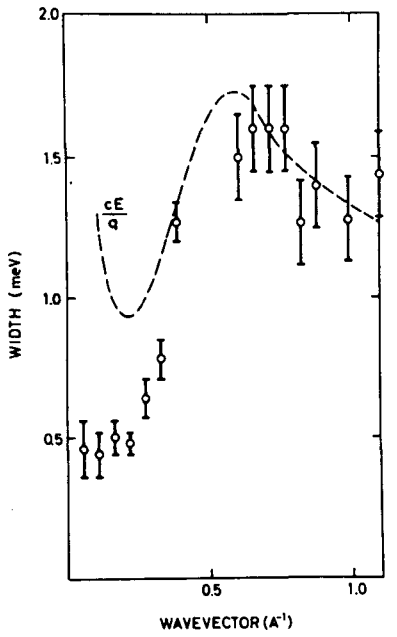

FIG. 13. Natural width of magnons propagating in the c-direction of Tb-10% Ho at 110° K. The experimental resolution, which is always smaller than the natural width, has been extracted from the measurements (after Ref. [17]).

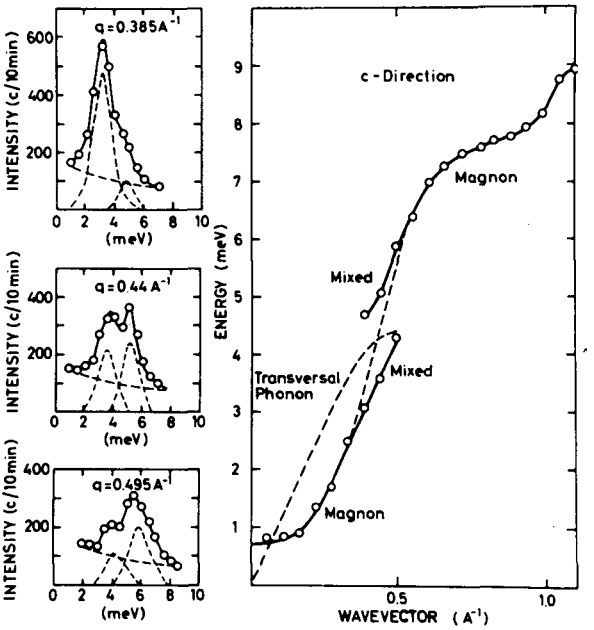

FIG.14. Neutron groups and excitation energies in the c-direction of Tb-10% Ho at 110°K. The scan used for these measurements was such that transverse phonons were not observed (after Ref. [17]).

reflect the exchange splitting of the Fermi surface. The residual broadening at low q is probably due to Umklapp processes [38].

A magnon-phonon interaction has been observed in Tb-10% Ho [16], as shown in Fig. 14. At the crossing of the magnon and transverse-phonon dispersion curves, there is a strong interaction leading to the creation of mixed magnon-phonon modes. The splitting at the crossing point of the unperturbed dispersion curves is 1.7 meV, which is approximately the same magnitude as has been observed in a magnetic insulator [39]. The magnon-phonon interaction is much weaker in pure Tb, and no coupling has been observed in the alloy between magnons and transverse phonons propagating in the a-direction, for which the crossing occurs at much higher energy.

An anomaly has also been observed in the magnon dispersion relation in the a-direction of the Tb-10% Ho alloy [16] with the characteristic form associated with a resonant mode and it has been ascribed to a resonant-magnon mode arising because the Ho moments, due to the smaller spin of Ho, are coupled comparatively weakly to the Tb host moments.

4. IRON GROUP METALS

Since the magnon energies in the iron group metals are much higher than those in the rare-earth metals it has only been possible to measure the magnon dispersion relation for rather small wavevectors, due to the intensity problems mentioned in section 2. Figures 15, 16, 17, and 18 show the results of such measurements on Fe [40], Fe-4% Si [10, 40],

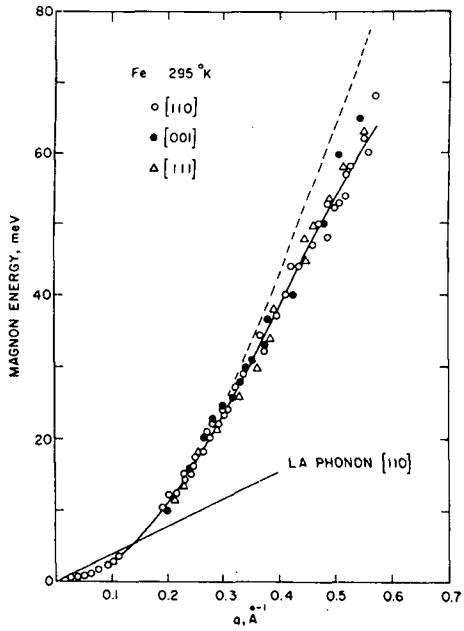

FIG.15. Experimental magnon dispersion relation in Fe at 295° K, measured with a triple-axis spectrometer. The broken line corresponds to the Heisenberg model with D = 281 meV A^2 (after Ref. [40]).

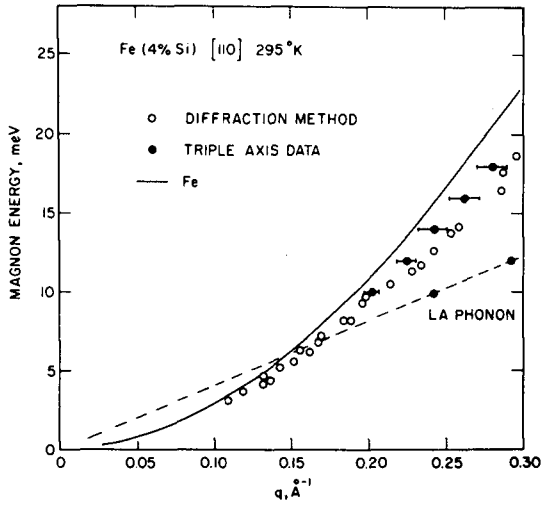

FIG.16. Experimental magnon dispersion relation in Fe-4% Si at 295° K, measured with a triple-axis spectrometer and with the diffraction method with polarized neutrons. The solid line corresponds to the (110) data of pure Fe (after Refs [40] and [10]).

hex Co [40, 41] and fcc Co [6]. Preliminary measurements on Cr-Mn by the diffraction method have also been reported [42]. The measurements on Fe-4% Si were performed because this crystal is easier to obtain than

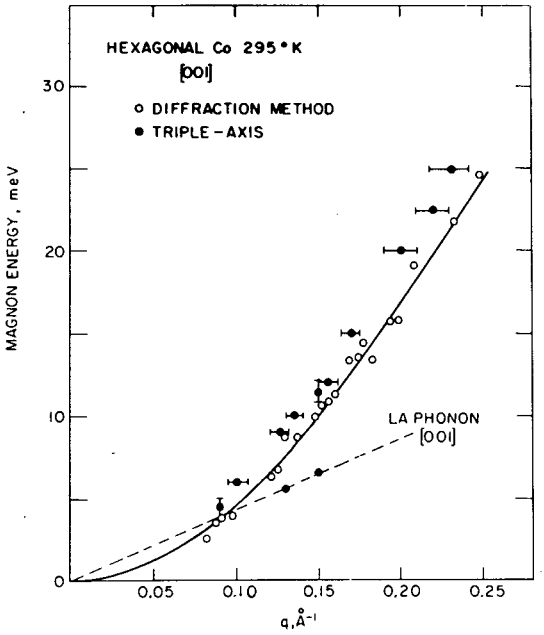

FIG.17. Experimental magnon dispersion relation in hcp Co at 295°K, measured with a triple-axis spectrometer and with the diffraction method with polarized neutrons (after Refs. [40] and [41]).

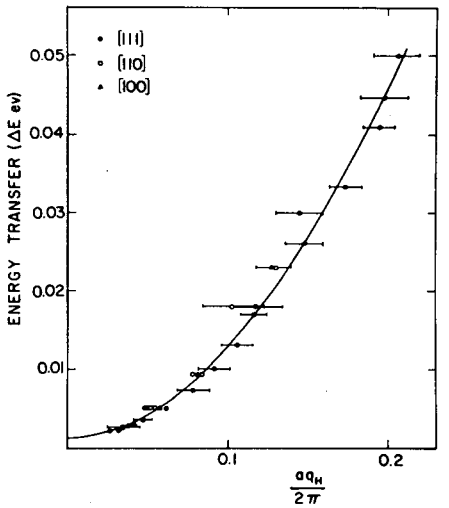

FIG.18. Experimental magnon dispersion relation in fcc Co at 295°K, measured by a triple-axis spectrometer (after Ref. [6]).

pure Fe and it was assumed that the 4% Si did not affect the magnon dispersion relation. Surprisingly, this is not the case, as seen from Fig. 16. No effects which show unambiguously that the magnetic electrons have an itinerant character have been observed in these magnon dispersion relations, probably because of the limited range of magnon energies

studied. The merging of the magnon branch into the single-particle excitations (see Fig. 2) has not been detected, and Kohn anomalies in the exchange due to the abrupt change in the electron distribution at the Fermi surface have not been unambiguously observed [43]. On the other hand, the role of the conduction electrons in the exchange is manifested in some instance by its long-range and temperature dependence.

The measurements have been analysed using the phenomenological Heisenberg exchange Hamiltonian (1), which for a Bravais lattice with negligible magnetic anisotropy gives the following magnon dispersion relation

$$\epsilon(\vec{q}) = S\left\{J(0)-J(\vec{q})\right\} \tag{16}$$

where

$$J(\vec{q}) = \sum_{\vec{R}_j} J(\vec{R}_j)e^{i\vec{q}\cdot\vec{R}_j} \tag{17}$$

is the Fourier transformed exchange parameter.

A series expansion for small $\vec{q}$ gives

$$\epsilon(\vec{q}) = S\sum_{\vec{R}_j} J(\vec{R}_j)\left\{\tfrac{1}{2}(\vec{q}\cdot\vec{R}_j)^2 - \frac{1}{24}(\vec{q}\cdot\vec{R}_j)^4 + \ldots\right\} \tag{18}$$

$$= Dq^2(1-\beta q^2 + \ldots) \tag{19}$$

where the exchange stiffness parameter D is

$$D = \frac{S}{2q^2}\sum_{\vec{R}_j} J(\vec{R}_j)(\vec{q}\cdot\vec{R}_j)^2 \tag{20}$$

and

$$\beta = \frac{1}{12q^2}\,\frac{\sum_{\vec{R}_j} J(\vec{R}_j)(\vec{q}\cdot\vec{R}_j)^4}{\sum_{\vec{R}_j} J(\vec{R}_j)(\vec{q}\cdot\vec{R}_j)^2} \tag{21}$$

For small $\vec{q}$ a quadratic dispersion relation is therefore expected, and the deviations at larger $\vec{q}$ from the quadratic dispersion relation are seen to depend on the range of the exchange interaction. Equation (21) shows that β is larger for a longer range interaction.

Table I shows the results of the analysis in terms of D and β of the dispersion relations in Figs 15, 16, 17, and 18 and the results of other measurements.

The values of β for Fe, Fe-4% Si, hex Co and fcc Co definitely indicate long-range exchange interactions, in agreement with predictions from the itinerant model [47]. These observations are in marked contrast to the results for magnetic insulators [9, 48], which follow quite closely the predicted behaviour for nearest neighbour interactions only. On the other hand, it is perhaps surprising that the results for Ni do not show deviations from a quadratic dispersion relation for small q.

The temperature dependence of magnon energies in Fe and Ni have been studied over a wide range of temperature using a triple-axis spectrometer [40], and small-angle scattering [12]. The temperature dependence of the stiffness constant derived from these measurements is shown in Fig. 19. An expression of the magnon energy in powers of T gives leading terms in both T^2 and $T^{5/2}$ for metals [49]

$$D = D_0 - D_1 T^2 - D_2 T^{5/2} \qquad (22)$$

The T^2 term results from magnon-electron interaction and the $T^{5/2}$ term from magnon-magnon interactions. The itinerant model should lead to a rather large T^2 term [49, 50], while it should be negligible in the localized model. The results of Fig. 19 were analysed in both models for $T < 0.4\,T_c$ [12]. Although the data can be described by a $T^{5/2}$ law, the value thus obtained for D_2/D_0 is at least an order of magnitude larger than expected [47] for short-range forces, as found from measurements of the dispersion relation (see above). The localized model therefore fails to give a consistent account of these two experiments. The itinerant model with both T^2 and $T^{5/2}$ terms gives, however, a good fit to the data with a reasonable value of D_1/D_0 [50].

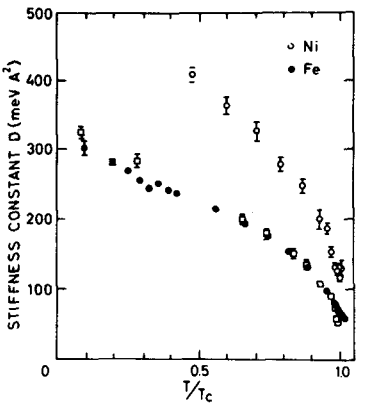

FIG. 19. Temperature dependence of the stiffness constant D for Fe and Ni obtained from small-angle scattering (circles) and triple-axis spectrometer measurements (squares) (after Refs. [12] and [40]).

There is good agreement between the triple-axis spectrometer data and the small-angle scattering data in Fig. 19, except for temperatures close to the transition temperature where the triple-axis results show a value of D tending to zero at T_c, whereas the small-angle scattering results seem to give a finite value of D at T_c. Further, in the small-angle scattering experiment significant scattering of spin-wave character was ob-

TABLE II. THE DISPERSION CONSTANTS D AND β OF IRON GROUP METALS AT 295°K

The stiffness constant D is given in units of meV · A^2 and β in A^2.

	Small-angle scattering		Diffraction method		Triple-axis spectrometry	
	D	β	D	β	D	β
Fe	256 ± 8	[43]			281 ± 10	1.0 [40]
Fe (4% Si)	286	[10]	266 ± 15	3.2 [10]	270	2 [40]
fcc Co (8% Fe)			275 ± 16	[44]	371	[6]
			384 ± 20	3.1 [43]		
hcp Co			490 ± 20	3.3 [41]	510	1.8 [40]
Ni	403 ± 7	[43]	340 ± 45	[45]		
			310 ± 40	[46]		
			374 ± 20	0 [43]		

served at temperatures above the Curie point (in Fe up to T_c + 20°K and in Ni up to T_c + 2°K), whereas no magnons were observed above the Curie temperature in the triple-axis spectrometer measurements. The magnetic excitations near the Curie point in Ni are discussed in a paper presented at this Symposium [51].

Only a few results on line widths have been reported, showing a strong temperature dependence of the magnon lifetimes in Ni [7, 12] and Fe [12, 40], but no detailed investigations have been performed. The results in Fig. 20, obtained from small-angle scattering measurements [12], were compared with theoretical calculations [52] of the lifetime due to magnon-magnon interactions in a nearest neighbour Heisenberg ferromagnet of spin $\frac{1}{2}$. In Ni the observed lifetime was very much shorter than the calculated, whereas the results for Fe agreed surprisingly well. However, this model is not expected to be adequate for metals where the magnon-conduction electron interaction should be large.

Magnon interactions also influence the neutron scattering cross-section by introducing an additional temperature dependence, which may be described in terms of a temperature dependence of the effective spin S_{eff}. Due to the kinematic magnon interactions S_{eff} is expected to vary as the mean spin $\langle S_z \rangle$, for long wavelength spin waves in a Heisenberg ferromagnet [53]. Results on Ni and Fe [12] show this additional strong temperature dependence of the scattering cross-section. In the case of Fe, the cross-section tends to decrease faster than $\langle S_z \rangle$, whereas the result for Ni appears to be in better agreement with $\langle S_z \rangle$. A decrease of the scattering cross-section due to kinematic magnon interactions has also been observed in Tb.

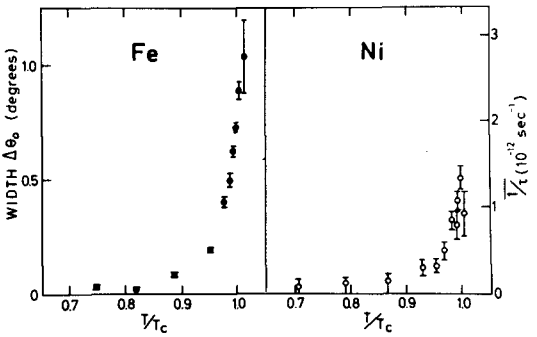

FIG. 20. The contribution $\Delta\theta_0$ of the magnon lifetime to the width of the cut-off edge of the measured angular distributions in Fe and Ni. Approximate average values of the inverse magnon lifetime derived from these values of $\Delta\theta_0$ are indicated by the scale on the right-hand ordinate (after Ref. [12]).

In an attempt to distinguish between the localized model and the itinerant model, the variation of the stiffness constant D with alloy concentration has been measured for iron group alloys [11, 54, 55]. The results show that, since the simple localized model with nearest neighbour interaction cannot explain the results for Fe-Cr, Fe-Ga and Fe-Al systems, it is necessary to take account of band effects. The fact that previous measurement on Fe-Ni could be explained in terms of the localized model is probably fortuitous [54].

5. CONCLUSIONS

Inelastic scattering of neutrons is the most powerful method at present available for studying magnon energies and lifetimes in solids, and it has already been extensively applied in elucidating the magnetic interactions in metals. It is clear, however, that such studies are in an early stage of development and that many problems remain to be solved.

The relatively low magnon energies found in the rare earth metals have allowed the determination of the magnon dispersion relation throughout the entire zone in Tb, with a correspondingly detailed experimental knowledge of the indirect exchange interaction. This work should clearly be extended to a wider range of materials, magnetic phases and temperatures. The application of a magnetic field in such experiments, although experimentally inconvenient, would give further useful information on the exchange and anisotropy forces. A more detailed study of the magnon energies and lifetimes as a function of temperature would provide further information on the relation between the conduction electrons and the magnetic interactions. In particular, a study of the magnon lifetime in the ferromagnetic phase should show the effect of the ordering on the exchange splitting of the energy bands. From the conduction electron energy bands, it should be possible to calculate both the exchange coupling between the magnetic ions and the damping of the magnons through absorption by the conduction electrons. Free-electron calculations have proved to give a very bad fit to the data. The preliminary studies of the interaction of magnons with phonons and impurities should be extended. It should also be possible to make detailed measurements on other rare-earth metals.

Preliminary measurements have already been made on Ho. Probably the maxima in $J(\vec{q})$ are more pronounced in Ho, since it forms a periodic structure over the whole temperature range of ordering. Measurements on Gd and Gd-Y alloys would permit studies of the exchange interaction in ferromagnetic and spiral structures, without having large anisotropy effects present [25].

The major problem in the study of magnon in the iron group metals lies in the extension of the measurements to higher energies, so that the exchange forces may be studied in more detail and characteristic effects associated with the itinerant nature of the magnetic electrons observed. Such an extension of the measurements involves formidable experimental problems, but should provide essential evidence on the nature of the interactions which produce magnetic ordering in these metals.

ACKNOWLEDGEMENTS

The author is indebted to A. R. Mackintosh for discussions and detailed comments on the manuscript. He further wants to thank A. D. B. Woods, M. W. Stringfellow and B. R. Cooper for providing unpublished results of their work.

REFERENCES

[1] RUDERMAN, M. A., KITTEL, C., Phys. Rev. 96 (1954) 99;
KASUYA, T., Progr. Theoret. Phys. (Kyoto) 16 (1956) 45;
YOSIDA, K., Phys. Rev. 106 (1959) 893.
[2] See GOLD, A. V., Proc. Int. Congr. Magnetism, 1967; J. appl. Phys. 39 (1968) 768.
[3] See DONIACH, S., Proc. Int. Congr. Magnetism, 1967; J. appl. Phys. 39 (1968) 751.
[4] IZUYAMA, T., Progr. Theor. Phys. Japan 23 (1960) 969.
[5] BROCKHOUSE, B. N., Inelastic Scattering of Neutrons in Solids and Liquids (Proc. Symp. Vienna, 1960), IAEA, Vienna (1961) 113.
[6] SINCLAIR, R. N., BROCKHOUSE, B. N., Phys. Rev. 120 (1960) 1638.
BJERRUM MØLLER, H., MOGENSEN, P. A., HOUMANN, J. C. G., KOWALSKA, A., Symp. Inelastic Scattering of Neutrons, Brookhaven, 1965.
[7] LOWDE, R. D., J. appl. Phys. 36 (1965) 884.
[8] FRIKKEE, E., RISTE, T., Proc. Int. Congr. Magnetism, (1964) 299.
[9] ALPERIN, H. A., STEINSVOLL, O., NATHANS, R., SHIRANE, G., Phys. Rev. 154 (1967) 508.
[10] SHIRANE, G., NATHANS, R., STEINSVOLL, O., ALPERIN, H. A., PICKART, S. J., Phys. Rev. Lett. 15 (1965) 146.
[11] HATHERLY, M., HIRAKAWA, K., LOWDE, R. D., MALLETT, J. F., STRINGFELLOW, M. W., TORRIE, B. H., Proc. phys. Soc. 84 (1964) 55.
[12] STRINGFELLOW, M. W., Proc. Phys. Soc., to be published (1968).
[13] STRINGFELLOW, M. W., AERE Rep. R -4535 (1966).
[14] BJERRUM MØLLER, H., HOUMANN, J. C. G., Phys. Rev. Lett. 17 (1966) 737.
[15] WOODS, A. D. B., HOLDEN, T. M., POWELL, B. M., Phys. Rev. Lett. 19 (1967) 908.
[16] BJERRUM MØLLER, H., HOUMANN, J. C. G., MACKINTOSH, A. R., Phys. Rev. Lett. 19 (1967) 312.
[17] BJERRUM MØLLER, H., HOUMANN, J. C. G., MACKINTOSH, A. R., Proc. Int. Congr. Magnetism 1967; J. appl. Phys. 39 (1968) 807.
[18] GYLDEN HOUMANN, J. C., "Magnon energies and exchange reactions in terbium, these Proceedings 2, SM-104/17.
[19] BAR'YAKHTAR, V. G., MALEEV, S. V., Soviet Phys. Solid State 5 (1963) 858.
[20] KAPLAN, T. A., LYONS, D. M., Phys. Rev. 129 (1961) 2072.
[21] LINDGÅRD, P. A., KOWALSKA, A., LAUT, P., J. Phys. Chem. Solids 28 (1967) 1357.
[22] BRINKMAN, W., J. appl. Phys. 38 (1967) 939.

[23] NIIRA, K., Phys. Rev. 117 (1960) 129.
[24] YOSIDA, K., MIWA, H., J. appl. Phys. 32, Suppl. (1961) 8 S.
[25] COOPER, B.R., to be published.
[26] WOODS, A.D.B., private communication.
[27] RHYNE, J.J., CLARK, A.E., J. appl. Phys. 38 (1967) 1379.
[28] NIELSEN, M., BJERRUM MØLLER, H., MACKINTOSH, A.R., to be published.
[29] STRINGFELLOW, M.W., WINDSOR, C.G., Proc. phys. Soc. 92 (1967) 408.
[30] GOODINGS, D.A., J. Phys. C 1 (1968) 125.
[31] ROTH, L.M., ZEIGER, H.J., KAPLAN, T.A., Phys. Rev. 149 (1966) 519.
[32] KOHN, W., Phys. Rev. Lett. 2 (1959) 393.
[33] KEETON, S.C., LOUCKS, T.L., Phys. Rev. (to be published).
[34] EVENSON, W.E., LIU, S.H., Bull. Am. phys. Soc. 13 (1968) 441.
[35] BROOKS, M.S.S., GOODING, D.A., RALPH, H.I., J. Phys. C 1 (1968) 132.
[36] KEFFER, F., LOUDON, R., J. appl. Phys. 32 (1961) 2S.
[37] ELLIOTT, R.J., STERN, H., Inelastic Scattering of Neutrons in Solids and Liquids (Proc. Symp. Vienna, 1960), IAEA, Vienna (1961) 61.
[38] LUTHER, A.H., TANAKA, T., to be published.
[39] DOLLING, G., COWLEY, R.A., Phys. Rev. Lett. 16 (1966) 683.
[40] SHIRANE, G., MINKIEWICZ, V.J., NATHANS, R., Proc. Int. Congr. Magnetism, 1967; J. appl. Phys. 39 (1968) 383.
[41] ALPERIN, H.A., STEINSVOLL, O., SHIRANE, G., NATHANS, R., J. appl. Phys. 37 (1966) 1052.
[42] MUHLESTEIN, L.D., SINHA, S.K., Bull. Am. phys. Soc. 13 (1968) 468.
[43] PICKART, S.J., ALPERIN, H.A., MINIKIEWICZ, V.J., NATHANS, R., SHIRANE, G., STEINSVOLL, O., Phys. Rev. 156 (1967) 623.
[44] FRIKKEE, E., Physica 32 (1966) 2149.
[45] RISTE, T., SHIRANE, G., ALPERIN, H.A., PICKART, S.J., J. appl. Phys. 36 (1965) 1076.
[46] FURRER, A., SCHNEIDER, T., HÄLG, W., Solid State Com. 4 (1966) 99.
[47] MARSHALL, W., Proc. Eighth Int. Conf. Low Temperature Physics (1962) 215.
[48] BROCKHOUSE, B.N., WATANABE, H., Inelastic Scattering of Neutrons in Solids and Liquids (Proc. Symp. Chalk River, 1962) 2, IAEA, Vienna (1963) 297.
[49] IZUYAMA, T., KUBO, R., J. appl. Phys. 35 (1964) 1074.
[50] MATHON, J., WOHLEFARTH, E.P., Proc. R. Soc. Series A 302 (1968) 409.
[51] KOMURA, S., LOWDE, R.D., WINDSOR, C.G., Magnetic excitations in nickel, these Proceedings 2, SM-104/110.
[52] COOKE, J.F., GERSCH, H.A., Phys. Rev. 153 (1967) 641.
[53] MARSHALL, W., MURRAY, G., Proc. Int. Congr. Magnetism, 1967, J. appl. Phys. 39 (1968) 380.
[54] LOWDE, R.D., SHIMIZU, M., STRINGFELLOW, M.W., TORRIE, B.H., Phys. Rev. Lett. 14 (1965) 698.
[55] ANTONINI, B., STRINGFELLOW, M.W., Proc. phys. Soc. 89 (1966) 419.

DISCUSSION

Yu. M. KAGAN: What is the reason for such a strong temperature dependence of the Fourier component of the exchange integral in the case of rare-earth metals?

H. BJERRUM MØLLER: The strongest effect on the temperature dependence of the spin-wave energies accrues from the fact that the z-component of the magnetic moment decreases as more and more spin waves are excited, so that $S_i \cdot S_j$ in the Hamiltonian decreases. In our analysis this effect has been included in the temperature dependence of the Fourier-transformed exchange parameter.

Yu. M. KAGAN: I should like to know why you believe that magnon-magnon interaction is much less than magnon-electron interaction.

H. BJERRUM MØLLER: We believe that magnon-electron interaction is the important process in limiting the lifetime of the magnons because of the temperature and wavelength dependence of the line width, which

is different from what ought to be observed for the other possible interactions.

R.A. COWLEY: Have you any idea of the microscopic origin of the magnon-phonon interaction in terbium?

H. BJERRUM MØLLER: We are at the moment doing further measurements on the magnon-phonon interaction and it is perhaps too early to discuss its origin now. However, at present we believe that the magnon-phonon coupling is due to the modulation of the exchange parameter in a phonon motion. It may be enhanced by a magnon-resonant mode observed at 4 meV in the Tb-10% Ho sample, which would explain the large difference between Tb and Tb-10% Ho.

B.N. BROCKHOUSE: If my memory of the literature serves me correctly, I do not think that there is much evidence for (or against) a large value for the quartic constant β in the dispersion curves for the spin waves in 3d metals.

J. ALS-NIELSEN: The parameter β giving information on the range of interactions in the 3d metals can also be determined by the q dependence of critical scattering. In contrast with the small value of β given in Table II of the paper for Ni, the critical scattering data indicate a higher value of β for Ni than for Fe and Co. This shows that there are experimental inconsistencies in the values of β for Ni.

R.I. SHARP: I am interested to know why the temperature dependence of the Kohn effect is much more prominent in terbium than in non-magnetic metals. Is it because the exchange integral $J(\vec{q})$ appears directly in the expression for the magnon energy, or because $I_{nn'}$ is especially large for terbium or for some other reason?

H. BJERRUM MØLLER: The temperature dependence of the Kohn effect in Tb is, we believe, entirely explained by the temperature dependence of the Fermi function and of the magnon energies.

A.R. MACKINTOSH: The essential difference is that in this case the Fermi surface itself is changing with temperature, whereas in the case of the phonon Kohn anomaly this is not so.

H. MAIER-LEIBNITZ: What do you think would be the chances (and also the importance) of measuring the single-particle excitations shown in Fig. 2(b) of your paper?

H. BJERRUM MØLLER: Unfortunately, I don't know the size of the band splitting. However, I think that the merging of the spin waves into the single-particle excitations takes place at some magnon wavevector. The reason why it has not been observed is probably the restriction of the measurements to rather low values of q and E. It would be interesting to observe the merging of the spin waves into the single-particle excitations, and this would represent the first experiment to show unambiguously that the magnetic electrons have an itinerant character.

W.L. WHITTEMORE: Mr. Bjerrum Møller noted that some interesting metals have large absorption cross-sections, and this leads to very difficult or impossible experimental situations. The new, high-efficiency chopping systems to be discussed at the Special Session concluding the Symposium may render such measurements much easier. This, of course, presupposes that time-of-flight techniques can be used for determining the dispersion curves. In this regard it may be interesting to note that Brugger and co-workers at Idaho have demonstrated the feasibility of using the time-of-flight technique for dispersion curve measurements.

H. BJERRUM MØLLER: The advantage of the triple-axis spectrometer method is that measurements can be restricted to a chosen direction in the crystal. This is important in measurements on the rare-earth metals, where the dispersion relation is not isotropic and we are interested in knowing the detailed shape of the dispersion relation for specific directions. With a time-of-flight instrument one would have to select the data which correspond to these specific directions in the crystals, and many items of data would be wasted. I very much doubt, therefore, whether the time-of-flight method can compete with the triple-axis spectrometer for such measurements.

B.N. BROCKHOUSE: Observation of the dispersion curves for the lattice vibrations in the fcc ferromagnetic 3d metals (Ni, Fe and some alloys) shows that these curves are rather smooth, with no obvious Kohn anomalies. On the other hand, the 3d electron bands are fairly flat, with consequent very high density-of-states. Do not these two facts together suggest that perhaps the itinerant electron model is not very good after all, and that low-lying single-particle excitations may not be observable?

A.R. MACKINTOSH: I think that the strongest evidence that 3d transition metal electrons are itinerant comes from Fermi surface measurements, the Haas-van Alphen effect, and so on. The Haas-van Alphen effect shows very clearly that in Fe, and more especially in Ni, the 3d electrons are, in some sense, itinerant.

As regards the Kohn effect, the important feature is not that the density-of-states is high but that the relevant pieces of Fermi surface connected by q are flat. We are far from absolutely certain what the Fermi surface looks like in iron, but pictures have been drawn and these pictures do not have the great flat regions found in the rare earths, or in chromiun for example.

To my mind there can thus be little doubt that the 3d electrons are itinerant in some way or other, and therefore that single-particle excitations must exist.

MAGNON ENERGIES AND EXCHANGE INTERACTIONS IN TERBIUM

J.C. GYLDEN HOUMANN
RISØ RESEARCH ESTABLISHMENT,
ROSKILDE, DENMARK

Abstract

MAGNON ENERGIES AND EXCHANGE INTERACTIONS IN TERBIUM. The magnon density of states, and hence the magnetic contribution to the specific heat, together with the exchange interaction between ions in the same sub-lattice have been calculated for Tb at 90°K, using experimental results obtained by inelastic neutron scattering.

The magnon dispersion relations for Tb at 90°K along all symmetry lines in the Brillouin zone have recently been published [1, 2]. In this paper an interpolation method for determining the magnon energies throughout the zone from these measurements is presented. This in turn is used to calculate the magnon density of states, and hence the magnetic contribution to the heat capacity, and also the exchange interaction between ions in the same hexagonal sub-lattice.

It was shown in Ref. [1] that the magnon dispersion relations can be accounted for by a Hamiltonian of the form

$$H = \sum_{i<j} J(\vec{R}_i - \vec{R}_j)\,\vec{S}_i \cdot \vec{S}_j + \sum_j \left\{ B S_{zj}^2 - \frac{1}{2} G\left[(S_{xj} + i S_{yj})^6 + (S_{xj} - i S_{yj})^6 \right] \right\} \qquad (1)$$

where $J(\vec{R}_i - \vec{R}_j)$ is the exchange interaction between ions at $\vec{R}_i$ and $\vec{R}_j$ and B and G describe the two-fold and six-fold anisotropies respectively. We have used $\vec{S}$ to denote the total angular momentum operator. In diagonalizing Eq. (1) [3, 4] it is convenient to consider the hcp lattice of Tb as two inter-penetrating hexagonal Bravais lattices and to introduce two Fourier transformed exchange parameters

$$J(\vec{q}) = \sum_{R_j} J(\vec{R}_j)\, e^{i\vec{q}\cdot\vec{R}_j}$$
$$J'(\vec{q}) = \sum_{R_{j'}} J(\vec{R}_{j'})\, e^{i\vec{q}\cdot\vec{R}_{j'}} \qquad (2)$$

where the sums in Eqs (2) are over all vectors from one atom to other atoms in the same sub-lattice ($\vec{R}_j$) and over all vectors to atoms in the other sub-lattice ($\vec{R}_{j'}$), respectively.

Analysis of the magnon dispersion relations [2] shows that the indirect exchange interaction in Tb is of very long range, and the measurements along symmetry lines are not therefore adequate by themselves to determine the interatomic exchange parameters. Consequently, a fitting procedure using such parameters does not provide a satisfactory method of obtaining magnon energies throughout the zone and an analytical interpolation scheme was therefore developed. The fundamental principle of this method is that, because of the symmetry of the reciprocal lattice, constant energy surfaces must meet the faces of the irreducible Brillouin zone normally. Furthermore, the constant energy contours on planes within the zone are continuous and analytical, and they may therefore be approximated by simple analytical expressions. The measurements and the symmetry of the zone are sufficient to determine four parameters in such an analytical expression, and a constant energy contour is therefore represented by a third-order polynomial or an ellipse.

A computer programme was written which uses as input selected points from the dispersion relations along symmetry lines. From this, analytical expressions for the constant energy contours are constructed and plotted on the faces of the irreducible zone. Figure 1 shows such computer plots for the acoustic and optical magnon energies. The contour lines around those critical points which are not symmetry points are represented by ellipses with the critical point at one focus. The energies within the zone are calculated by interpolating in the same way on planes normal to ΓA. This determines the energies on a relatively coarse mesh throughout the zone, from which values at any point may be obtained with satisfactory accuracy by linear interpolation.

To check the accuracy of this method, the energies of acoustic magnons were measured at the centre of the ΓMK plane and at a general point in the centre of the irreducible zone. The results were 9.65 ± 0.1 and 9.85 ± 0.1 meV, respectively, which may be compared with the values 9.75 ± 0.1 and 9.70 ± 0.1 meV obtained from the interpolation method. The magnon energy at an arbitrary point in the zone can therefore apparently be obtained from the interpolation method with an uncertainty very little greater than that of the measurements. The method has the advantages of great speed and simplicity, but is, in its present form, less suited to the calculation of phonon energies, where degeneracies between different branches cause difficulties [5].

The density of states $g(\epsilon)$ may readily be constructed from the energy contours on the planes normal to ΓA, since the area between two contour lines of different energy is proportional to the number of states in the plane between the two energies. The density of states for magnons in Tb at 90°K was determined in this way, and the result is shown in Fig. 2 which is a computer plot, smoothed in some places to eliminate spurious structure introduced by the method [5]. A number of Van Hove singularities [6] may be observed in the density of states and these can be related to features of the dispersion relations. For example, the pronounced peak at about 11 meV has its origin in maxima in the AH and HL directions, while the peaks at about 9 and 12 meV can be related to extrema in the

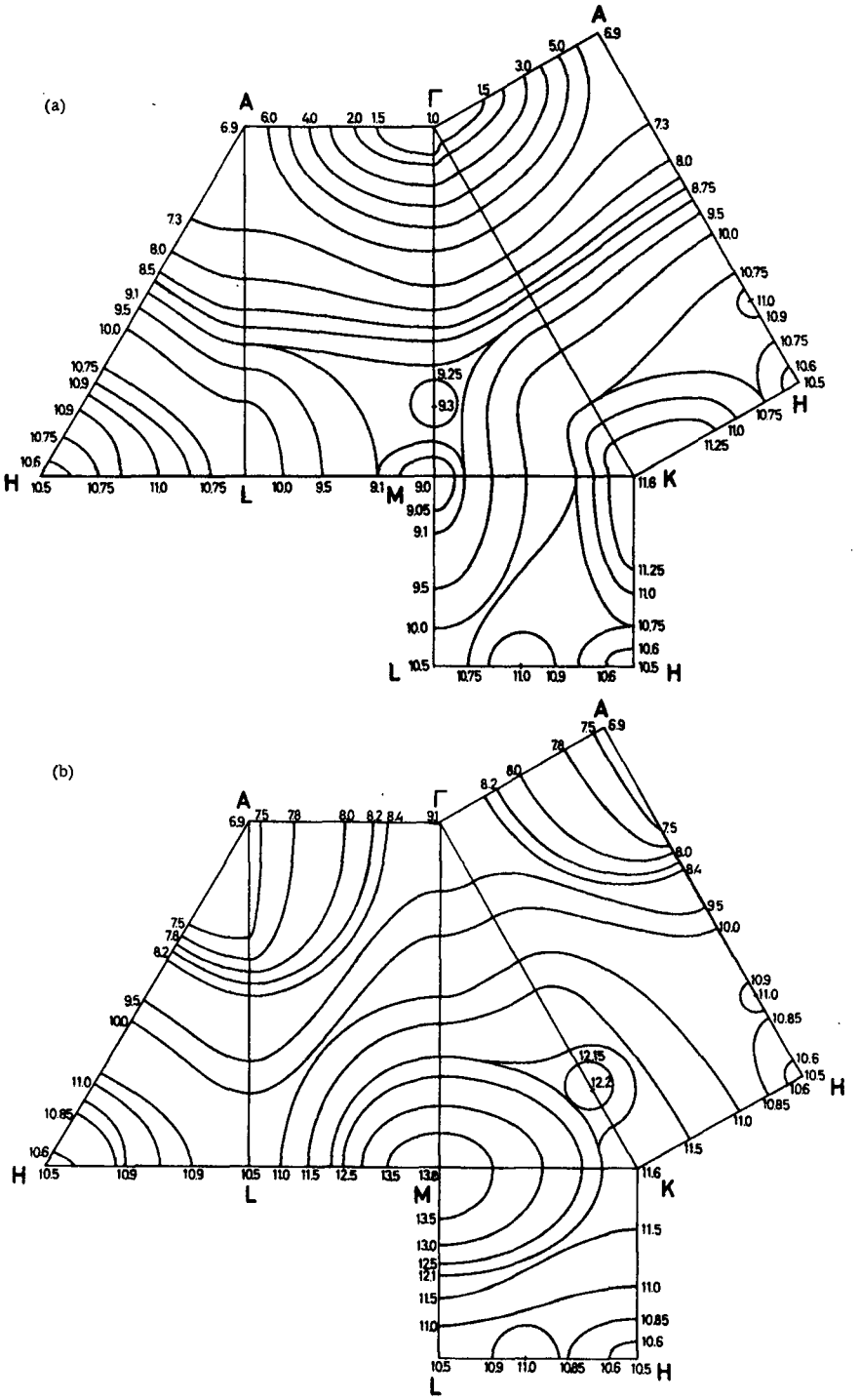

FIG.1. (a) Acoustic magnon energy contour lines in the unfolded irreducible zone for Tb at 90°K.
(b) Optical magnon energy contour lines in the unfolded irreducible zone for Tb at 90°K.

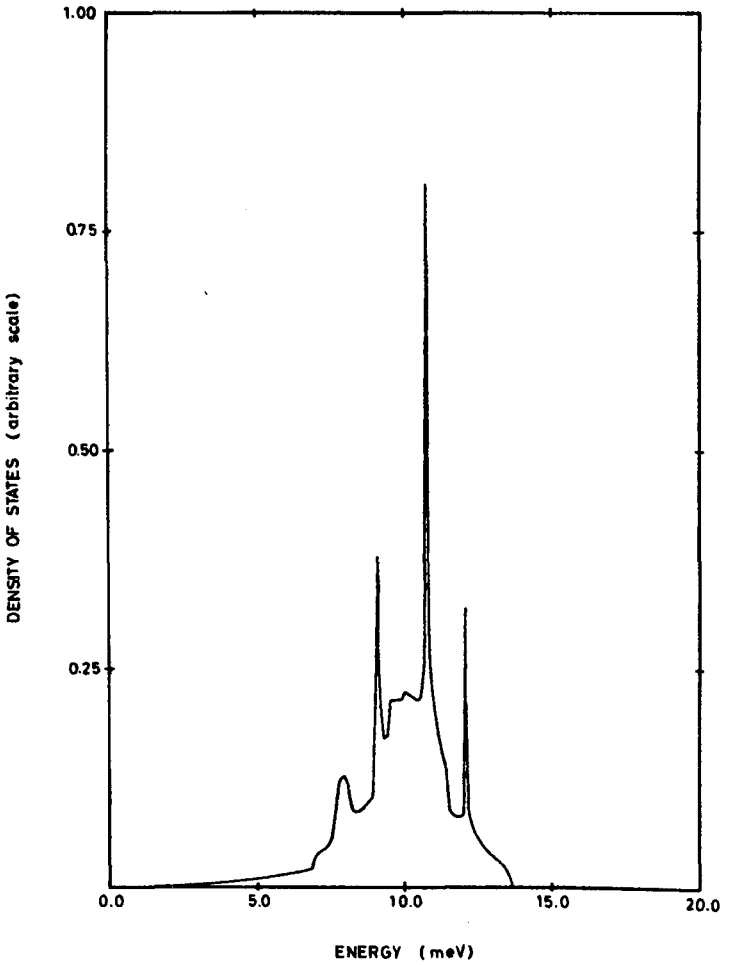

FIG. 2. Smoothed computer plot of the magnon density of states for Tb at 90°K. The density of states is normalized, so that the total number of states is one.

ΓM acoustic branch and ΓK optical branch, respectively. The energy gap at Γ is also evident.

At temperatures sufficiently low that renormalization of the magnon energies may be neglected, the magnetic contribution to the specific heat may be written

$$C_M = R \int \frac{\epsilon^2 g(\epsilon) \exp(\epsilon/kT) d\epsilon}{k^2 T^2 (\exp(\epsilon/kT - 1)^2} \qquad (3)$$

We have recently made measurements of magnon energies in Tb at 4.2°K and these show that, apart from effects associated with changes in the magnetic anisotropy, the dispersion relations do not change

markedly between 4.2 and 90°K. At 90°K the high-energy magnons make the largest contribution to C_M and, since these magnon energies are mainly determined by the exchange forces, we can use Eq. (3) as an approximation to the magnetic specific heat. We find

$$C_M\,(\mathrm{Tb})_{90°K} = 7.3 \pm 1.0\ \mathrm{J/mole\ degK\ (calculated)}$$

It was found in practice that C_M is rather insensitive to changes in $g(\epsilon)$, and the uncertainty quoted is therefore almost entirely due to the neglect of renormalization effects.

The magnetic specific heat may be estimated by assuming the relation [7]

$$C_M(\mathrm{Tb}) = C(\mathrm{Tb}) - C(\mathrm{Lu})$$

where C(Lu) is the heat capacity for Lu, which is non-magnetic. From the published measurements [8, 9], we find the result

$$C_M\,(\mathrm{Tb})_{90°K} = 8.5 \pm 1.0\ \mathrm{J/mole\ degK\ (experimental)}$$

TABLE I. INTERATOMIC EXCHANGE PARAMETERS (EXCHANGE BETWEEN ATOMS IN THE SAME SUB-LATTICE) FOR Tb AT 90°K

$\vec{R}$	Number of neighbours	Distance from central atom (Å)	$J(\vec{R})$ (meV)
(a, 0, 0)	6	3.60	0.0910
(0, 0, c)	2	5.69	-0.0345
(a, a, 0)	6	6.24	0.0117
(a, 0, c)	12	6.73	0.0043
(2a, 0, 0)	6	7.20	0.0105
(a, a, c)	12	8.44	0.0051
(2a, 0, c)	12	9.18	0.0017
(2a, a, 0)	12	9.52	-0.0003
(3a, 0, 0)	6	10.80	0.0070
(2a, a, c)	24	11.09	0.0031
(0, 0, 2c)	2	11.38	0.0010
(a, 0, 2c)	12	11.94	-0.0022
(2a, 2a, 0)	6	12.48	-0.0009
(a, a, 2c)	12	12.98	-0.0032

The major uncertainty in this value is the assumption that the lattice and electronic heat capacities of Lu and Tb are identical. Allowing for the uncertainties in the theoretical and experimental values, the agreement between them is satisfactory.

Since the dispersion relation for an arbitrary direction can be deduced from the interpolation method, it is possible, without further measurements, to obtain enough information for a complete and unambiguous determination of the interatomic exchange parameters. Since $J'(\vec{q})$ is generally complex, it is complicated to calculate the exchange between atoms in different sub-lattices. We have therefore so far only calculated the exchange parameters for atoms in the same sub-lattice but plan to complete the calculation of the exchange in the near future.

The details of these calculations may be found in Ref. [5] and the results are presented in Table I and Fig. 3. The interatomic exchange parameters have a markedly oscillatory character, as expected from the theory of indirect exchange [10]. These results are rather different from those of Goodings [11] who was forced, through lack of experimental data, to make certain assumptions about the form of $J(\vec{R})$. In particular, he found J(0, 0, c) to be small and positive, whereas in this calculation it is rather large and negative.

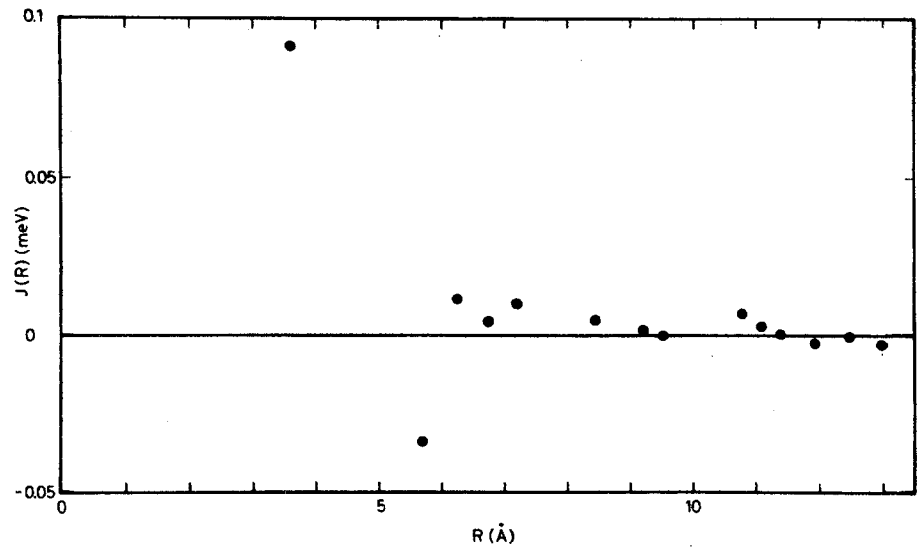

FIG. 3. Interatomic exchange parameters (interaction between atoms in the same sub-lattice) for Tb at 90°K obtained from the interpolation method.

ACKNOWLEDGEMENTS

It is a pleasure to thank Dr. H. Bjerrum Møller and Professor A. R. Mackintosh for many pleasant and stimulating discussions concerning this work.

REFERENCES

[1] BJERRUM MØLLER, H., GYLDEN HOUMANN, J.C., Phys. Rev. Lett. 16 (1966)737.
[2] BJERRUM MØLLER, H., GYLDEN HOUMANN, J.C., MACKINTOSH, A.R., Proc. Int. Congr. Magnetism, 1967; J. appl. Phys. 39(1968)807.
[3] NIIRA, K., Phys. Rev. 117(1960)129.
[4] LINDGÅRD, P.A., KOWALSKA, A., LAUT, P., J. Phys. Chem. Solids 28 (1967) 1357.
[5] GYLDEN HOUMANN, J.C., Thesis submitted to the Technical University of Denmark (1968).
[6] VAN HOVE, L., Phys. Rev. 89 (1953) 1189.
[7] LOUNASMAA, O.V., SUNDSTRÖM, Lorna J., Phys. Rev. 150 (1966) 399.
[8] JENNINGS, L.O., STANTON, R.M., SPEDDING, F.H., J. chem. Phys. 27 (1957) 909.
[9] JENNINGS, L.O., MILLER, R.E., SPEDDING, F.H., J. chem. Phys. 33 (1960) 1849.
[10] RUDERMAN, M.A., KITTEL, C., Phys. Rev. 96(1954)99.
[11] GOODINGS, D.A., J. Phys. C 1 (1968)125.

VIRTUAL MAGNON STATES IN DILUTE ALLOYS

N. KROÓ AND L. PÁL
CENTRAL RESEARCH INSTITUTE FOR PHYSICS,
HUNGARIAN ACADEMY OF SCIENCES,
BUDAPEST, HUNGARY,
AND
D. JOVIC
BORIS KIDRIČ INSTITUTE OF NUCLEAR SCIENCE,
VINČA, BELGRADE, YUGOSLAVIA

Abstract

VIRTUAL MAGNON STATES IN DILUTE ALLOYS. The effect of magnetic impurity atoms on the spin-wave spectrum of Fe and Ni has been studied with inelastic neutron scattering using the time-of-flight method. If weakly bound magnetic impurity atoms are randomly distributed in a ferromagnetic crystal, incoherent magnetic neutron scattering occurs with a resonance at the energy of the virtual level. From the width of this resonance the lifetime of the virtual state and from the energy the impurity-host to host-host exchange energy ratio can be determined. The magnetic origin of the observed resonance can be proved by repeating the measurements on magnetized samples.

In a Fe matrix the effects of Mn, Er, V and Cr atoms were studied. In Fe(Mn) an anomalous broad resonance was observed at $E_0 \sim 20$ meV. The angular distribution of the total scattered intensity has a maximum, indicating that $S_{Mn} \neq 0$ and that the density distribution of magnetic electrons of iron atoms near the Mn impurity has changed. In Fe(Er) and Fe(Cr) low-lying virtual levels were observed, with 0.6 meV and 1.6 meV energies, respectively. The results in Ni(V) and Ni(Cr) are also described. In Fe(V) a virtual level could not be seen in the observed scattered neutron spectra. The temperature dependence of the lifetime of the observed resonances was also studied between 80°K and the Curie point of the samples.

INTRODUCTION

Inelastic neutron scattering studies have become in the last decade an effective tool for understanding the microdynamics of both non-magnetic and magnetic crystals. The frequency spectrum of phonons and the dispersion relations of phonons and magnons have been measured in many substances. High-flux reactors and better equipment have increased the sensitivity of neutron spectroscopy. This fact has made it possible to measure the effect of impurity atoms on the phonon and magnon spectra. Several measurements of this type have been reported for phonons, whereas the study of the spin-wave (magnon) spectrum perturbed by magnetic impurities in magnetic crystals is at the very beginning.

The effect of the magnetic impurities on the spin-wave spectrum of an ideal Heisenberg ferromagnet has been investigated theoretically by several authors [1-4] but very few experimental facts are known as yet [5-9]. Calculations with first-neighbour interactions in cubic crystals show that an s-type virtual spin-wave state can be associated with the impurity if the impurity-host exchange J' is smaller than the host-host exchange J. The energy E_s of this state lies in the host spin-wave band and is a monotonic function of J'/J. If $\epsilon = J'/J$ de-

creases, the virtual level occurs at lower energies. Since the lifetime of a virtual level is inversely proportional to the host density of states, its lifetime will be the longer the lower the energy of a virtual level, that is, the smaller the value of ϵ is associated with it. These low-lying virtual s-like states are of particular importance even in the macroscopic thermodynamic behaviour of the impure ferromagnet, since these states give rise to a large density of states at the low-energy part of the spectrum where the density of spin-wave states of the unperturbed crystal is very small.

Calculations by Wolfram and Hall [10] show that the energy and lifetime of the virtual level depend on the temperature. Near the Curie point T_c, the lifetime is longer and the energy is slightly higher than at low temperatures. In the results of Hone, Callen and Walker [11] this energy shift does not appear.

The presence of weakly bound magnetic impurities in a ferromagnetic crystal changes the neutron scattering properties of the system. The double-differential scattering cross-section has an incoherent part with a Lorentzian-type resonance around the energy E_s. For neutron energy gain this cross-section formula, given by Izyumov and Medvedev [12], reads

$$\frac{d^2\sigma_{inc}}{d\Omega dE} = \frac{1}{2}(r_0\eta)\frac{k'}{k_0}[n(E_0)]F_{eff}(\kappa)[1 + (\vec{e}\vec{m})^2]\frac{1}{\pi}\frac{\Gamma_s}{\Gamma_s^2 + (E - E_s)^2} \qquad (1)$$

where $\vec{\kappa} = \vec{k} - \vec{k}_0$ and $n(E_0)$ is the population factor. The unit vector $\vec{e}$ points in the direction of $\vec{\kappa}$ and $\vec{m}$ in that of the magnetic field $\vec{H}$ and $\vec{\Gamma}$ is the width of the resonant level.

$F_{eff}(\kappa)$ is an effective form factor which is given by Izyumov as $F_{eff}(\kappa) = F'(\kappa)\sqrt{S'}, -F(\kappa)\sqrt{S}$, with S and $F(\kappa)$ giving the spin and form factor unprimed for the host and primed for the impurity atoms, respectively.

Recent results of Lovesey [13] give a more complicated formula for $F_{eff}(\kappa)$.

To study the properties of the virtual spin-wave states, iron and nickel based dilute alloys were chosen. In ferromagnetic matrices the magnetic origin of an observed resonance can be proved by measurements in a magnetic field. This field dependence does not occur in antiferromagnets, causing difficulty in the interpretation of data [7]. The impurity atoms were Mn, Er, and Cr in the Fe and V and Cr in Ni matrix. In Fe(Mn) the NMR measurements of Jaccarino et al. [14] indicate the existence of a low-lying virtual level. In Fe(Er) a level with very low energy, i.e. with very long lifetime, is expected because of the screening effect of 5s and 5p electrons in Er which allows only an indirect exchange between the 4f magnetic electrons of Er and the 3d electrons of the neighbour Fe atoms and this exchange via the conduction electrons is small.

MEASUREMENTS

The measurements on Fe(Mn), Fe(Er) and Fe(Cr) were performed in Budapest and those on Ni(V) and Ni(Cr) in Vinča. In Budapest a

conventional time-of-flight spectrometer [15] with liquid N cooled Be-filter and curved slit chopper before the sample was used. The spectrum of in-going neutrons was centred around 4.25 Å with a wavelength spread of $\Delta\lambda/\lambda = 12\%$. Data could be collected simultaneously at four angles in the horizontal plane. Detector banks were built up from 38-mm diameter BF_3 gas-filled proportional counters, each bank consisting of a layer of 10 detectors. The average efficiency of a bank for the incident neutrons was 40%. The flight-path was 4.52 m.

The time-of-flight spectrometer in Vinča also operates with Be-filtered neutrons, but with the slow chopper after the sample. The arm of the spectrometer can be moved in the vertical plane from 0-90°. The detector bank is composed of 9 BF_3 counters (25 mm diameter) in one layer.

The dilute alloys used as samples were all of the substitutional type with 3% impurity atoms except for Fe(Er) where, because of the limited solubility, 0.4% Er was used. The oxygen content of this last alloy was measured by activation analysis as 0.017%.

The term

$$g(E) = \frac{1}{\pi} \frac{\Gamma_s(T)}{\Gamma_s^2(T) + (E - E_s)^2} \qquad (2)$$

in (1) describes the shape of the virtual resonance. Cross-section (1) also depends on the effective form factor and on the value of $1 + (\vec{e}\vec{m})^2$. The observed incoherent inelastic contribution from the impurity atoms was studied in terms of these three factors.

The magnetic origin of the scattering can be proved by the magnetic field dependence of the cross-section. If one uses polycrystalline samples with randomly oriented crystallites, then without magnetic field $1 + (\vec{e}\vec{m})^2 = 4/3$, while with a magnetic field perpendicular to the scattering plane and strong enough to saturate the sample, this factor decreases to 1.

The function g(E) is normalized to 1. Therefore the total intensity scattered by the virtual level is proportional to the effective form factor.

The position and width of the observed resonance at a fixed angle determine the parameters E_s and Γ and according to the theory [10] Γ is a function of temperature.

The measurements were performed as follows. Time-of-flight spectra were taken at different angles on the dilute alloy and at the same angles on the pure host crystal. The measured spectra were compared after correction for change in nuclear scattering due to impurities in the alloy, for absorption and for the variation in sample thickness at different scattering angles. Corrections were taken also for detector efficiency and air out-scattering.

RESULTS

The scattering angles used at room temperature are listed in Table I. A result for each alloy can be seen in Figs 1-4. In two cases the magnetic field dependence of the observed additional scattering by

TABLE I. SCATTERING ANGLES USED AT ROOM TEMPERATURE

Alloy	Angles
Fe(Mn)	7°, 12°, 18°, 26°, 32°, 41°
Fe(Er)	10°, 16°, 25°, 35°, 40°
Fe(Cr)	17°, 23°, 29°, 35°, 41°, 47°, 53°
Ni(V)	20°, 30°, 40°
Ni(Cr)	20°, 30°

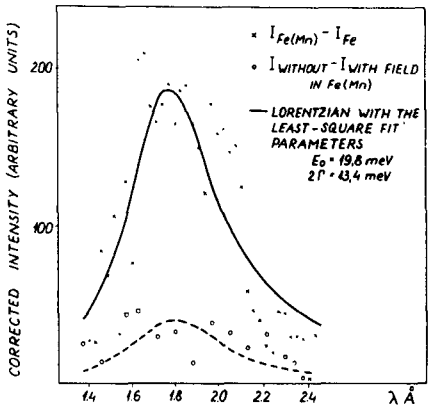

FIG.1. Virtual level in Fe(Mn). The full line is the calculated curve with the parameters of the least-square fit. The intensity variation with the applied $\vec{e} \perp \vec{m}$ magnetic field is also plotted.

the alloy, i.e. the difference between the scatterings with and without the magnetic field, is also plotted in the figures. As compared with the intensity change of 25% expected for magnetic scattering, the changes were found to be between 20 ± 6 % in FeMn and 28 ± 13 % in Ni(V).

The shape of the resonance was supposed to be Lorentzian and was fitted to the measured data by the least-squares method with three free parameters, E_s, Γ and a normalization constant, after folding the Lorentzian with our ingoing spectrum. From the results of Vashishta [16] for bcc and fcc host crystals, J' was calculated using for J the value obtained from the paramagnetic Curie temperature . The lifetime of the virtual level was calculated from Γ. The results are summarized in Table II.

For iron-based alloys the angular distribution of the total intensity scattered by the virtual level, i.e. the angular dependence of the effective form factor is given in Figs 5-7.

It is of interest to note that in Fe(Mn) around $\kappa \sim 2.5$ Å^{-1} the angular distribution has a maximum which does not follow from the data of Collins and Low [17]. This is not surprising since their data are given only for the $0 < \kappa < 1.5$ Å^{-1} region, which is below the

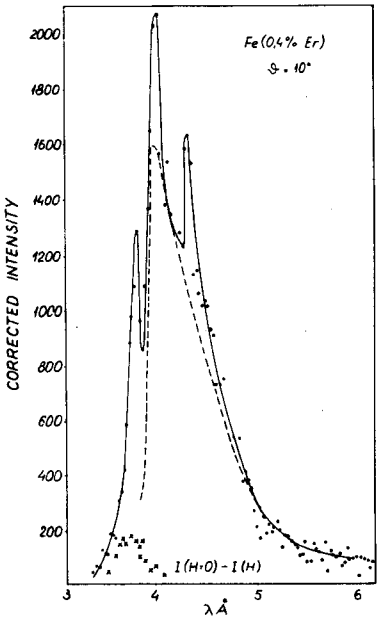

FIG. 2. Time-of-flight spectrum in Fe(Er) at $\vartheta = 10°$ with the ingoing spectrum (broken line) and the effect of an $\vec{e} \perp \vec{m}$ magnetic field.

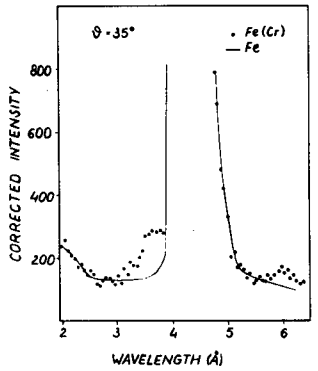

FIG. 3. Time-of-flight spectrum of Fe(Cr) at $\vartheta = 35°$ with the equivalent pure iron result.

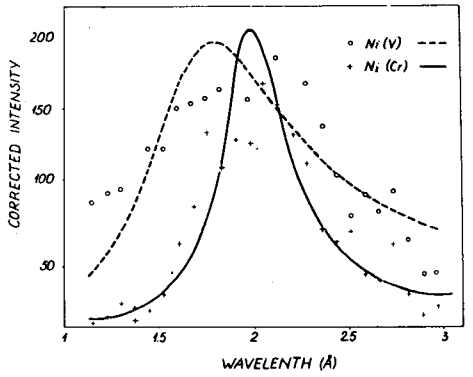

FIG. 4. Virtual level in o Ni(V) and + Ni(Cr) after subtraction of the intensity scattered by Ni.

TABLE II. PARAMETERS OF THE OBSERVED VIRTUAL LEVELS FROM THE LEAST-SQUARES FIT

Alloy	E_S (meV)	$2\Gamma_S$ (meV)	J'/J	τ (sec/10^{-13})
Fe(Mn)	19.8	13.4	0.16	0.5
Fe(Er)	0.67	0.4	0.0056	16.5
Fe(Cr)	1.6	1.0	0.013	6.6
Ni(V)	22.0	30.0	0.19	0.23
Ni(Cr)	18.4	10.0	0.15	0.64

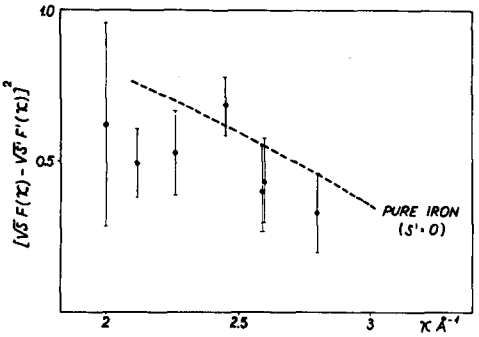

FIG. 5. Angular distribution of the total intensity of neutrons scattered by the virtual level in Fe(Mn). The broken line is the form-factor of pure iron.

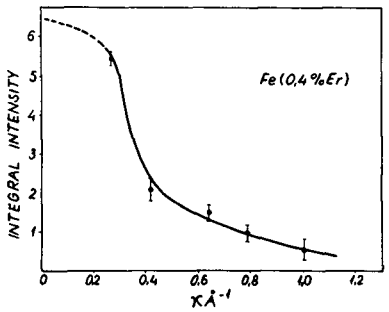

FIG. 6. Angular distribution of the total intensity scattered by the virtual spin-wave in Fe(Er).

κ range of the present study. Present data imply therefore a non-zero value of S' on the Mn atoms. All the other effective form factors are consistent with the values of $F'(\kappa)$ reported in Ref. [17]. The intensity distributions for Fe(Er) and Fe(Cr) are given in Figs 6 and 7.

The temperature dependence of the lifetime of the virtual level was studied in Fe(Cr). The measured level width as a function of temperature decreases when $T \sim T_c$. Therefore the lifetime increases when T approaches T_c. At the same time a small energy shift toward higher energies is observed.

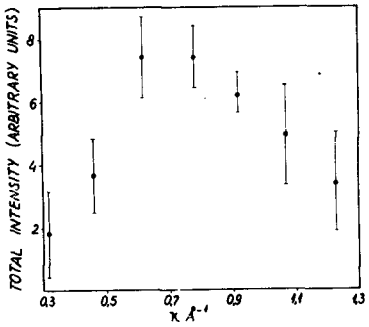

FIG. 7. Angular distribution of the total intensity in Fe(Cr).

DISCUSSION

The results are seen to prove the existence of virtual spin-wave levels in the alloys studied. In each case when the energy was lower, the lifetime was observed to be longer, in agreement with the predictions. On the other hand, the lifetime was always found to be shorter than the values predicted for Heisenberg isolators (Table II). This fact can be put down to the presence of conduction electrons in the alloy.

The metallic character of all the systems studied is reflected in addition by the change in the effective form factor as compared with the value calculated from the form factors of the free atoms in the alloy. The maximum, observed in the Fe(Mn) intensity distribution (Fig. 5), is probably caused by the decrease in the magnetic electron density of Fe atoms with Mn nearest neighbours. In Fe(Er) the intensity distribution shown in Fig. 6 reflects the long-range magnetic electron density perturbation around the impurity atoms.

The data in Ni(V) also show additional magnetic scattering as compared with the scattering of Ni. The broad maximum in the Ni(V) - Ni inelastic spectrum is observed in the energy region of the incoherent one-phonon peak. The total intensity of this additional effect cannot be explained by the scattering from vanadium atoms alone, because it would require at least $\mu_V = 6\mu_B$[1] while from Ref. [17] $\mu_V = -1.4\,\mu_B$. Clusters containing both the impurity and neighbour Ni atoms are assumed therefore to form the scattering unit. These clusters are randomly distributed and give rise to incoherent scattering.

The wide maximum superposed on the phonon spectrum prompts one to question the origin of the effect. Therefore it was decided to study in addition to Ni(V) the Ni(Cr) system where qualitatively the same result was expected. However, if the additional scattering is not connected with the phonons, the probability to find the maximum at the same energy is very small. In fact, a small shift of the Ni(Cr) maximum towards lower energies was observed and the width of this resonance is smaller.

The increase in the lifetime of the virtual spin-wave state was observed near T_c. The measured ratio of the width at room temperature

[1] μ_B = Bohr magnetons = 9.273×10^{21} erg/G.

to that at $T \sim T_c$ is 2, in good agreement with the results of Wolfram and Hall [10].

ACKNOWLEDGEMENTS

The authors are indebted to Dr. E. Kisdi-Koszó for all the computer programs and to Mr. G. Konczos for the preparation of the specimens.

REFERENCES

[1] WOLFRAM, T., CALLAWAY, J., Phys. Rev. 130 (1963) 2207-17.
[2] IZYUMOV, Yu., Proc. phys. Soc. 87 (1966) 505-19.
[3] ISHII, H., KANAMORI, J., NAKAMURA, T., Progr. theor. Phys., Japan. 33 (1965) 795.
[4] TAKENO, S., Progr. theor. Phys., Japan 30 (1963) 731.
[5] KROÓ, N., BATA, L., Phys. Lett. 24A (1967) 22.
[6] KROÓ, N., PÁL, L., Proc. Int. Congr. Magnetism, Boston, 1967; J. appl. Phys. 39 (1968) 453.
[7] BUYERS, W.J.L., COWLEY, R.A., HOLDEN, T.M., STEVENSON, R.W.H., Proc. Int. Congr. Magnetism, Boston, 1967; J. appl. Phys. 39 (1968) 1118.
[8] BJERUM MÖLLER, H., GYLDEN HOUMAN, J.C., MACKINTOSH, A.R., Phys. Rev. Lett. 19 (1967) 312.
[9] BJERUM MÖLLER, H., GYLDEN HOUMAN, J.C., MACKINTOSH, A.R., Proc. Int. Congr. Magnetism, Boston, 1967; J. appl. Phys. 39 (1968) 807.
[10] WOLFRAM, T., HALL, W., Phys. Rev. 143 (1966) 284.
[11] HONE, D., CALLEN, H., WALKER, L.R., Phys. Rev. 144 (1966) 283.
[12] IZYUMOV, Yu.A., MEDVEDEV, M.V., Zh. eksp. teor. Fiz. 48 (1966) 574.
[13] LOVESEY, S.W., Proc. phys. Soc. 91 (1967) 658.
[14] JACCARINO, V., WALKER, L.R., WETHEIM, G.K., Phys. Rev. Lett. 13 (1964) 752.
[15] BATA, L., KISDI, E., KROÓ, N., MUZSNAY, L., PÁL, L., SZLÁVIK, F., ZSIGMOND, G., Rep. KFKI 2 (1966).
[16] VASHISHTA, P., Proc. phys. Soc. 91 (1967) 372.
[17] COLLINS, M.F., LOW, G.G., Proc. phys. Soc. 86 (1965) 535.

INELASTIC SCATTERING OF POLARIZED NEUTRONS BY MAGNETO-VIBRATIONAL WAVES IN A SINGLE CRYSTAL OF bcc IRON

O. STEINSVOLL
INSTITUTT FOR ATOMENERGI,
KJELLER, NORWAY

Abstract

INELASTIC SCATTERING OF POLARIZED NEUTRONS BY MAGNETO-VIBRATIONAL WAVES IN A SINGLE CRYSTAL OF bcc IRON. It has been predicted theoretically that the scattering of neutrons by magneto-vibrational waves in a magnetic crystal should depend upon the polarization state of the incoming neutrons. Our measurements on a single crystal of bcc iron ($Fe_{0.96}Si_{0.04}$) have confirmed the theoretical expressions for the polarization effects. The widths of the inelastic diffuse reflections obtained by the diffraction method have been found to agree with the linear dispersion relation of phonons, and the velocity of sound derived from our measurements agrees with values found by other types of measurements. A direct proof has been given by using a flipper-chopper time-of-flight spectrometer that the polarization effects are connected with inelastic scattering processes. The different field and polarization dependence of the magneto-vibrational and spin-wave scattering has been used to resolve the scattering components present in the composite diffuse reflections. In principle, it is then possible to find values of the magnetic form factor for the ions for momentum transfers different from the reciprocal lattice vectors, and some preliminary results are presented of this new method.

1. INTRODUCTION

Polarized neutrons have been successfully applied in the study of spin-wave scattering from magnetic substances [1-7]. The great advantage of using polarized neutrons is that by magnetizing the sample along the scattering vector one separates that part of the inelastic scattering which is caused by spin-wave scattering from all other inelastic contributions.

For a ferromagnetic substance like metallic iron, the main other inelastic contribution will come from neutrons being scattered by elastic waves on the atomic lattice. According to the experimental geometry the neutrons may create or annihilate phonons, the quanta of the vibrational states of the crystal. The phonons are propagating in all directions on the chemo-crystalline lattice, but in a magnetic crystal-like iron where all atoms have a magnetic moment these vibrations will also be seen on the magneto-crystalline lattice - the orderly arrangement of the magnetic moments. The neutron will interact with both these lattices simultaneously by virtue of its mass and magnetic moment. This gives rise to nuclear-vibrational and magneto-vibrational scattering.

The phase difference between these two types of scattering effects will depend upon the polarization state of the incoming neutrons, similar to elastic scattering from magnetic substances. This should give rise to polarization effects for the inelastic vibrational scattering when the sample is magnetized vertical to the scattering vector [8-11]. For this field direction the spin-wave scattering will, however, not be polarization dependent.

The inelastic scattering of polarized neutrons by vibrational waves in a single crystal of iron has been studied both by the 'diffraction' method and by a flipper-chopper time-of-flight spectrometer [12-14]. The measurements have confirmed the theoretical predictions about the polarization dependence of vibrational scattering. The energy analysis of the scattered neutrons has proved that the polarization effects in the diffuse reflections are connected with an inelastic scattering process.

An attempt has been made to study the ratio between the vibrational scattering cross-sections for the two spin states of the neutrons. A knowledge of this ratio would in fact give the magnetic form factor for the magnetic ions for momentum transfers different from the reciprocal lattice vectors.

2. THEORY

2.1. Polarization effects in vibrational scattering

The differential coherent scattering cross-section for scattering of polarized neutrons with creation of vibrational quanta with wavevector $\vec{q}$ belonging to the vibrational mode s in the vicinity of a reciprocal lattice vector $2\pi\vec{\tau}$ of an iron crystal may be written:

$$\frac{d^2\sigma}{dEd\Omega} \propto \left\{\bar{b}^2 + 2\,\bar{b}p\,(\vec{P}\cdot\vec{Q}) + p^2\vec{Q}^2\right\} \left|\vec{K}\cdot\vec{V}_{\vec{q}s}\right|^2 \times$$

$$\times\, \delta\,[\vec{K} - \vec{q} - 2\pi\vec{\tau}]\;\delta\,[(\hbar^2/2m_0)\,(\vec{k}_f^2 - \vec{k}_i^2) + \hbar w_{\vec{q}s}] \qquad (1)$$

where $\bar{b}$ is the nuclear coherent scattering amplitude; p is the magnetic scattering amplitude; $\vec{P}$ is the polarization vector of the neutron beam; $\vec{k}_i$, ($\vec{k}_f$) is the wavevector of the ingoing (outgoing) neutron beam; $\vec{K} = \vec{k}_i - \vec{k}_f$

$$\vec{Q} = [\hat{m} - \hat{e}\,(\hat{e}\cdot\hat{m})] \qquad (2)$$

$\hat{e} = \vec{K}/|\vec{K}|$, i.e. the unit scattering vector; $\hat{m}$ is the unit magnetization vector; $\vec{V}_{\vec{q}s}$ is the polarization vector of the vibrational quanta created; $\hbar w_{\vec{q}s}$ is the energy of the vibrational quanta created; $\vec{q}$ is the quasi-momentum of the vibrational quanta; m_0 is the neutron mass; and $2\pi\vec{\tau}$ is a reciprocal lattice vector.

We have further:

$$p \propto f(\vec{K}) \qquad (3)$$

where $f(\vec{K})$ is the magnetic form factor for the iron atoms.

We see from Eqs (1) and (2) that when $\hat{m} \perp \hat{e}$, $\vec{Q} = \hat{m}$ and $\vec{Q}^2 = 1$. The two delta functions express the conservation of linear momentum (crystal + neutron) and energy in the system. The simultaneous fulfilment of these two conditions together with the dispersion relation for the quasi-particles (the phonons) involved, imposes upon the

scattering certain geometrical limitations which will be treated below. In this case we may write Eq.(1) as follows:

$$\frac{d\sigma}{d\Omega} \propto \left\{\bar{b}^2 + 2\bar{b}p\,(\vec{P}\cdot\vec{Q}) + p^2\vec{Q}^2\right\} \left|\vec{K}\cdot\vec{V}_{\vec{q}_s}\right|^2 U(\Delta E) \tag{4}$$

where the parenthesis takes care of the polarization dependence and the factor $U(\Delta E)$ determines the spatial dependence of the scattering. The scattering is only confined to certain directions in space [15-17].

2.2. Dispersion law and scattering surfaces

For small quasi-momentum values the quanta of the lattice vibrations have a linear dispersion relation, and we can write:

$$\omega(q) = c_s q \tag{5}$$

where c_s is the velocity of the disturbance propagating through the lattice (= velocity of sound). A Debye model may be assumed in which the velocity of the sound waves is independent of wavelength, direction and polarization.

Equation (5) has to be fulfilled together with the following equations:

$$\frac{\hbar^2}{2m_0}\left(\vec{k}_f^2 - \vec{k}_i^2\right) + \hbar\omega_{\vec{q}_s} = 0 \tag{6}$$

$$\vec{K} - \vec{q} - 2\pi\vec{\tau} = 0 \tag{7}$$

The simultaneous solution of these equations traces out a so-called scattering surface in reciprocal space. For small energy and momentum transfers and creation of phonons the scattering surface in reciprocal space is very close to an ellipsoid with the reciprocal point as a pole (or focal point) and the sphere of reflection as polar plane if the velocity of the neutrons is smaller than the velocity of sound in the crystal [15]. The momentum vector $\vec{k}_f$ may end anywhere on the surface giving rise to a diffuse reflection around the reciprocal lattice point. According to Lowde [16] the half width (semi-angle) of this reflection is given approximately by the following formula:

$$\Gamma/2 = \left[\left(\frac{c_s}{v}\right)^2 - 1\right]^{-\frac{1}{2}} \sin 2\theta_B \Delta\Phi \tag{8}$$

where v is the velocity of the neutrons, $2\theta_B$ is the Bragg angle for the reflection we are considering and $\Delta\Phi$ is a small angle of missetting of the crystal from the Bragg position Φ. From the measured width Γ for different values of $\Delta\Phi$ we may calculate the parameter c_s in the

dispersion relation for the phonons, Eq.(5), and see whether it agrees with the results of other measurements.

In Fig. 1 we have drawn the geometry of the scattering process in reciprocal space for an angle of misset $\Delta\Phi = 12°$ from the Bragg angle. A Debye model has been assumed, and the scattering curves in the equatorial plane around the reciprocal lattice point (110) have been plotted for vibrational scattering (the ellipse) and spin-wave scattering (the circle). An isotropic velocity of sound has been assumed ($c_s = 6000$ m/s) and a value $D = 266$ meV $\mathring{A}^2$ for the parameter in the spin-wave dispersion relation was used.

The Debye model assumed above in the derivation of the formulas and for the drawing does not hold in the real case. The subscript s in the cross-section formula, Eq.(1), characterizes vibrational quanta belonging to different vibrational modes. The polarization vectors $\vec{V}_{\vec{q}s}$ are different for the various modes, which may be labelled longitudinal (ℓ) and transverse (t) depending upon the approximate direction of $\vec{V}_{\vec{q}s}$ relative to q. The dispersion relations will be different for

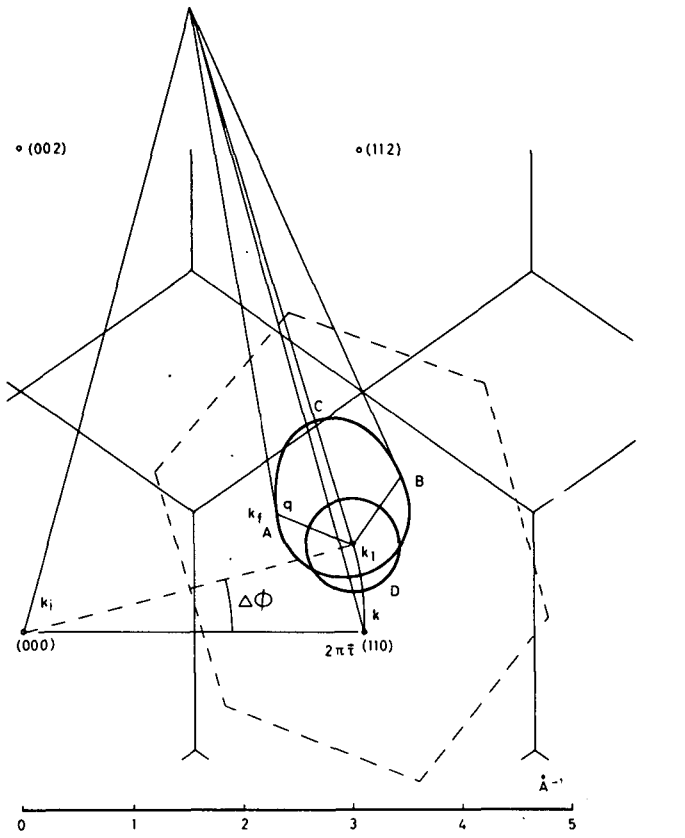

FIG.1. The geometry of the inelastic scattering around the (110) reciprocal lattice point in iron. After a positive misset $\Delta\Phi$ from the Bragg position the conservation laws are fulfilled along the scattering curves drawn with heavy lines. The ellipse applies to vibrational scattering while the circle applies to spin-wave scattering.

the various vibrational modes, and will also depend upon the crystallographic direction in which $\vec{q}$ is pointing. In fact, we will get several scattering surfaces around the reciprocal lattice point, each belonging to a different vibrational mode.

From the stiffness moduli, c_{ij}, for iron, we may calculate the velocity of sound for the transverse and longitudinal modes of vibration. Depending upon the propagation direction in the crystal the velocity of sound ranges from 5400 to 6400 m/s for the longitudinal modes and from 3000 to 3900 m/s for the transverse modes. This may be compared with the velocity of the neutrons applied, $\lambda = 1.07$ Å, i.e. v = 3700 m/s. The scattering surfaces should therefore be closed for longitudinal vibrational modes while they should be very wide and even open surfaces for the transverse modes. Closed scattering surfaces will give rise to diffuse reflections with good angular definition.

3. EXPERIMENTS APPLYING THE DIFFRACTION METHOD

3.1. The experimental set-up

The experiments were performed with an ordinary diffractometer for polarized neutrons ($\lambda = 1.07$ Å). A single crystal of $Fe_{0.96}Si_{0.04}$ 0.6 cm thick was used. The crystal was cut with the [100] direction normal to the surface of the crystal. In this way the crystal could be kept in the same position on the diffractometer and be magnetized along equivalent [110] directions, either along the scattering vector or normal to it. The crystal was magnetized by a permanent magnet giving a field of 3500 Oe. The depolarization in the crystal was very small.

3.2. The polarization dependence of the diffuse reflections

The experiments to confirm Eqs (1) or (4) were performed with the 'diffraction method'. The diffuse reflections around the reciprocal lattice vector $2\pi\tau_{(110)}$ were scanned by the counter. For each counter position two measurements were performed, with the radio-frequency flipper On and with the flipper Off. A plot of a typical series of measurements is shown in Fig. 2. The lower part of this figure shows the measured intensities when the magnetic field is vertical to the scattering vector and the misset is $\Delta\Phi = 12°$. As expected, we observe diffuse reflections with sharp cut-off angles on a slightly sloping background. The difference between the measured intensities when the R.F. flipper is Off and On should give the polarization-dependent part of the vibrational scattering. This difference is plotted on the second insert from the bottom in Fig. 2. The polarization-dependent background is partly due to disorder scattering and partly due to inelastic scattering where the neutrons interact with other vibrational modes than the longitudinal.

The upper part of Fig. 2 shows a similar scan where the magnetic field is parallel to the scattering vector. The polarization-dependent part of the diffuse reflection is in this case caused by spin-wave

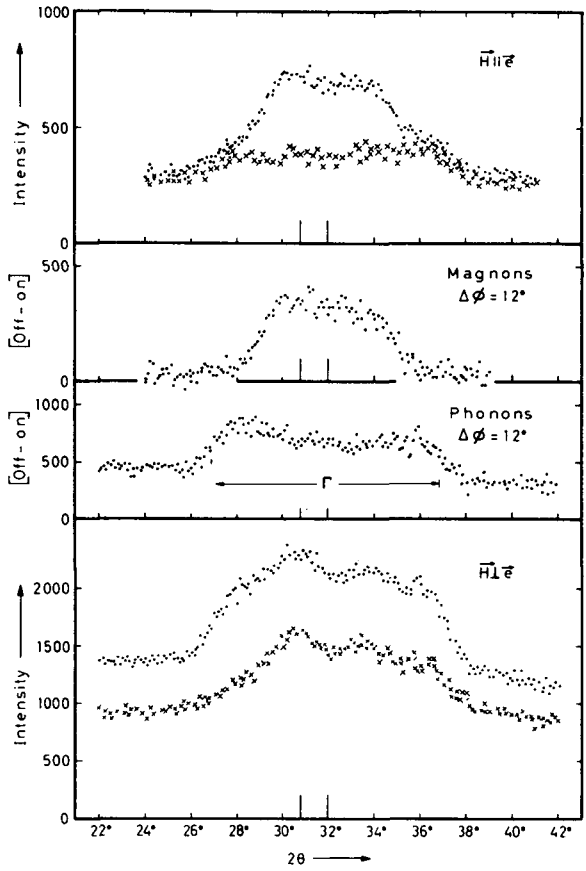

FIG. 2. The inserts at the top and bottom show the raw data obtained by scanning with the counter across the diffuse reflection when $\Delta\Phi = 12°$ with $\vec{H} \parallel \vec{e}$ and $\vec{H} \perp \vec{e}$. Crosses apply to data for R.F. on, and points to R.F. off. Subtracting the two types of data from each other, one obtains the angular behaviour of vibrational and spin-wave diffuse scattering.

scattering and the difference in the measured intensities with R.F. Off and On is plotted on the third insert from the bottom in Fig. 2. As expected, the two inelastic scattering processes give rise to diffuse reflections having different widths because the form of the dispersion relations is different. This is in accordance with Fig. 1.

3.3. Experimental determination of the dispersion relation

The diffuse reflections when $\vec{H} \perp \vec{e}$ were scanned by polarized neutrons in the way described above for a series of positive angles of misset. The widths of the diffuse reflections were estimated, and the half widths, $\Gamma/2$, plotted against the angle of misset, $\Delta\Phi$ (see Fig. 3). It is seen that the points are almost on a line. As the angle of misset is roughly proportional to the energy exchanged and the width proportional to the momentum exchanged, this points to a linear dispersion relation.

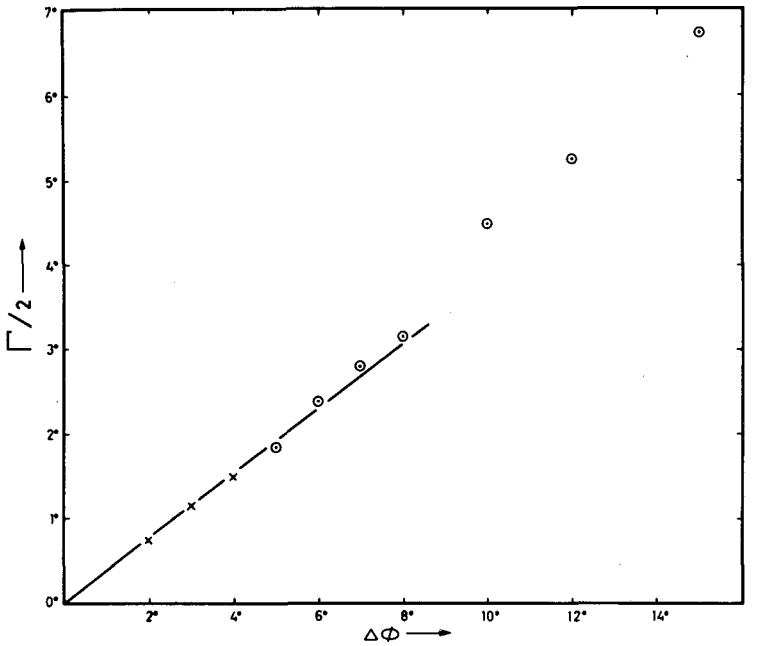

FIG.3. The estimated half widths, Γ/2, of the vibrational diffuse reflections plotted against the angle of misset ΔΦ. The slope of the line through 7 experimental points and the origin gives $c_s \approx 6000$ m/s as the sound velocity.

From the slope of the line through 7 experimental points and the origin, the velocity of sound can be estimated using Eq.(8). We find $c_s \approx 6000$ m/s. This is in good agreement with the sound velocity calculated for the longitudinal modes of vibration. This indicates that the polarization-dependent diffuse reflections when $\vec{H} \perp \vec{e}$ are caused by vibrational scattering.

4. EXPERIMENTS APPLYING THE FLIPPER-CHOPPER

The features of the flipper-chopper time-of-flight spectrometer have been described elsewhere [12-14]. We have applied this technique for $\vec{H} \perp \vec{e}$ using a similar disc-shaped crystal, $Fe_{0.96}Si_{0.04}$. The results of the measurements are shown in Fig. 4, where for comparison we also show the elastic reflection (110) as analysed by the apparatus. The elastic peak may be considered as the resolution function for the apparatus.

The measurements give a qualitative proof of the fact that the polarization effects in the diffuse reflections are connected with inelastic scattering processes. It is seen that for a positive angle of misset, some of the scattered neutrons have been slowed down, i. e. creation of vibrational quanta, whereas the opposite is true for a negative missetting angle.

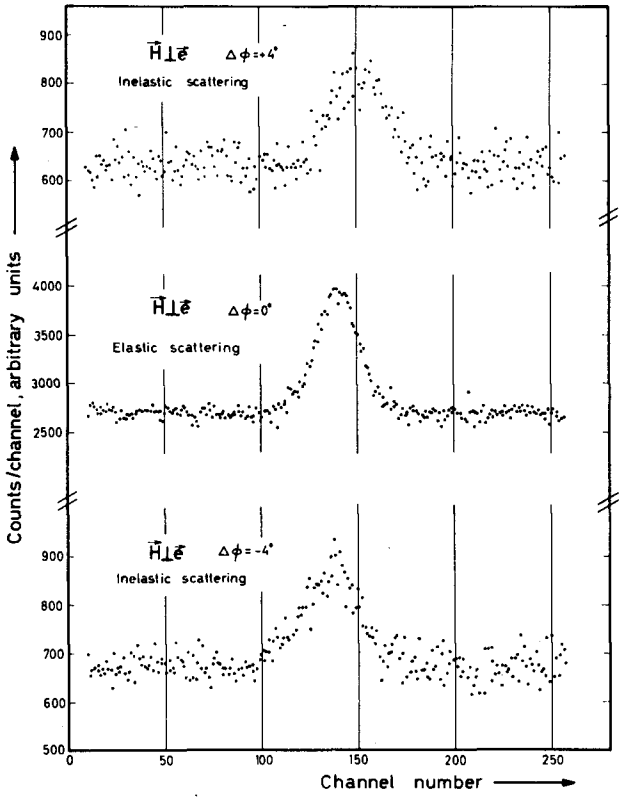

FIG.4. Time-of-flight measurements of scattered neutron energies by a flipper-chopper spectrometer for vertical field, $\vec{H} \perp \vec{e}$, and missetting angles $\Delta\Phi = \pm 4°$. The neutrons are either slowed down or speeded up in the scattering process. The time analysis of the elastic reflection (110) is shown for comparison in the middle insert.

5. EXPERIMENTAL DETERMINATION OF MAGNETIC SCATTERING AMPLITUDES FROM THE DIFFUSE REFLECTIONS

From Fig. 1. it is seen that the scattering in a diffuse reflection originates from a scattering surface in reciprocal space which surrounds the reciprocal lattice point. By studying the diffuse reflections one has therefore access to processes with momentum transfers which are different from the reciprocal lattice vectors. Increasing the angle of misset gradually the scattering surface will expand. In principle therefore, a great range of momentum transfers in all directions should be accessible.

It is seen from Eq. (4) that the cross-section for vibrational scattering is dependent upon the magnetic form factor $f(\vec{K})$ for the magnetic ions through the parameter p, the magnetic scattering amplitude. From the ratio between the scattered intensities due to vibrational scattering for positive and negative polarization it is therefore possible to find the value of $f(\vec{K})$.

It is found from the formulas and also seen from Fig. 2 that when $\vec{H} \perp \vec{e}$, spin-wave scattering still gives rise to a diffuse reflection. The scattered intensity for this field arrangement may, however, be estimated from the intensity of the polarization-dependent spin-wave scattering when $\vec{H} \parallel \vec{e}$. Scanning the diffuse reflections using polarized neutrons for horizontal and vertical field arrangement on the sample crystal makes it possible in principle to single out the intensity components caused by vibrational scattering. Background intensity caused by other scattering effects has to be subtracted. From Fig. 2 it is seen that some of this background scattering is also polarization dependent and is probably caused by magnetic incoherent scattering.

Because of the large experimental difficulties involved in such measurements, our preliminary values for the form factor obtained from vibrational scattering have large errors and differ very much from the values obtained in elastic reflections. This difference is certainly not due to any real physical effects, but is caused by the difficulties in estimating the correct background intensity. Looking away from the large systematic error introduced by such effects, our preliminary values show the right kind of variation across the diffuse reflections: the form factor decreases for larger momentum transfers.

Several interesting problems may be expected to be solved by such investigations. Especially for small scattering angles covalency effects should show up in the form factor [18]. New experiments are therefore being made under improved experimental conditions.

6. CONCLUSION

Our work has shown the great advantage and potential use of polarized neutrons for inelastic scattering experiments. The experimental difficulties are, however, much larger than for elastic scattering. With the ever increasing neutron fluxes available it seems probable that polarized neutrons will increasingly be applied in the field of inelastic scattering.

ACKNOWLEDGEMENTS

A part of this work was done at Brookhaven National Laboratory during a stay as a guest scientist under the Fulbright exchange program. The author would like to thank most sincerely the people in the Neutron Diffraction Group at BNL for all help and advice during the stay.

REFERENCES

[1] FERGUSON, G.A., Jr., SAENZ, A.W., J. Phys. Chem. Solids 23 (1962) 117.
[2] SAMUELSEN, E.J., RISTE, T., STEINSVOLL, O., Phys. Lett. 6 (1963) 47.
[3] RISTE, T., SHIRANE, G., ALPERIN, H.A., PICKART, S.J., J. appl. Phys. 36 (1965) 1076.
[4] SHIRANE, G., NATHANS, R., STEINSVOLL, O., ALPERIN, H.A., PICKART, S.J., Phys. Rev. Lett. 15 (1965) 146.
[5] ALPERIN, H.A., STEINSVOLL, O., SHIRANE, G., NATHANS, R., J. appl. Phys. 37 (1966) 1052.

[6] ALPERIN, H.A., STEINSVOLL, O., NATHANS, R., SHIRANE, G., Phys. Rev. 154 (1967) 508.
[7] PICKART, S.J., ALPERIN, H.A., MINKIEWICZ, V.J., NATHANS, R., SHIRANE, G., STEINSVOLL, O., Phys. Rev. 156 (1967) 623.
[8] SAENZ, A.W., Phys. Rev. 119 (1960) 1542.
[9] IZYUMOV, Yu.A., MALEEV, S.V., Sov. Phys. JETP 14 (1962) 1168.
[10] STEINSVOLL, O., Kjeller Rep. KR-65 (1963).
[11] IZYUMOV, Yu.A., Sov. Phys. Uspekhi 16 (1963) 359.
[12] STEINSVOLL, O., VIRJO, A., IFA Internal Work Rep. NF-5 (1967).
[13] VIRJO, A., STEINSVOLL, O., Kjeller Rep. KR-125 (1968).
[14] STEINSVOLL, O., VIRJO, A., Time-of-flight spectrometer using an electronic chopper for polarized slow neutrons, these Proceedings 2, SM-104/65.
[15] SEEGER, R.J., TELLER, E., Phys. Rev. 62 (1942) 37.
[16] LOWDE, R.D., Proc. R. Soc. Ser. A. 221 (1954) 206.
[17] WANIC, A., Nukleonika 9 (1964) 834.
[18] HUBBARD, J., MARSHALL, W., Proc. phys. Soc. 86 (1965) 561.

DISCUSSION

H. RAUCH: Your elastic flipper data show a background ratio smaller than 1 : 2, while according to the structure factor it should be better than 1 : 3. Is it possible that this discrepancy is caused by depolarization within the crystal at your field of only 3.5 kOe, which seems to be rather small? In our measurements on Co single crystals we have seen that a field higher than 5 kOe is necessary to avoid depolarization.

O. STEINSVOLL: The flipper-chopper data were obtained using a magnetic field of about 6.5 kOe across the crystal, and the depolarization was found to be low ($\approx$ 5-10%). When the experiment was performed the spectrometer was not too well optimized as regards polarization and flipping efficiency. The crystal was rather thick (6 mm), giving rise to high extinction effects for the case of elastic scattering; however, these do not influence the inelastic scattering processes. The preliminary data shown should therefore be taken only as a proof of the inelasticity of the scattering process giving rise to the polarization-dependent diffuse reflections.

S.K. SINHA: You would not in principle expect the form factor obtained from your experiments to agree with that obtained from Bragg scattering. In fact a detailed investigation of the difference would be very interesting in that it would enable one to study the deformation of the magnetic electron distribution due to the vibrational motion of the atom.

O. STEINSVOLL: Yes, this was precisely one of the reasons why we started such measurements. At our new reactor we now have an experimental set-up with a rotatable electromagnet, and this arrangement will enable us to make more reliable corrections for all the other scattering processes than was possible in the experiments reported above.

NEUTRON SCATTERING INVESTIGATION OF THE DYNAMICS OF THE CRITICAL STATE IN IRON

J. GORDON, Éva KISDI-KOSZÓ, L. PÁL AND I. VIZI
CENTRAL RESEARCH INSTITUTE FOR PHYSICS,
HUNGARIAN ACADEMY OF SCIENCES,
BUDAPEST, HUNGARY

Abstract

NEUTRON SCATTERING INVESTIGATION OF THE DYNAMICS OF THE CRITICAL STATE IN IRON. The inelasticity of critical scattering has been investigated in iron using the pulsed monochromatic neutron beam at the IBR-1 reactor in Dubna. The measurement covered the temperature range $-2.5 \times 10^{-3} \leq \tau \leq 6.5 \times 10^{-3}$ where $\tau \equiv T/T_c - 1$ and the critical temperature was approached within $\tau < 5 \times 10^{-4}$. The slight temperature dependence of the inelasticity was confirmed for $q = 5.7 \times 10^{-2}$ Å^{-1}, but the observed diffusion constant was found to be temperature independent and higher ($\mu = 16.5$) than the value ($\mu = 11$) reported earlier by other authors.

1. INTRODUCTION

Neutron scattering experiments offer one of the most powerful methods for the investigation of the critical magnetic state. Owing to its favourable magnetic and neutron scattering properties, iron has been extensively studied by this method.

The static properties of fluctuations, i.e. the temperature dependence of the correlation range and the susceptibility of iron, have been measured by several authors [1 - 4] and the correlation range and susceptibility were found to be $\xi(\tau) \sim \tau^{-0.68}$ and $\chi(\tau) \sim \tau^{-1.33}$; $\tau \equiv T/T_c - 1$, respectively.

The dynamics of the magnetic fluctuations were first studied by Van Hove [5] who introduced a thermodynamic spin diffusion model. This model predicts a slowing down of the fluctuations near the Curie temperature. A similar result was obtained from several microscopic theories [6 - 8].

The cold neutron experiments of Jacrot et al. [9] showed, however, an unexpected broadening of the energy distribution even near the Curie point. Later, Passell et al. [10] confirmed this observation and evaluated a temperature-independent spin diffusion constant as

$$2m\Lambda/\hbar = 11.0 \pm 0.6$$

This disagreement between experimental results and theory suggests that some of the processes involved have not been taken into account in the thermodynamic fluctuation model. Marshall [11] and Brout [12] have pointed out that for $q\xi > 1$, where $\hbar q$ is the momentum transfer of neutrons in the scattering process, collective excitations driven by fluctuation of magnetization may occur even above the transition temperatures.

The spin-wave-like behaviour for relatively high momentum transfer above the Néel point was observed by Nathans, Menzinger and Pickart [12] in antiferromagnetic $RbMnF_3$. No similar effect was found, however, in metallic ferromagnets.

Considering that in the recent inelastic scattering experiments the closest approach to the Curie point was $\tau = 2 \times 10^{-3}$ [10, 11], it was thought of interest to investigate the temperature dependence of the inelasticity closer to T_c.

2. EXPERIMENTAL

The spectrometer and the detection electronics together with the methods of temperature stabilization and homogenization have been already described in an earlier report [13].

The moderated neutron beam of the pulsed reactor IBR-1 is monochromatized by a magnetite monocrystal. The first order (111) reflection centred around the wavelength of 4.10 Å is used. A 24-min Soller collimator located between the monocrystal and the detector determines the wavelength resolution of the system.

The overall moderator-to-detector distance is 16.10 m, while the sample-to-detector vacuum flight path is 6.40 m. The scattered, transmitted or incident neutrons are counted by detectors of 11 cm × 13 cm surface. In the first set of experiments the detectors were located at fixed angle $\vartheta = 2.16°$. The pulses are transferred to a multichannel analyser with channel width $\theta = 16$ μsec and dead time $\tau = 25$ μsec. The analyser stores the counts of all the higher order reflections of the monocrystal and the fast neutron burst from the reactor, too. The fast neutron burst determines the '0' mark of the time scale. A 0.5 cm thick, 10 cm long and 3.5 cm wide, zone-melted 'Puron' iron sample of 99.99% purity was used with a 3 cm × 3 cm surface exposed to the neutrons. The temperature stability and homogeneity was found to be better than 0.2 deg during a 100-hour operation. The ratio of the scattered to transmitted intensity showed a maximum at $T_c = 1041°K$. Measurements were performed in 0.5 deg steps around the Curie point from $T - T_c = -1.5$ to 1.5°K and at temperatures $T_c - 2.5°K$ and $T_c + 6.5°K$.

3. DATA EVALUATION

Since the count-rate corrections and the choice of the energy and angular resolution functions play a decisive role in the evaluation of the parameters of inelasticity, the procedure used for the evaluation of the experimental data will be described in some detail.

3.1. Analyser dead-time corrections

In the case of pulsed reactors the count rate obtained during a reactor pulse may be so high as to result in an appreciable counting loss for analysers with conventional dead time. Thus it was necessary to work out a suitable method of dead-time correction. The dead-time corrections were found to be especially important in the measurement of incident beam distribution.

Assuming the neutron counts to have a Poissonian distribution the number of counts in the i^{th} channel with correction for dead time is

given by the formula

$$C_i = N \ln Y_i$$

where N is the number of reactor pulses and Y_i is given by the equation

$$Y_i = (N - m_{i-1} - m_{i-2} - m_{i-2}Y_i^k)/(N - m_i - m_{i-1}); \; K = (\tau - \theta)/\tau$$

where m_i is the measured number of counts in the i^{th} channel.

The validity of the correction was checked by comparison of the corrected spectrum data with those measured at a small count rate.

3.2. Background corrections

It was observed that a major fraction of the background of the scattered beam is due to diffuse incoherent scattering from the collimator plates. Whenever the background intensity originates from the 'forward' direction, i.e. from neutrons transmitted by the sample, the intensity has to be corrected by use of the formula

$$n_k = N_k - B_k f_k$$

where n_k and N_k are the corrected and measured intensities, B_k is the background in the k^{th} channel, respectively, f_k is the (temperature dependent) transmission factor.

3.3. Determination of the input beam parameters

Assuming a Γ-type time distribution of the neutrons which have left the moderator, the probability of a neutron count in the i^{th} channel is

$$P(t_j) \sim \sum_{j=0}^{i} t_j^{\alpha} \exp\left\{ - t_j/\tau \right\} \exp\left\{ - \left[(t_i - t_j - t_0)/\rho t_0 \right]^2 \right\} f(t_i - t_j) \qquad (1)$$

Here t_j is the time at which the neutron leaves the moderator, $t_i - t_j = c\lambda$, $t_0/c = \lambda_0$ is the maximum of the Gaussian wavelength distribution, and $f(t_i - t_j)$ is the correction for detector efficiency. The parameters α, τ, ρ and t_0 as determined by least-squares fit are $\alpha = 0.69 \pm 0.07$; $\tau = 133 \pm 10$ μsec, $\rho = 8.7 \pm 0.7 \times 10^{-3}$; $t_0 = 16420 \pm 16$ μsec. The measured distribution and the best fit are shown in Fig. 1.

3.4. Correction for angular resolution

Owing to the finite dimensions of the source, sample, detector and collimator, the measured effect is proportional to the value of the scattering cross-section averaged over all possible angles permitted by the geometry. The geometry of a system determines a weight function

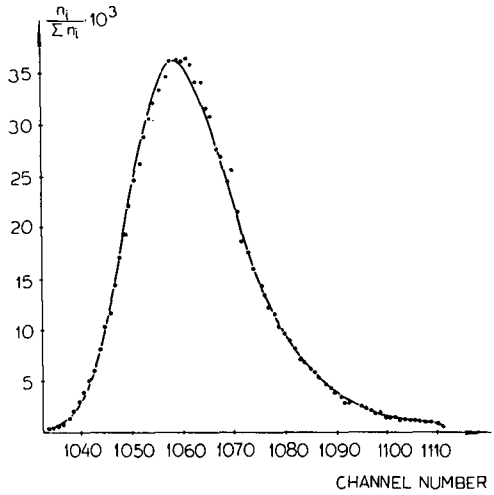

FIG. 1. Incident beam spectrum.

$A(\vartheta)$ of the scattering angles. Thus, the average cross-section is given by

$$\overline{\sigma(\vartheta)} = \int \sigma(\vartheta) A(\vartheta) d\vartheta \approx \sum_{k=1}^{m} A(\vartheta_k) \sigma(\vartheta_k) \Delta\vartheta$$

The distribution function $A(\vartheta)$ was evaluated by the Monte Carlo method for the geometry described in section 2. It proved to be sufficient to sum till m = 10. Figure 2 a shows the distribution function $A(\vartheta)$. In Fig. 2 b the cross-section $\sigma(\vartheta_{av})$ is compared with the averaged $\sigma(\vartheta) = \Sigma \sigma(\vartheta_k) A(\vartheta_k)$ as a function of the wavelength plotted on a time scale. Since the intensity of each element of the scattered beam is proportional to ϑ^2 and its half width on the wavelength scale is $\mu\vartheta^2$, it is not surprising that the averaged cross-section is narrower than the cross-section evaluated for the average angle. In our case the difference in half width is about 30%.

Two approximations implied in the above calculations have to be pointed out. First, the beam incident on the Soller collimator is taken to be isotropic. This approximation is reasonable since the angular divergence of the beam before the monocrystal is greater than that of the collimator. Secondly, λ_i is assumed to be independent of ϑ since the mosaic spread of the monocrystal is not greater than that of the collimator.

3.5. Distribution function of scattered neutrons

Assuming the inelastic scattering to be due to the diffusive motion of spins, the cross-section for small-angle scattering near T_c is given as

$$\sigma(\lambda_i, \lambda_s; \vartheta, K_1, \mu)\Delta\lambda_s = \text{const.}\, \lambda_i z x^3 \left[(K_1\lambda_i/2\pi)^2 + zx \right]^{-1} \left[\mu^2 z^2 + (x - x^{-1})^2 \right]^{-1} \Delta\lambda_s$$

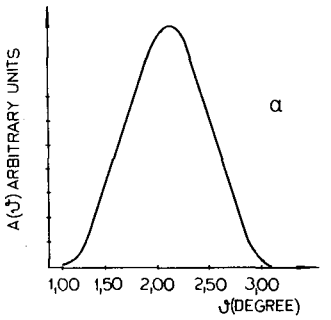

FIG. 2a. The A(ϑ) distribution function.

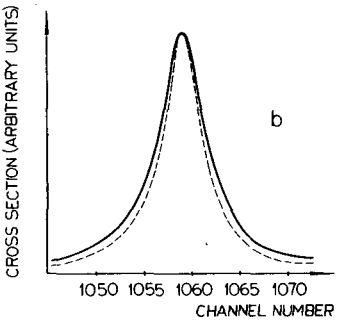

FIG. 2b. The scattering cross-section: —— without angular integration; – – – – with angular integration.

where $x = \lambda_i/\lambda_s$, λ_i being the incident and λ_s the scattered wavelength; $z = x + x^{-1} - 2\cos\vartheta$; and $\mu = \Lambda 2m/\hbar$ is the spin diffusion coefficient.

Considering that $\lambda_0 = ct_0$; $\lambda_i = c(t_i - t_j)$ and $\lambda_s = (t_\ell - t_j - \ell_R t_i)/(1-\ell_R)$ where ℓ_R is the 'reduced flight path'; $\ell_R = \ell/L$, ℓ being the sample-to-moderator, and L the moderator-to-detector distance, the experimental curve was fitted to the distribution function

$$R(t_\ell) \sim \sum_{j=0}^{i} \left[t_j^{\alpha} \exp\left\{-t_j/\tau\right\} \sum_i \exp\left\{-\left[(t_i - t_j - t_0)/\rho\, t_0\right]^2\right\} \sum_k A_k \sigma(\vartheta_k,\ t_i,\ t_j; t_\ell, K_1, \mu) \times f(t_i, t_j, t_\ell) \right] \tag{2}$$

Since in the neighbourhood of the Curie point K_1^2 does not play any important part in the evaluation of the diffusion parameter, its values were replaced by those obtained from angular distribution measurements as

$$K_1^2(T_c) = 0;\quad K_1^2(T_c - 2.5°) = 4 \times 10^{-4};\quad K_1^2(T_c + 6.5°) = 5.7 \times 10^{-4}$$

All calculated and measured distributions were normalized to unit area.

4. RESULTS AND DISCUSSION

Before evaluating the diffusion parameters by the method described in the previous section, the distribution measured at T_c was compared with that measured at T_c - 2.5°K and at T + 6.5°K using Smirnov's statistical test [14]. The distributions measured above and below the Curie point were found to be broader than that measured at T_c. The reliability of the disagreement with the Curie point curve was higher than 90%. Then, the normalized distribution (2) was fitted to the experimental curves making use of K_1^2 values listed at the end of the previous section. The calculations yielded a temperature-independent diffusion constant:

$$\mu = 16.5$$

The best fit and the experimental curve for T_c is shown in Fig. 3.

The disagreement between the diffusion constant evaluated from the present measurement and the values reported by other authors can be attributed most probably to the different procedures of data evaluation, particularly to the fact that no corrections for angular resolution have been made in the earlier calculations of the diffusion constant. It is apparent from Fig. 2a that, without correction for angular resolution, we would have $\mu = 13$, a value which is close to the recently reported $\mu = 11$ [10]. Of course, other reasons, like difference in sample purity, may also explain some of the disagreement.

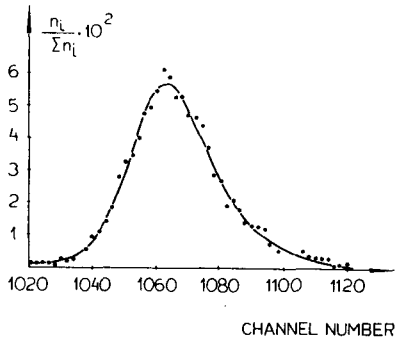

FIG. 3. Scattered neutron distribution: measured counts and the best-fit curve at $T = T_c$.

Finally, it is of interest to note that in this experiment $q\xi > 2.5$, thus the temperature-independent diffusion constant is related to processes occurring within a region of a radius smaller than the correlation length. With the present experimental technique it would be difficult to get any information about processes for which $q\xi < 1$.

REFERENCES

[1] SHULL, C. G., WILKINSON, M. K., Phys. Rev. 103 (1956) 516.
[2] LOWDE, R. D., Rev. mod. Phys. 30 (1958) 69.
[3] ERICSON, M., JACROT, B. J., Phys. Chem. Solids 13 (1960) 235.

[4] SPOONER, S., AVERBACH, B.L., Phys. Rev. 142(1966)291.
[5] Van HOVE, L., Phys. Rev. 95 (1954)1374.
[6] MORI, H., KAWASAKI, K., Progr. theor. Phys. 27 (1962) 529.
[7] De GENNES, P.G., VILLAIN, J., Phys. Chem. Solids 13 (1960)10.
[8] KAWASAKI, K., Phys. Rev. 142 (1966)164.
[9] JACROT, B., KONSTANTINOVIC, J., PARETTE, G., CRIBIER, D., Inelastic Scattering of Neutrons in Solids and Liquids (Proc. Symp. Chalk River, 1962) 2, IAEA, Vienna (1963)317.
[10] PASSELL, L., BLINOWSKI, K., BRUN, T., NIELSEN, P., Phys. Rev. 139A (1965)1866.
[11] MARSHALL, W., Critical Phenomena (Proc. Conf. Washington, D.C., 1965) National Bureau of Standards, Washington, D.C. (1966).
[12] NATHANS, F., MENZINGER, F., PICKART, S.J., Conf. Magnetism and Magnetic Materials, Boston, 1967, BNL Report No. 11634 (1967).
[13] GORDON, J., PELLIONISZ, P., VIZI, L., ZSIGMOND, G., SZKATULA, A., Nucl. Instrum. Meth. 55 (1967)151.
[14] Van der WAERDEN, B.L., Mathematische Statistik, Springer-Verlag Berlin (1957).

DISCUSSION

J. ALS-NIELSEN: Is the vertical collimation taken into account in your resolution function A (θ)?

J. GORDON: Yes, it is.

J. ALS-NIELSEN: You say that you neglected the correlation in the resolution function between energy transfer and momentum transfer. Could you please enlarge a little on your reasons for doing this, because it seems to me that this procedure can be a source of error?

J. GORDON: We do not believe that it leads to serious systematic error for the following reasons. First, if neglect of the correlation played an important role, the scattered distribution measured by the 'left-hand' and 'right-hand' detectors would be different. No such difference could be observed within the experimental error. Secondly, the systematic error partially cancels out when the distribution functions measured on both detectors are added.

R.D. LOWDE: I would like to pin you down a little more closely about exactly what happens to the diffusion constant as the temperature passes through T_c, as this question is far too important to be lumped into the remark that there is a temperature-independent diffusion parameter. There are dangerous myths in circulation about the matter already, since the analysis given at the Agency's 1962 Chalk River Symposium by the Saclay workers[1] was only purely preliminary and has only just been completed in a little-known article by Konstantinović (Bull. Boris Kidrič Inst. 17 (1966) 329). The position appears to be that the diffusion coefficient goes to zero if one makes both K and $T-T_c$ sufficiently small simultaneously. Are you able to contradict this?

J. GORDON: Not at the moment, I'm afraid, since our own investigations have not yet been taken far enough.

J. KONSTANTINOVIĆ: Permit me to add a few words in connection with Mr. Lowde's question. It is not certain that a scattering angle of 2.5° (which is the one in question) is small enough to test the scattering approximation. The instrumental resolution is also not good enough, for the uncertainty regarding the incident spectrum appears twice in the re-

[1] Inelastic Scattering of Neutrons in Solids and Liquids (Proc. Symp. Chalk River, 1962) 2, IAEA, Vienna (1963) 317.

sulting diffusion coefficient. Furthermore, we do not know the relationship linking the width of the measured spectrum with the widths of the incident and Lorentzian spectra. It appears that the diffusion coefficient decreases as the Curie point is approached, but in view of the above considerations and of the fact that the corrections made are very large it is not possible to be certain about this.

R.D. LOWDE: You mention collective modes above the Curie temperature: these were first explicitly discussed by Kawasaki in another insufficiently-known paper which appeared in 1963 (Prog. theor. Phys. 29 (1963) 156).

H. RAUCH: Why is your critical scattering spectrum not centred around the elastic line or your calculated line shown in Fig. 2b?

J. GORDON: The shift in the maximum of the scattered distribution as compared with the primary one is caused by the folding processes involved. The exponential term in the Γ-distribution function governs the shift.

H. RAUCH: I would stress that, especially at the Curie point, it is necessary to take an average over the sample temperature even when the range is only 0.2° C, and to include in this the temperature variation of κ as well. This gives a diffusion constant closer to that reported in the literature.

T. SPRINGER: As far as we know, the Curie temperature T_c depends on the purity, the crystalline structure and the dislocations and internal stresses, etc. of the sample. The presence of impurities or defects would thus induce a certain broadening of T_c, which could have a marked effect on the results of experiments very close to that point. This width of T_c could, for example, smooth out a fast change of the diffusion coefficient with T close to T_c. Was this considered when the conclusions from these data were discussed?

J. GORDON: At the Curie temperature we should be above the annealing temperature, and so the dislocations and internal stresses should not play any important part in the broadening. However, impurities may cause some additional broadening of the energy distribution, as is mentioned in the paper.

T. RISTE: At the meeting of the American Physical Society held in Washington in April 1968, Dr. Collins presented some recent work by the Brookhaven group on critical scattering in iron. The data were obtained at an extremely high resolution, and the resolution correction was carried out with the method of Cooper and Nathans. If I remember correctly, the temperature independence of the diffusion constant was confirmed and its numerical value agreed with the results of earlier work at Risø by Passell et al.

INELASTIC CRITICAL NEUTRON SCATTERING IN TERBIUM

O.W. DIETRICH AND J. ALS-NIELSEN
RISØ RESEARCH ESTABLISHMENT,
ROSKILDE, DENMARK

Abstract

INELASTIC CRITICAL NEUTRON SCATTERING IN TERBIUM. The critical neutron scattering above the Néel temperature T_N in Tb has been measured using both double-axis and triple-axis spectrometry. The parameters of the magnetic susceptibility and the spin relaxation function have been deduced in the temperature range $0.005 \lesssim (T - T_N)/T_N \lesssim 0.06$. Both the inverse correlation range κ_1, and the long wavelength susceptibility $\chi(\vec{Q})$ obey temperature power laws, with the exponents $\nu = 0.66 \pm 0.02$ and $\gamma = 1.33 \pm 0.02$, respectively. The results for the relaxation function show that thermodynamic slowing down of the spin fluctuations does occur in Tb when the temperature approaches the critical temperature.

INTRODUCTION

A neutron scattering experiment has been carried out to study the critical behaviour of the rare earth Tb above the Néel temperature. The magnetic structure of Tb has previously been investigated by neutron diffraction techniques [1, 2]. In the temperature region from 216 to 226°K Tb exhibits a magnetic phase with a spiral structure. In the spiral phase the spins are ferromagnetically aligned within the hexagonal planes of the hcp lattice, but rotate from plane to plane. The diffraction of neutrons from the spiral structure appears as satellite peaks to the nuclear Bragg reflection peaks, displaced in the direction of the hexagonal axis.

Short-range regions of spiral order persist in the disordered paramagnetic state above the Néel temperature $T_N = 226$°K. These regions give rise to broader and much less intense satellite peaks - the critical scattering. We have examined the longitudinal component of the critical scattering around a satellite of the (002) reflection. By measurements of the critical scattering using both triple-axis spectrometry and double-axis spectrometry, it has been possible to deduce the spatial spin correlation parameters and the spin relaxation parameters for temperatures in the range $0.005 \lesssim (T-T_N)/T_N \lesssim 0.06$. Results of critical scattering using a double-axis spectrometer have been reported previously [3, 4].

The experimental procedure and details of the data analysis are described and the results are discussed on the basis of the relevant theories. Special attention is given to the variation of the relaxation function as the temperature approaches T_N. The results show that thermodynamic slowing down of the spin fluctuations occurs in the close vicinity of the critical temperature, as predicted by the theory. Preliminary results on this effect have been published previously [5].

CRITICAL SCATTERING CROSS-SECTION

The cross-section for neutrons scattered magnetically from a wavevector $\vec{k}$ to a wavevector $\vec{k}'$ and from an energy E to an energy E', is generally expressed by the formula,

$$\frac{d^2\sigma}{d\Omega dE'} = \frac{N}{\hbar}\left(\frac{e^2\gamma}{mc^2}\right)\frac{k'}{k}\,|F(\vec{K})|^2 \sum_{\alpha\beta}\left(\delta_{\alpha\beta} - \frac{k_\alpha k_\beta}{k^2}\right) S^{\alpha\beta}(\vec{K},\omega) \qquad (1)$$

where $\vec{K} = \vec{k} - \vec{k}'$ and $\hbar\omega = E - E' = \hbar^2/2m(k^2 - k'^2)$. α and β denote the Cartesian co-ordinates x, y and z, the z-axis being along the spiral axis. The response function $S^{\alpha\beta}(\vec{K},\omega)$ is the Fourier transform over space and time of the spin pair correlation function, i. e.

$$S^{\alpha\beta}(\vec{K},\omega) = (2\pi)^{-1}\int_{-\infty}^{\infty} dt \sum_{\vec{R}} \exp(i\vec{K}\cdot\vec{R} - i\omega t)\,\langle S_0^\alpha(0)\, S_R^\beta(t)\rangle \qquad (2)$$

It is a reasonably good approximation in Tb to assume only scalar interactions between the spins, in which case only terms with α and β identical contribute to the cross-section. With $\vec{K}$ in the direction of the hexagonal axis, Eq. (1) further reduces to the sum of the two identical longitudinal terms S^{xx} and S^{yy}. The following calculations are confined to this case and the indices will be omitted.

$S(\vec{K},\omega)$ contains a static term, giving the Bragg scattering, and a diffusive term, describing the critical scattering. The diffusive term, $S_d(\vec{K},\omega)$, may be written in the following form [6]

$$S_d(\vec{K},\omega) = \frac{kT}{g^2\mu^2}\,\chi(\vec{K})\,\frac{\hbar\omega/kT}{1-\exp(-\hbar\omega/kT)}\,F(\vec{K},\omega) \qquad (3)$$

Here $\chi(\vec{K})$ is the wavevector dependent susceptibility, which gives the magnetic moment response to a sinusoidal magnetic field with wavevector $\vec{K}$. $F(\vec{K},\omega)$ is the wavevector and frequency-dependent relaxation function. The Fourier transform of $F(\vec{K},\omega)$ over ω, $f(\vec{K},t)$, describes the decay in time of the magnetic moment response, when the sinusoidal field is suddenly switched off at t = 0. If $\vec{K}$ equals the spiral wavevector Q of the ordered structure and if the field direction is in the basal plane, then the magnetic moment distribution created by this field will be more like the ordered structure than that for any other wavevector $\vec{K}$, and the susceptibility will achieve its maximum value $\chi(\vec{Q})$. When the field is switched off, the spin ordering with wavevector $\vec{K} = \vec{Q}$ will decay more slowly than that for any other value of $\vec{K}$.

Defining a deviation wavevector $\vec{q}$ with co-ordinates q_x, q_y and q_z as

$$\vec{q} = \vec{\tau}_{002} - \vec{Q} - \vec{K}$$

the susceptibility is expanded to second order in $\vec{q}$ around its maximum value for $\vec{q} = 0$

$$\chi(\vec{K}) \ (\kappa_1^2 + q_x^2 + q_y^2 + a^2 q_z^2)^{-1} = (\kappa_1^2 + \tilde{q}_a^2)^{-1} \tag{4}$$

The anisotropy parameter a is introduced to account for the symmetry properties of the hexagonal lattice and $\kappa_1 = \kappa_1(T)$ is the inverse correlation range.

Assuming an exponential time decay $f(\vec{K}, t) = \exp(-\Gamma(\vec{K}, T)|t|)$ for large times, $F(\vec{K}, \omega)$ will be a Lorentzian in ω for small energy transfers. $\Gamma(\vec{K}, T)$ is expanded to second order in $\vec{q}$ around its minimum value as

$$\Gamma(\vec{K}, T) = \Gamma(\vec{Q}, T) + \Lambda_x(\vec{Q}, T) \cdot (q_x^2 + q_y^2) + \Lambda_z(\vec{Q}, T) \cdot q_z^2 \tag{5}$$

The cross-section (1) for scattering around the (002-Q) satellite with small energy transfer is thus reduced to

$$\frac{d^2\sigma}{d\Omega dE'} \propto T(\kappa_1^2 + \tilde{q}_a^2)^{-1} \cdot \Gamma(\vec{K}, T)/(\Gamma^2(\vec{K}, T) + \omega^2) \tag{6}$$

Equation (6) contains 5 parameters to be determined from experimental data: the inverse correlation range $\kappa_1(T)$, the anisotropy constant a and the time decay parameters $\Gamma(\vec{Q}, T)$, $\Lambda_x(\vec{Q}, T)$ and $\Lambda_z(\vec{Q}, T)$.

MEASUREMENTS

Scan types

The measurements were performed at the DR 3 reactor at Risø. Both triple-axis and double-axis spectrometry were used to study the critical cross-section.

A triple-axis spectrometer may be set to count neutrons scattered with a certain wavevector $\vec{q}$ and a certain energy transfer ω, both subject to the limitations of the resolution of the apparatus. The measurements were carried out using a number of different types of scan. In Fig. 1 the three different types of scan performed with the triple-axis spectrometer are schematically indicated. These were ω-scans for $\vec{q} = 0$, and q-scans in the x and z direction for $\omega = 0$. Below each scan in Fig. 1 are shown three diagrams, which schematically illustrate the scattering configuration at the centre and in the wings of the scan. In the following, these scans are named type I, II and III scans. The type III scan is asymmetric due to overlapping with the nuclear (002) peak. The intensity distribution in these scans are the result of a folding of the cross-section (6) and the instrumental resolution function, which will be discussed later.

The triple-axis spectrometer scans were not sufficient to deduce the critical parameters, mainly because both $\chi(\vec{K})$ and $F(\vec{K}, \omega)$ depend

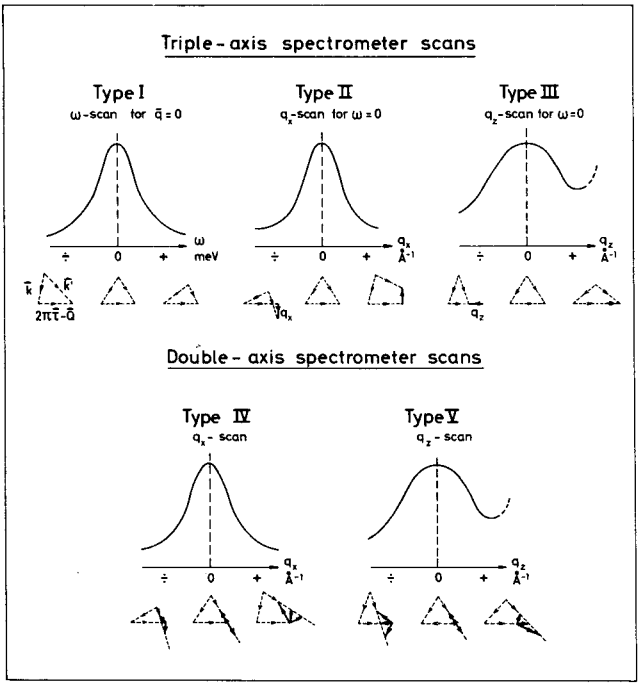

FIG. 1. The five different scan types used in the experiment. The three diagrams below each scan illustrate the scattering configuration at the centre and in the wings of the scan. The scans are numbered I - V. Notice that, for a double-axis spectrometer setting, neutrons representing different wavevector transfers are accepted by the neutron counter.

on $\vec{q}$. Therefore two independent scans were performed without energy analysis (types IV and V). In these scans, which are also taken along the x and z directions, all neutrons scattered in a certain direction are accepted by the counter. But such neutrons represent different $\vec{q}$'s and correspondingly different energies, as sketched in Fig. 1. The cross-section for a double-axis spectrometer setting is thus the integral of Eq. (6) over $\vec{q}$ and ω, taken along the direction of $\vec{k}$!

The triple-axis spectrometer measurements were carried out with a fixed incoming neutron wavelength of 2.14 Å. In the double-axis spectrometer measurements the neutron wavelength was 1.56 Å. Higher-order neutron contamination was eliminated by means of a velocity selector.

Temperature measurements

The measurement of the temperature and the temperature control have previously been described in connection with a study of the long-range magnetic order in Tb [2]. The temperature control kept the temperature of the sample stable to within ± 0.05°.

The thermocouple voltage corresponding to the critical temperature was determined by least-squares fitting of a temperature power law to the measured long-range order versus temperature curve, after correc-

tion for critical scattering and background [2]. The best fit corresponds to $T_N = 225.85 \pm 0.05°K$.

DATA ANALYSIS

The resolution function

If the triple-axis spectrometer is set at $\vec{q}_0$ and ω_0, the scattered intensity $I(\vec{q}_0, \omega_0)$ is

$$I(\vec{q}_0, \omega_0) = c \int R(\vec{q} - \vec{q}_0, \omega - \omega_0)\ \sigma(\vec{q}, \omega)\, d\vec{q}\, d\omega \tag{7}$$

for any cross-section $\sigma(\vec{q}, \omega)$. $R(\vec{q} - \vec{q}_0, \omega - \omega_0)$ is the instrumental resolution function, as given by the collimation and the mosaic spreads of the crystals. The resolution function is difficult to calculate accurately, but fortunately the Bragg-scattering cross-section is a δ-function in $\vec{q}$ as well as in ω, and R can therefore be measured with high accuracy by the line profiles of the (002-Q) long-range-order Bragg peak.

In the analysis of the critical data, the measured resolution function was approximated by the analytical expression,

$$\begin{aligned} R(q_x, q_y, q_z, \omega) \propto\ & \exp[-(q_y^2/\sigma_y^2) - (q_z^2/\sigma_z^2)] \\ & \times [(q_x^2/\sigma_x^2 + \omega^2/\sigma_\omega^2 + B(q_x/\sigma_x)(\omega/\sigma_\omega)^{+1})^{-1} - A] \end{aligned} \tag{8}$$

The values of the parameters in Eq. (8) were

$\sigma_x = 0.475 \times 10^{-2}$ Å^{-1} $\quad \sigma_z = 1.365 \times 10^{-2}$ $\quad A = 0.045$

$\sigma_y = 5.45 \times 10^{-2}$ Å^{-1} $\quad \sigma_\omega = 0.0525$ meV $\quad B = -1.943$

In the y and z directions the measured line profiles were nearly Gaussian in shape and the peak positions were independent of the settings of the other variables. There is, however, a strong correlation between q_x and ω, which is a characteristic feature of the triple-axis spectrometer and is known as the focussing effect in phonon and magnon investigations. The correlation is given in Eq. (8) by the cross-term in q_x and ω. Furthermore, the line profiles in q_x and ω had more intense tails than those of a Gaussian function, and it was appropriate to approximate the q_x and ω dependence of R as a Lorentzian function, cut off by subtraction of a constant A.

The resolution function for the double-axis spectrometer was well approximated by a product of exponentials in the variables q_x, q_y and q_z. The width parameters, similar to those of σ_y and σ_z in Eq. (8), were

$\sigma_x = 1.04 \times 10^{-2}$ Å^{-1} $\quad \sigma_y = 4.80 \times 10^{-2}$ Å^{-1} $\quad \sigma_z = 1.71 \times 10^{-2}$ Å^{-1}

Unfolding procedure

The data analysis of the critical scans was performed on an IBM 7090 computer, using an iteration procedure. The way in which each scan type depends on the critical parameters was first considered. Due to the effect of the resolution function, all parameters influence the shape of each scan, but one or two parameters are the most significant. These are indicated in Table I.

For each type of scan, preliminary values were selected for 4 of the parameters, and a least-squares fit to the measured intensities of the remaining parameter in the folded cross-section was performed. This procedure was continued until internal consistency was obtained for all 5 parameters over the temperature range of the measurements.

An example of the analysis of a type I scan is shown in Fig. 2. The filled circles are the measured intensities and the full line is the best fit of the folded cross-section, for $\hbar\Gamma(\vec{Q}, T) = 0.108$ meV. The dashed line is the unfolded intensity, which displays the importance of the resolution correction.

TABLE I. PARAMETERS IN THE DATA ANALYSIS

	Scan type	Most significant parameter	Least-squares fit parameter
Triple-axis spectr. scans	I	$\Gamma(\vec{Q}, T)$	$\Gamma(\vec{Q}, T)$
	II	κ_1 and Λ_x	Λ_x
	III	κ_1/a and Λ_z	Λ_z
Double-axis spectr. scans	IV	κ_1	κ_1
	V	κ_1/a	a

RESULTS

The results for the 5 parameters in the critical scattering cross-section are given in Figs 3, 4 and 5.

The lower part of Fig. 3 shows the inverse correlation range as a function of temperature in a double logarithmic plot. $\kappa_1(T)$ is found to vary as a power law,

$$\kappa_1(T) = 0.39\,[(T - T_N)/T_N]^{\nu} \qquad (9)$$

with $\nu = 0.66 \pm 0.02$. The uncertainty expresses the statistical scatter and does not involve possible systematic errors from the measurements. The upper part of Fig. 3 shows the anisotropy parameter a. This is within the experimental uncertainty found to be independent of temperature, with an average value $a = 0.47 \pm 0.01$.

$\Gamma(\vec{Q}, T)$ is shown in Fig. 4. This figure displays the important result that the spin fluctuations in Tb become slow when approaching

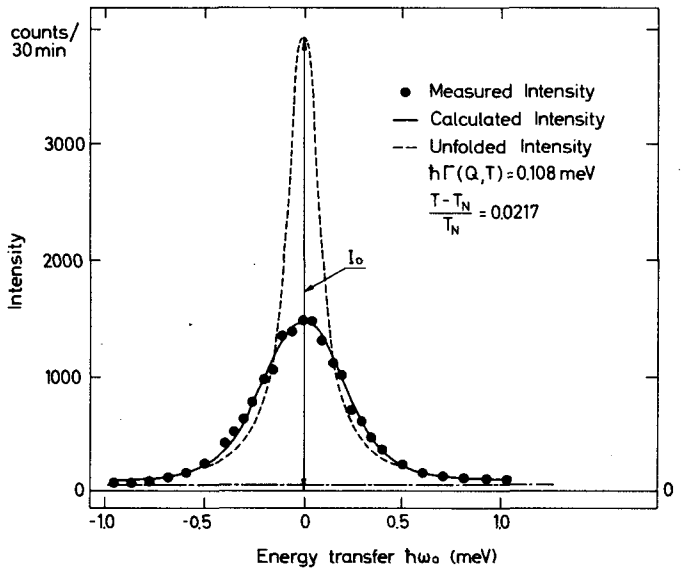

FIG. 2. Inelastic critical scattering at $(T-T_N)/T_N = 0.0217$ in a constant $\vec{q} = 0$, variable ω-scan (type I scan). The dashed-dotted line is the background count rate.

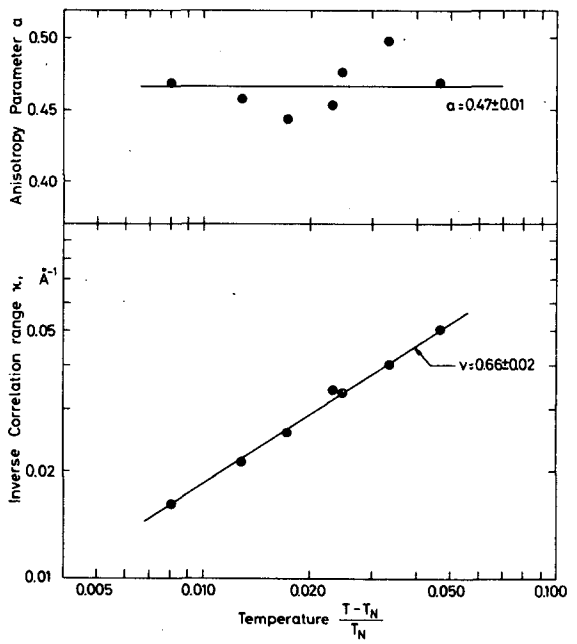

FIG. 3. Lower part: Inverse correlation range versus temperature in a double logarithmic plot. The straight line verifies the power law $\kappa_1 = 0.39\,[(T-T_N)/T_N]^{\nu}$, with $\nu = 0.66 \pm 0.02$.

Upper part: Anisotropy parameter a versus temperature. This parameter is independent of temperature within the experimental uncertainty, with an average value $a = 0.47 \pm 0.01$.

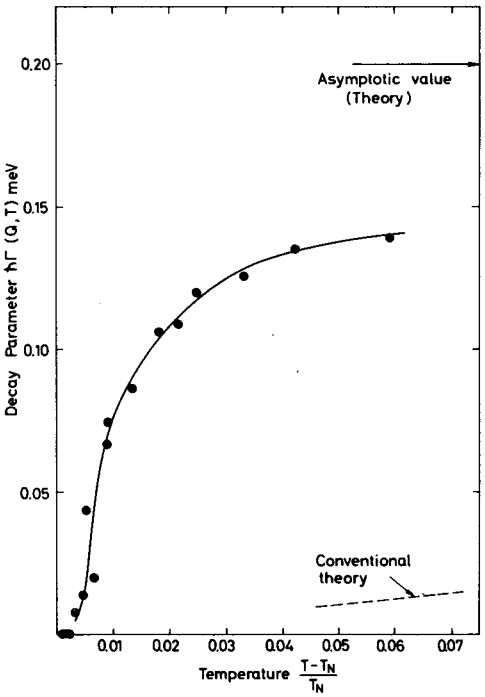

FIG. 4. Temperature variation of the time decay parameter $\Gamma(\vec{Q}, T)$. The results of the conventional theory are also shown.

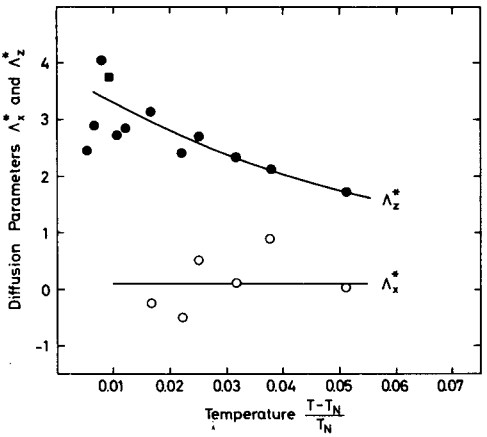

FIG. 5. Temperature variations of the time decay parameters Λ_x^* and Λ_z^*. The filled square point of Λ_z^* is the result of ω-scans for $q_z \neq 0$.

the critical temperature. This feature is expected from theory and is known as thermodynamic slowing down. The three points, shown close to T_N, were not unfolded because no broadening was observed of the corresponding scans relative to the width of the resolution function.

Therefore the points are depicted at zero energy, but it must be noticed that they are subject to the uncertainty of the resolution function width which is $\simeq$ 0.005 meV. Any detailed conclusion about how $\Gamma(\vec{Q}, T)$ tends to zero for $T \to T_N$ can therefore not be drawn from these results.

Figure 5 gives the two dimensionless diffusion parameters $\Lambda_x^* = 2m\Lambda_x/\hbar$ and $\Lambda_z^* = 2m\Lambda_z/\hbar$. Λ_x^* is the most difficult parameter to deduce of the five, due to the interrelation with κ_1 in the cross-section combined with the strong $q_x - \omega$ correlation in the resolution function. Reliable results could not be obtained close to T_N, but the results at higher temperatures seem to indicate that Λ_x^* is nearly zero independent of the temperature. Λ_z^* decreases slightly with increasing temperature from a value about 4 at T_N. As a check of the determination of Λ_z^*, 4 ω-scans were taken for q_z = 0.07, 0.10, 0.13 and 0.15 Å^{-1}, respectively. The shape of these scans depends more sensitively on Λ_z^* than the type III scans, but at the cost of intensity. The average value of Λ_z^*, as determined from these scans, is shown as a filled square in Fig. 5. The agreement with the results of the type III scans is good.

The unfolded peak intensity $I_0(\vec{q} = 0, \omega = 0)$, shown in Fig. 2, is proportional to $T\chi(\vec{Q}, T)/\Gamma(\vec{Q}, T)$. It is expected, that $T\chi(\vec{Q}, T)$ obeys a temperature power law, $T\chi(\vec{Q}, T) \propto [(T - T_N)/T_N]^{-\gamma}$, with $\gamma = 4/3$ for the Heisenberg model and $\gamma = 5/4$ for the Ising model, calculated in both cases for nearest neighbour interaction only. $T\chi(\vec{Q}, T)$ is shown in Fig. 6 in a double logarithmic plot, as calculated from the unfolded peak intensities of the type I scans and $\Gamma(\vec{Q}, T)$. A least-

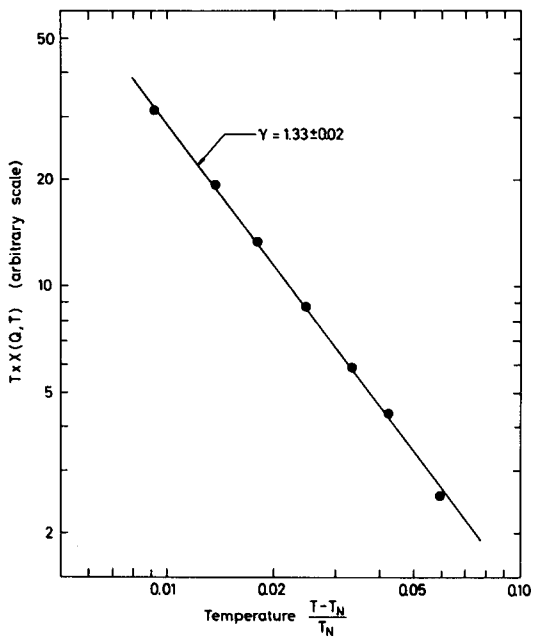

FIG. 6. Temperature variation of $T\chi(\vec{Q}, T)$, measured as the product of the unfolded peak intensities I_0 (see Fig. 2) and $\Gamma(\vec{Q}, T)$ from Fig. 4. The straight line in the double logarithmic plot verifies the power law $T\chi(\vec{Q}, T) \propto [(T-T_N)/T_N]^{-\gamma}$, with $\gamma = 1.33 \pm 0.02$.

squares fit of a power law to the points gives the exponent $\gamma = 1.33 \pm 0.02$, in excellent agreement with the result of the Heisenberg model.

Because of the involved process of analysis it has not been possible to determine reliable uncertainties in the critical parameters due to systematic errors. The sensitivity of the results to the background level and to changes in the other parameters has been tested and from this it was concluded that most of the results are reliable within 5%.

DISCUSSION

The theoretical evaluation of critical parameters and exponents has so far only been carried out for the Ising model and for the isotropic Heisenberg model, both with nearest neighbour interaction only. Although Tb is known to have highly anisotropic and long-range forces, the critical exponents measured for Tb are in excellent agreement with those evaluated for the Heisenberg model. Thus the theoretical values for ν and γ are 0.69 ± 0.02 and $\sim 4/3$, respectively [7], compared with the measured values $\nu = 0.66 \pm 0.02$ and $\gamma = 1.33 \pm 0.02$.

The anisotropy parameter a can be estimated to 0.4 in the molecular field approximation, assuming exchange interactions to third nearest neighbours only. Incidentally, this estimate is insensitive to the values of the three exchange interactions, when the condition for the stability of a spiral structure is utilized. This estimate is in reasonable agreement with the measured value of $a = 0.47 \pm 0.01$.

There is no satisfactory theoretical understanding of the fluctuation rates with time near a second-order phase transition [6], but the results for $\Gamma(\vec{Q}, T)$ can be compared with the conventional theory [5, 6] which predicts that fluctuations should slow down for thermodynamic reasons as the temperature is lowered to the critical temperature.

Approximating the ω-dependence of $F(\vec{K}, \omega)$ by a truncated Lorentzian, $\Gamma(\vec{Q}, T)$ is expressed in terms of the second and fourth-order moments as [6]

$$\Gamma(\vec{Q}, T) = \frac{\pi}{2\sqrt{3}} \frac{\langle \omega^2 \rangle^{3/2}}{\langle \omega^4 \rangle^{1/2}} \tag{10}$$

These two moments have been evaluated [5], using the exchange and anisotropy parameters for Tb determined from the measured magnon dispersion relations [8, 9]. The theoretical results are indicated in Fig. 4. This theory correctly predicts the asymptotic value $\Gamma(\vec{Q}, \infty)$, within the limits set by the uncertainties of extrapolating the experimental results and the present knowledge of the exchange and anisotropy parameters. The theory, however, predicts values for $\Gamma(\vec{Q}, T)$ which are too small by an order of magnitude for temperatures $(T - T_N)/T_N \simeq 0.06$. We conclude that, while the conventional theory is invalid except at infinite temperatures, dynamical slowing down of fluctuations does occur at a second-order phase transition, but that this effect is confined to an extremely narrow temperature range $(T - T_N)/T_N \lesssim 0.02$. Thermodynamic slowing-down was not observed in critical neutron experiments on Fe [10, 11], but has recently been reported for Ni [12] and $RbMnF_3$ [13].

ACKNOWLEDGEMENTS

The authors are indebted to Dr. W. Marshall and Mr. P.-A. Lindgård for discussions and co-operation concerning the theoretical evaluation of the diffusion parameter, and to Dr. H. Bjerrum Møller for valuable discussions on the resolution function of the triple-axis spectrometer.

REFERENCES

[1] KOEHLER, W.C., CHILD, H.R., WOOLAN, E.O., CABLE, J.W., J. appl. Phys. 34 (1963) 1335.
[2] DIETRICH, O.W., ALS-NIELSEN, J., Phys. Rev. 162 (1967) 315.
[3] DIETRICH, O.W., ALS-NIELSEN, J., Nordic Solid State Conf., Tylösand, Sweden (Aug. 1966); Conf. on Rare Earth Metals, Durham, England (Sept. 1966).
[4] ARROTT, A., WERNER, S.A., COOPER, M.J., NATHANS, R., SHIRANE, G., J. appl. Phys. 38 (1967) 969.
[5] ALS-NIELSEN, J., DIETRICH, O.W., MARSHALL, W., LINDGÅRD, P.-A., Solid State Comm. 5 (1967) 607.
[6] MARSHALL, W., in Critical Phenomena, NBS Misc. Publ. 273 (1966) 35.
[7] DOMB, C., SYKES, M.F., Phys. Rev. 128 (1962) 168.
[8] BJERRUM MØLLER, H., HOUMANN, J.C.G., Phys. Rev. Lett. 16 (1966) 737.
[9] GOODINGS, D., private communications.
[10] PASSELL, L., BLINOWSKI, K., BRUN, T., NIELSEN, P., Phys. Rev. 139 (1965) A1866.
[11] JACROT, B., KONSTANTINOVIC, J., PARETTE, G., CRIBIER, D., Inelastic Scattering of Neutrons in Solids and Liquids (Proc. Symp. Chalk River, 1962) 2, IAEA, Vienna (1963) 317.
[12] DRABKIN, G.M., ZABIDAROV, E.I., KASMAN, Ya.A., OKOROKOV, A.I., Sov. Phys. JETP 2 (1962) 336.
[13] NATHANS, R., MENZINGER, F., PICKART, S.J., Proc. Int. Conf. Magnetism, Boston (1967); J. appl. Phys. 39 (1968) 1237.

DISCUSSION

J. GORDON: Have you any explanation why the diffusion constant Λ_z rises as the critical temperature is approached?

O.W. DIETRICH: The theory does not predict thermodynamic slowing-down effects for the higher-order expansion coefficients of the decay parameter $\Gamma(K)$. From the simple theory, $\Gamma(K)$ is expected to be inversely proportional to the susceptibility $\chi(K)$, and thus from the K-dependence in $\chi(K)$ alone we expect $\Gamma(Q)$ and Λ to scale as $\Lambda = \Gamma(Q)/\kappa_1^2$. The measured ratio of $\Gamma(Q)\,\kappa_1^2$ does in fact increase when approaching T_N.

A.G. SJÖLANDER (Chairman): From talking to Professor Resibois about the time dependence of the spin-correlation function very close to the Curie point, I got the impression that asymptotic exponential decay in time may not occur. If so, this would introduce a temperature-dependent diffusion constant, though entailing an exponential decay in the correlation function. Would you comment on this?

O.W. DIETRICH: The asymptotic behaviour of the time decay of the correlation function is reflected in the shape of the frequency distribution for small energy transfers (Fig. 2 of the paper). We cannot detect any deviation from a Lorentzian shape in the unfolded frequency distributions and thus the exponential time decay is justified within the experimental uncertainty.

P.-A. LINDGÅRD: May I comment on the point raised by Mr. Gordon? In the presence of anisotropy the decay coefficient is (in the conventional theory using $1/\chi(Q-q) \sim \kappa_1^2 + q^2$) given by $\Gamma(q) = A\{\kappa_1^2 + q^2(1 + B\kappa_1^2)\} = \Gamma(Q,T) + \Lambda(Q,T)q^2$, where κ_1^2 is the short-range order parameter and A and B are constants expected to vary slowly with temperature. Therefore, at T_c $\Gamma(Q, T_c) = 0$, but $\Lambda(Q, T_c) \neq 0$. The temperature variation from these values is expected to be proportional to the inverse susceptibility. However, it would not be too surprising if the agreement with the conventional theory proved to be worse for $\Lambda(Q, T)$ than for $\Gamma(Q, T)$. One would expect that corrections due to spin-wave-type excitations, characterized by a certain wavelength dependence, would influence $\Lambda(Q, T)$ rather than $\Gamma(Q, T)$.

This provides a link with Mr. Sjölander's remark. As mentioned by Mr. Dietrich, the presence of additional poles in the relaxation function might explain the unexpected temperature dependence of the effective diffusion constant. However, a direct comparison between the experiment and the alternative theory of Resibois (which is valid, as far as I know, only for the limiting case of infinitely long-range, infinitely weak forces) may not be very relevant.

D. BALLY: Did you, Mr. Dietrich, correct your data for the vertical divergence of the beam or only for its height?

O.W. DIETRICH: The four-dimensional resolution function was measured on the Bragg-peak profiles. This function contains all the resolution corrections which have to be made to the measured intensities.

R.D. LOWDE: Allow me to do you the service of emphasizing that your new figure for γ, namely 1.33, really is an improved figure for this quantity (which you gave previously, in Ref. [5] of your paper, as 1.20), and is not just a misprint!

O.W. DIETRICH: Thank you!

SMALL-ANGLE CRITICAL MAGNETIC SCATTERING OF NEUTRONS IN Co

D. BALLY, M. POPOVICI, M. TOTIA,
B. GRABCEV AND A.M. LUNGU
INSTITUTE FOR ATOMIC PHYSICS,
BUCHAREST, ROMANIA

Abstract

SMALL-ANGLE CRITICAL MAGNETIC SCATTERING OF NEUTRONS IN Co. Angular distributions of the small-angle critical scattering of 1.25 Å neutrons in cobalt have been measured at temperatures up to 150°C above the Curie point for a large range of scattering vectors (κ = 0.03 - 0.6 Å^{-1}). The experimental data show that the asymptotic form of the instantaneous spin pair correlation function at large distances is that predicted by Fisher. The temperature dependence of the interaction range inferred from experimental data by using the Fisher correlation function is in agreement with theoretical predictions. The exponents of the temperature dependences of the reduced magnetic susceptibility and correlation range are found to be smaller in cobalt than in iron. The critical scattering data are in agreement with classical susceptibility measurements. The angular distributions at relatively large values of the scattering vector show the limited validity of the asymptotic spin correlation function. The variation with κ of the position of the maximum scattered intensity as a function of temperature is discussed.

INTRODUCTION

Neutron scattering has proved to be a useful tool for the investigation of second-order phase transitions in magnetic materials. During the last few years, critical neutron scattering measurements have been carried out in an increasing number of laboratories. An up-to-date review of the recent results can be found in Jacrot's lectures at the International Course on the Theory of Condensed Matter, Trieste, 1967 [1].

From the ferromagnetic metals of the first transition group, iron and nickel have been investigated in some detail. Information has been obtained on the spatial and temporal behaviour of spin fluctuations in these ferromagnetic metals. Some results on cobalt were reported in our previous communications [2, 3]. The aim of the present paper is to supplement these results with more detailed and accurate data on the instantaneous spin correlation function $\gamma(r) = \langle \vec{S}_0 \cdot \vec{S}_r \rangle_T$, obtained from the angular distribution measurements of the scattered neutrons. We have focused our attention on the correlation function behaviour at large distances to check Fisher's predictions [4] about its asymptotic form experimentally and to determine the temperature dependence of the susceptibility by a method different from the classical ones. To get information about the correlation function at intermediate distances, the measurements have been extended up to relatively large scattering angles.

EXPERIMENTAL METHOD

A high-purity polycrystalline cobalt sample 0.2 cm thick was heated by direct radiation in a vacuum aluminium oven capable of temperatures

up to 1300°C. The system used for sample temperature regulation and stabilization has been described in Ref. [5]. Near the critical point the uncertainty in the sample temperature was estimated to be ± 0.5°C considering the temperature dependence of the scattered intensity at the smallest angle of measurement. The angular distributions were measured using a 1.25 Å monochromatic neutron beam. The results were analysed within the static approximation. No correction for inelasticity of scattering was made because data on the spin fluctuations relaxation in cobalt are missing. Assuming the relaxation time of spin fluctuations in cobalt to be not less than that in iron as determined by Passell et al. [6], the expected changes in intensity due to the inelasticity of the scattering ought to be less than 5% at relatively small angles.

According to the explored angular range, Soller collimators with cadmium slits with 10', 30' and 60' horizontal angular divergences have been used. At the smallest scattering angles the resolution corrections (which appear to be very important) have been calculated by assuming a linear variation of inverse scattering intensity plotted against κ^2, the square of the scattering vector. The calculations were made using angular resolution functions with Gaussian forms of experimentally determined half-widths. At larger scattering angles the resolution corrections were made by Gaussian unfolding, using a successive approximation technique.

EXPERIMENTAL RESULTS

The corrected values of the inverse measured intensity for the smallest scattering angles are shown in Fig. 1 plotted against κ^2 for several temperatures above the critical one. For κ less than 0.1 $Å^{-1}$ the results obey practically a linear dependence. This can be considered as a consequence of the validity of the asymptotic correlation function in Ornstein-Zernike form $\gamma(r) \sim r_1^{-2}(e^{-k_1 r}/r)$, where the parameters r_1 and k_1^{-1} represent the effective range of direct interaction and the effective range of correlations, respectively. However, this is not the unique possibility, because Fisher has recently argued [4] that the correlation function could have the asymptotic form $\gamma(r) \sim e^{-k_1 r}/r^{1+\eta}$ leading also to a practically linear dependence of the results in Fig. 1 at small η. Because of the experimental errors it is very difficult to decide in favour of one of these correlation functions in a direct way by analysing the negative curvature of the distributions shown in Fig. 1. An indirect method of analysis has already been used for β-brass [7] and iron [8]. It consists in comparing the temperature dependences of the correlation range and of the zero-field susceptibility. The reduced zero-field susceptibility χ_0 is expected to vary as $\chi_0 \sim (1 - T_c/T)^{-\gamma}$ and the correlation range as $k_1^{-1} \sim (T - T_c)^{-\nu}$, so that $\gamma/2\nu = 1 - \eta/2$ [4].

The interpretation of the data for $\kappa^2 \leq 0.01$ $Å^{-2}$ has been performed by means of a Fisher and Burford first-order approximant [9] in the following form:

$$\chi^{-1}(\kappa, T) = r_1^2 [k_1^2 + \kappa^2/(1 - \eta/2)]^{1-\eta/2} \qquad (1)$$

where $\chi(\kappa, T)$ is the reduced scattering intensity, related to the spin correlation function by Fourier inversion. The reduced zero-field susceptibility is $\chi(0, T)$. Equation (1) corresponds to an Ornstein-Zernike correlation

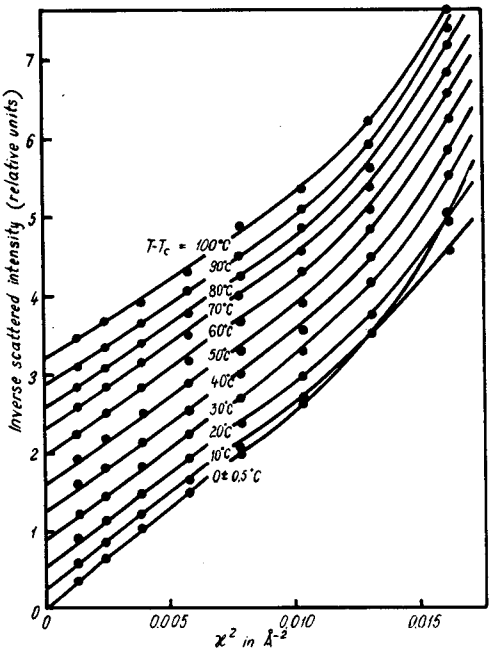

FIG. 1. Inverse of the corrected scattered intensity plotted against square of the scattering vector.

function when $\eta = 0$. Using a method of successive approximations for determining η, it was estimated that $\eta = 0.10 \pm 0.05$. The temperature dependences of the inverse correlation range and of the inverse reduced susceptibility, taken out from the experimental data using Eq. (1), are shown in Fig. 2. The value $\gamma = 1.19$ of the reduced susceptibility exponent in cobalt agrees with macroscopic results ($\gamma = 1.21$ [10] and $\gamma = 1.20$ [11]). It should be noted that the critical indices γ and ν of cobalt are considerably lower than those obtained for iron and nickel by the same method of critical neutron scattering. Our experimental data for iron, obtained with the same experimental device and analysed by the same technique as for cobalt, yield the values $\gamma = 1.34$ and $2\nu = 1.39$ leading to $\eta \cong 0.07$ [8]. The critical neutron scattering in nickel has given $\gamma = 1.30$ [1].

The indices γ and ν should be connected with the exponent β of the temperature dependence of the spontaneous magnetization near T_c by the relation (see Ref. [12] for references)

$$2\beta = 3\nu - \gamma \qquad (2)$$

obtained by assuming the equality of the critical indices below and above T_c. The value $\beta \sim 0.34$ for cobalt follows from Eq. (2). To our knowledge, direct determinations of the exponent β for cobalt have not yet been reported. However, the spontaneous magnetization data reported for cobalt [11, 13], if plotted on a logarithmic scale against $(T_c - T)$, exhibit a constant slope $\beta \sim 0.4$ for $T/T_c < 0.995$. (It should be noted that the data from Refs [11, 13] show that below T_c cubic cobalt and nickel obey practically the same reduced equation of state, while Mössbauer effect

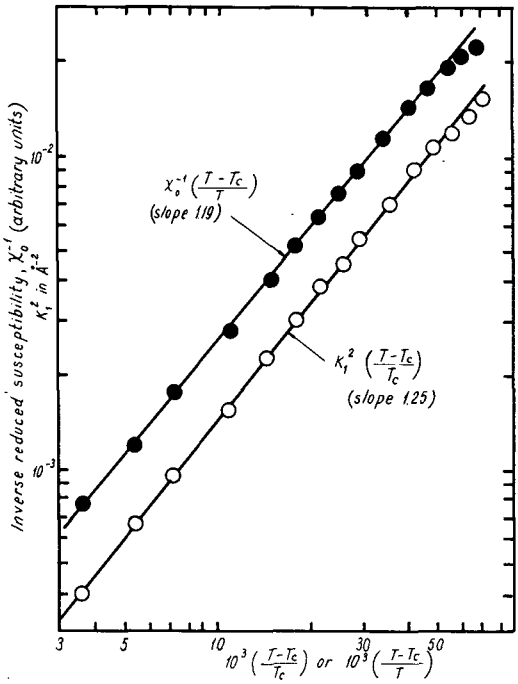

FIG. 2. Temperature variations of the reduced susceptibility and of the correlation range.

measurements showed that $\beta \sim 0.33$ in nickel for $T/T_c < 0.99$ [14].) The spontaneous magnetization data [11] suggest that the index β for iron is smaller than in cobalt and nickel, so that the value $\beta \sim 0.37$, following from neutron scattering data for iron by Eq. (2), appears plausible.

In Fig. 3 the reciprocal of the correlation ranges for Co, Ni and Fe, obtained from neutron scattering measurements, is plotted against $(T/T_c - 1)$ as ak_1 (a being the nearest neighbour distances: 2.55 Å in Co, 2.50 Å in Ni and 2.52 Å in Fe at temperatures near T_c). The data for cobalt and iron [8] have been obtained with the same device, while for nickel we used data from Ref. [15] where a somewhat different measuring technique was used.

The solid lines in Fig. 3 represent the theoretical predictions for ak_1 obtained in several approximations (De Gennes and Herpin [16] in the mean field approximation, Elliott and Marshall [17] and Fisher and Burford [9] for the $\frac{1}{2}$ spin Ising model for fcc and bcc lattices).

Although the Ising model is an over-simplified representation of the real physical picture, the results of Fisher and Burford [9] are capable of describing the values as well as the temperature dependence (they predict $2\nu \sim 1.29$) of the observed correlation ranges.

The temperature dependence of the interaction range is plotted against T/T_c in Fig. 4 as r_1^2/r_{1c}^2 (r_{1c} being the value of r_1 at $T = T_c$). The solid line represents the dependence $r_1^2 \sim T^{-1}$ roughly predicted by all the theories considered above. The values plotted in Fig. 4 have been deduced from the same experimental data by assuming first $\eta = 0$ and then $\eta = 0.1$.

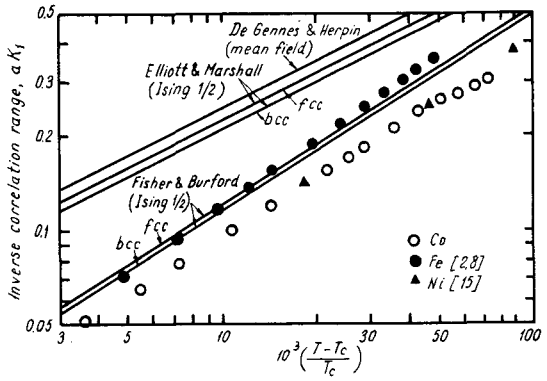

FIG.3. Temperature dependence of the inverse correlation range in Co, Ni, Fe(see text for explanation).

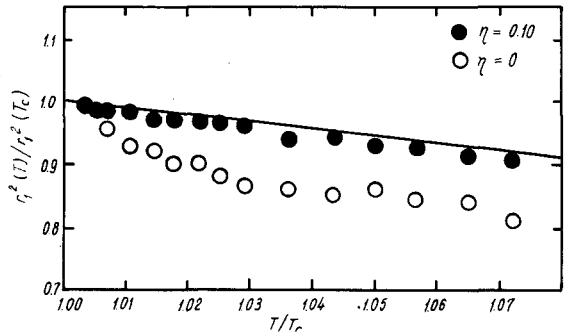

FIG.4. Temperature variation of the interaction range obtained by assuming $\eta = 0$ (○) and $\eta = 0.1$ (●). The solid line is the dependence $r_1^2 \sim T^{-1}$.

It appears that taking the non-zero value of η into account cancels out almost completely the deviations from theoretical in the temperature dependence of r_1 observed over the years in all measurements of critical scattering interpreted by means of the Ornstein-Zernike correlation function.

The theoretical values of the interaction range r_1 are rather insensitive both to calculation methods and to the crystal lattice. For the above-mentioned calculus approximations the results range between $r_{1c}/a = 0.408$ (mean field [16]) and $r_{1c}/a = 0.448$ (bcc Ising $\frac{1}{2}$ spin [9]).. All these calculations predict the equality (within 2%) of the interaction ranges r_{1c} for cobalt and iron.

The absolute values of the interaction ranges can be deduced either from the absolute measurements of the differential cross-section or by comparison of the relative scattering measurements with magnetic susceptibility data.

By using the measured values of the susceptibility [10, 11] (giving $\chi_0 = 10^{13}$ at $T-T_c \sim 7.5°C$) together with our data on the correlation range k_1^{-1}, the value $r_{1c}/a = 0.43 \pm 0.04$ for cobalt has been obtained from Eq.(1). The imprecision is due mainly to the uncertainty in the value of η used in this calculation.

The same procedure has been applied for iron by using the magnetic susceptibility data [18, 19] (indicating $\chi_0 = 10^{13}$ at $T-T_c \sim 5°C$) together with our data for the correlation range. It has been found that $r_{1c}/a = 0.39 \pm 0.04$. The direct determinations of r_{1c} in iron, performed by calibrating the critical scattering cross-section, yield the values $r_{1c}/a = 0.42 \pm 0.02$ [20] and $r_{1c}/a = 0.38$ [21].

A cross-verification of these data has been possible by comparing the intensities scattered by iron and cobalt for the same experimental set-up. The ratio of the differential cross-sections of cobalt and iron at T_c for the smallest scattering angles has been found to have a constant value of $\sim 2/3$, i.e. the squared calculated effective paramagnetic moment ratio of cobalt to iron. It follows that the interaction ranges at T_c have approximately the same value in both these ferromagnetic materials. The larger value of the interaction range in cobalt than in iron reported earlier [3] was due to considerable evaporation of the cobalt sample during the long-time measurements which was not taken into account.

By considering again the inverse angular distributions in Fig. 1, we note that the isotherm for $T = T_c$ intersects the other ones. This effect has been observed for iron too [2] and it has found a qualitative theoretical basis in the recent calculations of Fisher and Burford [9]. However, the experimental data show a stronger than theoretically predicted κ dependence of the maximum scattered intensity shift towards higher temperatures (Fig. 5).

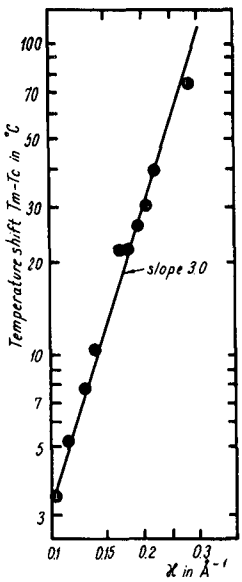

FIG. 5. Logarithmic plot of the temperature shift of the maximum scattered intensity against the value of the scattering vector.

This is not surprising because the data in Fig. 5 refer to large scattering angles where a deviation from the linearity of the data in Fig. 1 is observed. This deviation is not predicted by the theoretical calculations made in Ref. [9] (most probably because they neglect the interaction between more distant neighbours). It points out the limits of the validity of the asymptotic correlation function and can be described by including a κ^4 term in the inverse differential cross-section. From the uncorrected data for large scattering angles, the preliminary figure of about 30 Å^2 was obtained for

the ratio between the coefficients of the κ^4 and κ^2 terms in the angular distributions at temperatures near the critical one, by neglecting the non-zero value of η. This figure, which is a measure of the importance of the long-range couplings in the spin system, is to be compared with the reported values of 29 Å^2 for iron and 110 Å^2 for nickel [16].

More complete results concerning the spin pair correlation function in cobalt will be published.

REFERENCES

[1] JACROT, B., Int. Course Theory of Condensed Matter, Trieste, 1967.
[2] BALLY, D., GRABCEV, B., POPOVICI, M., TOTIA, M., LUNGU, A.M., Int. Congr. Magnetism, Boston, 1967.
[3] BALLY, D., POPOVICI, M., TOTIA, M., GRABCEV, B., LUNGU, A.M., Phys. Lett. 25A (1967) 595.
[4] FISHER, M.E., J. Math. Phys. 5 (1964) 944.
[5] TARINA, E., TIMIS, P., Rev. Roum. Phys. 12 (1967) 545.
[6] PASSELL, L., BLINOWSKI, K., BRUN, T., NIELSEN, P., Phys. Rev. 139 (1965) A1866.
[7] DIETRICH, O.W., ALS-NIELSEN, J., Phys. Rev. 153 (1967) 711.
[8] BALLY, D., POPOVICI, M., TOTIA, M., GRABCEV, B., LUNGU, A.M., Phys. Lett. (in press).
[9] FISHER, M.E., BURFORD, R.J., Phys. Rev. 156 (1967) 583.
[10] COLVIN, R.V., ARAJS, S., J. Phys. Chem. Solids 26 (1965) 435.
[11] GEISSLER, K.K., LANGE, H., Z. angew. Phys. 21 (1966) 357.
[12] FISHER, M.E., J. appl. Phys. 38 (1967) 981.
[13] MYERS, H.P., SUCKSMITH, W., Proc. R. Soc. Ser. A 207 (1951) 427.
[14] HOWARD, D.G., DUNLAP, B.D., DASH, J.G., Phys. Rev. Lett. 15 (1965) 628.
[15] JACROT, B., KONSTANTINOVIC, J., PARETTE, G., CRIBIER, D., Inelastic Scattering of Neutrons in Solids and Liquids (Proc. Symp. Chalk River, 1962) 2, IAEA, Vienna (1963) 317.
[16] DE GENNES, P.G., HERPIN, A., Comptes R. 243 (1956) 1611.
[17] ELLIOTT, R.J., MARSHALL, W., Rev. mod. Phys. 30 (1958) 75.
[18] ARAJS, S., COLVIN, R.V., J. appl. Phys. Suppl. 35 (1964) 2424.
[19] NOAKES, J.E., TORNBERG, N.E., ARROTT, A., J. appl. Phys. 38 (1966) 1264.
[20] GERSCH, H.A., SHULL, C.G., WILKINSON, M.K., Phys. Rev. 103 (1956) 525.
[21] SPOONER, S., AVERBACH, B.L., Phys. Rev. 142 (1966) 291.
[22] BALLY, D., GRABCEV, B., LUNGU, A.M., POPOVICI, M., TOTIA, M., J. Phys. Chem. Solids 28 (1967) 1947.

DISCUSSION

J. ALS-NIELSEN: The scaling law $2\beta = 3\nu - \gamma$ (Eq. (2) of your paper) worries me, because it does not hold for the two-dimensional Ising model, for which an exact solution exists, or for the three-dimensional Ising model, for which fairly accurate values have been found by series expansion techniques. Would you care to comment on this?

D. BALLY: The γ and ν parameters, determined from analysis of the experimental data using Fisher's results, correspond to the real ferromagnetic and not to the simplified model; that is, the initial model is not so restrictive for all the conclusions.

T. SPRINGER: Mr. Bally's curves showing the temperature dependence of the scattered intensity for a fixed scattering vector κ close to T_c prompt me to mention that at our laboratory Drs F. Maier and N. Stump have found the same qualitative behaviour for nickel, namely: (1) the characteristic shift of the position of the intensity maximum with changing κ; and (2) the second peak shown at smaller κ values. Interpreting this peak as

being due to spin waves with a square dispersion law, one can extract the stiffness constant, and its value agrees quite well with the results obtained by Stringfellow at Harwell.

J. GORDON: We have observed that phonon scattering, which increases with temperature, may also cause an effect similar to this shift of intensity maxima with changing κ. It would be a good idea to perform inelastic scattering investigations in order to separate the phonon and magnetic critical scattering effects.

R.D. LOWDE (Chairman): You mentioned, Mr. Bally, in your oral presentation, that you are interested in examining your "second maximum". This maximum is believed to be due to the spin waves, which are still very prominent at that point below the Curie temperature. Originally confined to a very small angle, they broaden out and cut across the scattering angle, thus producing first a rise and then a fall in the intensity. This is in fact what you term the "second maximum".

A good way of studying this – which we have adopted at Harwell – is to use the small-angle scattering technique, involving the taking of difference counts. Indeed, addressing himself to this very problem, Stringfellow has recently made a study of these phenomena in iron and nickel. He examines the spin-wave scattering by means of difference counting, and corrects for the critical magnetic dependence using the thermodynamic discussion of the French school, which we find adequately fits the facts.

We thus have here a method of separating this kind of scattering into components before we start asking what happens to the individual components as a function of various factors.

SPIN CORRELATIONS IN ONE, TWO AND THREE-DIMENSIONAL HEISENBERG PARAMAGNETS

C.G. WINDSOR
ATOMIC ENERGY RESEARCH ESTABLISHMENT,
HARWELL, DIDCOT, BERKS., ENGLAND

Abstract

SPIN CORRELATIONS IN ONE, TWO AND THREE-DIMENSIONAL HEISENBERG PARAMAGNETS. The spin correlations $\langle \vec{S}_0(0)\cdot\vec{S}_R(t)\rangle$ within a finite lattice of several thousand classical spins have been calculated by solving numerically the equation of motion of an initially random set of spins interacting through nearest-neighbour Heisenberg exchange interactions. Previous results on a simple cubic lattice have been extended to include all neighbours with separations up to three lattice spacings. The Fourier transformation over space and time to give the wavevector and frequency dependent scattering function $\mathscr{S}(\vec{q},\omega)$, may now be made to within a resolution in frequency of order $2JS/\hbar$. This function is closely related to the neutron scattering cross-section involving a momentum transfer $\hbar\vec{q}$ and an energy transfer $\hbar\omega$, and the calculations are compared with experimental measurements by Windsor, Briggs and Kestigian on a single crystal of $RbMnF_3$. Since the Hamiltonian of this salt is well known, this comparison may be made on an absolute scale without further parameters.

Similar calculations with a square lattice in two dimensions and with a linear chain have proved rather easier to compute with accuracy, on account of the smaller number of neighbours which contribute appreciably to the correlations within a given time. The results for a linear chain are compared with the quantum mechanical calculations of Carboni and Richards on a linear chain of ten spin half-particles.

1. INTRODUCTION

Van Hove [1] showed that the wavevector and frequency dependent scattering function $\mathscr{S}(\vec{q},\omega)$, which is closely related to the neutron inelastic scattering cross-section involving a momentum transfer $\hbar\vec{q}$ and an energy transfer $\hbar\omega$, may be expressed as the Fourier transformation over space and time of the pair correlation functions $\langle \vec{S}_0(0)\cdot\vec{S}_R(t)\rangle$. These functions give the probability that any given spin in a lattice is parallel to a neighbouring spin distant $\vec{R}$ observed at a later time t, and provide a more physical description of the dynamics of a spin system.

In the present case of a Heisenberg paramagnet at infinitely high temperatures, certain properties of the correlation functions are known from theoretical considerations. These properties have recently been reviewed by Marshall and Lowde [2]. In particular, the method of moments [2, 3] gives an expansion of the correlations useful at small times, while the diffusion method [3-5] gives an approximate expression for the correlations appropriate to large times.

The present method sets up a computer model of a Heisenberg paramagnet consisting of a few thousand classical spins interacting through nearest-neighbour exchange forces. The equation of motion of an initial random set of spins is then solved numerically and the pair correlations between an initial set of spin directions and the current directions evaluated as a function of time for various types of neighbour. Some preliminary results using the method have been given in an earlier paper [6]. The extension of the method to finite temperatures has been given by Vineyard,

Watson and Blume [7], while Carboni and Richards [8, 9] have solved the formidable difficulties of a quantum mechanical calculation in the case of a linear chain of ten spins. In the present paper the method and the results for a simple cubic lattice will be discussed. Space forbids more than a brief discussion of the results in one and two dimensions.

2. THE CALCULATION

An array of spin vectors of unit length was indexed according to a simple cubic, square, or linear lattice. The size of the array used was a compromise between statistical accuracy of the results and computing time and was not in this case limited by storage capacity. A set of initial spin directions corresponding to an infinite temperature was constructed using a pseudo-random number generator. The random character of the spin directions produced was in all cases checked by evaluating the averages $\langle \hat{S}_\alpha \rangle$ and $\langle S_\alpha^2 \rangle$ with α = x, y and z, which approached the values 0 and $\frac{1}{3}$ respectively.

The equation of motion of the spins is determined by the commutator of each individual spin $\vec{S}_R$ with the Hamiltonian

$$\frac{d\vec{S}_R}{dt} = \frac{i}{\hbar} [\mathscr{H}, \vec{S}_R] \tag{1}$$

In the case of a nearest-neighbour, isotropic exchange Hamiltonian

$$\mathscr{H} = \sum_{i>j} 2J\vec{S}_i \cdot \vec{S}_j \tag{2}$$

it is found that the commutator vanishes unless site R equals either i or j so that the sum over all pairs of spins reduces to a sum over those sites R' nearest neighbour to R, and the commutator can be evaluated to give the cross product

$$\frac{d\vec{S}_R}{dt} = -\frac{2J}{\hbar} \sum_{R' \text{nn} R} \vec{S}_R \times \vec{S}_{R'} \tag{3}$$

During a short finite Δt the change $\Delta\vec{S}_R$ in the unit vector on site R is then given by

$$\Delta\vec{S}_R = -\frac{2JS}{\hbar} \Delta t \sum_{R' \text{nn} R} \hat{S}_R \times \hat{S}_{R'} + O(\Delta t)^2 \tag{4}$$

When the spin changes $\Delta\vec{S}_R$ have been evaluated for all spins in the lattice, the spin vectors are updated and the whole procedure repeated. It is convenient to measure time in units of $\hbar/2JS$, the precession time of a spin in the molecular field of a neighbouring spin. For the motion to be accurately followed, it is necessary that the time increment Δt be a small fraction of this unit as each evaluation of Eq. (4) introduces an error of order $\frac{1}{2} z(2JS\,\Delta t/\hbar)^2$ in the spin directions, where z is the number of nearest neighbours. In nearly all the results presented here the value Δt = 0.005

time units has been used which, if the motion is followed for say four complete units of time, introduces a cumulative error of order 6% in the spin directions. Periodic boundary conditions were applied and to avoid any spurious effects resulting from this procedure the pair correlations considered were limited to neighbours whose separation was less than 20% of the lattice dimension.

In a classical system the expectation value occurring in the expression for the pair correlations may be interpreted as a straightforward average taken over all neighbours of the same type occurring in the lattice. Since the individual terms in the expectation value are of order unity, the statistical accuracy of the results depends on the number of terms in the average. If the lattice contains N spins and if there are Z_R neighbours of separation R to any given spin, then the statistical accuracy of the expectation value will be $(NZ_R)^{-\frac{1}{2}}$. This may be reduced by a factor $n^{\frac{1}{2}}$ by repeating the calculation n times with different initial spin configurations and averaging the results together. This procedure is inferior to an increase in lattice size, if this is possible, but is useful if computing time considerations necessitate the breakdown of the calculation into separate stages, or if storage capacity is limited.

To find the scattering function from the pair correlations, it is necessary to perform numerical Fourier transformations over space and time. The space transform gives a q and t dependent correlation function

$$\langle \vec{S}_{-\vec{q}}(0) \cdot \vec{S}_{\vec{q}}(t) \rangle = \sum_{R} e^{i\vec{q}\cdot\vec{R}} \langle \vec{S}_0(0) \cdot \vec{S}_R(t) \rangle \qquad (5)$$

where

$$\vec{S}_{\vec{q}}(t) = \sum_{R} e^{i\vec{q}\cdot\vec{R}} \vec{S}_R(t) \qquad (6)$$

This function is related to the relaxation function [2], since it describes the response of the spin system to a perturbation of wavevector $\vec{q}$. In practice it is only possible to perform the sum over R in the transform over a limited number of neighbours whose pair correlations have been computed. At small times this is not a serious limitation since the correlations decay rapidly with distance, however, as the time is increased the contribution to the sum from the more remote neighbours becomes appreciable. This may be seen by considering the computed function for $\vec{q} = 0$ which is simply the sum of the correlations over all neighbours $\Sigma_R \langle \vec{S}_0(0) \cdot \vec{S}_R(t) \rangle$. Conservation of total spin requires that, if all neighbours are included, this must be independent of time with the value $S(S+1)$. In practice it falls off from this value only after some characteristic time t_1 which increases as the number of neighbours included in the sum is increased. The computed space transform is thus only reliable at times up to t_1.

The scattering function $\mathcal{S}(\vec{q},\omega)$ can be obtained from $\langle \vec{S}_{-\vec{q}}(0) \cdot \vec{S}_{\vec{q}}(t) \rangle$ by a Fourier transformation over all time

$$\mathcal{S}(\vec{q},\omega) = \frac{1}{\pi} \int_0^\infty e^{-i\omega t} \langle \vec{S}_{-\vec{q}}(0) \cdot \vec{S}_{\vec{q}}(t) \rangle \qquad (7)$$

TABLE I. SPIN CORRELATIONS $Z_R \langle \vec{S}_0(0) \cdot \vec{S}_R(t) \rangle$ FOR A SIMPLE CUBIC PARAMAGNET

$t \times \frac{2JS}{\hbar}$	R = 000	100	110	111	200	210	211	220	221	222
0.0	1.000	0.000	-0.001	-0.004	-0.004	0.034	0.004	-0.031	0.062	0.006
0.2	0.926	0.073	-0.004	-0.003	-0.002	0.030	0.017	-0.026	0.049	0.008
0.4	0.736	0.250	+0.006	+0.001	+0.005	0.020	0.034	-0.014	0.034	0.008
0.6	0.503	0.424	0.048	0.010	0.020	0.012	0.040	+0.001	0.018	0.006
0.8	0.308	0.511	0.129	0.020	0.039	0.013	0.036	0.011	0.008	0.006
1.0	0.180	0.498	0.223	0.035	0.058	0.024	0.040	0.014	0.011	0.004
1.2	0.110	0.424	0.298	0.055	0.072	0.046	0.025	0.013	0.022	0.001
1.4	0.076	0.335	0.332	0.079	0.077	0.073	0.032	0.013	0.028	-0.002
1.6	0.060	0.265	0.328	0.101	0.072	0.104	0.056	0.017	0.022	-0.001
1.8	0.050	0.217	0.304	0.115	0.063	0.136	0.086	0.020	0.011	0.005
2.0	0.043	0.185	0.272	0.117	0.058	0.162	0.112	0.025	0.007	0.013
2.2	0.037	0.163	0.241	0.111	0.056	0.181	0.125	0.027	0.012	0.017
2.4	0.034	0.144	0.216	0.102	0.054	0.196	0.128	0.028	0.019	0.017
2.6	0.031	0.128	0.198	0.093	0.050	0.202	0.128	0.030	0.023	0.016
2.8	0.028	0.115	0.180	0.085	0.041	0.203	0.133	0.031	0.031	0.012
3.0	0.025	0.105	0.161	0.080	0.032	0.205	0.137	0.025	0.054	0.006
3.2	0.023	0.095	0.143	0.076	0.028	0.203	0.136	0.022	0.074	0.003
3.4	0.020	0.089	0.126	0.070	0.030	0.192	0.137	0.029	0.097	0.004
3.6	0.016	0.082	0.113	0.062	0.036	0.163	0.140	0.044	0.108	0.009
3.8	0.013	0.076	0.107	0.054	0.036	0.137	0.149	0.060	0.116	0.017
4.0	0.013	0.068	0.103	0.049	0.038	0.119	0.137	0.072	0.119	0.026
ERROR	0.005	0.013	0.018	0.014	0.013	0.025	0.025	0.018	0.025	0.014
Z_R	1	6	12	8	6	24	24	12	24	8

Difficulty occurs in evaluating the integral as in practice the correlations may only be computed up to some finite time t_0, and the decay of the correlations at large times may be rather slow. A simple truncation of the integral at time t_0 is unsatisfactory since this creates spurious structure in the transform. While an extrapolation of the pair correlations to infinite times with the $t^{-\frac{1}{2}d}$ time dependence predicted by diffusion theory in d dimensions is quite possible, this is hardly worth while since in practice t_0 is comparable with the characteristic time t_1 defining the time over which the space transform is reliable. In these circumstances the resolution of the energy transform is in any case of the order of $\hbar\pi/t_0$ and the truncation problem may be solved by including in the integrand of Eq. (7) a factor $\sin(\pi t/t_0)/\pi t/t_0$. This factor reduces to zero at $t = t_0$ and provides a degree of smoothing consistent with the truncation [10].

3. RESULTS FOR A SIMPLE CUBIC LATTICE

The pair correlations presented in Table I and shown in Fig. 1 were obtained by averaging the results of some 32 runs each with different initial spin configurations and with lattices containing between 1000 and 4096 spins. The number of neighbours whose correlations were calculated was variable and although neighbours out to 111 were always included, those between 200 and 222 were included in only about half the runs, and their correlations are therefore less accurate.

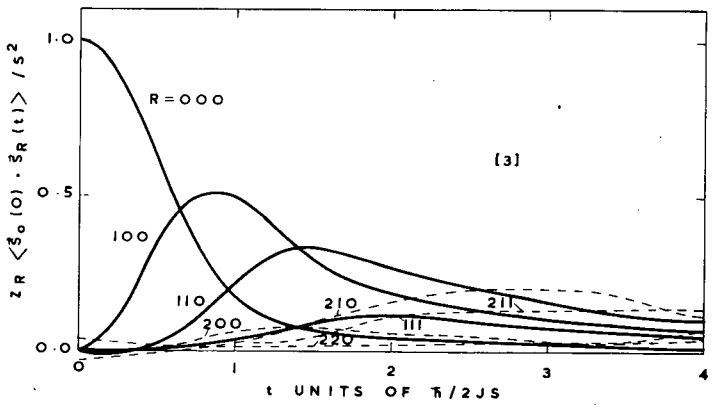

FIG. 1. The R and t dependent spin correlations for a simple cubic lattice. The curves are multiplied by the number of neighbours Z_R.

It is seen that, allowing for statistical error, all the correlations are positive. This is also observed in the results for one and two-dimensional lattices and appears to be a general result at infinite temperatures. At time zero the results confirm that all correlations other than the self term are zero. At small times they confirm the predictions of the moments theory [2] that the self-correlation function is parabolic with a curvature equal and opposite to that of the nearest-neighbour function, while the curvature of correlations with other neighbours is vanishingly small. The decay of the correlations at large times is close to that predicted by the

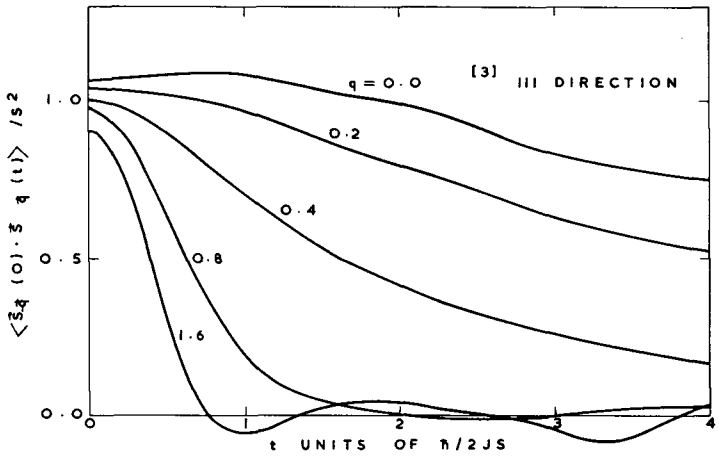

FIG. 2. The $\vec{q}$ and t dependent correlation function for a simple cubic lattice, for various values of $\vec{q}$, in units of π/a_0, along the 111 direction.

theory of spin diffusion in a quasi-continuous medium [1], where the correlations have the form

$$\langle \vec{S}_0(0)\cdot\vec{S}_R(t)\rangle = a_0^3 S(S+1)\exp(-R^2/4\pi\Lambda t)(4\pi\Lambda t)^{-3/2} \qquad (8)$$

where a_0 is the lattice constant. Agreement with the computed correlations is very poor at small times but at the largest times computed there is fair agreement if a diffusion constant $\Lambda = (0.35 \pm 0.03)2JSa_0^2$ is assumed. The coefficient here is close to the value 0.33 predicted by the theory of Mori and Kawasaki [4].

Figure 2 shows the correlation function $\langle \vec{S}_{-\vec{q}}(0)\cdot\vec{S}_{\vec{q}}(t)\rangle$ evaluated using Eq. (5) with the summation limited to the 125 neighbours within a cubic shell with corners at 222. The fact that the curve for $\vec{q} = 0$ remains within 10% of unity for times up to 2.6 units of $\hbar/2JS$ indicates that over this period the contribution from more distant neighbours than those included is not important. The irregularities in this curve and the fact that it passes above unity at small times are due to a statistical error of about 8%. This is much larger than the error on the pair correlations since a sum over many terms, each with its own error, is involved. At finite $\vec{q}$ the correlation function decays with time and shows features of the $\exp(-\Lambda q^2|t|)$ dependence predicted by diffusion theory. In particular the steepest gradient of the curves is nearly proportional to q^2 for small values of q and suggests a diffusion constant $\Lambda = 0.25\ 2JSa_0^2$. However other features in the curves demonstrate breakdown of diffusion theory. At small times the correlation function has zero gradient at all $\vec{q}$ vectors as predicted by the moments theory. Also the function is periodic in $\vec{q}$ and near the zone boundary has an oscillatory structure with negative regions. Although the statistical accuracy of this structure is questionable, the much more accurate results obtained in case of a linear chain also show these features.

Figure 3 shows the function $\mathcal{S}(\vec{R},\omega)$ obtained by Fourier transformation of the pair correlations over time. The curves have only a very small statistical error but the truncation of the correlations at $t_0 = 4\hbar/2JS$

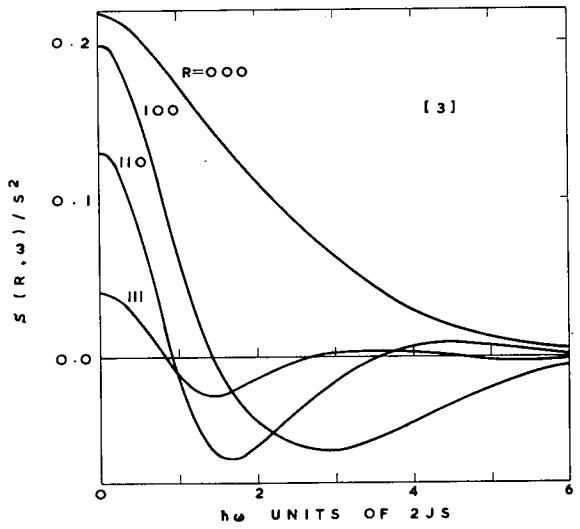

FIG.3. The R and ω dependent correlation function for a simple cubic lattice, in units of $(2JS)^{-1}$.

causes the resolution in energy to be limited to about 2JS. The curve labelled R = 0 represents the neutron scattering function from a polycrystalline specimen at large wavevectors [6], and since it represents a cross-section, it is necessarily positive.

Lastly the Fourier transform over time of $\langle \vec{S}_{-\vec{q}}(0) \cdot \vec{S}_{\vec{q}}(t) \rangle$, or equivalently the space transform of $\mathcal{S}(\vec{R}, \omega)$, gives the Van Hove scattering function $\mathcal{S}(\vec{q}, \omega)$. The dashed curves of Fig. 4 show the computed transforms for various $\vec{q}$ vectors along the 110 direction in reciprocal space, and have been scaled so that they may be compared with experimental measurements by Windsor, Briggs and Kestigian [11] on paramagnetic $RbMnF_3$. This simple cubic antiferromagnet has largely nearest-neighbour Heisenberg interactions (J = 0.28 meV) and a large spin (S = 5/2) and so approximates closely to the present Hamiltonian, and since the scattering function was measured on an absolute scale, it can be compared with theory without any adjustable parameters. The solid curves in the figure follow the Gram-Charlier series suggested by Collins and Marshall [12] which has the calculated area, second and fourth moments. Although the computed transforms have a statistical error of order 8% and a resolution in energy of order 2JS or 1.6 meV, they show good agreement with both the moments theory and with the experimental results. The computed scattering function shows a width in energy varying considerably with the direction of $\vec{q}$ within the zone. A comparison with experiment throughout the 110 plane of reciprocal space is shown in Ref. [11].

4. RESULTS FOR A SQUARE LATTICE AND A LINEAR CHAIN

Figure 5 shows the pair correlations calculated for various neighbours on a square lattice and on a linear chain. The square lattice con-

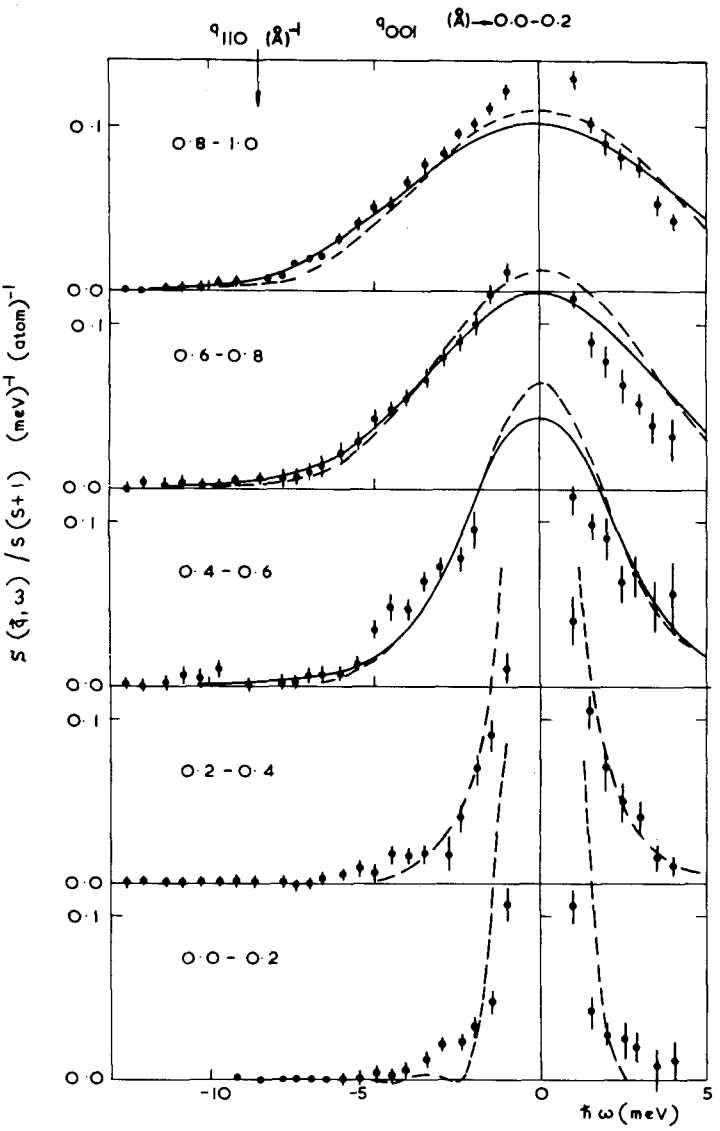

FIG. 4. The $\vec{q}$ and ω dependent scattering function for various values of $\vec{q}$ along the 110 direction in $RbMnF_3$ (dashed curve). The zone boundary is at 1.04 $Å^{-1}$ and q vectors at the centre of each range have been used in the calculation. The solid curve follows the Gram-Charlier expansion with the calculated moments. The points are experimental measurements on a $RbMnF_3$ single crystal at $3.5T_N$.

tained 2500 spins and was averaged over eight separate runs with different initial spin configurations to give a statistical accuracy of order 0.7% for each neighbour. The linear chain contained 4000 spins and was averaged over 5 runs to give 0.7% accuracy also.

The most striking change as the co-ordination number is reduced is the much smaller number of neighbours which contribute appreciably to the

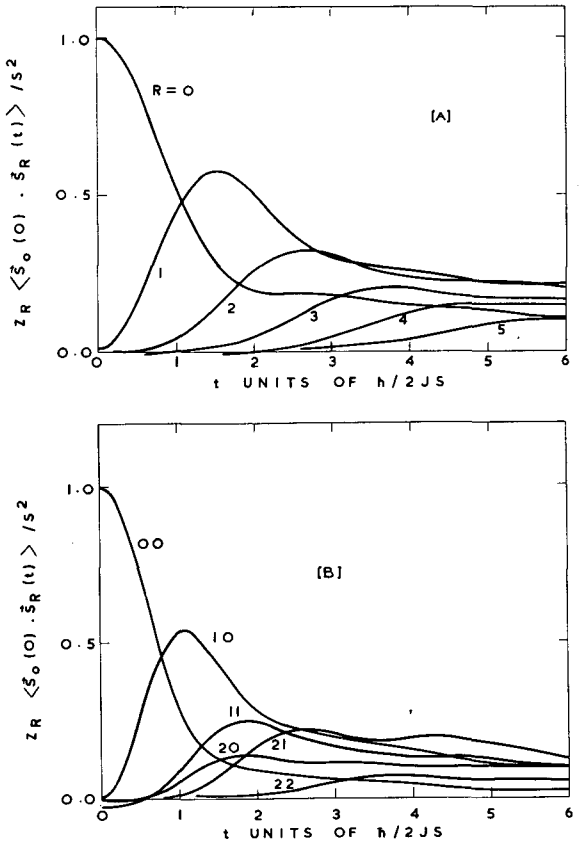

FIG. 5. The pair correlation functions for a square lattice (A), and for a linear chain (B).

correlations at a given time. This greatly reduces the amount of computation involved, and means that the space transforms may be evaluated with much greater accuracy. In both lattices some structure may now be seen in the correlation functions which in many cases can be identified with a particular process. In the linear chain results for example, a spin may diffuse to the adjacent site then back again to the original site giving a bump in the self-correlation function at the same position as the peak in the second-neighbour function. This type of process is more probable in lattices with a small co-ordination number and provides an explanation for the very slow decay of their correlations at large times.

The various Fourier transforms of the correlation functions have all been calculated but space limitations forbid a full discussion here. The linear chain $\mathscr{S}(\vec{R}, \omega)$ transforms are directly comparable with the results of Carboni and Richards [8, 9] for the spin-half case. There is remarkable agreement with their results particularly if a spin value $[S(S+1)]^{\frac{1}{2}} = \frac{1}{2}\sqrt{3}$ rather than one half is assumed.

ACKNOWLEDGEMENTS

The author is grateful to R.D. Lowde for useful discussions, and to P.M. Richards and F. Carboni for communicating their results on the linear chain.

REFERENCES

[1] Van HOVE, L., Phys. Rev. 95 (1954) 1374.
[2] MARSHALL, W., LOWDE, R.D., Rep. Progr. Phys. (1968).
[3] de GENNES, P. G., J. Phys. Chem. Solids 4 (1958) 223.
[4] MORI, H., KAWASAKI, K., Progr. theor. Phys. 27 (1962) 529.
[5] BENNETT, H.S., MARTIN, P.C., Phys. Rev. 138 A (1965) 608.
[6] WINDSOR, C.G., Proc. phys. Soc. 91 (1967) 353.
[7] VINEYARD, G.H., WATSON, R.E., BLUME, M., Int. Congr. Magnetism, Boston, 1967; J. appl. Phys. 39 (1968) 969.
[8] CARBONI, F., RICHARDS, P.M., to be published.
[9] CARBONI, F., Thesis, USAEC Rep. COO-1488-4 (1967).
[10] MOON, R.M., Phys. Rev. 136 A (1964) 195.
[11] WINDSOR, C.G., BRIGGS, G.A., KESTIGIAN, M., J. Phys. (in press).
[12] COLLINS, M.F., MARSHALL, W., Proc. phys. Soc. 92 (1967) 390.

DISCUSSION

A. RAHMAN: Permit me first to congratulate you on this most interesting piece of work, and then to enquire about a technical point: how did you satisfy yourself that the simple algorithm you have used is efficient enough?

C.G. WINDSOR: The criterion for accurate evaluation of the spin motions is that $\Delta t \ll \hbar/2JS$. This condition was checked by halving the Δt used and observing that the spin motion was changed by only a negligible amount.

R.D. LOWDE: You also have the sum rules, which tell you for instance that $\langle \vec{S}(-\vec{\kappa}) \cdot \vec{S}(\vec{\kappa}, t) \rangle$ should be independent of time, and the computation can be checked against these.

C.G. WINDSOR: The sum will be independent of time if the contributions from the neighbours not included in the calculation are negligible. The simple cubic results of Fig. 2 do not show significant deviations until times of order $3\hbar/2JS$.

R.D. LOWDE: Will you please comment on the range of κ over which the diffusion approximation appears to hold in your results?

C.G. WINDSOR: The diffusion approximation is characterized by an exponential decay of $\langle S_{-q}(0) \cdot S_q(t) \rangle$ with initial gradient proportional to q^2. This dependence was roughly satisfied by the calculations for q vectors as high as $0.5\pi/a_0$.

LINE SHAPE OF THE MAGNETIC SCATTERING FROM ANISOTROPIC PARAMAGNETS

P.-A. LINDGÅRD
RISØ RESEARCH ESTABLISHMENT,
ROSKILDE, DENMARK

Abstract

LINE SHAPE OF THE MAGNETIC SCATTERING FROM ANISOTROPIC PARAMAGNETS. The frequency dependence of the cross-section for magnetically scattered neutrons for low-energy transfer ($\hbar\omega \ll kT$) is conventionally expressed by $F^{\alpha\beta}(\vec{\kappa}, \omega)$, the Fourier transform of the normalized relaxation function. The second and fourth moments with respect to ω of $F(\vec{\kappa}, \omega)$ have been evaluated in the high-temperature limit for anisotropic materials described by a Hamiltonian containing Heisenberg interaction and axial anisotropy. A discussion, using the moments and the Gram-Charlier expansion, is given of the frequency dependence of $F(\vec{\kappa}, \omega)$.

Significant deviations are to be expected from the Gaussian line shape at large κ values and from the Lorentzian line shape at small κ values and at high temperatures. The results are compared with exact Ising model calculations and with measurements in the paramagnetic phase of rare earth metals, experimentally determined exchange and anisotropy parameters being used. As a first-order temperature correction, it is taken into account that the moments are proportional to $T/\chi(\vec{\kappa}, T)$, where $\chi(\vec{\kappa}, T$ is the wavelength-dependent susceptibility.

1. INTRODUCTION

Recently a number of measurements on the disordered phase of magnets having a large axial anisotropy, notably the rare-earth metals, have been reported [1, 2]. Consideration is here given to the effects this anisotropy will have on the interpretation of the experimental results. The frequency dependence of the paramagnetic and critical neutron scattering is conventionally [3-5] analysed by means of certain analytic approximations for the observed line shape, i.e. a Gaussian or a cut-off Lorentzian function. The moments of these functions can then be determined and related to the basic spin Hamiltonian. Recently Marshall and Collins [6] have discussed for the Ising model to what degree corrections to the Gaussian approximation for the paramagnetic line shape could be provided if a Gram-Charlier expansion[1] was used instead. They obtained a significantly better fit to the exact line shape. The coefficients in the expansion are determined by the moments of the spin-relaxation function higher than the second. This method is here used for estimating the line shape for the Heisenberg magnet with axial anisotropy.

2. AN EXACTLY SOLVABLE MODEL

The time dependence of the spin-relaxation function can be exactly solved for an Ising Hamiltonian with axial anisotropy and at high temperatures:

$$H = H_1 + H_2; \quad H_1 = -\sum_{i<j} 2J_{ij} S_i^z S_j^z; \quad H_2 = D \sum_i (S_i^z)^2 \qquad (1)$$

[1] This is an expansion in the derivatives of the Gaussian function.

As H_1 and H_2 commute, the time dependence of any operator p(t) is given as the product of the two time-dependent functions $g_1(t)$ and $g_2(t)$ giving the time evolution with respect to H_1 and H_2 respectively: $p(t) = p\, g_1(t) g_2(t)$. The frequency dependence of $P(\omega)$ is therefore given as the folding of the Fourier transforms of $g_1(t)$ and $g_2(t)$:

$$P(\omega) = \int e^{i\omega t} p(t) dt = p \int G_1(\omega') \, G_2(\omega - \omega') d\omega' \tag{2}$$

The neutron cross-section for paramagnets is related to the spin relaxation as follows [5]:

$$\frac{d^2\sigma}{d\Omega d\epsilon} \propto \sum_{\alpha\beta} (\delta_{\alpha\beta} - \hat{\kappa}_\alpha \hat{\kappa}_\beta) \sum_{n,p} \int dt \, e^{i\omega t + i\vec{\kappa}(\vec{n} - \vec{p})} \, R^{\alpha\beta}(\vec{n}-\vec{p}, t) \frac{\hbar\omega}{1 - e^{-\hbar\omega\beta}} \tag{3}$$

In the momentum space the spin-relaxation function is defined as

$$R^{\alpha\beta}(\vec{\kappa}, t) = \int_0^\beta d\lambda \langle e^{\lambda H} S^\alpha(-\vec{\kappa}, 0) e^{-\lambda H} S^\beta(\vec{\kappa}, t) \rangle \tag{4}$$

It is convenient to write

$$R^{\alpha\beta}(\vec{\kappa}, t) = R^{\alpha\beta}(\vec{\kappa}, 0) \times f^{\alpha\beta}(\vec{\kappa}, t) = \frac{N\chi^{\alpha\beta}(\vec{\kappa})}{g^2\mu^2} f^{\alpha\beta}(\vec{\kappa}, t)$$

in terms of the wavelength-dependent susceptibility $\chi^{\alpha\beta}(\vec{\kappa})$. $f^{\alpha\beta}(\vec{\kappa}, t)$ contains the full time dependence; it is normalized at t = 0 and is inversely proportional to the wavelength-dependent susceptibility.

The Fourier transform is denoted

$$F^{\alpha\beta}(\vec{\kappa}, \omega) = \int f^{\alpha\beta}(\vec{\kappa}, t) e^{i\omega t} dt \tag{5}$$

The time-evolution functions with respect to H_1 and H_2 have previously [7, 8] been calculated at high temperatures:

$$f_1^{\alpha\alpha}(\vec{\kappa}, t) = \sum_M g_M e^{i\omega_M t} \quad ; \quad \omega_M = \frac{2JM}{\hbar} \quad ; \quad \alpha = x \text{ or } y \tag{6}$$

g_M is the probability of finding the total spin M of neighbouring spins to a given site.

$$f_2^{\alpha\alpha}(\vec{\kappa}, t) = \frac{3}{2(2S+1)} \sum_{m=-S}^{S} \left(1 - \frac{m(m+1)}{S(S+1)}\right) e^{-i\omega_m t} \quad ; \quad \omega_m = \frac{D}{\hbar}(2m+1)$$

$$\alpha = x \text{ or } y \tag{7}$$

$f_i^{\alpha\beta}(\vec{\kappa}, t) = 1$ otherwise. $F_1^{xx}(\vec{\kappa}, \omega)$ is well approximated by a Gaussian, and the neutron cross-section is therefore proportional to

$$\frac{d^2\sigma}{d\Omega d\epsilon} \propto \frac{S(S+1)}{3}\frac{T}{T-T_c}(1-\hat{\kappa}_z^2)\delta(\omega)$$

$$+\frac{(1+\hat{\kappa}_z^2)}{2(2S+1)}\sum_{m=-S}^{S}[S(S+1)-m(m+1)]\frac{e^{-(\omega-\omega_m)^2/2\langle\omega^2\rangle_1}}{(2\pi\langle\omega^2\rangle_1)^{\frac{1}{2}}} \qquad (8)$$

For a polycrystal an elastic peak will be observed together with a smeared-out distribution of evenly spaced crystal field levels. For a large crystal field splitting compared with the exchange broadening, the second distribution will be discrete and the method of moments is not necessary; however, for a small crystal field splitting compared with the exchange broadening, the line shape will be close to a Gaussian and the deviation may be determined by a Gram-Charlier expansion. In Fig.1 is shown a comparison of line shapes, one based on a direct calculation of Eq.(8), the other obtained by a Gram-Charlier expansion by means of second and

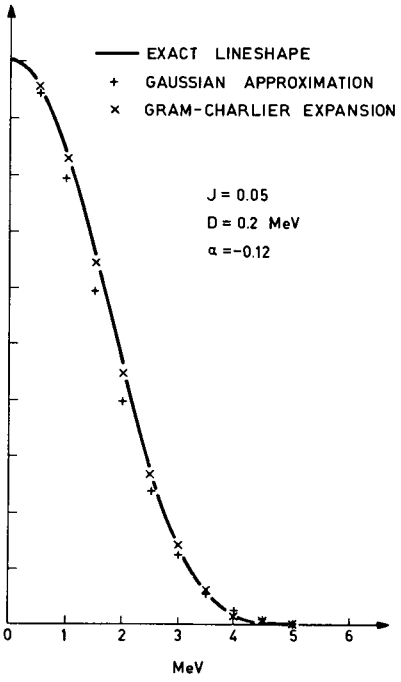

FIG.1. The line shape for the Ising model with axial anisotropy. The good fit provided by the Gram-Charlier expansion gives confidence in the method for this type of problem.

fourth moments of $F^{\alpha\beta}(\vec{\kappa},\omega)$ with respect to H_1+H_2, easily obtained from $f_1^{\alpha\beta}$ and $f_2^{\alpha\beta}$. They are

$$\langle\omega^2\rangle = \langle\omega^2\rangle_1 + \langle\omega^2\rangle_2$$

and

$$\langle\omega^4\rangle = \langle\omega^4\rangle_1 + \langle\omega^4\rangle_2 + 6\langle\omega^2\rangle_1\langle\omega^2\rangle_2$$

3. HEISENBERG INTERACTION WITH AXIAL ANISOTROPY

The Hamiltonian is $H = H_1 + H_2 + H_3$, where

$$H_3 = -\sum_{i<j} 2J_{ij}\tfrac{1}{2}(S_i^+S_j^- + S_i^-S_j^+)$$

H_2 does not commute with H_3. Therefore the frequency distribution of the cross-section is no longer a simple folding of the separate distributions for H_2 and H_1+H_3. Equation (8) is no longer valid, although we expect it to give the qualitative features as follows (the exchange interaction and the anisotropy are assumed to be of comparable magnitude):

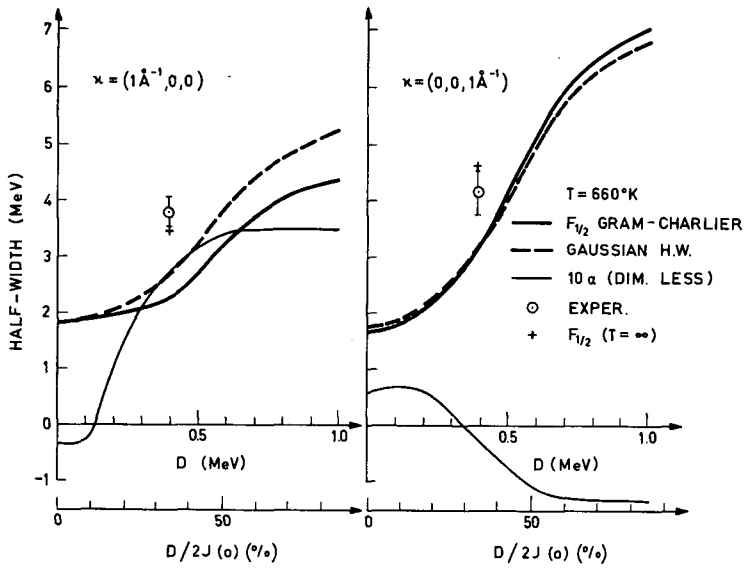

FIG. 2. The half-width $F_{\frac{1}{2}}$ for the Gram-Charlier approximated line, the corresponding Gaussian half-width and the (dimensionsless) shape parameter α_S as functions of the anisotropy (for κ = 1 Å in the x and z-directions, T = 660°K). The experimental half-width at 660°K (o) and the T = ∞ theoretical value (+) are shown. The lower scale shows the ratio of the anisotropy energy to the exchange energy (D/2J(0)) in per cent.

(1) A narrow central peak around $\omega = 0$ proportional to $(1 - \hat{\kappa}_z^2)$. The width of this peak is mainly determined by the exchange interaction (H_3).

(2) A broader peak proportional to $(1 + \hat{\kappa}_z^2)$, the width of which is determined mainly by the width of the crystal field levels. For a polycrystal we therefore expect the combination of these contributions as a 'Lorentzian-like' line shape with a narrow central peak and large (truncated) wings. This was observed in erbium by Holden et al. [1].

For a detailed analysis we are confined to the method of moments. The second and fourth moments of $F^{\alpha\beta}(\vec{\kappa}, \omega)$ have been calculated for this purpose. The latter has not previously been reported for the present Hamiltonian

$$H = -\sum_{i<j} 2J_{ij}\vec{S}_i \cdot \vec{S}_j + D\sum_i (S_i^z)^2$$

$$\langle\omega^2\rangle^{\alpha\alpha} = \frac{Xg^2\mu^2}{3kT\chi^{\alpha\alpha}(\vec{\kappa})}\left\{\langle\omega^2\rangle_{ex} + \frac{D^2}{5}(4X-3)\right\} \qquad \alpha = x \text{ or } y \tag{9}$$

$$\langle\omega^2\rangle^{zz} = \frac{Xg^2\mu^2}{3kT\chi^{zz}(\vec{\kappa})}\langle\omega^2\rangle_{ex}$$

$$\langle\omega^4\rangle^{\alpha\alpha} = \frac{Xg^2\mu^2}{3kT\chi^{\alpha\alpha}(\vec{\kappa})}\left\{\langle\omega^4\rangle_{ex} + \frac{1}{5}(4X-3)\left[\frac{8X}{3}\sum_m J_{om}^2 D^2 (7-4e^{i\vec{\kappa}\cdot\vec{m}})\right.\right.$$

$$-\frac{16X}{3}\sum_m J_{om}^3 D(1-e^{i\vec{\kappa}\cdot\vec{m}}) \tag{10}$$

$$\left.\left. + \frac{1}{7}D^4(12X-17)\right]\right\} \qquad \alpha = x \text{ or } y$$

$$\langle\omega^4\rangle^{zz} = \frac{Xg^2\mu^2}{3kT\chi^{zz}(\vec{\kappa})}\left\{\langle\omega^4\rangle_{ex} + \frac{1}{5}(4X-3)\left[\frac{16X}{3}\sum_m (J_{om}^2D^2 + J_{om}^3 D)(1-e^{i\vec{\kappa}\cdot\vec{m}})\right]\right\}$$

where $\langle\omega^{2n}\rangle_{ex}$ are the well-known moments for the pure Heisenberg interaction [8], $X = S(S+1)$ and in the molecular field approximation at high temperatures

$$\frac{Xg^2\mu^2}{3\chi^{\alpha\alpha}(\vec{\kappa})} = \left[kT - \frac{2X}{3}J(\vec{\kappa})\left(1 + \frac{1}{kT}\frac{D}{30}(4X-3)\right)\right] \qquad \alpha = x \text{ or } y$$

(11)

$$\frac{Xg^2\mu^2}{3\chi^{zz}(\vec{\kappa})} = \left[kT - \frac{2X}{3}J(\vec{\kappa})\left(1 - \frac{1}{kT}\frac{2D}{30}(4X-3)\right)\right]$$

As a first-order temperature dependence of the moments the inverse proportionality to the wavelength-dependent susceptibility is taken into account [10, 5]. In a recent experiment on the critical scattering from terbium [2] the general prediction of the 'thermodynamic slowing-down' was verified; however, the detailed temperature dependence did not follow that of the inverse susceptibility. An experimental investigation of the temperature dependence of moments at $T > T_c$ would be valuable.

From the expressions for the moments we notice that the peak proportional to $(1 - \hat{\kappa}_z^2)$ has a line shape close to that expected for pure exchange interaction, the wings, however, being somewhat truncated because of the anisotropy that enters in moments higher than the second. In particular we note that the width goes to zero as κ^2 for small $\vec{\kappa}$. The width proportional to $(1 + \hat{\kappa}_z^2)$ does not vanish at $\vec{\kappa} = 0$ in the presence of anisotropy. In a neutron scattering experiment it is probably not easy to separate the contributions from the $\alpha\alpha$ (α = x or y) and the zz part. Therefore it may be convenient to consider moments of the more involved function

$$S(\vec{\kappa}, \omega) = \sum_{\alpha\beta} (\delta_{\alpha\beta} - \hat{\kappa}_\alpha \hat{\kappa}_\beta) \chi^{\alpha\beta}(\vec{\kappa}) F^{\alpha\beta}(\vec{\kappa}, \omega)$$

which is the one directly measurable. These moments are obtained from Eqs (9)-(11) by performing the summation and normalization. The moments $\langle\omega^4\rangle_S$ of $S(\vec{\kappa}, \omega)$ contain $\hat{\kappa}_z^2$ terms, introduced by the first factor in $S(\vec{\kappa}, \omega)$; such terms are, or course, not present in the line width because of the fundamental spin-spin relaxation.

For a discussion of the line shape using the moments we choose as an example terbium, for which both the paramagnetic scattering [1] and the exchange parameters are known[2]. Figure 2 shows the variation of the line shape as measured by $\alpha_S = \langle\omega^4\rangle_S / 3\ \langle\omega^2\rangle_S^2 - 1$ as a function of the direction of $\vec{\kappa}$ and the magnitude of the anisotropy. In agreement with our previous anticipations, the total line shape for $\vec{\kappa} = (\kappa, 0, 0)$ tends to become more 'Lorentzian-like' (α_S increases) as the anisotropy increases, whereas that for $\vec{\kappa} = (0, 0, \kappa)$, which does not contain the central peak, becomes broader and more square-like (α_S decreases) with increasing anisotropy. We further note that $\alpha_S \sim 0$ for D = 0, indicating that the pure exchange-broadened line shape at $\kappa = 1$ Å is nearly, but not exactly Gaussian. The dependence on the direction of $\vec{\kappa}$ is for this distribution due to the anisotropy of the (hcp) lattice. Furthermore, the figure shows the line width $F_{1/2}$ at half maximum for the Gram-Charlier approximated line and that obtained in the Gaussian approximation (calculated at T = 660°K). The error introduced in the second moment as determined by the Gaussian approximation and the measured half-width is in general for $|\alpha_S| \leq 1$ about

---

[2] For the exchange and anisotropy parameters a 9-parameter least-squares fit to the terbium dispersion relation at 90°K is used [9]. Listed by increasing bond length they are: $J^{(i)}$ = 35; 46; -12; 9; 13; -10; 2; 6 ($\times 10^{-3}$ meV); D = 0.39 meV. A good agreement with this value for the anisotropy parameter is obtained from the susceptibility measurements by Hegland et al. [11] when these are analysed at high temperatures on the basis of Eq. (11) instead of on the basis of the (extrapolated) difference in the paramagnetic transition temperatures.

$40 \times \alpha_S$ %. This becomes a very substantial error at the smaller κ values (up to at least half the Brillouin zone). At small κ values α_S tends to infinity for $\kappa \rightarrow 0$ for the pure Heisenberg interaction, as an indication of a Lorentzian line shape. As is seen from expressions (9) and (10), this is not the case in the presence of the anisotropy, where α_S tends to a finite value, although the peak proportional to $(1 - \hat{\kappa}_z^2)$ shows the 'dynamical' narrowing or slowing-down. Finally a comparison is made with the experimental half-width for terbium at 660°K from Ref. [1] interpreted as $(\langle \omega^2 \rangle^{\text{experimental}} \ln 4)^{1/2}$. The agreement with the theoretical value for T = 660°K is poor, while it is considerably better for the infinite temperature value. This fact supports the conclusion in Ref. [2] that the moments of $F^{\alpha\beta}(\vec{\kappa}, \omega)$ remain at the limiting high-temperature value in a large temperature range, and only in a narrow region close to the transition temperature T_c are they reduced to zero as a consequence of the 'thermodynamic' slowing-down.

ACKNOWLEDGEMENTS

I thank Dr. W. Marshall for suggesting the problem. It is a pleasure to acknowledge valuable discussions with Dr. A. D. B. Woods and his colleagues.

REFERENCES

[1] CABLE, J. W., COLLINS, M. F., WOODS, A. D. B., Proc. 6th Rare Earth Res. Conf., Gatlinburg, Tenn., 1967 (unpublished);
HOLDEN, R. M., POWELL, B. M., WOODS, A. D B., Proc. Int. Conf. Magnetism, Boston, 1967; J. appl. Phys. 39 (1968) 457.
[2] ALS-NIELSEN, J., DIETRICH, O., MARSHALL, W., LINDGÅRD, P. A., Sol. State Com. 5 (1967) 607.
[3] Van VLECK, J. H., J. Chem. Phys. 5 (1937) 320; Phys. Rev. 55 (1939) 924.
[4] De GENNES, P. G., J. Chem. Phys. Sol. 4 (1958) 223.
[5] MARSHALL, W., AERE Harwell Rep. T. P. 200 (1966) (unpublished); LOWDE, R. D., MARSHALL, W., Rep. Progr. Phys. (to be published).
[6] COLLINS, M. F., MARSHALL, W., Proc. phys. Soc. (to be published).
[7] COLLINS, M. F., WINSOR, C. G., Proc. phys. Soc. 90 (1067) 1015.
[8] COLLINS, M. F., Proc. Int. Conf. Magnetism, Boston, 1967; J. appl. Phys. 39 (1968) 533.
[9] MØLLER, H. B., HOUMANN, J. C. G., Phys. Rev. Lett. 16 (1966) 737.
[10] MORI, H., KAWASAKI, K., Progr. theor. Phys. 27 (1962) 529.
[11] HEGLAND, D. E., LEGVOLD, S., SPEDDING, F. H., Phys. Rev. 131 (1963) 158.

DISCUSSION

C. G. WINDSOR: B. Rainford at Harwell has measured the scattering widths from cerium metal at several temperatures and finds that relaxation via the conduction electrons gives the dominant contribution to the width. Could this process explain your terbium widths in excess of the theory?

P.-A. LINDGÅRD: I agree that the rare earths are far too complicated to be described by the Hamiltonian which I have used, and a fair comparison with observed line widths must take account of all relaxation mechanisms. In the case of terbium, however, unlike cerium, the exchange broadening is expected to be the dominant feature.

MAGNETIC EXCITATIONS IN NICKEL

S. KOMURA, R.D. LOWDE AND C.G. WINDSOR
ATOMIC ENERGY RESEARCH ESTABLISHMENT,
HARWELL, DIDCOT, BERKS., ENGLAND

Abstract

MAGNETIC EXCITATIONS IN NICKEL. The Fourier transform of the spin correlation function $\langle \underline{S}_o \, \underline{S}_r(t) \rangle$ has been measured by means of neutron scattering, and its evolution studied as the temperature is carried through the order-disorder transition point from the low to the high-temperature extreme situations. The correlation is exhibited in detail over the complete Brillouin zone for the range of energies up to 0.11 eV at 0.5, 0.9, 1.1 and 1.6 times T_c. At the highest temperature the distribution is well explained by the elementary theory of Stoner paramagnetism if an exchange enhancement calculated in random-phase approximation is introduced. At low temperature the correlation shows a sharp ridge corresponding to spin-wave excitations; below 60 meV the spin-wave peaks all fall close to a parabola extrapolated from the quadratic dispersion law of previous low-energy determinations, but at higher energies they fall away from this parabola in a manner agreeing with the calculation of Thompson and Myers. As the temperature is taken through the phase-transition point, critical enhancement of the susceptibility such as would be predicted using the random-phase approximation is not observed. The approach to criticality from either side is characterized instead by a pronounced anticipation of the features of the susceptibility on the other side of the Curie point. Away from a region closely confined to the origin, the transition through T_c is smooth; indeed the correlation functions at 0.9 T_c and 1.1 T_c are strikingly similar. In the critical region the susceptibility is dominated by spin-wave-like peaks rather than paramagnons; it is suggested that the explanation might lie in the existence of large fluctuations of the band splitting near T_c.

INTRODUCTION

The excitations of electrons in the transition metals are of perennial interest, since it is such a complex task to understand them theoretically. Quantitative calculations of their spectra are nowadays beginning to appear in increasing numbers, illustrating a variety of different mathematical treatments, and it is much to be hoped that comparison of these with experiment will illuminate the problem. For instance, the comparison may indicate to what degree the electron interactions and correlation effects distort the picture presented by the simple non-interacting-electron one-particle theory [1]. The ferromagnetic transition metals are of special significance in this connexion, since they exhibit in the same substance the paramagnetic state, the ferromagnetic state with an energy splitting between spin-up and spin-down bands, and the still obscure "critical" phenomena of the passage (as a function of temperature) through the phase transition.

In this paper we present some further results of our study of the magnetic electrons in nickel from this point of view, using the powerful technique of neutron scattering.

According to the simple theories of non-interacting electrons, the excitations above the ground states of transition metals that are paramagnetic at low temperature are normally confined to a well-defined region of wave-vector—frequency $(\underline{K},\omega)$ space. Fig 1a actually drawn for ferromagnetic nickel, will serve as an example

where the principal feature illustrated is that large-energy excitations cannot be achieved at small K. The band splitting Δ in ferromagnets, however, introduces the complication that the excitations with and without spin flip have different character; those without spin flip have, for each spin sub-band, a nature similar to those of figure 1a, while those with spin flip are lifted or depressed by Δ on the energy scale. Both types of excitation also give rise to the so-called collective modes, in the latter case the spin wave modes. (We ignore the plasma modes at present, which are normally so high in energy that they need not be discussed in the work at hand). Figure 1b shows the excitations with spin reversal as calculated for nickel along the [100] axis by Thompson & Myers [2] from a non-interacting electron theory. The generalised susceptibility $\chi(\underline{K},\omega)$ [defined as $dM(\underline{K},\omega)/dH(\underline{K},\omega)$] is governed by these excitations, and in non-interacting one-electron theory for metals at $0^{\circ}K$ is non-zero only in regions derived as for figure 1.

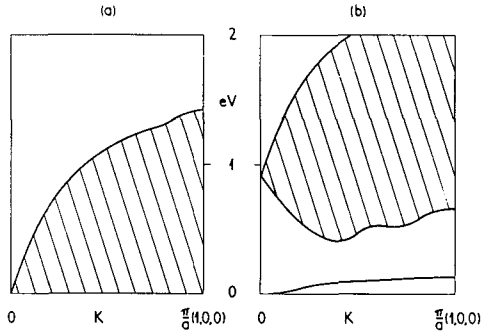

FIG.1. Regions of non-zero spin correlation in a material like nickel at low temperatures, according to simple non-interacting electron theory. (a) for the zz correlation; (b) for the xx and yy correlations. (Based on Ref. [2]).

It can be shown that the generalised susceptibility $\chi(\underline{K},\omega)$, the spin correlation function

$$\mathcal{S}^{\alpha\alpha}(\underline{K},\omega) = \frac{1}{2\pi}\int_{-\infty}^{\infty} e^{-i\omega t}\langle s_K^{\alpha}(t)s_K^{\alpha\dagger}\rangle\, dt\,, \qquad (1)$$

and through the latter the neutron cross-section as a function of momentum transfer $\hbar\underline{K}$ and energy transfer $\hbar\omega$

$$\frac{\partial^2\sigma}{\partial\Omega\partial E} = \frac{2}{3}(r_0\gamma)^2(k'/k)\,|F(\underline{K})|^2 \sum_{\alpha}\mathcal{S}^{\alpha\alpha}(\underline{K},\omega)\,, \qquad (2)$$

are all interrelated functions, so that in particular $\mathcal{S}$ or χ can be obtained in detail from the neutron scattering [3]. [Eqs (1) and (2) employ conventional notation throughout, with α=x,y,z; eq (2) is written for the restricted case of a cubic magnet not having preferred domain directions in the ordered state]. We have used this fact to determine $\sum_{\alpha}\mathcal{S}^{\alpha\alpha}(\underline{K},\omega)$ for nickel over a range of temperatures from $0.46T_c$ to $2.3T_c$, and present some of the results below. The whole Brillouin zone has been covered for a range of energies up to 0.11eV, and data are set out in detail for temperatures of 0.46, 0.90, 1.10 and 1.62 times T_c.

We have previously investigated the behaviour of $\chi''(\underline{K},\omega)$ in nickel at $1.62T_c$ [4]. The generalised susceptibility was shown to give a good absolute fit out to $\frac{1}{2}K_{max}$ with calculations for a free-electron gas with an effective intra-atomic Coulomb repulsion parameter $I_{eff} = 0.4$eV and susceptibility enhancement taken into account through the random-phase approximation [5,6]. A fit of comparable quality over the whole Brillouin zone was later found, employing a five 3d-band model in tight-binding approximation with I_{eff} the only adjustable parameter [7]. The susceptibility at $1.6T_c$ is thus fairly well understood using the itinerant-electron model of Stoner with RPA exchange enhancement. On the other hand, our early measurements of the temperature dependence of the scattering, covering a limited range of $\underline{K}$ and ω, indicated that the critical divergence of the enhancement factor predicted by RPA theory for temperatures approaching the transition point was essentially absent [8]; the scattering changed smoothly and continuously through T_c and into the ordered region [9]. Those studies, in fact, suggested that the currently available theories are satisfactory at the highest temperatures but break down totally as the Curie temperature is approached.

The spin wave energies at very small wave-vectors in nickel have already been accurately measured, both by neutron scattering [10-12] and by thin-film ferromagnetic resonance [13]. These methods have given among other things the stiffness coefficient D in the quadratic dispersion law $E_{sw} = DK^2 + O(K^4)$, and recent measurements on nickel by Stringfellow [12] show that D varies from a value 0.403 ± 0.007 eV Å^2 at room temperature ($0.46T_c$) to about a third of this value near the Curie point. The so-called diffraction technique has been used by Pickart et al [11] to extend the observed range of K to about 0.3Å^{-1}; no departure from the quadratic frequency dependence was observed. In the present study we are able to extend the range of the observed K's considerably beyond what has previously been attained.

Thompson and Myers succeeded in fitting the observed spin-wave stiffness of nickel, employing in their calculation reasonable input parameters. It would appear, therefore, that simple theories are adequate to describe nickel at the easily understood extremes of high and low temperatures, but unsatisfactory for the intermediate region.

THE EXPERIMENT

Our time-of-flight spectrometer at PLUTO [14] was used to give some $\sim 10^5$ incident neutrons sec^{-1} of energy 14.9 meV ($\lambda = 2.34$ Å) at a resolution E_o/dE_o of 14 and a pulse repetition frequency of 550 sec^{-1}. Scattered neutrons were detected as a function of their flight time over a 225 cm path by 8 pairs of scintillation counters at different scattering angles; the vertical and horizontal angular divergences of each counter pair were 1.5° and 0.75° respectively. The sample was an isotopic ^{60}Ni single crystal of effective volume 1.5 cm^3, and was mounted (in a furnace, except for the room temperature measurements) so that the equatorial plane of the detectors was a (100) plane. At each temperature some 56 time-of-flight spectra were taken for different crystal settings, normalised together, and placed on an absolute scale by means of a vanadium-sample calibration run.

The data at each temperature were sorted, according to the mean values of $\underline{K}$ and ω corresponding to the time channels, into the compartments of a mesh of spacing 0.1 $Å^{-1}$ in K and 5 meV in $\hbar\omega$. (The instrumental resolution at, for instance, a neutron energy gain of 32 meV was 0.1 $Å^{-1}$ in K and 4 meV in $\hbar\omega$, so that this mesh is rationally related to the parameters of the spectrometer). Mean values of $\sum \mathcal{S}^{\alpha\alpha}$ were then derived for each compartment from eq(2), approximating the atomic form factor $F(\underline{K})$ analytically by $\exp -0.04K^2$ (K in $Å^{-1}$). Since $\mathcal{S}$ is periodic in the reciprocal lattice, the scattering vector $\underline{K}$ may be replaced by the wave-vector q reduced to the first Brillouin zone, and this reduction was performed. Anisotropy in the degree that would justify a four-dimensional treatment was not found, and so finally all data at the same K were collapsed onto the single variable K with a resulting improvement in the statistics.

RESULTS

Figure 2 shows the data for one particular time-of-flight setting as recorded at seven different temperatures. It refers to an arrangement, shown inset at the top of the figure, in which the scattered neutron wave-vector passes through the 200 reciprocal lattice point at an energy gain of 32 meV to give the q and and ω dependence shown in the lowermost scales. The magnetic scattering at this setting is largely concentrated in the small-q region. Two spin-wave peaks are clearly seen at either side of the local origin of q at $\frac{1}{2}T_c$; these gradually broaden with increase of temperature, crossing T_c apparently continuously, until at the highest temperatures they merge into a hump having just a slight dip at the smallest $\underline{q}$ vectors.

Comprehensive contour diagrams of $\frac{1}{3}\sum \mathcal{S}^{\alpha\alpha}$ at four temperatures are given in figure 3. The spacing of the contours is logarithmic, each contour representing double the scattering intensity of the adjacent contour; an evenly spaced set of contours would imply an exponential change of the function. Some of the structure in the diagrams arises from the statistical error inherent in the scattering measurements, which is of order 2.5 scale units. The ridge at low energies in figure 3a, some trace of which is seen in each diagram, is due to coherent nuclear scattering from phonons. (^{60}Ni has a nuclear σ_{coh} of 1 barn and no nuclear-spin disorder scattering).

DISCUSSION

The spin-wave region

At $0.5T_c$ the scattering shows a well-defined ridge, which in the energy range up to 60 meV corresponds closely to the spin-wave parabola extrapolated from the low-energy measurements [12]. At higher energies the line of the ridge curves over in strikingly good agreement with the calculation of Thompson and Myers [2], whose results are shown in the figure for the symmetry directions [100] and [110] on the assumption that there are 0.6 holes per atom in the 3d band. Thompson and Myers' calculation was fitted to a D of 0.390 eV $Å^2$, so that of course the parabolic part is bound to be satisfactory; however, beyond the quadratic region the behaviour of their dispersion law is dictated by the supposed band structure of nickel.

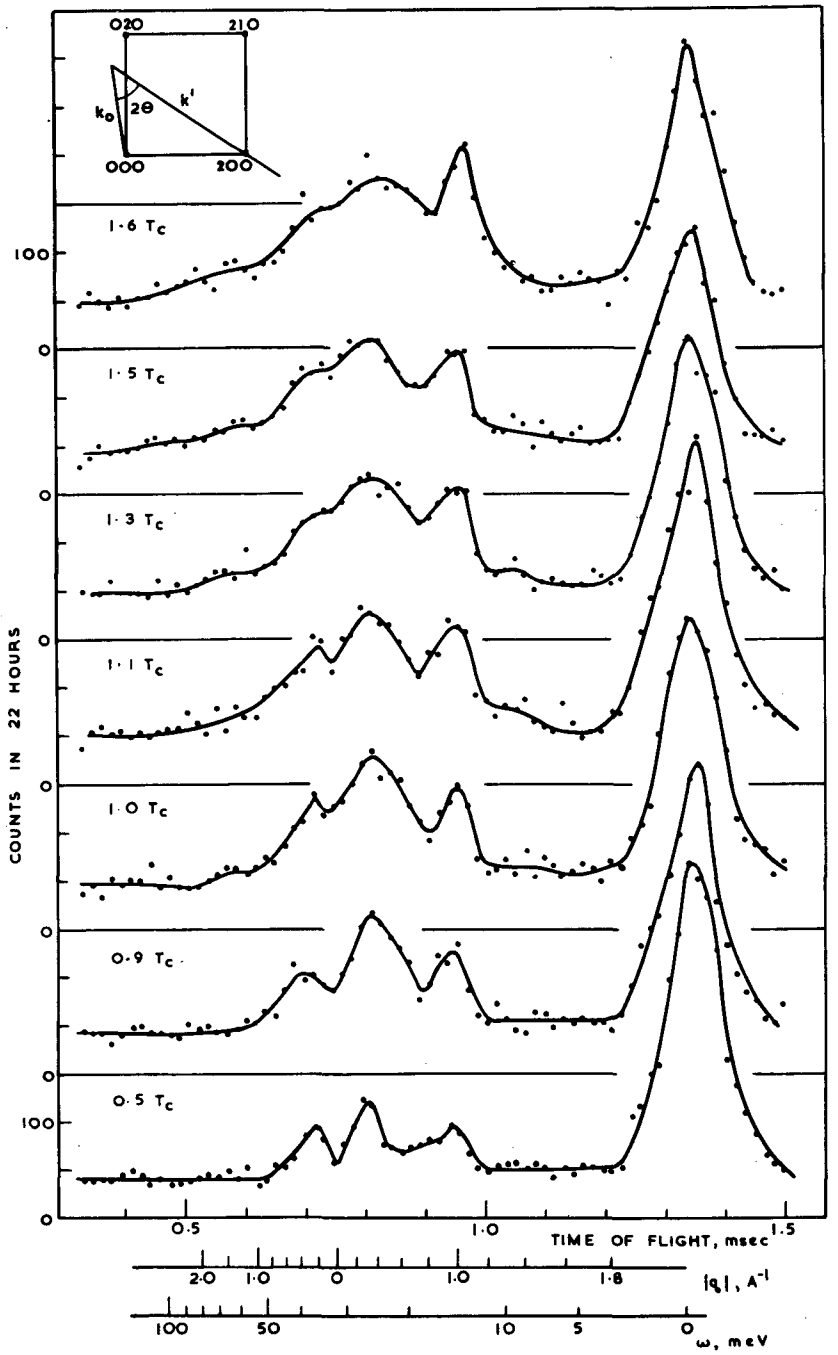

FIG. 2. Neutron time-of-flight spectra taken with a nickel crystal at various temperatures. The incident wavevector and the direction of scattering are shown in an inset at the top. The magnetic scattering is concentrated in the double peaks around the position q = 0, with a phonon peak to the right and an elastic peak to the extreme right.

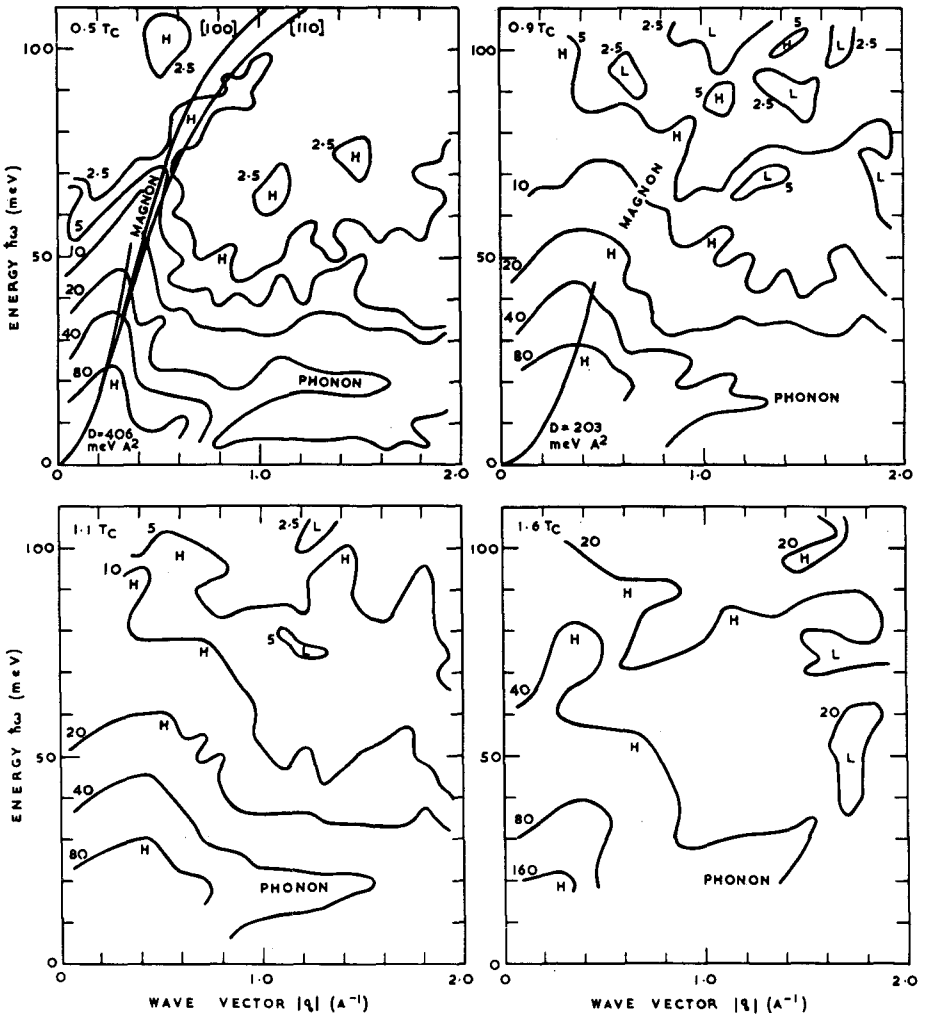

FIG.3. Contour maps of the measured spin correlation function $\frac{1}{3}\sum_{\alpha} \mathcal{S}^{\alpha\alpha}(q,\omega)$ for nickel at four different temperatures, with high (H) and low (L) regions marked. The contour labels are expressed in units of $10^{-2}\,eV^{-1}\,atom^{-1}$.

There is some suggestion of an unforseen second ridge at about two-thirds the energy of the acknowledged spin-wave one. Our present data are insufficiently extensive to decide whether or no this is real.

The spin-wave intensity undoubtedly comes from $\mathcal{S}^{xx}+\mathcal{S}^{yy}$, but these functions should give little else over the remainder of figure 3a. The conspicuous bank of intensity in figure 3a which can be seen building up towards the low-energy region, and which is represented by a set of roughly horizontal contour lines, may accordingly on our present understanding be attributed to $\mathcal{S}^{zz}$.

Paramagnetism

Turning directly to the diagram for $1.6T_c$ at (d), a comparatively simple distribution is seen that is known [7] to be in reasonable agreement with the tight-binding five-3d-band calculation for the paramagnetic phase by Allan et al employing a susceptibility enhancement (in random-phase approximation) of 3. The theoretical contours, not reproduced here, themselves produce a low-energy bank of intensity with horizontal contour lines reminiscent of those that were remarked upon at figure 3a. Above T_c there is no difference between $\mathcal{S}^{xx}$ and $\mathcal{S}^{zz}$, and it is interesting to see that something qualitatively recognisable as this bank of intensity along the axis of abscissae persists throughout the whole temperature range covered in the investigation. There can be little doubt that it corresponds to the excitation of electrons by thermal agitation in such a way that the electrons involved remain close to the Fermi surface.

Spin waves at elevated temperatures

At (b), $0.90T_c$, $M(T)/M(0)$ is 0.59; $\Delta(T)/\Delta(0)$ might be expected to be about 0·5. Both renormalisation of the spin wave energy and broadening of the line are apparent at (b), while the outstanding thing about (b) and (c) taken together is their close similarity. Indeed, such limited measurements as we have taken at temperatures very close to the Curie point suggest that there is a completely steady and continuous evolution from (b) to (c). At $0.90T_c$ a parabola for the stiffness constant 0.203 eV Å^2 (half the value for room temperature) is drawn to represent the long-wavelength results of Stringfellow at that temperature [12], and is seen to join smoothly on to the renormalised magnon ridge. Very near T_c itself, Stringfellow finds at small q that $E_{sw}(T)/E_{sw}(0)$ is about ≈ 0.3, while from figure 3d for intermediate q's it is evidently about a half and for large q's about 0.8-0.9.

At $1.10T_c$, although the conception of clear-cut spin-wave peaks at constant $\underline{K}$ has apparently been lost, there still remain peaks in the distribution-in-q at constant ω; the residual ridge in $\mathcal{S}$ is so unmistakable that one would confidently draw a partial dispersion curve. So far as these vestigeal spin-wave-like phenomena are concerned, the main consequence of raising the temperature far above T_c seems to be that the ridge dies away gently, after a degree of movement yet to be investigated, into the general detail of the paramagnetic susceptibility.

The critical region

The smooth transition from (b) to (c) [8,9] is one of the more remarkable features of the data. Until recently, the theoretical prediction would have been that with lowering of the temperature from infinity enhancement of the susceptibility would take place in the way discussed by Doniach and Engelsberg and by Berk and Schrieffer [15]. According to this view the limitless increase of the enhancement factor would compress the correlation function more and more towards the axis of abscissae, creating a sharply peaked surface on which could be identified the dispersion curve of a new quasiparticle, the paramagnon. This situation, as described by the random-phase approximation,

would become more and more pronounced as the critical temperature was approached, until on passing the actual transition point band splitting would abruptly set in and two-thirds of the susceptibility (the xx and yy parts) would begin to be lifted out of the top of the diagram.

However, so far as can be discerned, none of this happens in the manner that used to be envisaged.

A qualitative explanation

As long ago as 1963, Kawasaki [16] published an account of collective modes at elevated temperatures in the Heisenberg ferromagnet in which the very phenomena we have described were forseen. According to his formulae, a 'Heisenberg substance' with the constants of nickel would suffer only a slight reduction of D on attaining the Curie temperature, and some kind of broadened modes would persist into the paramagnetic phase. The discussion was based on Mori's statistical-mechanical theory, with the central physical idea that the spin motions are determined with regard to what appear to be the local conditions of equilibrium. Thus local regions of short-range order at and above the Curie temperature act as miniature ferromagnets and support forms of motion on a local scale that have much in common with the dynamics of the ground state.

Clearly the corresponding idea in the theory of metals at high temperatures is that of a local, fluctuating band splitting. As the Curie temperature is approached from above, the band splitting undoubtedly undergoes fluctuations of mean value zero but of boundlessly increasing magnitude. At temperatures where this effect is marked, it would follow that on a local scale a paramagnetic metal makes extensive excursions into the ferromagnetic phase region, and that its susceptibility consequently partakes more strongly of the character of the ordered state than has hitherto been conceded. Likewise on approaching T_c from below one could say that the collapse of $\Delta(T)$ and the divergence of its fluctuations tend to work in opposite directions, so that in the upshot the spin wave peaks just below T_c are at higher energies than would otherwise have been thought.

CONCLUSIONS

We have documented in figure 3 the fact that a simple account can be given of the susceptibility of nickel at both the low and high temperature extremes, but that elementary molecular-field-theory ideas fail entirely to explain the phenomena associated with passing through the order-disorder transition point. Materially away from the origin of $(\underline{K},\omega)$ space the transition from well-defined spin waves to paramagnetic disorder takes place in a completely smooth manner, the predictions of "criticality" as hitherto taken from theories using the random-phase approximation being correct only for the initial stages of the departure from the temperature extreme ($T=0$ or ∞). The effects were foretold by Mori and Kawasaki. It would seem likely that the current theories of magnetic metals essentially lack, in this connexion, the concept of a fluctuating, or locally fluctuating, band splitting.

REFERENCES

[1] See, e.g. HERRING, C., in Magnetism 4 (RADO, G.T., SUHL, H., Eds), Academic Press, New York (1966). A valuable review has been written especially for experimental physicists by THOMPSON, E.D: Adv. Phys. 14 (1965) 213.
[2] THOMPSON, E.D., MYERS, J.J., Phys. Rev. 153 (1967) 574.
[3] IZUYAMA, T., KIM, D.J., KUBO, R., J. phys. Soc. Japan 18 (1963) 1025.
[4] CABLE, J.W., LOWDE, R.D., WINDSOR, C.G., WOODS, A.D.B., J. appl. Phys. 38 (1967) 1247.
[5] LOWDE, R.D., WINDSOR, C.G., Phys. Rev. Lett. 18 (1967) 1136.
[6] DONIACH, S., Proc. phys. Soc. 91 (1967) 86.
[7] ALLAN, G., LOMER, W.M., LOWDE, R.D., WINDSOR, C.G., Phys. Rev. Lett. 20 (1968) 933.
[8] LOWDE, R.D., WINDSOR, C.G., J. appl. Phys. (1968 ; in press).
[9] LOWDE, R.D., WINDSOR, C.G., Solid State Comm. 6 (1968 ; in press).
[10] HATHERLY, M., HIRAKAWA, K., LOWDE, R.D., MALLETT, J.F., STRINGFELLOW, M.W., TORRIE, B.H., Proc. phys. Soc. 84 (1964) 55.
[11] PICKART, S.J., ALPERIN, H.A., MINKIEWICZ, V.J., NATHANS, R., SHIRANE, G., STEINSVOLL, O. Phys. Rev. 156 (1967) 623.
[12] STRINGFELLOW, M.W. (in the press).
[13] NOSE, M., J. phys. Soc. Japan 16 (1961) 2475.
[14] DYER, R.F., LOW, G.G.E., Inelastic Scattering of Neutrons in Solids and Liquids (Proc. Symp. Vienna, 1960), IAEA, Vienna (1961) 179.
[15] DONIACH, S., ENGELSBERG, S., Phys. Rev. Lett. 17 (1966) 750; BERK, N., SCHRIEFFER, J.R., Phys. Rev. Lett. 17 (1966) 433.
[16] KAWASAKI, K., Prog. theor. Phys. 29 (1963) 156.

DISCUSSION

H. BJERRUM MØLLER: The time-of-flight method has been successful in the measurements on Ni above all, I think, because the dispersion relations for magnons in different directions are more or less identical, at least for the small q region studied in the experiment.

In the case of rare-earth metals this is not the case, and the time-of-flight method would not be so successful there.

R.A. COWLEY: To what extent are your results inconsistent with the localized Heisenberg model? Since $S(\vec{\kappa},\omega)$ on the Heisenberg model is still quite uncertain, it seems difficult to decide which aspects of your results are associated with general magnetic phenomena and which are peculiar to the itinerant electron model.

R.D. LOWDE: There is one big qualitative discrepancy with the distributions of the Heisenberg model, and that is in the κ dependence of the energy widths at small κ in the paramagnetic state, where the localized-electron model requires κ^2 and the electron gas κ. We obtain κ. To fit the facts even roughly in the paramagnetic state the Heisenberg description requires an altogether excessive range of forces, covering some tens of interatomic distances. It is, of course, true that in the lower temperature regions the Heisenberg theory would give some broad distribution of intensity, and it would be interesting to know this; but failing a dramatic turnabout in the theory of magnetism, the question arises how much effort should go into 'rescuing' a model when it patently does not apply. We are, in fact, making calculations for both models and detailed comparisons with theory will be available eventually.

C.G. WINDSOR: Further to Dr. Cowley's question, I would point out that, for nearest-neighbour Heisenberg paramagnets, both experiment[1] and theory[2] show that the diffusion region with Lorentzian line shapes and widths proportional to q^2 extends to half the zone boundary distance. In paramagnetic nickel, Lorentzian line shapes have been observed only at 1/20th of the zone boundary distance. This can be explained only in terms of very long-range Heisenberg interactions.

T. RISTE: Your observation of single-particle modes even at room temperature is very interesting, Mr. Lowde, and I should like to know with what degree of certainty you can ascribe the general intensity to this kind of excitation rather than, for example, to multiple-phonon scattering.

R.D. LOWDE: With the isotope of nickel used, the nuclear cross-section is only 1 barn and phonon scattering and multiple-phonon scattering can be definitely excluded as explanation of the intensity.

T. RISTE: I should also like to comment on the fact that you only examined $\mathcal{S}^{xx}$ and $\mathcal{S}^{yy}$ among the transverse spin correlation functions. You seem to have forgotten xy-type correlations, which also make a contribution, as is evidenced by the fact that the spin-wave cross-section is polarization-dependent and that polarization results from the scattering of an initially polarized beam.

R.D. LOWDE: We have not "forgotten" xy-type correlations. In an experiment with unpolarized neutrons we measure $\chi^{xy} + \chi^{yx}$, which is zero.

---

[1] Windsor, Briggs, Kestigian, Proc. phys. Soc. (in press).

[2] These Proceedings 2, SM-104/112.

SPIN WAVES AROUND THE NEEL TEMPERATURE IN MnO

N. KROÓ AND L. BATA
CENTRAL RESEARCH INSTITUTE FOR PHYSICS,
HUNGARIAN ACADEMY OF SCIENCES,
BUDAPEST, HUNGARY

Abstract

SPIN WAVES AROUND THE NÉEL TEMPERATURE IN MnO. The spin-wave spectrum has been investigated in antiferromagnetic MnO near the Néel temperature by inelastic scattering of cold neutrons using the time-of-flight method. No abrupt change was found in the spectrum during the phase transition. The average lifetime of magnons is a monotonical function of the temperature even around $T_N = 125°K$. In the 110-125°K range the average energy change of scattered neutrons at a fixed angle decreases with increasing temperature. In the same temperature range an additional high intensity coherent elastic peak is to be seen with a κ value half that of the [111] antiferromagnetic super-reflection. It is known from classical and neutron diffraction data that the extraordinary temperature anomaly in the heat capacity and the disappearance of the rhombohedral distortion of the crystal occur also in the range from 110 to 125°K.

The comparison of measured time-of-flight spectra at $T < T_N$ and $T > T_N$ clearly shows the existence of collective spin-excitations in the paramagnetic phase.

INTRODUCTION

Inelastic neutron scattering is a useful tool for the study of the dynamics of paramagnets. Much work of this kind has been carried out on different materials [1-3]. Among them antiferromagnetic MnO is of considerable interest because the magnetic short-range order persists even at temperatures much higher than the Néel point and the heat capacity exhibits an extraordinary anomaly around the temperature of the phase transition. The value of the Néel point was found to be about 117°K from susceptibility or heat capacity and 125°K from neutron diffraction measurements.

The first inelastic scattering studies on paramagnetic MnO showing the effect of short-range order on the scattered neutron spectra were carried out by Brockhouse and Iyengar [3]. The cold neutron scattering work of Satya Murthy, Venkataraman, Usha Deniz, Dasannacharya and Iyengar [4] proved the existence of collective spin excitations even in samples at room temperature.

The aim of the present work was to study the change of the spin-wave excitations around the phase transition point.

EXPERIMENT

The measurements were carried out on a polycrystalline MnO sample prepared by decomposing $MnCO_3$ at 1000°C under a dry hydrogen atmosphere to powder form and pressing it into bricks, then sintering in the same atmosphere at 1000°C for 2 hours. The sample was placed in a liquid N_2 cryostat where its temperature could be varied between ~ 90°K and room temperature. Inelastic neutron scattering spectra of the sample were taken on a conventional type time-of-flight spectrometer using a cooled

TABLE I. SCATTERING ANGLES AND TEMPERATURES USED IN THE EXPERIMENT

Scattering angle (ϑ)	Temperatures (K°)
18°	109, 140
25°	109, 116, 120, 125, 132, 140, 270
35°	109, 118, 124, 130, 136, 143
41°	109, 118, 124, 130, 136, 143
47°	109, 118, 124, 130, 136, 143
53°	109, 118, 124, 130, 136, 143

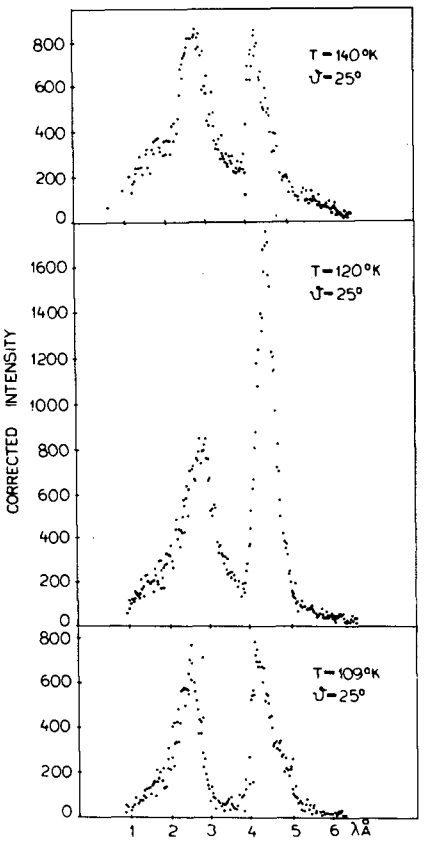

FIG.1. Corrected time-of-flight spectra at $\vartheta = 25°$ and different temperatures.

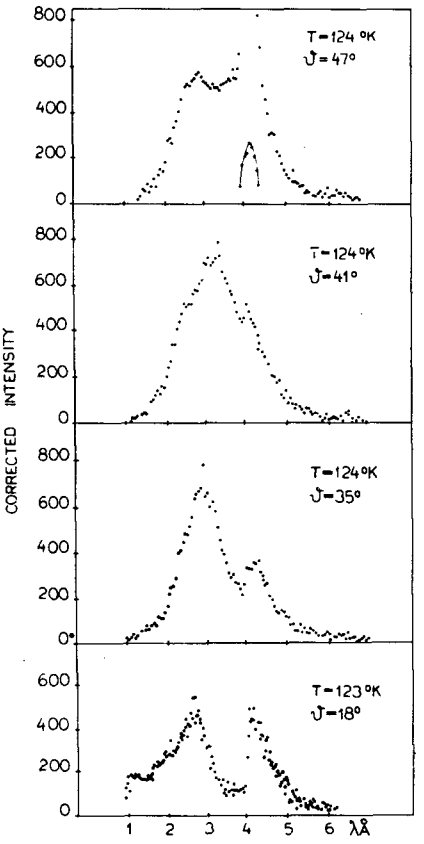

FIG.2. Spectra at $T = T_N$ and different scattering angles.

Be-filter and a semi-monochromatizing, curved chopper before the sample. The scattering angles and temperatures are listed in Table 1. The results are corrected for background, air out-scattering and detector efficiency. Some of the results are plotted in Figs 1-2. Figure 1 shows three runs at $\vartheta = 25°$. One of them is far below, the other far above T_N. The third curve was measured at T near T_N. It shows an extraordinarily high elastic peak. The κ value associated with this coherent maximum is half that of the [111] antiferromagnetic super-reflection. The inelastic parts of the spectra are very similar, but the break occurring on the low energy side of the spectra shifts with increasing temperatures to lower energies. In Fig. 2 the results obtained at $T \sim T_N$ are shown. As the angle increases towards the [111] reflection at about 49°, the inelastic magnon peak shifts to smaller energies in agreement with the quasi-momentum conservation law, averaged over the polycrystal [5]. According to this relation the contribution to the scattering from a set of lattice planes, characterized by the reciprocal lattice vector $\vec{\tau}$, is restricted to the interval

$$\kappa(\vartheta, \omega) - q(\omega) \leq 2\pi\tau \leq \kappa(\vartheta, \omega) + q(\omega) \qquad (1)$$

with sharp breaks at $\kappa(\vartheta, \omega) - q(\omega) = 2\pi\tau$ or $\kappa(\vartheta, \omega) + q(\omega) = 2\pi\tau$ where ϑ is the scattering angle. Making use of these equations, a point of the average dispersion relation can be determined from the measured position of the break in a time-of-flight spectrum taken at a fixed angle [6].

RESULTS

The inelastic part of the observed time-of-flight spectra was analysed using Eq. (1) for the calculation of points in the average dispersion curves from the breaks measured at different scattering angles. The change in the slope of this break is strongly related to the change in the lifetime of magnons. In Fig. 1 this break is well pronounced and with rising temperatures it shifts toward smaller energy changes. Figure 3 shows the average energy of the interval in which the break occurs as a function of temperature at two scattering angles. The shift with rising temperatures occurs under T_N only. In the paramagnetic phase no change in the position of the break could be observed. The shift occurs in the same temperature interval as that observed for the decreasing rhombohedral distortion [7]. The altering position of the break, which is several meV, definitely reflects the change in the average dispersion relation and cannot be explained by the small variation of the rhombohedral distortion angle. The dispersion curves at two different temperatures are plotted in Fig. 4. The

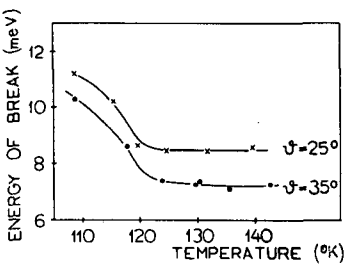

FIG. 3. The shift of breaks with varying temperature at two scattering angles.

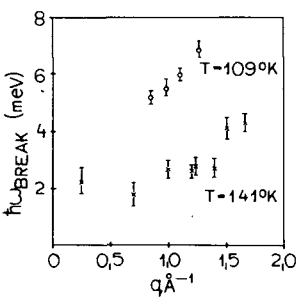

FIG. 4. Average dispersion curve at $T < T_N$ and $T > T_N$.

curve at 141°K, thus above, is found to be at lower energies than that at 109°K, thus below T_N = 125°K. The difference in energy between the two curves, at a fixed value of q, is about 3 meV.

The change in the slope of the inelastic break in the time-of-flight spectrum is a measure of the change in the lifetime of magnons. As seen in Fig. 5, this quantity is within experimental error a monotonical function of temperature, without abrupt change around T_N.

The elastic peak intensity has also been studied at the angles and temperatures given in Table I. Besides incoherent nuclear scattering, the [111] antiferromagnetic super-reflection was also observed. The temperature dependence of the super-reflection intensity is plotted in Fig. 6. In addition to this coherent elastic peak, in a small temperature region around T_N, a second peak was also observed at the $[\frac{1}{2}\frac{1}{2}\frac{1}{2}]$ angular position, as seen in Fig. 1. The temperature dependence of this second reflection is also plotted in Fig. 6. The sample was cooled down to about 105°K and slowly warmed up to higher and higher temperatures. At each point the peak intensity was measured after holding the sample at the same temperature for two hours.

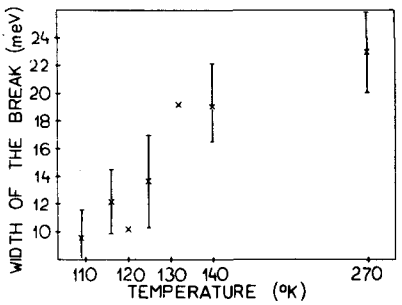

FIG. 5. The change in the slope of the break with temperature.

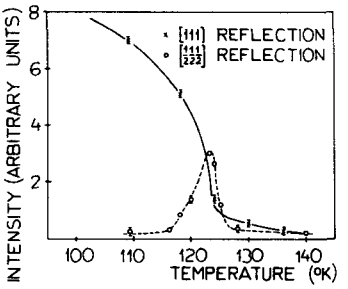

FIG. 6. The intensities of the [111] and $[\frac{1}{2}\frac{1}{2}\frac{1}{2}]$ reflections at different temperatures.

DISCUSSION

The inelastic spectra above T_N are similar to those observed at $T < T_N$. This shows that collective spin excitations exist in the paramagnetic phase. The variation of the lifetime around T_N is slow without any irregularity within the experimental error. This result indicates that if q is not too small, spin waves are not appreciably influenced by critical fluctuations. The case of long wavelength spin waves, i.e. small q values, could not be studied owing to the relatively small resolution of the time-of-flight spectrometer and because of the more complicated scattering patterns around $\vartheta = 49°$.

The average dispersion curves are seen to be different at 109 and 141°K. The slope of the curves above $q \sim 1$ Å^{-1} is the same within the experimental error in both cases, but due to the change in the anisotropy term, a shift greater than 3 meV is observed in the dispersion relation. This change of the anisotropy energy occurs in the temperature region of the decreasing rhombohedral distortion.

The Néel temperature of MnO was found to be 125°K (Fig. 6). Around this temperature an additional coherent elastic peak was observed, with $[\frac{1}{2}\frac{1}{2}\frac{1}{2}]$ Miller indices in the magnetic unit cell. This peak could be observed between ~ 116 and ~ 126°K. Remembering that susceptibility and specific heat measurements gave T_N = 116°K while from the [111] super-reflection line measured by neutron diffraction T_N ~ 125°K, the temperature interval between these two values is seen to be that of the new reflection at ϑ = 25°.

The possible existence of two phase transitions, one of first order at a lower temperature and a second of second order at a higher temperature, seems to be compatible with present data and consistent with considerations based on group theory [8].

ACKNOWLEDGEMENTS

The authors are indebted to Professor L. Pál for helpful discussions and to Mr. G. Konczos for preparing the samples.

REFERENCES

[1] BROCKHOUSE, B.N., Phys. Rev. 99 (1955) 601.
[2] CRIBIER, D., JACROT, B., Inelastic Scattering of Neutrons in Solids and Liquids (Proc. Symp. Chalk River, 1962) 2, IAEA, Vienna (1963) 309.
[3] IYENGAR, P.K., BROCKHOUSE, B.N., Bull. Am. phys. Soc. 3 (1958) 195.
[4] SATYA MURTHY, N.S., VENKATARAMAN, G., USHA DENIZ, K., DASANNACHARYA, B.A., IYENGAR, P.K., Inelastic Scattering of Neutrons (Proc. Symp. Bombay, 1964) 1, IAEA, Vienna (1965) 433.
[5] EGELSTAFF, P.A., AERE Rep. R-4101 (1962).
[6] KROÓ, N., BORGONOVI, G., SKÖLD, K., LARSSON, K.-E., Inelastic Scattering of Neutrons (Proc. Symp. Bombay, 1964) 2, IAEA, Vienna (1965) 101.
[7] BLECH, J.A., AVERBACH, B.L., Phys. Rev. 142 (1966) 287.
[8] SÓLYOM, J., private communication.

DISCUSSION

T. RISTE: Have you compared your observed dispersion law above T_N with the predictions of the dynamic scaling laws?

N. KROÓ: Unfortunately we have had no time to make this comparison yet, but we intend to perform it as soon as possible.

R.D. LOWDE (Chairman): It is fascinating to see the anomalous behaviour of MnO around the Néel temperature documented in increasingly clear detail. The ordered state of this substance at low temperatures is one in which the first neighbour shell makes no contribution to the magnetic energy (if we ignore fluctuations), because the interactions to the neighbours cancel out in pairs. At higher temperatures, however, this cancellation is inexact, and in the region of the Néel temperature the first neighbours in particular may be expected to exert a good deal of influence. Thus, as the Néel point is approached from above, it would not be surprising if other kinds of fcc ordering proved to play some part, in addition to the kind that is destined to take over with further lowering of the temperature. Perhaps an explanation along these lines would account for your data without the necessity of supposing that there are two transition points.

EXCHANGE INTEGRALS IN MAGNETITE*

K.T. MÖGLESTUE**
REACTOR CENTRUM NEDERLAND,
PETTEN (N.H.), THE NETHERLANDS

Abstract

EXCHANGE INTEGRALS IN MAGNETITE. From available experimental data the values of the three average nearest-neighbour magnetic exchange integrals in magnetite have been calculated. The calculation is based upon the results of Brockhouse and Watanabe, Alperin et al. and Dimitrijević et al. Brockhouse and Watanabe measured the energy of the acoustic magnons at the zone boundary in the [001] direction by means of a triple-axis neutron spectrometer. They also found the energy of the lowest optic magnons for zero wavevector. For small magnon wavevectors, $\vec{q}$, the theoretical expression for the acoustic branch may be expanded in powers of $\vec{q}$. Using the 'diffraction method', Alperin et al. and Dimitrijević et al. measured the coefficient of the quadratic term, a_2, of this expansion. The result of the present calculation is $J_{AA} = -1.52 \pm 0.46$ meV, $J_{AB} = -2.42 \pm 0.04$ meV and $J_{BB} = 0.31 \pm 0.07$ meV. Here J_{AA}, J_{AB} and J_{BB} are the average magnetic exchange integrals between nearest neighbour A-A ions, A-B ions, and B-B ions respectively.

This result has been compared to earlier determination of J_{AB} and J_{BB} where it was assumed that J_{AA} vanishes. The conclusion of this comparison is that all three exchange integrals should be taken into account on interpreting spin-wave data on magnetite. The exchange integrals J_{AA} and J_{BB} have been studied as a function of a_2. It has been found that J_{BB} is almost independent of a_2, while J_{AA} exhibits a very strong dependence on it.

Based upon the exchange interaction constants of the present investigation, the complete spin-wave dispersion curve has been computed for the [001] direction. There is a good agreement between the computed curve and the experimental points given by Watanabe and Brockhouse.

1. INTRODUCTION

The structure of magnetite at room temperature is known to be the cubic spinel structure with space group $Fd3m\text{-}O_h^7$. Eight of the tetrahedral sites (A sites) are occupied by Fe^{3+} ions and sixteen of the octahedral sites (B sites) are occupied by an equal number of Fe^{3+} and Fe^{2+} ions. Above the Verwey transition temperature at 119°K a rapid exchange of electrons takes place [1-3]. This exchange is so rapid that all ions at the B sites may be considered equal. Thus one may expect three types of nearest-neighbour exchange interactions between magnetic ions: one between the ions of the A sites, another between the ions at different types of sites and the third type between the ions of the B sites.

It has earlier been assumed that the interaction between a pair of ions of the A sites is negligible, and that the interaction between a pair of ions of the B sites is small compared to the interaction between the ions of different types of sites. The aim of the present investigation was to check this hypothesis, using published experimental data on the spin-wave dispersion curves.

The spin-wave dispersion relation for magnetite has been computed by several authors [4-7]. In some of this work it has either been assumed that a simple relationship existed between the exchange integrals or that

* Work sponsored jointly by Institutt for Atomenergi, Norway and Reactor Centrum Nederland.
** On leave from Institutt for Atomenergi, Kjeller, Norway.

both the A-A and the B-B interactions vanish. Without any restrictions of this kind Kaplan [7] has given the expressions for the acoustic and the first optic branch of the spin-wave dispersion relation for small spin-wave momenta. Glasser and Milford [5] have calculated the general formula for the spin-wave energies in the [100] direction.

For pure magnetite the spin-wave dispersion curve has been observed previously by inelastic neutron scattering techniques [8-14]. Experiments employing the diffraction method have been performed to measure the acoustic branch for small spin-wave momenta [8-12]. Using a triple-axis instrument Brockhouse and Watanabe [13] have measured the entire acoustic branch and the lower energy parts of two of the optic branches at room temperature. At 77°K Alperin et al. [9] and Torrie [14] have measured the acoustic branch. Their results are not essentially different from those at room temperature.

2. THEORY

As mentioned in the introduction, the entire spin-wave dispersion curve has been calculated by Glasser and Milford [5]. From their analysis it follows that the energy, E_0, of the lowest energy optic branch at zero magnon momentum is

$$E_0 = 12J_{AB}\,(S_A - 2S_B) \tag{1}$$

Here J_{AB} is the magnetic nearest-neighbour exchange interaction constant between an ion at an A site and an ion at a B site. S_A is the spin of the A site ions, S_B is the average spin of the ions at the B sites. This equation determines J_{AB} uniquely.

Further, the energy E_a of the acoustic magnons at the Brillouin-zone boundary in the [100] direction is

$$E_a = 6J_{AB}\,(S_A - 2S_B) - 4(J_{AA}S_A - J_{BB}\,S_B) - \{[6J_{AB}(S_A + 2S_B) - 4(J_{AA}S_A + J_{BB}\,S_B)]^2 - 16J_{AB}^2\,S_A S_B\}^{\frac{1}{2}} \tag{2}$$

Here J_{AA} and J_{BB} are the magnetic exchange interaction constants between a pair of A site ions and a pair of B site ions, respectively. The expressions for E_a and E_0 are derived for zero external magnetic field.

For small magnon wavevectors, $\vec{q}$, the expression for the energy, E, of the acoustic branch may be expanded as follows:

$$E = (\hbar^2/2m_0)(a_0 + a_2 q^2 + a_4 q^4 + \ldots) \tag{3}$$

where m_0 is the mass of the neutron. For zero magnetic field a_0 vanishes. For a_2 Kaplan [7] gives the expression

$$a_2 = \frac{(11/2)J_{AB}\,S_A S_B - J_{AA}S_A^2 - 2J_{BB}\,S_B^2}{2\hbar^2(S_A - 2S_B)}\,a^2 m_0 \tag{4}$$

where a is the lattice constant. This equation may also be obtained from the general equation for the energy of the acoustic branch given by Glasser and Milford [5].

3. RESULTS AND DISCUSSION

From available data on pure magnetite it is possible to determine the three-nearest-neighbour magnetic-exchange interaction constants. For pure magnetite Brockhouse and Watanabe [13] have measured $E_0 = 58 \pm 1$ meV and $E_a = 75 \pm 1$ meV. By means of the diffraction method the quantity a_2 of Eq. (3) has been determined by several authors [8-12]. The experimental values range from 243 [10] to 330 [12]. J_{AA} and J_{BB} can be found as a function of a_2, using the values of E_a and E_0 mentioned above. From the result of this analysis shown in Fig. 1 it is found that J_{BB} is almost insensitive to variations in a_2, while J_{AA} depends very strongly on it. This is also reflected in the large standard deviation that has been found for J_{AA}. In comparison, the shift of J_{AA} due to variations of E_a and E_0 within the uncertainty limits is of no significance.

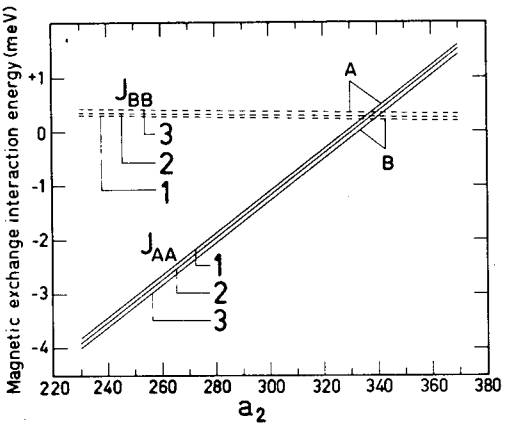

FIG. 1. Exchange constants J_{AA} and J_{BB} as functions of a_2 for different values of E_0 and E_a. The full curves represent J_{AA}, the dashed lines represent J_{BB}. Curves 1, 2 and 3 are computed for E_a = 74, 75 and 76 meV, respectively. For all of these E_0 = 58 meV. Lines A and B coincide with the curves calculated for E_a = 75 and for E_0 = 57 and 59 meV respectively.

The value of a_2 reported by Riste et al. [8] and Ferguson and Sáenz [10] are both at the lower limit of the range of experimental values. They require an antiferromagnetic exchange interaction which is stronger than the A-B interaction. This is not in accordance with what is generally expected. Excluding those two results because of this, what remains are the values reported by Jacrot and Cribier [12] (a_2 = 330), Alperin et al. [9] ($a_2 = 297 \pm 15$) and Dimitrijević et al. [11] ($a_2 = 285 \pm 15$). These determinations are all performed at room temperature. The result of Jacrot and Cribier is at the upper limit of the range of experimental values. It leads to a value of J_{AA} close to zero, which is in agreement with the assumption made in most of the work published hitherto [6,7,13,14]. As nothing has been stated about the accuracy of this determination, it is

not possible to tell what weight it should be given. It has therefore not been used. The mean value of the two remaining determinations of a_2 is $a_2 = 291 \pm 11$.

It can be mentioned that in their discussion Alperin et al. [9] obtained their value by a least-squares fit of a quartic spin-wave curve (Eq. (3)) to their experimental data. The fit would not improve significantly on taking higher-order terms into account. With a quadratic fit only, they get a value of a_2 agreeing with the result of Ferguson and Sáenz [10].

Assuming $a_2 = 291 \pm 11$, J_{AA} and J_{BB} have been calculated. The result is given in Table I. The standard deviations are based upon the standard deviations in E_a, E_0 and a_2. For comparison, the values of the exchange interaction constants quoted by Glasser and Milford [5] and Torrie [14] are also included in this table.

TABLE I. NEAREST-NEIGHBOUR MAGNETIC EXCHANGE CONSTANTS IN Fe_3O_4
The standard deviations are given in units of the last decimal.

Source	J_{AA}(meV)	J_{AB}(meV)	J_{BB}(meV)
Present work	-1.52(46)	-2.42(4)	0.31(7)
Glasser and Milford [5]	0	-2.4	0.24
Torrie [14]	0	-2.20(22)	0.6(6)

In agreement with earlier results, the A-B interaction is found to be the largest. The B-B interaction is ferromagnetic and an order of magnitude smaller. The A-A interaction, however, is antiferromagnetic and more than half of the A-B interaction. This result is not in accordance with earlier assumptions [4, 5, 13, 14], but agrees with predictions based upon molecular field theory made by Néel [15].

Earlier authors [4-6, 13, 14] have, assuming either that $J_{AA} = 0$ or that $J_{AA} = J_{BB} = 0$, attempted to fit computed dispersion curves to the data of Brockhouse and Watanabe [13]. The latter assumption has not led to a satisfactory fit for all wavevectors. Glasser and Milford [5] used both the acoustic and the first optic branch of Brockhouse and Watanabe in their determination of J_{AB} and J_{BB}. For this purpose they first determined the best J_{AB}. As a correction they applied $J_{BB} = -J_{AB}/10$. They obtained a good agreement between their calculation and the experimental data. Torrie [14] limited himself to the acoustic branch to obtain J_{AB} and J_{BB}. The agreement he obtained between calculation and experiment is good for this branch, but his exchange integrals imply that $E_0 = 53 \pm 5$ meV. On the other hand, the exchange integrals quoted by Glasser and Milford [5] lead to $a_2 = 315$. This shows that all three exchange integrals should be taken into account when interpreting the experimental data on magnetite.

Based upon the exchange integrals of the present investigation, the complete spin-wave dispersion relation for the [001] direction has been computed. This is shown in Fig. 2. In this figure the experimental points given by Brockhouse and Watanabe have also been indicated. As in the work of Glasser and Milford, there is a good agreement between the calculated curve and the experimental points.

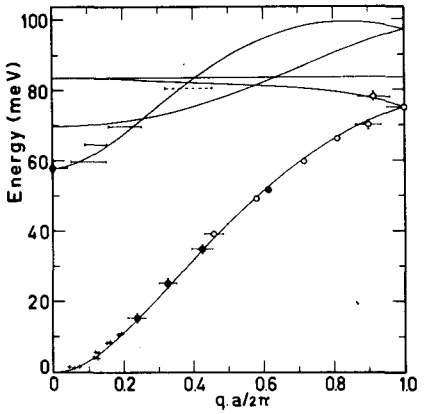

FIG.2. Computed spin-wave dispersion curve in the [001] direction. The curves are based upon the values of the exchange integrals given in Table I. The experimental points are those given by Ref. [13].

Numerical calculations show that the agreement does not change significantly on varying the value of J_{AA}. However, from Fig. 1 we see that J_{AA} takes a value significantly different from zero in the region where experimental values of a_2 have been reported. The conclusion, therefore, is that also J_{AA} should be taken into consideration when discussing magnetite.

Numerical analysis also shows that the optic branch that intersects the energy axis at 70 meV (Fig. 2) is most sensitive to variations in J_{AA}. To establish a better value of J_{AA}, this branch should be measured.

ACKNOWLEDGEMENTS

The author wishes to express his gratitude for the helpful discussions with Mr. E. Frikkee, Dr. B.O. Loopstra and Mr. E.J. Samuelsen.

REFERENCES

[1] VERWEY, E.J.W., HAAYMAN, P.W., Physica 8 (1941) 979.
[2] ITO, A., ÔNO, K., ISHIKAWA, Y., J. phys. Soc. Japan 18 (1963) 1456.
[3] BAUMINGER, R., COHEN, S.G., MARINOV, A., OFFER, S., SEGAL, E., Phys. Rev. 122 (1961) 1447.
[4] CALLEN, E., Phys. Rev. 150 (1966) 367.
[5] GLASSER, M.L., MILFORD, F.J., Phys. Rev. 130 (1963) 1783.
[6] MILLS, R.E., KENAN, R.P., MILFORD, F.J., Phys. Rev. 145 (1966) 704.
[7] KAPLAN, H., Phys. Rev. 86 (1952) 121.
[8] RISTE, T., BLINOWSKI, K., JANIK, J., J. Phys. Chem. Sol. 9 (1959) 153.
[9] ALPERIN, H., STEINSVOLL, O., NATHANS, R., SHIRANE, G., Phys. Rev. 154 (1967) 508.
[10] FERGUSON, G.A., Jr., SÁENZ, A.W., Phys. Rev. 156 (1967) 632.
[11] DIMITRIJEVIĆ, Z., KRAŠNICKI, S., RŽANY, H., TODOROVIĆ, J., WANIĆ, A., Phys. Stat. Sol. 15 (1966) 119; Phys. Stat. Sol. 22 (1967) K55.
[12] JACROT, B., CRIBIER, D., J. phys. Rad. 23 (1962) 494.
[13] BROCKHOUSE, B.N., WATANABE, H., Inelastic Scattering of Neutrons in Solids and Liquids (Proc. Symp. Chalk River, 1962) 2, IAEA, Vienna (1963) 297; Phys. Lett. 1 (1962) 189.
[14] TORRIE, B.H., Solid State Comm. 5 (1967) 715.
[15] NÉEL, L., Ann. Phys. 3 (1948) 137.

DISCUSSION

W. BALTENSPERGER: Exchange constants cannot at present be calculated from a priori theory, and I would like to draw attention to the possibility of other measurements capable of providing further information on exchange. The phonon spectrum of a magnetic substance is weakly dependent on the magnetic state, i.e. the spin correlations, and the theory of this effect (on which a publication is to appear in Helvetica Physica Acta) involves the first and second derivatives of the exchange constants with respect to the distances and the angles between the atoms, including non-magnetic atoms, which carry the superexchange interaction. The dependence of the exchange constants on volume can be obtained from pressure measurements. The changes in the phonon spectrum with magnetic order, however, show how the exchange parameters vary with other structural deviations. The relative change of the phonon frequency is only of the order of 10^{-3} to 10^{-2} .

K. T. MÖGLESTUE: The exchange integrals can be calculated if one knows the electronic configuration of the solid. Measurement of the magnetic exchange constants also provides a check on that part of the calculated interaction arising from the unpaired electrons.

R.D. LOWDE (Chairman): You spoke about the sensitivity of the calculated magnon spectrum to the parameters you put in. I think I may have missed your indication of what those frequencies would have become if you had used a wider range of credible J values. You rejected some J's and I wonder whether that rejection can be justified by the answer you get.

K.T. MÖGLESTUE: In the lower range we had a_2 values equal to about 240, implying that J_{AA} is larger than J_{AB} . I can imagine, intuitively, that such an AB structure would no longer be stable, thanks to the strong A interaction.

MAGNETIC EXCITATIONS IN COBALTOUS OXIDE

W.J.L. BUYERS, G. DOLLING, J. SAKURAI
AND R.A. COWLEY
ATOMIC ENERGY OF CANADA LTD.,
CHALK RIVER, ONT., CANADA

Abstract

MAGNETIC EXCITATIONS IN COBALTOUS OXIDE. Neutron inelastic scattering experiments on single-crystal cobaltous oxide (CoO) show that magnetic excitations exist in this material both above and below the transition temperature (293°K). The measurements were made with a triple-axis crystal spectrometer at the NRU reactor, Chalk River. In the paramagnetic phase, two distinct bands of excitations have been observed. These correspond to transitions between the spin-orbit levels of the Co^{2+} ion. The ratio of the measured transition frequencies (0.61) and the temperature dependence of the intensities of the bands support this assignment. The spin-orbit coupling parameter, -2.13 ± 0.05 (10^{12} cps) is only 40% of the free-ion value, possibly because of a dynamic Jahn-Teller effect. Two bands of excitations have also been observed in the antiferromagnetic state, but their origins are believed to be quite different from those described above. They correspond, respectively, to transitions from the ground state of the Co^{2+} ion to its conjugate ($j = 1/2$) state and to the lowest state of the next spin-orbit level ($j = 3/2$). At the temperature of the experiment (110°K) the latter transition is the lower of the two transitions at approximately 5 (10^{12} cps). Both transitions exhibit weak dependence on wave vector. A spin-wave model for these magnetic excitations leads to a next-nearest-neighbour exchange constant of 0.35 ± 0.02 (10^{12} cps), and indicates that the nearest-neighbour exchange constant and the tetragonal distortion are both small. The transition temperature of this model in the molecular field approximation is 240°K, in reasonable agreement with experiment.

1. INTRODUCTION

At high temperatures cobaltous oxide (CoO) is paramagnetic and has the rocksalt crystal structure. Below 293°K (the Néel temperature, T_N), it distorts to an antiferromagnetic tetragonal structure in which the atomic magnetic moments are arranged in ferromagnetic sheets parallel to (111) crystallographic planes [1,2,3,4]. The orbital magnetic moment of the Co^{2+} ion is not completely quenched by the crystalline field, and there are several low-lying excited states of the system which might be expected to influence its magnetic properties significantly, as discussed by Kanamori [5] and by Tachiki [6].

In section 2 we present experimental results for the dispersion relations of both phonon and magnon excitations at temperatures above and below T_N. A discussion of the phonon excitations will be given elsewhere [7]; here we shall consider possible interpretations only of the magnetic excitations, above T_N in section 3 and below T_N in section 4.

2. EXPERIMENTS

The determination of the magnon and phonon dispersion relations was performed by observing the coherent, inelastic scattering of slow neutrons by single crystal specimens [8], with the aid of a triple-axis crystal spectrometer mounted at facility C5 of the NRU reactor, Chalk River. The spectrometer was operated throughout in its constant $\vec{Q}$ mode [9], where $\hbar\vec{Q}$ is

the momentum change suffered by the scattered neutrons, and measurements were made of excitations having reduced wave vectors $\vec{q}$ along three directions of high symmetry, (00ζ), $(\zeta\zeta 0)$ and $(\zeta\zeta\zeta)$; $2\pi\zeta/a$ is a coordinate of $\vec{q}$ and a is the lattice constant. In this paper we shall for convenience refer to symmetry axes and wave vectors appropriate to the high temperature cubic phase of CoO, even when dealing with the low temperature tetragonal phase. Owing to the small size of the distortion, and the multi-domain character of our specimen, we are unable to distinguish between excitations propagating along the a or c axes.

Some typical scattered neutron distributions are shown in Figs. 1 and 2. In Fig. 1 the results of scans with a wave vector transfer, $\vec{Q}$, of $(2,2,0)2\pi/a$ at 425°K and 110°K are shown. The results clearly show the presence of some scattering with a frequency of about 5 (10^{12} cps) at both temperatures, and further scattering with a frequency of 7 at 110°K. Figure 2 shows two distributions obtained at 110°K, for wave vectors close to the (002) reciprocal lattice point. It does not seem possible to understand all our measured distributions in terms only of the phonon spectrum of CoO [7]. In particular, the peaks M1 and M2 are incompatible with any reasonable description of the normal modes, and are therefore believed to arise from magnetic excitations. The peak marked LA however arises from scattering by the longitudinal acoustic phonon propagating along the (00ζ) direction. The initial results in the paramagnetic phase were obtained for $\vec{q}$ along the cube body-diagonal (Λ), at a temperature of 330°K. Subsequent measurements for the other two high symmetry directions (Δ,Σ) were made at 425°K, and Fig. 3 is a composite of all these high-temperature results. The complete results at 110°K are shown in Fig. 4.

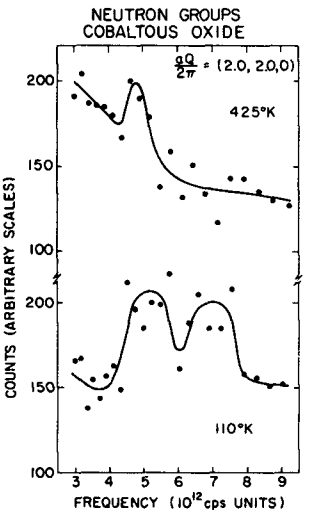

FIG. 1. Observed neutron groups for two constant-Q scans at 110°K and 425°K. The peaks are believed to arise largely from magnetic scattering and show the decrease in intensity at a frequency of 7.0 at 425°K. The rise in intensity at low frequency at 425°K is associated with the paramagnetic scattering.

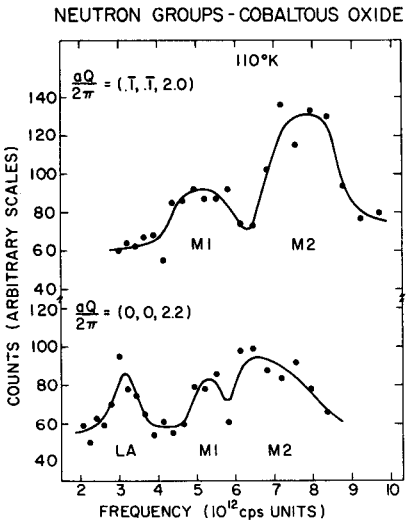

FIG.2. Two distributions obtained at 110° K. The peaks labelled M1 and M2 are from the magnetic excitations and LA from the longitudinal acoustic normal mode of vibration.

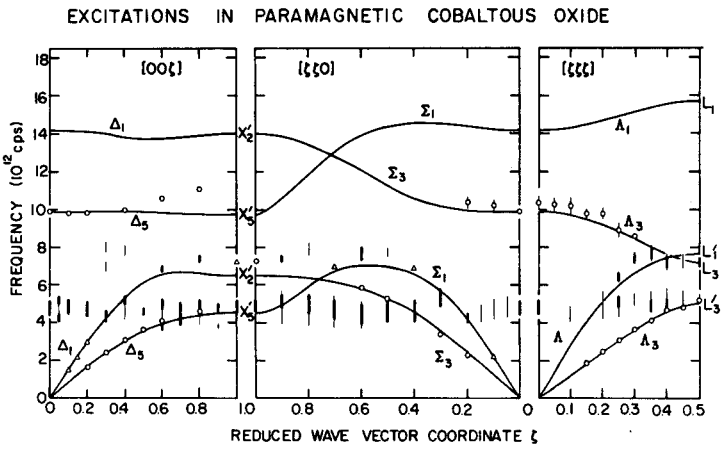

FIG.3. The experimental results in the paramagnetic phase of CoO. The results for the [00ζ] and [ζζ0] directions are at 425° K and [ζζζ] at 330° K. The circles arise from sharp peaks, and the bars from broad peaks. The thin vertical bars indicate broad distributions of low intensity. The solid lines are a shell model best fit to the phonon dispersion curves. The magnetic curves are then seen to be a flat branch at a frequency of 4.8 and a weaker branch at about 7.8.

Standard group-theoretical methods were used in conjunction with the character tables of Koster [10], to label the various branches of these spectra that could be identified with phonon excitations. Considerable experimental difficulty was experienced, however, in making assignments within the frequency range 4.5 to 7.5 x 10^{12} cps, owing to the magnetic scattering in this region. We shall label the lower and upper broad bands M1 and M2 respectively. At 110°K, both bands gave rise

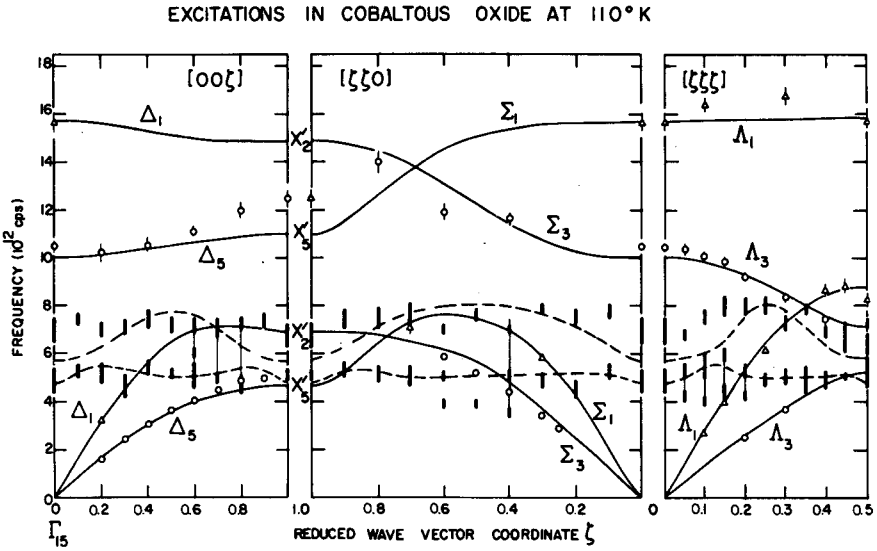

FIG.4. The complete experimental results at 110°K. The circles arise from sharp peaks in the scattered distributions, while the bars represent the broad peaks. The thin lines connecting the bars indicate the presence of weaker intensity near the broad peaks. The labels are the standard group theoretical labels for the phonon branches in the NaCl structure. The solid lines show a best-fit shell model to the phonon dispersion curves, and the dotted lines a magnon model with only second-nearest-neighbour interaction.

to neutron scattering of comparable intensity, but at 425°K the intensity from the upper band was only just observable. The lower frequency band was still readily observed, however. The variation in the intensity of these bands as a function of momentum transfer was difficult to determine because of the presence of phonons with similar frequencies. However, where phonon scattering is likely to be unimportant, the intensity decreased somewhat as the momentum transfer increased.

3. MAGNETIC EXCITATIONS ABOVE THE NEEL TEMPERATURE

At 425°K, two broad bands of magnetic excitations are observed (Fig. 3), with the higher frequency band M2, at 7.8×10^{12} cps, much less intense than the lower band M1 at about 4.8×10^{12} cps. These bands may be understood in terms of the single ion energy level diagram of Co^{2+} in CoO, as shown in Fig. 5. The ground state ^4F configuration of the free ion is split by the cubic field to give a Γ_4 orbital triplet of lowest energy. The spin orbit coupling then further reduces the twelve-fold degeneracy ($S = 3/2$) of this effective $\ell = 1$ state to give three states with quantum numbers $j = \ell + S = 5/2, 3/2, 1/2$. The lowest of these is the $j = 1/2$ Kramers doublet. Since both bands of excitations show little dispersion, a description of them in terms of the properties of a single ion is reasonable. A simple interpretation of the results is then obtained (see Fig. 5) by identifying the M1 and M2 bands with transitions A, between the $j = 1/2$ and $j = 3/2$ levels, and B, between the $j = 3/2$ and $j = 5/2$ levels, respectively. The latter transition is weaker both because there are fewer ions in the $j = 3/2$ state than in the $j = 1/2$ state at 425°K, and

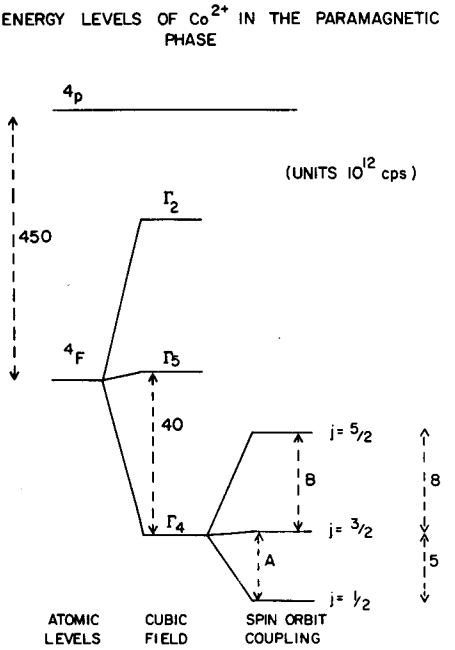

FIG.5. The energy level diagrams of Co^{++}, in the paramagnetic state, showing the effects of the cubic crystal field, and the spin-orbit interaction.

also because its higher frequency leads to a smaller neutron scattering cross-section. The ratio of the frequencies of the two bands, on this picture, should be 0.60, independent of the numerical value of the spin-orbit coupling parameter, λ. Experimentally, we obtain 0.61 $\pm$ 0.07. However, to give the observed energies, this scheme requires a reduction in the value of λ from -5.4 (10^{12} cps) for the free ion, to -2.13 in the crystal.

4. MAGNETIC EXCITATIONS BELOW THE NEEL TEMPERATURE

4.1 Molecular Field Approximation

In the antiferromagnetic state, the results show two almost constant-frequency branches (Fig. 4), again suggesting that the results may be explained largely by the single-ion properties. The effect of applying a molecular field to the unperturbed spin-orbit states of Co^{2+} is shown in Fig. 6. The degeneracy of all the j multiplets is removed to give a complicated energy level spectrum. The calculation is performed within the molecular field approximation by introducing a Heisenberg exchange interaction, J_2, between next-nearest neighbours (nearest neighbours do not contribute to the molecular field); the single ion Hamiltonian is thus

$$-\frac{3}{2}.\lambda\ \vec{\ell}.\vec{S} + 2J_2 Z_2 \langle S \rangle\ S^z \qquad (4.1)$$

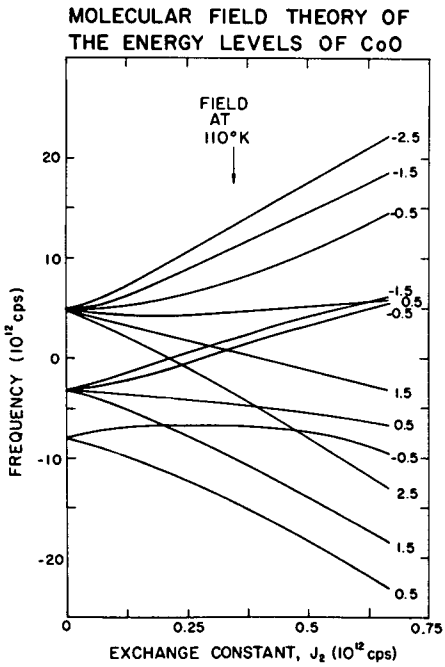

FIG. 6. The energy levels of the ground-state multiplet of Co^{2+} in the antiferromagnetic state, as a function of second-nearest-neighbour exchange parameter. The arrow shows the value of J_2 which gives the correct splitting for the lowest two states in CoO. The spin-orbit coupling parameter is $\lambda = -2.13 \times 10^{12}$ cps, and the tetragonal distortion is not included. The numbers at the right-hand side give the Z component of the total angular momentum, $j = \ell + S$, of each state.

where Z_2 is the number of next-nearest neighbours and $\langle S \rangle$ is the thermal average value of S^z:

$$\langle S \rangle = \sum_n \langle n|S^z|n \rangle \exp(-E_n/kT) / \sum_n \exp(-E_n/kT) \qquad (4.2)$$

For any given value of J_2, a self-consistent set of energy levels E_n is determined by an iterative procedure. An exchange interaction $J_2 = 0.347 \pm 0.02$ (10^{12} cps) leads to two energy levels lying 4.5 and 7.8 (10^{12} cps) above the ground state, as shown in Fig. 6. These correspond quite closely to the energies of the two bands observed experimentally, and essentially perfect agreement may readily be obtained by adding a small term $c\ell_z^2$ to the Hamiltonian (4.1) to represent the tetragonal distortion. A suitable value for the constant c is -0.7 ± 0.2 (10^{12} cps). The values of J_2 and c given by Kanamori [5] are 0.45 and -3.0 respectively.

4.2 Spin Waves in CoO

If we restrict the exchange interactions to be of the Heisenberg form between first and second nearest neighbour Co^{2+}

ions only, then an appropriate Hamiltonian for the magnetic electrons in the Γ_4 state is

$$\sum_i \left[-\frac{3}{2}\lambda\, \vec{\ell}(i)\cdot\vec{S}(i) + c\ell_z(i)^2 \right] + \sum_{ij} J(ij)\, \vec{S}(i)\cdot\vec{S}(j) \tag{4.3}$$

The spin waves may then be calculated with the help of pseudo-boson techniques (see, for example, Grover [11]).

The results, neglecting the nearest neighbour exchange interaction J_1, are shown in Fig. 4. It is seen that there is reasonable agreement with experiment although the theory predicts too large a dispersion. An estimate of J_1 may be obtained from the paramagnetic susceptibility measurements of La Blanchetais [12], since this quantity depends on the sum of J_1 and J_2: we obtain $J_1 = 0.021$ (10^{12} cps), which is indeed much smaller than the molecular field result for J_2. Recalculation of the magnon frequencies including this nearest neighbour constant J_1 showed only small changes ($\leq 0.2 \times 10^{12}$ cps) from the $J_1 = 0$ results. Strictly speaking, the magnon dispersion relation is more complex than described above, since the spin direction is not quite along the tetragonal axis (the deviation is about 10°). The anisotropy which gives rise to this deviation [13] will also split the doubly degenerate spin wave modes for each domain into two separate branches. However, it is expected that these splittings will be quite small, probably about 0.2×10^{12} cps. The origin of the broad scattered neutron distributions associated with the magnetic excitations below T_N is probably the slightly different frequencies of these modes, and also the fact that if $J_1 \neq 0$ then the frequencies of modes in different domains will also be slightly different.

5. DISCUSSION

Perhaps the most striking feature of the above results and analysis is the unusually low value of the spin-orbit coupling constant λ which has been invoked to understand the magnetic excitations. It seems difficult to understand how the covalent bonding of the Co^{2+} to the neighbouring oxygen ions, or the interaction with higher states, can reduce it to only 40% of the free-ion value. This reduction of the spin-orbit parameter may constitute evidence for a dynamic Jahn-Teller effect as described by Ham [14].

In the antiferromagnetic phase, the results are in good qualitative agreement with a model involving an almost negligible nearest neighbour exchange constant $J_1 = 0.021$, a second nearest neighbour constant $J_2 = 0.347$ and a tetragonal distortion parameter of -0.7 (all quantities in units 10^{12} cps). Agreement might well be improved by including states of higher energy than the lowest two, since interaction with such higher states would tend to reduce the dispersion of the upper band.

No striking experimental evidence was obtained for a magnon-phonon interaction. The absence of the effect is seen to be reasonable when the mechanism for the coupling of magnons

and phonons is considered. These may interact because the electrostatic field of the ions is altered by the presence of a phonon, and this in turn disturbs the energy levels. In the cause of UO_2 where a strong interaction was observed [15], the anisotropy from the crystal field in the ground state is comparable with the molecular field energy. In CoO, however, this is not the case as the distortion energy is only about 15% of the molecular field energy. Since the magnon-phonon interaction in UO_2 is about 20% of the anisotropy energy, we expect a magnon-phonon interaction in CoO of about 0.15 (10^{12} cps), a value well below the experimental resolution.

Further detailed experiments are needed to achieve a more complete understanding of the magnetic properties of CoO. Experiments at much greater resolution might well separate the different branches which contribute to the broad bands of excitations seen at present, and in this connection, a single domain specimen would be most valuable. More detailed checks of the theory would be provided by measurements both of higher frequency excitations and of the temperature dependence of the magnetic excitations particularly in the range 110°K to room temperature. It is planned to attempt some of these experiments in the near future.

REFERENCES

[1] ROTH, W.L., Phys. Rev. 110 (1958) 1333.

[2] VAN LAAR, B., Phys. Rev. 138 (1965) A584.

[3] VAN LAAR, B., SCHWEIZER, J., LEMAIRE, R., Phys. Rev. 141 (1966) 538.

[4] SAITO, S., NAKAHIGASHI, K., SHIMOMURA, Y., J. Phys. Soc. Japan 21 (1966) 580.

[5] KANAMORI, J. Prog. Theor. Phys. (Kyoto) 17 (1956) 177, 197.

[6] TACHIKI, M., J. Phys. Soc. Japan 19 (1964) 454.

[7] SAKURAI, J., BUYERS, W.J.L, COWLEY, R.A., DOLLING, G., Phys. Rev., to be published.

[8] See chapters 1, 5 and 6 of Thermal Neutron Scattering (EGELSTAFF, P.A. ed) Academic Press, New York (1965).

[9] BROCKHOUSE, B.N., "Inelastic scattering of neutrons in solids and liquids", IAEA, Vienna (1961) 113.

[10] KOSTER, G.C., Solid State Physics, Vol. 5, p. 174 (SEITZ, F., TURNBULL, D., Eds.) Academic Press, New York (1957).

[11] GROVER, B., Phys. Rev. 140 (1965) A1944.

[12] LA BLANCHETAIS, C.H., J. Phys. Radium 12 (1951) 765.

[13] UCHIDA, E., FUKUOKA, N., KONDOH, H., TAKEDA, T., NAKAZUMI, Y., NAGAMIYA, T., J. Phys. Soc. Japan 19 (1964) 2088.

[14] HAM, F.S., Phys. Rev. 138 (1965) A1727.

[15] DOLLING, G., COWLEY, R.A. Phys. Rev. Letters 16 (1966) 683.

DISCUSSION

C.G. WINDSOR: The spin-orbit interaction in CoO could be found independently, could it not, by analysis of the susceptibility at high temperatures.

R.A. COWLEY: Kanamori et al. attempted this, but since the exchange constants are unknown, the result obtained is ambiguous.

C.G. WINDSOR: Can you explain the low value for J_1/J_2 compared with the value of about unity found in MnO?

R.A. COWLEY: Not in detail, but I see no reason to expect the exchange in CoO to be the same as in MnO. If the interaction is largely superexchange through the O^2 ions, it is not surprising that the 90° interaction of nearest neighbours is smaller than the 180° interaction of next-nearest neighbours. Further, the ferromagnetic direct interaction is likely to be larger for the closest neighbours. Adding these two effects it is perhaps possible to understand why $|J_1| < |J_2|$.

PARAMAGNETIC SCATTERING OF NEUTRONS BY TRIVALENT RARE-EARTH IONS IN AN OCTAHEDRAL CRYSTAL FIELD

A. FURRER, W. HÄLG AND T. SCHNEIDER
DELEGATION FÜR AUSBILDUNG UND HOCHSCHULFORSCHUNG,
SWISS FEDERAL INSTITUTE FOR REACTOR RESEARCH,
WÜRENLINGEN, SWITZERLAND

Abstract

PARAMAGNETIC SCATTERING OF NEUTRONS BY TRIVALENT RARE-EARTH IONS IN AN OCTAHEDRAL CRYSTAL FIELD. The energy distribution of neutrons scattered by trivalent rare-earth compounds has been measured at room temperature. The paramagnetic lines, corresponding to transitions within the ground-state multiplet of the rare-earth ion split by the octahedral crystal field, are superposed on the nuclear parts of the energy distribution. Experimental conditions and computational methods are described to determine the position and shape of the paramagnetic lines. The resulting values of the crystal field splitting and the paramagnetic line width are discussed.

1. INTRODUCTION

The properties of paramagnetic salts have been investigated in a number of ways, chief of which are paramagnetic resonance experiments and susceptibility measurements including the study of anisotropy. The disadvantages of these methods are that single crystals are required for accurate work and certain substances cannot even be investigated because there are no allowed transitions between the levels which give rise to paramagnetism. Moreover, impurities could affect the results, a fact which is of great importance in substances such as the rare earths which are often not available in the highly purified condition.

One of the most versatile experimental methods has proved to be direct measurement of energy levels by inelastic scattering of thermal neutrons, where the difficulties and restrictions mentioned above do not exist. We used this technique to investigate several rare-earth compounds in the paramagnetic state. There are three main interactions which control the properties of the rare-earth ion in a crystal: (i) the Coulomb interaction between electrons, which has the effect of coupling the individual angular momenta into total orbital and spin angular momenta L and S; (ii) the spin-orbit interaction, which couples L and S to give J; (iii) the crystalline electric field, which partly raises the $(2J+1)$-fold degeneracy of a given J. In the rare-earth transition group, the unfilled electron shell is an inner 4f shell, so that the interaction with the electric field of neighbouring ions is small and usually comparable with the energy of thermal neutrons. Thus, when neutrons are magnetically scattered from the rare-earth ions, the scattered neutrons leave the sample with discrete energies corresponding to the crystal field splittings.

Up to the present, crystal field splittings have been observed by the inelastic neutron scattering method in a great number of rare-earth compounds. However, analysis of the measured energy distributions has not always given satisfactory results. In section 2 an experimental procedure is proposed to evaluate both the position and the shape of the paramagnetic part exactly. This is exemplified in section 3 for the case of $Ce_xY_{1-x}As$. We have chosen compounds where x takes the values 1 and 0.7 to investigate especially the effect of paramagnetic exchange broadening. This is shown in section 4, where it is found that the spin-lattice interaction has to be taken into consideration for the interpretation of line widths at room temperature.

2. EXPERIMENTAL DETAILS

The inelastic scattering of slow neutrons by polycrystalline paramagnetic solids provides information about both the dynamics of the crystal lattice and the paramagnetic behaviour. If one is interested only in the latter, the question of how to separate paramagnetic scattering from other inelastic components, such as vibrational scattering arises. In some cases one may base such a separation merely on the different response of the paramagnetic and vibrational cross-sections to an external magnetic field. However, when a magnetic field is applied, the behaviour of the energy levels is thereby more complicated than in the case of single crystals, where the lines diverge linearly.

The best method for distinguishing between paramagnetic scattering and vibrational scattering is provided by the double-differential cross-sections themselves. If the coherent scattering of neutrons does not constitute the major part of the vibrational scattering, the latter can be completely treated by the incoherent approximation [1] whose cross-section is given by

$$\frac{d^2\sigma^{inc}}{d\Omega d\omega} = \text{const}\ \frac{g(\omega)}{\omega}\ \frac{k}{k_0}\ Q^2\ (n + \frac{1}{2} \pm \frac{1}{2})\ e^{-2W(Q)} \qquad (1)$$

where $g(\omega)$ is the phonon frequency distribution function; k and k_0 denote the wave number of the scattered and incoming neutrons, Q is the momentum transfer, n is the Bose-Einstein occupation number and $e^{-2W(Q)}$ is the Debye-Waller factor. The paramagnetic scattering cross-section can be expressed in the form [2]

$$\frac{d^2\sigma^{para}}{d\Omega d\omega} = \text{const}\ \frac{k}{k_0}\ |F(Q)|^2\ P_Q(\omega) \qquad (2)$$

where $F(Q)$ is the magnetic form factor and $P_Q(\omega)$ is the scattering law which describes the paramagnetic behaviour of the rare-earth compounds. We call particular attention to the fact that cross-sections (1) and (2) are strongly Q dependent. Therefore, if at least two energy distributions are measured at different scattering angles θ, one can extract the paramagnetic scattering function from the measured spectra.

To demonstrate this, it is useful to sum up cross-sections (1) and (2) into a total cross-section $f(Q_{ij}, \omega_j)$ defined as the number of neutrons scattered due to one-phonon and paramagnetic processes:

$$f(Q_{ij}, \omega_j) = \alpha(Q_{ij}, \omega_j)\, g(\omega_j) + \beta(Q_{ij}, \omega_j) P_Q(\omega_j) \qquad (3)$$

The coefficients α and β may easily be derived from Eqs (1) and (2), still paying regard to the detector efficiency. i is the running index attached to the energy distributions measured at different scattering angles, while the index j denotes the channel number of the experimental spectra.

It will be seen from Eq. (3) that an exact solution must take into consideration the Q dependence of the paramagnetic scattering law $P_Q(\omega)$. However, in the high-temperature region $P_Q(\omega)$ is expected to be near Gaussian in shape [3] and the Q dependence may be neglected. We have reliable experimental evidence that this supposition is true for the $Ce_xY_{1-x}As$ compounds.

3. APPLICATION TO CERIUM COMPOUNDS

We report in this section on experimental results of the trivalent rare-earth compounds CeAs and $Ce_{0.7}Y_{0.3}As$ having a NaCl structure. The lattice constant of CeAs has a value of 6.074 Å [4] which is diminished by a factor of 0.032 for $Ce_{0.7}Y_{0.3}As$. Because of the octahedral electrostatic field of the neighbouring charges, the ground state $F_{5/2}$ of the Ce^{3+} ion splits into a double state Γ_7 and a quartet Γ_8. This means that with thermal neutrons just one crystal field transition can be observed, since at ordinary temperatures only the lowest multiplet is populated. Thus we may expect very clear and incontestable experimental results.

The experiments were performed at room temperature by means of a rotating crystal time-of-flight spectrometer at Karlsruhe with 4.04 Å incident neutrons. The polycrystalline powder specimens were in the form of flat 50 mm × 30 mm × 3 mm plates set up in the transmission position. Time-of-flight spectra were measured at sixteen scattering angles θ ranging from 10° to 90° and typical ones are shown in Figs 1 and 2. The main features observed are: (i) a pronounced component of quasi-elastic scattering, which is found to be strongly dependent upon the momentum transfer Q; (ii) from Fig. 2 it may be seen very clearly how the paramagnetic scattering law $P_Q(\omega)$ is superposed on the phonon frequency distribution function $g(\omega)$. At small scattering angles, a single peak appears in the time-of-flight spectrum; with increasing scattering angle θ this peak splits into a pair of twins, thus demonstrating the decrease in the paramagnetic scattering due to the form factor as well as the increase in the vibrational scattering; (iii) Fig. 1 shows an unusually large count rate at large energy transfers. This effect is neither caused by sample impurities nor is it of magnetic origin and at present we can offer no convincing explanation for this.

The analysis of the time-of-flight spectra was carried out according to the method described in section 2. Since neutron scattering data for

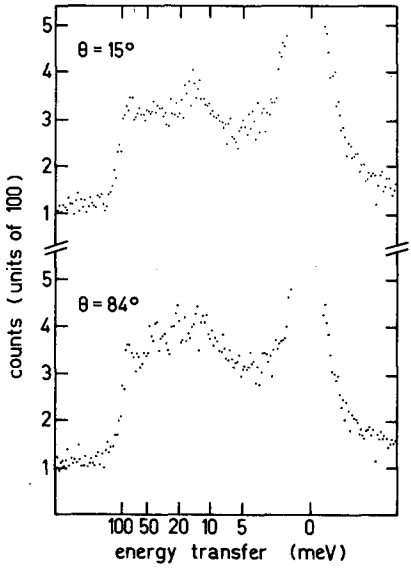

FIG. 1. Time-of-flight spectrum of CeAs at 15° and 84° scattering angles.

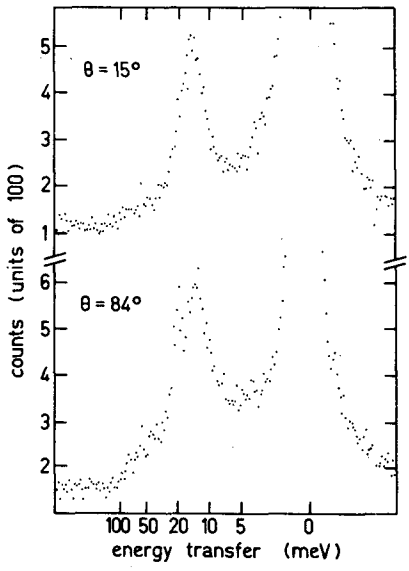

FIG. 2. Time-of-flight spectrum of $Ce_{0.7}Y_{0.3}As$ at 15° and 84° scattering angles.

the magnetic form factor of cerium are not yet available, we used the approximation given by Trammell [5] and calculated by Blume, Freeman and Watson [6]. The resulting paramagnetic scattering functions $P_Q(\omega)$ are presented in Fig. 3. The position of the paramagnetic line indicates that the crystal field splitting has a value of 12.2 ± 1.0 meV in CeAs, which is consistent with previous measurements [7, 8], and a value of 12.5 ± 1.0 meV in $Ce_{0.7}Y_{0.3}As$. The equality of the crystal field splittings is remarkable and seems to confirm the idea of a simple point-charge ionic model for the calculation of energy levels. The

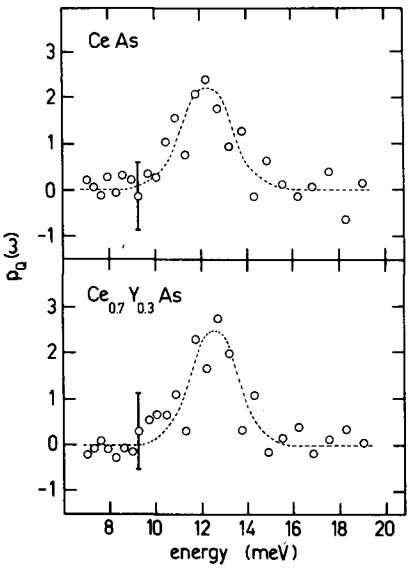

FIG.3. Paramagnetic scattering law $P_Q(\omega)$ for CeAs and $Ce_{0.7}Y_{0.3}As$.

paramagnetic line width has a value of 2.5 meV for CeAs and 2.3 meV for $Ce_{0.7}Y_{0.3}As$. We shall discuss this in the next section.

4. INTERPRETATION OF THE LINE WIDTH

To obtain maximum resolution of the spectrum, the experiments should be designed as far as possible to minimize all contributions to the line width. There are two major causes of the broadening of paramagnetic line widths: (i) the interaction between the paramagnetic ions and the lattice; and (ii) the interaction between the various ions themselves. The mechanism of spin-lattice interaction is one in which the thermal vibrations of the lattice give a fluctuating crystalline electric field. To avoid this interaction it is best to work at low temperatures. However, at these low temperatures usually only the lowest doublet state is populated so that the crystal field splitting cannot be measured with the chosen incoming neutron wavelength. The second broadening process arises from the interactions between the dipoles. Above the Néel point this broadening shows no dependence on temperature and can only be reduced by separating the magnetic carriers. Two main types of interaction between the ions have been recognized, the dipole-dipole and the exchange interactions. Usually the dipole-dipole interaction is negligible in paramagnetic salts and only the exchange interaction has to be taken into consideration.

Susceptibility measurements for CeAs [9] show magnetic ordering below 7.5°K, indicating an exchange of 1 meV at most. When replacing 30% of the cerium ions by yttrium, the exchange for Ce is diminished [10] and is expected to be smaller than the threshold value for magnetic ordering. Figure 3 thus provides direct information about the exchange in CeAs. The half-width of the paramagnetic scattering function $P_Q(\omega)$

may be described by

$$\Gamma = \sqrt{\Gamma_{ex}^2 + \Gamma_{sl}^2 + \Gamma_{in}^2} \tag{4}$$

where Γ_{ex} and Γ_{sl} denote the half-widths of the exchange and spin-lattice broadening respectively. Γ_{in} is the half-width associated with the instrumental resolution function and amounts to 1.4 meV in the range of the paramagnetic line. Γ_{ex} can now be evaluated by applying Eq. (4) to the paramagnetic scattering functions shown in Fig. 3. Its second moment $\langle \hbar^2\omega^2 \rangle_{ex}$ has a value of about 1 meV^2 and is in good agreement with estimates based on molecular field expressions [7].

The spin-lattice interaction is generally treated as giving relaxation effects characterized by a relaxation time τ, which is a measure of the rate at which a spin reverses direction and either takes from, or gives to, the lattice a quantum of energy. Since relaxation processes give half-widths of the order of $1/2\pi\tau$ sec^{-1}, our data on cerium arsenide compounds suggest an order of magnitude of about 10^{-13} sec for the spin-lattice relaxation time at room temperature.

5. CONCLUSION

With the aid of thermal neutron scattering we investigated the crystal field splitting in paramagnetic salts. The position as well as the width of the resulting lines are in good agreement with spectroscopic data and estimates on exchange and spin-lattice interaction. The exchange and spin-lattice interactions are derived from the comparison of the line widths between the pure rare-earth compound and the diluted one having nearly 0°K ordering temperature.

More detailed information about the spin-lattice interaction could be obtained by working at various temperatures. At present there is increasing interest in the relaxation behaviour of exchange-coupled ion clusters which may have shorter relaxation times than isolated ions. Moreover, there is considerable evidence that the possibility of magnetic ordering is determined by the balance between crystal field and exchange forces [11]. Further experimental work on mixed $Ce_xY_{1-x}As$ compounds is currently in progress to illuminate some of these questions.

ACKNOWLEDGEMENTS

We are very much indebted to Prof. G. Busch and Dr. O. Vogt, who originally directed our attention to this interesting field, for stimulating discussions. We especially acknowledge the collaboration of Dr. O. Vogt who kindly prepared the specimens. Furthermore we wish to thank Dr. W. Gläser for the use of the facilities at Karlsruhe and Mr. P. von Blanckenhagen and Mr. Hagen for experimental assistance.

REFERENCES

[1] MOZER, B., OTNES, K., PALEVSKY, H., Proc. Int. Conf. Lattice Dynamics, Pergamon Press, London (1965) 63.
[2] VAN HOVE, L., Phys. Rev. 95 (1954) 1374.
[3] De GENNES, P.G., J. Phys. Chem. Solids 4 (1958) 223.
[4] PENG, K., private communication.
[5] TRAMMELL, G.T., Phys. Rev. 92 (1953) 1387.
[6] BLUME, M., FREEMAN, A.J., WATSON, R.E., J. chem. Phys. 37 (1962) 1245.
[7] RAINFORD, B., TURBERFIELD, K.C., BUSCH, G., VOGT, O., AERE Rep. R 5638 (1967).
[8] FURRER, A., HÄLG, W., SCHNEIDER, T., Helv. Phys. Acta 40 (1967) 821.
[9] BUSCH, G., VOGT, O., Phys. Lett. 20 (1966) 152.
[10] COOPER, B.R., Phys. Rev. 163 (1967) 444.
[11] TRAMMELL, G.T., Phys. Rev. 131 (1963) 932.

DISCUSSION

C.G. WINDSOR: I should like to know in greater detail how you were able to separate the magnetic contribution to the scattering from the phonon contributions.

A. FURRER: It can be seen from Eq. (3) that both the vibrational and the paramagnetic scattering cross-sections have their own characteristic dependence upon the momentum transfer Q of the scattered neutrons. Therefore, if i denotes the number of energy distributions measured at different scattering angles, the unknown functions $g(\omega_j)$ and $P_Q(\omega_j)$ can be evaluated by solving the system of i equations for every channel number j. However, this procedure is only applicable to high temperatures, where the paramagnetic scattering function is almost constant over the whole Q region.

T. RISTE: This paper, among others at this session, has demonstrated the need for a reliable method of extracting the magnetic intensity component. I should like to point out that such a method, involving the use of a polarized beam, is now available. If you bring the beam to the sample with the polarization along the scattering vector, the magnetic scattering occurs with complete polarization reversal. This is true for scattering in connection with any kind of magnetic substance, and applies equally well to elastic, inelastic, coherent and incoherent scattering. Thus the magnetic component may be extracted by analysing the polarization of the scattered beam. Moon, Koehler and myself expect to be publishing a paper on the subject in due course.

A. FURRER: The fact that the polarization of the scattered neutrons can be analysed constitutes in general the most powerful evidence for the existence of magnetic scattering. However, for the case of rare-earth salts, the method you describe might not be successful. The fact is that a crystal field transition within the ground state multiplet occurs without involving a change in the total angular momentum of the atom. Therefore, on grounds of spin conservation I believe that the polarization of the scattered neutrons will be maintained.

MOLECULAR DYNAMICS

(Session D)

Chairmen: D. JOVIC
T. RISTE

INVESTIGATION OF THE DYNAMICS OF WATER MOLECULES IN CRYSTALLO-HYDRATES BY NEUTRON INELASTIC SCATTERING

A. BAJOREK*, J.A. JANIK, J.M. JANIK**, I. NATKANIEC,
K. PARLIŃSKI, Yu.N. POKOTILOVSKY
AND M. SUDNIK-HRYNKIEWICZ
JOINT INSTITUTE FOR NUCLEAR RESEARCH,
DUBNA, USSR, AND
INSTITUTE OF NUCLEAR PHYSICS, CRACOW, POLAND
AND
V.E. KOMAROV, R.P. OZEROV AND S.P. SOLOVEV
KARPOV INSTITUTE OF PHYSICAL CHEMISTRY,
MOSCOW, USSR

Abstract

INVESTIGATION OF THE DYNAMICS OF WATER MOLECULES IN CRYSTALLO-HYDRATES BY NEUTRON INELASTIC SCATTERING. Translatory and rotatory frequencies of crystallization molecules of water were determined by the neutron inelastic scattering method in several crystallo-hydrates. The results are compared with those obtained from infrared and nuclear magnetic resonance experiments.

1. INTRODUCTION

Crystallized compounds containing water have been studied by the neutron inelastic scattering method (INS) by Boutin et al. [1], Prask and Boutin [2], and Bajorek et al. [3].

The present INS study concerns the following compounds: ice, $Li_2SO_4.H_2O$, $LiClO_4.3H_2O$, $NiSO_4.7H_2O$, $NiSO_4.6H_2O$, $LiCl.H_2O$, and $La_2Mg_3(NO_3)_{12}.24H_2O$. In these compounds both the configurations of water molecules and the types of hydrogen bonds differ significantly (see section 2) and it was thought that these differences might be reflected in the INS spectra. It was also felt that an INS study of $La_2Mg_3(NO_3)_{12}.24H_2O$ might furnish some useful data for a better understanding of the role played by this substance in nuclear polarization.

Section 2 gives information on the structure of the substances. Section 3 describes the experimental method applied. Section 4 presents the results obtained and a discussion mainly based on their comparison with other INS data but also with those obtained by infrared techniques.

2. STRUCTURE OF HYDRATES INVESTIGATED

Information on the structure of the compounds in question is given in this section from the point of view of the crystallo-chemistry of hydrogen and in particular of hydrogen bonds. Detailed information is given in the references.

* Structural Research Laboratory of the Jagiellonian University, Cracow.
** Chemical Physics Laboratory of the Jagiellonian University, Cracow.

The most complete data on the structure of ice are those from neutronographic studies [4]. The crystal is composed of an infinite three-dimensional lattice of hydrogen bonds. Each oxygen atom in this lattice is in the centre of a tetrahedron. Hydrogen atoms are either statistically or dynamically situated in two positions between oxygen atoms (Fig. 1).

The $Li_2SO_4.H_2O$ structure was studied by X-ray diffraction [5-7] and by neutron diffraction [8, 9]. The H_2O molecules are mutually bound by hydrogen bonds, forming a one-dimensional chain of bonds . . O--H. . . . O--H. ., similar to that in ice. The remaining hydrogen bonds of water molecules connect this chain to SO_4 tetrahedrons. This configuration, rather exceptional for hydrates, is reflected in many physical properties of $Li_2SO_4H_2O$ [10]. Water molecules in this crystal are structurally equivalent (Fig. 2). The 2_1 axis joins two such molecules in the elementary cell.

In $LiClO_4.3H_2O$ the hydrogen bonds, according to neutron diffraction data [11], are closed, joining $Li(OH_2)_6$ octahedrons with ClO_4 tetrahedrons (Fig. 3) (Li--O--H. . . O--Cl). All water molecules are connected together by the 6_3-symmetry axes and are structurally equivalent.

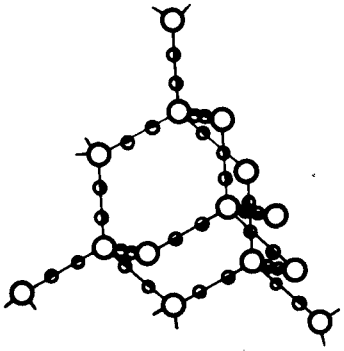

FIG. 1. The structure of ice. Large circles – oxygen atoms, small circles – hydrogen atoms. Hydrogen positions are occupied with a 50% probability.

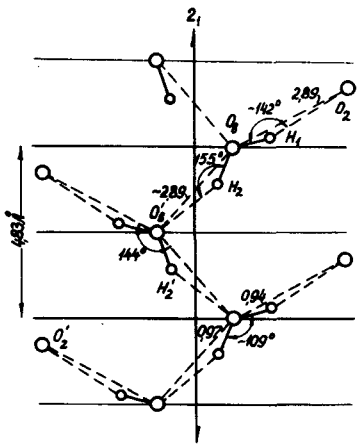

FIG. 2. Hydrogen bonds in the $Li_2SO_4.H_2O$ structure. O_B - oxygen atoms of water molecules, O_2 - oxygen atoms of SO_4 - tetrahedrons.

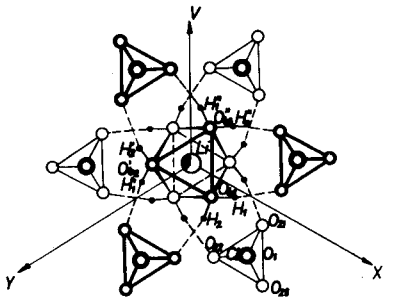

FIG.3. A projection of the $LiClO_4 . 3H_2O$ structure along the hexagonal axis.

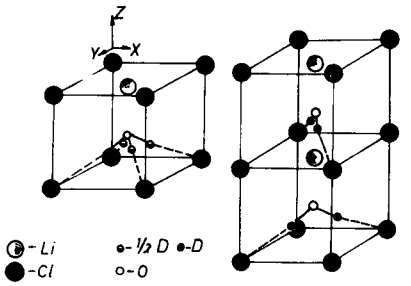

FIG.4. The structure of $LiCl.D_2O$. Model a: hydrogen atoms may jump between two positions. Model b: statistical distribution of hydrogen atoms in either one or another position.

In $LiCl.H_2O$ the hydrogen bonds are also closed and they join O and Cl atoms together (O--H....Cl) (Fig. 4). Preliminary neutron diffraction studies [12] led to the conclusion that there are two different orientations of water molecules in the $LiCl.H_2O$ crystals.

The crystallo-hydrates $NiSO_4 . 7H_2O$ and $NiSO_4 . 6H_2O$ have not yet been studied neutronographically. On the basis of röntgenographic studies [13-16] one may accept that in $NiSO_4 . 6H_2O$ the hydrogen bonds join together the $Ni(OH_2)_6$ octahedrons and SO_4 tetrahedrons, forming closed hydrogen bonds Ni--O-- H....O--S. It is suggested that in $NiSO_4 . 7H_2O$ the additional water molecule enters in between, forming Ni--O--H....O--H....O--S bonds.

3. EXPERIMENTAL METHOD

The measurements were performed on a time-of-flight spectrometer for inelastic, incoherent scattering of neutrons [17] installed at the IBR pulsed reactor at Dubna. The majority of measurements were made with the following parameters of the spectrometer:

Duration of slow neutron pulse ~ 200 μsec
Path length: moderator-sample 20.4 m
Path length: sample-detector 1.76 m
Fixed energy of scattered neutrons 5.0 meV
Resolution $d\lambda/\lambda$ in the energy transfer region from 5 meV to 110 meV 3.5%
Scattering angle 90°.

Polycrystalline samples, whose thickness was ~1 mm (approximately 85% of neutron transmission), were placed in a cryostat which allowed measurements to be performed at any temperature between that of liquid nitrogen and room temperature.

The scattered neutron intensity measured in this spectrometer is, after making the necessary corrections and after normalization to a constant value of incident neutron flux, proportional to the cross-section $d^2\sigma/d\Omega dE$ (with phonon creation). The results are presented in the form of scattered neutron intensity versus analyser channel number (with background subtracted after making a smooth line from it). The energy transfers were obtained from the peak values as were the frequencies of corresponding phonon peaks in cm^{-1}. These frequencies are shown in the tables below together with the data of other authors obtained either by INS or i.r. techniques.

4. RESULTS AND DISCUSSION

4.1. Ice

Our INS results are presented in Fig. 5 and in Table I. The peaks are distributed into three groups, corresponding to H_2O rotational motion (group III), H_2O translational motion (group II), and bending deformation of the hydrogen bond (group I). It is interesting to note that group I appears as a distinct and intense band for the two substances only (ice and $Li_2SO_4 . H_2O$) for which there is a chain of hydrogen bonds between pairs of H_2O molecules, and is either much weaker or even does not appear for hydrates in which the hydrogen bonds are closed.

In Table I our data are presented together with other INS data of Burgman et al. [18] and with i.r. data of Giguere and Arraudeau [19] for comparison. There is good agreement between the two INS results. The i.r. data show the appearance of more peaks, though some of them are very weak. In particular, in the translational vibration region (group II) there are five peaks in i.r. and only three in INS. Of the five i.r. peaks only two, i.e. one at 154 cm^{-1} and one at 225 cm^{-1}, are distinct and completely formed as peaks. Their agreement with INS is good. It should be pointed out that according to an analysis performed by Springer [20] there are nine optical modes for the ice tetrahedron lying below three librational modes. What in Table I are called groups I and II should be covered by these nine frequencies. In fact, if one takes into account both INS and i.r. results there are nine frequencies in groups I and II which have been demonstrated experimentally.

As concerns group III, the INS data show the appearance of a fairly broad band with a maximum value at 601 cm^{-1} (peak g). On its left shoulder there are certainly some unresolved peaks around 800-900 cm^{-1}. The high intensity of peak g may arise only from hydrogen motions. We consider that the 601 cm^{-1} corresponds to H_2O twisting (as its intensity in i.r. is very small) and the i.r. peaks around 800-900 cm^{-1} to two other rotational modes of H_2O, in agreement with suggestions of Giguere and Arraudeau [19]. It should be pointed out that, according to estimations of Cross et al. [21], the torsional frequency in the ice tetrahedron should be 570 cm^{-1}, which is quite close to our value of 601 cm^{-1}.

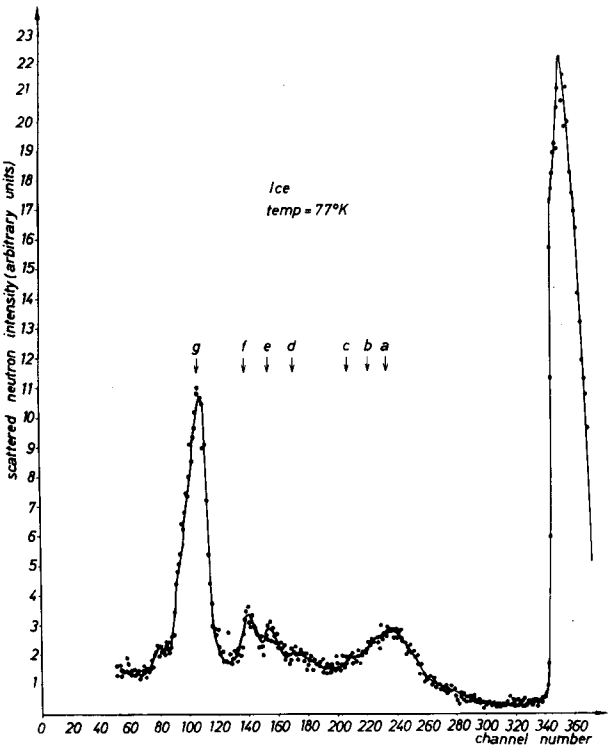

FIG. 5. The INS spectrum if ice.

4.2. $Li_2SO_4.H_2O$

As seen from Fig. 6 and Table II, the peaks, as those for ice, are distributed in three groups arising from hydrogen bond deformation (group I), H_2O translational motion (group II), and H_2O rotational motion (group III). In Table II the INS data of Prask and Boutin [2] and the i. r. data of J. M. Janik et al. [22], Miller et al. [23] and Shukarev et al. [24] are also presented.

Group I, i. e. low-frequency hydrogen motions, appears, as shown by Prask and Boutin [2], in many INS spectra of hydrates. As discussed in section 4.1, this group appears also in the INS spectrum of ice. It is believed that these motions are connected with deformations of hydrogen bonds at which atoms move perpendicularly to the chain of hydrogen bonds. It should be pointed out that this low frequency band is very pronounced in $Li_2SO_4.H_2O$, as in ice, this perhaps being connected with a similarity of inter-H_2O hydrogen bond structure in the two substances.

We interpret the three INS peaks belonging to group II, in agreement with theoretical predictions of Cross et al. [21] (more precisely with the statement that translatory H_2O motions should appear in the region 125 to 200 cm^{-1}), as arising from H_2O translations. There is also a possibility that one of these frequencies (probably that at 235 cm^{-1}, i. e. frequency e in our spectrum) corresponds to methyl-oxygen stretching. This stretching frequency usually appears between the translational and rotational ones as

TABLE I. PEAK FREQUENCIES IN ICE OBTAINED IN VARIOUS EXPERIMENTS

This work INS Temp. 77°K (cm^{-1})	Burgman et al. [18] INS Temp. 268.6°K (cm^{-1})	Giguere and Arraudeau [19] i.r. Temp. 113°K (cm^{-1})	Interpretation
			Group I
a 57	52	70 - 80 ?	hydrogen bond deformation
b 69	~69	100 ?	
c 87	~86	122	
			Group II
d 159		154	H_2O-transl.
		190	
e 215	210		
		225	
		259	
f 291	275	295	
			Group III
g 601	632	570	H_2O-rot. (T) Two of these peaks are H_2O-rot. (W, R)
		800	
		840	
		900	

estimated by Sartori et al. [25]. Although the value obtained by Sartori et al. is evidently too high (637 cm^{-1}), a sequence: translational vibrations, MeO stretching, librational vibrations seems probable. Another possibility suggested by Shukarev et al. [24] is that the i.r. peak at 480 cm^{-1} corresponds to MeO stretching.

There are arguments for believing that the frequencies indicated in the table by asterisks arise from internal vibrations of SO_4 groups. As shown in the i.r. study of J. M. Janik et al. [22], all these peaks appear practically unchanged in dry Li_2SO_4 which does not contain H_2O molecules. The intensities of corresponding peaks in INS spectra do not conflict with the assumption that they are not connected with hydrogen atom motions.

There remain three frequencies belonging to group III which we believe are caused by three types of rotational motions of H_2O molecules (rocking, twisting and wagging).

The sharp peak at 343 cm^{-1} in our INS spectrum is so strong that it evidently arises from hydrogen. It is surprising that this peak was not observed by Prask and Boutin [2]. The sharpness may be treated as proof of the flatness of the corresponding phonon branch, which, on the basis

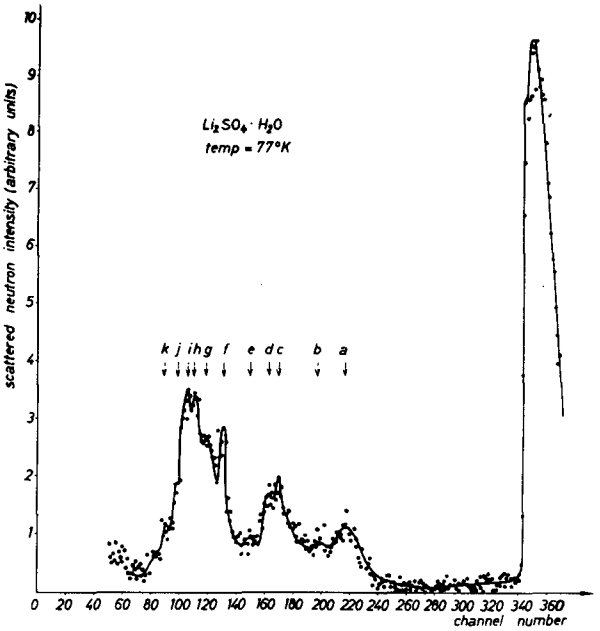

FIG. 6. The INS spectrum of $Li_2SO_4 . H_2O$.

of arguments given in the paper of J. A. Janik et al. [26], should be a characteristic of phonons connected with H_2O librational motions (twisting). It should be pointed out that the barrier value for twisting obtained in nmr measurements by Holcomb and Pederson [27] implies for the twisting frequency a value of 365 cm^{-1}, in fairly good agreement with our value of 343 cm^{-1}. Of the other two peaks (h and j), one at 556 cm^{-1} appears also in i.r. and, as pointed out by J. M. Janik et al. [22], is shifted to lower frequencies ($\sim$ 495 cm^{-1}) for the deuterized substance. We believe that the two peaks arise from two other H_2O rotational motions, wagging and rocking.

4.3. $LiClO_4 . 3H_2O$

It should be pointed out that the three water molecules in this substance are structurally equivalent, as are the two in $Li_2SO_4 . H_2O$. Therefore we may compare the two substances, while stressing the fact that $Li_2SO_4 . H_2O$ has a hydrogen bonded zig-zag structure of water molecules, whereas hydrogen bonds in $LiClO_4 . 3H_2O$ are closed.

Figure 7 and Table III present our INS results. The peaks are distributed in three groups. There is slight evidence of a low-energy hydrogen bond deformation peak (group I). The i.r. data of J. M. Janik et al. [22] and of Shukarev et al. [24] are presented in Table III for comparison and for help in interpreting peaks.

As the H_2O molecules in the $LiClO_4 . 3H_2O$ crystal are all in the same crystallographic positions, there should be three translational peaks of the H_2O groups. From the five peaks of group II, 128, 157, 209, 277 and

TABLE II. PEAK FREQUENCIES IN CRYSTALLINE $Li_2SO_4 . H_2O$ OBTAINED IN VARIOUS EXPERIMENTS

This work INS Temp. 77°K (cm^{-1})	Prask and Boutin [2] INS Temp. 293°K (cm^{-1})	J.M. Janik et al. [22] i.r. Room temp. (cm^{-1})	Miller et al. [23] i.r. Room temp. (cm^{-1})	Shukarev et al. [24] i.r. Room temp. (cm^{-1})	Interpretation
					Group I
a 76					Hydrogen bond deformation
b 103	107				
					Group II
c 164					H_2O-transl.
d 186	203				
e 260	260				
					Group III
f 343					H_2O-rot(T)
			367		?
g 448		414, 438 *	437 *	435 *	ν_2-SO_4
		480	480	480	LiO
h 556	524	580	577	570	H_2O-rot
i 617 *	672 *	638, 650 *	646 *	632, 642 *	ν_4-SO_4
j 769	832	835			H_2O-rot
k 1014 *		1019 *		980 *	ν_1-SO_4
	1280 *	1120 *		1110 *	ν_3-SO_4

304 cm^{-1}, which are observed in the INS spectrum, three doubtless arise from H_2O translations. It is possible that either the 277 cm^{-1} or 304 cm^{-1} peak corresponds to the MeO stretching frequency.

The peak at 380 cm^{-1} probably arises from H_2O twisting, in view of its sharpness and intensity. It should be noted that such a peak, although situated at various positions for various hydrates, appears in a very similar shape for $Li_2SO_4 . H_2O$, $NiSO_4 . 6H_2O$ and $NiSO_4 . 7H_2O$, and its interpretation in $Li_2SO_4 . H_2O$ was strongly confirmed by agreement with nmr experiment, as pointed out in section 4.2. Nuclear magnetic resonance studies for $LiClO_4 . 3H_2O$ performed by Pietrzak [28] give 350 cm^{-1} as the twisting frequency, in fairly good agreement with the present study.

Other rotational peaks of H_2O groups are probably those at 456 cm^{-1} and 515 cm^{-1}. The i.r. spectrum shows a broad band with maximum at circa 550 cm^{-1} in this region. This broad band is shifted towards lower

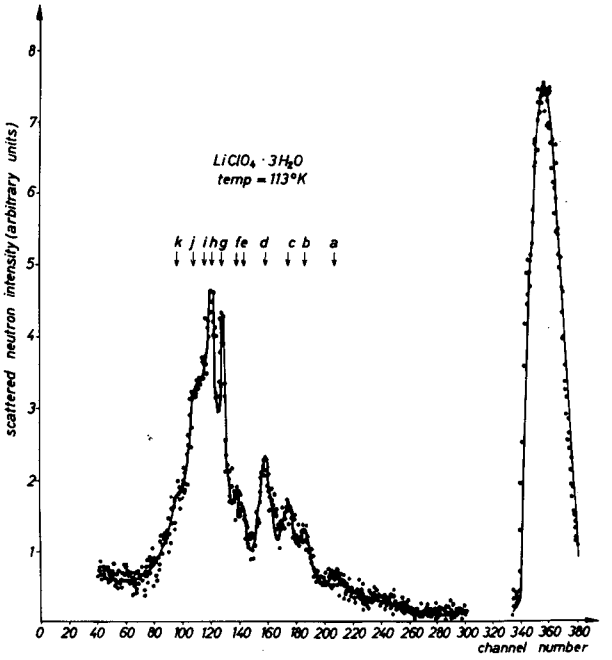

FIG. 7. The INS spectrum of $LiClO_4 . 3H_2O$.

frequencies after deuterization, so it must contain rotational H_2O peaks, but probably overlapped on ClO_4 internal frequencies.

The peak (j) at circa 617 cm^{-1} (INS) is, owing to its coincidence with i.r. for both $LiClO_4 . 3H_2O$ and for water-free $LiClO_4$, ascribed to the vibration of the ClO_4 ion. This peak and another one seen in i.r. at 1090 cm^{-1} are indicated by asterisks in Table III.

4.4. $NiSO_4 . 7H_2O$ and $NiSO_4 . 6H_2O$

Our INS results for $NiSO_4 . 7H_2O$ and $NiSO_4 . 6H_2O$ are presented in Figs 8 and 9. The peaks are distributed in two groups, one arising, we believe, from rotatory motions and the other from translatory vibrations. No group I, connected with hydrogen bond deformation, was observed for either substance. In Table IV the INS peak values and the i.r. data of J. M. Janik et al. [22] are presented together with those of Gamo [29].

It should be pointed out that vibrations of H_2O groups in both $NiSO_4 . 7H_2O$ and $NiSO_4 . 6H_2O$ lie in a higher frequency region than those for $Li_2SO_4 . H_2O$.

The two spectra, that for $NiSO_4 . 7H_2O$ and that for $NiSO_4 . 6H_2O$, are very similar (in fact almost identical), suggesting the same features of H_2O dynamics in the two substances and hence a negligible effect of the seventh H_2O molecule. As no extra peaks appeared after introducing the seventh water molecule, it may be deduced that this water molecule has a smooth spectrum, suggesting a much weaker bonding than other H_2O molecules.

TABLE III. PEAK FREQUENCIES IN CRYSTALLINE $LiClO_4 . 3H_2O$ OBTAINED WITH INS AND i.r.

This work INS Temp. 113°K (cm^{-1})	Janik et al. [22] i.r. Room temp. (cm^{-1})	Shukarev et al. [24] i.r. Room temp. (cm^{-1})	Interpretation
			Group I
a 90			
			Group II
b 128			
c 157			Three of these frequencies should be H_2O - transl.
d 209			
e 277			
f 304			
			Group III
g 380			H_2O-rot. (T)
h 456			H_2O-rot.
i 515	Broad band ~550	Broad band ~550	
j 617*	625 *	624, 630 *	ν_4-ClO_4
k 866		938	?
	1090 *	1080 *	ν_3-ClO_4

As seen from Table IV, in the lower frequency region (group II) there are three peaks in our INS spectrum (denoted a, b, c) which either all arise from H_2O translations or, possibly, c corresponds to an MeO stretching.

The peak g at 981 cm^{-1} is the only one in the INS spectrum which we may attribute to the internal vibration in the SO_4 group (if this interpretation is correct). This is certainly due to a domination of these seven H_2O groups over only one SO_4 in $NiSO_4 . 7H_2$ (whereas in $Li_2SO_4 . H_2O$ this is not the case). Other SO_4 frequencies are seen only in i.r. [22]. They appear at about the same positions as in $Li_2SO_4 . H_2O$ and as in water-free $NiSO_4$. All peaks attributed to SO_4 groups are indicated by asterisks in Table IV.

We interpret the peak at 469 cm^{-1} (d) as H_2O twisting in view of its similarity to the corresponding one in $Li_2SO_4 . H_2O$, in its intensity, sharpness, and shift in the deuterized substance. The two other frequencies, e and f, which, as we believe, arise from two other H_2O rotational motions also appear in the i.r. as weak bonds which disappear after

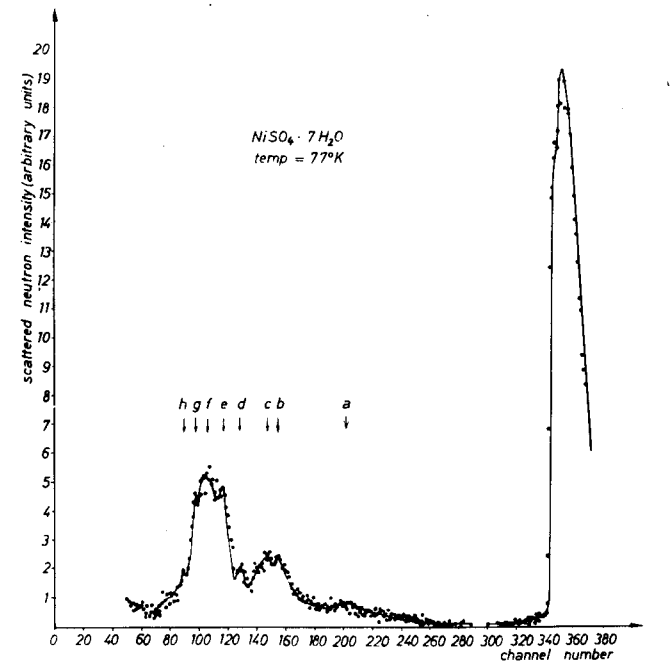

FIG. 8. The INS spectrum of $NiSO_4 . 7H_2O$.

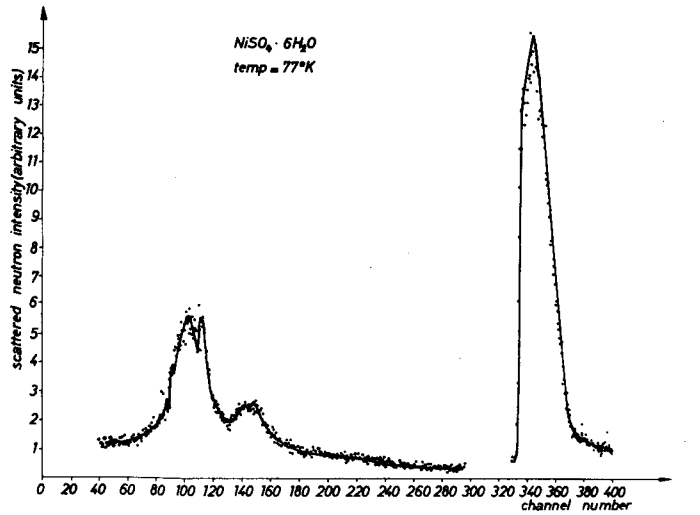

FIG. 9. The INS spectrum of $NiSO_4 . 6H_2O$.

TABLE IV. PEAK FREQUENCIES IN CRYSTALLINE $NiSO_4 . 7H_2O$ OBTAINED WITH INS AND i.r.

This work INS Temp. 77°K (cm^{-1})	Janik et al. [22] i.r. Room temp. (cm^{-1})	Gamo [29] i.r. Room temp. (cm^{-1})	Interpretation
			Group II
a 215			H_2O- -translations
b 244			
c 358			
			Group III
d 469	470		H_2O-rot. (T) and ν_2-SO
e 617	615		H_2O-rot. (W)
	630 *		ν_4-SO_4
f 770	790	760	H_2O-rot. (R)
g 981	990, 1100 *		ν_1-SO_4

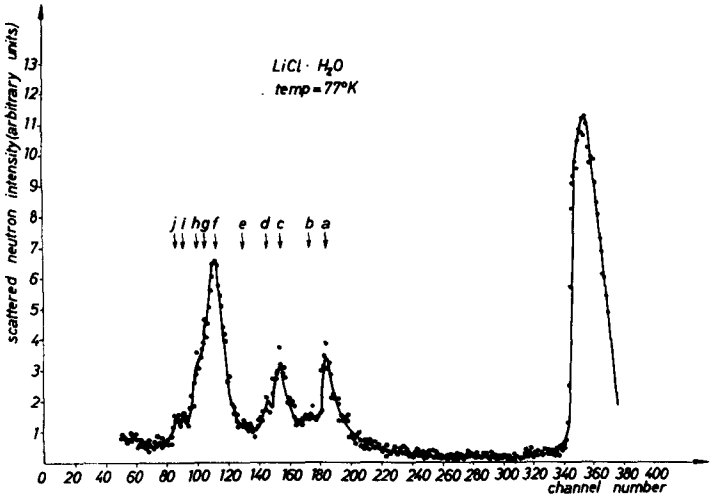

FIG.10. The INS spectrum of $LiCl.H_2O$.

TABLE V. THE INS PEAK FREQUENCIES IN CRYSTALLINE $LiCl.H_2O$

This work INS Temp. 77°K (cm^{-1})	Interpretation
	Group II
a 130	H_2O-translation
b 156	?
c 218	H_2O-translation
d 259	?
e 350	MeO stretching
	Group III
f 529	H_2O-rotations
g 634	H_2O-rotations
h 727	H_2O-rotations
i 951	overtones?
j 1121	overtones?

deuterization. It is hard to determine the shifts as the $NiSO_4.7D_2O$ spectrum differs in too many details from that of $NiSO_4.7H_2O$.

4.5. $LiCl.H_2O$

It should be pointed out that owing to the large absorption cross-section for neutrons of Li and Cl, the scattered neutron intensity distribution may in this case be almost entirely attributed to H_2O molecules.

The INS spectrum obtained by us is presented in Fig. 10. As there are no reliable i.r. data for this substance, the interpretation may be made only on the basis of an analogy with other INS spectra of hydrates.

It is evident that two quite intense peaks (a) and (c) belonging to what was called group II for previous substances, arise from H_2O translations. Peak e may perhaps be connected with LíO stretching.

A broad maximum which forms group III has its peak value at 529 cm^{-1} (f) and it probably contains all rotational frequencies of H_2O groups.

Table V presents all INS peak values and their rough interpretation.

4.6. $La_2Mg_3(NO_3)_{12}.24H_2O$

The INS spectrum is presented in Fig. 11. Table VI presents frequencies corresponding to peak values. On the basis of an analogy with INS spectra of other hydrates we believe that the observed peaks of group II,

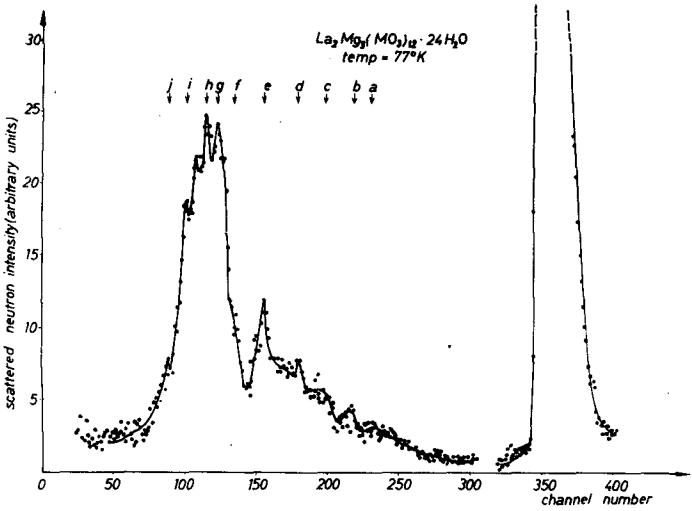

FIG. 11. The INS spectrum of $La_2Mg_3(NO_3)_{12} \cdot 24H_2O$.

TABLE VI. PEAK FREQUENCIES IN CRYSTALLINE $La_2Mg_3(NO_3)_{12} \cdot 24H_2O$

This work INS Temp. 77°K (cm^{-1})	Janik et al. [22] i.r. Room temp. (cm^{-1})	Interpretation
		Group II
a 161		
b 202		H_2O-translations
c 298		
		Group III
d 387		
e 460	Broad band at 430	
f 516		H_2O-rotations
g 653	Broad band at 620	

i.e. those at 161, 202 and 198 cm^{-1}, arise from H_2O translations, and peaks belonging to group III, i.e. those at 387, 460, 516 and 653 cm^{-1}, arise from H_2O rotations. As there are probably four unequivalent situations of H_2O molecules in the crystal, we may expect more peaks than those observed and interpreted as translational and rotational. It is possible that they have not been resolved.

An i.r. measurement of this substance was made by J. M. Janik et al. [22]. The i.r. spectrum shows in the same frequency region two broad maxima, one at ~430 cm^{-1} and the other at ~620 cm^{-1}, in rough agreement with our INS data.

All peaks discussed are probably connected with hydrogen motions and not with internal frequencies of NO_3 groups, as the latter ones appear at frequencies higher than 700 cm^{-1}.

It should be pointed out that a knowledge of the rotational levels of H_2O molecules in $La_2Mg_3(NO_3)_{12}.24H_2O$ may be of some importance in attempting to understand its use for polarization of nuclei. From the point of view of polarization experiments it is important to know the magnitude of splitting of the ground level of torsional vibrations of water molecules around the c-axis (i.e. the axis in the molecular plane). To evaluate this splitting it is necessary to know the barrier to rotation. It is possible to obtain this from the torsional frequency. We assume that this frequency lies in the region 280-650 cm^{-1}, i.e. the energy region 48-80 meV. Assuming further that the potential energy has the form

$$V = \frac{1}{2} V_0 (1 + \cos 2\phi) \qquad (1)$$

we might, by using tables of eigenvalues of the Mathieu equation given in the paper of Stejskal and Gutovsky [30], evaluate the barrier from the torsional frequency, but only for the frequency region corresponding to energies 35-50 meV. It is therefore necessary to extrapolate the barrier versus frequency dependence to higher energies. As it was found in the region 35-50 meV that barriers evaluated from the potential (1) and those obtained from harmonic potential differ by a constant value of 20 meV, we assume that this is valid for energies up to 80 meV. On the basis of this assumption, we obtain the result that barriers corresponding to torsional peaks lying in the energy region 48-80 meV are 350-900 meV. The splitting of the ground level estimated on the basis of formulas given by Das [31] is $2 \times 10^{17} - 5 \times 10^{10}$ meV.

ACKNOWLEDGEMENTS

We express our thanks to Professor F. L. Shapiro for his interest and discussions as well as for suggesting the measurements with $La_2Mg_3(NO_3)_{12}.24H_2O$ in view of its importance for nuclear polarization experiments. We also thank Professor T. G. Balitcheva for her interest, for preparing samples, and for enabling us to learn the results of i.r. studies.

REFERENCES

[1] BOUTIN, H., SAFFORD, G.J., DANNER, H.R., J. chem. Phys. 40 (1964) 2670.
[2] PRASK, H.J., BOUTIN, H., J. chem. Phys. 45 (1966) 699; 3284.
[3] BAJOREK, A., MACHEKHINA, T.A., PARLIŃSKI, K., Inelastic Scattering of Neutrons (Proc. Symp. Bombay, 1964) 2, Vienna (1965) 355.
[4] PETERSON, S.W., LEVY, H.A., Acta crystallogr. 10 (1953) 70.
[5] ZIEGLER, G.E., Z. Kristallogr. 89 (1934) 456.
[6] LARSON, A.C., HELMHOLZ, L., J. chem. Phys. 22 (1954) 2049.

[7] LARSON, A.C., Acta crystallogr. 18 (1965) 717.
[8] RANNEV, N.B., DATT, I.D., TOVBIS, A.B., OZEROV, R.P., Kristallografiya 10 (1968) 914.
[9] SMITH, H.G., PETERSON, S.W., LEVY, H.A., Meeting Am. crystallogr. Ass. 1961.
[10] CHARLES, S., SMITH, H., LONDON, H.H., Bull. Am. phys. Soc. 24 (1949) 6; JAFFE, H., Phys. Rev. 75 (1949) 1625; BUREVICH, V.M., ZHELUDEV, I.S., Kristallografiya 5 (1960) 805. MARIČIĆ, S., PRAVDIĆ, V., VEKSLI, Z., Croat. chem. Acta 33 (1961) 187.
[11] DATT, I.D., RANNEV, N.V., OZEROV, R.P., Kristallografiya 13 (1968) 2.
[12] DATT, I.D., RANNEV, N.V., OZEROV, R.P., Kristallografiya (in press).
[13] BEEVERS, C.A., LIPSON, H., Z. Kristallogr. 83 (1932) 123.
[14] BEEVERS, C.A., SCHWARTZ, C.M., Z. Kristallogr. 91 (1953) 157.
[15] ZALKIN, A., RUBEN, H., TEMPLETON, D.H., Acta crystallogr. 17 (1964) 235.
[16] BAUR, W.H., Acta crystallogr. 17 (1964) 1167.
[17] PARLIŃSKI, K., SUDNIK-HRYNKIEWICZ, M., BAJOREK, A., JANIK, J.A., OLEJARCZYK, W., Research Applications of Nuclear Pulsed Systems (Proc. Panel Dubna, 1966), IAEA, Vienna (1967) 179.
[18] BURGMAN, J.O., ŚCIESIŃSKI, J., SKÖLD, K., to be published.
[19] GIGUERE, P.A., ARRAUDEAU, J.P., C. r. Acad. Sci. 257 (1963) 1692.
[20] SPRINGER, T., Nukleonik 3 (1961) 110.
[21] CROSS, P.C., BURNHAM, J., LEIGHTON, P.A., J. Am. chem. Soc. 59 (1937) 1134.
[22] JANIK, J.M., PYTASZ, G., DYREK, M., STANEK, T., Acta phys. polonica (in press).
[23] MILLER, F.A., CARLSON, G.L., BENTLEY, F.F., JONES, W.H., Spectrochim. Acta 16 (1960) 135.
[24] SHUKAREV, S.A., BALISHEVA, T.G., LAVROV, B.B., Vest. Leningr. gos. Univ. (in press).
[25] SARTORI, G., FURLANI, C., DAMIANI, A., J. inorg. nucl. Chem. 8 (1958) 119.
[26] JANIK, J.A., BAJOREK, A., JANIK, J.M., NATKANIEC, I., PARLIŃSKI, K., SUDNIK-HRYNKIEWICZ, M., Acta phys. polonica (in press).
[27] HOLCOMB, D.F., PEDERSON, B., J. chem. Phys. 36 (1962) 3720.
[28] PIETRZAK, J., Thesis, Poznań, 1966.
[29] GAMO, I., Bull. chem. Soc. Japan 34 (1961) 760.
[30] STEJSKAL, E., GUTOVSKY, H., J. chem. Phys. 28 (1958) 388.
[31] DAS, I., J. chem. Phys. 25 (1965), 896; 27 (1957) 763.

DISCUSSION

O.K. HARLING: In our recent inelastic downscattering studies on ice we found that the centroid of the torsional band was located at considerably higher energies, $\approx$ 93 meV.

DISPERSION RELATION FOR SKELETAL VIBRATIONS IN DEUTERATED POLYETHYLENE*

L.A. FELDKAMP**, G. VENKATARAMAN† AND J.S. KING
DEPARTMENT OF NUCLEAR ENGINEERING,
UNIVERSITY OF MICHIGAN,
ANN ARBOR, MICH., UNITED STATES OF AMERICA

Abstract

DISPERSION RELATION FOR SKELETAL VIBRATIONS IN DEUTERATED POLYETHYLENE. The low-frequency vibrations in polyethylene have been studied previously, utilizing the incoherent scattering technique which yields an amplitude-weighted density of states. In the present work the dispersion relations have been obtained directly by observing the coherent scattering from a deuterated sample. This represents the first such measurement on a crystalline polymer. A target in which the molecular chain axes were approximately parallel was prepared by stretching polycrystalline material. The FWHM of the rocking curve for the (002) reflection was measured to be 9°. Constant-Q and constant-E scans were made on the University of Michigan triple-axis spectrometer at room temperature to observe phonons propagating along the chain direction. The resulting dispersion curve for the ν_5 mode follows generally the calculated curve of Tasumi and Krimm with systematically lower frequencies. The maximum frequency of 1.36×10^{13} Hz agrees with the cut-off frequency determined previously from the incoherent scattering spectrum.

1. Introduction

The molecular and lattice dynamics of polyethylene (Fig. 1(a).) have heretofore been studied extensively by infrared absorption and Raman scattering [1], and by incoherent neutron scattering [2-6]. The general features of such data are in fair agreement with those predicted by dispersion curves based on the assumption of infinite non-interacting chains. This model, however, is not able to explain either the frequency splitting observed in the optical data or certain peaks in neutron spectra. Consequently, a crystalline model in which two planar chains pass through each orthorhombic unit cell in the c-direction (Fig. 1(b).) has been the basis for recent calculations of the c-direction dispersion relations and polarization vectors [7,8]. Low-frequency dispersion curves are shown in Fig. 2. Good agreement has been attained for the optical q=0 frequencies and splittings and for the maximum frequencies of the transverse and longitudinal lattice vibrations as observed in the incoherent neutron data. Other structure in neutron spectra has been identified with certain q=0 intercepts of the calculated dispersion curves [5,6]. Detailed comparison of theory with the shape of experimental frequency spectra has, unfortunately, been less successful. In the

* Work supported in part by the US National Science Foundation under grant number GK1943.
** National Science Foundation Graduate Fellow.
† Visiting Scientist from Bhabha Atomic Research Centre, Trombay, Bombay, India.

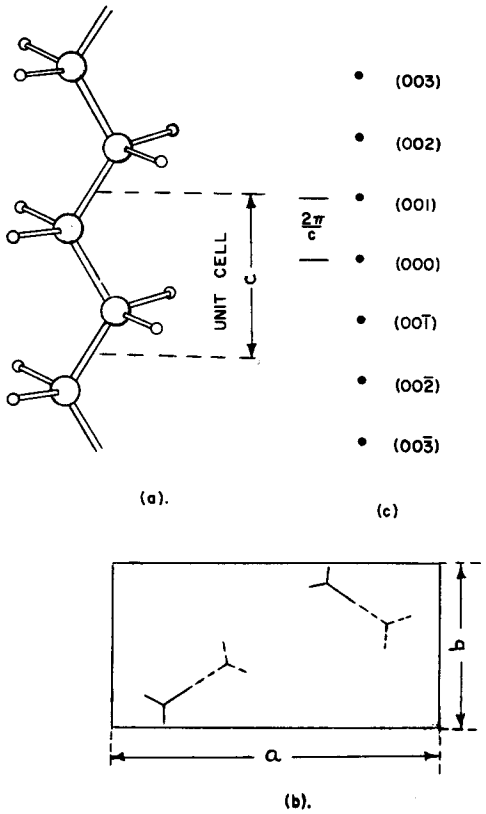

FIG.1. (a) Polyethylene single chain; (b) polyethylene unit cell in the ab plane; (c) reciprocal lattice in the c-direction for uniaxially oriented polyethylene. Off-axis reciprocal lattice points are smeared into rings concentric with the c-axis.

work reported here, a deuterated sample was used in conjunction with standard coherent scattering techniques to measure directly the dispersion relations for the predominantly longitudinal skeletal vibrations. This is the first such measurement on a polymer.

2. Experiment

The target, whose dimensions were 4 in. x .9 in. x .08 in., was prepared by pressing granules of 98% deuterated material for five to ten minutes at 160°C and later stretching to 500% elongation. This process produced a specimen in which the c-direction of crystallites are approximately oriented along the stretch direction. A neutron diffraction rocking curve using the (002) reflection disclosed the "mosaic" to be 9°; the a- and b- axes are randomly oriented perpendicular to c [9]. The reciprocal lattice appropriate to this uniaxially oriented target is shown in Fig. 1. (Note the similarity to pyrolytic graphite

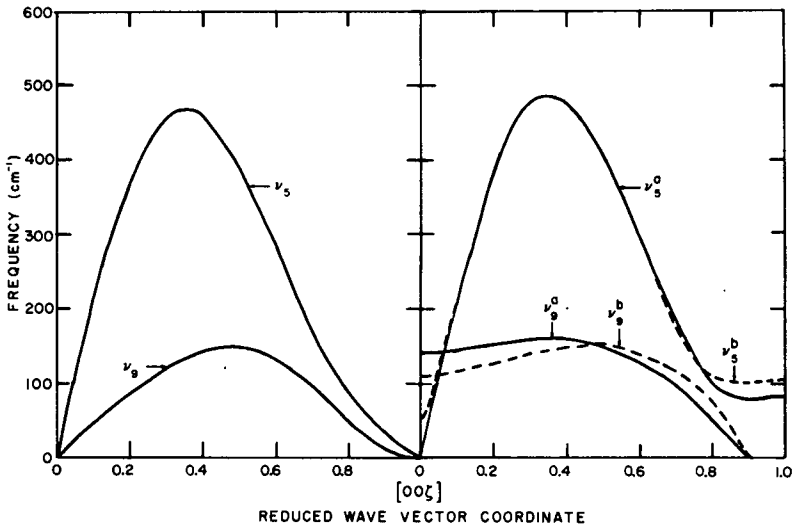

FIG.2. Calculated deuterated polyethylene low-frequency c-direction dispersion curves [7] for single chain (left) and crystal (right). The labelling of modes is that of Ref. [8].

[10].) Unambiguous results may be obtained only when the momentum transfer $\underline{Q}$ lies along $\hat{c}$ so that only vibrations with a longitudinal component are visible.

Because of screw symmetry about the c-axis, the structure factor zone is twice as large as the Brillouin zone, making it convenient to utilize a double-sized zone, i.e. $q_{max}=2\pi/c$, in performing experiments. This and the relatively small direct lattice constant in the c-direction (here taken to be 2.54 Å [7]) restricts the choice of reciprocal lattice points around which to work.

Although there are four branches in the frequency region of interest, the structure factor for two of these is identically equal to zero for $\underline{q}$ in the c-direction because of the demand of symmetry that equivalent atoms in the two chains be exactly out of phase. Structure factors for the remaining two branches based on the polarization vectors of Lynch [7] are displayed in Fig. 3. In view of this, the main effort was directed toward observation of the upper mode, ν_5^a.

Scans were made at room temperature using the University of Michigan triple axis spectrometer which was operated in downscattering to various fixed final energies (28.2 mev, 30.4 mev, 66.1 mev). Since the dispersion curve under primary consideration was known to reach its maximum frequency somewhere in the center, it was appropriate for purposes of focussing to divide the curve at its maximum and to treat the two parts separately. The Q_z region beyond the (002) point was chosen for investigation of the first portion of the

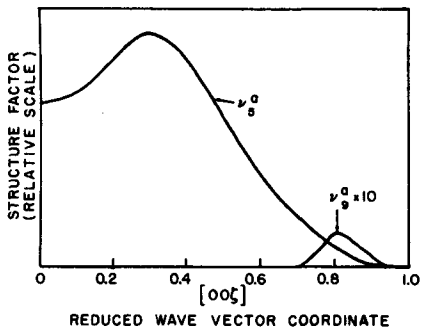

FIG.3. Calculated [7] structure factors for modes ν_5^a and ν_9^a. The quantity plotted is proportional to $\left(\sum_{\text{atoms in unit cell}} \text{(scattering length)} \times \text{(polarization vector component in c-direction)}\right)^2$. The structure factors for modes ν_5^b and ν_9^b are zero.

curve and regions beyond the (001) and (003) points for the other.

The measurement was complicated by several factors: 1) the small signal to background caused by the small amount of target material, by the relatively high frequencies involved, and by the strongly decreasing (calculated) structure factor for $\frac{q}{q_{max}} > 0.3$; 2) the appreciable incoherent cross section of deuterium; and 3) the large mosaic of the target. In spite of (1) and (2), it was generally possible to obtain reasonably good single phonon peaks with either constant-Q or constant-energy transfer modes of scanning. This was expected on the basis of calculations performed using the resolution function formulation of Cooper and Nathans [11], a simple model for the dispersion surface off the c-axis, and a gaussian representation of the mosaic. Calculated phonon widths were found to be in reasonable (10%) agreement with those observed. The mosaic and the relatively large slope were shown to be responsible for the experimental observation that constant-energy phonons tended to be superior to those obtained by constant-Q, especially for small values of energy transfer. Further, the possible frequency- or q-shift in the peak position attributable to the mosaic was assessed to be negligible under "focussed" conditions, but appreciable for small ϵ under defocussed conditions. (In this case, "focussed" means operating beyond a (00ℓ) reciprocal lattice point, rather than in front of it. Focussing in the full sense cannot, of course, be achieved easily in a case such as this.)

3. Results and Discussion

The collected data are shown in Fig. 4. Good consistency is observed between points obtained by the two

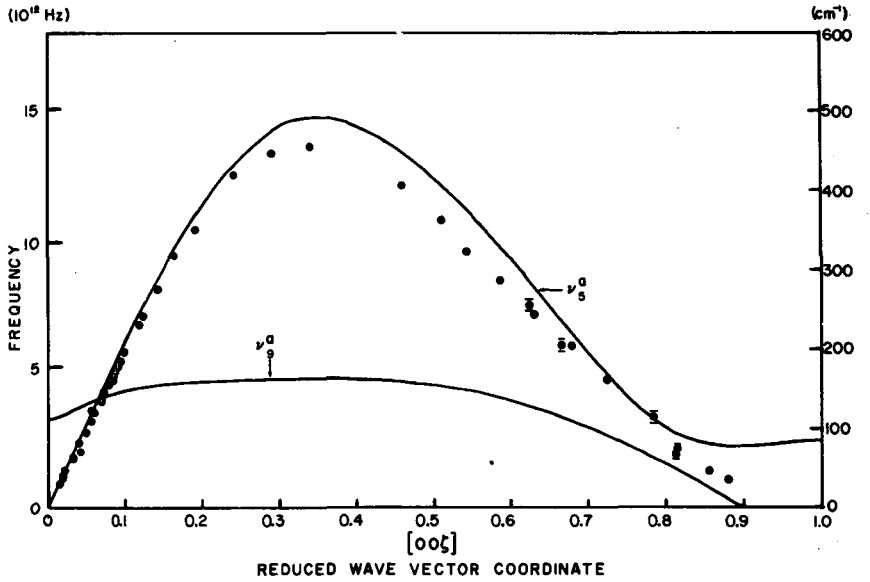

FIG. 4. Comparison of experiment with calculated [7] ν_5^a and ν_9^b dispersion curves.

types of scan and between points obtained using different analyzer energies. Except where indicated, the estimated uncertainties in q or ϵ due to statistics and resolution are comparable with or smaller than the size of the filled circles. As may be seen, the points lie on a rather smooth curve. Comparison with the corresponding calculated ν_5^a curve [7] shows that while there is reasonable overall agreement the experimental frequencies tend systematically to be lower than those predicted. A disagreement of this sort is not surprising since the force field used in the calculation was derived on the basis of optical data alone.

Beyond $q=0.8\ q_{max}$, the data diverges from the calculation by failing to level off, and at first sight there seems to be a disagreement between theory and experiment. The discrepancy appears to be further enhanced when one notes that an infrared band has been observed near the frequency of the calculated $q=q_{max}$ intercept, and has been established as belonging to the appropriate symmetry species by a dichroism measurement [12]. Closer examination, however, suggests that the discrepancy is probably more apparent than real. Now the ν_9 branch would have strictly transverse polarization if the single chain model were applicable. The presence of interchain forces mixes in a weak longitudinal component especially for large q as indicated in Fig. 3. Thus, in the region $q \gtrsim 0.8\ q_{max}$, both ν_5^a and ν_9^a have somewhat comparable structure factors, and although that for ν_5^a has a higher value,

the advantage is offset by the extreme flatness of the dispersion curve in this region. On this basis, it is conceivable that in our experiments ν_5^a disappears beyond 0.8 q_{max}, and that ν_9^a appears via its longitudinal component. Unfortunately, the observed intensities are too weak to substantiate this statement quantitatively.

The maximum frequency observed was $1.36 \pm .01 \times 10^{13}$ HZ (452 ± 3 cm^{-1}) at $q=0.34$ q_{max}. The position is in excellent agreement with calculation. Although the frequency is 7% lower than calculated, the ratio .86 of the measured deuterated to normal polyethylene peak frequencies (using Myers' [4,6] value of 525 cm^{-1} for $(CH_2)_n$ obtained from incoherent scattering) is in agreement with the calculated [7,8] ratio.

4. Conclusion

The dispersion relation for skeletal vibrations in deuterated polyethylene has been measured using a uniaxially oriented sample and found to be in fair agreement with theory. It is expected that the method used here can be extended to other chain polymers in order to provide a test for force fields derived from optical data. Further details of the lattice vibrations will become accessible when polymer crystals of sufficient size become available.

Acknowledgments

The authors wish to thank Mr. D. K. Steinman for performing the target stretching and Professor G. C. Summerfield and Dr. J. E. Lynch, Jr., for stimulating and helpful discussions concerning the theoretical aspects of this problem. A Michigan Memorial-Phoenix Project grant provided funds for purchase of the target material. One of us (G.V.) would like to thank The University of Michigan for the award of a fellowship made possible through funds provided by the Institute of Science and Technology and the General Electric Foundation.

REFERENCES

[1] See, for example, ZBINDEN, R., Infrared Spectroscopy of High Polymers, Academic Press, New York and London (1964).
[2] DANNER, H.R., SAFFORD, G.J., BOUTIN, H., BERGER, M., J. chem. Phys. 40 (1964) 1417.
[3] MYERS, W.R., DONOVAN, J.L., KING, J.S., J. chem. Phys. 42 (1965) 4299.
[4] MYERS, W.R., SUMMERFIELD, G.C., KING, J.S., J. chem. Phys. 44 (1966) 184.
[5] LYNCH, J.E., SUMMERFIELD, G.C., FELDKAMP, L.A., KING, J.S., J. chem. Phys. (to be published).

[6] MYERS, W.R., RANDOLPH, P.D. (to be published).
[7] LYNCH, J.E., Doctoral thesis, University of Michigan, 1968.
[8] TASUMI, M., KRIMM, S., J. chem. Phys. 46 (1967) 755.
[9] GEIL, P.H., Polymer Single Crystals, Interscience Publ., New York (1963) 421.
[10] DOLLING, G., BROCKHOUSE, B.N., Phys. Rev. 128 (1962) 1120.
[11] COOPER, M.J., NATHANS, R., Acta Crystall. 23 (1967) 357.
[12] BANK, M., KRIMM, S., private communication.

DISCUSSION

G.S. PAWLEY: The appearance of only two modes of vibration with acoustic behaviour for long wavelengths seems to me indicative of an error in the calculation.

L.A. FELDKAMP: The reason for the peculiar behaviour of the calculated ν_9 curves is the following: in the matrix transformation from internal (valence) force constants to Cartesian force constants, a small amount of computer truncation error occurred, with the result that the Cartesian force constants do not quite satisfy the sum rule. The similar calculation of Tasumi and Krimm [8] was performed wholly in internal co-ordinates and hence the difficulty did not arise.

J.W. WHITE: Have you seen any of the other modes of polythene indicated by the calculations and the neutron incoherent scattering spectrum?

L.A. FELDKAMP: To the extent that the calculated eigenvectors are nearly correct, we have seen the branches which it is, in principle, possible to see (cf. Fig.3). It is conceivable that some phonons belonging to ν_9^a could be seen with the method used by Dolling to obtain information about the transverse branch in pyrolytic graphite; however, the presence of non-zero incoherent scattering coupled with the probable flatness of ν_9^a is the likely reason why our efforts in this direction have so far not been successful. The optic branches seem to be out of reach because of their high frequencies and relative flatness.

J.W. WHITE: Have you any data on the temperature dependence of the phonon group widths?

L.A. FELDKAMP: No. This did not seem to be a fruitful task because the usual difficulty of subtracting the contribution from resolution is substantially increased when dealing with a target such as this.

J.W. WHITE: This work is of basic interest to those concerned with polymer dynamics. I should like to congratulate the authors, and can already substantiate their view that studies of this kind should be and will be extended by announcing that we have been able to measure the corresponding acoustic modes in fully deuterated and oriented polyoxymethylene, using time-of-flight methods.

FREQUENCY DISTRIBUTIONS OF SYNDIOTACTIC POLYVINYLCHLORIDE*

J.E. LYNCH Jr.**AND G.C. SUMMERFIELD
DEPARTMENT OF NUCLEAR ENGINEERING,
UNIVERSITY OF MICHIGAN,
ANN ARBOR, MICH., UNITED STATES OF AMERICA

Abstract

FREQUENCY DISTRIBUTIONS OF SYNDIOTACTIC POLYVINYLCHLORIDE. The incoherent neutron scattering cross-section for a harmonic crystal can be determined from a set of frequency distributions. We compute these frequency distributions for crystalline, syndiotactic polyvinylchloride. We use the force constants introduced by Opaskar and Krimm for the saturated hydrocarbons. We also include a diagonal torsional force constant of 0.06 mdyn Å/rad^2. We ignore intermolecular forces in this calculation except for the inclusion of an ϵ^2 dependence in the frequency distributions at small ϵ. We present representative calculations to indicate the resolution needed to determine the details of the frequency spectra.

INTRODUCTION

The incoherent neutron cross-section for a harmonic crystal is

$$\frac{d^2\sigma}{d\Omega d\epsilon} = \frac{k'N}{2\pi\hbar k}\int_{-\infty}^{\infty} dt\ e^{i\epsilon t/\hbar} \sum_s C_s^2\ e^{-Z_s(0)+Z_s(t)} \tag{1}$$

where $\hbar k$ and $\hbar k'$ are the initial and final neutron momenta, ϵ is the energy transfer, C_s is the incoherent scattering length of the s^{th} atom in a unit cell, and N is the number of unit cells.

The function $Z_s(t)$ is just

$$Z_s(t) = \sum_{\alpha\gamma}\int_{-\infty}^{\infty} d\epsilon' \frac{\hbar^2 \operatorname{csch}(\beta\epsilon'/2)}{4\epsilon' M_s} K_\alpha K_\gamma G^s_{\alpha\gamma}(\epsilon') e^{i\epsilon' t/\hbar}\ e^{\beta\epsilon'/2} \tag{2}$$

and $G^s_{\alpha\gamma}$ is given by

$$G^s_{\alpha\gamma}(\epsilon') = \frac{1}{N}\sum_{j\vec{q}} \gamma_j^{\alpha s *}(\vec{q})\gamma_j^{\beta s}(\vec{q})\delta(\epsilon - \hbar\omega_j(\vec{q})) \tag{3}$$

The indices j and $\vec{q}$ refer to the phonon branch and wavevector respectively; $\gamma_j^{\alpha s}(\vec{q})$ is the α^{th} component of the dynamical matrix eigenvector; the normalization is such that

$$\sum_{\alpha s} \gamma_j^{\alpha s *}(\vec{q})\gamma_{j'}^{\alpha s}(\vec{q}) = \delta_{jj'} \tag{4}$$

and $\omega_j(\vec{q})$ is the phonon frequency.

* Work supported by the US National Science Foundation Grant No. GK 1709.

** US Atomic Energy Commission Predoctoral Fellow. Present address: Department of Mechanical Engineering, Ohio State University, Columbus, Ohio.

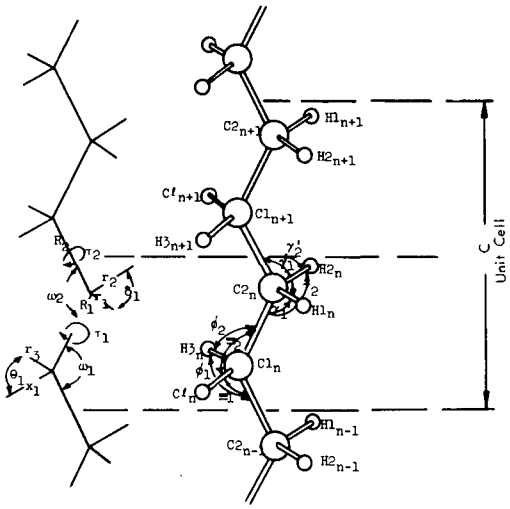

FIG. 1. Syndiotactic polyvinylchloride chain structure and internal co-ordinates.

We compute the G's as given in Eq. (3) for syndiotactic polyvinylchloride, $(CH_2\ CHC\ell)_n$.

CALCULATIONS

Syndiotactic polyvinylchloride in the planar conformation has the structure shown in Fig. 1. We take the bond angles to be 109°28'. We use the following bond lengths

$$\begin{aligned} r[\,C\text{-}H] &= 1.093\,\text{Å} \\ r[\,C\text{-}C] &= 1.54\,\text{Å} \\ r[\,C\text{-}C\ell] &= 1.798\,\text{Å} \end{aligned} \tag{5}$$

Except $r[\,C\text{-}C\ell]$, these values agree with the values quoted by Schachtschneider and Snyder [1] for polyethylene. We use the force constants introduced by Opaskar and Krimm [2] for the saturated hydrocarbons. In addition we use a torsion force constant of 0.06 mdyn Å/rad^2. This torsion force corresponds essentially to that found in polyethylene [3, 4].

We ignore the intermolecular forces in computing the normal frequencies of this molecule. The intermolecular forces are rather weaker than the intramolecular forces. We expect that the characteristics of the frequency distribution should not be affected by this approximation except for small ϵ. This was found to be the case for polyethylene [3, 4].

This molecule has C_{2v} symmetry. This symmetry permits us to use the phase between equivalent atoms in adjacent chemical repeat units δ_c in place of the phonon wavevector

$$Cq_c = 2\delta_c \tag{6}$$

where q_c is the component of the phonon wavevector along the chain axis.

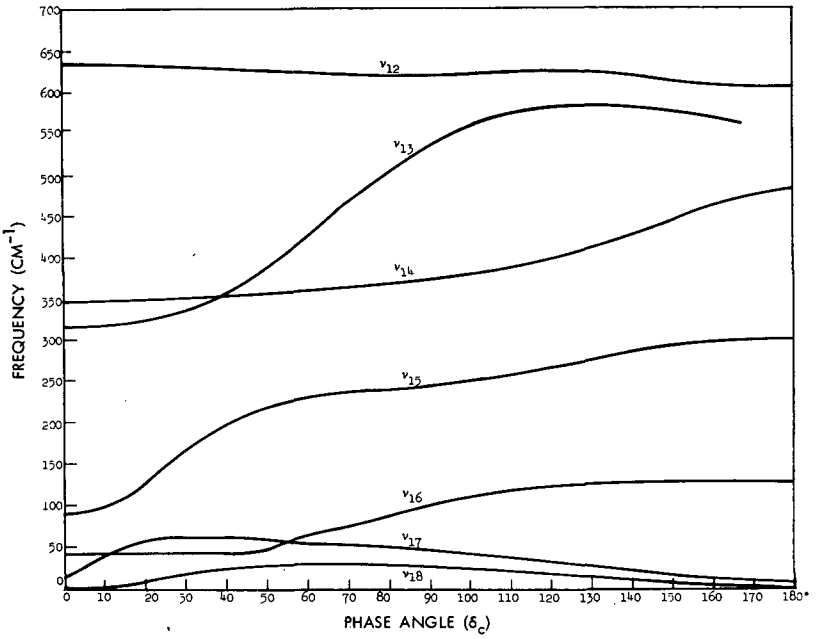

FIG. 2. Single-chain polyvinylchloride dispersion relations (F_T = 0.06 mdyn -Å/rad²).

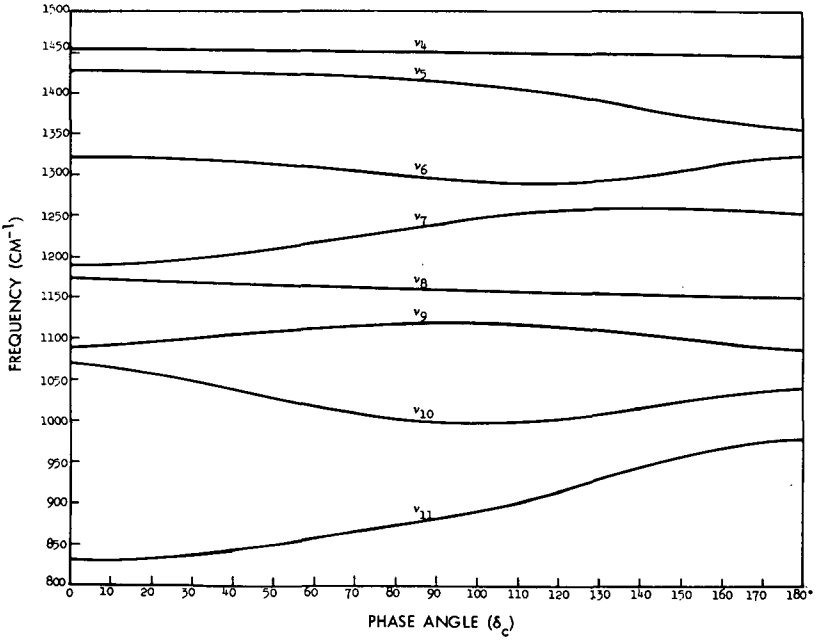

FIG. 3. Single-chain polyvinylchloride dispersion relations (F_T = 0.06 mdyn - Å/rad²).

The phonon dispersion relations are shown in Figs 2 and 3.

If we take the 3-axis to lie along the chain, we can profitably define transverse and longitudinal frequency distribution as follows:

$$G_L^s(\epsilon) = G_{33}^s(\epsilon)$$
$$G_T^s(\epsilon) = \frac{1}{2}\{G_{11}^s(\epsilon) + G_{22}^s(\epsilon)\} \quad (7)$$

Since $G_{11}^s(\epsilon)$ and $G_{22}^s(\epsilon)$ are almost equal, we only need $G_L^s(\epsilon)$ and $G_T^s(\epsilon)$ to determine the cross-section for stretched samples [3, 4]. The frequency distributions for H1 and H2 (see Fig. 1) are essentially equal and we plot these in Figs 4 and 5. The frequency distributions for H3 are plotted in Figs 6 and 7.

DISCUSSION

We can see from Fig. 2 that the ν_{18} torsion mode lies entirely below 0.006 eV. This mode has never been directly observed and it arises from our inclusion of a rather arbitrary torsional force constant of 0.06 mdyn Å/rad^2. We have therefore not included the frequency distribution curve below 0.006 eV. In this region we simply extrapolate the calculated curves to zero as ϵ^2.

It would be most useful to have measurements of the frequency distribution for these very small energy transfers. We might point out that this is equally true for polyethylene in which there is also considerable structure at very low values of ϵ.

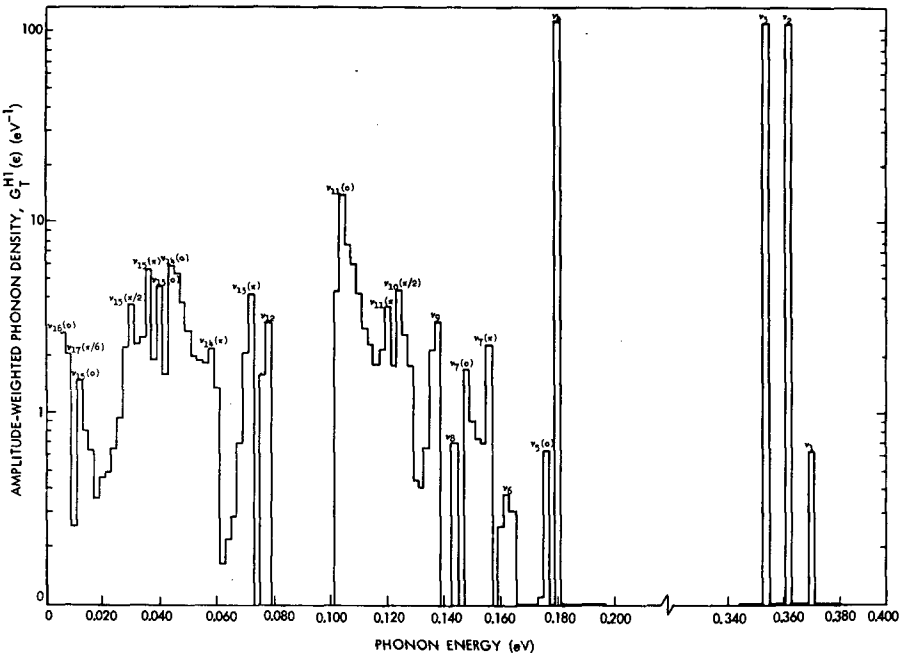

FIG. 4. Single-chain polyvinylchloride transverse (H^1 or H^2) hydrogen frequency function.

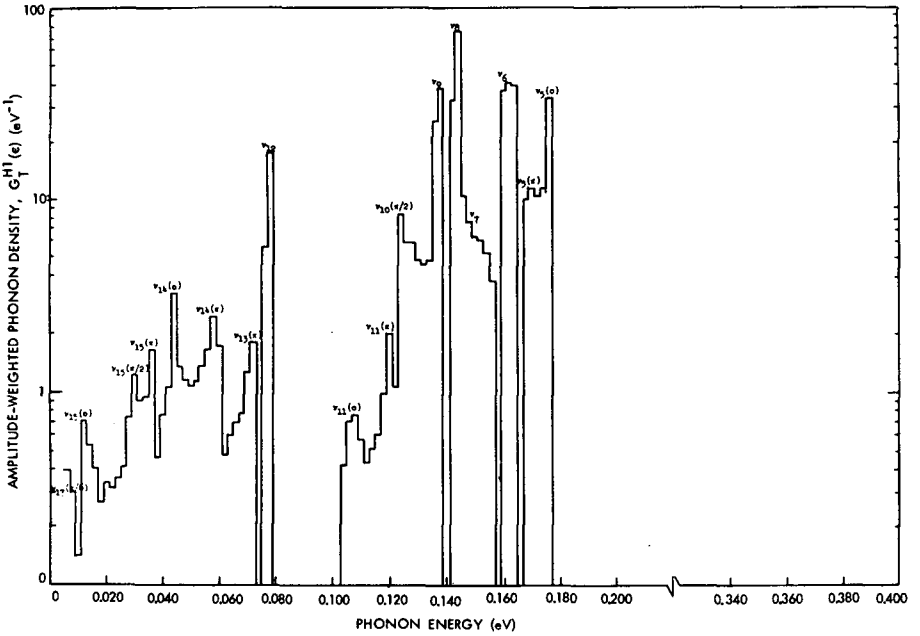

FIG. 5. Single-chain polyvinylchloride longitudinal (H^1 or H^2) hydrogen frequency function.

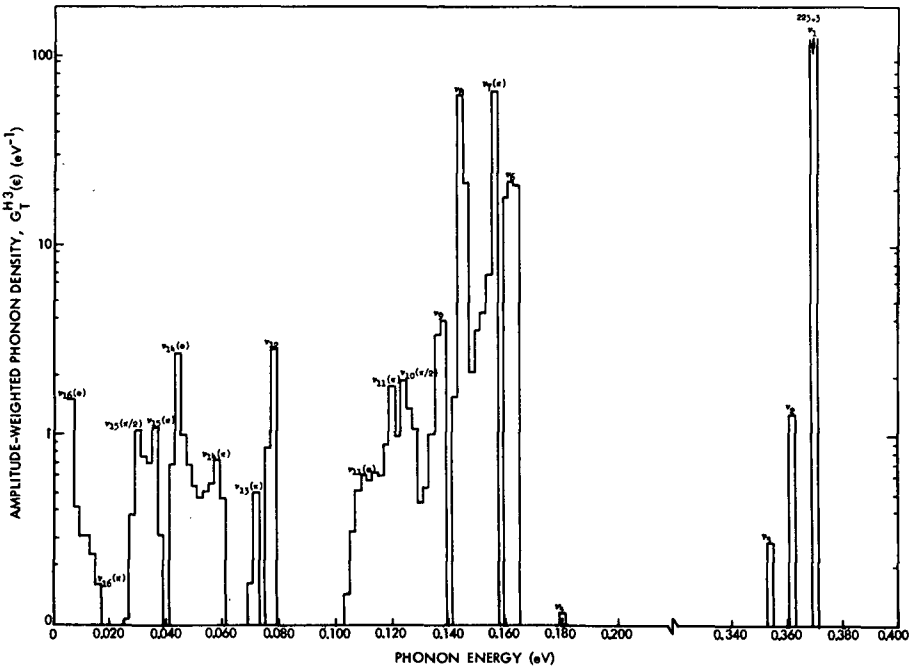

FIG. 6. Single-chain polyvinylchloride transverse (H^3) hydrogen frequency function.

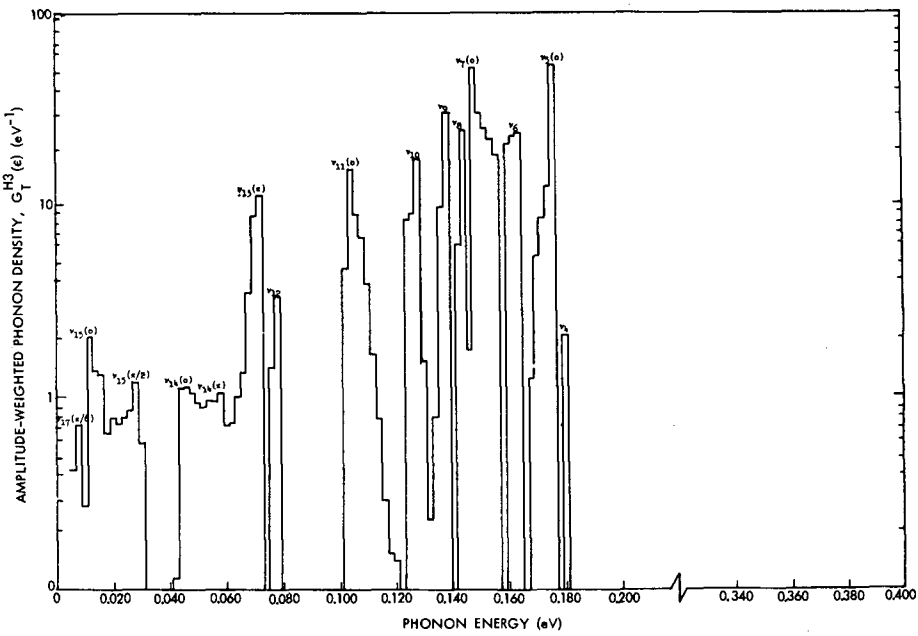

FIG. 7. Single-chain polyvinylchloride longitudinal (H^3) hydrogen frequency function.

One other piece of experimental data which would be quite valuable is a measurement of the Debye-Waller factor, $e^{-Z_s(0)}$, for $\vec{K}$ oriented parallel and perpendicular to the chain axis. From our frequency distribution, we calculate the $Z_s(0)$ factors at 100° K to be

Transverse orientation:

$$Z_{H1}(0) = Z_{H2}(0) = 0.035\ \text{Å}^2\text{K}^2 \tag{8}$$

$$Z_{H3}(0) = 0.022\ \text{Å}^2\text{K}^2 \tag{9}$$

Longitudinal orientation:

$$Z_{H1}(0) = Z_{H3}(0) = 0.021\ \text{Å}^2\text{K}^2 \tag{10}$$

$$Z_{H3}(0) = 0.022\ \text{Å}^2\text{K}^2$$

Approximately 50% of the transverse coefficients and 10% of the longitudinal coefficients are contributed by the modes below 0.006 eV. Thus the measurement of these coefficients will provide us with information about the low lying modes for which our calculation is open to question.

REFERENCES

[1] SCHACHTSCHNEIDER, J. H., SNYDER, R. G., Spectrochim. acta 19 (1963) 117.
[2] OPASKAR, C., KRIMM, S., (to be published); OPASKAR, C., thesis, University of Michigan (1967).
[3] LYNCH, J. E., Jr., thesis, University of Michigan (1968).
[4] LYNCH, J. E. et al., J. chem. Phys. (to be published).

DISCUSSION

H. PRASK: On what information did you base your choice of force constants, and did your calculation give agreement with Q = 0 frequencies obtained by Raman and infrared measurements?

J.E. LYNCH: The internal co-ordinate force constants used are those of Opaskar and Krimm for PVC. This set of constants is an augmented version (including the carbon-chlorine stretching constant) of the well-known set by Schachtschneider and Snyder for the saturated hydrocarbons.

B.N. BROCKHOUSE: To what extent are the patterns for such materials as this, or for the polyethylene dealt with in the preceding paper, fixed by symmetry or by well-known bond constants? Is there any hope of using the incoherent neutron results to adjust the force constants and hence to improve the models? It seems to me that, for this to be possible, the initial model must be fairly close to the truth.

J.E. LYNCH: The dispersion relations, at least as regards the $S_c = 0$ and $S_c = \pi$ intercepts, are generally quite insensitive to the symmetry of the molecule for the saturated hydrocarbons. This explains why the basic force constants used here reproduce the measured infrared and Raman frequencies quite well for a large number of molecules of different symmetry. These are well-known force constants (Schachtschneider and Snyder; Opaskar and Krimm).

The incoherent neutron results should certainly be used to improve or determine the force constants which affect the lowest frequency motions, such as the internal rotation force constant or the carbon-carbon stretching constant.

AN INVESTIGATION OF THE POLYPEPTIDE, POLY-L-GLUTAMIC ACID, USING NEUTRON INELASTIC SCATTERING

W.L. WHITTEMORE
GULF GENERAL ATOMIC INCORPORATED,
SAN DIEGO, CALIF., UNITED STATES OF AMERICA

Abstract

AN INVESTIGATION OF THE POLYPEPTIDE, POLY-L-GLUTAMIC ACID, USING NEUTRON INELASTIC SCATTERING. The polypeptides are synthetic polymers of amino acids with many similarities to natural proteins. In a large number of cases, one of the conformations for both the synthetic and natural proteins is the α-helix. The simplest of the synthetic polymers with no side chains is polyglycine and the simplest of the synthetic polymers with a small side chain (methyl group) is polyalanine. Dispersion curves have been computed by Gupta for both of these polymers. Polyglutamic acid is similar to polyalanine in that the composition of the basic residue and radius of helix is the same. Polyglutamic acid has a more complicated side chain which will contribute a number of additional natural frequencies that are expected to be essentially independent of conformation. On the other hand, the dispersion curves already derived for polyalanine in the α-helix form should be correct in many specific details for polyglutamic acid.

An experimental study has been undertaken for polyglutamic acid at room temperature using the techniques of inelastic neutron scattering. In the first measurements, 'cold' neutrons from a reactor were used to investigate the energy level structure up to $\simeq$ 3 kT for both conformations of the polymer. In addition, the scattering of monoenergetic high-energy neutrons ($>$ 0.15 eV) provided by an electron Linac was used to study energy levels above 3 kT. These latter measurements permit comparisons to be made between the calculated and measured results for a much larger range of frequencies (and hence permit a check for a larger number of dispersion curves). This extension of the experimental results to higher frequencies has made it possible to check on the earlier assumption that only the lower frequencies are altered when the conformation is changed. This assumption underlies the evaluation of changes in internal energy with conformation from only the 'cold' neutron data, as is done with the present data.

An experiment was performed to evaluate the frequencies associated with motion of water molecules adsorbed on the sodium salt of polyglutamic acid. The water was present only to the extent of about one molecule to each two or three residues. A number of distinct frequencies attributable only to the adsorbed water were observed which indicate a variety of bonding of the water molecule to the host polypeptide.

I. INTRODUCTION

Although the simplest of the polymers is polyethylene, the simplest of the biopolymers is polyglycine, which is a member of the polypeptide family. The polypeptides are synthetic polymers of amino acids. As such these exhibit many properties of natural proteins, including the possibility usually to exist in one or more conformations. It was early recognized that the α-Helix form of polyglutamic acid (PGA) possessed many similarities to the conformed structure of DNA and RNA. It is therefore not surprising that PGA as well as many of the polypeptides have received continuing attention and that continued effort is directed toward measurement of bond strengths, particularly those involved with molecular conformation. The purpose of the investigation reported here is to apply the technique of thermal neutron inelastic scattering to some of the problems connected with biopolymers.

II. GENERAL DISCUSSION

Three of the polypeptides, progressing from the simplest with no side chain to one with a simple methyl side chain and, finally to one with a complex side chain, are polyglycine, polyalanine and polyglutamic acid. These and many other polypeptides have been extensively studied by Raman, infra-red and X-ray techniques. The structure has been identified and location of many of the frequencies associated with the complex molecular structure has been found. A suitable discussion of these and other facets of the problem has been given by Gupta et al. [1]. Physical chemistry measurements have been performed to attempt to evaluate the bond strengths, particularly those which are altered in the process of changing conformation such as α-Helix to random-coil in PGA.

It has been noted [2] that the energy transfer bands on which most reliance can be placed for many structural studies are generally those due to: (1) NH stretch ($3310\ cm^{-1}$ and $700\ cm^{-1}$); (2) NC = O out-of-phase mode (Amide I, $1630\ cm^{-1}$ and $1685 - 1700\ cm^{-1}$) and (3) NH out-of-plane deformation (Amide II, $1530 - 1560\ cm^{-1}$). It may be noted that these all lie in a range of neutron energies from $\sim 0.1 - 0.3$ eV. For a study of polypeptide conformation Miyazawa [3] has shown that a large range of frequencies in the Amide group (CONH) is important. He has identified and evaluated nine characteristic energies ranging from Amide A ($3280\ cm^{-1}$) to Amide VII ($206\ cm^{-1}$). Of considerable interest is the fact that Miyazawa notes that only a few of the lowest frequencies (in the range $200-600\ cm^{-1}$) have intensities which vary significantly with conformation (structural transitions) of the molecule. As will appear below, it may be that changes in intensity of the higher frequencies also accompany changes in conformation. This will be one of the interests in studying the scattering patterns for neutrons with higher energies ($E > 0.1$ eV) since in the end one hopes to derive a proper phonon distribution to describe each conformation and, from these, to derive the bond strength.

Of considerable assistance in analyzing neutron inelastic scattering measurements are dispersion curves calculated for a specific polypeptide. Gupta et. al. [1] have been instrumental in making such calculations for several biopolymers specifically for use in comparing theory with neutron scattering results. Although polarization vectors are not available, the dispersion curves are available for polyglycine [1] and preliminary results as well for polyalanine [4] in the planar zigzag conformation. When polyalanine dispersion curves are available for the α-Helix conformation it will be highly instructive to compare these with neutron results. Since it may be some additional time before similar theoretical results are available for polyglutamic acid, the dispersion curves for the α-Helix conformation of polyalanine may profitably be compared with these measurements since many similarities undoubtedly exist between these two molecules in the α-Helix conformation. The major difference lies in the complexity of the side chain and its interactions. The calculations of Gupta indicate some changes in intensity to be expected for Amide frequencies above $600\ cm^{-1}$ as the conformation is changed.

III. EXPERIMENTAL RESULTS AND DISCUSSION

As discussed above, polyglutamic acid (PGA) and its sodium salt (Na-PGA) are members of the polypeptide family with rather complex side chains. In the conformed structure (α-Helix) the molecule assumes a helical structure with about 3.7 residues per helix. Neutron inelastic scattering occurs predominantly from the bound hydrogen in the molecule. In an earlier study [5], "cold" neutrons were used to study the frequency distributions of PGA and Na-PGA. These data were analyzed to yield approximate frequency distributions (in the single phonon approximation) and, from these, the appropriate thermodynamic quantities and some estimates of the strength of conformational bonds. For convenience Figure 1 shows the more prominent frequencies for PGA and Na-PGA. The composition of a residue is shown in this Figure as well.

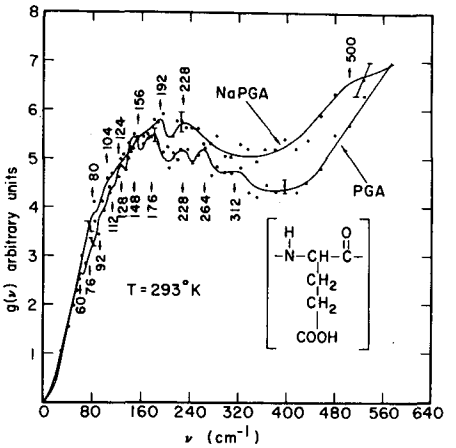

FIG.1. Frequency distribution $g(\nu)$ of PGA and its sodium salt derived in the one-phonon approximation. The ordinate is in arbitrary units. The abscissa and the noted frequencies are expressed in wave numbers (cm^{-1}).

In a pair of experimental runs using a cold neutron energy gain scatter ing technique, the neutron spectra for "dry" and "wet" Na-PGA were studied. Figure 2 shows these results. The small weight of adsorbed water was remo' in a vacuum furnace (~ 50°C) after the "wet" specimen was run. The quantity of water corresponded to an average density of about one water molecule per five or six residues, so it is most likely that single molecules of water inter· acted with the large host molecule. An average difference curve is shown in Figure 2. One can view this resulting curve as the sum of (1) the interactions between the water molecule and the host molecule, as well as (2) any enhanced motion of the host molecule made obvious by the presence of the water. Since no dispersion curve is available for the host molecule, we are not able to comment on (2). The difference curve shows a large peak at about 550 cm^{-1} together with distribution of other peaks for lower energy. In some degree the appearance of this curve is similar to that for the scattering of liquid water. It will be remembered that the usual model for liquid water considers that the molecule executes torsional motion essentially about the oxygen molecule, bending the two hydrogen bonds (each hydrogen atom in

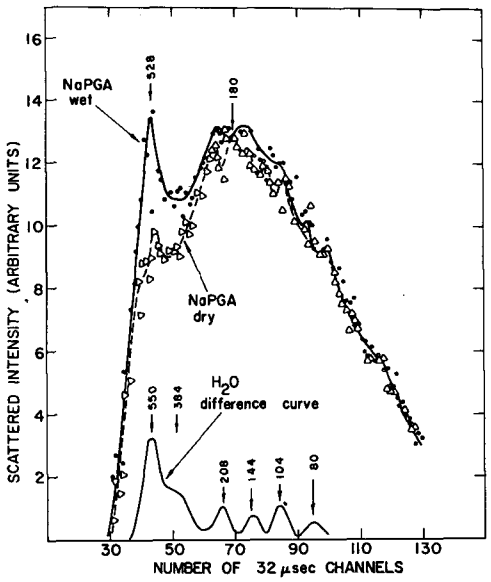

FIG. 2. Neutron spectra for 'dry' and 'wet' Na-PGA. The difference spectrum is due to adsorbed water. The identified peaks are expressed in wave numbers (cm^{-1}).

one molecule bonded to other molecules). Since this peak in the present case at 550 cm^{-1} is so close to that in liquid water, one may suspect that most atoms of the individual water molecules adsorbed on Na-PGA tend to be tightly bound and that the molecule executes hindered rotations (torsional motion) much the same as in liquid water. The large number of lower frequencies (probably connected with other arrangements of binding) present a qualitative picture somewhat different from that in liquid water and must await a normal mode calculation before complete interpretation.

Reference to Figure 1 shows that cold neutron scattering results become imprecise for energy transfers greater than about 600 cm^{-1}. No substantial gain in intensity is possible by heating the specimen (to take advantage of the Boltzmann factor) since the elevated temperatures will destroy the biomolecular conformations. To investigate the energy transitions in these higher regions (> 600 cm^{-1} ≅ 0.075 eV), warm neutron sources will generally be needed. A technique using incident neutrons with energy up to ≃ 1.0 eV (≃ 8000 cm^{-1}) has been developed using an electron Linac as a neutron source [6]. A program for applying this technique to the study of polyglutamic acid has been initiated. The first results were obtained for scattering at a number of angles (30° - 120°) and for incident neutron energies of 0.179 and 0.257 eV. Typical results are shown in Figures 3 and 4, where the evaluated data are presented as a function of energy transfer.

As was noted in Section II, no dispersion curves exist for polyglutamic acid nor for the α-Helix conformation of polyalanine (which might be similar even though the side chain in polyalanine is smaller). Therefore, it will not be possible to identify with certainty the prominent peaks seen in Figures

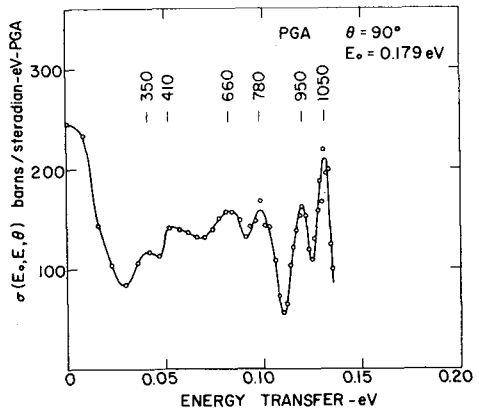

FIG.3. Energy exchange cross-sections of PGA for neutrons with E_0 = 0.179 eV scattered at 90°. Tentatively identified peaks are expressed in wave numbers (cm^{-1}).

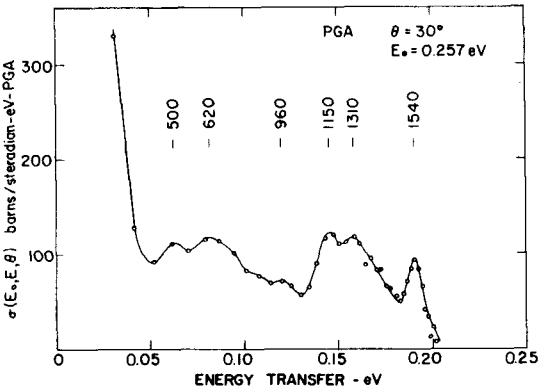

FIG.4. Energy exchange cross-sections of PGA for neutrons with E_0 = 0.257 eV scattered at 30°. Tentatively identified peaks are expressed in wave numbers (cm^{-1}).

3 and 4. However, using the theoretical work of Miyazawa [3] and Gupta et al. [1], we have attempted to make assignments for the frequencies shown in the Figures. These are listed in the Table. When similar data exist for Na-PGA it will be instructive to investigate the intensity of the listed frequencies to evaluate any change in these with conformations.

Data of the type exhibited in Figures 3 and 4 (when sufficiently numerous and when measured for both PGA and Na-PGA) can be used to derive a Scattering Law [7]. The extrapolation technique [7] (which evaluates a quantity proportional to the molecular frequency distribution) can be used above ν = 600 cm^{-1} (see Figure 1) to supplement the frequency distributions already derived using cold neutrons [5]. These data, when available, may make it possible (1) to integrate the thermodynamic quantities over the full range of frequency and (2) to check Gupta's suggestion [4] that the frequencies above 600 cm^{-1} may vary in intensity as the molecular conformation is changed.

TABLE I. TENTATIVE ASSIGNMENT OF FREQUENCIES FOR SCATTERING IN PGA OF EPITHERMAL NEUTRONS

$\nu(cm^{-1})$	Assignment
350	C = O rocking or C-C torsion
410	C-C-C deformation
500	C = O out of plane bend (Amide VI)
620	Skeletal deformation along helix
660	Amide V; N-H out of plane
780	CH_2 rocking
960	(CH_2 twist)
1050	C-C- stretch
1150	C-C stretch
1310	CH_2 wag
1535	N-H deformation and C-N stretch (Amide II)

IV. SUMMARY

1. The observed neutron scattering pattern for an isolated water molecule gives evidence that the molecule is tightly bonded to Na-PGA.

2. High energy monoenergetic neutrons (> 0.1 eV) give scattering patterns which indicate numerous well defined excitations in PGA. Using the same neutron probe for PGA and Na-PGA should make it possible to study directly any change in intensity of the higher frequencies (> 600 cm^{-1}) with change in conformation.

ACKNOWLEDGMENTS

The author gratefully acknowledges helpful discussions with Drs. P. A. Egelstaff, V. D. Gupta, and D. E. Parks. Mr. A. K. Hom capably processed all data reported herein for the high energy neutron experiments.

REFERENCES

[1] GUPTA, V. D., TREVIÑO, S., BOUTIN, H., Vibration spectra of polyglycine, to be published in Jour. of Chem. Phys. Available as preprint from Picatinny Arsenal, Dover, N. J.

[2] ELLIOTT, A., BRADBURY, E. M., DOWNIE, A. R., HANBY, W. E., "Conformation of polypeptide chains in the solid state", Polyamino Acids, Polypeptides, and Proteins (Proc. Intl. Symp. University of Wisconsin, 1961) 255.

[3] MIYAZAWA, T., "Characteristic amide bonds and conformations of polypeptides" (op. cit.) 201.

[4] Private communication with Dr. V. D. Gupta, Picatinny Arsenal, Dover, N. J., and presently, Physics Department, Indian Institute of Technology, Kanpur, India.

[5] BOUTIN, H., WHITTEMORE, W. L., Investigation of the α-helix-random-coil transition in polyglutamic acid by slow neutron scattering, Jour. of Chem. Phys. 44 (1966) 3127.

[6] WHITTEMORE, W. L., Neutron Differential Scattering, Annual Summary Report, October 1, 1965 through September 30, 1966, USAEC Rep. GA-7439, General Dynamics, General Atomic Division.

[7] EGELSTAFF, P. A., "The theory of the thermal-neutron scattering law", Proc. Symposium on Inelastic Scattering of Neutrons in Solids and Liquids (Proc. Symp. IAEA Vienna, 1960) Vienna (1961) 25.

DISCUSSION

L.J. SLUTSKY: At least when one is dealing with a solution, one would expect a molecule not altogether in the helical form to consist of alternating helical and coil segments; one might further expect that the non-helical segments would be more likely to form inter-molecular hydrogen bonds. Therefore, because of the co-operative nature of the transition it is not possible to proceed directly from a low concentration of water molecules, helical segments or protonated -COO^- groups to a negligible concentration of adjacent water molecules, helical units, etc.

W.L. WHITTEMORE: I doubt whether this remark applies to our case, where we used the dried samples exclusively.

J.W. WHITE: Could you explain the lack of correspondence between the energies of the peaks you observed using different incident energies in your downscattering experiments?

W.L. WHITTEMORE: The individual peaks show a generally consistent behaviour with momentum transfer, as has been demonstrated by plotting a scattering law for these data obtained at several angles and two incident energies.

J.W. WHITE: At a given incident energy, do the spectra change greatly with scattering angle? How do you overcome the effects of multiphonon scattering at the high momentum transfers involved in your experiments?

W.L. WHITTEMORE: By using small momentum transfers we can reduce the effects of multiphonon processes. To obtain the data, very small scattering angles are required for the large incident energies.

J.J. RUSH: In Fig. 1 of your paper, showing the frequency distributions derived from the cold-neutron work, you indicate a number of 'peaks' below 250 cm^{-1}. Presumably the indicated maxima are taken from Raman or infrared measurements, but it seems to me that the resolution and statistical accuracy of the neutron measurements do not justify the assignment of any peaks in this region.

W.L. WHITTEMORE: The listed frequencies are indeed those reported by workers using optical techniques. They indicate regions where it seemed reasonable to look for evidence of the existence of peaks, but I admit that little such evidence emerges.

J.J. RUSH: With reference to your "baking" the water out of your sample at 50° C, what is the melting or decomposition point of the compound? Is there any possibility that the resulting changes in the spectra are due to some other change in the sample?

W.L. WHITTEMORE: Our biophysicist friends tell us that 'dry' samples will not be affected by temperatures somewhat in excess of 50° C. Thus, our treatment of the specimen was quite gentle!

G. JANNINK: The ordered α configuration is probably associated with singularities in the acoustic frequency spectrum (assuming that the random distribution of the residues does not affect acoustic modes). In the coil configuration these singularities vanish. This effect should be observable if the experiment were performed at a one-phonon level, but it would seem to be washed out at the temperature at which you operate.

W.L. WHITTEMORE: I believe that you are right; in any case this can be checked by using better instrumental resolution and lower sample temperatures.

H. MAIER-LEIBNITZ: The usefulness of all work in this field would seem to be hampered at present by poor resolution, and I wonder what resolution we should aim at. I should also be interested to hear participants' views on what is the importance of observing peaks for various momentum transfers.

W.L. WHITTEMORE: I consider that resolutions of 1-5% in energy would be a useful goal. In reply to your second point, it is quite likely that the different modes of motion will exhibit a quite different dependence on momentum exchange. Measurement of this dependence can therefore help in the assignment of the individual peaks.

H.H. STILLER: Changes in confirmation will mostly affect the low-frequency modes, for instance the hindered rotations of atomic groups involving large numbers af atoms. We have estimated that to observe this a resolution of at least 10^{-5} eV would be required. As to measurements with finite momentum transfers, I think they are important, because different κ-dependencies make it possible to identify different motions.

J.W. WHITE: Very interesting chemical information could be extracted from the momentum transfer dependence of inelastic scattering spectra at high as well as at low energy transfers. For example the dispersion (or lack of it) of intramolecular modes is of particular interest.

I would like to point out, however, that multiphonon processes may set a limit to the usefulness of this work, especially for incoherent scattering. Low-angle scattering experiments should be performed now, for downscattering with energy transfers up to 500 meV, in order to see what can be done with selected molecules.

O.K. HARLING: It certainly appears that κ-dependent measurements of inelastic neutron scattering spectra are useful. These measurements can best be performed by downscattering for energy changes much larger than κT. It would also appear particularly important to be able to measure the scattering distributions to small κ, so that good extrapolations can be made to $\kappa = 0$ (where multiphonon effects will be zero). This kind of operation is of course inherently difficult because it requires large incident energies, up to several eV for the higher molecular vibrational frequencies, and at the same time needs small scattering angles and very high resolutions. Hot sources in reactors, associated with instruments of the type reported in my paper (SM-104/81) and electron-accelerator-based spectrometers such as those at General Atomics and the Rensselaer Polytechnic Institute, are particularly suitable for these types of measurement. The accelerator-based instruments, in particular, appear to be very competitive and have not yet been refined to the same degree as the reactor-based equipment.

G.C. SUMMERFIELD: I should like to comment further on the multiphonon question. In the neutron cross-section at these high energy and momentum transfers, the multiphonon contributions from the low-energy modes can effectively shift the positions of the high-energy singularities in the frequency distribution, as well as broadening them. Thus, the singularities observed in this cross-section do not correspond directly to the singularities in the frequency distribution, and one cannot simply interpret the peaks in the cross-section as being singularities in that distribution.

W.L. WHITTEMORE: This point is a valid one, and indicates the real reason for performing these measurements for large energy transfers under conditions giving low momentum transfers.

L.J. SLUTSKY: One should bear in mind that, even in the perfectly helical form with which we are dealing, a 'crystal' contains some 100 unit cells. Therefore, when discussing 'singularities' in the frequency distribution, we should remember that there is a definite upper limit to the Fourier components of the spectrum, which are in fact independent of the chain-length, boundary condition and accidents of local environment. I do not believe that we should expect to find singularities in the sense that we find them in crystalline solids.

H.H. STILLER: I wonder whether, with these large and complicated molecules, the observation of large energy transfers is really important. The high-frequency modes are in general optically active. I therefore consider that, in future, neutron investigations should be concentrated rather on very small energy transfers, which can also be done in upscattering.

W.L. WHITTEMORE: Even though the optical measurements produce – so I understand – data for $\vec{q} = 0$, the neutron data yield information on the 'flatness' of the optical branch. This would be at least one reason for continued high-energy neutron measurements on these complicated molecules.

H. PRASK: As I understand your results to date, you have not been able to do the measurements on the Na-PGA salt to verify whether the downscattering measurements are conformation-sensitive for the two different PGA conformations.

Have you compared your downscattering results on PGA with infrared and Raman measurements, to ascertain whether the neutron results give any new information on the high-frequency modes in this polypeptide?

W. L. WHITTEMORE: This comparison has not been made yet.

G. CAGLIOTI: It has been generally implied during this discussion that the optic branches of internal modes are extremely 'flat'. This might well not be the case if the intermolecular forces are large. An experimental study of this point seems to be desirable.

W. L. WHITTEMORE: This would constitute an example of the value of neutron measurements in the high-energy transfer region. Such measurements should of course be made for small momentum transfers, so as to reduce the effect of multiphonon processes.

LATTICE DYNAMICS OF HEXAMETHYLENETETRAMINE

B.M. POWELL
ATOMIC ENERGY OF CANADA LTD.,
CHALK RIVER, ONT., CANADA

Abstract

LATTICE DYNAMICS OF HEXAMETHYLENETETRAMINE. The frequencies of the normal modes of vibration of the organic molecular crystal deuterated hexamethylenetetramine (DHMT) have been measured using inelastic neutron scattering techniques. The measurements were made along the high symmetry directions [00ζ], [ζζζ], [ζζ0] and [½½ζ] at 296°K, using the triple-axis spectrometer in its constant-$\vec{Q}$ mode of operation at the NRU reactor, Chalk River. DHMT is a simple molecular crystal which crystallizes in a body-centred-cubic structure. The molecules have cubic symmetry, and it is believed that the intramolecular forces are much stronger than the intermolecular ones. The molecules can thus be considered as rigid units with three translational and three librational degrees of freedom. For any general wave-vector there will thus be six normal modes, each comprising both translational and librational components. The effect of the librational components can be seen in the very different neutron group intensities observed along similar directions in reciprocal space, e. g. (200)→(221) and (330)→(331). The frequencies of certain triply degenerate modes are (units 10^{12} cps): H_{15} (1. 96 ± 0. 04); H'_{15} (0. 95 ± 0. 02); Γ'_{15} (1. 06 ± 0. 04). Cochran and Pawley have proposed a simple model for normal hexamethylenetetramine and calculated dispersion curves in the symmetry directions. The present results indicate that the model is a reasonable approximation and, by fitting the observed frequencies, the parameters of the model for DHMT can be determined.

1. INTRODUCTION

In many molecular crystals the intramolecular forces are thought to be much stronger than the intermolecular ones. In these cases the molecules may be considered as rigid units having three translational and three librational degrees of freedom. The lattice dynamics of such crystals has only recently been developed, and it is of interest to determine to what extent the dynamics of such crystals can be described within the framework of conventional phenomenological theories. Hexamethylenetetramine (HMT) $(CH_2)_6N_4$ is a highly symmetric organic molecular crystal which crystallizes in the body-centred cubic structure. It has space group $I\bar{4}3m$, and the molecule also has the symmetry $\bar{4}3m$. Raman [1], Infra-red [2] and X-ray diffraction [3] measurements indicate that treating the molecules as rigid units is a good approximation for HMT, the lowest intramolecular vibration frequencies being a factor of five higher than the intermolecular vibration frequencies. The present paper describes measurements of the frequencies of these intermolecular or lattice modes of the molecular crystal deuterated hexamethylenetetramine (DHMT). The dispersion curves are analyzed in terms of a simple dynamical model, from which may be calculated the normal mode frequency distribution function.

2. EXPERIMENT

2.1 Experimental Details

Single crystals were grown from 98% deuterated DHMT powder by slow evaporation of a saturated solution in ethyl

alcohol. The specimen used in the experiment consisted of three single crystals having a total volume of 3-4 cms^3. Since HMT sublimes slowly at room temperature the specimen was sealed in an aluminum can. The crystals were oriented with the $[1\bar{1}0]$ axis vertical, and the measurements were carried out at 296°K on the triple-axis spectrometer at NRU reactor Chalk River. The incident and scattered neutron beams are in the horizontal plane in this system. The constant momentum transfer mode [4] with neutron energy loss was used throughout.

2.2 Discussion of Results

Since the molecules have six degrees of freedom, for a general wave-vector there will be six normal "lattice" modes, each having both translational and librational components. To assign the measured frequencies to the correct modes, a dynamical model proposed by Cochran and Pawley [5] for normal HMT was used in the initial stages. Using this model the "inelastic structure factor", which is the principle term in the coherent one-phonon scattering cross-section, is calculated for the deuterated material. This quantity is compared with the observed neutron group intensities, and assignments of the observed frequencies are made to obtain approximate agreement between the two. A least-squares fit to the observed frequencies is then carried out using these assignments, and new inelastic structure factors are calculated. One such iteration was needed to achieve satisfactory agreement between the calculated structure factors and the observed neutron group intensities. The dispersion curves obtained in this way are shown in Fig. 1. Measurements were made along the Δ, Λ, Σ and D directions. Connected error bars are shown on two points in the D direction, indicating that the neutron groups for these pairs of points were not experimentally resolved. The experimental accuracy of all other frequencies is typically 2 or 3%.

Group theoretical labels have been assigned to the branches on the assumption that the molecules are centrosymmetric. In effect this assumes a point group symmetry O_h^9 instead of the actual T_d^3 symmetry. Reasons for making this assumption and its effect on the labelling scheme will be discussed in section 4. All branches with subscript 1 (except Δ_1') are pure translational modes, while branches with subscript 2 (together with Δ_1') are pure librational modes with the axis of libration parallel to the direction in which $\vec{q}$ is changing along any particular branch. Thus, for example, D_1 is a pure translational mode with polarization vector parallel to [001], while D_2 is a pure librational mode with axis of libration parallel to [001]. All other branches are of mixed translational-librational character, the proportion of each type of displacement varying with wave-vector. Certain branches, including all branches representing pure libration, are shown as dashed lines in Fig. 1; the structure factor calculations indicate that none of these modes should be observed with the crystal in the present orientation (except by possible spurious double scattering processes [6]). Indeed Cochran [7] has pointed out that if the momentum transfer vector $\vec{Q}$ is parallel to a symmetry axis of the molecule then a pure librational mode cannot be observed. The lack of experimental points on the $\Delta_5 0$, $\Lambda_3 0$ and $\Sigma_3 0$ branches

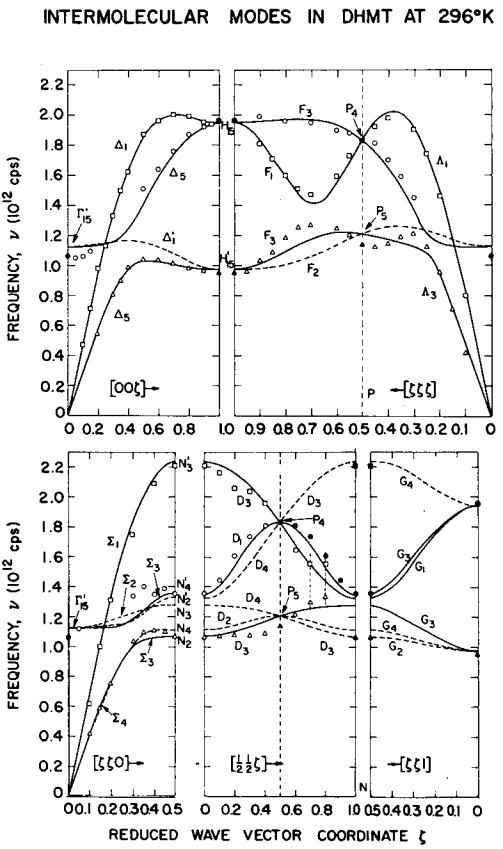

FIG.1. Intermolecular modes at 296°K in DHMT. The experimental observations are shown as squares, circles and triangles, the various symbols being used to provide simple differentiation among the branches. Points appearing more than once in the figure are shown as filled points. Solid and dashed lines represent the best least-squares fit to the experimental results; the dashed lines refer to modes which cannot be observed with the crystal in the $[1\bar{1}0]$ orientation.

(0 indicates optical, A indicates acoustical) as $\zeta \to 0$ in Fig. 1 arises from the experimental difficulty of observing these particular modes. These modes become mainly librational as $\zeta \to 0$, and despite the prediction of favourable structure factors by the model, very long counting times have been necessary for their observation. The experimental points are seen to lie generally on smooth curves, and so it might be hoped that a comparatively simple model could be used to interpret them.

3. THEORETICAL ANALYSIS

Theoretical models for the dynamics of molecular crystals have been proposed by Hahn and Biem [8], Biem [9], and by Cochran and Pawley [5]. Using the known values of elastic constants and of the triply degenerate librational mode Γ_{15}' to estimate the unknown model parameters, the latter authors have calculated the dispersion curves of normal HMT in symmetry

directions. The model postulates force constants representing forces and couples exerted on a molecule by its first and second nearest neighbours only. Because of the high symmetry of this crystal, the number of independent parameters is reduced to twelve. On making the additional assumption that the molecules are centrosymmetric, the number of parameters is further reduced to ten, five for each type of neighbour and a further reduction to eight parameters is achieved by imposing certain equilibrium conditions. Using this model, a least-squares fit has been made to the experimental frequencies, and the best fit is shown in Fig. 1 by the solid and dashed lines. It can be seen that the overall fit is quite good, with Δ_1, Δ_5, Λ_1 and Σ_1 branches being fitted very closely. The fit is poorer for the Λ_3A, $\Sigma_3$0 and D_3A branches however and the frequency of the mode P_5 is not predicted very accurately. Similarly the agreement between the measured and calculated frequencies of the optical mode Γ_{15}' at $\zeta \rightarrow 0$ is only fair. The values of the parameters obtained for this fit are shown in Table I, and the parameters used by Cochran and Pawley for normal HMT are also given for comparison.

Using the parameters from the best fit, a frequency distribution for the lattice modes of DHMT has been calculated by the extrapolation procedure of Gilat and Raubenheimer [10]. The distributions for the translational and librational components of the modes are shown in Fig. 2. The librational frequencies are seen to lie in a band extending from 1.00 to 1.30 (10^{12} cps), but there are tails to the librational distribution arising from the modes of mixed character. The comparatively narrow band of librational frequencies, which lies on the low frequency tail of the translational frequencies, emphasizes the fact that the model tends to produce either almost pure translational or almost pure librational modes. Comparatively

TABLE I. MODEL PARAMETERS

Parameter	Best Fit (This work)	Values from Ref. [5]
A	6.39 ± 0.08	5.0
B	0.33 ± 0.04	0.123
Q	0.86 ± 0.21	0.495
R	-1.03 ± 0.13	0.495
A'	3.80 ± 0.10	4.0
B'	-0.06 ± 0.03	0.123
Q'	1.10 ± 0.33	0.495
R'	0.36 ± 0.19	0.495

The parameters are in units of 10^3 dynes cms^{-1}. The notation is that of reference [5]. The values quoted from this reference are for the model from which the published dispersion curves have been calculated.

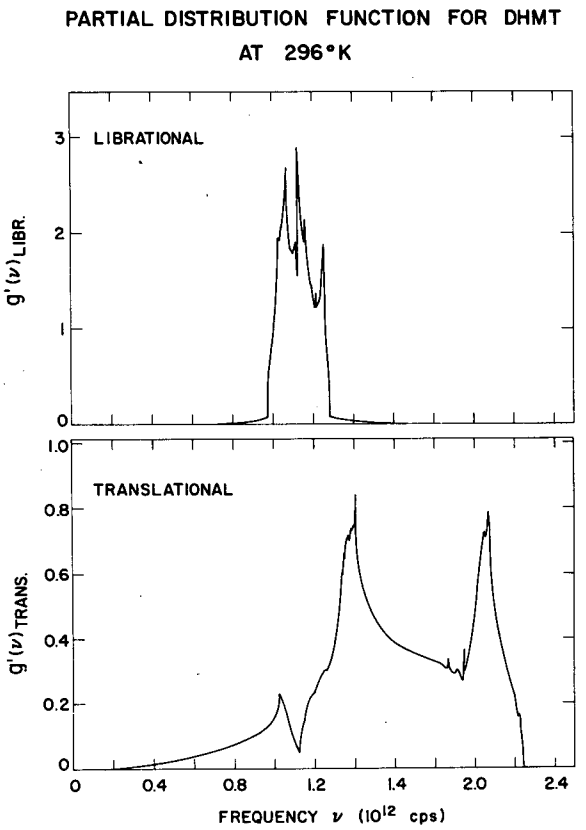

FIG. 2. Distribution functions for translational and librational components of lattice modes in DHMT.

few modes, at least in symmetry directions, are of significantly mixed character. The total frequency distribution shown in Fig. 3 is seen to be dominated by the librational component, with the translational component providing a smaller high frequency tail. The arrows shown on Fig. 3 indicate the movement of prominent features if the distribution is calculated using the parameters obtained from the fit for DHMT, but with the mass and moment of inertia of the molecule appropriate to normal HMT. This displaced frequency distribution is then appropriate to normal HMT on the very plausible assumption that the intermolecular forces are unchanged on replacing deuterium by hydrogen. Measurements of the frequency distribution of normal HMT have been made by Becka [11] and by Bührer et al. [12] using the inelastic incoherent scattering of neutrons from powdered specimens. While certain features of these measured distributions can be correlated with the calculated distribution for normal HMT (not shown), the overall shapes of the calculated and measured distributions are rather different.

The calculated frequency distribution for normal HMT has been used to compute the temperature variation of the heat capacity C_V and the derived Debye temperature θ_D, and the

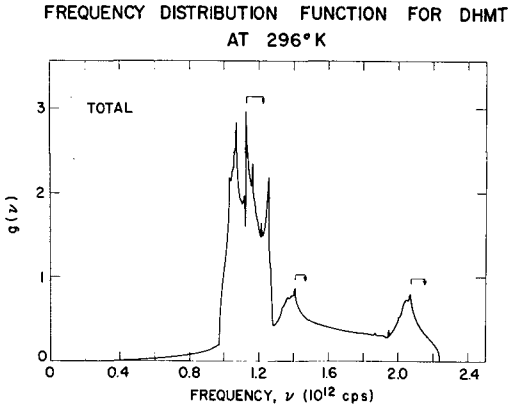

FIG.3. Calculated frequency distribution function for lattice modes in DHMT.

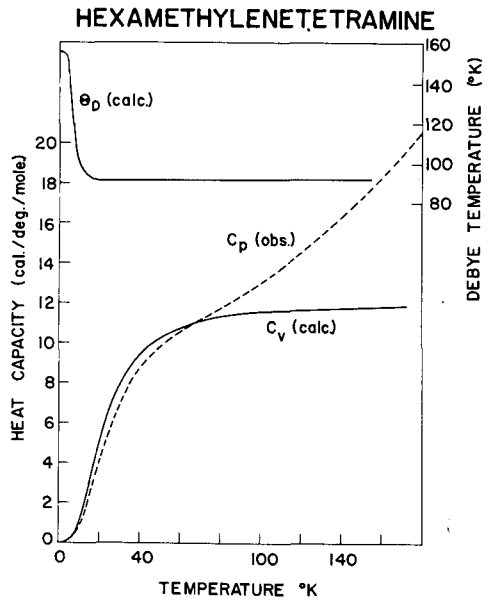

FIG.4. Temperature variation of the heat capacity C_v and Debye temperature θ_D calculated for HMT, compared with the observed heat capacity C_p.

results are shown in Fig. 4. The heat capacity C_p of normal HMT has been measured by Chang and Westrum [13], and their observations are shown as the dashed line on Fig. 4. It can be seen that the calculated heat capacity saturates at quite low temperatures and at higher temperatures the measured heat capacity is much larger than the calculated value, the difference increasing with increasing temperature. This discrepancy arises mainly because at higher temperatures the measured heat capacity includes contributions due to the excitation of relatively high frequency intramolecular modes of vibration, and these modes are specifically excluded from the model on which the calculated

heat capacity is based. More surprising is the fact that at low temperatures the calculated C_v is significantly greater than the measured C_p. In making this comparison is must be remembered that the heat capacity has been calculated from a frequency distribution appropriate to 296°K; and also that the frequencies used for the long wavelength acoustic modes are very dependent on the model since the experimental measurements are not very accurate in this region. Nevertheless the discrepancy between the calculated and measured heat capacities seems too large to be accounted for by these approximations and may imply an unusually large temperature dependence of the normal mode frequencies. The variation of θ_D with temperature is also unusual, since it reaches a constant value at a rather low temperature.

4. DISCUSSION

To obtain better agreement between the measured and fitted frequencies, several improvements to the model may be made. For example the assumption of molecular centrosymmetry could be removed, thus adding two more adjustable parameters. Recent calculations by Pawley [14], however, based on Kitaigorodskii's interatomic potential functions [15], indicate that the assumption of centrosymmetry is a very good one for normal HMT. Those force constants which would be zero in a centrosymmetric molecule are estimated to be about 1% of the small force constants in Table I. It is therefore physically reasonable and expedient to utilize this higher symmetry (O_h^9) in carrying out the group-theoretical analysis and mode labelling shown in Fig. 1. No additional degeneracies are introduced as a result of the higher symmetry, and indeed, the analysis based on T_d^3 [16] leads to remarkably similar results. Further discussion of these matters will be given in a future publication.

The range of intermolecular forces may be extended to include more distant neighbours, again adding more adjustable parameters to the theory. However, from the structure of the crystal it would be expected that neighbours more distant than next nearest would have a very weak effect. A further variation would be to introduce interatomic rather than intermolecular forces. If such forces, between atoms on different molecules, are postulated with force constants as adjustable parameters, then the large number (22) of atoms in the HMT molecule will introduce a very large number of constants, unless drastic assumptions are made regarding which interatomic bonds contribute to the intermolecular forces. A further possibility is to assume a specific analytic expression [15], containing few constants, for the interatomic or intermolecular potential, and calculate the necessary force constants by direct differentiation of the potential. This approach has been used by Pawley [17] for other molecular crystals. Since comparatively few adjustable parameters may be needed, this procedure could be the most useful one.

These approaches are essentially all variations of the same model, and all may be expected to improve the agreement with the experimental frequencies shown in Fig. 1. An additional branch, having rather weak intensity, and not shown in the figure, has been observed in the Σ direction however. The

branch has a frequency of 1.70×10^{12} cps at $\zeta = 0.05$, decreases in frequency as ζ increases, crossing the Σ_1 branch and appearing to become degenerate with the $\Sigma_3 0$ branch near N_4'. None of the models mentioned above appears able to predict such a dispersion curve, and alternative explanations are being considered. The branch may arise from a small second crystal, misoriented relative to the bulk of the specimen, although no evidence of such a crystal has been detected in examinations of the Bragg reflections. The possibility that it is a mixed inter-intramolecular mode appears unlikely due to its low frequency. The branch may be due to a defect mode of the 2% hydrogen in the crystal. Using the frequency distribution of the DHMT host lattice, it is hoped to calculate such defect modes in order to check this possibility. Some evidence of this additional branch has been observed in other symmetry directions, and further experiments are planned to attempt to elucidate its behaviour and origin.

5. SUMMARY

Measurements of the frequencies of the normal modes of vibration of deuterated hexamethylenetetramine have been described, and the experimental results presented. A simple theoretical model has been fitted to the observed frequencies. With the parameters determined from the fitting procedure calculations of the frequency distribution and of the temperature variation of the heat capacity and the Debye temperatures of both deuterated and normal HMT have been made. Improvements in the model are discussed, and possible explanations for an "additional" branch which has been observed are mentioned.

ACKNOWLEDGEMENTS

The author would like to thank his colleagues at Chalk River Nuclear Laboratories for helpful advice and discussion during this work, and particularly Dr. G. Dolling for his invaluable assistance. He would also like to thank Drs. S.H. Chen and V. Dvorak for a preprint of their paper and Dr. G.S. Pawley for much helpful correspondence.

REFERENCES

[1] COUTURE-MATHIEU, L., MATHIEU, J.P., CREMER, J., POULET, H., J. Chim. Phys. 48 (1951) 1.

[2] CHEUTIN, A., MATHIEU, J.P., J. Chim. Phys. 53 (1956) 106.

[3] BECKA, L.N., CRUICKSHANK, D.W.J., Proc. Roy. Soc. A273 (1963) 455.

[4] BROCKHOUSE, B.N., Inelastic Scattering of Neutrons in Solids and Liquids, IAEA, Vienna (1961) 113.

[5] COCHRAN, W., PAWLEY, G.S., Proc. Roy. Soc. A280 (1964) 1.

[6] DOLLING, G., WOODS, A.D.B., Thermal Neutron Scattering (EGELSTAFF, P.A., Ed.) Academic Press, New York (1965) 196.

[7] COCHRAN, W., Rep. Progr. in Phys. 26 (1963) 1.

[8] HAHN, H., BIEM, W., Phys. Stat. Sol. 3 (1963) 1911.
[9] BIEM, W., Phys. Stat. Sol. 3 (1963) 1927.
[10] GILAT, G., RAUBENHEIMER, L.J., Phys. Rev. 144 (1966) 390.
[11] BECKA, L.N., J. Chem. Phys. 37 (1962) 431.
[12] BÜHRER, W., HÄLG, W., SCHNEIDER, T., Report AF-SSP-9 Delegation fur Ausbildung und Hochschulforschung, E.I.R.
[13] CHANG, S-S., WESTRUM, E.F., J. Phys. Chem. 64 (1060) 1547.
[14] PAWLEY, G.S., private communication.
[15] KITAIGORODSKII, A.J., J. Chim. Phys. 63 (1966) 6.
[16] CHEN, S.H., DVORAK, V., to be published.
[17] PAWLEY, G.S., Phys. Stat. Sol. 20 (1967) 347.

DISCUSSION

E.E. SÁNDOR: Since Mr. Powell some years ago made very extensive and accurate measurements on the thermal diffuse scattering of X-rays by hexamine single crystals, I wonder whether he is considering calculating the thermal diffuse scattering distribution expected on the basis of his neutron measurements. It would be interesting to see whether this would agree better with the measurements than the results of earlier calculations. It would also provide a kind of indirect check on the correctness of his model.

B.M. POWELL: I agree that the calculation of the thermal diffuse scattering of X-rays by DHMT would be a useful, although indirect, check on the correctness of the model, and I intend to carry out these calculations.

E.E. SÁNDOR: Is it possible that the predominance of pure translational and librational modes in the frequency spectrum, as compared with the relative unimportance of mixed modes, is partly the result of assuming that the crystal is centrosymmetric? Would a non-centrosymmetric treatment not alter this predominance?

B.M. POWELL: I do not think that the assumption of centrosymmetry is the sole reason for the predominance of almost pure modes. I have a simple non-centrosymmetric model of HMT, using interatomic forces, and this model shows an effect very similar to the present one – i.e. it also tends to produce few significantly mixed modes.

G.S. PAWLEY: It should be pointed out, in connection with Mr. Sándor's first remark, that for comparison of experimental X-ray diffuse scattering with that calculated for any model, the two-phonon scattering must be included. This calculation has been done for the model proposed by Cochran and myself[1] and should be published soon.

I now have two questions for Mr. Powell. First, did the process of improving the inelastic scattering cross-sections after model fitting cause any alterations in mode assignments?

B.M. POWELL: It's not so much a question of changing assignments as using the cross-section to make the assignment in the first place.

[1] See Ref.[5] of the paper.

One might see perhaps a whole group, and one then decides, on the basis of the cross-section, which frequency belongs to which branch.

G.S. PAWLEY: Well, that is very encouraging in connection with any future work on more complicated systems.

My second question is: what variation in frequencies is necessary to account for the specific heat variation observed? This should then be compared with the results of Becka and Cruickshank from X-ray structure analysis.

B.M. POWELL: The difference between the calculated specific heat C_V and the measured specific heat C_P is approximately 10% at low temperatures. The characteristic temperatures introduced by Becka and Cruickshank also vary by approximately 10% between 300 and 30° K. The temperature variation of the normal mode frequencies which is implied by this variation thus seems large enough to explain the discrepancy between the calculated and measured specific heats.

W. COCHRAN: I would like to draw the attention of Mr. Whittemore and other practitioners of the art of inelastic incoherent scattering to Mr. Powell's results. The model should certainly make possible an accurate calculation of the spectrum and might make possible an assessment of the importance of multiphonon processes.

R. STOCKMEYER: Have the elastic constants and the optical frequencies been measured for deuterated hexamine, or did you extrapolate the values from those known from ordinary hexamine?

B.M. POWELL: The elastic constants and optical frequency have not yet been measured for deuterated hexamine. The values of the elastic constants have not been used in the least-squares fit and the optical frequency used is that measured in the experiment. The elastic constants then obtained from the fit agree quite well with those of normal hexamine. The measured optical frequency in deuterated hexamine, when scaled to apply to normal hexamine, agrees with the measured frequency in normal hexamine to within $\sim 10\%$.

R. STOCKMEYER: You have shown dispersion curves in which the librational and translational branches cross. In my study of the very similar case of adamantane I have found that the assumptions made regarding the symmetry of the molecular force field (e.g. the assumption of a superposition of central interatomic forces) decide whether or not the branches split. Do you consider the cross-points to be well confirmed irrespective of this?

B.M. POWELL: I am surprised that any model for a crystal such as hexamine or adamantane splits up the librational and translational branches, except possibly in special directions. I would expect that all branches will generally be of mixed translational-librational character. In the present fitting no assumption as to the character of the measured frequencies was made. It is only by looking at the eigenvectors of the fitted model that the character of any given branch can be decided. As I said in the paper, branches are generally of mixed character, but in certain high-symmetry directions branches representing a pure type of displacement do occur.

G. CAGLIOTI: Reverting to the matter of the 'flatness' of the internal molecular modes and looking at the dispersion relations for intermolecular modes which you obtained, I wonder whether it would be fair to say that in this system the 'flatness' of the ω versus q dispersion relation for

the higher-frequency optic branches is confined to a range of about two frequency units.

B.M. POWELL: The pure librational intermolecular modes actually show less dispersion than the range you have indicated. In general one would expect the higher-frequency intramolecular modes to show even less dispersion, but I do not know precise values for this.

J.W. WHITE: Have you been able to see any of the higher-energy intramolecular modes? I wonder whether the same intramolecular force law would describe, even qualitatively, the small dispersion which would be expected in their case.

B.M. POWELL: The lowest intramolecular mode frequency is about 10^{13} cps, and I have not looked at frequencies as high as this. I have seen no evidence for these intramolecular modes in the frequency range (up to 3×10^{12} cps) used in the experiment.

G.S. PAWLEY: The results reported in this paper have been used in a least-squares fitting of a model using the 6-exp or Buckingham atom-atom potential function. The nitrogen atom interactions were assumed to be the same as the carbon atom interactions. One feature of the fitting is that the optic mode at zero wave number is consistently too high when the rest of the dispersion curves are well fitted.

SLOW-NEUTRON SCATTERING AND ROTATIONAL FREEDOM OF METHYL GROUPS IN SEVERAL ORGANIC COMPOUNDS

S.B. HERDADE
INSTITUTO DE ENERGIA ATÔMICA,
SÃO PAULO, BRAZIL

Abstract

SLOW-NEUTRON SCATTERING AND ROTATIONAL FREEDOM OF METHYL GROUPS IN SEVERAL ORGANIC COMPOUNDS. The total cross-sections of CH_3NO_2, $(CH_3)_2CO_2$, $(CH_3)_2SO$, $(CH_3CO)_2O$, CH_3CH, $(CH_3)_2SiCl_2$ and dimethyl polysiloxane (silicone oil) have been measured for neutrons with wavelength λ_n in the range 5 - 10 Å. The scattering cross-sections per H atom, σ_s/H, may be approximated by straight lines $\sigma_s/H = a_s + b_s\lambda_n$, for $\lambda_n > 5$ Å. An empirical correlation is observed to exist between the slopes b_s and the barrier heights for internal rotation of CH_3 groups in the molecules, and a calibration curve is plotted using some of the experimentally determined slopes and published values of barrier heights determined by other methods. From the slopes 12.3 ± 0.5 b/Å-H for $(CH_3)_2SiCl_2$, and 12.3 ± 0.3 b/Å-H for dimethyl polysiloxane, it is concluded that the internal rotation of CH_3 groups in these compounds is practically free. An average barrier height of ~ 1 kcal/mole is estimated for $(CH_3CO)_2O$, from the experimentally determined slope 10.8 ± 0.3 b/Å-H.

INTRODUCTION

Total cross-section measurements may be still considered a useful complementary technique to other more advanced methods in the study of the dynamics of hydrogenous groups in molecules by inelastic scattering of slow neutrons [1-4]. For cold neutrons ($E_n \ll 0.025$ eV) the total scattering cross-sections of hydrogenous compounds, as a function of neutron wavelength, can be approximated by straight lines with slopes determined by the inelastic scattering involving an energy gain by the neutrons from the molecules in populated excited states.

The slope of the scattering cross-section per H atom, σ_s/H, of ammonium compounds was found to be a simple function of the barrier for hindered rotation of the NH_4 ion in the crystal [5]. An empirical calibration curve plotted for these compounds has been used to estimate the barrier heights for internal rotation of methylbenzenes [5], on the basis that the CH_3 groups and the NH_4 ion have approximately the same 'effective rotational mass' for neutron scattering.

In the present paper, a new calibration curve is presented for methyl compounds in the range 0 to 3 kcal/mole. This curve is utilized to evaluate the internal rotational freedom of CH_3 groups in acetic anhydride, dimethyl-dichloro-silane, and dimethyl-polysiloxane (silicone oil).

EXPERIMENTAL RESULTS AND DISCUSSION

The total neutron cross-sections of nitromethane, acetone methyl acetate, dimethyl-sulphoxide, acetic anhydride, acetonitrile, dimethyl-dichloro-silane and dimethyl polysiloxane (silicone oil) have been measured

TABLE I. CORRELATION BETWEEN COLD-NEUTRON SCATTERING CROSS-SECTION SLOPES AT ROOM TEMPERATURE (296° K) AND BARRIERS TO INTERNAL ROTATION FOR SEVERAL METHYL COMPOUNDS

Compound	Wavelength range of least-squares fit (Å)	Scattering cross-section slopes (b/Å-H)	Barrier heights from literature (kcal/mole)	Method
CH_3NO_2	6.0 - 8.0	12.9 ± 0.6	0.0063 [9]	μ-wave
$CH_3C \equiv CCH_3$	4.0 - 11.0	12.4 ± 0.3 [3]	< 0.01 [10]	
m-, p- xylene, toluene, mesitylene	4.0 - 11.0	11.4 ± 0.3 [5]	0.190 - 0.540 [11, 12]	Low temperature heat capacity
$(CH_3)_2CO$	7.0 - 10.0	11.6 ± 0.3	0.783 [13]	μ-wave
$(CH_3)_2CO_2$	7.0 - 10.0	10.6 ± 0.4	1.17 [14]	μ-wave
o-xylene	4.0 - 11.0	9.5 ± 0.3 [5]	1.850 [11]	Low temperature heat capacity
$(CH_3)_2SO$	6.0 - 10.0	8.0 ± 0.3	2.9 [15]	μ-wave

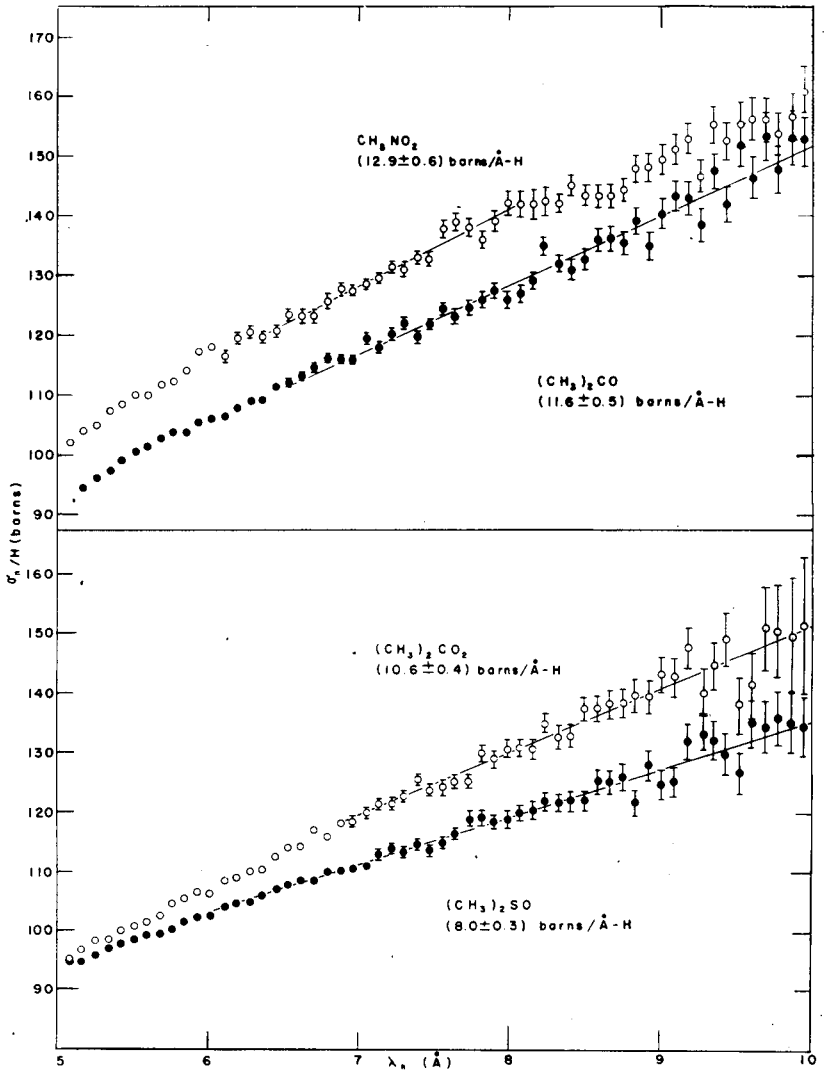

FIG.1. Neutron scattering cross-sections per hydrogen atom of nitromethane, acetone, methyl acetate and dimethyl-sulphoxide in the neutron wavelength range 5 to 10 Å. Slopes were calculated by a weighted least-squares fit to the data. Only statistical errors are indicated.

as a function of neutron wavelength in the range 5 to 10 Å (0.0035 to 0.0008 eV) using a curved slit slow-neutron chopper and time-of-flight spectrometer [6, 7] in operation at the IEA-R1 research reactor. All samples were in the liquid state, at room temperature (296° K) and were contained in aluminium cells such as to present a thickness of 0.25 cm. The number of molecules per square centimetre, n, of each sample has been determined from the measured internal dimensions of the cells and

the density of the liquid at room temperature. The internal dimensions of the cells were checked by measuring the total cross-section of H_2O, and comparing the results with the corresponding data published in the Barn Book [8]. Uncertainties in the n values amount to about 3%.

Scattering cross-sections per H atom, σ_s /H, were calculated by subtracting the absorption cross-section [8] from the total cross-section per molecule and dividing the result by the number of H atoms in the molecule. Results for nitromethane, acetone, methyl acetate and dimethyl-suphoxide are presented in Table I and plotted in Fig. 1. Slopes were calculated by a weighted least-squares fit to the data. Only statistical errors are indicated. Included in Table I are results obtained by Rush et al. [3, 5] for dimethyl-acetylene and methyl-benzenes.

Due to the large incoherent scattering cross-section of hydrogen, Bragg scattering is in general not observed in hydrogenous samples. Nevertheless, the coherent scattering cross-section of nitrogen is appreciable so that, for CH_3NO_2, a liquid diffraction break is observed at about 8.2 Å. This coherent scattering introduces an additional uncertainty in the slope of the scattering cross-section curve. The wavelength range of least-squares fit to the data of CH_3NO_2 (6.0 to 8.0 Å) does not include the Bragg break.

Table II and Fig. 2 present the results for dimethyl-dichloro-silane, dimethyl-polysiloxane, and acetic anhydride.

An empirical correlation may be established between the cross-section slopes and the average barrier heights for internal rotation of the methyl groups in the molecules. Corrections for other low-frequency motions of the molecules in the liquid state would result in a small reduction in the slopes attributed to internal rotation, but these corrections are difficult to estimate. A calibration curve (slopes versus barrier heights) for methyl compounds, using the data from Table I, is presented in Fig. 3. The values for the barriers heights were taken from microwave spectroscopy and low-temperature heat-capacity measurements published in the literature [9-15]. Using this calibration curve and the cross-section slopes obtained for dimethyl-dichloro-silane, dimethyl-polysiloxane (silicone oil), and acetic anhydride, the average barrier heights for internal rotation of methyl groups have been estimated for these compounds and are presented in Table II.

TABLE II. ESTIMATED BARRIER HEIGHTS FOR INTERNAL ROTATION OF CH_3 GROUPS IN DIMETHYL-DICHLORO-SILANE, DIMETHYL-POLYSILOXANE (SILICONE OIL) AND ACETIC ANHYDRIDE

Compound	Wavelength range of least-squares fit (Å)	Scattering cross-section slopes (b/Å-H)	Estimated barrier heights (kcal/mole)
$(CH_3)_2SiCl_2$	6.0 – 10.0	12.3 ± 0.5	~ 0
Dimethyl-polysiloxane	5.0 – 10.0	12.3 ± 0.3	~ 0
$(CH_3CO)_2O$	6.0 – 10.0	10.8 ± 0.3	~ 1

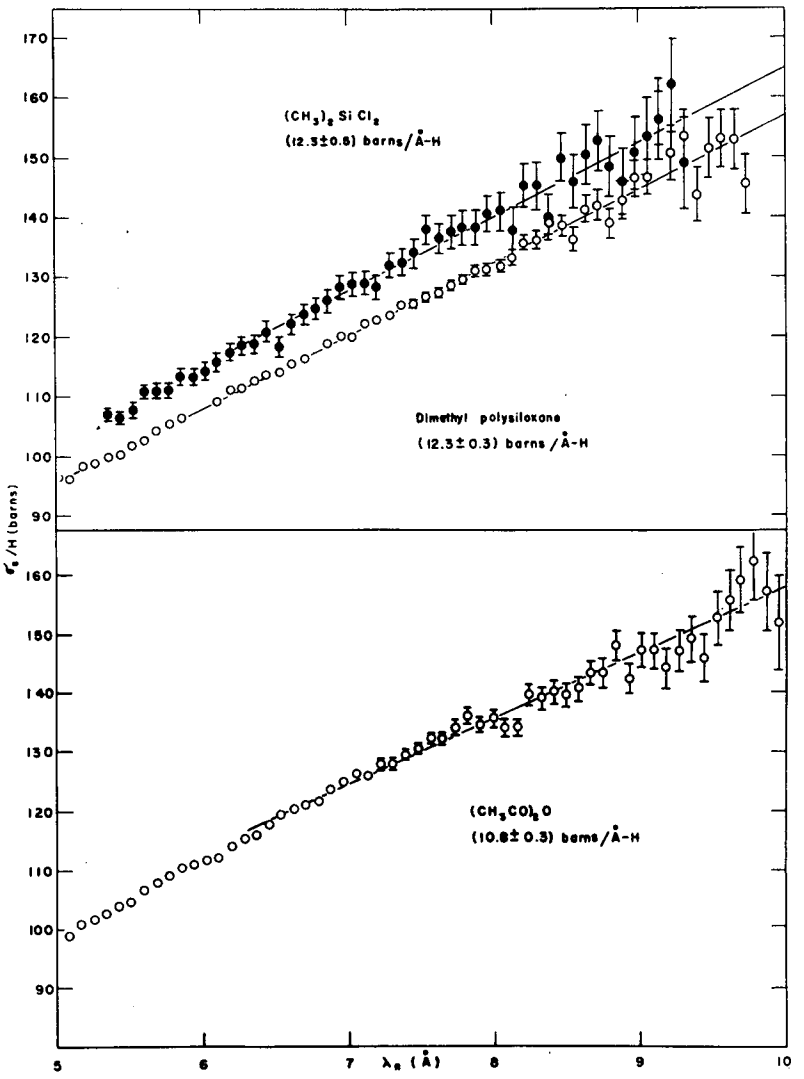

FIG. 2. Neutron-scattering cross-sections per hydrogen atom of dimethyl-dichloro-silane, dimethyl-polysiloxane (silicone oil) and acetic anhydride in the neutron wavelength range 5 to 10 Å. Slopes were calculated by a weighted least-squares fit to the data. Only statistical errors are indicated.

Dimethyl-dichloro-silane is used in the preparation of silicone polymers such as dimethyl-polysiloxane. The internal rotation of methyl groups in these compounds seems to be free, as had already been predicted [16-17].

The average barrier for internal rotation of the CH_3 groups in acetic anhydride has been estimated to be ~ 1 kcal/mole.

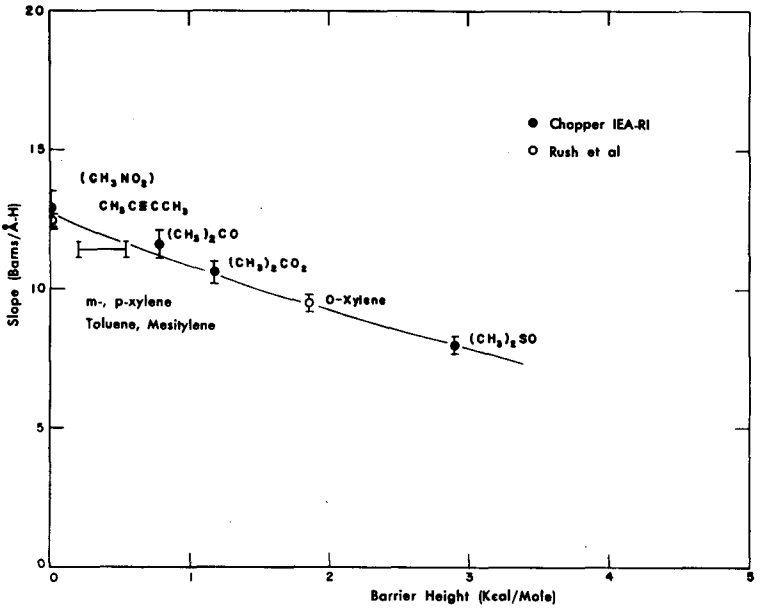

FIG.3. Calibration curve (slopes versus barrier heights) for methyl compounds covering the range from 0 to 3 kcal/mole. Black circles correspond to measurement with the IEA-R1 chopper and time-of-flight spectrometer presented in this paper; open circles and the horizontal bar correspond to measurements by Rush et al. with a crystal spectrometer.

The barrier for internal rotation of the CH_3 group in acetonitrile is expected to be zero. Nevertheless, proton magnetic resonance measurements [18] resulted in a barrier of 2.6 kcal/mole for CH_3CN in the solid state (low temperatures). This barrier has been attributed to intermolecular forces within the crystal.

The neutron scattering cross-section σ_s /H versus λ_n, for acetonitrile, is presented in Fig. 4 as measured in the liquid state at room temperature. The slope 12.6 ± 0.3 b/Å-H corresponds to a free rotation of the CH_3 group, probably indicating that the influence of intermolecular forces is negligible for this compound in the liquid state.

As all substances in this paper can be considered as non-associated liquids, this last comment may be also extended to them.

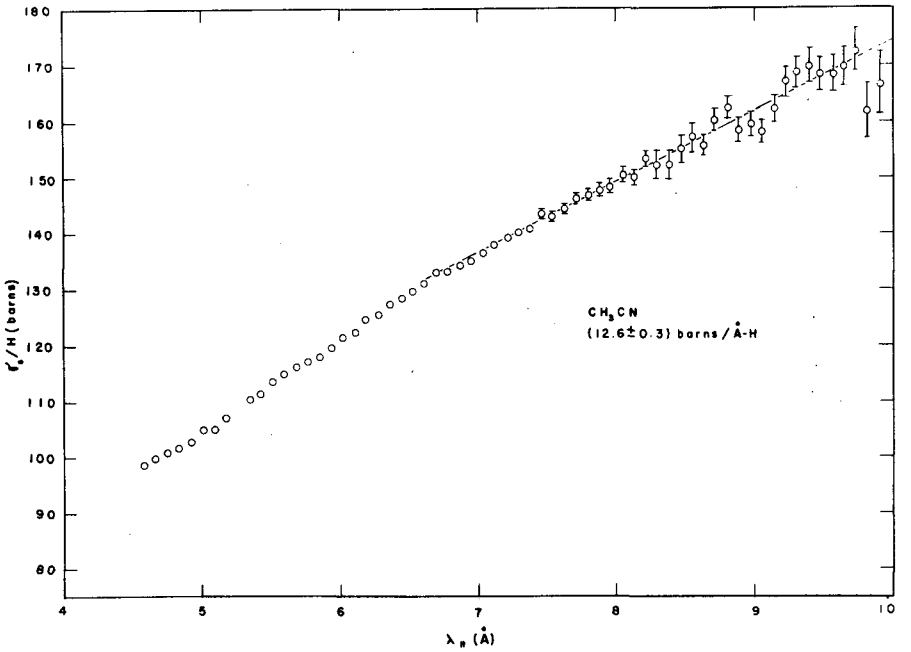

FIG.4. Neutron-scattering cross-section per hydrogen atom of acetonitrile in the neutron wavelength range 4 to 10 Å. Cross-section slope for $\lambda_n > 6.5$ Å has been determined by a weighted least-squares fit to the data. Only statistical errors are indicated.

REFERENCES

[1] RUSH, J.J., TAYLOR, T.I., J. phys. Chem. 68 (1964) 2534.
[2] JANIK, J.M., Inelastic Scattering of Neutrons (Proc. Symp. Bombay, 1964) 2, IAEA, Vienna (1965) 262.
[3] RUSH, J.J., HAMILTON, W.C., Inorg. Chem. 5 (1966) 2238.
[4] RUSH, J.J., LEUNG, P.S., TAYLOR, T.I., J. chem. Phys. 45 (1966) 1312.
[5] RUSH, J.J., TAYLOR, T.I., HAVENS, W.W., J. chem. Phys. 37 (1962) 234.
[6] HERDADE, S.B., AMARAL, L.Q., RODRIGUEZ, C., VINHAS, L.A., Rep. IEA-136 (1967).
[7] AMARAL, L.Q., VINHAS, L.A., RODRIGUEZ, C., HERDADE, S.B., Nucl. Instrum. Meth. (to be published).
[8] HUGHES, D.J., SCHWARTZ, R.B., Neutron Cross Sections, Rep. NBL-325 (1958) 2nd ed.
[9] TANNENBAUM, G., MYERS, R.J. GWINN, W.D., J. chem. Phys. 25 (1956) 42.
[10] LOWE, J.P., PARR, R.G., J. chem. Phys. 44 (1966) 3001, Table I.
[11] WULF, C.A., J. chem. Phys. 39 (1963) 1227.
[12] SIMPSON, K.O., BEYNON, E.T., J. phys. Chem. 71 (1967) 2796.
[13] SWALEN, J.D., COSTAIN, C.C., J. chem. Phys. 31 (1959) 1562.
[14] WILSON, E.B., "The problem of barriers to internal rotation in molecules", Advances in Chemical Physics 2, Interscience Publishers, New York (1959).
[15] DREIZLER, H., DENDL, G., Z. Naturf. Tl a 20 11 (1965) 1431.
[16] ROCHOW, E.G., "Silicones", Modern Chemistry for the Engineer and Scientist (ROBERTSON, G.R., Ed.), McGraw-Hill (1957).
[17] ROCHOW, E.G., Le CLAIR, H.G., J. inorg. nucl. Chem. 1 (1955) 92.
[18] STEJSKAL, E.O., WOESSNER, D.E., FARRAR, T.C., GUTOWSKY, H.S., J. chem. Phys. 31 (1959) 55.

DISCUSSION

J.J. RUSH: I have one or two comments on this paper. First of all, it should be pointed out that such a correlation of cross-section slopes versus rotation barrier is only reasonable if the barrier shapes are the same in each case. The cross-section variations are dependent, not directly on the barriers, but on the energy states below the barrier available for energy-gain scattering by the cold neutrons. There is also, as Mr. Herdade said, a contribution from whole-molecule motions.

Secondly, I would like to mention that since I completed my own total cross-section work at Columbia, Leung and Taylor have extended these measurements to a systematic study of cross-sections versus temperature. Their results also show an excellent empirical correlation with the freedom of rotation of ammonium ions and methyl groups. In view of this, Leung, Taylor and myself have performed some simple cross-section computations in an attempt to put this crude but somewhat useful method on a semi-quantitative basis. We have assumed a harmonic oscillator model for the torsional oscillation and optical translational modes, and a Debye spectrum for the acoustic modes; we have used data on a series of ammonium salts and methyl-substituted crystals for neutron and i.r. data. In almost every case we are able to reproduce the temperature and wavelength dependence of the cross-section to within 10-15%.

T. SPRINGER: I understood Mr. Rush to say that a theoretical correlation was established between the scattering cross-sections and the barrier heights: was this done assuming a cosine-shaped angular dependent potential for the hindered rotations, this potential directly connecting the torsional frequency with the barrier height?

J.J. RUSH: Perhaps I did not make myself quite clear. In our cross-section calculations we did not use rotational barriers; we assumed single frequencies for the torsional and translational modes and calculated cross-sections using the peak energies assigned from neutron and i.r. spectra. I don't believe that a more sophisticated approach is justified for fitting such integral data on relatively complex solids.

COHERENT INELASTIC NEUTRON SCATTERING BY MOLECULAR GASES

Measurements on C_2F_6 and rotation-vibration coupling calculations for CD_4*

J.M. CARPENTER** AND N.A. LURIE
DEPARTMENT OF NUCLEAR ENGINEERING,
UNIVERSITY OF MICHIGAN,
ANN ARBOR, MICH., UNITED STATES OF AMERICA

Abstract

COHERENT INELASTIC NEUTRON SCATTERING BY MOLECULAR GASES: MEASUREMENTS ON C_2F_6 AND ROTATION-VIBRATION COUPLING CALCULATIONS FOR CD_4. Two investigations of neutron scattering by molecular gases are presented. In the first measurements of the scattering law for room temperature hexafluoroethane (C_2F_6) gas, performed at the MTR velocity selector, are reported, as obtained for scattering angles between 4.8° and 90°. The scattering law shows several inelastic scattering maxima of small amplitude. One at approximately 11 meV is interpreted as due to energy transfer with the internal torsional vibrational mode previously unobserved due to both Raman and infrared inactivity. This is to be compared with 8 meV which has been reported from analysis of specific heat data for liquid and solid C_2F_6, and about 12 meV inferred from vibrational relaxation measurements. Another, less well-defined, at 27 meV is thought to correspond to the doubly-degenerate infrared-active rocking mode. Another band centred at approximately 17 meV is possibly due to two-quantum process involving several vibrational modes.

The zeroth Placzek moment (diffraction pattern) is extracted from the data – it substantiates the staggered structure determined by other techniques. The first and second Placzek moments are computed from the data. Measured half widths are extracted from the data and show what appears to be a de Gennes narrowing. Multiple scattering effects are evident even though the target transmission was quite high (95%).

The second investigation is a theoretical study. The scattering law for slow neutron scattering by molecular gases is considered for processes in which one vibrational quantum is exchanged. Formulas are derived using the technique of invariant imbedding and without the usual approximation of separating the intermediate scattering function for rotational and vibrational motions. These formulas permit rigorous quantum mechanical calculation of the scattering law for both spherical and diatomic molecules, for both coherent and incoherent scattering. Calculations for CD_4 gas are presented and compared to the calculations and experiments of West, Brugger and Griffing. The effect of the separation of rotational and vibrational scattering functions is discussed.

The present paper deals with two aspects of the coherent inelastic scattering of neutrons by molecular gases. The first part describes experiments performed at the MTR velocity selector, in which the inelastic scattering cross-section for hexafluoroethane (C_2F_6) was measured. The second part describes related calculations of the effects of molecular rotation on the cross-section of deuteromethane (CD_4) for processes in which one quantum of energy is exchanged with an internal vibrational mode.

* Work supported in part by the US National Science Foundation and by the US Atomic Energy Commission.
** Address at the time of the experimental portion of this work, Phillips Petroleum Co., Idaho Falls, Idaho.
† US Atomic Energy Commission Predoctoral Fellow.

HEXAFLUOROETHANE

Several features of the scattering from gaseous C_2F_6 are of interest. Due to the fact that selection rules prevent its observation by either infrared-absorption or Raman scattering methods, the frequency of the internal torsional vibration has not been directly determined. Frequencies of internal torsional oscillation appear to be of interest from the standpoint of better understanding forces between unbonded atoms in molecules. The effects of the coherent scattering on the quasi-elastic (rigid-molecule) scattering and the vibrationally-inelastic scattering, although understood in principle, are of interest because of the difficulty of calculating the cross-sections. The use of the method of neutron inelastic scattering to investigate molecular motions requires refinement of present calculational methods and, it is hoped, the development of useful approximations.

Measurements of the cross-section for gaseous ethane (C_2H_6) by Straker [1] and by Strong and Brugger [2] have shown the torsional frequency in that molecule to be 33 meV, which is in good agreement with the results of other methods of measurement. C_2F_6 has received less attention than C_2H_6. However, the frequencies of all internal vibrations have been directly measured [3-5] except the torsional frequency [6]. These are given in Table I, as

TABLE I. NORMAL MODES OF C_2F_6[a]

Species	Notation	Frequency		Degeneracy	Activity[b]
		cm^{-1}	meV		
A_{1g}	$\bar{\nu}_1$	1417	178	1	R
A_{1g}	$\bar{\nu}_2$	808	101	1	R
A_{1g}	$\bar{\nu}_3$	348	43.5	1	R
A_{1u}	$\bar{\nu}_4$	89	11	1	Inactive
A_{2u}	$\bar{\nu}_5$	1117	139.5	1	I
A_{2u}	$\bar{\nu}_6$	714	89.3	1	I
E_g	$\bar{\nu}_7$	1250	156.3	2	R
E_g	$\bar{\nu}_8$	619	77.4	2	R
E_g	$\bar{\nu}_9$	372	46.5	2	R
E_u	$\bar{\nu}_{10}$	1251	156.3	2	I
E_u	$\bar{\nu}_{11}$	523	65.4	2	I
E_u	$\bar{\nu}_{12}$	216	27	2	I

[a] Data from Ref. [5], except for the torsional frequency ν_4 which is the result of the present work.
[b] I = infrared, R = Raman.

TABLE II. INTERATOMIC DISTANCES IN C_2F_6[a]

C-F	1.33 Å
C-C	1.51 Å
F...F	2.16 Å
C...F	2.34 Å
F...F gauche	2.76 Å
F...F trans	3.49 Å
∢ CCF	108°

[a] Data from Ref. [11].

taken from Ref. [5]. While early specific heat data [7,8] from the solid and liquid gave a barrier height against internal torsion which can easily be interpreted to yield a torsional oscillation frequency of 8.5 meV, it is felt [9] that condensed-phase data are not necessarily applicable to the molecule in the gas phase.

A value of approximately 100 cm^{-1} (12.4 meV) for the frequency of torsional oscillation has been inferred from vibrational relaxation measurements [10] on C_2F_6 gas.

C_2F_6 is structurally similar to ethane [11,12] and consists of two fully-fluorinated methyl groups, CF_3, connected by a single carbon bond. The methyl groups are oriented in a staggered configuration. Table II gives interatomic distances for the various types of atom-pairs in the molecule. The torsional oscillation consists of rotations of the CF_3 groups relative to one another, about the carbon bond.

Using a carbon mass of 12 amu and a fluorine mass of 19 amu, the moments of inertia calculated from the data of Table II are

$$I_A = I_B = 273.2 \text{ amu Å}^2$$

$$I_C = 179.2 \text{ amu Å}^2$$

The Sachs-Teller effective rotational-translational masses of carbon and fluorine on C_2F_6 are respectively

$$M_C = 114.8 \text{ amu}$$

$$M_F = 63.8 \text{ amu}$$

while the molecular mass M = 138 amu. The scattering from both carbon and fluorine is totally coherent, with cross-sections from BNL-325,

$$\sigma^C = 5.5 \text{ b}$$

$$\sigma^F = 4.0 \text{ b}$$

both scattering lengths having the same sign.

EXPERIMENTAL INFORMATION

Measurements of the cross-section of C_2F_6 were performed at the MTR velocity selector [13]. The target material was originally supplied by the DuPont Company and kindly transmitted to us by Dr. Charles E. Hathaway of the University of Oklahoma. Infrared and mass spectrograms indicated that the sample was of extremely high purity, containing less than 0.01% of both C_2HF_5 and CF_3CF_2Cl. About 0.1% air was evident, probably introduced when the sample was transferred to the mass spectrometer.

Two sets of data were accumulated. In the first, 15 banks of $^{10}BF_3$ detectors were used at scattering angles between 15° and 105°. A He atmosphere [14] was maintained around the target and in the scattered flight paths. The incident neutron energy was 20.1 meV with an elastic-scattering resolution of 1.1 meV FWHM. The target was held in an aluminium cylinder of 2.00-in. diameter, 5.5 in. high, with 0.020-in. walls. The cylinder axis was perpendicular to the scattering plane. An evacuated dummy was used during background counting. At the target pressure of 131 lb/in^2 abs and temperature, 302°K, the average target area density for the 1.4-in. wide beam, was computed from the target mass to be 10.6×10^{20} molecules/cm^2. The measured target transmission for the incident energy was 95 ± 1% which corresponds roughly to the attenuation computed assuming elastic scattering and using the data of Table II, 37.7 b/molecule. (Neglecting interference scattering gives 35.0 b/molecule.)

In the second set of measurements, two banks of He^3 detectors were used at scattering angles of 4.8° and 8.2°, in an evacuated flight path [2]. The target container was essentially identical to that used in the first series except that 0.020-in. cadmium discs were included at 1-in. vertical intervals to reduce multiple scattering [2]. Measurements were made at incident energies of 39.6 and 50.0 meV, with elastic-scattering resolution of 1.9 and 2.7 meV FWHM respectively.

Only the data at 50.0 meV and 8.2° are discussed below: the inelastic-scattering amplitude was too low and the background too high to allow the inelastic scattering to appear clearly for the other conditions.

The more complete information, presented below in the form of the scattering law, was derived from the first set of data. The most distinct indication of the torsional oscillation frequency was obtained in the second set of measurements. We discuss first the results of the 'large angle' data, that is, the first set, then the small-angle information.

DATA TREATMENT

After background subtraction the data, which were proportional to $\partial^2\sigma/\partial\Omega\partial\lambda$, the differential cross-section per unit scattered-neutron wavelength λ, were reduced to the symmetric form of the scattering law

$$\frac{\partial^2\sigma}{\partial\Omega\,\partial\lambda} = \frac{\partial^2\sigma}{\partial\Omega\partial\epsilon}\left|\frac{\partial\epsilon}{\partial\lambda}\right| = \frac{k}{k_0}\, e^{\frac{-\beta\epsilon}{2}} S(\kappa,\epsilon)\left|\frac{\partial\epsilon}{\partial\lambda}\right| \qquad (1)$$

Here, ϵ is the neutron energy gain, $\hbar\kappa$ is the momentum transfer and $|\partial\epsilon/\partial\lambda|$ is the Jacobian transforming between energy and wavelength. The cross-section and thus the scattering law were normalized using

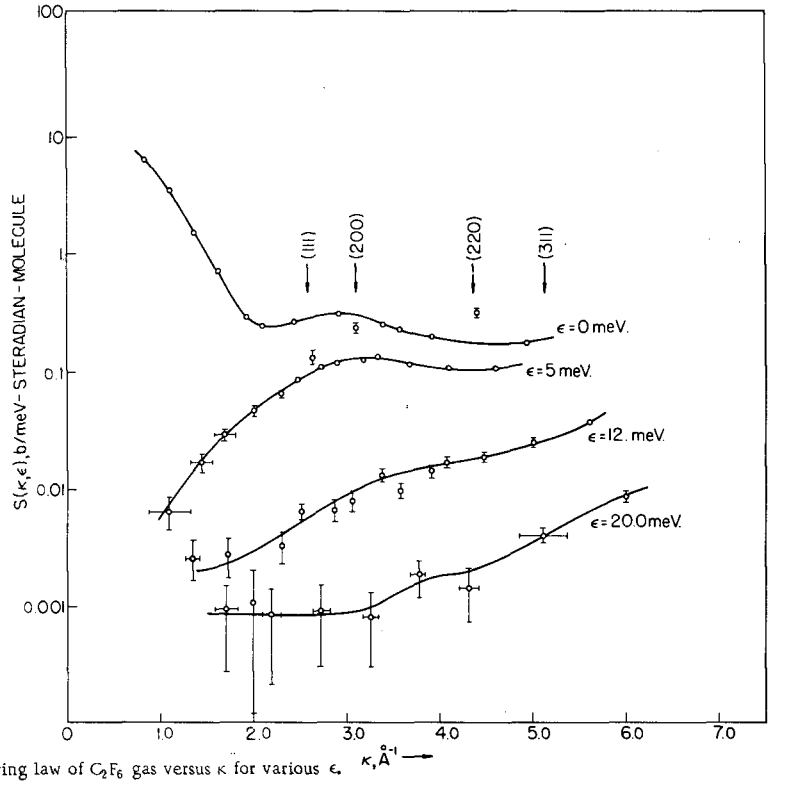

FIG. 1. Scattering law of C_2F_6 gas versus κ for various ϵ.

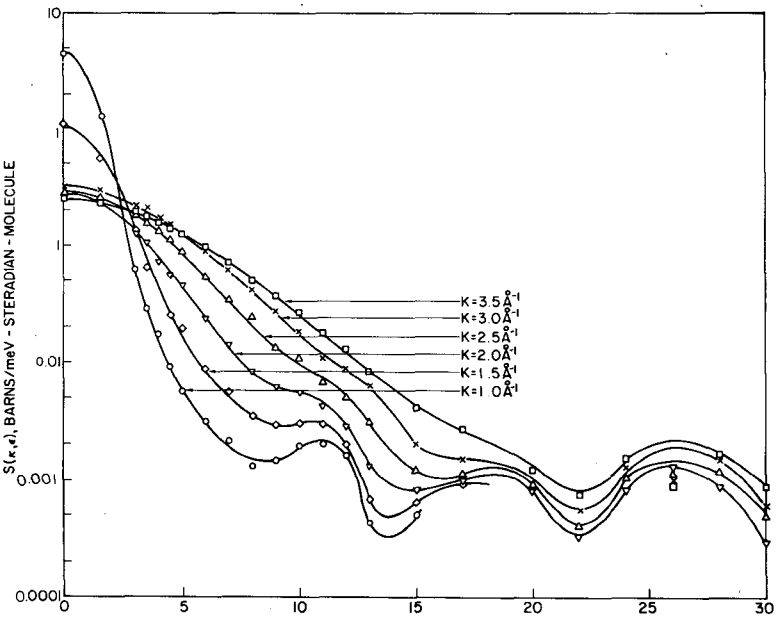

FIG. 2. Scattering law of C_2F_6 gas versus ϵ for various κ.

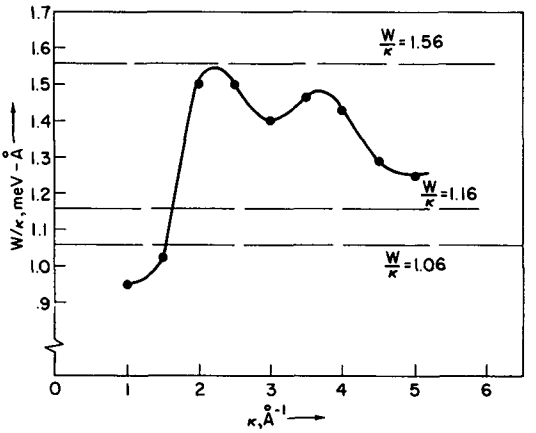

FIG. 3a. Half-width at half maximum of the quasi-elastic peak of C_2F_6 gas.

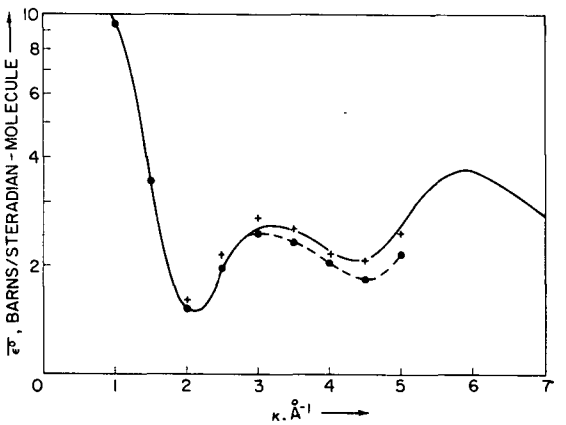

FIG. 3b. Zeroth Placzek moment (diffraction pattern) of C_2F_6 gas. Solid line, exact calculation without Debye-Waller factors; crosses, data moment; solid points, approximate moment Eq. (6).

the known target area density and detector efficiency, and the measured beam monitor counting rate, to give the result in barns/molecule. The scattering law was then plotted against κ for some thirty values of the energy transfer from 0 to 35 meV. Figure 1 shows the symmetric scattering law for a few values of the energy transfer. Error bars reflect statistical errors only.

On the curve for $\epsilon = 0$ arrows designate the expected locations of elastic scattering peaks due to the aluminium target holder. Smooth curves through these data were drawn by hand, averaging several sets for neighbouring values of ϵ in the range of larger energy transfers where this procedure led to improved statistical accuracy. The scattering law was then replotted against ϵ for various values of κ, as shown in Fig. 2, using points read from the smooth curves of $S(\kappa, \epsilon)$ versus κ. No error flags are appended to these curves since these are difficult to estimate. It is felt that the presentation of S versus ϵ for fixed κ's is more appropriate for the present purposes than that of S versus κ for fixed ϵ's.

DISCUSSION

Several features of the scattering from C_2F_6 are of note from Figs 1 and 2. The influence of interference scattering is plainly evident, as a modulating effect on the scattering law for all energy transfers. The energy-transfer width of the 'quasi-elastic' peak, which is due to translational and rotational motions of the molecule, is seen to increase with increasing momentum transfer. Several maxima appear in Fig. 2 for energy transfers of 11, 16-20, and 26 meV, which become unresolved at the larger momentum transfers due to translational-rotational broadening. These features are now discussed in greater detail.

The elastic peak width, presented as the half width at half maximum, W, divided by κ, is shown in Fig. 3a, plotted against κ. In the sense of an effective-mass calculation, as that of Krieger and Nelkin [15] or McMurry [16], the scattering law should be the sum of several Gaussians with widths W given by

$$W = [(4 \ln 2)\ (\hbar^2\kappa^2/2M_{eff}\ \beta)]^{\frac{1}{2}} \qquad (2)$$

where $\beta = 1/k_BT$, and M_{eff} is the effective mass of the scatterer. Using the Sachs-Teller masses of C and F given above, two values are obtained from Eq.(2)

$$\begin{aligned} W &= 1.16\ \kappa \text{ for C} \\ &= 1.56\ \kappa \text{ for F} \end{aligned} \qquad (3)$$

where κ is in $Å^{-1}$ and W in meV. Using the molecular mass as the effective mass

$$W = 1.06\ \kappa \qquad (4)$$

Except for the points at $\kappa = 1.0$ and $1.5\ Å^{-1}$, W/κ varies between 1.16 and 1.56 for κ up to $5\ Å^{-1}$. The treatment of molecular rotations by the effective-mass approximation is supposed only to apply for direct scattering; we presume the 'low' points to be due to the influence of interference scattering, although possibly due to hindrance of the free translations. The widths have been corrected for experimental resolution and the plotted points are the square root of the difference between the square of the resolution width and the square of the observed width.

The three lowest Placzek moments [17] of $\exp(\beta\epsilon/2)\ S(\kappa,\epsilon)$ have been derived from the data. These are defined

$$\overline{\epsilon^n} = \begin{cases} 2\int_0^\infty \epsilon^n \cosh\frac{\beta\epsilon}{2}\ S(\kappa,\epsilon)\,d\epsilon & \text{n even} \\ 2\int_0^\infty \epsilon^n \sinh\frac{\beta\epsilon}{2}\ S(\kappa,\epsilon)\,d\epsilon & \text{n odd} \end{cases} \qquad (5)$$

and have been obtained by numerical integration of functions of the form $S(\kappa, \epsilon) = \exp[\text{polynomial in } \epsilon]$ which were fitted to the data so as to give less than about 5% error in the computed integrals.

The moment of order zero, $\overline{\epsilon^0}$, which is the diffraction pattern, is shown in Fig. 3b. Also shown are an approximate calculation, assuming a Gaussian shape,

$$\overline{\epsilon^0} \approx S(\kappa, 0)\ W\ (\pi/\ln 2)^{\frac{1}{2}} \qquad (6)$$

and an exact calculation using the structural data given earlier. Agreement is seen to be excellent between the integral data moment and the exact calculation, which gives us confidence in our normalization (and in the consistency of the BNL-325 cross-sections). Also, the data verify the structure which was determined by electron diffraction [11, 12]. The approximate moment, Eq. (6), is low at larger κ presumably because the large ϵ contributions are not accounted for.

Comparing Figs 3a and 3b, the maxima and minima in the widths W/κ are found approximately at the minima and maxima of $\overline{\epsilon^0}$, thus showing a de Gennes [18] narrowing effect. The 'low' points occur where $\overline{\epsilon^0}$ increases due to constructive interference of waves scattered from all pairs of nuclei.

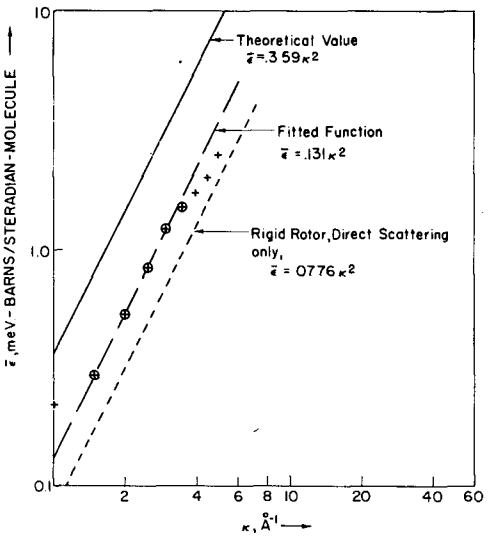

FIG. 4. First Placzek moment of C_2F_6.

The first moment $\bar{\epsilon}$ is shown in Fig. 4. Placzek [18] has found that the interference scattering does not contribute to $\bar{\epsilon}$ so that for the present case using Placzek's results

$$\bar{\epsilon} = \frac{1}{4\pi}\left[2\,\sigma_c/M_c + 6\,\sigma_F/M_F\right]\frac{\hbar^2\kappa^2}{2} \qquad (7)$$

$$= 0.359\,\kappa^2\ \text{b - meV/steradian}$$

where κ is in Å^{-1}. This relationship is shown in Fig. 4 along with the corresponding value computed using the Sachs-Teller masses given earlier, for which

$$\bar{\epsilon} = 0.0776\ \kappa^2 \tag{8}$$

The first moment of the data was fitted in the range $1.5 \leq \kappa \leq 3.5$ to the function

$$\bar{\epsilon} = 0.131\ \kappa^2 \tag{9}$$

which lies between the exact and Sachs-Teller approximate values. At $\kappa = 1$, $\bar{\epsilon}$ is closer to the Placzek value, which may reflect the small importance of vibrationally inelastic scattering for smaller κ, or may be due to the influence of multiple scattering. For $\kappa > 3.5$, the data first moment is lower than the fitted line, perhaps because the integration of the data was truncated beyond 35 meV.

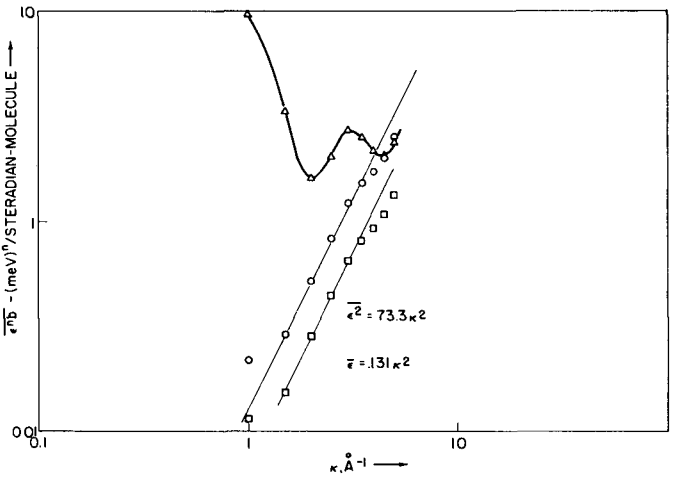

FIG. 5. Zeroth, first and second Placzek moments of C_2F_6 from the data.

The second Placzek moment, computed similarly from the data, is shown in Fig. 5 with the zeroth and first data moments. Placzek's theory indicates that the second moment is of the form

$$\overline{\epsilon^2} = \sum_{s,s'} \frac{\sigma_{ss'}}{4\pi} \left[\frac{h^4 \kappa^4}{4 M_s M_{s'}} \left\langle e^{i\vec{\kappa}\cdot(\vec{b}_s - \vec{b}_{s'})} \right\rangle + \frac{\hbar^2}{M_s M_{s'}} \left\langle e^{i\vec{\kappa}\cdot(\vec{b}_s - \vec{b}_{s'})} \, (\vec{\kappa}\cdot\vec{p}_s)(\vec{\kappa}\cdot\vec{p}_{s'}) \right\rangle \right] \tag{10}$$

where $\langle\ \rangle$ denotes an average over system quantum states, $\vec{p}_s$ is the momentum operator for the s^{th} nucleus, $\vec{b}_s$ is the position operator for the s^{th} nucleus M_s its mass, and $\sigma_{ss'}$ is the cross-section for scattering from the ss' pair. The first term is of order κ^4. In an expansion of

the second term of Eq.(10) the leading term is $\langle(\vec{\kappa}\cdot\vec{p}_s)(\vec{\kappa}\cdot\vec{p}_{s'})\rangle = \frac{1}{3}\kappa^2\langle\vec{p}_s\cdot\vec{p}_{s'}\rangle$ which is of order κ^2, and exhibits no interference effects; the data second moment has been fitted to the function $\overline{\epsilon^2} = 7.33\kappa^2$. The point at $\kappa = 1$, which falls above the fitted function, may be high because of multiple scattering or due to the fact that no resolution-broadening correction was made in these moments. The latter correction is small except at $\kappa = 1$.

The behaviour of $S(\kappa,\epsilon)$ as a function of ϵ for fixed κ, as in Fig. 2, is best discussed with reference to the data of Table I. Modes of frequency $\bar{\nu}_{12}$, 27 meV have been identified in the infrared spectrum, and as one of the frequencies of symmetry species E_μ. We attribute the maximum around 26 meV as due to exchange of one quantum of vibrational energy with these same modes.

The rather broad peak around ϵ = 16 to 20 meV may possibly be due to several effects involving two quanta of energy exchange. It is noted from Table I that $\bar{\nu}_3 - \bar{\nu}_{12} = 16.5$ meV and $\bar{\nu}_9 - \bar{\nu}_{12} = 19.5$ meV so that this peak may represent several two-quantum processes in which, for example, the neutron (gaining energy) de-excites a mode of frequency $\bar{\nu}_3$ and excites a mode of frequency $\bar{\nu}_{12}$. The cross-section for all possible such processes involving $\bar{\nu}_3$, $\bar{\nu}_9$, and $\bar{\nu}_{12}$ has been computed earlier [19]. It is too small to account for the peak by two orders of magnitude. Multiple scattering one-quantum events may possibly be the cause, but the magnitude of this effect has not been computed.

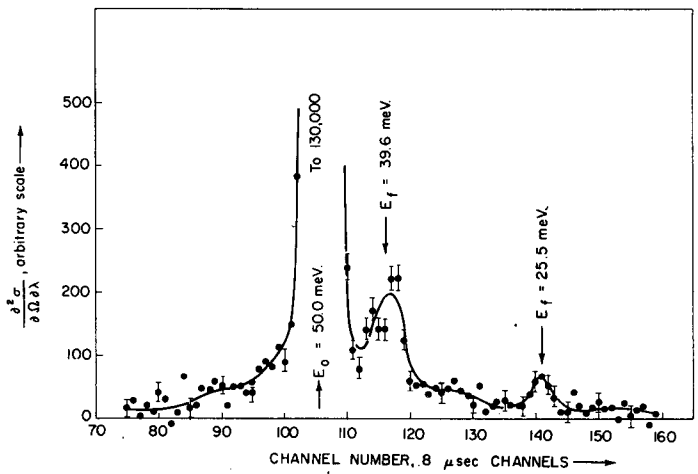

FIG. 6. Cross-section $\partial^2\sigma/\partial\Omega\,\partial\lambda$ of C_2F_6, for incident energy 50.0 meV, scattering angle 8.2°.

The peak at 11 meV is attributed to energy exchange with the torsional oscillation mode, hitherto not directly observed. The cross-section for inelastic scattering, exchanging one quantum with that mode has been calculated [20] and is found to be approximately equal to the area under the 11-meV peak of Fig. 2, although the calculated area is lower by about a factor of 2. This may be due to over-optimistic treatment of the data shown briefly in Fig. 1. The 11-meV torsional frequency corresponds closely with the vibrational relaxation result of reference [10].

That the 11-meV peak cannot be a quantum-rotational peak such as is observed for light molecules has been established by calculations for rigid molecules, approximating the symmetric-top C_2F_6 by a spherical-top [21] having moments of inertia equal to the mean of those of C_2F_6, and a linear molecule [22] of similar moment of inertia. The scattering law appears nearly Gaussian in both cases.

It is noted that the observed scattering law is not well represented by a Gaussian in its wings, but appears too broad, probably due to multiple scattering in this rather thin target.

In Fig. 6 the results of the small-angle scattering experiment are given for incident energy 50.0 meV and scattering angle 8.2°. The data are presented as the cross-section per unit scattered neutron wavelength. No absolute normalization was possible in this case, and only an approximate background subtraction was made, the background having been determined from the data at channels corresponding to very large energy transfers. A prominent peak at a final energy 39.6 meV (energy transfer 10.4 meV) is clearly the same as that found in Fig. 2 at 11 meV. The 26-meV peak of Fig. 2 is found here at final energy 25.5 meV (energy transfer 24.5 meV). The 16-20-meV band is merely suggested, which might be taken to indicate that it was present in the 'large angle' data due to greater multiple scattering in that target, or that it depends quite strongly on momentum transfer κ, which was chosen to be smaller in the small-angle experiments in order to resolve the inelastic peaks better.

ROTATION-VIBRATION COUPLING CALCULATIONS FOR CD_4

In calculations of the scattering law for molecular gases, one must take into account each degree of freedom of the molecule. The usual approach to such calculations is to evaluate the intermediate scattering function for each motion (that is, translation, rotation, vibration) separately. The influence of possible coupling[1] between motions is usually thought to be small and therefore is ignored. In this section of the paper we describe an attempt to explicitly evaluate the scattering law for one-quantum processes without the approximation of separating the intermediate scattering function for rotational and vibrational motions.

EXPRESSION FOR THE SCATTERING LAW

The symmetric scattering law for slow-neutron scattering from a system of molecules is given formally by the well-known Zemach and Glauber formula [23]

$$S(\vec{\kappa},\epsilon) = \frac{1}{2\pi\hbar} e^{\beta\epsilon/2} \int_{-\infty}^{\infty} dt\, e^{-i\epsilon t/\hbar} \sum_{\nu\mu} a_{\nu\mu} \langle \chi_{\nu\mu} \rangle_T \qquad (11)$$

[1] The 'coupling' spoken of here is that which is associated with the neutron interaction, not that in which rotation and vibration are coupled in the molecular Hamiltonian [28].

which describes a scattering event with momentum gain $\hbar\vec{\kappa}$ to the neutron and energy gain ϵ. Here $\beta = 1/k_B T$, and the thermally averaged intermediate scattering function is

$$\langle \chi_{\nu\mu} \rangle_T = \sum_{fi} P_i \langle \psi_i | e^{iHt/\hbar} e^{i\vec{\kappa}\cdot\vec{r}_\nu} | \psi_f \rangle \langle \psi_f | e^{-iHt/\hbar} e^{-i\vec{\kappa}\cdot\vec{r}_\mu} | \psi_i \rangle \tag{12}$$

with $a_{\nu\mu} = A_\nu A_\mu + \delta_{\nu\mu} C_\nu^2$. H is the Hamiltonian of the system, A_ν is the bound coherent scattering length and C_ν is the bound incoherent scattering length of the ν^{th} atom whose position is $\vec{r}_\nu$, and P_i is the Boltzmann factor.

The vector position of the ν^{th} atom can be expressed as

$$\vec{r}_\nu = \vec{R} + \vec{b}_\nu + \vec{u}_\nu \tag{13}$$

where $\vec{R}$ is the position of the centre of mass, $\vec{b}_\nu$ is the equilibrium vector displacement of the ν^{th} atom from the centre of mass, and $\vec{u}_\nu$ is its instantaneous displacement from equilibrium.

Assuming that the Hamiltonian is completely separable we can rewrite Eq. (12) as

$$\langle \chi_{\nu\mu} \rangle_T = \langle \chi_{\nu\mu} \rangle_T^{trans} \langle \chi_{\nu\mu} \rangle_T^{RV} \tag{14}$$

The translational part is well known. The rotation-vibration part cannot be completely separated since all of the operators in $\langle \chi_{\nu\mu} \rangle_T^{RV}$ do not commute. Usually in computations, however, they are completely separated and a thermally averaged intermediate scattering function is evaluated for each motion. Agreement of resulting computations with experiment has previously been taken as evidence that this assumption is not too drastic [24].

If we make the assumption that rotations occur on a time scale that is long compared to vibrations, we can write

$$\langle \chi_{\nu\mu} \rangle_T^{RV} = \langle e^{i\vec{\kappa}\cdot\vec{b}_\nu(t)} \; V_{\nu\mu} \; e^{-i\vec{\kappa}\cdot\vec{b}_\mu} \rangle_T \tag{15}$$

where $\vec{b}_\nu(t)$ is the usual Heisenberg operator and

$$V_{\nu\mu} = \langle e^{iH^\nu t/\hbar} e^{i\vec{\kappa}\cdot\vec{u}_\nu} e^{-iH^\nu t/\hbar} e^{-i\vec{\kappa}\cdot\vec{u}_\mu} \rangle_T \tag{16}$$

Equation (16) can be reduced using a set of normal mode displacements to the Zemach-Glauber result [23]

$$V_{\nu\mu} = \prod_\lambda V_{\nu\mu}^{(\lambda)}$$

where

$$V_{\nu\mu}^{(\lambda)} = \exp\left\{\frac{-\hbar}{4\omega_\lambda}\left[(\vec{\kappa}\cdot\vec{\gamma}_\nu^{(\lambda)})^2 + (\vec{\kappa}\cdot\vec{\gamma}_\mu^{(\lambda)})^2\right]\coth\frac{\hbar\omega_\lambda\beta}{2}\sum_{n=-\infty}^{\infty} e^{in\omega_\lambda t}\, e^{-n\hbar\omega_\lambda\beta/2}\right.$$

$$\left.\times\, I_n\left(\frac{(\vec{\kappa}\cdot\vec{\gamma}_\nu^{(\lambda)})(\vec{\kappa}\cdot\vec{\gamma}_\mu^{(\lambda)})\hbar}{2\omega_\lambda\sinh(\hbar\omega_\lambda\beta/2)}\right)\right\} \tag{17}$$

and where $I_n(X)$ is the modified Bessel function, and $\vec{\gamma}_\nu^{(\lambda)}$ is the mass weighted amplitude for the ν^{th} nucleus in the λ^{th} normal mode. In approximation we keep only the first term in the small argument power series expansion of the Bessel function, and we replace the Debye-Waller factor by unity. Including terms up to one-quantum and ignoring all terms involving products of excited states the vibrational factor becomes

$$V_{\nu\mu} = 1 + \sum_\lambda Z^2(\vec{\kappa}\cdot\vec{\gamma}_\nu^{(\lambda)})(\vec{\kappa}\cdot\vec{\gamma}_\mu^{(\lambda)}) \tag{18}$$

where

$$Z_\lambda^2 = \left(\hbar/4\omega_\lambda\sinh\frac{\beta\hbar\omega_\lambda}{2}\right)\exp(i\omega_\lambda t - \hbar\omega_\lambda\beta/2)$$

If this expression were inserted into the thermal average (Eq.(15)), and the whole thing evaluated directly, we would have an essentially exact result

$$\langle\chi_{\nu\mu}\rangle_T^{RV} = \langle e^{i\vec{\kappa}\cdot\vec{b}_\nu(t)}\; e^{-i\vec{\kappa}\cdot\vec{b}_\mu}\rangle_T + \sum_\lambda\langle e^{i\vec{\kappa}\cdot\vec{b}_\nu(t)} Z_\lambda^2(\vec{\kappa}\cdot\vec{\gamma}_\nu^{(\lambda)})(\vec{\kappa}\cdot\vec{\gamma}_\mu^{(\lambda)})\, e^{-i\vec{\kappa}\cdot\vec{b}_\mu}\rangle_T \tag{19}$$

Using the technique of imbedding invariant parameters [20], the one-quantum terms have the form

$$\frac{\partial^2}{\partial\alpha\,\partial\alpha'}\langle e^{i\vec{\kappa}\cdot\vec{d}_\nu(t)}\; e^{-i\vec{\kappa}\cdot\vec{d}_\mu}\rangle_T\Big|_{\alpha=\alpha'=0} \tag{20}$$

where $\vec{d}_\nu(t) = \vec{b}_\nu(t) + \alpha Z\vec{\gamma}_\nu^{(\lambda)}$. The thermal averages in Eq.(20) above clearly have the same form as in the rigid rotor problem and therefore can be evaluated exactly [25].

We shall examine the case of the spherical molecule and give the result for the other class of molecules for which rigorous calculations are feasible, namely the linear molecule. Using the well-known matrix elements for the spherical molecule, Eq.(20) can be evaluated and the one-quantum part of the rotation-vibration intermediate function becomes

$$\langle\chi_{\nu\mu}\rangle_T^{'g} = \exp\{-it\hbar\kappa^2/2M - t^2\kappa^2/2M\beta\}\sum_{JJ'} P_J$$

$$\times\,(2J+1)(2J'+1)\, e^{it(E_J - E_{J'})/\hbar}\sum_{\ell\lambda} Z^2 Q_{\nu\mu}^{\lambda}(\kappa,\ell) \tag{21}$$

where

$$Z^2 Q^{\lambda}_{\nu\mu}(\kappa, \ell) = \frac{\partial^2}{\partial\alpha\partial\alpha'} \{j_\ell(\kappa b_\nu)\, j_\ell(\kappa b_\mu)\, P_\ell(\vec{\hat{d}}_\nu \cdot \vec{\hat{d}}_\mu)\}_{\alpha=\alpha'=0} \tag{22}$$

an explicit expression for Q is given in the Appendix.

After Fourier transformation, the one-quantum scattering law for spherical molecules is

$$S'(\vec{\kappa}, \epsilon) = \sqrt{\frac{\beta}{4\pi E_R}}\, \frac{1}{N}\, e^{\beta\epsilon/2} \sum_{\nu\mu} a_{\nu\mu} \sum_{JJ'} P_J\, (2J+1)\, (2J'+1)$$

$$\times \sum_{\lambda} \frac{\exp\{-(\epsilon + E_R - E_J + E_{J'} - \hbar\omega_\lambda)^2 \beta / 4E_R\}}{4\omega_\lambda \sinh \hbar\omega_\lambda\beta/2}\, e^{-\beta\hbar\omega_\lambda/2} \sum_{\ell} \hbar Q^{\lambda}_{\nu\mu}(\kappa, \ell) \tag{23}$$

where

$$E_R = \hbar^2 \kappa^2 / 2M$$

For the linear diatomic molecule the result is somewhat simpler since there is only one mode [26] and the displacements are colinear with the bond. The one-quantum part of the scattering law is

$$S'(\vec{\kappa}, \epsilon) = \sqrt{\frac{\beta}{4\pi E_R}}\, \frac{1}{N}\, e^{\beta\epsilon/2} \sum_{\nu\mu} a_{\nu\mu} \sum_{JJ'} P_J\, (2J+1) \frac{\hbar^2\kappa^2}{4\omega\hbar \sinh(\hbar\omega\beta/2)}$$

$$\times (\vec{\hat{b}}_\nu \cdot \vec{\gamma}_\nu)\, (\vec{\hat{b}}_\mu \cdot \vec{\gamma}_\mu) \exp\left\{\frac{-\beta}{4E_R} (\epsilon + E_R - E_J + E_{J'} - \hbar\omega)^2\right\} e^{-\beta\hbar\omega/2}$$

$$\times \sum_{\ell} (2\ell+1)(2\delta_{\nu\mu} - 1)^\ell\, [C^{J\ell J'}_{00}]^2 \left[\frac{\ell j_\ell(\kappa b_\nu)}{\kappa b_\nu} - j_{\ell+1}(\kappa b_\nu)\right]$$

$$\times \left[\frac{\ell j_\ell(\kappa b_\mu)}{\kappa b_\mu} - j_{\ell+1}(\kappa b_\mu)\right] \tag{24}$$

CALCULATIONS FOR CD_4 GAS

Using formula (23) derived above, calculations have been performed for CD_4 gas. Experiments have also been performed for CD_4 [5] and the vibrational motions have been observed to contribute to the scattering law for high energy transfers (above about 72 meV). Although the calculations of Griffing [21] are generally in excellent agreement, there is some disagreement at the energies where vibrations are important.

As pointed out by West, Brugger and Griffing [21], only two frequencies will contribute to the scattering law as measured, the triply degenerate modes of 0.123 eV and the doubly degenerate 0.135 eV modes. Calculations according to Eq.(24) of the scattering law for those energy transfers reported in Ref.[2] above 72 meV are shown in Fig. 7. Also shown are the data and Griffing's calculation from Ref.[21].

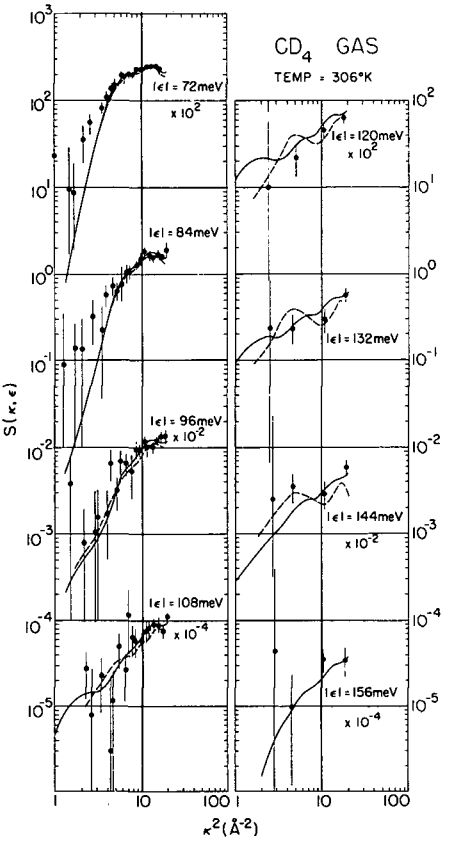

FIG. 7. Scattering law for CD_4 gas. The dashed line and the data are from Ref. [21]. The solid line is the result of the present work.

The present calculation appears to agree somewhat better with the data than Griffing's calculation. Statistical error in the data in this experimentally difficult region makes comparison against the measurements not too meaningful. We note, as stated in Ref.[21], that the disagreement between calculation and experiment at small κ is probably an experimental effect. A minor error exists in Griffing's normalization of the displacements for the triply degenerate modes. This probably affects those calculations at the highest energy transfers so that a direct comparison of the present results with those of Griffing is not meaningful at this time either. Nonetheless we believe that the present theory represents an improvement in the calculation since it properly accounts, to lowest order in κ^2, for the coupling in the interaction between rotational and vibrational motions.

ACKNOWLEDGEMENTS

One of us (JMC) wishes to acknowledge the hospitality of the Phillips Petroleum Company and the Idaho Nuclear Corporation during the course of the C_2F_6 experiments, and to express deep gratitude to the personnel of the Nuclear Technology Branch for their help in all aspects of that work, notably H.L. McMurry, R.M. Brugger, P.D. Randolph, G.W. Griffing and Don Jackson; and for help in certain of the computations W.R. Gavin and Mrs. Eldene Moss. Special thanks are given to Y.D. Harker and W.R. Myers for performing the small-angle experiments. We both wish to thank Mr. Yoon Il Chang, who computed the normal-mode displacements and programmed the CD_4 calculations. We are grateful to Dr. Griffing for supplying us with the numerical results of his CD_4 calculations. Use of the University of Michigan's IBM 7090 is also gratefully acknowledged.

APPENDIX

The expression Q in Eq.(22) evaluated for CD_4 gives the following results

$$Q^{\lambda}_{dd'}(\kappa,\ell) = \frac{j^2_\ell(\kappa b)}{b^2}\{\ell^2 C_1 C_2 P_\ell + (\ell+1)(\ell+2) P_\ell C_5^2 C_8 C_9 + \ell(\ell+1)$$

$$\times [(P_{\ell+1} - C_5 P_\ell)(C_8 C_1 + C_2 C_9) - C_8 C_9 P_\ell]$$

$$+ (\ell+1)[(P_{\ell+1} - C_5 P_\ell)(C_6 - C_1 C_3 - C_2 C_4 - C_5 C_1 C_2)/C_7$$

$$- 2C_5 C_8 C_9 P_{\ell+1}]\} - \frac{j_\ell(\kappa b)\, j_{\ell+1}(\kappa b)}{b}\kappa$$

$$\times \{\ell P_\ell C_1 C_2 + (\ell+1)(P_{\ell+1} - C_5 P_\ell) C_2 C_9\}$$

$$- \frac{j_{\ell+1}(\kappa b)\, j_\ell(\kappa b)}{b}\kappa \{\ell C_1 C_2 P_\ell + (\ell+1)(P_{\ell+1} - C_5 P_\ell) C_1 C_8\}$$

$$+ j^2_{\ell+1}(\kappa b)\kappa^2 C_1 C_2 P_\ell$$

$$Q^{\lambda}_{dd}(\kappa,\ell) = \kappa^2 C_1^2 (\ell j_\ell(\kappa b)/\kappa b - j_{\ell+1}(\kappa b))^2$$

The constants C_1 through C_9 have the following definitions

$$C_1 = (\vec{b}_d \cdot \vec{\gamma}^{(\lambda)}_d) \qquad C_3 = (\vec{b}_d \cdot \vec{\gamma}^{(\lambda)}_{d'})$$

$$C_2 = (\vec{b}_{d'} \cdot \vec{\gamma}^{(\lambda)}_{d'}) \qquad C_4 = (\vec{b}_{d'} \cdot \vec{\gamma}^{(\lambda)}_d)$$

$C_5 = (\vec{b}_d \cdot \vec{b}_{d'})$

$C_6 = (\vec{\gamma}_d^{(\lambda)} \cdot \vec{\gamma}_{d'}^{(\lambda)})$

$C_7 = C_5^2 - 1$

$C_8 = (C_3 - C_5 C_2)/C_7$

$C_9 = (C_4 - C_5 C_1)/C_7$

The arguments for the Legendre polynomials are all C_5. The normal-mode eigenvectors used are those given by Pope [27]. Other parameters used in the calculations are: $b = 1.093 \times 10^{-8}$ cm, $I = 10.66 \times 10^{-40}$ g cm^2, $C_c = 0$, $A_c = 0.664 \times 10^{-12}$ cm, $C_d = -0.399 \times 10^{-12}$ cm, $A_d = 0.677 \times 10^{-12}$ cm.

REFERENCES

[1] STRAKER, E.A., J. chem. Phys. 43 (1965) 4134.
[2] STRONG, K.A., BRUGGER, R.M., J. chem. Phys. 47 (1967) 421.
[3] RANK, D.H., PACE, E.L., J. chem. Phys. 15 (1947) 396.
[4] NIELSON, J. R., RICHARDS, C.M., McMURRY, H.L., J. chem. Phys. 16 (1948) 67.
[5] CARNEY, R., PIOTROWSKY, E.A., MEISTER, A.G., BRAUN, J.H., CLEVELAND, F.F., J. molec. Spectros. 7 (1961) 209.
[6] BUCKER, H.P., NIELSON, J. Rud, J. molec. Spectros. 11 (1963) 243.
[7] PACE, E.L., ASTON, J.G., J. Am. chem. Soc. 70 (1948) 566.
[8] MANN, D.E., PLYLER, E.K., J. chem. Phys. 21 (1953) 1116.
[9] LOWE, J.P., private communication (1966).
[10] LAMBERT, J.D., SALTER, R., Proc. R. Soc. Ser. A 253 (1959) 277.
[11] BRANDT, J.L., LIVINGSTON, R.L., J. Am. chem. Soc. 76 (1953) 2096.
[12] SWICK, D.A., KARLE, I.L., J. chem. Phys. 23 (1955) 1499.
[13] BRUGGER, R.M., EVANS, J.E., Nucl. Instrum. Meth. 12 (1961) 75.
[14] BRUGGER, R.M., Nucl. Instrum. Meth. 32 (1964) 303.
[15] KRIEGER, T.J., NELKIN, M.S., Phys. Rev. 106 (1957) 290.
[16] McMURRY, H.L., Nucl. Sci. Engng 15 (1963) 429.
[17] PLACZEK, G., Phys. Rev. 86 (1952) 377.
[18] DeGENNES, R.G., Physica 25 (1959) 825.
[19] CARPENTER, J.M., SCHAEFER, R.A., Neutron Thermalization and Reactor Spectra (Proc. Symp. Ann Arbor, 1967) 1, IAEA, Vienna (1968) 293.
[20] CARPENTER, J.M., J. chem. Phys. 46 (1967) 465.
[21] WEST, R.E., BRUGGER, R.M., GRIFFING, G.W., Phys. Rev. 148 (1966) 163.
[22] LURIE, N.A., J. chem. Phys. 46 (1967) 352.
[23] ZEMACH, A.C., GLAUBER, R.J., Phys. Rev. 101 (1956) 118.
[24] JANIK, J.A., KOWALSKA, A., Thermal Neutron Scattering, (EGELSTAFF, P.A., Ed.) Academic Press, New York (1965).
[25] RAHMAN, A., J. nucl. Energy 13 (1961) 128.
[26] YOUNG, J.A., KOPPEL, J.U., Phys. Rev. 135 (1964) A603.
[27] POPE, N.K., Can. J. Phys. 30 (1952) 597.
[28] BUZANO, C., DeMICHELIS, F., RASETTI, M., Phys. Rev. 167 (1968) 97.

DISCUSSION

O.J. EDER: Could you please comment on the kind of rotational spectrum which you expect from a vibrational-rotational transition?

J.M. CARPENTER: We have looked at the spectrum for the one-quantum processes, as broadened by the rotational motion, and it appears similar to the spectrum for scattering by a rigid molecule, exhibiting the same sort of rotational sideband at small momentum transfers.

O.J. EDER: Did you do any calculations on translation-rotation interaction?

J.M. CARPENTER: No, the treatment applies to the dilute, freely-translating gas. Of course, with this assumption, centre-of-mass translational motion is independent of rotational motion and the translational intermediate scattering function is rigorously separable.

G.S. PAWLEY: Can you explain in greater detail the process of "collision narrowing"?

J.M. CARPENTER: It is really very difficult to discuss this matter on a theoretical basis at the present stage in our investigations. However, it seems more or less satisfactory to think of the phenomenon as a process in which molecules in the vicinity of the one with which the neutron is colliding form with that molecule a larger system, so that the scattering is no longer associated with a single molecule and the shape of the cross-section is altered. Under certain conditions, the effect is to narrow the line. I emphasize that our conclusion as to the reason for the line narrowing is tentative, pending verificatory calculations.

THE MOLECULAR DYNAMICS OF METHANE IN ARGON*

O.J. EDER
PHYSICS INSTITUTE,
REACTOR CENTRE SEIBERSDORF, AUSTRIA,
AND
P.A. EGELSTAFF
SOLID STATE PHYSICS DIVISION,
ATOMIC ENERGY RESEARCH ESTABLISHMENT,
HARWELL, DIDCOT, BERKS., ENGLAND

Abstract

THE MOLECULAR DYNAMICS OF METHANE IN ARGON. The inelastic and quasi-elastic scattering of 5.3 Å neutrons has been studied for the system methane in argon at 86°K. The experimental data have been taken for two concentrations (1.6 and 3.2 molar %) and six scattering angles. A discussion of the changes in the scattering pattern as compared to scattering experiments on pure methane performed under comparable conditions is presented.

A comparison with our experimental data is made, using a new approach for the rotational motion of the methane molecules. We assume that the methane molecules rotate nearly freely at short times and undergo rotational diffusion at long times, while discussing the centre-of-mass motion in terms of a modified 'itinerant oscillator model'. The data are consistent with the view that the argon atoms form a 'cage' around the methane molecules in which the rotation is continuously but weakly hindered and where the long-time translational motion can be described by simple diffusion, but for the short-time behaviour some new approach is needed.

1. INTRODUCTION

Recent investigations of hydrogen in argon and neon [1] have provided evidence of a rather broad localized frequency spectrum and a strong broadening of the quasi-elastic peak not typical for argon, but caused by the specific dynamical properties of hydrogen in argon.

We now chose to investigate methane in argon and compare the results with those obtained for pure liquid methane, again taking advantage of the almost only incoherently scattering methane molecules and the large differences in the scattering cross-sections of methane and argon. In the case of hydrogen in argon there is a region between the quasi-elastic peak and the ortho-para peak ($E_{rot}(J = 1) = 14.7$ meV) where we could see the centre-of-mass motion of the hydrogen molecules well separated from its rotational motion. As we shall see in section 2, this is no longer true for CH_4 in argon, due to the much smaller separation of the rotational levels ($E_{rot}(J = 1) = 1.3$ meV) caused by the small rotational constant of methane. The question of how methane molecules behave in the solid and liquid state, or as a solvent in different host lattices has been investigated by infrared, Raman spectroscopy [2-8] and neutron scattering techniques [9-12].

In section 2 we will discuss several models for the rotational and translational motion and give the experimental details in section 3. In

* Work performed in the Solid State Physics Division at AERE, Harwell, UK.

section 4 the experimental results are presented together with the conclusions from a comparison of model calculations with the experimental data.

2. THEORY

The general formalism of van Hove [13] extended to molecules gives for the double-differential scattering cross-section of slow neutrons the expression

$$\frac{\partial^2\sigma}{\partial\Omega\partial\omega} = \frac{k'}{k_0}\frac{1}{2\pi}\int dt\ \exp\{-i\omega t\}\left[\sum_{l,\alpha}(a^{\alpha 2}_{l\,coh}+a^{\alpha 2}_{l\,inc})F^{\alpha\alpha}_{ll}(Q,t) + \sum_{l}{}'\sum_{\alpha\beta}{}' a^{\alpha}_{l\,coh}a^{\beta}_{l\,coh}F^{\alpha\beta}_{ll}(Q,t) + \sum_{lm}{}'\sum_{\alpha\beta}{}' a^{\alpha}_{l\,coh}a^{\beta}_{m\,coh}F^{\alpha\beta}_{lm}(Q,t)\right] \quad (1)$$

The dash at the summation sign indicates summation for different indices only, $\vec{k}_0$, $\vec{k}'$ denote incident and scattered neutron wavevectors, $\hbar\omega$ and $\hbar Q$ energy and momentum transfer, $a_{l\nu}$ the scattering length of the γ^{th} nucleus in the l^{th} molecule, and $F(\vec{Q},t)$ the intermediate scattering function.

In Eq.(1) we have neglected spin correlations within a molecule following Zemach and Glauber [14] and Sinha and Venkataraman [15] who showed that these effects are negligible as long as the rotational constants of molecules are small compared to kT.

The three terms in Eq.(1) describe the incoherent scattering of the individual nuclei, the intramolecular coherent scattering and the intermolecular coherent scattering.

One usually defines the first two terms as incoherent molecular scattering and for methane they will give the main contribution to the cross-section

$$\frac{\partial^2\sigma_s}{\partial\omega\partial\Omega} = \frac{k'}{k_0}\frac{1}{2\pi}\int \exp\{-i\omega t\}\sum_{l}\sum_{\alpha\beta}(a^{\alpha}_{l\,coh}a^{\beta}_{l\,coh}) + \delta_{\alpha\beta}\,a^{\alpha 2}_{l\,inc})F^{\alpha\beta}_{ll}(Q,t) \quad (2)$$

If we now collect the scattering of all possible pairs of nuclei in a single methane molecule, we find

$$\frac{\partial^2\sigma_s}{\partial\Omega\partial\omega} = \frac{k'}{k_0}\frac{1}{2\pi}\int \exp\{-i\omega t\}\,[4(a^2_{\rho\,coh}+a^2_{\rho\,inc})F_{\rho\rho}(Q,t) + (a^2_{c\,coh}+a^2_{c\,inc})F_{cc}(Q,t) + 12\,a^2_{\rho\,coh}F_{\rho\rho'}(Q,t) + 8\,a_{\rho\,coh}a_{c\,coh}F_{\rho c}(Q,t)] \quad (3)$$

One can usually simplify this expression by neglecting the interaction between different modes of motion of the molecules considerably. At temperatures where most of the molecules are in their vibrational ground state this assumption has only to be critically considered for the interaction between centre-of-mass motion and rotational motion, but is generally believed to hold true for spherical top molecules since the anisotropic forces are small. With these assumptions in mind, we can write the intermediate scattering function as a product consisting of a rotational and a translational part, while finding that the vibrations of the molecules in the ground state only give rise to a vibrational Debye-Waller factor.

$$F_s(Q,t) = \sum_{\alpha,\beta} (a^{\alpha}_{coh}\, a^{\beta}_{coh} + \delta_{\alpha\beta}\, a^{\alpha 2}_{inc})\, F^{tr}_{s}(Q,t)\, F^{rot}_{\alpha\beta}(Q,t)\, F^{vib}_{\alpha\beta}(Q,t) \tag{4}$$

2.1. Vibrational motion of the methane molecules

Pope [16] has given the contribution of the vibrations to the intermediate scattering function without change in the vibrational state as

$$F^{vib}_{\alpha\beta}(Q,t) = \exp\{-2\,W^{vib}_{\alpha\beta}\} \tag{5}$$

$$2\,W^{vib}_{\alpha\beta} = Q^2 \gamma_{\alpha\beta} \tag{6}$$

with

$$\gamma_{\alpha\beta} = \sum_{\lambda} \frac{1}{12\,\omega_\lambda}[(C^{\lambda}_{\alpha})^2 + (C^{\lambda}_{\beta})^2] \tag{7}$$

with C^{λ}_{α} being the magnitude of the eigenvector corresponding to the λ^{th} vibrational state at the α^{th} nucleus with the eigenfrequency ω_λ.

For the position of an atom α in a molecule 1 we have

$$\vec{R}_{1\alpha} = \vec{R}_1 + \vec{b}_{1\alpha} + \vec{u}_{1\alpha}$$

where $\vec{R}_1$ is the centre-of-mass, $\vec{b}_{1\alpha}$ the equilibrium position of the atom α and $u_{1\alpha}$ the vibrational displacement from the equilibrium position.

2.2. Rotational motion of the methane molecules

Sears [17] introduced for rotational motion a rotational distribution function $G_s(\Omega_0, \Omega, t)$ in terms of rotational relaxation functions $F_l(t)$ and the rotation matrices $D^{l}_{m,n}$

$$F^{rot}_{\alpha\beta}(Q,t) = \frac{1}{8\pi^2} \int d\Omega_0 \int d\Omega \, \exp\{-i\vec{Q}\vec{b}_{\alpha}(0)\} \, \exp\{i\vec{Q}\vec{b}_{\beta}(t)\} G_s(\Omega_0, \Omega, t) \tag{8}$$

where

$$G_s(\Omega_0, \Omega, t) = \sum_{\substack{l \\ m,n}} \frac{2l+1}{8\pi^2} F^l_{m,n}(t)\, D^l_{m,n}(\Omega\Omega_0^{-1})$$

$$= \sum_{\substack{l \\ m,n}} \frac{2l+1}{8\pi^2} F^l_{m,n}(t) \sum_{\mu} D^l_{n\mu}(\Omega)\, D^{l*}_{m\mu}(\Omega_0) \tag{9}$$

With the normalization and initial conditions

$$\int G_s(\Omega_0, \Omega, t)\, d\Omega = 1 \tag{10}$$

$$G_s(\Omega_0, \Omega, 0) = \delta(\Omega\Omega_0^{-1}) \tag{11}$$

This implies

$$F^l_{mn}(0) = \delta_{m,n} \qquad \text{for all } l \tag{12}$$

Using the orthogonality of the rotation matrices and writing for

$$F^l_{00}(0) = F_l(t) \tag{13}$$

one finds

$$F^{rot}_{\alpha\beta}(Q, t) = \sum_{l=0}^{\infty} (2l+1)\, j_l(Qb_\alpha)\, j_l(Qb_\beta)\, F_l(t) \tag{14}$$

where j_l are the spherical Bessel functions of order l.

It is convenient to discuss the rotational behaviour in terms of $F_1(t)$. In Fig. 1 we show the classical limit of the relaxation function $F_1(t)$ for liquid methane obtained by Gordon [18] by Fourier inversion of the infrared data by Ewing [7]. Gordon pointed out that the conclusions drawn from both infrared and Raman experiments are consistent with each other. As one can see by inspection, the methane molecules appear to rotate essentially freely in time intervals of about 10^{-13} sec, while for intermediate time regions from $1 - 3 \times 10^{-13}$ sec the hindering produces a significant effect and for time intervals larger than 3×10^{-13} sec the rotational motion can be described by a random reorientation process. The results for higher rotational relaxation functions show qualitatively the same behaviour and are therefore not shown. To gain a deeper understanding of the rotational motion of methane molecules, we have calcu-

lated the rotational relaxation functions for several models using m- and $\vec{J}$-diffusion models introduced by Gordon [18], the results by Sears for classical free rotation and a model which combines free rotation for short times with rotational diffusion for long times. In the m-diffusion model a free rotational step is terminated by randomizing the components of the angular momentum $\vec{J}$ of the molecular rotation, while keeping its magnitude $\vec{J}$ and the spatial orientation of the molecule unchanged. In the $\vec{J}$-diffusion model the magnitude of $\vec{J}$ is distributed over a Boltzmann distribution in addition to randomizing the components of $\vec{J}$.

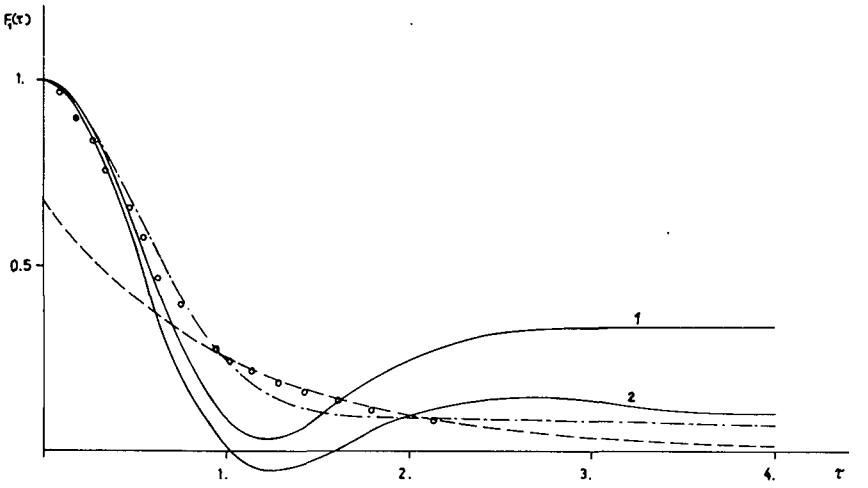

FIG.1. Classical free rotational relaxation functions of order 1: (1) is a model for free rotation (2) is a model for free rotation at short times and rotational diffusion for long times with $D_r = 0.5 \times 10^{12}$ sec^{-1}. The empirical values for the relaxation function for liquid methane (ooo) and rotational diffusion (---) adjusted to the long-time behaviour of the experimental CH_4 data; (-.-.-) the m-diffusion model by Gordon [18]. $\tau_0 = 1.0$, $\tau = \sqrt{BkT}\, t/\hbar$ (B... rotational constant).

The rate $1/\tau_0$ determines time intervals after which interactions terminate the free rotationof the molecule and force it to change its rotational state according to the m- or $\vec{J}$-diffusional behaviour. The number of molecules which are in their (n+1) diffusion step at a time t is given by a Poisson distribution.

While for a number of non-spherical molecules Gordon could fit experimentally determined $F_1(t)$ and $F_2(t)$ data very well using these models, we found that neither of these models could describe the rotational behaviour of the spherical methane molecules in the liquid state satisfactorily. The parameter τ_0 is the only variable parameter in the calculations and was chosen so as to fit the experimental $F_1(t)$ data for small t values. Gordon's rotational diffusion models are in principle 'collision models' – m-diffusion without an instantaneous energy transfer and $\vec{J}$-diffusion with instantaneous energy transfer – and show a long-time behaviour of the relaxation functions much more like a free rotation over the time scale that cold neutrons can observe than a random reorientation, depending, of course, on the collision rate. This indicates that for spherical molecules the hindering is not caused by 'collisions' but is a much weaker con-

tinuous hindering process which appears to randomize the molecular rotation in time intervals of about 3×10^{-13} sec.

The $\vec{J}$-diffusion model calculations are not shown in Fig. 1 because we could not bring them to show the right short-time behaviour without becoming negative for long times. We show for m-diffusion the characteristic differences between the exponentially decaying relaxation function of liquid methane and the shape of the m-diffusion relaxation function which decays much more slowly. For calculating the rotational part of the intermediate scattering function, we use two approaches:

(i) We assume that methane molecules rotate freely in liquid argon and treat them quantum mechanically

(ii) We assume that the methane molecules rotate freely in liquid argon at short times and perform rotational diffusion at long times.

For the rotational relaxation functions we find in the first case (see Griffing[1] [19] and Sears [17]

$$F_l^{rot} = \frac{1}{Z_{rot}} \sum_{j,J}{}' \frac{(2j+1)(2J+1)}{2l+1} \exp\{-Bj(j+1)/kT\} \exp\{l\omega_{jJ} t\} \tag{15}$$

$$Z^{rot} = \sum_{j} (2j+1)^2 \exp\{-Bj(j+1)/kT\} \tag{16}$$

$$\omega_{jJ} = B[j(j+1) - J(J+1)] \tag{17}$$

The dash at the summation sign indicates that (jJ1) must fulfil the triangle relations [20].

For the second case we take

$$F_l(t) = F_l^0(t) - \frac{1}{2l+1}[1 - \exp\{-l(l+1) D_r t\}] \tag{18}$$

where $F_l^0(t)$ stands for the classical limit of the rotational relaxation function for freely rotating molecules obtained by Sears [17]

$$F_l^0(t) = \frac{1}{2l+1}\left[1 + 2\sum_{n=1}^{l}\left(1 - \frac{n^2 kT\, t^2}{I}\right)\exp\left\{-\frac{n^2 kT\, t^2}{2I}\right\}\right] \tag{19}$$

The rotational diffusion constant D_r governs the deviations from the free rotational behaviour of the molecules. As an example we presented $D_r = 0.5 \times 10^{12}\,\mathrm{sec}^{-1}$ in Fig. 1.

---

[1] The author wishes to thank G. Griffing for a computer program for methane which was used in the calculations after modification to include simple diffusion.

If one assumes the Stokes expression to hold (which describes the motion of a molecule under the influence of a viscous force and torque), we find for the ratio of the rotational to the translational diffusion coefficient

$$D_r / D_{tr} \simeq 0.75\, b \tag{20}$$

For $D_{tr} = 2.45 \times 10^{-5}$ cm^2 sec^{-1} and $b = 1.093$ Å^{-1} one gets $D_r \simeq 0.15 \times 10^{12}$ sec^{-1}.

If we assume our picture of the rotational relaxation progress Eq.(18) to be a fair one, then the quasi-elastic peak should be broadened by rotational diffusion, this broadening being angle independent. Since we did not observe any broadening for the 20° scattering angle, the next question is, which broadening would we have observed within our experimental resolution and the statistical accuracy of the data. This puts an upper limit on the rotational diffusion constant and we found that $D \lesssim 0.2 \times 10^{12}$ sec^{-1}.

It is obvious that in the solid an expression of this kind cannot be expected to be right for molecules which can rotate, since it implies that there is rotational motion only if there is also translational motion. On the whole one can expect such a classical relation to hold better for heavy molecules at temperatures where higher rotational states are excited.

For methane in argon at 86°K rotational states with $J < 5$ are probable and we found that the quantum mechanical treatment of free rotations gave a reasonable result (Fig. 3).

2.3. Centre-of-mass motion of methane molecules in argon

As is well known, the simple diffusion model describes the long-time behaviour of the molecular dynamics fairly well. If we take the classical form of the self-correlation function and correct it to first order in $\hbar$ for quantum mechanical effects (see Schofield [21] we find for the translational part of $S_s(Q,\omega)$

$$S_s^{tr}(Q,\omega) \simeq \exp\left\{\frac{\hbar\omega}{2kT}\right\} \frac{1}{\pi} \frac{DQ^2}{(DQ^2)^2+\omega^2} \tag{21}$$

This form of the scattering law will only be valid in the vicinity of the quasi-elastic peak. The deviations of the half-width of the quasi-elastic peak from the simple behaviour

$$\Delta\omega = 2\, DQ^2 \tag{22}$$

does not show up for the Q-values of our experiment for $D = 2.45 \times 10^{-5}$ cm^2 sec^{-1}.

One might expect to improve the theory by using more complicated models and we are at present investigating the results of using the 'advanced itinerant oscillator model' of Damle et al. [22] for an impurity problem.

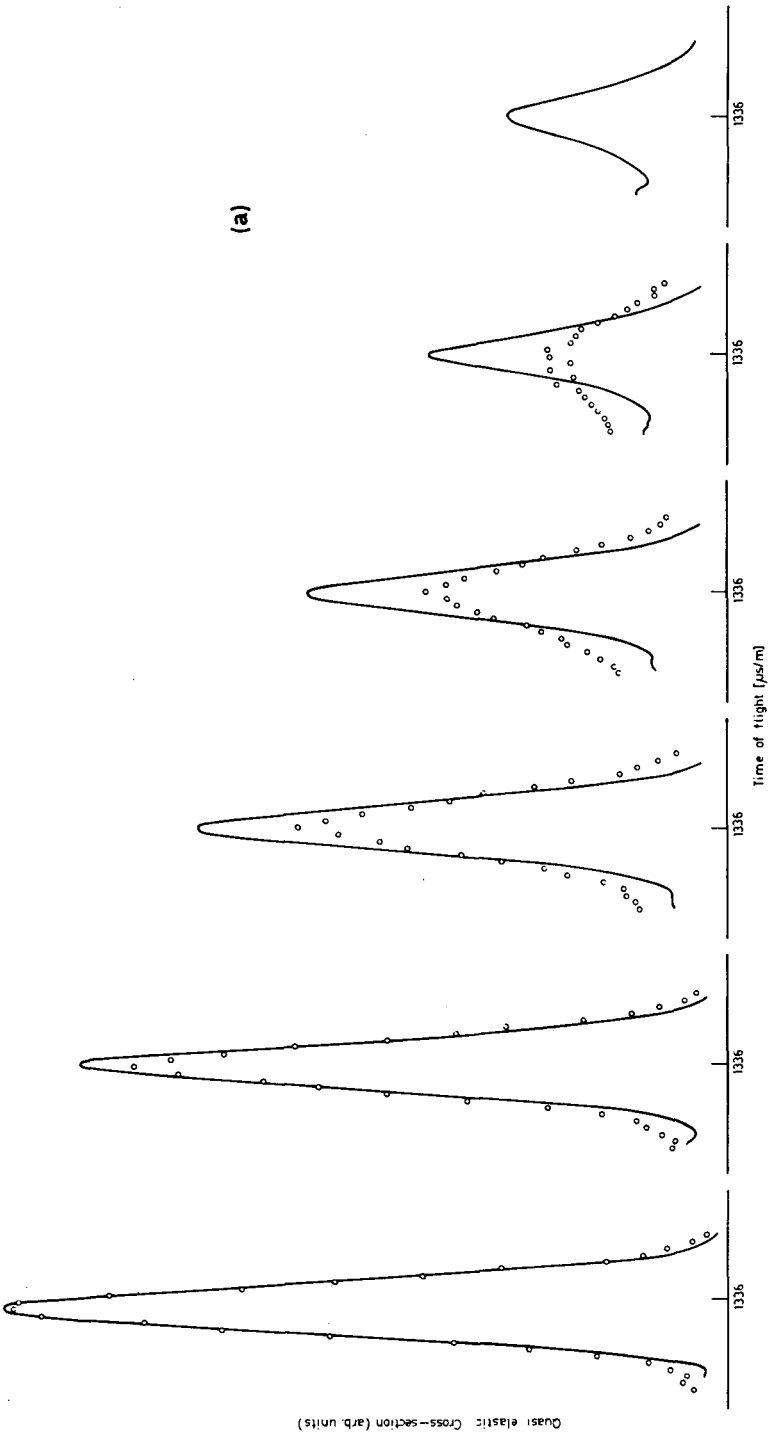
(a)
Quasi elastic Cross-section (arb. units)
1336
1336
1336
1336
1336
Time of flight (μs/m)

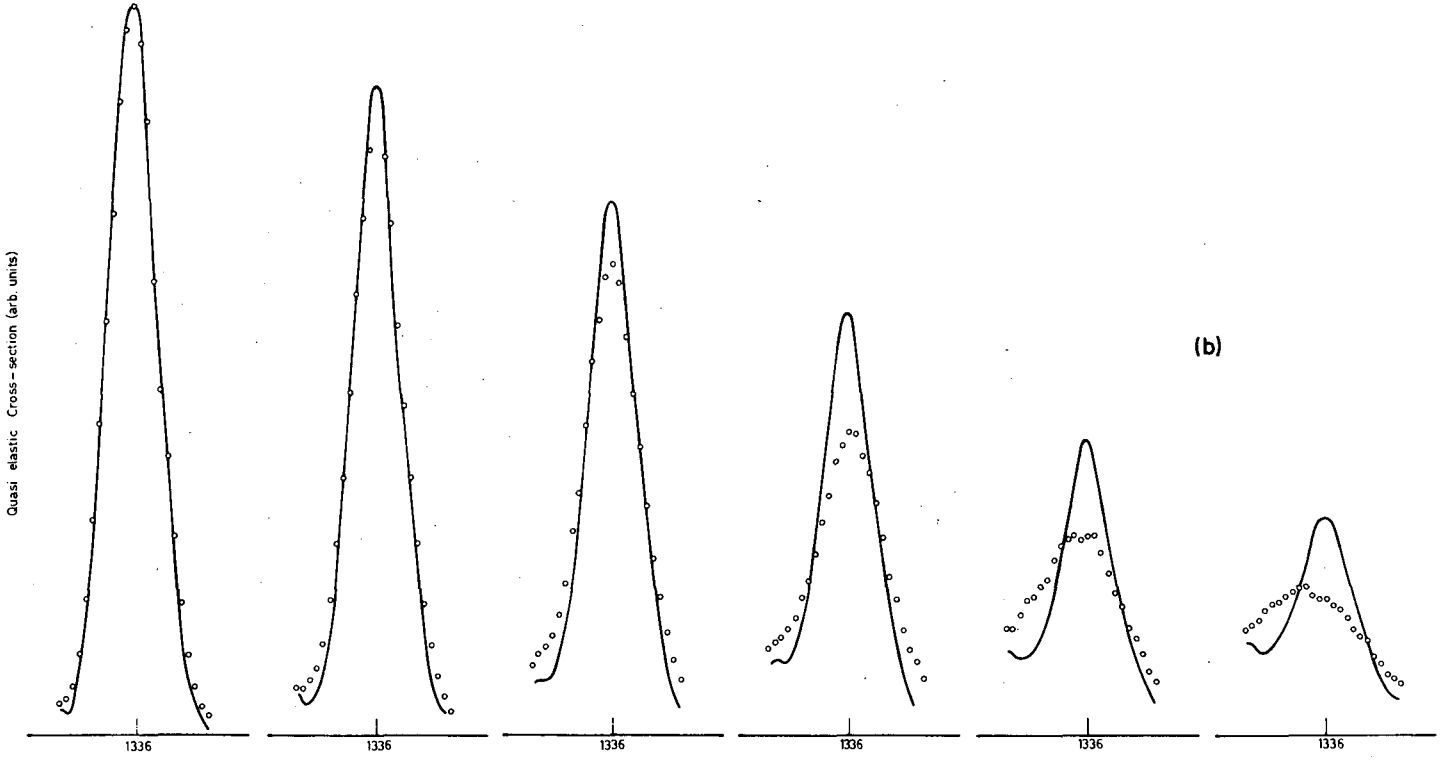

FIG. 2. Comparison of the quasi-elastic scattering patterns for (a) liquid methane at 92° K with solid methane at 89° K and (b) the liquid system methane (1.6%) in argon at 86° K with solid methane at 89° K. Solid methane is shown by the full line in both figures. Incident time of flight 1336 μsec/m; scattering angles 20°, 30°, 45°, 60°, 75° and 90°.

3. EXPERIMENTAL TECHNIQUE

3.1. Apparatus and sample

The experiment was performed on the cold neutron time-of-flight spectrometer at DIDO Harwell, described by Harris et al. [23]. A neutron beam remoderated in a liquid H_2 chamber, filtered by a cooled polycrystalline Be block and a Bi filter is chopped and monochromated by a curved slot rotor.

We used 5.3-Å neutrons in our experiment. The BF_3-counter banks were arranged 1.27 m from the sample at angles of 20°, 30°, 45°, 60°, 75° and 90°.

The methane-argon samples have been prepared by freezing a known amount of pure argon into an evacuated cylinder and adding a known amount of CH_4. The cylinder was heated slightly and the gases CH_4 and argon were allowed to mix. After filling the sample and cooling it down to 86°K, the sample was left for twenty-four hours to obtain thermal equilibrium. A rough measurement of the vapour pressure showed that the vapour pressure of the liquid system CH_4 in argon is lower than both the vapour pressures of argon and methane, this indicates that CH_4 and argon form a solution at the concentrations considered. The concentrations used in our experiment were 1.6 and 3.2 mol.% of CH_4 in argon.

A chemical analysis showed that the concentrations quoted agreed in all our samples to within 1% with the figures quoted. A typical analysis of the argon gas provided by the manufacturer showed that the degree of purity was 99.995%. It was produced from 99.95% argon treated with heated metallic calcium, then liquified and evaporated into cylinders, generating its own pressure. The methane used was 99% pure.

The sample holder was built of twelve stainless steel tubes (0.25-in. outer diameter and 0.004-in. wall thickness) arranged in an overlapping manner with 0.215-in. mutual separation, giving an approximate effective thickness of 0.214-in. The angle between beam and sample was 45°. The overall size of the sample was larger than the beam (2 in. × 1 in.). The sample was mounted in a liquid nitrogen cooled cryostat and kept at a temperature of 86°K. He gas with a pressure of 400 mmHg was used as a heat exchange medium. Using the vapour pressure of argon as an indicator of the temperature, a heater was switched automatically into our cooling system thus keeping the temperature within 86 ± 0.3°K. Temperature and pressure of the sample were recorded throughout the experiment. Regular checks of the transmission of the sample showed no significant changes. The transmission for our samples were approximately 92 and 84% respectively.

We used these two concentrations to find out if there is any concentration-dependent effect in our results, but apart from an increase in multiple scattering our results were independent of concentration. We will follow up this point and investigate multiple scattering, having in this case an identical geometry for two different scattering powers in our sample.

A preliminary result for the shape and size of the multiple scattering is shown in Fig. 3 for the 90° counter.

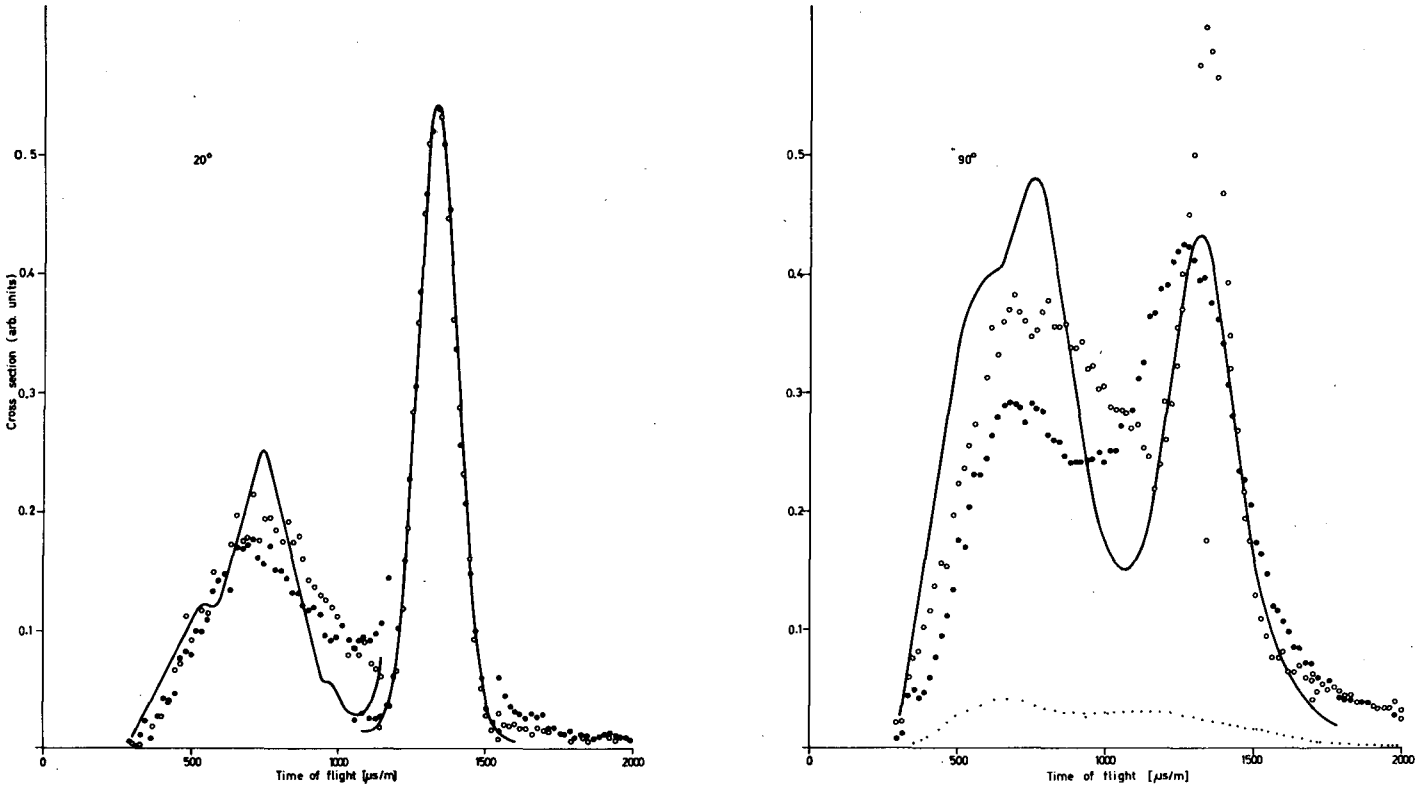

FIG.3. A comparison of the complete scattering pattern of solid methane (ooo) at 89°K and methane in argon at 86°K (●●●) with a model calculation using simple diffusion and the quantum mechanical treatment for free rotations for two scattering angles. Incident time of flight 1336 μsec/m.

3.2. Data collection and processing

The neutron pulses of seven BF_3-counter banks and three monitors have been stored on magnetic tape as a function of their time of arrival with respect to a start pulse from the rotor.

During a run of approximately 48 hours the input of every single BF_3-counter bank has been coded differently at 12-h intervals to check the consistency of the data taken and to permit the rejection of data in which, e.g., a counter had failed, without losing all the data. The magnetic data were then converted onto data cards.

The processing of the data consisted in subtracting 'background counts' from 'sample counts' channel by channel, normalizing for the incident flux, correcting for relative differences in the counter banks and the counter efficiency.

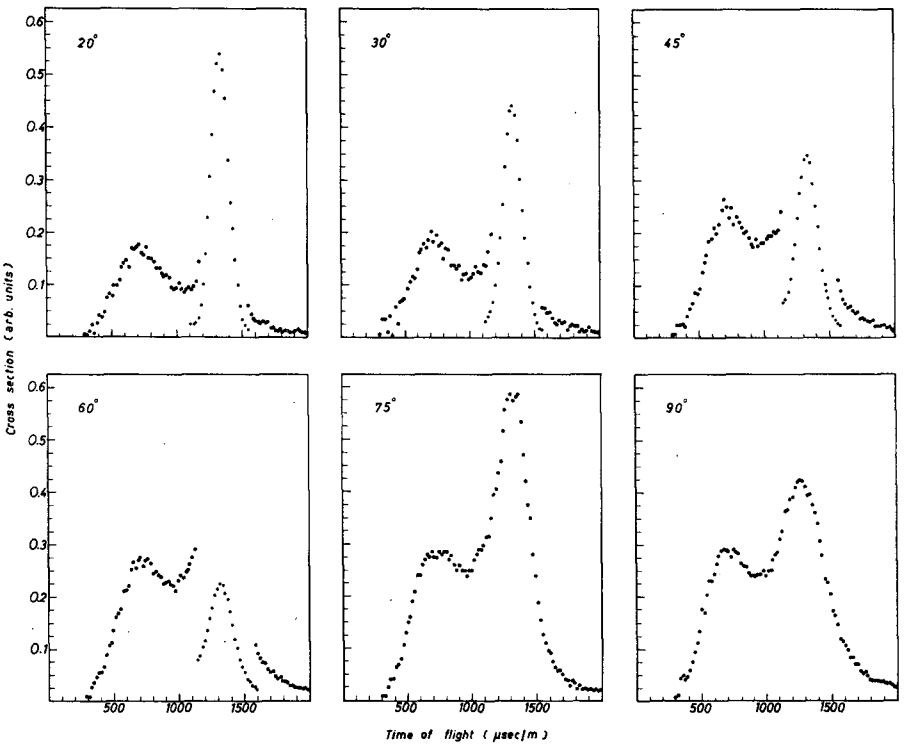

FIG. 4. The scattering pattern for methane (1.6%) in argon at 86°K for six scattering angles. Incident time of flight 1336 μsec/m; T = 86°K.

4. RESULTS AND CONCLUSIONS

In Fig. 2(a) we show the results for the quasi-elastic scattering cross-section for six scattering angles for liquid methane at 92°K as compared to solid methane at 89°K, and in Fig. 2(b) a comparison of the quasi-elastic scattering of the liquid system methane (1.6%) in argon at

86° K with solid methane. One can see that the quasi-elastic behaviour of methane in argon shows a clear broadening ($D = 2.45 \times 10^{-5}$ cm^2 sec^{-1}) but is still more pronounced than the quasi-elastic scattering of liquid methane. This can be explained only partly by the slightly higher diffusion coefficient of methane ($D = 2.7 \times 10^{-5}$ cm^2 sec^{-1} at 98°K). Since the decrease of the quasi-elastic peak is governed by the Debye-Waller factor to which the translational and rotational motions contribute, we have to conclude that either the rotations of methane in argon at 86° K are more free than the rotations in liquid methane at 92°K, or that the CH_4 molecules are not distributed randomly in the argon matrix but tend to form clusters.

It is obvious from the data shown in Figs 3 and 4 that the diffusional scattering is not sufficient to describe the translational part of the scattering law. We should also correct our data using the rotational relaxation functions deduced from infrared absorption and Raman scattering measurements for CH_4 in argon to discuss the translational motion unambiguously. For the time being we can say that none of the relaxation functions shown in Fig. 1 describes the rotational scattering much better than the quantum mechanical treatment of the free rotations. The data show, however, that the rotations are slightly hindered. The fact that the classical rotational relaxation functions described are not adequate may stem partly from the approximate way of going from classical mechanics to quantum mechanics which produces the highest error for low population numbers.

In a forthcoming paper on liquid methane at several temperatures we will use the experimentally determined rotational relaxation functions and try to find a model for the centre-of-mass motion.

REFERENCES

[1] EDER, O.J., CHEN, S.J., EGELSTAFF, P.A., Proc. phys. Soc. 89 (1966) 833.
[2] KEVOK, J., ROBINSON, G.W., J. chem. Phys. 36 (1962) 3137.
[3] ABRAMOWITZ, S., BROIDA, H.P., J. chem. Phys. 39 (1963) 2383.
[4] CABANA, A., SAVITSKY, G.B., HORNIG, D.F., J. chem. Phys. 39 (1963) 2942.
[5] HARROLD, J.H., thesis, Toronto (1949).
[6] PLINT, C.A., thesis, Toronto (1953).
[7] EWING, G.A., J. chem. Phys. 40 (1964) 179.
[8] CRAWFORD, M.F., WELSH, H.L., HARROLD, J.H., Can. J. Phys. 30 (1952) 81.
[9] HARKER, Y.D., BRUGGER, R.M., J. chem. Phys. 42 (1965) 275.
[10] WHITTEMORE, W.L., Nucl. Sci. Engng 18 (1964) 182.
[11] DESANNACHARYA, B.A., VENKATARAMAN, G., Phys. Rev. 156 (1966) 196; DESANNACHARYA, B.A., VENKATARAMAN, G., USHA DENIZ, K., Inelastic Scattering of Neutrons (Proc. Symp. Bombay, 1964) 2, IAEA, Vienna (1965) 157.
[12] JANIK, J.A., JANIK, J.M., MELLOR, J., PALEVSKY, H., J. Chem. Phys. Solids 25 (1964) 1091.
[13] Van HOVE, L., Phys. Rev. 95 (1954) 249.
[14] ZEMACH, A.C., GLAUBER, R.J., Phys. Rev. 101 (1956) 118.
[15] SINHA, S.K., VENKATARAMAN, G., Symp. Inelastic Scattering of Neutrons by Condensed Systems, Brookhaven, 1965 .
[16] POPE, N.K., Can. J. Phys. 30 (1952) 597.
[17] SEARS, V.F., Can. J. Phys. 45 (1967) 237.
[18] GORDON, R.G., J. chem. Phys. 43 (1965) 1307.
[19] GRIFFING, G.W., Phys. Rev. 124 (1961) 1489.
[20] ROSE, M.E., Elementary Theory of Angular Momentum, John Wiley and Sons Inc., New York (1957).
[21] SCHOFIELD, P., Phys. Rev. Lett. 4 (1960) 239.
[22] DAMLE, P.S., SINGWI, K.S., SJÖLANDER, A., to be published.
[23] HARRIS, D., COCKING, S.J., EGELSTAFF, P.A., WEBB, F.J., Inelastic Scattering of Neutrons in Solids and Liquids (Proc. Symp. Chalk River, 1962) 1, IAEA, Vienna (1963) 107.

STUDY OF THE FREQUENCY DISTRIBUTION IN UNSTRETCHED AND STRETCHED RUBBER BY NEUTRON INELASTIC SCATTERING

E. TUNKELO
REACTOR LABORATORY,
TECHNICAL UNIVERSITY OF HELSINKI, FINLAND,
AND
A. BAJOREK, I. NATKANIEC, K. PARLIŃSKI AND
M. SUDNIK-HRYNKIEWICZ
JOINT INSTITUTE FOR NUCLEAR RESEARCH,
DUBNA, USSR

Abstract

STUDY OF THE FREQUENCY DISTRIBUTION IN UNSTRETCHED AND STRETCHED RUBBER BY NEUTRON INELASTIC SCATTERING. A neutron inelastic scattering study of unvulcanized natural rubber in the normal state and stretched to about five times its original length was performed using time-of-flight techniques in the pulsed reactor IBR at JINR, Dubna. The energy analysis was performed with a beryllium filter and in some of the experiments with the additional Bragg reflection from a large single-crystal of zinc to obtain a better resolution. Scattering together with the strain of the sample both parallel and perpendicular to the scattering vector was studied.

The results were analysed in terms of the frequency distribution function, assuming single-phonon scattering to be dominant. The density of the low-energy modes was found to be reduced by stretching. This may be attributed to the unlinear change of elastic constants in stretching, making the initial slope of the dispersion curves more steep. The high-energy modes were found to stay almost unchanged. An additional band of frequencies was found in the region of 10-12 meV in the case of the strain parallel to the scattering vector. This can be attributed to flattening of the dispersion curves in this energy region. Summarizing, one may say that the stretching of the sample shifts part of the low-energy modes to higher energies, probably by making the dispersion curves more steep in the beginning and bending them more flat in the 10-12 meV region for phonons travelling in the direction of the strain.

1. INTRODUCTION

The peculiar elastic behaviour of rubber has been studied very extensively [1], using a variety of experimental techniques. While it has been possible to describe the macroscopic properties rather accurately both for an understanding and for the technical use of rubber, the behaviour at the microscopic or atomic level has not been studied very much using direct methods at the atomic level. As the inelastic scattering of neutrons offers a method which gives direct view of the atomic or molecular dynamics, it was considered possible to gain some new information using this technique.

Natural rubber was selected for the material to be studied. It is a cis-polymer of isoprene:

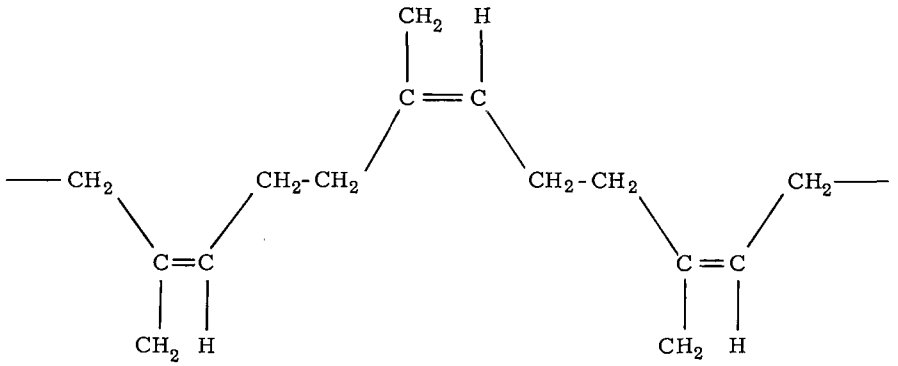

The basic formula $(C_5H_8)_n$ shows that the scattering will be almost completely due to hydrogen atoms, so that the frequency spectrum will readily be given by the inelastic scattering pattern.

When unvulcanized natural rubber is stretched, its long molecules tend to orient themselves in the direction of strain, thus producing regions of rather high symmetry. This is often called crystallization of rubber upon stretching. This behaviour is quite typical of natural rubber and not so clearly observed in vulcanized and many synthetic rubbers. In the crystallized form the interaction of neighbouring molecules is different from that of uncrystallized regions. This will not effect the high-frequency vibrations of the molecules but will certainly change the low-frequency ones which are intermolecular in nature. X-ray studies have shown conclusively that the crystalline regions extend no more than a few hundred Å units even in the direction of the molecular chains. As the average length of the polymer chain is much greater, each single molecule must contribute in several crystallized regions. Thus rather large unoriented regions between the crystallites will be left. In these regions no large changes in the dynamics are expected. This fact will make the effects seen in the inelastic scattering pattern rather smaller than the actual change in the vibration spectrum in the crystallized domains.

Natural rubber can be crystallized as well by cooling it below room temperature. The rate of crystallization depends on the temperature, having its maximum value at -22°C. Thus cooling a rubber sample to this temperature will produce a more or less completely crystallized material after a few hours.

Based on these facts, the program for this study was as follows. A rubber sample was cooled to -22°C, allowed to crystallize and then cooled quickly to liquid nitrogen temperature to quench the thermal motion leading thus to a better resolution in the experiment. This provided the reference spectrum of the vibrations in crystallized rubber. Then the rubber sample was cooled down to liquid nitrogen temperature from room temperature, first unstretched and then stretched, giving thus two spectra which had the only difference that the sample was

stretched in between. The stretched sample was measured with the strain parallel with and perpendicular to the scattering vector by rotating the sample around the horizontal axis.

2. EXPERIMENTAL METHOD AND RESULTS

Measurements were done using the time-of-flight spectrometer at the pulsed reactor IBR-1 of the JINR [2]. This instrument has a very high resolution as in the analysing device a large single crystal of Zr is used in addition to the conventional Be filter. The high resolution of the

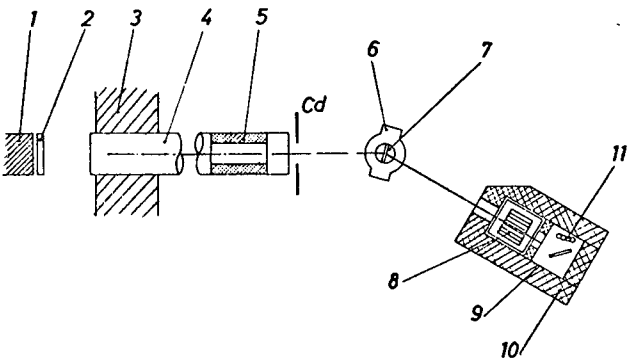

FIG.1. Lay-out of the experiment. 1. IBR pulsed reactor; 2. moderator; 3. shielding; 4. evacuated tube; 5. collimator; 6. cryostat; 7. sample holder; 8. cooled Be; 9. Zn monocrystal; 10. borated paraffin shielding; 11. BF_3 counters.

instrument was utilized only in the first measurement on thermally crystallized rubber. The rest of the measurements were performed using the conventional Be-filter detector method, i.e. placing the detector immediately after the Be filter. This method gives, of course, a higher count rate. It was used for the better statistical accuracy thus obtainable and as the effects expected were mainly in the low-energy region of the frequency spectrum.

The lay-out of the experiment is shown in Fig.1. The sample was held in a liquid nitrogen cooled cryostat [3]. Its position could be turned round the vertical axis so that the sample could be placed so that the change of the wavevector (Q) in the scattering process was (approximately) either parallel or perpendicular to the stress in the sample. Measurements were made at a scattering angle of 90°, the sample being placed at 45°. The transmission of the sample was 0.9. The stretching of the sample was done in the sample holder. It was stretched to slightly more than 4 times the original length and then folded to 4 layers so that the amount of material in the beam was the same as before.

The results of the measurements are given in Fig.2 which shows the scattered intensity from crystallized natural rubber. Frequency spectra

of unstretched and stretched rubber derived from measurements are shown in Fig. 3. These do not reproduce the fine details which can be seen in Fig. 2 because these measurements were done with lower resolution using the Be filter alone.

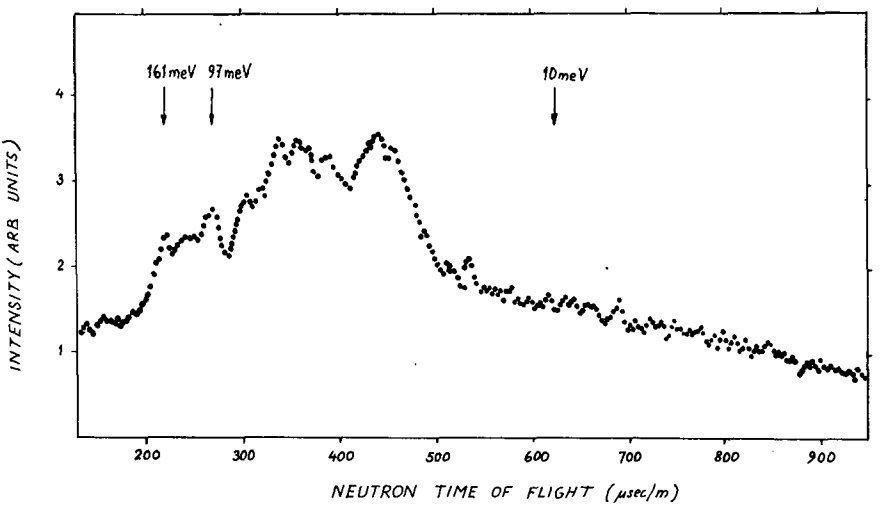

FIG. 2. Scattered intensity from crystallized natural rubber.

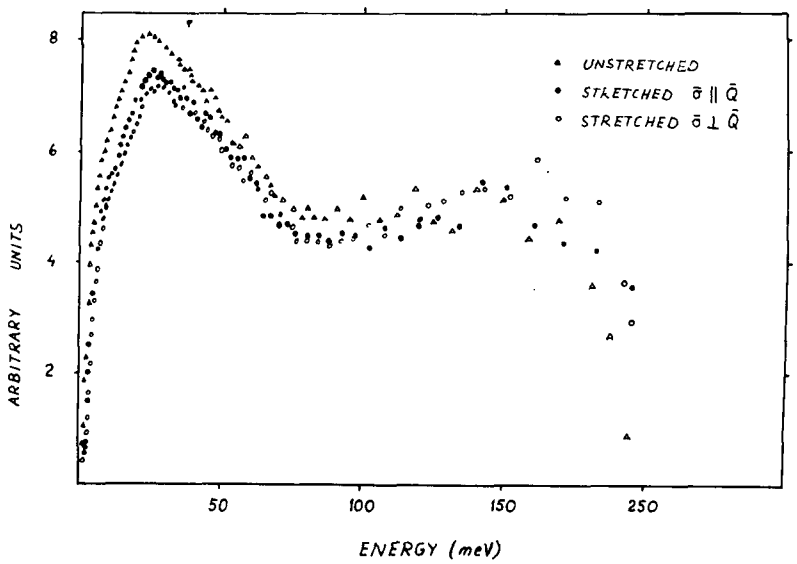

FIG. 3. Generalized frequency function of unstretched and 400% stretched natural rubber.

3. DISCUSSION

Figure 2 includes a large number of details of the frequency spectrum of rubber. The two high-energy peaks with energies of 161 and 97 meV are known from infrared measurements and are assigned to C-H rocking.

In stretching one does not expect the high-energy modes to be much affected because of their intermolecular nature. We therefore studied the low-energy part of the frequency spectra of stretched and unstretched rubber. Unfortunately, the effect is rather small. There seems to be less and less low frequency ($\epsilon \sim 3 - 5$ meV) when one goes from unstretched to stretched rubber and from the $\vec{Q}$ parallel to the $\vec{Q}$ perpendicular positions. This could be the effect of stiffening of the surrounding of a molecule by the orientation produced by the strain.

In addition there seems to be change in the region of 10-12 meV. An additional band or a new concentration of frequencies seems to be observed in this region in the stretched rubber when $\vec{Q}$ is parallel to the strain. This might be produced by the flattening of the dispersion curves in this energy region.

Summarizing, one may say that stretching the rubber seems to shift part of the low-energy modes to higher energies, probably by making the dispersion curves more steep in the low-energy part (< 5 meV) and producing some flattening of the dispersion curves in the 10-12 meV region for phonons having their polarization vector in the direction of the strain.

ACKNOWLEDGEMENTS

The authors are indebted to Prof. F.L. Shapiro and Prof. J.A. Janik for encouragement for this work and fruitful discussions. One of the authors (E.T.) is particularly grateful for the hospitality of the Joint Institute for Nuclear Research and its staff during his stay in Dubna.

REFERENCES

[1] BILLMEYER, F.W., Jr., Textbook of Polymer Chemistry, Interscience, New York (1957).
[2] PARLIŃSKI, K., SUDNIK-HRYNKIEWICZ, M., BAJOREK, A., JANIK, J.A., OLEJARCZYK, W., Research Applications of Nuclear Pulsed Systems (Proc. Panel Dubna, 1966), IAEA, Vienna (1967) 179.
[3] SUDNIK-HRYNKIEWICZ, M. et al., Nucleonika 12 (1967) 387.
[4] KLEY, W. et al., Proc. Symp. Inelastic Scattering of Neutrons by Condensed Systems, Brookhaven (1965).

DISCUSSION

W. GISSLER: Have you observed any broadening of the elastic line originating from the damped modes in the amorphous state?

E.H. TUNKELO: The elastic line may be slightly broadened. However, the broadening, if any, is of the same order as the experimental resolution, and for that reason we did not wish to say anything about it in the paper.

SUMMARY

A.R.MACKINTOSH
TECHNICAL UNIVERSITY,
LYNGBY, DENMARK

It is customary to begin a conference summary with a complaint about the impossibility of reviewing so many papers (in this case over one hundred) and an apology for the inadequacy of one's efforts to do so. I am happy to follow this convention and to remind you that the following remarks are nothing more than a personal opinion about the present state of the art and science of inelastic neutron scattering, illustrated where appropriate by references to work presented at this Symposium, or to papers published since the last IAEA Neutron Scattering Symposium in Bombay. These remarks will necessarily be biased by my own interests, which are those of a solid state physicist, primarily interested in metals, and with a limited competence in the techniques of neutron scattering.

We have some reason for considering ourselves as a privileged minority among those scientists who study the properties of condensed matter, since inelastic neutron scattering is the most expensive experiment in the field. Our justification for spending so much time and money is, of course, that it is also incomparably the most powerful method of obtaining information about the dynamics of condensed systems. The neutron interacts sufficiently strongly with the nuclei and magnetic moments that the scattering from reasonably sized samples is normally easy to measure, but sufficiently weakly that the distribution of the scattered neutrons contains information about the unperturbed system. The energies and momenta characteristic of the excitations in condensed systems are comparable with those of thermal neutrons, so that both the energy and momentum change of the neutron in the scattering process may readily be measured. A detailed study of the scattering cross-section, as a function of energy and momentum transfer, then allows the determination of the time dependent pair correlation functions, which play a central role in the description of the dynamics of the system. To provide a satisfactory physical description of the system, we must construct a model which predicts the dynamical motion of its constituents from a knowledge of the forces between them, and compare the results with experiment. Such models may readily be constructed for simple, highly ordered systems, but become less satisfactory as the complexity increases or the degree of ordering decreases.

I shall therefore begin by discussing phonons in metals, which generally have simple crystal structures. Their electronic structures are also simple if the conduction electron wave functions are derived from atomic s and p states, because the conduction bands are then almost parabolic and the electronic structures can be described in terms of a weak pseudo-potential. Calculations of phonon spectra in which the pseudo-potential is determined from first principles meet with variable success and Kagan [1] showed us that it is necessary to take into account non-pair forces to stabilize the crystal structure of, for instance, Sn. The phonon spectra of metals contain implicitly a great deal of information about the conduction electrons, and Schneider and Stoll [2] have used the dispersion relations for simple metals to determine empirical pseudo-potentials, which in turn may be used

to calculate other electronic properties, such as the distortion of the Fermi surface and the transport properties, with a considerable degree of success. A particularly interesting series of experiments on disordered binary and ternary alloys of Tl, Pb and Bi has been carried out by Ng and Brockhouse [3]. To a good approximation, the phonon spectra in these alloys appear to depend only upon electron concentration, which implies that the pseudopotentials for the three metals are probably rather similar. An approximation which is normally made in the calculation of phonon spectra in simple metals is the use of some form of free electron dielectric function, and this leads to errors in the prediction of Kohn anomalies, which are due to singularities in the dielectric function at wavevectors determined by the true Fermi surface. The behaviour of the Kohn anomalies in the Pb-Tl system [3] is in agreement with the predictions of the rigid band model, and such experiments are of particular interest to metal physicists because they provide one of the few ways of obtaining explicit information about the Fermi surface of disordered alloys. The dielectric function reflects the quantization of the electron energy levels in a magnetic field and Cowley [4] has calculated the resulting change in the phonon energies and lifetimes for K, which is a good approximation to the free electron model. These effects require very large magnetic fields but should nevertheless be observable in favourable cases.

The flat Fermi surfaces characteristic of transition metals give rise to large anomalies in the dielectric function and hence in the phonon spectra, and these have recently been studied as a function of electron concentration in the Nb-Mo system by Powell, Martel and Woods [5]. In this Symposium Sakamoto and Hamaguchi [6] have shown that the addition of a small amount of Ni to Cu perturbs the phonon spectrum significantly, despite the similarity between the dispersion relations for the pure metals. In this connection, it seems surprising that magnetic ordering has such a small effect on the phonon spectra of the 3d transition metals. For instance, De Wit and Brockhouse [7] observed only a very small difference between the paramagnetic and ferromagnetic phases of Ni, despite the fact that the Fermi surface is known to be drastically modified by the transition. It appears that the dielectric function must be largely determined by states sufficiently far from the Fermi level to be little affected by the magnetic ordering. The a priori calculation of the phonon dispersion relations for a transition metal is a formidable task because the d-electrons preclude the use of a pseudopotential for representing the electron-ion coupling, and the dielectric function must also be calculated from first principles. A formalism for performing such calculations has recently been presented by Sinha [8] however, and further discussed in this Symposium by Cohen, Martin and Pick [9].

These theoretical methods may also be applied to insulators and may therefore be used to justify phenomenological models, like the shell model and its extensions, and to calculate from first principles the parameters of such models, which have been extensively used to interpret the data on the dispersion relations of non-metals which have been presented at this Symposium. A new and interesting problem in lattice dynamics is presented by the measurements of Brun et al. [10] and the earlier results of Lipshultz et al. [11] on the quantum crystal ^{4}He. In this case, the zero-point vibrations of the atoms are so large that the conventional energy expansion about the equilibrium positions cannot be used, and new theoretical methods have

therefore been developed. The agreement between theory and experiment is not at present particularly good, and rapid developments in both may be anticipated.

In the Bombay Symposium, Elliott and Maradudin [12] emphasized the efficacy of neutron scattering for studying the local and quasi-local phonon modes which are produced by the addition of a small amount of impurity with a very different mass from that of the host, and since then a considerable number of experiments have been performed in this field [13]. In this Symposium, Nicklow et al. [14] and Als-Nielsen [15] have presented the first results on coherent scattering from local phonon modes due to light impurities. The former authors have shown that the $\vec{q}$-dependence of the scattered intensity is in accord with the simple mass-defect theory and that the mode is highly localized, but the changes in the band modes in both cases make it clear that force constant changes occur, and this is in agreement with previous experiments on quasi-local modes. A related experiment is that of Buyers and Cowley [16] on mixed crystals of KBr and RbBr. Phonons remain well-defined excitations in such a system, though considerably broadened, but the theory of concentrated disordered systems is extremely difficult, and it is not therefore surprising that there is substantial disagreement between experiment and theory in this case.

As the number of atoms in the unit cell increases, a transition occurs from solid state physics to physical chemistry and my competence as a reviewer declines rapidly. It would clearly be desirable to study complicated molecular crystals by coherent neutron scattering from single-crystal samples, but this is usually technically impossible at present, so we must generally be satisfied with frequency distributions deduced from incoherent scattering, to which the hydrogen atoms make the dominant contribution. There is clearly much useful information about molecular dynamics to be obtained from such studies, however, particularly if the background from coherent scattering, multiphonon processes etc. can be reliably subtracted. In this respect, the results of Powell [17] on deuterated hexamethylenetetramine are of particular importance. As well as being the first detailed study of the dispersion relations in a molecular crystal by coherent scattering, these experiments provide the parameters for a microscopic model of the vibrations of this material. From this model, the incoherent scattering by normal hexamethylenetetramine can be calculated and compared with experimental results on polycrystalline samples, as a test of the methods of interpretation normally used in such experiments.

A great extension in our knowledge of magnon dispersion relations has occurred since the Bombay Symposium, and this has had an important effect on the understanding of magnetic interactions in solids. The rare-earth metals have been studied in most detail because, in some cases, their strong magnetic scattering and convenient range of magnon energies outweighs the disadvantage of the high neutron absorption. The magnon dispersion relations in ferromagnetic Tb have been measured in great detail, as described by Møller [18], and Houmann [19] has used the results to construct a density of states and deduce the interionic exchange forces. The interactions of magnons with other excitations have also been studied. In addition, the dispersion relations have been examined in the spiral phase of Tb [18] and in the cone phase of Er by Woods, Holden and Powell [20]. The situation in the magnetic transition metals is not so happy because the very high magnon energies at present preclude measurements at large wave-

vectors. An important contribution has been made by Komura, Lowde and Windsor [21] who have measured the spin correlation function for Ni over a wide energy and momentum range. By plotting their results in terms of contour maps, they have been able to observe the departure of the magnon dispersion relation from a parabola in the ferromagnetic phase, and the persistence of magnon-like behaviour through the transition. In magnetic insulators, the results can generally be interpreted in terms of short-range exchange constants although, for various technical reasons, few complete dispersion relations have so far been measured. The short range of the magnetic forces in insulators make them suitable for the quantitative study of local modes, and the first measurements by coherent scattering on localized modes outside the continuum were made by Buyers et al. [22] on MnF_2 doped with Co.

It has become apparent in recent years that neutron scattering provides one of the most powerful techniques for studying phase transitions. The persistence of the crystalline order through magnetic transitions is experimentally convenient, and important developments have recently occurred in measuring the time dependence of the fluctuations in the critical region. At this conference Dietrich and Als-Nielsen [23] presented further studies of the phase transition in Tb and, by paying extremely careful attention to the experimental resolution of their apparatus, they were able to observe the predicted thermodynamic slowing down of the critical fluctuations at the transition temperature. This phenomenon has also been studied by Nathans, Menzinger and Pickart [24]. The dynamical behaviour of the spins near the transition is very poorly understood, and the assumption of an exponential time decay is clearly much too crude, since spin-wave peaks have been observed in the paramagnetic phase of $RbMnF_3$ [24] and, even more strikingly, in CoF_2 by Martel, Cowley and Stevenson [25]. Whether excitations are actually seen as peaks at finite energy transfer in the disordered phase seems to depend on the degree of damping, but even when they are not observed, incipient collective oscillatory behaviour is frequently present, as in the experiments on Ni mentioned earlier [21], and must be taken into account in the theory. In displacive ferroelectrics, the collective modes may be little damped, but Buyers et al. [26] have shown that the critical scattering in KDP may be interpreted in terms of a heavily overdamped oscillatory mode.

When all order is lost, both theory and experiment become difficult, and our understanding of liquids is still relatively primitive. They may be divided into the categories of simple, monatomic liquids and complex, molecular liquids; but unfortunately even simple liquids are not, in practice, particularly simple. At short times a vibrational, solid-like behaviour appears to dominate, while over long periods a diffusional gas-like behaviour is observed, and the problem is to construct a theory which encompasses these two limits while interpolating satisfactorily between them. In this connection the computer calculations, or "computer experiments", of Rahman [27] are particularly important, because they give much more detailed information about the correlation functions of a fairly realistic system than the neutron experiments are at present able to. They indicate that heavily damped longitudinal phonons exist in a liquid at large wavevectors and have a dispersion relation connected with the structure factor. Transverse fluctuations are also important, in agreement with experimental observations. It would seem most profitable in the future to test fundamental

theories and models against these calculations before applying them to the experimental results on real liquids. As discussed by Larsson [28], incoherent scattering from molecular liquids gives valuable information on the rotation-vibration spectra of the molecules and, at small energies, on the hindered rotations.

The most striking technical innovation which has been presented in the conference is the use of autocorrelation methods in time-of-flight spectrometry [29-31]. By allowing a large increase in the duty cycle, these techniques give a corresponding increase in intensity which promises to extend considerably the range of experiments which can be performed by the time-of-flight method. In general, technical progress is proceeding through refinements and developments in existing methods and equipment and of these the most significant, of course, is the construction of an increasing number of high flux reactors. Because of its great flexibility, the triple-axis crystal spectrometer will probably remain the most powerful method for the study of the energies and lifetimes of excitations in solids. There have been recent improvements in methods of calculating and measuring the resolution function for the instrument [32, 33] and these have been crucial in interpreting experiments on inelastic critical scattering and the lifetimes of excitations. Hot sources [34], which are particularly useful for the study of high-energy excitations, and cold sources [35] for high-resolution experiments are being developed, while existing fluxes are being utilized more efficiently by improvements in monochromators and the increasing use of ^{3}He detectors. A relatively cheap method of increasing count rates is by taking pains to grow bigger and better crystals, for use both as monochromators and samples, and this is an aspect of experimental technique which has not in the past been given the emphasis which it deserves.

It has been clear for some time that the measuring of the positions of neutron groups is subject to the law of diminishing returns, and we have frequently been warned that hard times are just around the corner for neutron scatterers. Fortunately there is a tremendous amount of interesting information to be obtained from line shapes and intensities, and in this Symposium we have seen a trend towards such measurements, which I expect to continue strongly. Line widths tell us about interactions between excitations, while intensities give, for example, phonon eigenvectors, as described by Cochran [36], and information about magnetic anisotropy and magnon renormalization. We may expect to see more extensive studies of local modes and disordered alloys, with particular emphasis on the effect on the excitations of changes and disorder in the force constants. The use of polarized beams in magnetic measurements will increase and the study of magnons in transition metals will be extended to higher energies, where it is hoped that the merging of magnons into single-particle excitations may be clearly demonstrated. The effects on the excitation spectrum of changes in the thermodynamic environment of the sample will be further studied by the application of magnetic fields or pressure. Preliminary experiments on the effects of pressure have been reported at the Symposium by Quittner, Vukovich and Ernst [37]. I believe that there will be an increasing preponderance of experiments which use coherent scattering from single crystals, even for the study of complex molecular solids. In all of these experiments access to a high-flux reactor will be a great advantage, but I do not feel that anyone with originality, imagination, patience and a more modest reactor has any reason to despair.

The explanation of those experimental results which have already been obtained clearly requires substantial developments in the theory. Because of the ease with which band structure calculations can now be performed and the reliability of the results, first principles calculations of force constants and phonon spectra in non-metals and transition metals, and of the indirect exchange interaction and magnon spectra in rare-earth metals, are now conceivable. On a more fundamental level, the theory of quantum crystals and its application to ^{4}He requires further development. The problem of excitations in disordered systems is very poorly understood and neutron scattering gives the most explicit experimental information on this question. Further investigation of the effect of long-range force-constant changes and finite concentration on local modes is required, and this is related to the general problem of the propagation of excitations through a system with disordered force constants. The time dependence of the critical fluctuations at phase transitions and the dynamics of liquids need further theoretical study. In this repsect, computer calculations on fairly large systems of the type described in this conference by Rahman [27] and Windsor [38] are likely to prove of great assistance in constructing a fundamental theory.

The value of conferences devoted to inelastic neutron scattering has sometimes been questioned and it is true that, since it is such a versatile technique, its practitioners embrace a wide spectrum of interests. However, I believe that the subject still has sufficient coherence that we all have much in common, and I have found something of interest in almost all of the papers which I have diligently listened to while gathering material for this summary. In particular the session on developments in technique and the opportunities for informal discussions have been valuable, I am sure, for all of us, and are almost enough in themselves to make these symposia worth continuing. It has been a great pleasure for those of us working in Denmark to welcome our colleagues from other countries to this Symposium. We hope that they enjoyed their visit and we look forward to seeing them in Copenhagen again.

REFERENCES

[1] KAGAN, Yu. M., these Proceedings 1, SM-104/203.
[2] SCHNEIDER, T., STOLL, E., these Proceedings 1, SM-104/4.
[3] NG, S.C., BROCKHOUSE, B.N., these Proceedings 1, SM-104/53.
[4] COWLEY, R.A., these Proceedings 1, SM-104/47.
[5] POWELL, B.M., MARTEL, P., WOODS, A.D.B., Phys. Rev. (to be published).
[6] SAKAMOTO, M., HAMAGUCHI, Y., these Proceedings 1, SM-104/24.
[7] De WIT, G.A., BROCKHOUSE, B.N., J. appl. Phys. 39 (1968) 451.
[8] SINHA, S.K., Phys. Rev. 169 (1968) 477.
[9] COHEN, M.H., MARTIN, R.M., PICK, R.M., these Proceedings 1, SM-104/29.
[10] BRUN, T.O., SINHA, S.K., SWENSON, C.A., TILFORD, C.R., these Proceedings 1, SM-104/146.
[11] LIPSHULTZ, F.P., MINCKIEWICZ, V.J., KITCHENS, T.A., SHIRANE, G., NATHANS, R., Phys. Rev. Lett. 19 (1967) 1307.
[12] ELLIOTT, R.J., MARADUDIN, A.A., Inelastic Scattering of Neutrons (Proc. Symp. Bombay, 1964) 1, IAEA, Vienna (1965).
[13] See MACKINTOSH, A.R., BJERRUM MØLLER, H., in Localized Excitations in Solids, Plenum Press, New York (1968) for a recent review.
[14] NICKLOW, R.M., VIJAYARAGHAVAN, P.R., SMITH, H.G., DOLLING, G., WILKINSON, M.K., these Proceedings 1, SM-104/85.
[15] ALS-NIELSEN, J., these Proceedings 1, SM-104/18.

[16] BUYERS, W.J.L., COWLEY, R.A., these Proceedings 1, SM-104/42.
[17] POWELL, B.M., these Proceedings 2, SM-104/50.
[18] BJERRUM MØLLER, H., these Proceedings 2, SM-104/205.
[19] HOUMANN, J.C.G., these Proceedings 2, SM-104/17.
[20] WOODS, A.D.B., HOLDEN, T.M., POWELL, B.M., Phys. Rev. Lett. 19 (1967) 908; and to be published.
[21] KOMURA, S., LOWDE, R.D., WINDSOR, C.G., these Proceedings 2, SM-104/110.
[22] BUYERS, W.J.L., COWLEY, R.A., HOLDEN, T.M., STEVENSON, R.W.H., J. appl. Phys. 39 (1968) 1118.
[23] DIETRICH, O.W., ALS-NIELSEN, J., these Proceedings 2, SM-104/21.
[24] NATHANS, R., MENZINGER, F., PICKART, S.J., J. appl. Phys. 39 (1968) 1237.
[25] MARTEL, P., COWLEY, R.A., STEVENSON, R.W.H., J. appl. Phys. 39 (1968) 1116.
[26] BUYERS, W.J.L., COWLEY, R.A., PAUL, G.L., COCHRAN, W., these Proceedings 1, SM-104/48.
[27] RAHMAN, A., these Proceedings 1, SM-104/95.
[28] LARSSON, K.-E., these Proceedings 1, SM-104/200.
[29] GOMPF, F., REICHARDT, W., GLÄSER, W., BECKURTS, K.H., these Proceedings 2, SM-104/67.
[30] COLWELL, J.F., MILLER, P.H., WHITTEMORE, W.L., these Proceedings 2, SM-104/77.
[31] PÁL, L., KROÓ, N., PELLIONISZ, P., SZLÁVIK, F., VIZI, I., these Proceedings 2, SM-104/6.
[32] COOPER, M.J., NATHANS, R., Acta Crystallogr. 23 (1967) 357.
[33] BJERRUM MØLLER, H., Risø Rep. 178 (1968).
[34] ABELN, O., DREXEL, W., GLÄSER, W., GOMPF, F., REICHARDT, W., RIPFEL, H., these Proceedings 2, SM-104/69.
[35] DAVIES, F., RODGERS, A.L., TODD, M.C.J., ROSS, D.K., SANALAN, Y., WALKER, J., BELSON, J., CLARK, C.D., MITCHELL, E.W.J., TUCKEY, G.S.G., these Proceedings 2, SM-104/116.
[36] COCHRAN, W., these Proceedings 1, SM-104/121.
[37] QUITTNER, G., VUKOVICH, S., ERNST, G., these Proceedings 1, SM-104/123.
[38] WINDSOR, C.G., these Proceedings 2, SM-104/112.

EXPERIMENTAL METHODS

(Special Session)

Chairman: H.MAIER-LEIBNITZ
Rapporteur: B.N. BROCKHOUSE

ON-LINE COMPUTER-CONTROLLED TRIPLE-AXIS NEUTRON SPECTROMETERS AT THE HFIR*

M.K. WILKINSON, H.G. SMITH, W.C. KOEHLER,
R.M. NICKLOW AND R.M. MOON
SOLID STATE DIVISION,
OAK RIDGE NATIONAL LABORATORY,
OAK RIDGE, TENN., UNITED STATES OF AMERICA

Abstract

ON-LINE COMPUTER-CONTROLLED TRIPLE-AXIS NEUTRON SPECTROMETERS AT THE HFIR . Two computer-controlled triple-axis neutron spectrometers have been constructed and installed at horizontal beam ports of the High Flux Isotope Reactor (HFIR). These spectrometers have been designed to provide maximum flexibility for use in many different types of investigations. The monochromator cavity contains both a polarizing and a non-polarizing crystal, and since either crystal can be selected and accurately positioned by external controls, the spectrometers can be modified relatively quickly for experiments requiring either polarized or unpolarized neutrons. Each spectrometer is controlled on-line by its own computer, a Programmed Data Processor-8 (PDP-8), through pulsed motors that drive up to six spectrometer axes. The advantages of this system lie in the flexibility of experiment control by stored programs on magnetic tape, which are brought into the fast memory when the conditions of the experiment dictate it. In addition to controlling the spectrometer, each computer has interfacing that allows control of auxiliary equipment such as shutters, velocity selectors, electromagnets, strip-chart recorders, and temperature controllers.

Completely automatic crystal spectrometers have recently been installed at two of the four horizontal beam ports of the High Flux Isotope Reactor (HFIR) at the Oak Ridge National Laboratory. These spectrometers, which are triple-axis instruments of the type developed by Brockhouse, have been designed to provide maximum flexibility for use in a wide variety of neutron scattering investigations. Either polarized or unpolarized neutrons can be obtained readily on monochromatization, and the third axis can be used for either polarization or energy analysis.

A schematic diagram, which indicates the main components of these spectrometers, is shown in Fig. 1. The reactor beam tubes have an inside diameter of four inches and extend into the beryllium reflector to a position where the thermal neutron flux is close to 10^{15} neutrons/cm^2/sec. Collimators within the beam tube can easily be installed and removed, and two ports through the shutter allow the selection of neutron beams with different dimensions. There is a large cavity between the shutter and monochromator shield, where additional collimating slits, neutron filters, and velocity selectors can be installed, and this auxiliary apparatus can be provided with external controls for selection and adjustment. When the shutter is closed and the beam tube is filled with water, access is permitted to this cavity during reactor operation. All three primary axes of the spectrometer can be moved continuously and automatically through large angles. The neutron energy from the monochromating crystal can be varied

* Research sponsored by the US Atomic Energy Commission under contract with Union Carbide Corporation.

over an unusually large range, because the scattering angle ($2\theta_M$) can be changed from -12° to +120°. The scattering angle from the specimen (Φ) has a range from -90° to +150°, and the scattering angle from the analyzing crystal ($2\theta_A$) ranges from -100° to +130°. The beam stop is mounted on an arm attached directly to the monochromator shield, so that it moves simultaneously with the monochromatic beam.

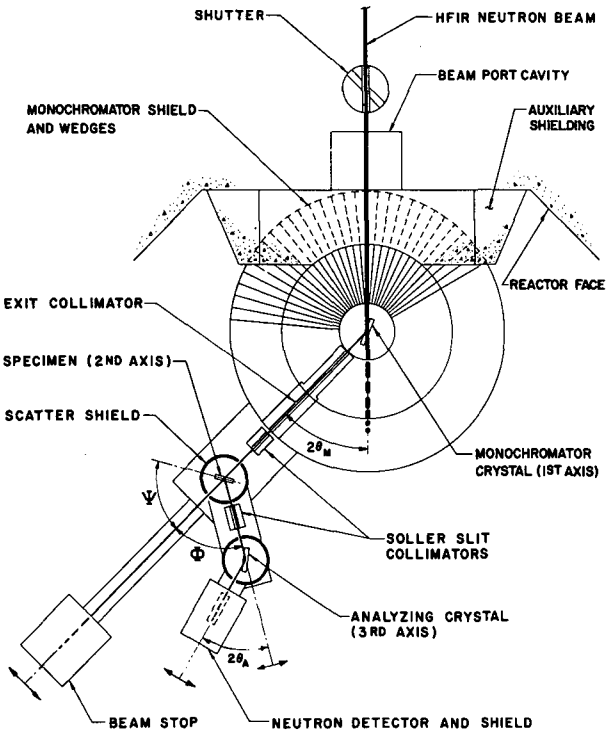

FIG. 1. Schematic diagram of triple-axis neutron spectrometer at the HFIR.

A cut-away diagram of the monochromator shield, which consists of four major sections, is shown in Fig. 2. The dome of this shield is made of Brookhaven concrete, a high-density concrete mixed with steel aggregate, and it is stationary. The shield containing the exit port for the monochromatic beam is mounted on a 40-mm gun mount and can be rotated precisely to vary the angle of scattering from the monochromator. This rotating section of the shield is also mainly of Brookhaven concrete, but the central part, which absorbs the main beam from the HFIR, is laminated steel and borated paraffin. The dome is supported on a stationary central base of Brookhaven concrete, and the entire unit shown in the figure fits snugly into a saddle shield of Barytes concrete, which mounts against the reactor shield around the beam port. As shown in the figure, the large monochromator scattering angles can be obtained without shielding problems by a system of wedges that form part of the rotating section of the shield.* These wedges are mounted on two cam tracks in the stationary

*This system of wedges is very similar to the system first designed for a triple-axis spectrometer at Brookhaven National Laboratory by A. Kevey.

dome, so that with rotation of the shield, each wedge is lifted vertically above the incident beam from the reactor. Therefore, at all positions of the monochromator shield, clearance has been provided for a neutron beam with a square cross section two inches on a side. The void in the shielding around this beam is a pie cut with an angle of about 20°. The wedges are made of laminated steel and borated paraffin, and they have been carefully adjusted to give clearance between adjacent wedges of approximately 0.025 inch.

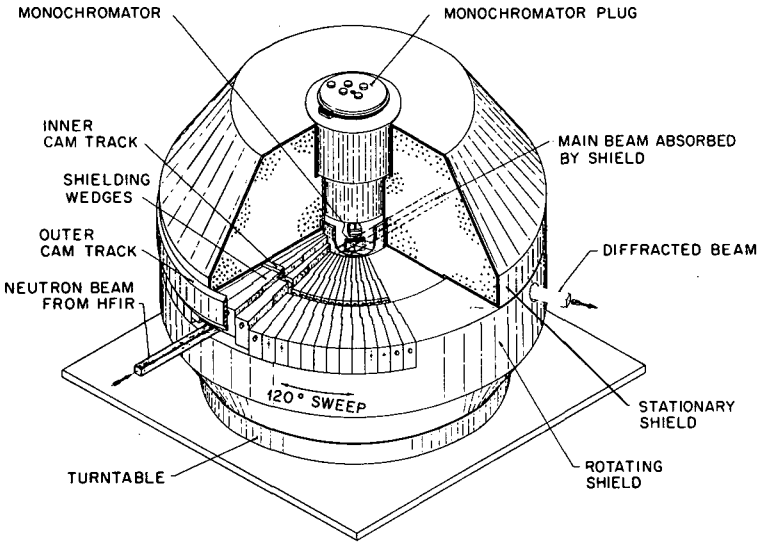

FIG. 2. Cut-away drawing of monochromator shield. (Although only one monochromator is shown, both a polarizing and a non-polarizing crystal can be attached to the monochromator plug.)

The minimum shielding in any direction through the monochromator shield is approximately 36 inches. Consequently, since there is a relatively large cavity for the monochromator, the shield is quite massive, extending 92 inches in diameter and 86 inches in height. The total weight, including the saddle shield, is approximately 84,000 pounds, and the weight of the rotating section is about one-third of the total. The entire shield is mounted on a two-inch steel base-plate that is supported on roller skids, so that it can be moved away from the reactor wall. Accurate repositioning can be accomplished easily by steel support tracks and guide tracks that have been carefully installed in the floor.

The cavity for the monochromating crystal is a cylinder that is 18 inches high with a diameter of 18 inches. This relatively large cavity was designed to permit the installation of both a polarizing crystal and a non-polarizing crystal. These crystals are suspended below the monochromator plug and controlled externally from the top of the plug. Either crystal can be selected and positioned accurately by the external controls, and when access to the crystals or to the cavity is necessary, the monochromator plug can be removed from the shield with an overhead crane. The monochromator plug is mechanically connected to the rotating section of the shield through an angle divider, which requires the monochromating

crystal to rotate at one-half the angular rotation of the exit collimator. The polarizing crystal in current use is an alloy of 92% cobalt with 8% iron, and it is mounted between the pole pieces of a small permanent magnet. The entire magnet assembly can be lowered to a position below beam height when a polarized beam is not used. The non-polarizing monochromating crystal (usually beryllium, zinc, or germanium) is mounted on a standard goniometer head, which can be raised above beam height when not in use. Since any type of slit system, including a magnetic guide field, can be installed easily in the exit collimator, the spectrometer can be converted very quickly for use with either polarized or unpolarized neutrons.

The initial operation of one spectrometer has been limited primarily to inelastic scattering investigations using unpolarized neutrons, whereas the other spectrometer has been used as a polarized beam instrument. Each spectrometer is directly interfaced to its own computer, a Programmed Data Processor-8 (PDP-8), and it is controlled by programs stored on a magnetic tape unit (DECtape 55). The interfacing includes analog-to-digital converters, digital-to-analog converters, and interrupt registers for the purpose of controlling auxiliary equipment such as shutters, radio frequency coils, electromagnets, histogram plotters, and temperature controllers. The various axes of the spectrometer are driven by Slo-syn pulsed motors. The angles Φ, Ψ, Θ, and $2\Theta_A$ are changed by 250 in-oz motors, and the rotating monochromator shield is driven through the angle $2\Theta_M$ by an 1800 in-oz motor. The smaller motors usually operate at speeds to vary the angles at a rate of 45°/min, while the large motor varies $2\Theta_M$ at 6°/min. However, these angular rates are determined by the program and they can be changed easily. The basic motor drive programs are those of Busing, Levy, and their associates [1], and the programs also permit starting and stopping at lower speeds to reduce wear on the gears.

Several computer programs have been written for various experimental techniques. These include the "constant Q" and "constant E" methods of operation (including flipping techniques for use with polarized neutrons), calculation of focusing effects, calculation of dominant higher order scattering processes, and automatic data collection and processing for form factor measurements. Although the 4000-word fast memory is sufficiently large to contain individual programs such as the "constant Q" method, it is not sufficient for all of the desired programs. Therefore, they are stored on an auxiliary magnetic tape unit, which is relatively slow but possesses a large capacity. The programs are called into the fast memory only when the conditions of the experiment dictate it.

The spectrometer that has been used for inelastic scattering investigations with unpolarized neutrons is shown in the photograph of Fig. 3. To reduce background scattering from entering the neutron detector, three special shields have been installed. The shield at the exit collimator, which is borated paraffin enclosed in Boral, reduces background from air scattering in that region and from scattering by the exit collimator and Soller slits before the sample. The shield around the sample specimen is made from Boral and must be installed to absorb the thermal neutrons scattered by Bragg reflections that occur in random directions. With large single crystals as specimens, the random Bragg scattering not only contributes to the background of the experiment, but it is a serious radiation hazard to personnel. The shield around the analyzing crystal was formed from B_4C in epoxy and it reduces the number of stray neutrons that might enter the detector from any direction. With the shielding arrangement shown in the photograph, the background not associated with scattering from the sample is approximately one neutron per minute. A low temperature cryostat is shown mounted on the sample table. This cryostat allows

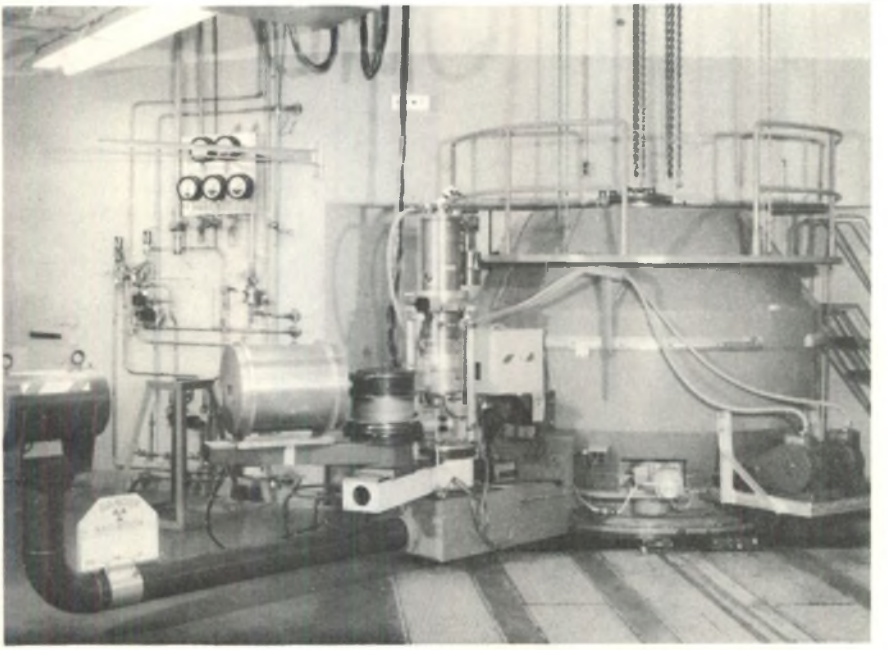

FIG. 3. Photograph of triple-axis neutron spectrometer at beam port HB-3 of the HFIR.

precise positioning of a single crystal at any temperature down to the liquid helium region. Continuous and automatic rotation of the specimen about a vertical axis is accomplished with a separate 50 in-oz pulsed motor that turns the cryostat with respect to its mounting bracket.

The second spectrometer, which is presently used in its polarized beam mode of operation, utilizes the (200) Bragg reflection of a thin rectangular 0.92 Co-0.08 Fe single crystal as monochromator and polarizer. The polarization of the beam (neutron moment up) is maintained by a magnetic collimator, which is constructed with bar magnets and soft iron sheets and produces a magnetic field of about 200 gauss inside the collimator. A radio frequency coil is used to flip the moment direction of the polarized neutrons, and this coil is located in a magnetically shielded guide field region of approximately 110 gauss. The flipping ratio, which represents the efficiency of polarization and flipping, has been measured to be 90 with a beam 3/4-in. square and 120 with a beam 1/4-in. square. An electromagnet capable of producing a magnetic field of 24 kilogauss in a 3/4-in. gap is located on the specimen table, and for flexibility of operation the magnet can be rotated about a horizontal axis to provide either a horizontal or vertical magnetic field. For some experiments additional guide field sections, consisting of small permanent magnets and soft iron, have been required to rotate the direction of polarization from vertical to horizontal and from horizontal to vertical. The system is ideally suited to investigations in which the polarization of the scattered beam is analyzed, and energy analysis is performed simultaneously. A number of experiments have demonstrated the power and versatility of polarization analysis techniques in investigations of incoherent scattering, paramgnetic scattering, magnon scattering, and magnetic structure analysis.

ACKNOWLEDGEMENTS

The authors wish to acknowledge the efforts of many scientists and engineers at ORNL, whose hard work and close cooperation helped to produce these excellent neutron scattering facilities. In particular, they wish to express their appreciation to D. L. Holcomb, who was the engineer in charge of the project, and to R. M. Beckers, J. T. Howe, J. K. East, W. E. Busby, E. S. Cantrell, E. Madden, R. T. Roseberry, and J. W. Reynolds, who participated in the detailed design, construction, and installation. They are also indebted to H. A. Levy, W. R. Busing, R. D. Ellison, and S. P. King for considerable assistance in writing programs for the computer.

REFERENCE

[1] BUSING, W. R., ELLISON, R. D., LEVY, H. A., KING, S. P., and ROSEBERRY, R. T., The Oak Ridge Computer-Controlled X-ray Diffractometer, ORNL-4143 (unpublished)(January 1968).

McMASTER UNIVERSITY NEUTRON CRYSTAL SPECTROMETERS

B.N. BROCKHOUSE, G.A. deWIT*, E.D. HALLMAN AND J.M. ROWE**
DEPARTMENT OF PHYSICS,
McMASTER UNIVERSITY,
HAMILTON, ONT., CANADA

Abstract

McMASTER UNIVERSITY NEUTRON CRYSTAL SPECTROMETERS. Three crystal spectrometers of unusual and differing designs have been constructed over the past five years. The spectrometers feature new design principles, which at once greatly decrease cost and improve instrument flexibility. In particular, the angular ranges of most variables extend upwards of 145°. Extensive use is made of commercial machinists' rotary tables; these are available with accuracy of a few hundredths of a degree and a backlash of a tenth, at modest cost.

Analysing spectrometers employ two side-irradiated helium three counters mounted on arms ~ 15 cm in length which move within cylindrical shielding. One counter records signal, the other background.

Crystals are copper slabs, normally used in reflection from (200) or (220) planes. The mosaic spreads were increased by mechanical deformation. Extensive studies of different methods of deformation have been made; the best appears to involve repeated bending and straightening of the crystal round a vertical radius (~ 90 cm) at room temperature. Improvements in reflectivity by a factor of four, and integrated reflectivities of ~ 10 minutes of arc have been obtained. The theoretical limit has not been reached, however.

At the McMaster University reactor two instruments use the same original beam, one of them an unconventional multiple-axis spectrometer which offers the possibility of use of multiple analysers. Borated water in iron tanks (protected by magnesium ingots) is used for shielding.

An instrument at the NRU reactor at Chalk River employs a dual monochromator deep within the experimental hole. After double reflection from {220} planes of two parallel crystals, the now monoenergetic beam emerges along its original direction. The specimen is at a position fixed in space, thus making spectrometer construction simple. Because of the double reflection the beam should be more than usually monochromatic and the background low.

(Double monochromators using two polarizing crystals (e.g. Fe) may provide the long-sought improved (over cobalt) monochromator for polarized beam work.)

Both spectrometers are fully automatic with all the usual capabilities. The control units employ IBM (0-24) card punches as card readers. Extremely simple logic permits complete non-linear control of six independent variables, in one or two analysing spectrometers.

I. INTRODUCTION

This paper describes a line of neutron crystal spectrometers of unusual characteristics. The design principles employed are directed towards mechanical and electrical simplicity, flexibility in operation, ease of construction and repair. Design, supervision of construction, assembly and testing of the instruments were largely carried out by graduate students. Commercial components intended for non-scientific applications were used whenever possible. Capital

---

* Post-doctorate Fellow (1966-7), now at Rutgers University, New Brunswick, New Jersey, USA.
** Now at Argonne National Laboratory. Some of this material formed part of a Ph.D. thesis (1966).

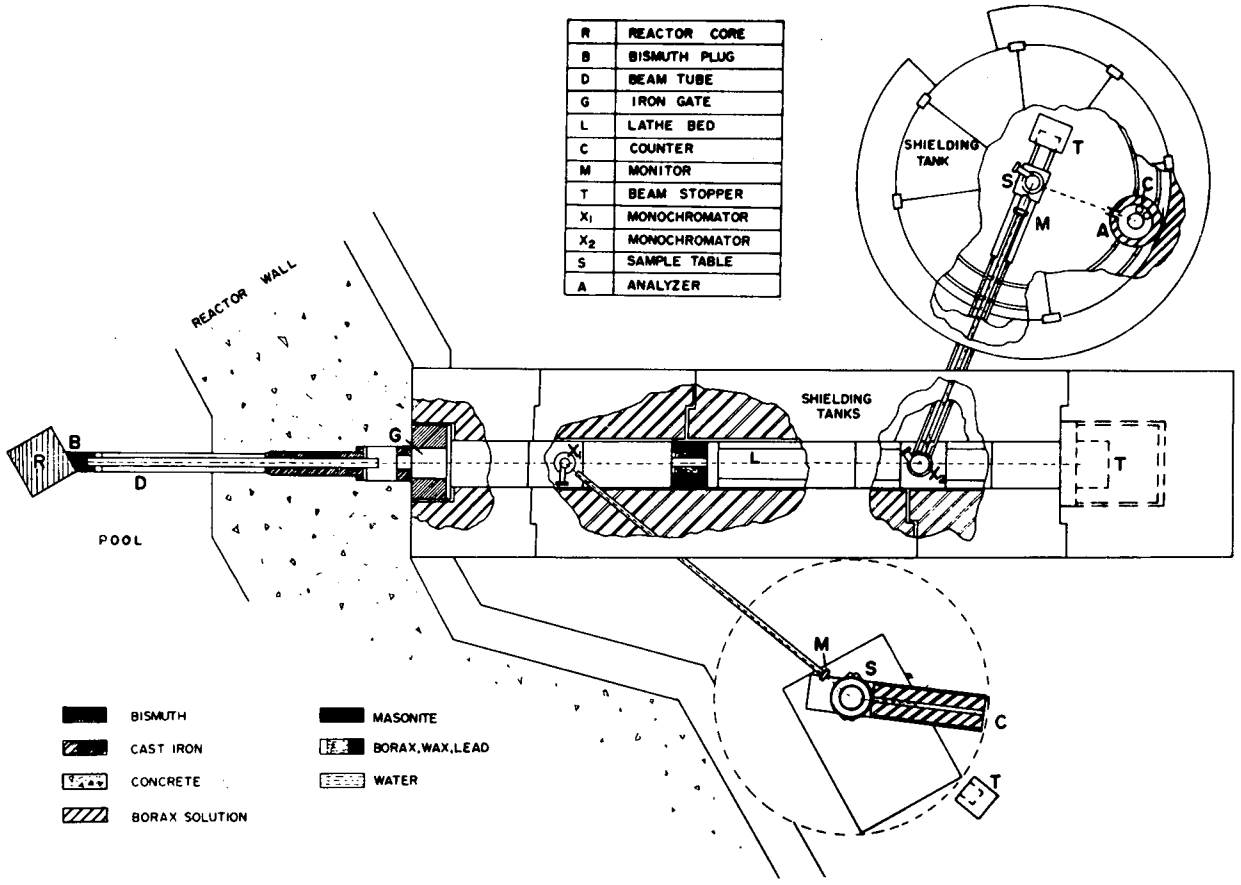

FIG.1. Schematic layout (to scale) of the spectrometer installation at the McMaster University Reactor.

costs were low in comparison with those for other instruments which have been built. The instruments (and the principles and procedures used in their design) are especially suited for Universities or Research Institutes which are isolated or lack extensive supporting facilities.

A program of improvement of monochromator crystals has been carried on with considerable success. By mechanical deformation the reflectivities of copper crystal have been improved by factors of four or more without much increase in the angular widths of the reflections. A factor of about two remains before the theoretical limit is reached.

Particularly for the McMaster installation the design was partly dictated by the rather limited space available close to the reactor.

II THE McMASTER UNIVERSITY INSTALLATION

The layout of the installation, which at present involves a powder diffractometer and an unconventional multiple-axis spectrometer, is shown in Fig. 1. The McMaster University Reactor is a light water-moderated reactor of swimming pool type, which is usually operated at 2 megawatts with a central flux of $\sim 2 \times 10^{13}$ n/cm^2/sec. The simple beam tube (3 inch diameter) commences within a re-entrant bismuth plug which reduces the fast neutron and gamma content of the beam. (It also reduces the slow neutron beam considerably, we think, and needs re-design). The simple gate (of cast iron, lead and borated plastic) is raised and lowered by a commercial chain pulley arrangement.

The large iron shielding tanks, made of 1/4 inch plate and welded construction, are filled with a solution of 0.5% borax in water. They are protected by magnesium ingots immersed in the solution and connected with the iron tanks. A current flows in such a direction as to prevent the iron going into solution.

Provision has been made to take off a monoenergetic beam by reflection from a fairly transparent monochromator (Al and Si have been used) to supply the fairly conventional powder diffractometer shown at the bottom of Fig. 1. The monoenergetic beam is brought out through a horizontal slot (8 cm. high) in the tank. The fixed take-off angle (38.7° at present) can be changed, though with some difficulty.

The instrument has lately been modified from the state shown in Fig. 1 to include an auxiliary third axis, in addition to the ordinary detector. An aluminum crystal is used as monochromator at all times and need not be changed The instrument is then used for powder work in the ordinary way. A perfect crystal is mounted on the auxiliary axis. For studies of rocking curves, etc. the beam is successively diffracted in parallel position by the monochromator, the specimen and the auxiliary perfect crystal into the detector. Rocking of the specimen crystal gives its true rocking curve

unbroadened by the monochromator (provided that the interplanar spacings of the specimen and the perfect crystal are the same).

The white beam from the reactor continues through a three inch aperture to the monochromator for the second instrument. Since this is (at present) the final instrument in the series, a copper monochromator crystal is used here. The monochromator is mounted on a half-angling mechanism, which in turn is mounted on a lathe bed along the line of the white beam. The design is somewhat similar to that of the Chalk River rotating crystal spectrometer [1]. When the monochromator is moved along the lathe bed and the half-angling mechanism is suitably adjusted, the monoenergetic beam passes through horizontal slots in the tanks to the fixed specimen position S within the circular shielding tank.

The specimen is mounted on a motor-driven and cam-indexed rotary machinist's table. The specimen is observed by analyzing spectrometer(s) which are constrained to move on a large machined casting of diameter 90.221 inches (circumference 7.2 metres). A steel machinist's rule stretched around the casting reads the angular positions (ϕ) of the analyzers directly in fractions of a degree (1 cm. = 0.50^{o}). The analyzers are moved by motor-driven spur gears which engage a standard 24 pitch steel rack, circularly mounted on the casting. With the chosen diameter of the rack circle, each tooth in the rack represents 0.20^{o} in ϕ.

The half-angling mechanism for the monochromator is a modified version of one described earlier [1]; it uses steel ball bearings to achieve the half angling instead of roller bearings. The rotation of the half-angler is coupled to the motion along the lathe bed by telescopic rods which pass through a second horizontal slot in each of the tanks from the specimen position to the half-angular. Thus the monochromator crystal is always properly oriented. It was originally hoped that the energy would be continuously variable; so far, however, it has been necessary to keep the slots filled with shielding material in order that the background might be acceptable ($\sim$ 0.4 cpm).

The analyzers (or detectors) are not mechanically coupled to the specimen position; instead they are carried on wheels which move in circular v-grooves cut in the large casting. Thus the analyzers are constrained to view the specimen from the desired angle. This method of construction is extremely flexible and provides large angular coverage ($-160^{o} < \phi < 160^{o}$). The instrument could readily be converted to entirely different uses, such as a curved crystal spectrometer.

The intent in the original design had been to use many analyzers for a single specimen. So far, this has not been done, for operational reasons. Up to ten analyzers could be used with the existing designs,and, indeed, the recording capability for ten detectors was provided in the original instrumentation.

Aside from the casting discussed above, all angular motions in the three instruments are provided by machinist's rotary tables. Sixteen of these are used in various applications, ranging from six-inch tables [B. Elliott, U.K., load ~ 50 kg., ~$200 each] to twenty-five inch tables [Troyke, U.S.A., load ~500 kg, ~ $1500 each]. All have precisions of better than 0.02° or 0.03° and backlash of less than 0.1°.

The tanks and other apparatus were designed with a particular view toward flexibility in future use. They can be re-assembled in various configurations. The end tank (extreme right) has provision for bringing out a white beam, and also for installation of a third instrument, which would employ the double monochromator principle (§ III), but with the two monochromators reflecting in the vertical plane.

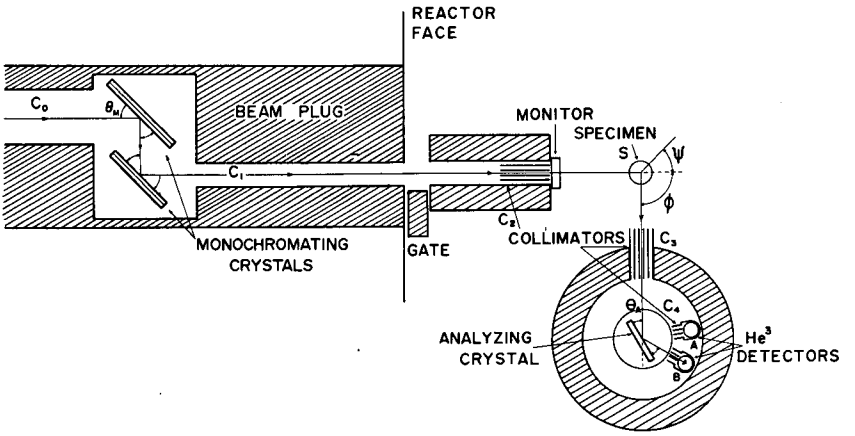

FIG. 2. Schematic layout (not to scale) of the spectrometer at the NRU reactor. The double monochromator uses (220) planes of copper in reflection. The monitor counter is a ^{235}U fission counter.

III THE McMASTER UNIVERSITY SPECTROMETER AT CHALK RIVER

A spectrometer of unusual and successful design was installed at hole E2 of the NRU reactor at Chalk River in June, 1967, and has been in continuous use since then. The schematic diagram is shown in Fig. 2. The spectrometer employs a double monochromator in which the monoenergetic beam is reflected in succession from two matched crystals in parallel positions. The crystals are rigidly mounted on a machinist's table deep within the reactor hole. The initial collimator (C_0) is about twice the width of the outgoing collimator (C_1). A reflected beam is obtained for scattering angles ($2\theta_M$) of ~ 60° to 120°, which are changed by rotation of the table.

For the monochromators used, (220) planes of copper, the limits are 1.28 Å < λ_o < 2.21 Å or 50.1 meV > E_o > 16.7 meV.

The most useful features of the spectrometer arise from its simplicity and resulting low cost. Because only the

monochromatic beam emerges from the reactor hole, the shielding required is comparatively modest. The specimen position is fixed in space independent of the incident energy, and as a result, the design of the rest of the apparatus is greatly simplified.

In addition, the beam should be of unusual purity because of the double reflection, and the background should be unusually low. We have not yet fully realized these advantages, partly because of some errors in design. It would be better if a Soller slit collimator were inserted in C_2, and a set of horizontal Soller slits placed between the two monochromating crystals. It is necessary for the reflecting planes of the crystals to be accurately parallel, but the two crystals should not have any other principal planes parallel to each other. The existing monochromators are, in fact, aligned parallel in both ways; as a result a weak contaminant is present, produced by double reflection from (331) planes. This last defect is particularly annoying because we had actually thought of this difficulty, and then forgot it at the crucial stage. We hope to change the instrument to conform to these ideas in the near future.

The loss in intensity occasioned by the use of the double monochromators depends on the efficiencies of the two monochromators. Considerable efforts were made to obtain as high efficiencies as possible (§V). We believe our losses to be of the order of factors of 3, depending on the wavelength. While this apparatus was under construction we learned of a somewhat similar project being undertaken by R. Stedman at Studsvik, Sweden. The detailed arrangements are, however, very different.

IV THE ANALYZING SPECTROMETERS

The analyzing spectrometers used in both instruments are shown to scale in Fig. 3, with a horizontal view in Fig. 2. Two detectors are used, which view the analyzing crystal through identical Soller collimators; one counts Bragg-scattered neutrons, the other diffusely-scattered neutrons. The first gives the signal, the second gives a result which approximates the background and which indicates certain types of contaminant peaks.

Cheap and standard components were used as far as possible because it was intended to build a considerable number of the analyzers for use in multiple detector systems. The small and simple solid state amplifier/discriminators are mounted close to the detectors, which move inside the fixed boron/paraffin shielding. Separate drives are used for the crystal and detector tables; half-angling is electrical.

The Soller collimators used are considerably modified versions of a Chalk River design. They are produced by milling parallel slots in brass or aluminum plates using ganged jewellers saws. They are quite cheap. Slit spacings of 0.6 mm are produced with lengths up to 20 cm. or more. Cadmium-

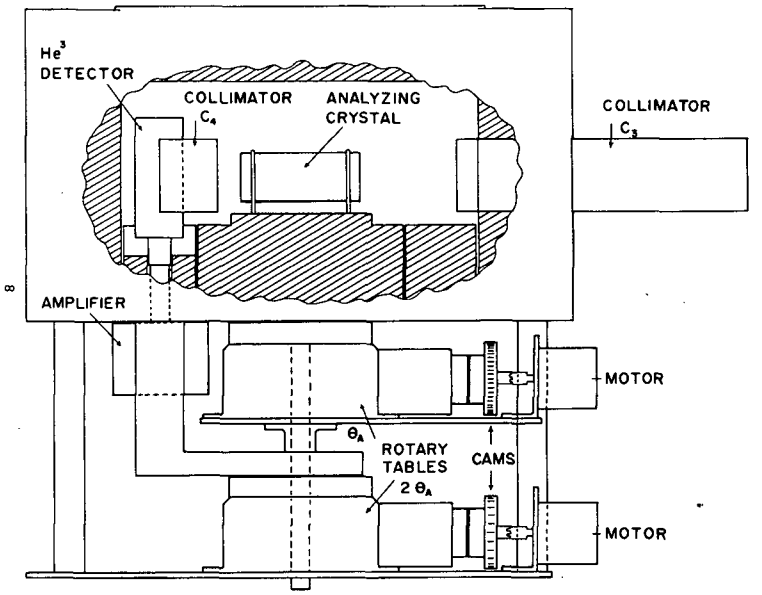

FIG.3. The analysing spectrometer (to scale).

plated steel shim stock is used for the separators. Separators can be easily inserted or removed, and are used in the numbers needed for the angular acceptance desired.

V MONOCHROMATOR CRYSTALS

In the absence of extinction the figure of merit for the reflectivity of a crystal is easily seen to be given by the approximate expression

$$\frac{\lambda^3 L}{\sin 2\theta} \frac{|F_o|^2}{v^2}$$

where L is a length, either a measure of the maximum permissible size, from physical considerations, for a crystal which removes neutrons only weakly from the beam, or a characteristic length for removal of neutrons from the beam by absorption, scattering etc., F_o is the usual elastic structure factor (i.e. the scattering length b for a crystal with one atom per unit cell), and v is the volume of a unit cell. Of metallic crystals Be is far and away the most promising monochromator according to this criterion. Of other metallic crystals with natural isotopic content which are easily obtainable as large crystals, Cu offers probably the best possibilities; though not quite as good as Fe, it is considerably better than Al and still more so than Pb (at room temperature).

Large copper slabs (5 cm x 15 cm x 1.2 cm), obtained from Research Crystals Inc. of Virginia, were used as monochromators. The crystals were oriented with (200) or (220) major faces.

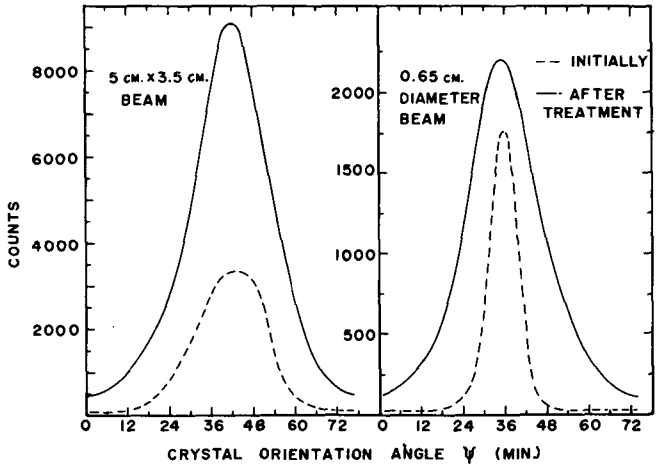

FIG. 4. The intensity of 1.30-Å neutrons Bragg-reflected from a (200) plane of copper crystal, in parallel position with the monochromator (the 220 plane of a comparatively perfect silicon crystal), as a function of the orientation of the copper crystal, for the copper crystal as received and after several deformations.

The crystals were studied by rocking them in parallel position against the (220) plane of a comparatively perfect silicon crystal. Some results for one such crystal are shown in Fig. 4. With the full beam (left), some of the reflected neutrons miss the detector. With a smaller diameter beam (right), the detector collects nearly all the scattered neutrons and an absolute reflectivity can be obtained:

$$R \equiv \int r(\psi)\,d\psi = \int \frac{I(\psi)\,d\psi}{I_o}$$

where I_o is the main beam intensity measured with the detector in the straight-through position ($\phi=0$), and ψ is the crystal orientation angle.

From Fig. 4 several features can be seen. As received, the crystals often showed greater rocking curve widths for the large beam than for the small, indicating the presence of large scale misalignment of different parts of the crystal. The reflectivities (R) of the crystals as received were quite low-typically 1 or 2 minutes of arc, (see Table I).

The crystals were deformed in various ways, including, among others, those listed in Table I, with considerable increases in reflectivity resulting. The widths of the rocking curves also increased. Obviously deformation could profitably be continued at least to the point at which the small and large beam curves had similar widths. Saturation occurred, however, and often no improvements were effected beyond a certain number of deforming operations. Bending of the crystal was carried out in the plane normal to the reflecting plane and to the plane of reflection, in order to minimize residual effects after straightening of the crystal again.

TABLE I

Integrated Reflectivities and Mosaic Spreads (FWHM) of Some Deformed Copper Crystals (λ=1.30 Å)

Crystal and Major Plane		Deformation Type	Stress, (Lb/in^2)	Rocking Curve Width (Min.) W	Reflectivity (Min.) R
1	(200)	As Received		9 ± 2	2.4 ± 0.2
		Straight Press	5000	25 ± 2	8.2 ± 0.2
2	(200)	As Received		17 ± 2	7.5 ± 0.2
		2-36" Radius Bends	2000	20 ± 2	8.7 ± 0.2
		6-36" " "	2000	32 ± 2	9.5 ± 0.5
3	(200)	As Received		12 ± 2	1.6 ± 0.2
		6-48" Radius Bends	500	14 ± 2	5.5 ± 0.5
		Straight Press	2000	16 ± 2	6.4 ± 0.5
		2-36" Radius Bends	600	14 ± 2	6.8 ± 0.5
		2-36" " "	4000	20 ± 2	6.6 ± 0.5
		Straight Press	10,000	23 ± 2	6.8 ± 0.5
4	(220)	As Received		14 ± 2	1.2 ± 0.2
		2-36" Radius Bends	400	22 ± 2	6.6 ± 0.2
		1-36" " "	1300	22 ± 2	6.9 ± 0.2
		1-36" " "	2000	22 ± 2	7.3 ± 0.2
		3-36" " "	2000	24 ± 2	8.7 ± 0.5
		3-36" " "	4000	32 ± 2	8.9 ± 0.5
		1-24" " "	3500	31 ± 2	8.5 ± 0.5
5	(220)	Initially Straightened	250	28 ± 2	8.1 ± 0.5
		2-36" Radius Bends	800	32 ± 2	10.0 ± 0.5
		1-36" " "	3500	27 ± 2	8.4 ± 0.5

After each bending the crystal was straightened by a straight press at the same stress as that used for the bending.

Calculations of the integrated reflectivities expected for an ideally imperfect absorbing crystal were carried out following Bacon and Lowde (see ref [2]). The results are shown in Fig. 5. If the mosaic width is identified with the width of the rocking curve, then the measured reflectivities can also be plotted. It can be seen that the measured values lie much too low - by a factor of about two. The model of an ideally imperfect crystal - one in which there is a Gaussian distribution of "mosaic blocks" and no primary extinction - does not seem to hold very well. It is probable that calculations for this model give the maximum possible reflectivity

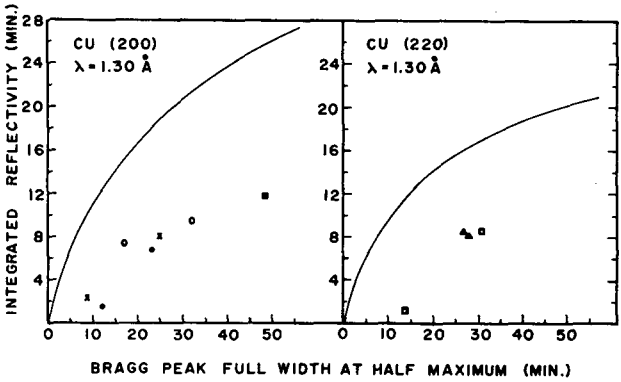

FIG. 5. The measured and calculated integrated reflectivities for a number of copper crystals, plotted as a function of the widths of the rocking curve (for the small beam). Where the same symbol is used more than once it indicates the same crystal in different states of deformation.

and thus give an upper bound to the theoretical reflectivity. At the same time inadequacies in the experiments probably tend to lower measured reflectivities. Even so, the possible gain of an additional factor of two in reflectivity is worth considerable effort, especially in view of the fact that any improvement is squared or cubed, since more than one monochromator is used in the apparatus.

More complete results will be presented elsewhere. Additional work remains to be done.

VI CONTROL UNIT AND ELECTRONICS

The electronics are comparatively conventional and will not be described here. The control units offer complete non-linear control [1] of up to six variables (eg $2\theta, \phi, \psi$ etc). They are based upon IBM 0-24 card punches which are used as card readers.

The duplicating feature of the punches includes "reading" of cards. Each lateral advance of the card provides potentially 12 bits of information, corresponding to the twelve horizontal rows on the card. A punch in a certain row instructs a certain motor-driven variable to move one increment in a particular direction. Thus the twelve rows provide for instructions to six variables to move in one of two directions, right or left. Since a particular variable cannot move in two directions at once, many combinations are forbidden as instructions for movement of variables. These "forbidden combinations" can be used as operational instructions, e.g. "count", "insert filter", "turn on magnet", "skip to new card" etc. No auxiliary store is employed; the card advances laterally one column, the instructions in it are executed, and then the card advances to the next column, etc. This simple logic makes the control unit reliable and cheap.

As far as the control unit is concerned the nature of the variables concerned, or the increments in which they move, does not matter. In the spectrometers described here, single increments of 0.1^{o} in the angular variables are employed. Thus in "constant Q" and similar applications, round-off errors of up to 0.05^{o} are encountered. The six variables give the usual non-linear capabilities for two analyzing spectrometers, or capability for three-dimensional work with a single spectrometer.

VII THE DOUBLE MONOCHROMATOR

In the double monochromator arrangement the two crystals are similar and in parallel position. A neutron reflected from the planes of a particular "mosaic block" in the second crystal has been reflected from a "mosaic block" in the first crystal whose planes are exactly parallel to the mosaic block originally considered.

The integrated reflectivity for the combination is thus given in terms of the reflectivities of the individual crystals by

$$R_c = \int_{-\infty}^{+\infty} r_1(\psi) \quad r_2(\psi) \quad d\psi \ .$$

The expression bears out the intuitively obvious "rules-of-thumb" that, for best results, the two crystals should be arranged exactly parallel and have approximately equal rocking curves $r_i(\psi) = r_i(\psi - \psi_{oi})$.

If the rocking curves are assumed to be Gaussian and we let $x = \psi - \psi_o$, then

$$r_1(x) = \frac{R_1}{\sqrt{2\pi}\ \sigma_1} \exp\left(-\frac{x^2}{2\sigma_1^2}\right) \qquad \text{etc.}$$

where R_1 is the integrated reflectivity. If $R \equiv R_1 \simeq R_2$ and $\sigma \equiv \sigma_1 \simeq \sigma_2$ then the integrated reflectivity of the combination is:

$$R_c = \int_{-\infty}^{+\infty} \frac{R^2}{2\pi\sigma^2} \exp\left(-\frac{x^2}{\sigma^2}\right) dx$$

$$= \frac{R^2}{\sigma} \quad \frac{1}{2\sqrt{\pi}}$$

The ratio of the reflectivity for the double monochromator to that for a single component R_c/R, is given by the expression

$$\frac{R_c}{R} = \frac{R}{\sigma} \quad \frac{1}{2\sqrt{\pi}} = 0.663 \ \frac{R}{W} \ .$$

where W is the F.W.H.M. of the rocking curve.

If the rocking curve were square rather than Gaussian then the ratio R_c/R would haye the value R/W.

It should be noted that the "width" of the combined rocking curve is smaller than that of the individual curve, for Gaussians by a factor $\sqrt{2}$. Thus, the resolution will be improved over that obtained with the corresponding single monochromator.

For the two crystals (#4, #5) which were used in the Chalk River instrument, the results of Table I show that

$$\frac{R_c}{R} \simeq 0.2$$

for a wavelength of 1.30 Å. For the wavelengths $1.28 < \lambda < 2.21$Å employed in the instrument, the ratio should be considerably better.

ACKNOWLEDGEMENTS

The authors wish to thank the members of their group at McMaster, Dr. S. H. Chen, Dr. E. C.Svensson, Mr. S. C. Ng, Mr. A. P. Miiller, Mr. W. A. Kamitakahara and Mr. J. R. D. Copley, for contributions to the design and construction of the instruments, and for many of the computer programs which are used with the instruments. In particular, Dr. Chen carried out the original design of the diffractometer at McMaster, and Dr. Svensson wrote the original "constant $\vec{Q}$" and "constant E" programs for the instruments. We are grateful also to Mr. P.D. Stevens-Guille and the Engineering Branch of A.E.C.L. at Chalk River for carrying out the detailed design of the in-pile plug for the Chalk River spectrometer, and to the authorities and staff at Chalk River for their enlightened policy and valuable co-operation in this program. The work was supported by grants from the National Research Council of Canada and two of us (E.D.H. and J.M.R.) held NRC postgraduate studentships.

REFERENCES

[1] BROCKHOUSE, B.N., Inelastic Scattering of Neutrons in Solids and Liquids, IAEA, Vienna,(1961) 113.

[2] BACON, G.E., Neutron Diffraction, Oxford Press, London, (1962).

THE BATTELLE NORTHWEST ROTATING CRYSTAL AND PHASED CHOPPER SLOW NEUTRON SPECTROMETER*

O.K. HARLING
PACIFIC NORTHWEST LABORATORY,
RICHLAND, WASH.,
UNITED STATES OF AMERICA

Abstract

THE BATTELLE NORTHWEST ROTATING CRYSTAL AND PHASED CHOPPER SLOW NEUTRON SPECTROMETER. A hybrid spectrometer consisting of a phased chopper and rotating crystal is described. This system combines the advantages of a crystal monochromator with the time-of-flight method of analysing scattered neutron spectra. A coarse chopper, 80% transmission, is phased with the rotating crystal to provide suppression of order contamination and reflections off unwanted planes as well as a substantial reduction in background due to fast neutrons and incoherently scattered slow neutrons. The chopper can also be used to convert the spectrometer to a time-of-flight diffractometer.

The monochromating section of this spectrometer permits the selection of neutron energies from ~ 15 to ~ 1000 meV. This wide range of operating energies is achieved with conservative operating conditions for the rotors which have functioned with high reliability. Burst widths at the sample positions of 8-12 μsec are obtained for typical operating conditions. Collimator angles from 0.08° to 1.75° are readily available. Copper and aluminium single crystals have been used in the crystal rotors. These are usually oriented so that the 001 axis is the rotation axis. This orientation provides four reflections from the (200) or the (220) planes per revolution and permits use of even narrower spacing planes like the (240).

Intensities are adequate for typical inelastic scattering experiments even at energies of ~ 0.5 eV where most phased chopper systems cannot operate or do so with rather poor resolution. For example, at 0.25 eV the pulsed beam intensity is ~ 5.6×10^4 neutrons/min with $\Delta E_0 = 1.46\%$ and a Δt_0 of 12 μsec at the 4-m detector bank. The scattered neutron spectra are analysed by time-of-flight simultaneously at 11 angles in the range from 15° to 165°. High pressure ^{3}He counters are used for detectors. The performance and operating experience with the spectrometer is discussed. Typical experimental results are shown. Possible areas for improvements are described.

I. INTRODUCTION

The Battelle Rotating Crystal Time-of-Flight Spectrometer[1] (RXS) uses a rotating crystal monochromator and a phased chopper to produce a high quality, pulsed, monochromated beam. This hybrid system has now been in successful operation for several years. Improvements in performance over the original configuration have been obtained by various refinements. These include development and use of better time-of-flight (TOF) detectors and the addition of a movable long flight path. Performance and typical results with the present configuration will be presented here, along with possibilities for future improvements.

II. DESCRIPTION OF THE SPECTROMETER

A. General Arrangement

The schematic diagram of Fig. 1 shows the general arrangement of the mechanical components of the RXS. A white beam is

* Work performed under US Atomic Energy Commission Contract AT(45-1)-1830.

obtained for this spectrometer from one of the Hanford production reactors. A pulsed monochromatic beam is obtained for TOF scattering studies by the combined action of a mechanical chopper and a rotating single crystal. The chopper, which operates in phase with the crystal rotor, has a duty cycle of about 4%. At 6000 rpm the chopper bursts are ∿100 μs wide. With the 2 m flight path between chopper and crystal this provides adequate time resolution to prevent significant reflection of neutrons from unwanted crystal planes and to eliminate order contamination. At this modest speed of 6000 rpm first order neutron energies up to 0.5 eV can be selected without other

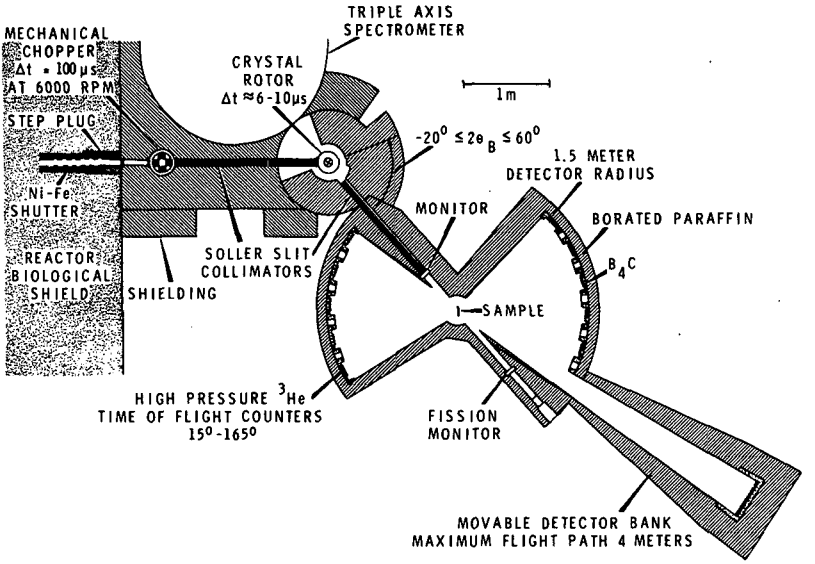

FIG.1. Plan view of Battelle Northwest rotating crystal spectrometer.

Bragg contamination. Increases in rotor speed to 9000 rpm permit use of neutrons with energies to ∿1.0 eV. Initial energies down to ∿0.015 eV can be used but emphasis has been in the tenth eV range. An important function of the coarse chopper, and one which greatly improves the quality of the monochromated beam, is the reduction in the number of neutrons which can be incoherently scattered from the rotating crystal. The cost in intensity for using this mechanical selector is 20% for typical operating energies. In addition to selecting crystal planes with different spacings, the energy resolution can be varied over a wide range with Soller slit collimators. Each collimator is about 1.5 m long and permits a maximum beam size of 5 x 10 cm. Nickel or steel shims can be inserted to vary the collimation from 1.75° to 0.08°.

The pulsed Bragg beam is scattered from the sample and the scattered neutron spectra are analyzed by TOF in the conventional manner. Scattering detectors are inside a completely shielded scattering chamber. The TOF detectors can be located at any angle from 15° to 165° on flight paths of 1 and 1.5 m. A movable flight path is also available which has a maximum sample

to detector distance of 4 m. This long flight path can be used at scattering angles of 15°, 90°, or 150°. It is particularly valuable in looking at small angles or small k scattering where the best possible resolution function is desirable.

B. Crystal Monochromators

Optimum monochromators for rotating crystal spectrometers are more difficult to obtain than for stationary crystal arrangements. Additional requirements like high mechanical strength must be met. It is desirable, in an arrangement like the RXS, to rotate about an axis of high symmetry; for example the 001 direction for a cubic crystal. This permits the selection of several different d spacing planes merely by adjusting the phase of the chopper and crystal rotors. In this way one can also obtain more than two monoenergetic bursts per revolution. In order for this selection to be successful, a monochromator must be obtained which has good reflection properties from the several planes of the same type which come into the Bragg condition during one revolution and the same must hold true for any other set of planes which is to be used with the same orientation of the monochromator. The monochromators we are using on the RXS are principally cylinders of aluminum and plates of copper. The aluminum cylinders are 10 cm high by 3.8 cm in diameter and are rotated about the cylinder axis which is also the 001 crystallographic direction. This arrangement permits use of the (220), (200), and (240) planes in transmission. The copper crystal is a plate 0.75 cm thick, 4.5 cm wide, and ∿9 cm high. It is cut with the (200) plane parallel to the face of the plate and is also rotated about the 001 direction. This geometry gives good results with the (220) planes which are in the transmission mode.

Although the monochromators we are using on the RXS are adequate, we know that substantial improvements are achievable. We are currently using a beryllium monochromator on the Battelle 3-Axis Spectrometer[2] which has two to three times better reflectivity than the copper and aluminum crystals used on the RXS. Unfortunately it is difficult to obtain good beryllium crystals and we have therefore used another approach. Single crystals like copper can be easily obtained with rather high perfection. In fact, this perfection is one of the main problems with their use. Secondary extinction can be very severe in even thin plates of copper. Thin slabs (∿1.5 mm) of a similar single crystal to that used for the rotating crystal monochromator, mentioned above, exhibited increases in reflectivity of a factor of two when deformed plastically. By making composite crystals composed of thin copper slabs we have produced higher integrated reflectivities and mosaics tailored to the needs of the spectrometer. A composite crystal composed of two copper slabs, each 0.20 cm x 2.5 cm x 10 cm, was fabricated for use as a rotating crystal. The two slabs were carefully oriented, and then plotted in an aluminum sleeve with a low melting point alloy of bismuth and thin. This monochromator had approximately 50% greater reflectivity in transmission than a single crystal slab of about the same size. Indicative of what may be accomplished with this slab technique is the result obtained at our laboratory by Smith[3] who used 5 cold worked slabs of copper crystal to fabricate a composite monochromator

with a total thickness of 0.9 cm. This composite had an integrated reflectivity of ∿3 times that of an equal single thickness of unworked copper crystal. Measurements were made in the transmission mode using the (200) plane and with the slabs adjusted for a 0.3° mosaic. The performance of this 5 slab composite is comparable with that obtained with a good beryllium crystal.

C. Time-of-Flight Detectors

Good TOF detectors for inelastic scattering should combine a number of characteristics which include high efficiency, good signal to noise ratio, low inherent background, reliability, ease and reproducibility of calibration as well as a small contribution to the resolution function. The latter requirement means that the counter must be sufficiently thin in space and the electronic jitter must not be excessive.

After studying the available possibilities, we obtained high pressure ^{3}He proportional counters made to our specifications. These counters have 8 atm of highly enriched ^{3}He, several percent methane and ∿0.1 atm krypton which is used to improve the pulse height distribution by increasing the stopping power of the filling and for matching the gas gain of the various counter tubes. The resolution element due to the thickness of these counters is unimportant for the 4 m flight path. Electronic jitter[4] is ∿0.75 μs and therefore is negligible. Operating characteristics of these counters seem to leave little to be desired. Their pulse height distribution, Fig. 2, is very sharp with a FWHM for the thermal peak of ∿12% for a single counter tube. They can be set to within ∿1% of the same operating efficiency merely by use of an oscilloscope. Efficiency for 0.1 eV neutrons is 68% compared to 15% for the previously used 2 atm BF_3 tubes.

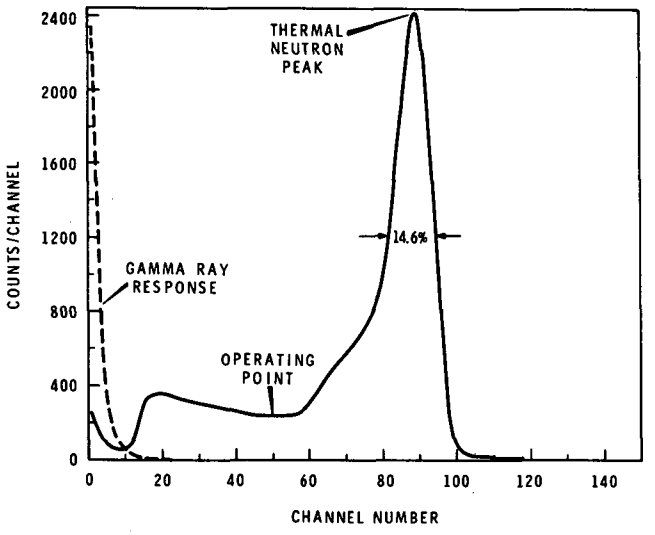

FIG. 2. Pulse height distribution of 5-8 atm ^{3}He counters. Solid curve is neutron response and dashed curve is response for a 2 mR/h ^{137}Cs source.

For typical experiments with the RXS 5 counter tubes are used at each scattering angle to give a detector solid angle of ∿0.022 sr. Thirty tubes must be used at 4 m to obtain approximately the same solid angle. Since high efficiency counters of this type are expensive this illustrates one of the problems involved in using longer flight paths. Other problems in increasing the flight path are the need for better shielding since the background goes up with the square of the flight path while the signal remains constant assuming a fixed detector solid angle. For large area detectors of the type required at distances like 4 m the inherent or unshieldable background component can become an important problem. We have found that the lower operating voltages of the ^{3}He counters contribute greatly to reduction in spurious backgrounds.

D. Time-of-Flight Diffraction

It is interesting that the RXS system which is designed for inelastic scattering, is also suited for TOF diffraction measurements. By bringing the second collimator to the zero degree position the RXS can be operated as a TOF diffractometer. Diffraction measurements can be made with a sample placed in the

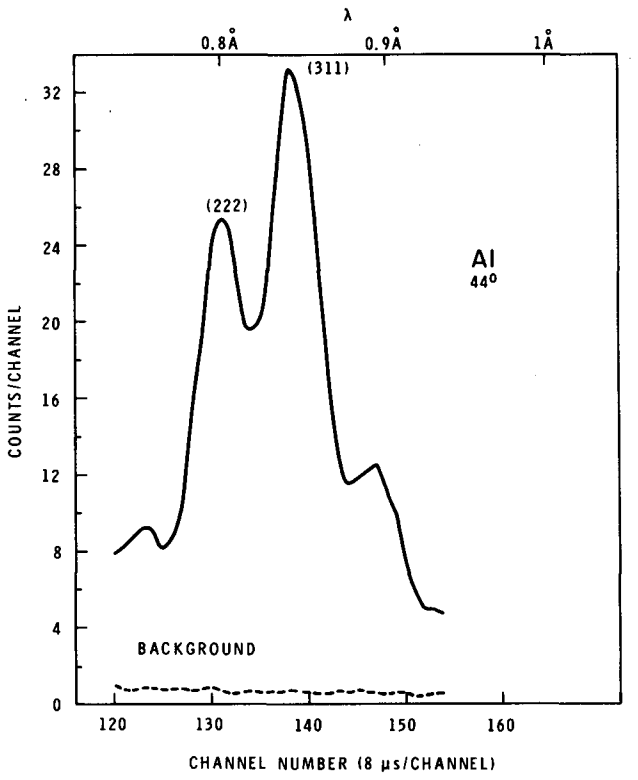

FIG.3. Part of diffraction pattern obtained with chopper of RXS at 6000 rpm. Sample is 1.75-cm thick slab of polycrystalline aluminium.

normal sample position. With the angular spread of the counter banks decreased for adequate angular resolution, TOF diffraction spectra can be obtained simultaneously for a range of Bragg angles if desired. This has the advantage that most of the various crystal planes can be observed at a Bragg angle where neutrons will be coming from the most intense part of the reactor spectrum. Data can, of course, be combined from the various scattering detectors by computer technique so that shorter running times are possible than for single angle TOF diffractometers.

With the present coarse chopper and no modifications we have obtained a time resolution $\Delta t/t$ of $\sim$4% for 0.025 eV neutrons with a chopper speed of 6000 rpm and TOF detectors placed in the 1.5 m detector positions. This resolution is adequate to separate the (222) and (311) reflections in a polycrystalline aluminum sample at a scattering angle of 44°, Fig. 3. Higher chopper rpm and use of the 4 m flight path would improve the time resolution by a factor of $\sim$2. Running time for data of the quality shown in Fig. 2 is only a few minutes using a 10% scatterer. It is clear that count rate can easily be traded for resolution by the addition of a simple low speed chopper or by insertion of additional collimation into the existing chopper. If, in addition, TOF diffraction data is accumulated simultaneously at a number of scattering angles, a competitive diffractometer results.

In addition to the added capability of being able to use an inelastic scattering spectrometer for diffraction, which might be of considerable advantage to small laboratories which cannot justify two separate instruments or two separate reactor beam holes, there may be unique advantages to such an arrangement in special cases. For example, if the sample is difficult to move which might be true for high pressure cells or low temperature experiments and it is desired to have both diffraction information from the sample, then the multipurpose spectrometer could have considerable advantages.

III. SPECTROMETER PERFORMANCE

In the design and operation of the RXS high resolution has been emphasized. Figs. 4 and 5 show some calculated resolution on downscattered neutrons and on energy change for an initial energy of 0.25 eV. The Soller slit collimation is 0.139° which approaches the best (0.08°) angular resolution available. The monochromator is Cu (220) in transmission. Resolutions are given for counter banks at a 15° scattering angle, flight paths are 1.5 and 4.0 m, rotor speeds are 6000 rpm and a 3.8 cm x 10 cm sample is assumed. Measured intensity under these operating conditions is 5.6×10^4 n/min on the sample. This is not a high intensity but is adequate for many scattering experiments.

Figure 6 presents raw data taken with a $\sim$10% scattering sample of $ZrH_{0.5}$. Running time was 2 days. Time-of-flight data are shown for the 30° counter bank at a flight path of 1.5 m and for the 15° counter bank at 4.0 m. These spectra were obtained simultaneously with counters of about the same solid angle, 0.02 sr. The one phonon vibration peak in the metal

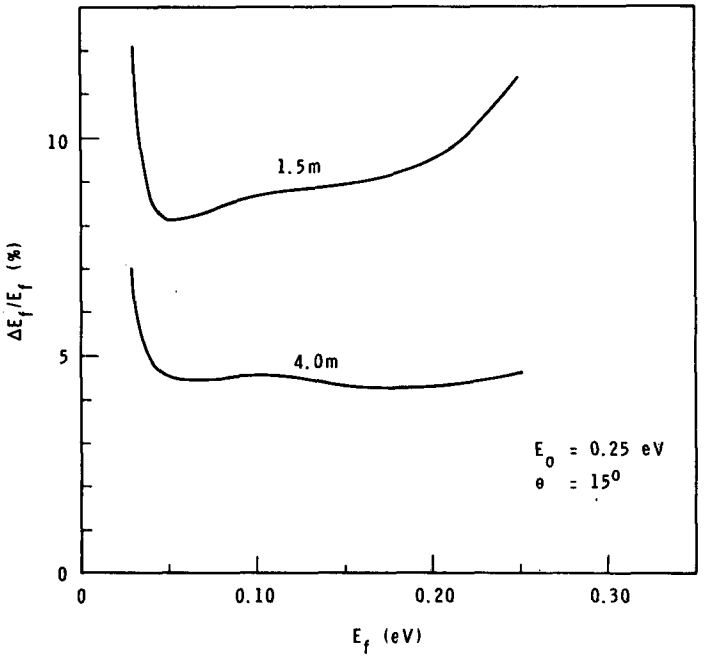

FIG.4. Resolution on scattered neutron energy, E_f.

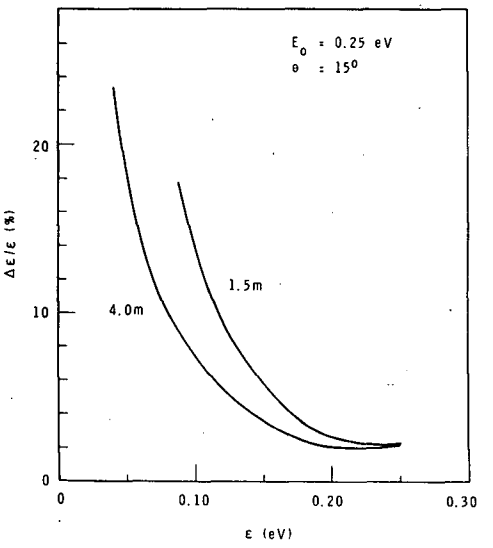

FIG.5. Resolution on energy change, $\epsilon = E_{0i} - E_f$.

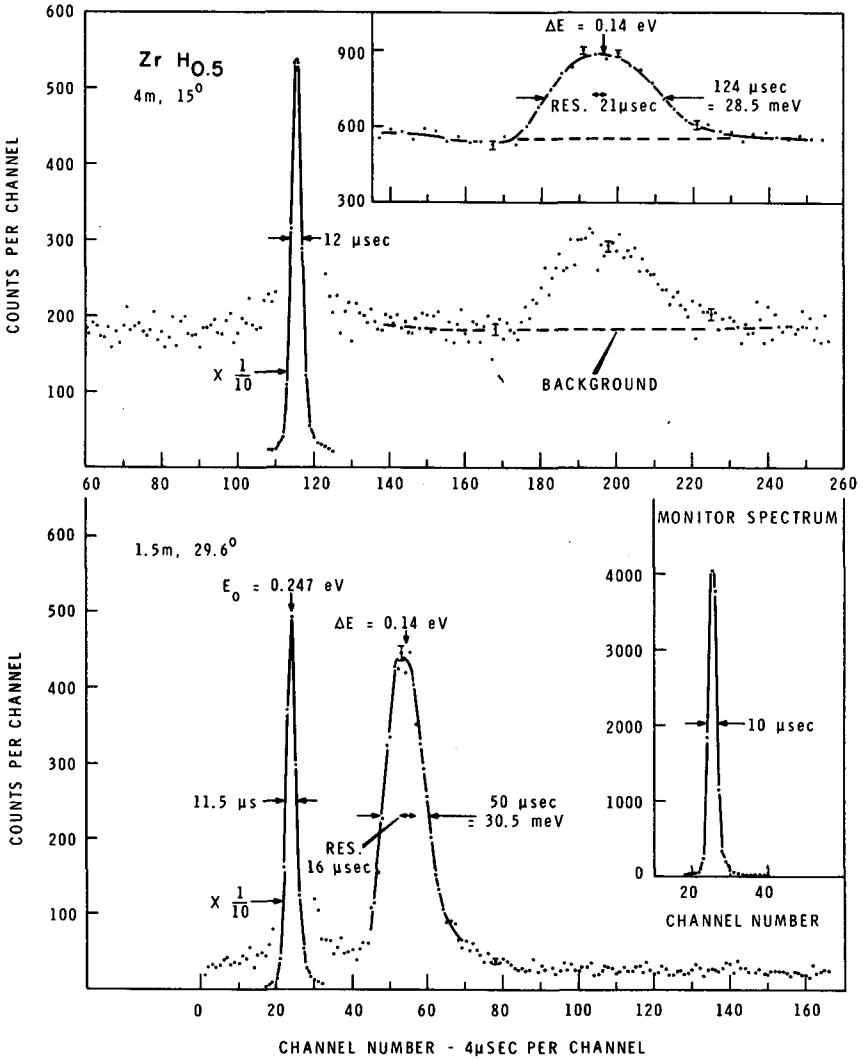

FIG. 6. Time-of-flight data for $ZrH_{0.5}$ in 1.5-m counter bank at 29.6° and in 15° counter bank at 4.0 m, $E_0 = 0.247$. Insets show one phonon peak with channels summed in groups of three and monitor spectrum with TOF distribution of beam incident of sample.

hydride is clearly resolved in both the 1.5 and 4.0 m counters. However, the resolution function at the inelastic peak is only ∿17% of the measured width in the 4 m counter while it is ∿30% in the 1.5 m counter. This sort of resolution is excellent by present standards for slow neutron inelastic scattering.[5] The time-of-flight distribution in a thin monitor counter placed in front of the sample is also shown on Fig. 6. Counts from the monitor are delayed 300.8 μ sec. The width of the elastic peak in the 4.0 m counter is only 2.5 μs larger than that of the monitor which is 4.5 m away. This indicates the small magnitude of the initial energy spread which was 1.46% = $\Delta E_o/E_o$, and the

relative independence between initial energy spread and initial time spread of the monochromatic beam in a rotating crystal spectrometer under some operating conditions. Because of this limited correlation it is sometimes possible to simultaneously approach optimization of the initial energy spread, the time spread and the repetition rate. With mechanical velocity selectors the initial energy spread and time spread are closely correlated and the same flexibility for optimization is not available. Furthermore, should pulsed magnetic coherent scattering become practical then it will be a simple matter to fully exploit this advantage of the crystal TOF spectrometers.

From Fig. 6 it is clear that a substantial price is paid in signal to background (S/N) whenever the flight path is increased. For constant solid angle and assuming no improvement in shielding the background increases as the flight path squared. Since improving the resolution involves spreading the signal over a larger interval in time, and most backgrounds are more or less time independent, this also acts to decrease the S/N. These problems are well illustrated in Fig. 6 where in going from a 1.5 to 4 m flight path the signal (the one phonon $ZrH_{0.5}$ peak) is spread out by a factor of 2.5 and the counter size is increased by a factor of 7. Without better shielding the S/N should change by a factor of 19 and it actually does change by approximately this amount as can be seen from the figure.

The RXS has been in successful operation for several years and has performed with high reliability. The monochromating section consisting of crystal and chopper rotor has been practically trouble free. Rotor bearings have shown no significant wear even on rotors which have run more than a year. Experiments have been successfully run over a wide range of operating conditions. Results for scattering from water at initial energies up to 0.61 eV will be presented in another session of this symposium.

LIST OF REFERENCES

[1] HARLING, O. K., Rev. Sci. Instr. 37, (1966) 697.

[2] KOTTWITZ, D. A. and LEONARD, B.R., "The Scattering Law For Room Temperature Light Water" in Inelastic Scattering of Neutrons in Solids and Liquids, IAEA, Vienna (1963), Vol 1, p. 359.

[3] SMITH, R. B., Some Measurements of the Neutron Scattering Law for Light Water at 95°C, USAEC Document BNWL-345 (August 1967).

[4] HARLING, O. K., Nucl. Instr. and Meth. 34 (1965) 141.

[5] BRUGGER, R.M., HARKER, Y.D., Compilation of Resolutions and Intensities of Slow Neutron, Inelastic Scattering, Time-of-Flight Instruments, USAEC Document, IDO-17134 (January 1966).

THE CHALK RIVER ROTATING CRYSTAL SPECTROMETER

A.D.B. WOODS, E.A. GLASER AND R.A. COWLEY
ATOMIC ENERGY OF CANADA LTD.,
CHALK RIVER, ONT., CANADA

Abstract

THE CHALK RIVER ROTATING CRYSTAL SPECTROMETER. The Chalk River rotating crystal spectrometer previously described by Brockhouse has been modified in several major respects. The most significant changes were (1) the replacement of the beryllium filter by a single-crystal-quartz filter to allow passage of the complete thermal spectrum, (2) the installation of a phased rotating collimator to eliminate higher order and other undesirable reflections, (3) the use of an axis of rotation of high symmetry of the rotating crystal to allow selection from a large variety of incident-neutron energies, (4) the use of a 2.5 cm diameter rotating crystal to improve resolution, (5) the replacement of the $^{10}BF_3$ neutron detectors by ^3He detectors to improve both resolution and intensity characteristics and (6) the use of magnetic tape recording with a direct computer connection to improve the data handling. Under present operating conditions the apparent time-of-flight width of a small-angle vanadium pattern for neutrons of incident wavelength 3.71 Å is about 36 μs compared with 76 μs obtained using 4.04-Å neutrons before these changes were made.

1. INTRODUCTION

Neutron spectrometers for inelastic scattering studies of atomic and magnetic spin motions in condensed systems are generally one of two basic types: pulsed-beam, time-of-flight instruments and crystal spectrometers. The choice between these types of spectrometer depends largely on the particular experiment to be done. In order to pulse the beam in an acceptable manner the time-of-flight spectrometer must use only a very small fraction (~ 1%) of the available neutrons of the desired energy. This loss is offset both because scattered neutrons of all energies may be detected simultaneously and also because an array of detectors may be used at a very large number of scattering angles about the specimen. Such spectrometers are therefore most useful when the neutron scattering function, S, is desired for a large and continuous range of energy transfers ($\hbar\omega$) and momentum transfers ($\hbar\vec{Q}$). On the other hand a crystal spectrometer usually observes just one energy at one scattering angle at any one time (it is possible to extend these somewhat but the practical limit appears to be about three analyser-detector systems). This disadvantage is offset by the relative simplicity of the apparatus, the ease of data handling and, particularly, the ability to program the spectrometer so that it can record neutron energy distributions at a preselected value of the wave vector transfer $\vec{Q}$. (Time-of-flight machines can in principle also give constant $\vec{Q}$ results but the expense and effort involved are prodigious). The crystal spectrometer is thus most useful in those situations where it is desired to have distributions over a small range of energies at certain particular values of $\vec{Q}$.

Since the first rotating crystal spectrometer was conceived and built by Brockhouse [1,2] several similar instruments have come into operation throughout the world. Although in principle they are not as versatile as phased-rotor time-of-flight spectrometers and, in addition suffer loss of intensity because of the normally low reflectivity of the rotating crystal itself, nevertheless there are certain advantages over the multi-chopper unit: 1) because the neutron beam is deflected at the rotating crystal through the angle $2\theta_m$ (see Fig. 1) the specimen is not in line with the main beam from the reactor, and fast neutron backgrounds are therefore generally easier to keep low; 2) beam areas can generally be made much larger than with multi-chopper systems; 3) the apparatus is simpler, more reliable, and very much cheaper than a corresponding multi-chopper system.

The principles, design considerations, and operating characteristics of both the Chalk River triple axis spectrometer and the rotating crystal spectrometer have been discussed in detail by Brockhouse [2]. This report describes the present state of the Chalk River rotating crystal spectrometer. Major changes have been made to the monochromating system, the detector system, and the data handling system which have improved the resolution, intensity and the utility of the instrument.

Some of the performance characteristics of this instrument are given in the compilation of Brugger and Harker [3]. These characteristics were obtained using $^{10}BF_3$ rather than ^3He detectors and $2\theta_m = 120^\circ$ rather than 105° and are therefore now slightly different.

2. DESCRIPTION OF THE SPECTROMETER

Figure 1 shows a schematic diagram of the spectrometer. The neutron beam from the reactor passes through a 180 cm long, 5 cm x 5 cm collimator and a filter of 35 cm of single crystals of quartz, located within the reactor shielding and cooled with liquid nitrogen to a temperature of about 80°K. This filter has a transmission of about 55% for 1.8 Å neutrons and a high attenuation of epithermal and fast neutrons.

The beam then passes through a thin monitor counter and the rotating collimator before being Bragg-reflected by the rotating aluminum single crystal monochromator. The rotating collimator and crystal are driven in phase at a speed of 8000 rev/min by similar hysteresis synchronous motors which are supplied by the same 400 cycles/sec motor-generator. The rotating collimator, of honeycomb construction, is 5 cm long. The slits are made of brass plated with 0.05 mm of cadmium and are encased in an aluminum cylinder which rotates with the collimator in order to reduce the effects of air friction. The openings through the collimator are 3 mm in width x 12 mm in height. The rotating collimator is connected to its motor by a flexible coupling and the whole assembly (motor and collimator) is mounted so that it may be rotated about its vertical axis to adjust the phasing relative to the rotating crystal. A vernier scale provides fine adjustment. Through suitable phasing of the collimator and monochromator it is possible to eliminate, almost entirely, all reflections except the one desired. This arrangement allows use of a monochromator

spinning about an axis of high symmetry, thereby facilitating the changing of monochromator plane and, hence, incident neutron wavelength. A subsidiary, but nevertheless significant, advantage of the rotating collimator is that it reduces by over 95% the "white radiation" caused by thermal diffuse scattering from the monochromator. This contamination can make a significant contribution to the observed intensity [2] because in the absence of the rotating collimator it occurs at all times and not just in the bursts.

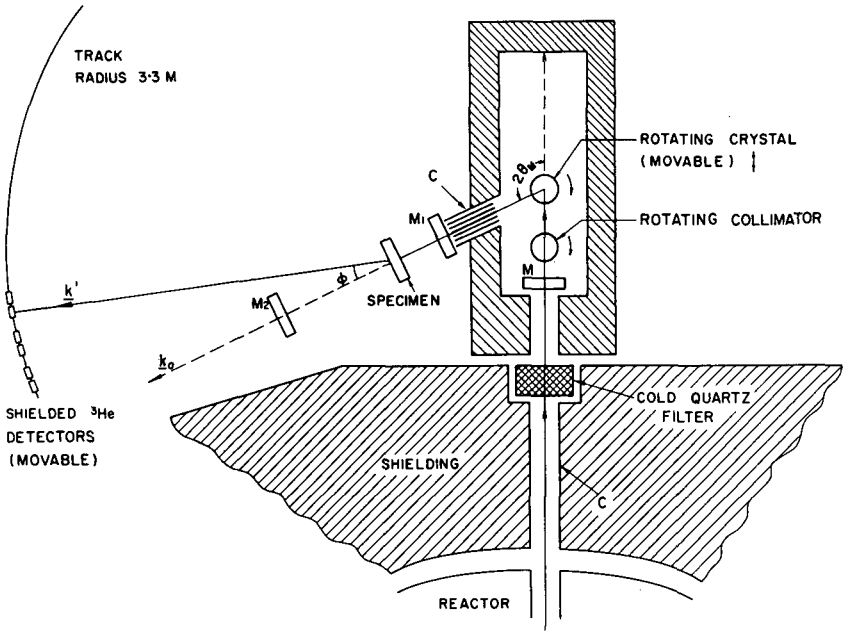

FIG.1. Schematic diagram of rotating crystal spectrometer.

The present monochromator consists of a cylindrical aluminum single crystal, 6 cm long and 2.5 cm in diameter. Mounting is by means of a shaft through a hole drilled through the long axis of the crystal. The shaft rotates in small sealed ball bearings secured in the end plates of a cylindrical aluminum housing and is coupled to the lower end of the drive motor. A mirror attached to the other end of this motor reflects a light beam onto a photocell twice per revolution. The resultant pulses start the electronic timing circuits which measure neutron time-of-flight. The monochromator crystal now in use has a mosaic spread of about 0.25°. Since it is oriented with a (110) plane horizontal, reflections from the (111), (002), (220), and (113) planes, etc. are readily available. The Bragg angle, $2\theta_m$, (see Fig. 1) is set to 105° but can, if desired, be increased to a maximum angle of 150°. The collimation between the monochromator and specimen can be varied but is typically about 0.75°.

The neutron wavelength is determined by the measured time-of-flight between the two monitor counters M1 and M2 (Fig. 1) in the diffracted beam. These are enriched uranium fission counters with an efficiency of 2×10^{-4}. Only one face of each counter is coated with uranium and the faces are flat to better than 1 mm. The geometry of these monitors does not, therefore, make any significant contribution to the measured time width of the neutron burst at the specimen position.

The specimen table is equipped with an angular scale and vernier and can be manually set and locked. It is suitable for mounting specimens in a cryostat or furnace, if required. With $2\theta_m$ at 105°, the scattering angle ϕ, at the specimen, can be varied from 0° to about 95°. For $2\theta_m = 150°$, ϕ can vary from 45° to 140°. The detector bank is 330 cm from the specimen and consists of six counters with their long axis vertical. Each of these has an active length of about 40 cm, a width of 3.8 cm and a thickness (in the beam) of 1.5 cm. They are filled with eight atmospheres of ^{3}He plus two atmospheres of Kr and operate at 1950 volts. These detectors have a significantly higher sensitivity and make a much smaller contribution to the resolution width than the 6.3 cm diameter $^{10}BF_3$ detectors which they replace [2]. A large part of the improvement in resolution, as discussed in section 4, can be attributed to these new detectors.

A block diagram of the electronic components of the system is shown in Fig. 2. The timing scaler and time delay scaler circuits were designed by R.A. McNaught. The magnetic tape system uses a Potter 905 tape transport with 24 track magnetic tape. The start pulse from the rotating crystal gates a 4.0 or 2.67 megacycle crystal oscillator in the timing scaler. When a neutron is detected in one of the six ^{3}He counters or in monitor counters M1 and M2, the number of channels elapsed since the start pulse as well as the counter identifications number is encoded and written on the magnetic tape as a binary number. A variety of channel widths are available but 8 μs is usual for the present apparatus. The tape runs continuously during recording at a speed of about 1.2 cm per second; at this speed a reel of tape conveniently records for somewhat more than 24 hours. At present 512 time channels are used per detector channel. The electronic system could be used with up to 30 detectors and 1024 time channels per detector, but only 8000 channels of data can be read off the tape at one pass. The data stored on the magnetic tape is read off, usually daily, via a telephone cable connection to a Digital Equipment Corporation PDP-1 computer, located about 600 meters from the spectrometer [4]. The reading of a tape for one day's run takes about 20 minutes at a tape speed of 75 cm per second. The spectra may be displayed and simple operations such as addition and subtraction of spectra may be carried out before they are punched out on paper tape for further analysis on the CDC G-20-3100 computer system (section 3). A number of scalers and a typewriter read-out record total count for each detector, and counting rate meters record the total count rate in the ^{3}He and monitor counter channels. A 100 channel kicksorter can be set to record the first 100 channels of the time distribution from any preselected detector or combination of detectors. The channel width is independent of that selected for the magnetic tape unit so that it is possible to display either a part or the

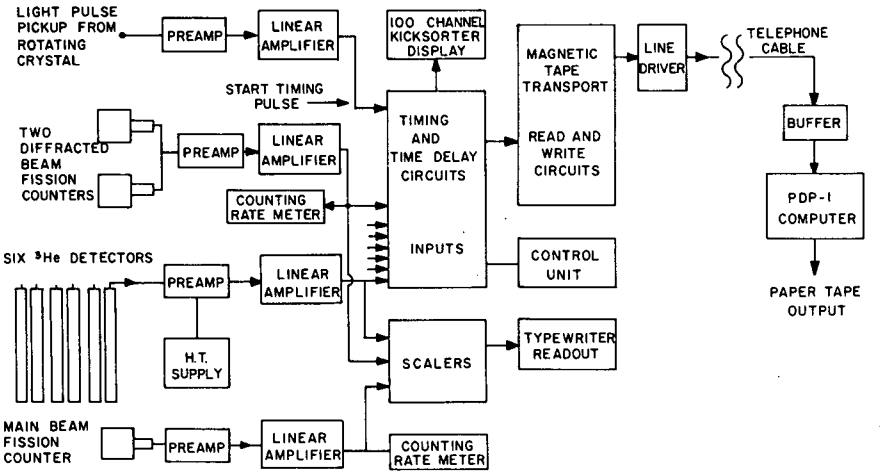

FIG. 2. Block diagram of electronics.

whole of any spectrum. The spectrum stored in the kicksorter is not usually used in data analysis but rather for monitoring the experiment and for calibration purposes.

Figure 3 is a plot of position along the entire flight path for neutrons reflected from various planes in the rotating crystal vs time. This diagram is used to determine the optimum spacing between the rotating collimator and the rotating crystal and also to determine the amount by which the collimator

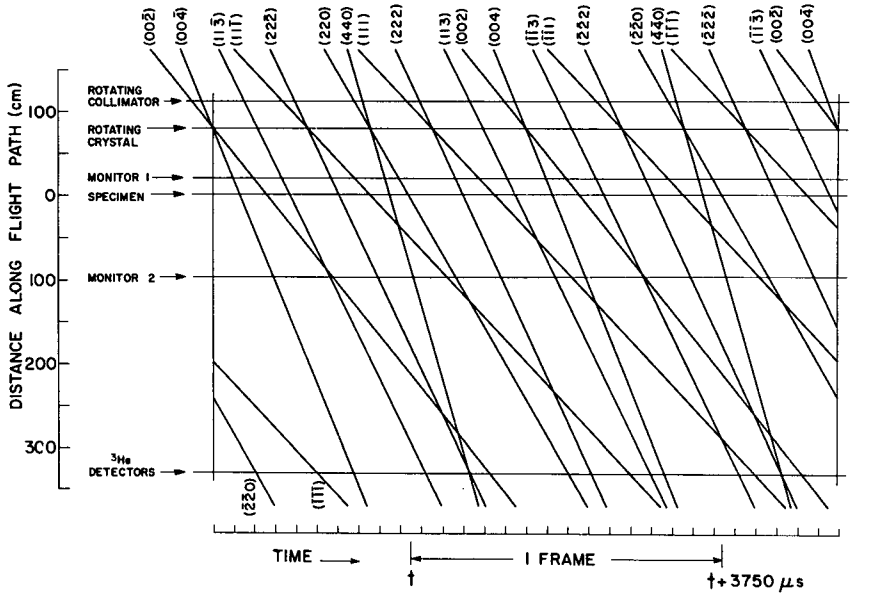

FIG. 3. Rotating crystal-rotating collimator phasing diagram for a fcc crystal (in this case aluminium) with (110) plane horizontal and $2\theta_m = 105°$.

assembly must be rotated to change from one crystal plane to another. Time measurements along the horizontal line marked "rotating collimator" may be expressed in terms of angular rotation of the collimator assembly (180° = 1 frame = 3750 μs) and, by means of the vernier scale, the desired adjustment may be made. In practice, a "rocking curve" of intensity in the counters is then done with a scaler. Identification of planes may be verified from a time distribution obtained in the monitor counters. Stability of the phase relation between the rotating crystal and collimator has been found to be adequate, once set, and only occasional small adjustments to the phasing are required. The need for these is determined by the intensity in the monitor counters in the diffracted beam.

Elastic scattering from a vanadium specimen in conjunction with the peaks in the monitor counters is used to give the final calibration. It is, of course, necessary for this to be consistent with the calibration deduced from the geometry of the spectrometer.

3. DATA HANDLING

Simple operations on the recorded spectra such as additions of runs, subtraction of background, and plotting can be carried out using the PDP-1 computer. More complex operations such as conversion of time-of-flight (wavelength) distributions to energy distributions and location of peaks is done using the CDC G-20-3100 computer system. Programs are available which allows this machine to take the paper tape output from the PDP-1 and perform the required analysis.

Time-of-flight distributions are readily converted to energy distributions through the relation $N(\lambda)d\lambda = N(E)dE$ with the k'/k_0 factor in the expression for the cross-section being removed at the same time.

The location of peaks in the distributions is done (1) by finding the highest count in the spectrum, (2) testing on each side of this high count until, on the basis of a suitable statistical criterion, the wings level off or begin to rise again, (3) determining the centre of gravity of this peak on the basis of both flat and sloping backgrounds, (4) storing this section of the spectrum separately and (5) finding a new peak by locating the highest count in the remainder of the spectrum. A statistical criterion is involved to determine which of these peaks are significant. The energy and width of each acceptable peak is calculated and printed out. The system works best for those peaks which are statistically well defined and which are a small number of channels (about five) wide.

The output of this data handling program includes most of the conventional features such as addition, subtraction, and normalization of spectra, summing arbitrary groups of channels, plotting and line printer output of both time-of-flight and energy distributions.

4. PERFORMANCE

In its present arrangement the instrument is most useful for those experiments which involve a continuous distribution of neutron energy transfers up to about 25 meV. It may also be used of course for the observation of energy transfers far in excess of this and it has been used successfully in experiments involving the observation of discrete peaks in solids and in liquid helium.

Table I shows the full widths at half height of neutrons scattered from vanadium at several angles of scattering using incident neutrons of three different energies, and compares these widths with those calculated on the basis of the expressions given by Brockhouse [2]. The improvement in the width of the vanadium pattern over those in ref. [2] is considerable and has been brought about mainly through the reduction in size of the rotating crystal and the use of the

TABLE I

Time width of distribution, in μsec, for neutrons elastically scattered from vanadium.

	λ = 3.71 Å			λ = 2.27 Å			λ = 1.47 Å		
ϕ →	10°	45°	90°	10°	45°	90°	10°	45°	90°
Observed	34	33	36	27	27	29	-	22	24
Calculated[a]	43	39	46	25	25	31	19	19	22
Reference [2][b]	76[c]	-	60	-	-	-	-	-	-
Reference [3][d]	-	56[b]	-	-	36[e]	-	-	24[f]	-

a The parameters used in the calculation, Ref. [2], were: L_o = 690 cm, L_1 = 79 cm, L_2 = 330 cm, R_m = 0.9 cm, Δ_D = 0.75 cm, ω_m = 836 rad/sec, δ_c = 0.01 rad, δ_m = 0.004 rad, Δ_s = 0.3 cm, and $2\theta_m$ = 105°.

b λ = 4.05 Å

c ϕ = 15°

d Principal differences between these and measurements in top row were the use of $^{10}BF_3$ detectors and $2\theta_m$ = 120°

e λ = 2.48 Å

f λ = 1.61 Å

^{3}He detectors. In addition to the wavelengths shown in Table I neutrons of wavelength 1.22 Å, obtained using a (115) reflection from the monochromator have also been used successfully although the intensity is low in this case. Examples of energy distributions of initially 1.47 Å neutrons scattered from liquid helium are given in another paper presented to this Symposium [5].

5. CONCLUSION

This paper has described the present status of the Chalk River rotating crystal spectrometer and some of its performance characteristics. The improvements described make the instrument very useful particularly for those experiments in which the scattered neutrons have a continuous distribution over a small range of energies.

ACKNOWLEDGEMENTS

The authors are grateful to R.A. McNaught for the design and building of the time-of-flight encoder and associated circuitry, to I.L. Fowler for the excellent ^{3}He detectors, to the tandem accelerator group for their cooperation in our use of the PDP-1 computer, and to colleagues at Chalk River and B.N. Brockhouse for advice, encouragement, and assistance.

REFERENCES

[1] BROCKHOUSE, B.N., Bull. Am. Phys. Soc. 3 (1958) 233.

[2] BROCKHOUSE, B.N., Inelastic Scattering of Neutrons in Solids and Liquids, IAEA, Vienna (1961) p. 113.

[3] BRUGGER, R.M., HARKER, Y.D., Compilation of resolutions and intensities of slow neutron, inelastic scattering, time-of-flight instruments, USAEC Rep. IDO-17134 (1966) p. 23.

[4] McNAUGHT, R.A., Nuc. Instr. Meth. 31 1 (1964) 106.

[5] WOODS, A.D.B., COWLEY, R.A., High energy excitations in liquid helium, these Proceedings, SM-104/45.

THE DOUBLE-CHOPPER NEUTRON SPECTROMETER AT ISPRA

K. KREBS
REACTOR PHYSICS DEPARTMENT,
JOINT NUCLEAR RESEARCH CENTER,
EURATOM, ISPRA (VARESE), ITALY

Abstract

THE DOUBLE-CHOPPER NEUTRON SPECTROMETER AT ISPRA. This paper contains a description of the new double-chopper facility which is operated in the EURATOM research centre at Ispra. The instrument was designed for use in solid and liquid state research. It consists of two phased triple-slotted rotor discs, both are made of heavy material (K-monel) and have a diameter of 29 cm. These rotors are able to reduce fast neutron and gamma radiation to such an extent that no filters or additional rotating collimators are needed. Each rotor is coupled to a reluctance motor driving unit by means of a thin flexible steel rod. The motor shaft of each driving unit runs on oil-lubricated precision ball-bearings. Rotor and driving motor are included within the same vacuum case so that no rotating seals are needed. The maximum operational speed was set to 22 000 rev/min corresponding to a safety factor of about 2 against yield stress in the rotor material. The width of each curved fluted slot is 12 mm at one end and increases linearly to 36 mm at the other end. The a.c. motor of the first chopper unit is fed from a frequency generator which itself is driven by a frequency-stabilized d.c. motor. The second chopper unit is driven by a pulsed d.c.-a.c. thyristor power converter, the pulsation frequency of which is derived from pick-up signals coming from the first unit. Thus there exists no connection at the power side between the two motors and beating problems are avoided. The phase angle between the chopper discs can be changed by shifting the control pulses coming from the first chopper.

The neutron beam of the 5-MW Ispra-I reactor is being collimated and can be switched off by means of steel-lead shutters. Measurements are done simultaneously at twelve angular positions using ^{3}He-or BF_3-counters. The analyser system consists of a PDP-8 computer with a special 12-input time-of-flight converter.

INTRODUCTION

Neutron scattering experiments done within the last decade have shown that measurement of the inelastic component gives essential information on the dynamics of matter. The full power of the method demands measurements over a larger part of neutron energy and momentum space. This is possible if one can do scattering measurements with neutrons of different initial energies and under different scattering angles.

Several experimental methods to select mono- or quasi-monochromatic neutrons from the thermal spectrum of a reactor are known. The instrument described in this paper belongs to the group of mechanical neutron selectors and is based on the principle of using two slotted rotors to chop a continuous beam of neutrons twice. By a suitable choice of the phase difference between the two rotors it is possible to select neutrons of a certain energy. The method has been discussed in detail by Lowde [1].

One of the main problems with mechanical selectors is the following: one wants to select a certain neutron energy from the thermal spectrum but one also likes to keep down the fast neutron and gamma-ray background. To meet the shielding requirements, one may introduce filters with high cross-section for fast neutrons and gamma radiation, e.g. bismuth or quartz. However, such filters will also reduce the intensity of thermal

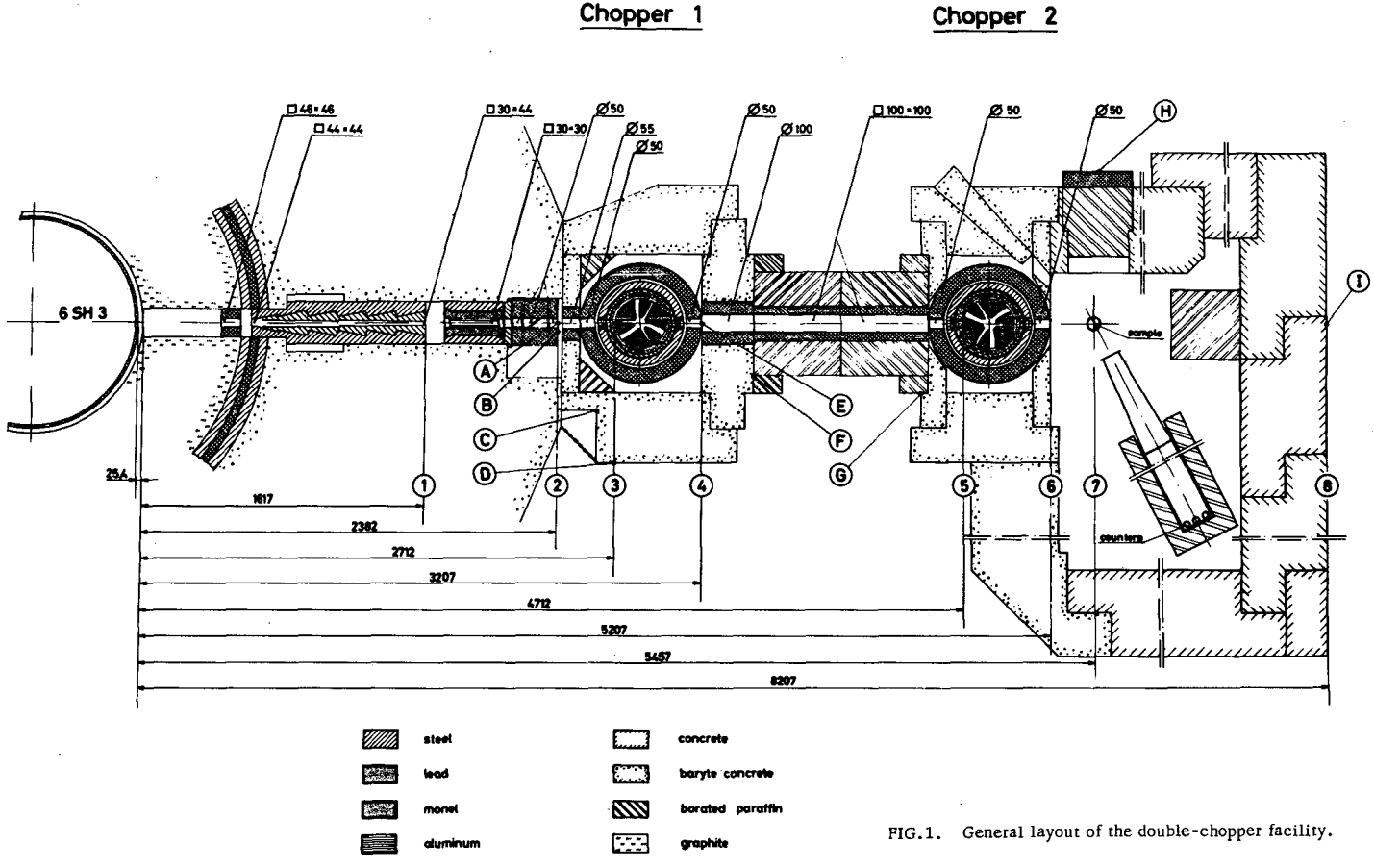

FIG.1. General layout of the double-chopper facility.

neutrons. Obviously, the simplest way is to use rotors which fulfil both requirements, selection and shielding, simultaneously. This can be done by the use of heavy rotors with curved slots which stop gamma radiation as well as fast neutrons. The running of heavy and also phase-coupled rotors presents technical difficulties which have led to the development of instruments with more than two rotors. In this case, fast neutron shielding and slow neutron selection is not done by the same rotors, and gamma-ray elimination is usually neglected. In the present paper a version which uses only two heavy rotors will be described.

DESCRIPTION OF INSTRUMENT AND ASSOCIATED EQUIPMENT

The main parts of the spectrometer facility (Fig. 1) are a collimator with variable collimation angle, a rotating lead shutter which may eventually accommodate some filter material, a sliding lead door connected to the safety system of the facility, the two-rotor system for energy selection, a suitable sample holder and finally a shielded counter system. The energy analysis of the scattered neutrons is made by the time-of-flight method over a flight path between 1 to 2 m. As detectors we use BF_3 or He^3 counters. An advantage of multiple-rotor systems as compared to triple-axis spectrometers lies in the possibility of detecting scattered neutrons under different scattering angles and for all energies simultaneously. For this purpose the counters are arranged within one large shielding block which allows the simultaneous detection of all neutrons which are scattered into a 90°-sector; in addition scattering is also observable at 135°.

For the storage of data obtained under up to 12 different scattering angles we use a PDP-8 computer[1] with a special 12-input time-of-flight converter [2]. This converter associates a channel number corresponding to the time-of-arrival of a neutron with a number identifying the counter which was involved. This information – a single 12-bit word for each of up to 12 counters – is then sent directly to the computer without using any additional interface electronics. The observation time interval can be shifted by a preselected delay, and the total number and the widths of channels are also variable. All operations are synchronized by a 4-MHz quartz controlled clock. The converter is able to accept several neutrons of the same chopper burst unless their times-of-arrival fall within the effective dead time of the analysing system (less than 50 μsec). A special time-of-flight program [3] allows accumulation of data in 3072 channels which may be sub-divided, it controls print-out or punching of stored data and it displays the data in various ways on an oscilloscope.

The essential parts of the spectrometer are the two chopping rotors. They are made of K-monel (2/3 Ni and 1/3 Cu), have a diameter of 29 cm with a thickness of 9.6 cm at the centre decreasing to 3.2 cm towards the edge. Each rotor weighs 32 kg. Three curved and fluted slots are cut across the diameter, the openings are 20 mm high and 12 and 36 mm wide, with corners rounded off to reduce undue stresses in the rotor material.

The rotation of a heavy rotor disc at high speed presents major technical problems because of the high stored energy and possible gyroscopic effects. In the present case the following solution was chosen (Fig. 2):

[1] Manufactured by Digital Equipment Corp. Maynard, Mass., USA.

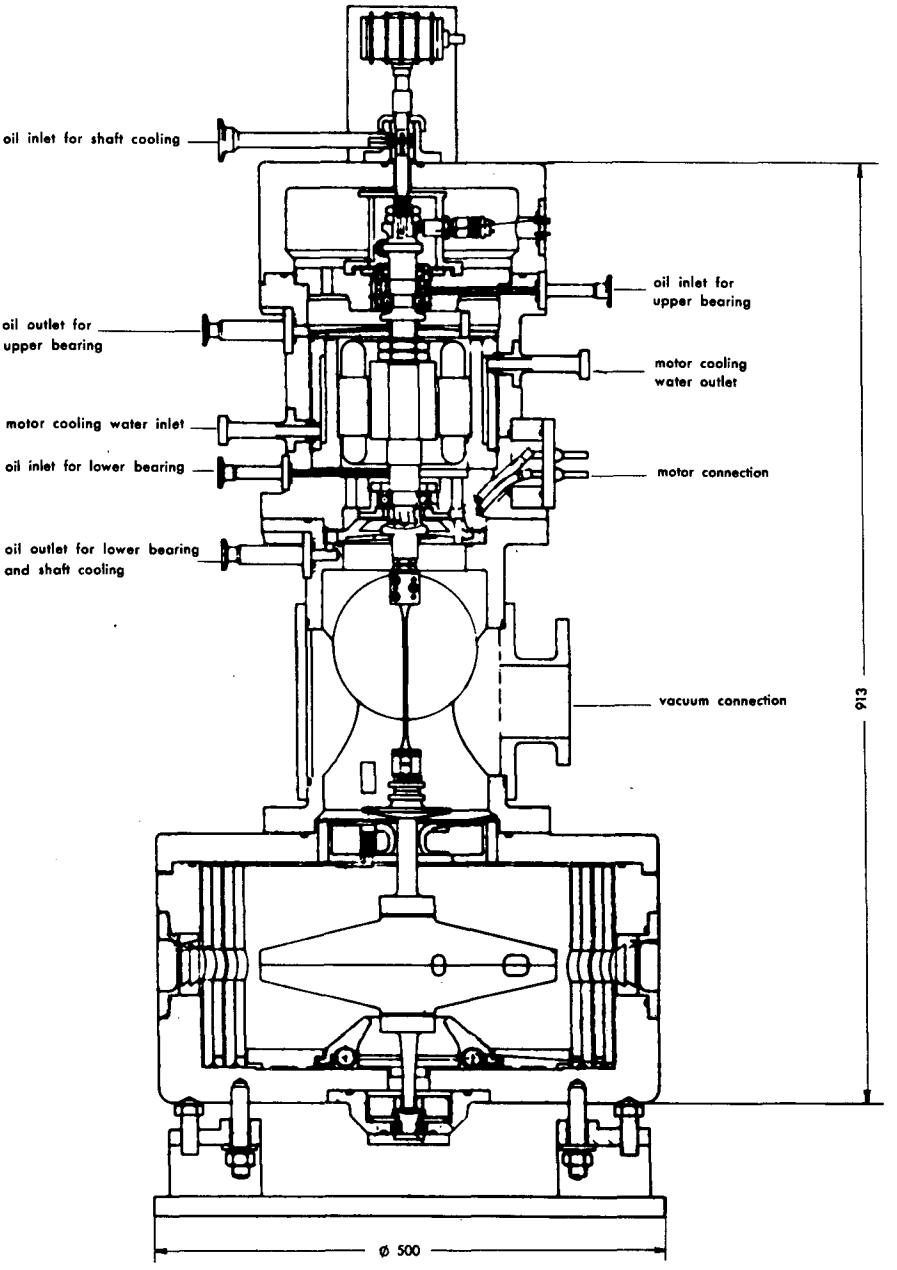

FIG. 2. Single chopper unit.

The chopper disc is suspended freely on a thin shaft, thus it behaves approximately like a gyroscopic pendulum and does not create strong non-axial effects upon the bearings. Moreover, the motor is kept under vacuum, thus avoiding rotating seals with high circumferential speeds.

The rotor of the driving motor runs on high precision ball bearings which are lubricated by oil droplets delivered by a vacuum-tight oil circulation system. The amount of oil is controlled carefully by oil-flow meters and the bearing temperatures are monitored constantly by thermocouples which are connected to the safety switch-off system of the facility. Should the thin shaft break, e.g. due to a bearing failure, three emergency bearings have been built in which allow the chopper disc to spin to rest as freely as possible. The functioning of these safety bearings has been checked thoroughly during the test period of the facility.

The lower part of the vacuum housing of the driving unit is equipped with two movable combined lead-steel rings which are acting as protection in case of a rotor explosion. For this case – which could set free up to 80 000 m.kp of rotational energy at 22 000 rev/min – also additional protection devices have been constructed: heavy lead rings around the chopper housing, heavy concrete blocks and some steel wire expansion devices holding rings and blocks together. Towards the reactor an automatic beam shutter is built in, which in its open position contains an inclined disc of a high strength Al-alloy able to stop small fragments with a high impact velocity which might arrive before the door could be closed.

The safety factor of the chopper disc against yield stress is 2 at 22 000 rev/min without considering stress concentrations around holes, it decreases to 1.5 at 25 000 rev/min [4]. At this speed the acceleration at the rim of the disc corresponds already to 100 000 g. The critical velocities of the rotating part of each chopper unit have been calculated [5], the most important second critical speed of bending, corresponding to a string-like vibration of the thin shaft lies at 29 500 rev/min. This value lies well above the maximum operational speed which – for safety reasons – has been chosen as 22 000 rev/min. The driving heads themselves have been tested to work up to 40 000 rev/min.

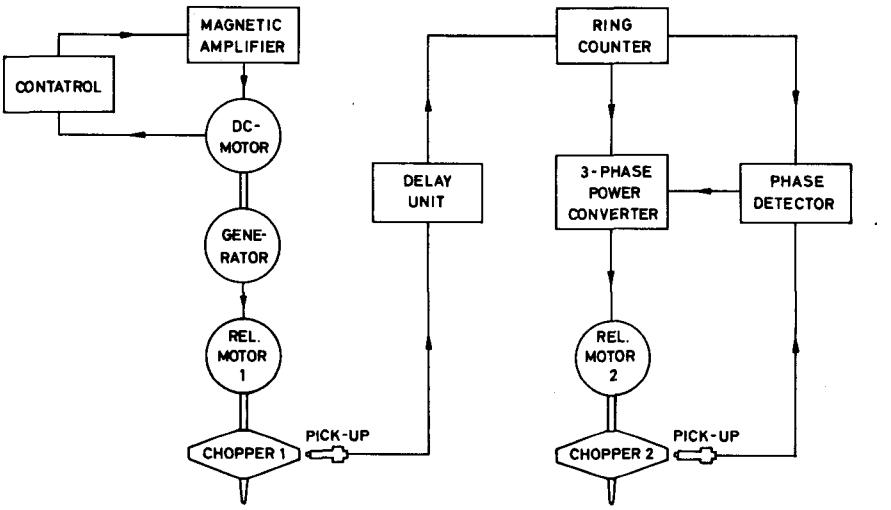

FIG.3. Block diagram of the electrical driving system.

The electrical driving system is the following (Fig. 3). Both chopper units are equipped with identical 1.5-kW synchronous reluctance motors[2] which are water-cooled and run in vacuum. The motor of chopper 1 is fed from a d.c. motor hf-generator set[2]. The frequency is kept constant to better than 0.1% by an analog-digital regulation device[3] which controls the power of the d.c. motor. With pick-up signals obtained from chopper 1 the pulsation frequency of a d.c.-a.c. thyristor power converter [6] is controlled. The output of this converter drives chopper 2. In this way no beating problems on power level occur between the two choppers. Moreover, it is also easy to shift the phase between the two discs simply by shifting the control pulses coming from chopper 1.

SPECTROMETER CHARACTERISTICS

The two monel discs have a radius of $r = 14.5$ cm, the radius of curvature of the three slots is $R = 35$ cm. The entrance openings have a width of $a = 1.2$ cm and the distance between the chopper centres is $D = 200$ cm. Thus the full width of a neutron pulse at half height is

$$\Delta\tau = \frac{a}{\omega r} = \begin{cases} 72\ \mu\text{sec at } 11\,000 \text{ rev/min } (3.4 \text{ meV}) \\ 36\ \mu\text{sec at } 22\,000 \text{ rev/min } (13.6 \text{ meV}) \end{cases}$$

The standard deviation of the distribution of the neutron times-of-flight in the pulse which arrives at the detector in a distance x from the centre of the second chopper is given by [7]

$$\sigma^2(x) = \frac{\Delta t^2}{48} + \left(x + \frac{D}{2}\right)^2 \frac{\Delta t^2}{12\ D^2}$$

where Δt is the 'open time' of the entrance slot ($\Delta t = 2\Delta\tau$). The second term in this formula is due to the spreading-out in time of the pulse as it travels away along the flight path. Since the standard deviation of a triangular pulse is related by $\sigma = \Delta\tau/\sqrt{6}$ to its half width $\Delta\tau$, the full width at half maximum of a triangular time distribution as measured at x becomes

$$\Delta\tau_x = \left[1 + \left(\frac{2x+D}{D}\right)^2\right]^{1/2} \frac{\Delta\tau}{\sqrt{2}}$$

or, with $t_x = x/v_0 = x/2R\omega$,

$$\frac{\Delta\tau_x}{t_x} = \left[1 + \left(\frac{2x+D}{D}\right)^2\right]^{1/2} \sqrt{2}\,\frac{a\,R}{x\,r}$$

---

[2] Manufactured by Elettrorava, Torino-Savonera, Italy.

[3] Manufactured by Bompard-Danielli & Co., Torino, Italy.

For the present system (with x = 210 cm) we obtain then the following values

$$\Delta\tau_x = \begin{cases} 166\ \mu\text{sec at } 11\,000 \text{ rev/min } (3.4 \text{ meV}) \\ 83\ \mu\text{sec at } 22\,000 \text{ rev/min } (13.6 \text{ meV}) \end{cases}$$

and $\Delta\tau_x / t_x = 0.06$, independent of ω. For $x >> D$ this value would go down to 0.04.

Figure 4 shows a time-of-flight spectrum as measured in the direct beam at 11 140 rev/min without sample and at a distance of x = 210 cm from the centre of the second chopper. The observed half width is $\Delta\tau = 170\ \mu$sec, which compares well with the calculated value above.

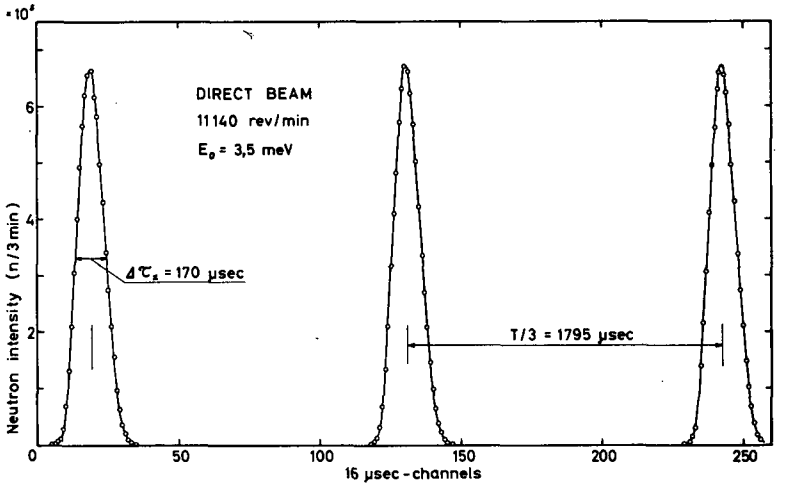

FIG.4. Time-of-flight distribution in the direct beam.

For the case of inelastic scattering by a process with sharp energy transfer from E_0 to E_f one obtains still a broadened peak. Its standard deviation is given by [7]

$$\sigma^2(x) = \frac{\Delta t^2}{48} + \left[s + \frac{D}{2} + \left(\frac{E_0}{E_f} \right)^{3/2} y \right]^2 \frac{\Delta t^2}{12\ D^2}$$

s and y are the distances between scatterer and the centre of the second chopper and scatterer and detector respectively. This expression may be rewritten as

$$\Delta\tau_y \approx \left[1 + \left(\frac{2s + D + 2y\,(E_0/E_f)^{3/2}}{D} \right)^2 \right]^{1/2} \frac{\Delta\tau}{\sqrt{2}}$$

and leads, with s = 60 cm, y = 150 cm, E_0 = 3 meV and E_f = 28 meV, to a value of $\Delta\tau_y = 104\ \mu$sec at 11 000 rev/min. This corresponds to a reso-

lution broadening of $\Delta\tau_y/t_y = 0.16$ for the observation of a sharp energy transfer of 25 meV. For down-scattering from $E_0 = 10$ meV to $E_f = 5$ meV this value would be 0.11. However, with the help of the $\Delta\tau_y$-formula experiments can be corrected for this broadening.

The neutron intensity at the sample position is given by

$$I = \frac{6R}{\pi D}\left(\frac{a}{r}\right)^2 \Phi_R \left(\frac{E_0}{E_m}\right)^2 \exp\left(-\frac{E_0}{E_m}\right)\frac{\Omega_R}{4\pi}$$

Using for Φ_R the thermal flux at the entrance to the beam tube (2×10^{13} n cm^{-2} sec^{-1}), one obtains at the sample position ($E_m \approx 40$ meV)

$$I \approx \begin{cases} 10^5 \text{ n/cm}^2 \text{ min at } 11\,000 \text{ rev/min } (3.4 \text{ meV}) \\ 10^6 \text{ n/cm}^2 \text{ min at } 22\,000 \text{ rev/min } (13.6 \text{ meV}) \end{cases}$$

Finally, Fig. 5 shows the time-of-flight spectrum of $Ca(OH)_2$ under a scattering angle of 90° and measured with 5 ^{3}He-counters in parallel. The measuring time in this case was 160 min.

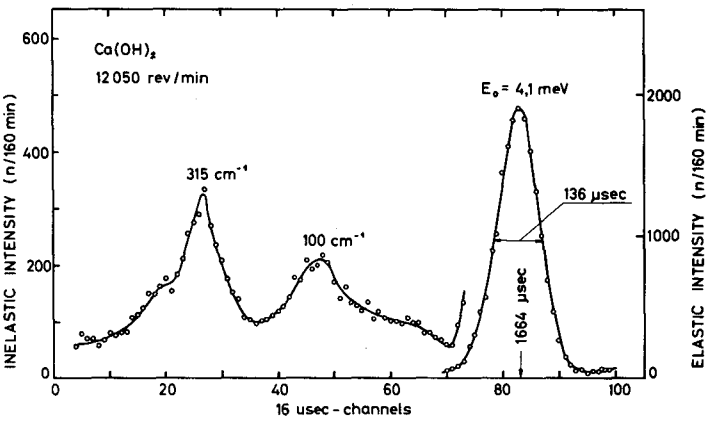

FIG. 5. Time-of-flight spectrum of $Ca(OH)_2$.

ACKNOWLEDGEMENTS

The idea of building a double-chopper spectrometer with heavy rotors was suggested to me by Dr. W. Kley, to whom I am also grateful for providing the necessary material support. For their active participation during the development, construction and test period of this facility I should like to express my gratitude especially to R. Freidhof, H. Geist, W. Pütz and W. Will.

REFERENCES

[1] LOWDE, R.D., J. nucl. Energy A 11 (1960) 69.
[2] COLOMBO, G., COPPO, N., STANCHI, L., Nucl. Instrum. Meth. 59 (1968) 86.
[3] METZDORF, J., EURATOM Rep. (to be published).
[4] BIGGIO, M., GEIST, H., EURATOM Rep. (to be published).
[5] BIGGIO, M., EURATOM Rep. EUR 3883e (1968).
[6] EDER, J., ROEBBELEN, D., EURATOM Rep. (to be published).
[7] ROYSTON, R.J., Nucl. Instrum. Meth. 30 (1964) 184.

MEASUREMENT OF THE VIBRATIONAL SPECTRA OF MOLECULES BY MEANS OF THE DOWN SCATTERING OF NEUTRONS

M.M. BEG* AND D.K. ROSS
PHYSICS DEPARTMENT,
UNIVERSITY OF BIRMINGHAM,
BIRMINGHAM, ENGLAND

Abstract

MEASUREMENT OF THE VIBRATIONAL SPECTRA OF MOLECULES BY MEANS OF THE DOWN SCATTERING OF NEUTRONS. A fast chopper has been used in conjunction with a beryllium-filtered detector to measure the down-scattering cross-section of a number of samples. An expression is derived for the overall resolution function which gives values of less than 15% in energy in the range 20-100 meV. The data is reduced to the form of the scattering law and is then compared with values obtained from an assumed form of the frequency distribution using the program LEAP. This program can be used to calculate the scattering law along the locus of the observed points in Q, w space. Data is presented for ammonium chloride, zirconium hydride, water and benzene. In the case of water, the agreement with the Haywood frequency distribution is good except that the hindered rotation peak appears at a slightly lower energy.

INTRODUCTION

The ideal detector for measuring thermal inelastic neutron scattering cross-sections is one with a high efficiency of detection for neutrons in a small energy band, the mean value of which can be varied at will. A good approximation to these conditions is provided by an arrangement consisting of an analysing crystal and a detector. This is the method used in the triple-axis spectrometer and it is equally applicable to a system which uses time-of-flight for the primary energy selection. It does, however, give rather a poor overall efficiency because in general to get the required energy resolution, only a small angular spread can be used whereas there are many experiments in which only a coarse resolution in momentum transfer is necessary. Several experiments have therefore made use of the properties of the beryllium cut-off to provide a window detector which accepts only neutrons with energy between zero and 0.005 eV. Thus Brockhouse [1] used an incident monoenergetic beam from a crystal spectrometer and filtered a beam of the neutrons scattered in the sample by passing it through a block of polycrystalline beryllium which removed all those with energy greater than 0.005 eV. The ratio of filtered to incident flux then gave a measure of the down-scattering cross-section.

An alternative technique used by Webb et al. [2] makes use of the pulse of thermalized neutrons that arises when a pulse of fast neutrons is produced in an accelerator target surrounded by moderating material. These polyenergetic neutrons are allowed to pass down a long flight tube to the sample position so that their time of arrival is a function of their energy. The scattered neutrons are then filtered and detected on a time-of-flight scale.

A third technique, which uses a reactor and neutron chopper in place of the accelerator and moderating block of the second technique, is possible. The purpose of this paper is to describe the considerations involved and to report on some results obtained with such a system. It is felt that this arrangement has considerable advantages over the first method mentioned because the whole range of incident energies is collected simultaneously, and because intensity is available at higher energies (up to 0.5 eV in the present case), while intensities with a crystal monochromator are limited because of diminishing crystal reflectivities. On the other hand, it has advantages over the accelerator case in that the range of energies examined can be varied by altering the chopper speed, the sharp cut-off of the transmission function guarding against overlap, and also in that it has a useful focusing effect due to the scanning action of the chopper. Further, even the present rather primitive arrangement compared quite favourably in intensity and resolution with the accelerator experiment.

These techniques are basically down-scattering experiments and therefore the availability of intensity and resolution for large energy changes, without the handicap of the Boltzmann factor, make possible investigations otherwise impracticable using neutrons. A major disadvantage is that with a small final energy, the momentum transfers become large for large energy transfers and the results are therefore increasingly smeared out due to multiphonon effects. Further with only a single value of momentum change for each energy change the extrapolation technique of Egelstaff [3] cannot be used to obtain a frequency distribution directly. However these difficulties can to some extent be overcome, in favourable cases, using the program LEAP [4].

The experiment described became possible because of the availability of a fast chopper [5] on the E1 hole of the HERALD Reactor at AWRE Aldermaston. This reactor is a 5-MW(th) light-water-moderated swimming-pool type and although the thermal flux at the source position is only 10^{13} n cm^{-2} sec^{-1}, the epithermal flux is relatively high. Due to the property of choppers that the overlap distance (the distance from the chopper at which the fast neutrons from one pulse catch up with the slow ones from the previous one) is independent of rotor frequency, it was possible to run the chopper at a fraction of the design speed while still using the 10-m flight station. The longer burst time that this produced was in fact desirable because, while increasing the intensity of the pulse, it was still rather less than the time spread due to the velocity spread of the slow neutrons travelling from the sample to the detector. An essential feature of the design was therefore to keep the sample as close to the detector as possible. This involved using the shortest possible piece of beryllium consistent with adequate attenuation of thermal and epithermal neutrons. Thus to reduce the transmission of unwanted neutrons by multiple scattering, i.e. 'diffusion' through the filter, it was constructed from 1-in. slabs of beryllium separated by a 0.005-in. thick layer of ^{10}B. Using this arrangement 12 cm of Be were sufficient and, although ideally the filter should be cooled, with this length only some 40% of the cold neutrons are lost by thermal diffuse scattering.

As this type of experiment is mainly useful for polycrystalline or amorphous samples, a large sample size is not an embarrassment. Thus the sample can be placed at a small angle to the beam ($\theta = 15°$) so that the

primary scattering ($\propto$ thickness/sin θ) is increased relative to the multiple scattering ($\propto$ thickness, if one assumes that the first scatter is isotropic).

APPARATUS

The general layout of the apparatus is shown in Fig. 1. It is situated on a radial hole that looks directly at the reactor core through 4 in. of lead and 4 in. of beryllium.

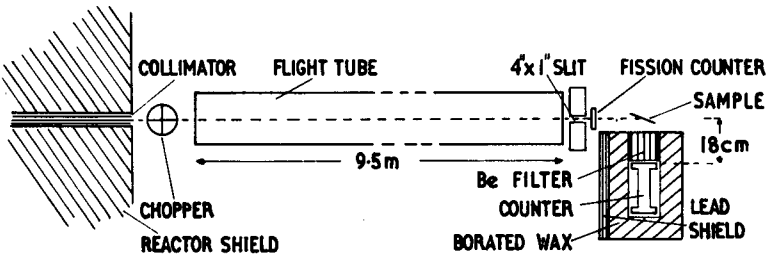

FIG. 1. Experimental arrangement.

The rotor, which is constructed from depleted uranium, duranickel and steel, is 10 in. in diameter and is designed to rotate at speeds of up to 15 000 rev/min. It contains two perpendicular sets of seven straight slits, each slit being 2 in. deep by 0.060 in. wide. When these lie parallel to the beam direction, they line up at one edge with a similar set mounted within the beam tube. The latter taper from 4 in. high by 0.22 in. wide near the beam plug to 2 in. high by 0.040 in. wide at the exit and serve to define the angular divergence of the beam. When the rotor is rotating in the appropriate direction, this arrangement transmits neutrons in the range of reciprocal velocity between zero and $1.69 \times 10^{-2} \times P$ μsec/m, where P is the rotor period in μsec and where the penetration of neutrons through the corners of the slit has been allowed for by use of an effective radius [6], $R^1 = R - (1/\Sigma)$ where Σ is the macroscopic removal cross-section of the rotor material. In the first third of this range of reciprocal velocity the transmission is constant while in the remaining part it drops steadily to zero.

The neutrons from the rotor pass down an evacuated flight tube 9.5 m long where they are first collimated down to 4 in. high by 1 in. wide and then traverse a parallel plate fission chamber. Beyond this monitor the beam reaches the sample and a fraction of it is scattered towards a beryllium filter. Those neutrons with energy less than 0.005 eV pass to the detector. Coarse collimation is provided by the ^{10}B between the slabs of the filter.

The detector is a lithium fluoride-zinc sulphide screen, viewed by a photomultiplier, the gamma-pulses being eliminated by pulse-shape discrimination [7]. The active layer was a total of 8 in. from the mid point of the beam. Beyond the sample the residual beam was allowed to pass on to a remote beam trap. The whole arrangement was shielded with borated wax.

RESOLUTION OF THE SYSTEM

The overall resolution of the beam is made up from various contributions which arise as follows:

(a) Terms giving rise to a time uncertainty independent of the energy of the incident neutron.

(1) The uncertainty due to the opening time of the slits combined with that due to the uncertainty in the flight-path length after scatter.

These effects must be considered together because there is some correlation between the time the neutrons are transmitted and the part of the sample which they strike. An accurate calculation would be tedious because of the complicated geometry so a measured value of the overall pulse length Δt_a taken from an observation of the gamma flash, is used.

$$\Delta t_a = 1.25 \times 10^{-3} \text{ P}$$

where P is the rotor period. If it is assumed that the scan time Δt_b is given to a good approximation by

$$\Delta t_b = \frac{dP}{2\pi L_1}$$

where d is the width of the beam at the sample position and L_1 is the flight-path length, then the combined uncertainty can be written

$$\Delta t_1^2 = (1.25 \times 10^{-3} \text{ P})^2 - \left(\frac{dP}{2\pi L_1}\right)^2 + \left(\frac{dP}{2\pi L_1} \pm d\bar{\tau}_2\right)^2 \qquad (1)$$

where $\bar{\tau}_2$ is the average reciprocal velocity after scatter and the sign depends on the direction of rotation.

(2) The uncertainty due to the length of the timing channel, $\Delta t_2 = 40\,\mu$sec in this case.

(3) The uncertainty due to the range of reciprocal velocities transmitted by the filter

$$t_3 = \Delta\tau_2 \, L_2$$

where L_2 is the distance from sample to detector and $\Delta\tau_2$ is the range in reciprocal velocities.

(b) The term due to the uncertainty in the energy change due to the range of final energies, ΔE_2.

(c) The term due to the uncertainty in the incident time of flight due to the uncertainty in L_1

$$\frac{\Delta\tau_1}{\tau_1} = \frac{\Delta L_1}{L_1}$$

To proceed further we require values of the average transmitted energy $\overline{E}_2$, the rms deviation in the final energy $\sigma(E_2)$, the mean final reciprocal velocity τ_2, and the rms deviation in the final reciprocal velocity, $\sigma(\tau_2)$. These may be defined in terms of the distribution in energy of the detected neutrons, $f(E_2)$, as follows.

$$\overline{E}_2 = \int_0^{0.005} E_2 f(E_2)\, dE_2 \Big/ \int_0^{0.005} f(E_2)\, dE_2$$

$$\sigma^2(E_2) = \int_0^{0.005} E_2^2 f(E_2)\, dE_2 \Big/ \int_0^{0.005} f(E_2)\, dE_2 - (\overline{E}_2)^2$$

and similarly for $\overline{\tau}_2$ and $\sigma(\tau_2)$, where here the limits of integration are now 1000 μsec/m to ∞ and the distribution is called $f'(\tau_2)$.

If $f(E_2)$ is defined to arise from a discrete energy change $\hbar\omega = E_1 - E_2$, it may be expressed

$$f(E_2)\, dE_2 = e^{-\int \Sigma(x, E_2)\, dx} \epsilon(E_2)\, I(E_1)\, \frac{\Sigma_s(E_1)}{4\pi} \sqrt{\frac{E_2}{E_1}}\, S(Q, \omega)\, dE_2 \Delta\Omega \qquad (2)$$

where $\Sigma(x, E_2)$ is the removal cross-section at a point x after the scatter; $\epsilon(E_2)$ is the detector efficiency; $I(E_1)$ is the incident flux; $\Sigma_s(E_1)$ is the total scattering cross-section of the sample; $S(Q, \omega)$ is the scattering law for the sample and $\Delta\Omega$ is the acceptance angle of the beryllium filter. Now for $\hbar\omega >> 0.005$ eV and for scattering through 90°

$$Q^2 \propto E_1 + E_2$$

and therefore Q and hence $S(Q, \omega)$ do not vary significantly over the range of integration. Further we can assume that the efficiency of the detector does not vary significantly with E_2, and also that $I(E_1)$ and $\sqrt{E_1}$ are constant over the range considered.

Thus we can write for any value of ω

$$f(E_2) \propto e^{-\Sigma(E_2)t} \sqrt{E_2} \qquad (3)$$

and

$$f'(\tau) \propto e^{-\Sigma(\tau_2)t}\, \tau^{-4} \qquad (4)$$

where t is the length of the Be filter. If we make the assumption that the removal cross-section is due entirely to the residual cross-section of beryllium, the means and variances may be calculated numerically, making allowance for the contribution from the penetration of neutrons with energies

lying between the two lowest Bragg edges. The results of this calculation are as follows

$$\bar{E}_2 = 0.034 \text{ eV}$$

$$\sigma(E_2) = 0.0014 \text{ eV}$$

$$\bar{\tau}_2 = 1330 \ \mu\text{sec/m}$$

$$\sigma(\tau_2) = 440 \ \mu\text{sec/m}$$

We may now express the overall resolution function

$$\frac{\Delta\omega}{\omega} = \frac{\hbar\omega + E_2}{\hbar\omega} \sqrt{\frac{4\Delta t^2}{L_1^2} \times \frac{\hbar\omega + \bar{E}_2}{(72.3)^2} + 4\left[\frac{\Delta L_1}{L_1}\right]^2 + \frac{\Delta E_2^2}{(E_2 + \hbar\omega)^2}} \qquad (5)$$

The form of the overall resolution width is shown in Fig. 2 in which ΔE refers to full width at half height where it can be seen that the energy uncertainty dominates at low energy while the time uncertainty dominates at high energy.

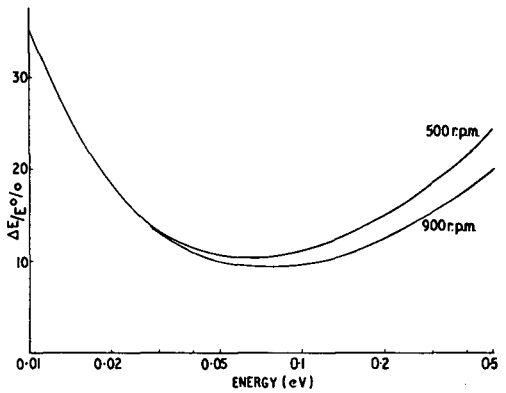

FIG. 2. Energy resolution at two chopper speeds.

EXPERIMENTAL RESULTS

Neutrons scattered from the sample which pass through the Be filter were recorded by a 400-channel time-of-flight analyser. A typical run took about three days. The time-of-flight data was corrected for constant background, streaming of elastically scattered neutrons through the Be filter and the incident neutron spectrum. The corrected data was then converted to the scattering law $S(Q,\omega)$, defined as follows

$$S(Q,\omega) = A \frac{\vec{k}_0}{\vec{k}} \frac{d^2\sigma}{d\Omega d\tau} \tau^3 \qquad (6)$$

where $\vec{k}_0$ is the incident neutron wavevector; $\vec{k}$ = scattered neutron wavevector; $d^2\sigma/d\Omega d\tau$ = double-differential scattering cross-section on time-of-flight scale; τ = time taken by neutrons to travel one metre; and A is a constant.

From the scattering law, the frequency distribution has been obtained by using the one-phonon expansion formula [8].

$$f(\omega) \propto \frac{\omega}{Q^2} S(Q,\omega) \left[1 - e^{-\hbar\omega/k_B T}\right] e^{2W} \qquad (7)$$

where e^{-2W} is the Debye-Waller factor; k_B is the Boltzmann's constant; and T is the absolute temperature.

Using the above method, the inelastic scattering from samples of NH_4Cl, ZrH_2, H_2O and benzene have been investigated. The fast neutron chopper was run at two different speeds, viz 500 and 900 rev/min, to obtain more flux at low or high incident energies respectively.

NH_4Cl

The inelastic scattering cross-section was measured at ambient and liquid nitrogen temperatures. Three main levels at 0.024, 0.046 and around 0.185 eV were found. Levels thought to be combination levels of those at 0.024 and 0.046 eV were also indicated around 0.065, 0.09 and 0.13 eV.

At liquid nitrogen temperature (~100°K) the peak at 0.046 eV was more prominent and was shifted towards the higher energy side by about 1 meV. The width of this peak was also reduced at 100°K and was just larger than the experimental resolution. The main object of using this sample was to compare the performance of the apparatus with other methods. The results were found to be in good agreement with Brockhouse [1], Venkataraman [9] and Janik [10].

The time-of-flight spectrum of NH_4Cl at liquid nitrogen temperature, corrected for background and the incident spectrum, is given in Fig. 3.

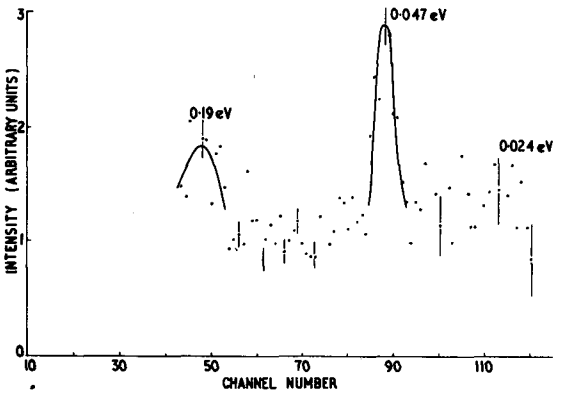

FIG. 3. Time-of-flight spectrum for NH_4Cl at liquid nitrogen temperature (chopper speed 900 rev/min).

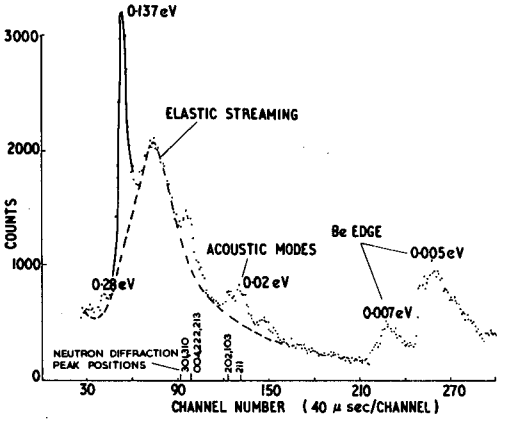

FIG. 4. Raw time-of-flight data for ZrH_2 (chopper speed 500 rev/min).

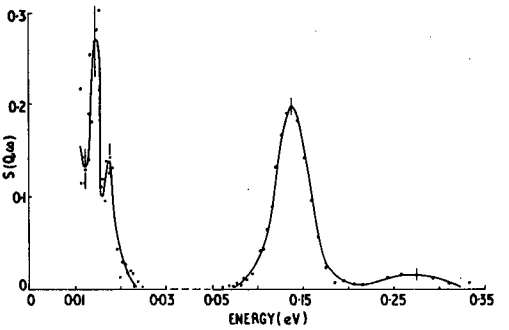

FIG. 5. Scattering law $S(Q, \omega)$ for ZrH_2.

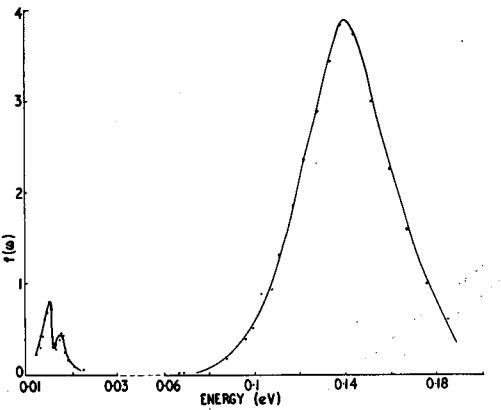

FIG. 6. Frequency distribution for ZrH_2.

ZrH_2

The metallic hydrides are examples of alloys in which the motions of one component are theoretically simple to analyse. The fact that the neutrons are scattered by hydrogenous materials in a simple manner makes neutron scattering a very useful technique in the study of the nature of hydrides.

The neutrons are scattered mainly by the hydrogen atoms and the majority of the modes are involved in the optical vibration. Because of the small percentage of acoustic modes the width of the optical peak is only slightly dependent on 'Q'.

Many workers [11, 12] have found optical levels in the Zr-H system with H/Zr ratios varying from 1.0 to 2.0. The frequency reported for the optical level is about 0.137 eV (which is claimed to be inactive in infrared). Pelah et al. [13] in their cold neutron experiment also report a continuum of acoustic vibrations.

A typical time-of-flight spectrum is shown in Fig.4. The spectrum shows the optical peaks, the elastic streaming through beryllium filter, acoustic modes and two beryllium Bragg edges at large times of flight. As the elastic scattering from ZrH_2 shows coherent effects, the data had to be corrected for the neutron diffraction patterns of ZrH_2. A separate experiment, using a double-axis crystal spectrometer, was performed to correct the raw data for coherent elastic streaming through the Be filter. Neutron diffraction data shows that $ZrH_{2.0}$ is ϵ phase and has a body-centred-tetragonal structure. The peak positions are marked in Fig.4. Corrected data is shown in the form of the scattering law (Fig.5). Figure 6 shows the frequency spectrum derived from the scattering law using Eq.(7). To calculate $f(\omega)$, a rough value of the Debye-Waller factor is first calculated from the position of the optical peak, from the Einstein model [14], using the relation

$$m\omega^2 \overline{U^2} = (n+\tfrac{1}{2})\hbar\omega \tag{8}$$

where $n = x(1-x)^{-1}$; $x = \exp(-\hbar/k_B T)$, $\overline{U^2}$ is the mean square displacement Zr and H atoms; and m is the mass of hydrogen atom.

$\overline{U^2}$ is related to the Debye-Waller factor by

$$e^{2W} = e^{Q^2\overline{U^2}} = e^{\alpha\lambda}$$

where $\alpha = \hbar^2 Q^2/2mk_B T$.

A preliminary value of $\lambda = 0.182$ is obtained by taking $m = 1$ and $\hbar\omega = 0.137$ eV and a rough frequency distribution is obtained. This $f(\omega)$ is fed into LEAP [4] which normalizes the area under $f(\omega)$ to unity and then calculates a value of λ given by

$$\lambda = 2\int_0^\infty \frac{k_B T}{\hbar\omega} \coth \frac{\hbar w}{k_B T} f(\omega)\, d\omega \tag{9}$$

The new value of λ is used to calculate $f(\omega)$ again, using Eq.(7). The process is iterated until the value of λ obtained from Eq.(9) is the same as used in Eq.(7). A final value of $\lambda = 0.24$ is obtained.

As shown in Fig.6 the frequency spectrum consists of two main portions. There are some acoustic modes extending up to about 0.022 eV and an optical peak at 0.137 eV. The acoustic modes have an area of nearly 1%. The ratio of areas under the two parts of the spectrum depends exponentially on the Debye-Waller factor used. Although the acoustic modes have very small weight, they affect the integration (9) to a great extent.

The acoustic modes in Fig.6 show two peaks around 0.015 and 0.018 eV, but there may be large uncertainties in this region due to the coherent elastic correction.

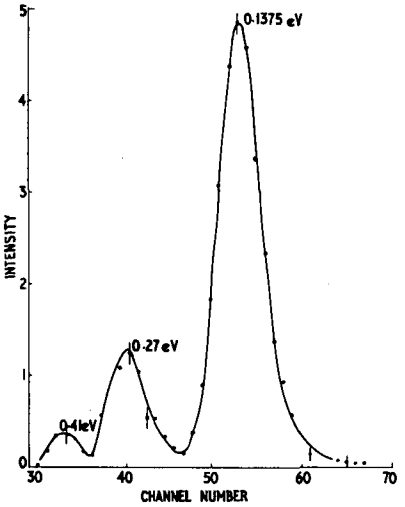

FIG.7. Raw data corrected for background and the incident spectrum, showing optical levels in ZrH_2 on time-of-flight scale (chopper speed 900 rev/min).

To study optical levels in ZrH_2, the chopper was run at a higher speed (900 rev/min) to obtain better resolution at high energies. Fig.7 shows the time-of-flight spectrum corrected for background and the incident spectrum. The positions and energy widths of optical levels are given below and are compared with those given by other workers (Tables I and II).

It should be noted that in spite of the low cross-section at the incident energies it is the 0.005 eV cross-section (80 b) that governs the chance of multiple scattering and so the sample was designed to give 10% scattering at this energy.

H_2O

A number of experiments have been performed on light and heavy water [17,18]. Most of these use cold neutrons and energy levels around 0.01, 0.022 and 0.05-0.07 eV have been observed [19,20].

TABLE I. PEAK POSITION (eV)

Source	1st Level	2nd Level	3rd Level
Pelah [13]	0.134 ± 0.015		
Whittemore [11]	0.14	0.28	
Harling [12]	0.14 ± 0.0025	0.278 ± 0.0096	0.411 ± 0.019
Present work	0.137 ± 0.002	0.27 ± 0.005	0.41 ± 0.010

TABLE II. WIDTH (meV)

	Observed	Resolution	Corrected	Whittemore [11]	Harling [12]
First level 0.137 eV	27.8	16.4	22.9 ± 5.4	18	26.4 ± 0.6
Second level 0.27 eV	73.5	45.8	56. ± 18	22	52.2 ± 3.7
Third level 0.41 eV	112.5	86.	72. ± 25		72 ± 6

The low-energy levels (0.01 and 0.022 eV) are attributed to acoustic and optical modes of motion with the molecule as a dynamic unit and the broad peak around 0.06 eV is due to hindered rotation of the H_2O molecule in the field of surrounding molecules. In infrared data [21] vibrational peaks are found at approximately 0.2 eV and around 0.37 eV to 0.45 eV. For these vibrational levels the population factor $e^{-\hbar\omega/k_BT}$ will be so small that they can only be studied by energy loss measurements. Egelstaff and Schofield [22] attributed about half the total number of degrees of freedom to the vibrational modes and about a third to the hindered rotations. The number of acoustic modes is much smaller, while that of diffusive modes is negligible.

A water sample giving approximately 15% scattering has been studied using the inverted filter technique at room temperature. The sample was placed at 25° to the incident beam and the scattered neutrons were detected at 90°. A broad peak around 0.06 eV was detected. Energy transfers around 0.02, 0.2 and 0.4 eV were also indicated. Haywood's data [16] was used to calculate the scattering law $S(Q,\omega)$, using six phonon terms, for the 90° scattering angle. In the calculation of $S(Q,\omega)$ half the weight is given to the modes around 0.02 and 0.06 eV and two delta functions at 0.2 and 0.43 eV with a weighting of 0.16 and 0.33 respectively are added using LEAP. The scattering law thus calculated has been compared with the experimental points in Fig. 8.

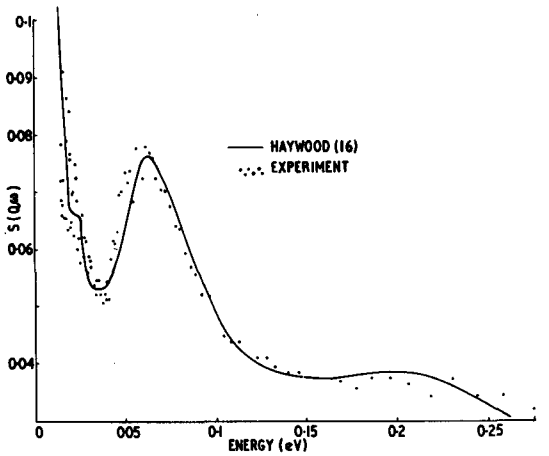

FIG. 8. Scattering law for H_2O.
..... Experimental points
____ Haywood [10]

Since H_2O has a much bigger Debye-Waller factor than ZrH_2 and there are large Q values associated with large energy transfers at 90°, the two delta functions at high energies cannot be observed as sharp peaks in the double-differential scattering cross-section. This fact is also shown by LEAP calculations on Haywood's data, with which the present results show good agreement.

BENZENE

Inelastic scattering of neutron from liquid benzene has been studied by several authors [15]. But it has been very difficult to study all the possible energy transfers using one experimental technique. Boffi, Molinari and Parks [23] formulated a model for liquid benzene in which the vibrations were treated exactly with the aid of the phonon expansion formula [24]. The rotational and translational motions were treated using the reduced mass formalism suggested by Kreiger [25] and on the perfect gas model. The BMP model predicts some modes of vibration closely spaced around 0.38 eV and well separated from the next highest set of vibration modes which spread from about 0.1 to 0.2 eV. The lowest normal vibration was predicted to be 0.05 eV. The BMP model also gives a peak around 0.01 eV due to the approximate treatment of the rotational and thermal motions. From Raman spectra in solid benzene energy levels at 0.008 and 0.012 eV are known [26], probably due to torsional vibrations of the benzene molecules in the field of its neighbours. In the present experiment a liquid benzene sample with 15% scatter at room temperature was used. The scattering law $S(Q,\omega)$ thus measured is shown in Fig. 9. At the lower energy values there is very good agreement with the scattering law using $P(\beta)$ given by Gläser [15]. $S(Q,\omega)$ was calculated with LEAP using two phonons. Experimental results agree well with the BMP model at higher energy transfers. This can be expected since, due to the uncertainty principle, at large energy values the observation time is small. Hence the neutrons observe the scattering system as that described by a 'gas' of harmonic oscillators, which is essentially the BMP theory [20].

The energy levels around 0.38 eV cannot be observed separate from the multiphonon background in this experiment, as explained for H_2O sample.

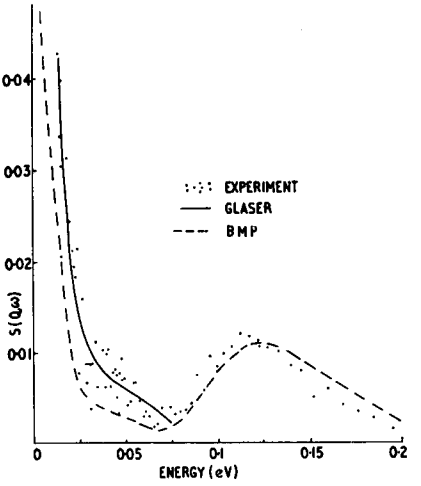

FIG. 9. Scattering law for benzene.
..... Experimental points
_____ Glaser [15]
_ _ _ BMP model [23]

CONCLUSION

The experiment provides a very good method for studying inelastic scattering of neutrons from solids and liquids. Some energy transfers which cannot be studied using cold neutrons are accessible in this experiment. The technique is particularly useful for molecular phases which only exist at low temperatures.

The energy resolution of the apparatus in the energy range of 0.028 to 0.2 eV lies between 10 and 15% which compares very well with other more sophisticated experiments. Improvements can be made by using larger flight paths and higher chopper speeds. Elastic scattering background can be reduced by using a longer beryllium filter at liquid nitrogen temperature. Also the correction is made more easily for incoherent scatterers.

The technique has proved useful for preliminary inelastic studies of new substances and for measurements where a range of momentum transfers is not required.

ACKNOWLEDGEMENTS

The authors are indebted to the staff of the HERALD reactor, in particular to Mr. G.S.B. Tuckey and Mr. J.M.A. Reichelt for their continued assistance. They are also grateful to the Science Research Council, London for financial support. One of them (M.M.Beg) would like to express his thanks to the Commonwealth Scholarship fund for the grant which made the work possible.

REFERENCES

[1] BROCKHOUSE, B.N. et al. Inelastic Scattering of Neutrons in Solids and Liquids (Proc. Symp. Vienna, 1960), IAEA, Vienna (1961) 113; 531.

[2] PAN, S.S., WEBB, F.J., Nucl. Sci. Engng 24 (1965) 194.

[3] EGELSTAFF, P.A., SCHOFIELD, P., Nucl. Sci. Engng 12 (1962) 260.

[4] McLATCHIE, R.F.L., private communication.

[5] MASLIN, E., REICHELT, J.M.A., The AWRE fast neutron chopper, AWRE Rep. NR/P-4/62.

[6] ROSS, D.K., The Nestor neutron chopper, AER Rep.M-622.

[7] WRAIGHT, L.A., Harris, D.H.C., Nucl. Instrum. Meth. 33 (1965) 181.

[8] LARSSON, K.-E. Inelastic Scattering of Neutrons (Proc. Symp. Bombay, 1964) 2, IAEA, Vienna (1965) 3.

[9] VENKATARAMAN, G., USHA, K., IYENGAR, P.K., VIJAYARAGHAVAN, P.R., ROY, A.P., Inelastic Scattering of Neutrons in Solids and Liquids (Proc. Symp. Chalk River, 1962) 2, IAEA, Vienna (1963) 253.

[10] JANIK, J.A., Inelastic Scattering of Neutrons (Proc. Symp. Bombay, 1964) 2, IAEA, Vienna (1965) 243.

[11] WHITTEMORE, W.L., Inelastic Scattering of Neutrons (Proc. Symp. Bombay, 1964) 2, IAEA, Vienna (1965) 314.

[12] HARLING, O.K., Symp. Inelastic Scattering of Neutrons by Condensed Systems, Brookhaven National Laboratory 1965.

[13] PELAH, I. et al., Phys. Rev. 108 (1957) 1091.

[14] BERGSMA, J., Inelastic Scattering of Neutrons in Solids and Liquids (Proc. Symp. Vienna, 1960), IAEA, Vienna (1961) 501.

[15] GLÄSER, W., EHRET, G., MERKEL, A., Inelastic Scattering of Neutrons, IAEA, Vienna (1965) 167.

[16] HAYWOOD, B.C., J. nucl. Energy 2 (1967) 249.

[17] BROCKHOUSE, B.N., Nuovo Cim. Suppl. 9 (1958) 45.

[18] LARSSON, K.-E., DAHLBORG, U., Reactor Sci. Tech. 16 (1962) 81.

[19] LARSSON, K.-E., HOLMRYD, S., OTNES, K., Inelastic Scattering of Neutrons in Solids and Liquids, IAEA, Vienna (1961) 329.

[20] ROSS, D.K., SANALAN, Y., Neutron Thermalization and Reactor Spectra (Proc. Symp. Ann Arbor, 1967) 1, IAEA, Vienna (1968) 477.

[21] WALGRAFEN, G.E., J. Chem. Phys. 40 (1964) 3249.

[22] EGELSTAFF, P.A., SCHOFIELD, P., Contemp. Phys. 6 (1965) 453.

[23] BOFFI, V.C., MOLINARI, V.G., PARKS, D.E., Conf. Neutron Thermalization, Brookhaven National Laboratories, 1962.

[24] SJÖLANDER, A., Ark. Fys. 14 21 (1958) 315.

[25] KREIGER, T.J., NELKIN, M.S., Phys. Rev. 106 (1957) 290.

[26] FRUHLING, A., Ann. Phys. 6 (1951) 401.

THE SPECTROMETER FOR THERMAL-NEUTRON INELASTIC SCATTERING STUDIES AT THE IBR PULSED REACTOR

E. MALISZEWSKI AND V.V. NITC
JOINT INSTITUTE FOR NUCLEAR RESEARCH,
DUBNA, USSR,
Izabela SOSNOWSKA
INSTITUTE OF EXPERIMENTAL PHYSICS,
UNIVERSITY OF WARSAW,
AND
J. SOSNOWSKI
INSTITUTE FOR NUCLEAR RESEARCH,
SWIERK, POLAND

Abstract

THE SPECTROMETER FOR THERMAL-NEUTRON INELASTIC SCATTERING STUDIES AT THE IBR PULSED REACTOR. The design of the spectrometer for studies of inelastic coherent scattering of thermal neutrons by single crystals at the IBR reactor is described. A polychromatic pulse neutron beam is scattered by a single-crystal sample and the energy of scattered neutrons is analysed by three analysing single crystals (for three different beams of scattered neutrons). The time-of-flight technique is used to measure the incident neutron energy. The spectrometer is adapted for simultaneous structure and lattice dynamics studies of solids. Special features of this spectrometer and its applications are discussed.

1. INTRODUCTION

Two methods are commonly used for neutron investigations of the phonon dispersion relations of solids: (i) the triple-axis crystal spectrometer method; and (ii) the time-of-flight (TOF) method [1, 2]. Both methods can be applied at steady-state neutron sources. However, with pulsed neutron sources, like the IBR reactor at the Joint Institute of Nuclear Research in Dubna, only the TOF method can be used efficiently. It has been applied at the IBR reactor for phonon-dispersion relations measurements in bismuth single cyrstals [3, 4]. In these experiments, the pulsed neutron beam was monochromized by a zinc single crystal and then scattered on the bismuth single crystal.

The energy of the scattered neutrons was analysed, using the time-of-flight technique. The geometry of this experiment will be called 'direct geometry'. The intensities of phonon peaks were rather low. However, because the background at the IBR reactor is very low, it was possible to carry out the experiment and to measure some dispersions relations.

To increase the intensity of phonon peaks, the possibility of using 'inverted geometry', suggested by F. L. Shapiro, was studied. Zinc, copper, aluminium and bismuth single crystals were used as samples [5, 6]. As compared with the 'direct geometry', the intensities of the phonon peaks were increased by a factor of 5.

On the basis of the above-mentioned measurements, Sosnowski [7] proposed the design of an 'inverted geometry' spectrometer for coherent inelastic scattering of thermal neutrons to be used at the IBR pulsed reactor at Dubna. In the meantime (1963-65) Buras et al. elaborated the TOF method for crystal-structure analysis of powdered and single crystals [8-11]. Buras discussed also the possibility of simultaneous studies – using one sample – of structure and lattice dynamics of solids by applying the time-of-flight technique [12, 13]. At the same time Janik et al. [14] developed the 'inverted geometry' method for incoherent inelastic scattering of neutrons enabling frequency distribution measurements to be made at the IBR reactor.

In the present paper the principle of an 'inverted geometry' TOF spectrometer for measurements of dispersion relations with simultaneous checking of the structure is described. The design of this spectrometer and its applications are discussed briefly.

2. THE PRINCIPLE OF THE SPECTROMETER

Figure 1(a) shows schematically the 'inverted geometry' TOF spectrometer. A polychromatic pulsed neutron beam from source P passes collimator C_1 and is scattered by the single-crystal sample S of known orientation in the laboratory system. The energy of the incident neutrons is a function of time and can be measured using the time-of-flight technique. The energy of inelastically scattered neutrons can be fixed for a certain measurement by a proper setting of the angle θ_A and in that way the detector records neutrons of a well-defined energy. The pulses from the detector are fed to the multichannel time-analyser triggered by the pulsed reactor. Knowing the length of the flight path, the scattering angle θ_A and the measured dependence of neutron intensity on time

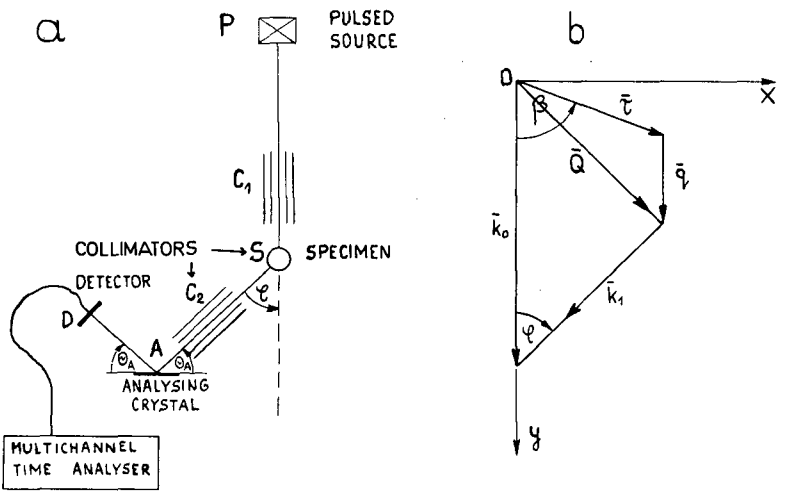

FIG.1. (a) The principle of the 'inverted geometry' time-of-flight spectrometer. (b) The principle of measurement in reciprocal space. $\vec{k}_0$ = incident neutron wavevector; $\vec{k}_1$ = scattered wavevector; $\vec{\tau}$ = reciprocal lattice vector; $\vec{q}$ = phonon wavevector; $\vec{Q}$ = momentum transfer.

(measured by the detector connected to the multichannel time-analyser), the energies and momenta of neutrons before and after the scattering can be easily found.

The energy and momentum conservation laws – using the conventional notation – are as follows:

$$\vec{Q} = \vec{k}_0 - \vec{k}_1 = \vec{\tau} + \vec{q} \tag{1}$$

$$\epsilon \hbar\omega = \frac{\hbar^2 k_0^2}{2m} - \frac{\hbar^2 k_1^2}{2m} \tag{2}$$

where $\epsilon = +1$ and $\epsilon = -1$ for the neutron energy loss and gain, respectively. The corresponding reciprocal lattice diagram is shown in Fig. 1(b). The vector $\vec{k}_1$ is fixed for a certain measurement. The direction of $\vec{k}_0$ is fixed throughout the experiment but, as stated above, its length depends on the neutron flight time between the source and the sample. By a proper choice of φ and β and the length of $\vec{k}_1$ one can study phonon-dispersion relations along any chosen direction in the reciprocal space.

For the situation shown in Fig. 1(b) Eqs (1) and (2) transform into the following formula:

$$\omega_\tau = \frac{\hbar}{2m} \{q^2 + 2q\tau \sin\beta (\cot\beta + \cot\varphi) + \tau^2 [-1 + 2 \sin\beta \cos\beta (\cot\beta + \cot\varphi)]\} \tag{3}$$

As an example, a typical set of $\omega_\tau(q)$ curves for a copper single crystal for $\tau = [200]$ and q in the [020] direction is shown in Fig. 2.

In this case: $\beta = 90°$, and curves for scattering angles $\varphi = 30°$, 45°, 90°, 135° are presented.

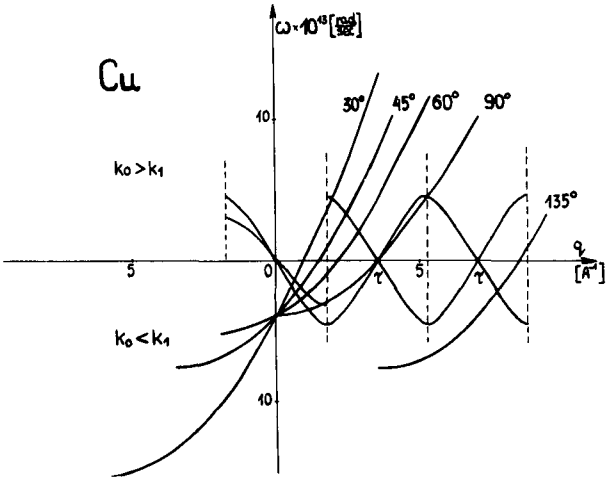

FIG. 2. Diagram of ω_τ (q) for a copper single crystal for $\tau = [2, 0, 0]$ and q in the [020] direction where $\beta = 90°$ and $\varphi = 30°$, 45°, 90° and 135°. The additional curves represent phonon-dispersion relations for copper.

FOCUSING

The principles of focusing for the triple-axis spectrometer have been elaborated in Refs [15 - 18]. The results presented in Ref. [17] have been adapted to our case, as presented below.

The vectorial divergency of the vector $\vec{k}_0$ (Fig.1(b)) is parallel to $\vec{k}_0$ (for an ideal collimation) and the following equation holds:

$$\vec{n} \cdot \delta\vec{k}_0 = 0 \tag{4}$$

where $\vec{n}$ is the vector normal to $\vec{k}_0$ (Fig.1(b)). By differentiating Eqs (1) and (2), one obtains

$$\left\{\left(\frac{m}{\hbar}\right)\nabla\omega - \vec{k}_0\right\} \delta\vec{k}_0 = 0 \tag{5}$$

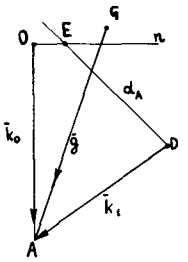

FIG.3. The focusing principle

Focusing takes place if Eqs (4) and (5) are satisfied simultaneously, i.e. if the vector

$$\left\{\left(\frac{m}{\hbar}\right)\nabla\omega - \vec{k}_0\right\} \tag{6}$$

is parallel to $\vec{n}$.

Focusing for the analyser (see Fig. 3) takes place if

$$\left\{\frac{m}{h}\nabla\omega - \vec{k}_1\right\} \tag{7}$$

is parallel to $\vec{d}_A$, where $\vec{d}_A$ is normal to the analysing plane.

The triangle OAD corresponds to Eq.(1). There are two straight lines, parallel to $\vec{n}$ and $\vec{d}_A$, passing through points 0 and D respectively. They cross at E. The vector $\vec{g} = (m/\hbar)\nabla\omega$ is shown as vector GA. Focusing takes place if conditions (6) and (7) hold simultaneously, i.e. if points G and E overlap.

If the experiment is set up so that $\vec{q}$ is parallel to the chosen direction [hkl] in the reciprocal space, then vector $\vec{k}_0$ is also parallel to the direction [hkl]. In this case $\vec{g} \parallel \vec{k}_0$.

The above discussion shows that the focusing principle can be applied to the inverted geometry TOF spectrometer in a similar way as to the triple-axis spectrometer.

3. DESCRIPTION OF THE SPECTROMETER

The inverted geometry permits measurements to be carried out in a convenient way for several scattering angles simultaneously. Figure 4 shows the design of the inverted-geometry TOF spectrometer enabling measurements at three different angles to be carried out simultaneously. The circular shield (3) has a window for the incident beam collimator (2) and another window for three collimators KII. It is set up on the base (9). The shield (3) has a vertical hole. The specimen table (10) is mounted in its lower part. Three arms of the spectrometer RI, RII, RIII have a common axis (7) which is situated below the specimen table. The arms are mounted on three carriages running on one rail. Collimators KII determining the scattering angles φ are located on special arms RI, RII, RIII. Each arm is equipped with an analysing system consisting of the table S and the arm RA connected with a shielded detector (26). The coupling between table S and arm RA is 1 : 2. The specimen table is adapted to bear heavy arrangements (of a few hundred kg) if necessary.

The positions of the specimen table (10), the arms RI, RII, RIII and the arm RA connected with the table S are controlled by a special remote control system, in accordance with a preset program. The spectrometer can be also controlled directly by a computer and the measured data can be sent to a computer.

A special collimator for structure investigations can be mounted in the shield (3). In this way the spectrometer can be used simultaneously for studies of lattice dynamics and structure.

4. INTENSITY AND RESOLUTION

The resolution of the TOF spectrometer described is determined partly by the width of the thermal neutron pulse from the moderator. As is known from previous experiments, the shape of the neutron pulse is asymmetric. Experiments at Dubna [19, 20] have shown that the width of the thermal neutron pulse can be decreased significantly by poisoning the moderator with a substance which strongly absorbs thermal neutrons. The neutron peaks then become almost symmetrical.

Based on the earlier results, the neutron intensities for the described spectrometer working at a large pulse reactor of a mean power 1 MW can be calculated. The results of calculations presented in this paper have been based on the following assumptions:

Distance between moderator and sample	15 m
Sample volume	50 cm^3
Cross-section of the beam	4 cm × 4 cm
Efficiency of the detector	35%

The calculations led to the following results:

(a) For inelastic scattering

intensity of the phonon peak at maximum	10^3 $\frac{\text{counts}}{1\,\text{h} \times 64\,\mu\text{s channel}}$
signal to background ratio	10
resolution $\frac{\Delta\lambda}{\lambda}$ ($\Delta\lambda$ = half width of the peak)	1.5%

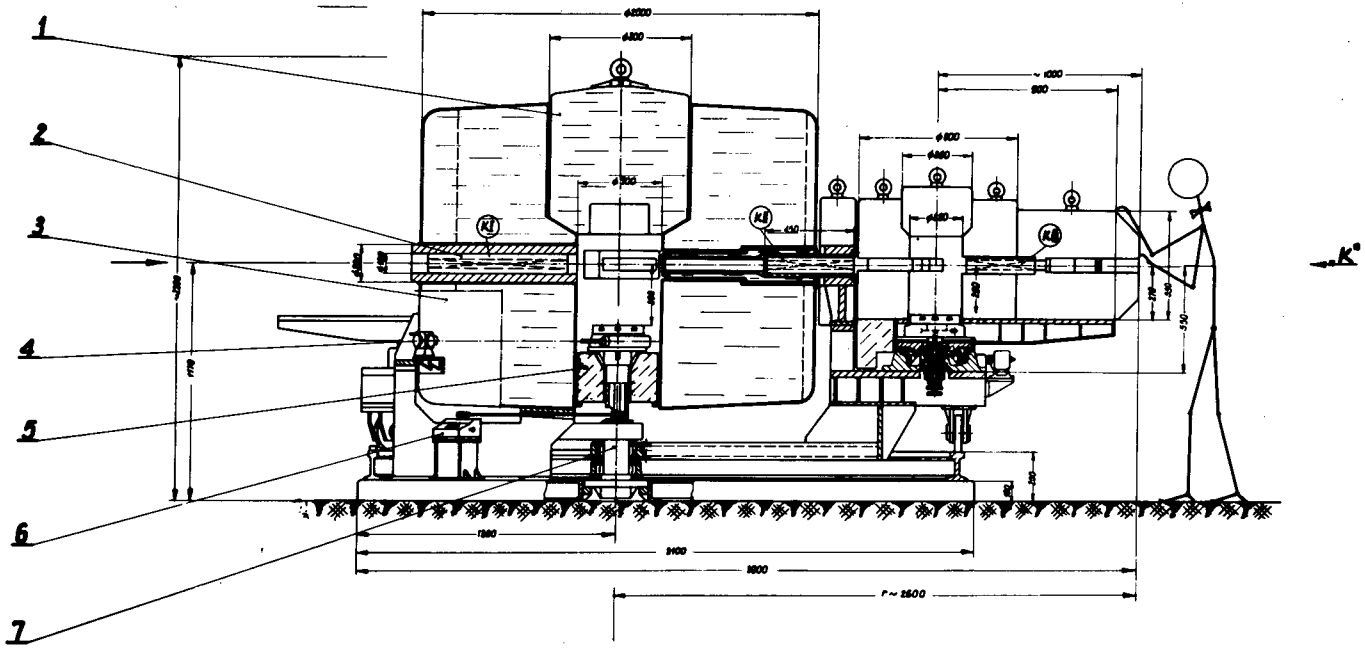

FIG.4. Plan for the spectrometer: (a) vertical section;

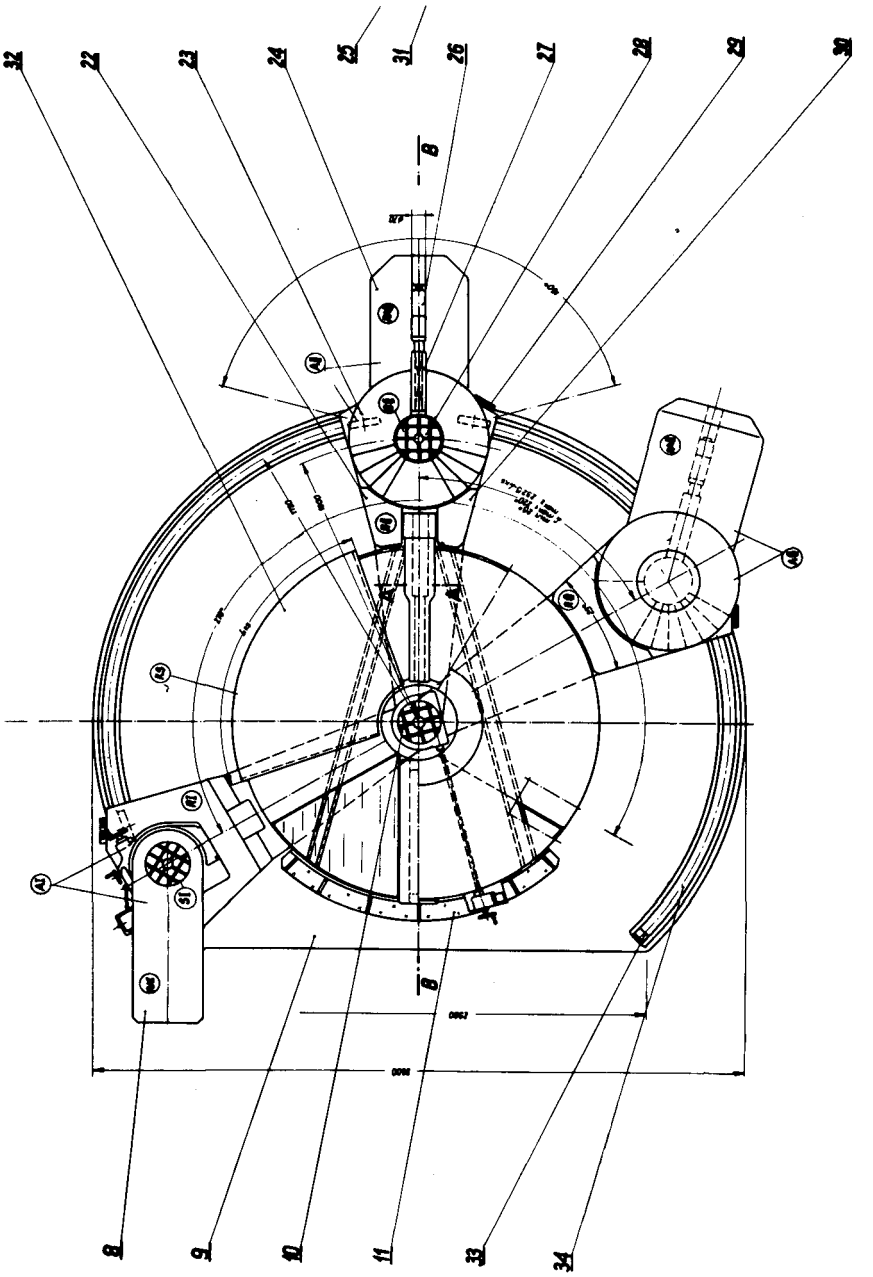

(b) horizontal section.

(b) For elastic scattering

intensity of the Bragg's reflection $8 \times 10^3 \frac{\text{counts}}{1\,\text{min} \times 64\,\mu\text{s channel}}$

signal to background ratio 100

resolution $\frac{\Delta\lambda}{\lambda}$ ($\Delta\lambda$ = half width of the peak) 1%

5. SUMMARY

The TOF spectrometer described permits various investigations to be carried out:

(1) Measurements of phonon-dispersion curves with good resolution and intensity

(2) Simultaneous studies of the influence of static external fields on lattice dynamics and structure of solids [12, 13]

(3) Simultaneous studies of the influence of pulse external fields on the internal dynamics and structure of solids [7].

In this experiment the pulses of the external field (external magnetic field) can be synchronized with the neutron pulse. Phase shifts between the two pulses can also be applied and used for transient effect studies [12, 13].

ACKNOWLEDGEMENTS

The authors wish to express their thanks to Professor B. Buras for valuable discussions and help in the course of the design of the spectrometer and to Professor F.L. Shapiro for his helpful consultations concerning the experiments in Dubna. Thanks are due to Mr. A. Holas for mathematical help. The authors are also indebted to Mr. R. Post M.E., Mr. A. Starzyński E.E., and Mr. A. Opatowski M.E. from the Institute of Nuclear Research, Świerk, for the technical design of the spectrometer.

REFERENCES

[1] EGELSTAFF, P.A., Ed., Thermal Neutron Scattering, Academic Press (1965).
[2] STEVENSON, R.W.H., Ed., Phonons in Perfect Lattices and Lattices with Point Imperfections, Oliver-Boyd, Edinburgh (1966).
[3] NITC, W.W., SOSNOWSKA, I., SOSNOWSKI, J., Dubna Rep. JINR-P-1847 (1964).
[4] SOSNOWSKA, I., SOSNOWSKI, J., Dubna Rep. JINR 2409 (1965).
[5] SOSNOWSKA, I., SOSNOWSKI, J., unpublished data.
[6] MALISZEWSKI, E., MALEKHINA, T., PAK-GWAN-O, NITC, W.W., unpublished data.
[7] SOSNOWSKI, J., Internal Rep., Institute of Nuclear Research, Świerk.
[8] BURAS, B., Nukleonika 8 (1963) 259.
[9] BURAS, B., LECIEJEWICZ, J., NITC, W.W., SOSNOWSKA, I., SOSNOWSKI, J., SHAPIRO, F.L., Int. Conf. peaceful Uses atom. Energy (Proc. Conf. Geneva, 1964) 7, UN, New York (1965) 447.
[10] SOSNOWSKA, I., SOSNOWSKI, J., KISELOV, S.V., OZEROV, R.P., Dubna Rep. JINR 2653 (1966).
[11] BURAS, B., MIKKE, K., LEBECH, B., LECIEJEWICZ, J., Phys. Stat. Sol. 11 (1965) 567.
[12] BURAS, B., Research Applications of Nuclear Pulsed Systems (Proc. Panel Dubna, 1966), IAEA, Vienna (1967) 17.

[13] BURAS, B., Seminar on Intense Neutron Sources, Santa Fe, New Mexico, USAEC-ENEA, 1966.
[14] PARLIŃSKI, K., SUDNIK-HRYNKIEWICZ, M., BAJOREK, A., JANIK, J.A., OLEJARCZYK, W., Research Applications of Nuclear Pulsed Systems (Proc. Panel Dubna, 1966), IAEA, Vienna (1967) 179.
[15] COLLINS, M.F., Brit. J. appl. Phys. 14 (1963) 805.
[16] PECKHAM, G.E., AERE Rep. R-4380 (1964).
[17] PECKHAM, G.E., SAUNDERSON, D.H., SHARP, R.I., Brit. J. appl. Phys. 18 (1967) 473.
[18] BERGSMA, J., van DIJK, C., Rep. BNL-940 (C-45).
[19] NITC, W.W., SOSNOWSKA, I., SOSNOWSKI, J., SHAPIRO, F.L., Dubna, Rep. JINR 2081 (1965).
[20] SOSNOWSKA, I., Ph.D. thesis, Warsaw University (1967).

THE "SMALL κ" METHOD OF NEUTRON MOLECULAR SPECTROSCOPY*

R.M. BRUGGER, K.A. STRONG AND D.M. GRANT**
IDAHO NUCLEAR CORPORATION,
IDAHO FALLS, IDAHO, UNITED STATES OF AMERICA

Abstract

THE 'SMALL κ' METHOD OF NEUTRON MOLECULAR SPECTROSCOPY. In slow neutron inelastic scattering experiments at the MTR it has been shown that discrete peaks can be observed in the neutron inelastic scattering spectra by observing the spectra at small momentum changes $\hbar\kappa$. Similar peaks are not observed in data at higher momentum changes because the widths of the elastic and inelastic peaks which are proportional to $\sqrt{\kappa^2 T/M}$ are large enough to overlap. Here T is the absolute temperature and M is the effective mass. Lowering T and increasing M narrows the peaks to some extent, but often the former change induces a phase change in the sample under study. The most effective way to narrow the peaks so that they do not overlap and can be observed as discrete peaks is to make κ small. In the MTR experiments this is achieved by observing the scattering at smaller angles and with incident neutrons of a higher energy. Because the inelastic scattering intensity is small compared to the elastic scattering, much care must be given to suppressing the background, multiple scattering, and air scattering. Data showing the transitions between librational levels in liquid neopentane will be shown to demonstrate the effectiveness of the small κ method of neutron molecular spectroscopy.

1. INTRODUCTION

Thermal neutrons have unique capabilities as probes to study the intramolecular vibrations of molecules. Many experiments have been directed toward these studies as is demonstrated by past publications [1] and the number of papers on the subject presented at this meeting. Many of the experiments have used cold neutrons because of their accessibility and relative good energy resolution. Others have used warmer neutrons at easily accessible scattering angles. New information about molecules has been obtained from these experiments, but the data have sometimes been discouraging when the experiments were directed at observing intramolecular vibration transitions unhindered by intermolecular forces.

The desire to observe intramolecular vibrational transitions has led us to a new experimental approach. In this approach the experimental equipment is arranged so that the inelastically scattered neutrons in the energy exchange ΔE range of interest will undergo as small a momentum exchange $\hbar\kappa$ as is compatible with instrumental resolution and counting statistics. Small κ's are required because the width of a transition peak is directly proportion to κ. To reach small κ's it is necessary to use warm incident neutrons (50 to 100 meV) and observe the inelastic scattering at smaller than usual scattering angles. This approach which we refer to as the "small κ" method has made it possible to resolve intramolecular transitions [2] which are unobservable by infrared methods and appear only as broad bands in previous neutron scattering experiments [3].

* Work performed under the auspices of the US Atomic Energy Commission.

** Temporary research assignment at MTR sponsored by Associated Western Universities. Present address, University of Utah, Salt Lake City, Utah.

In Section 2 the theoretical basis for the small κ method is outlined, and in Section 3 a few theoretical neutron scattering law curves are presented to demonstrate its relative effectiveness over prior methods. Section 4 details some of the experimental difficulties which had to overcome in perfecting the method. An example of actual data for liquid neopentane is given and discussed in Section 5.

2. THEORY

In order to describe intramolecular vibrations we shall use the McMurry-Russell [4] scattering model which was originally developed for water. At the same time we use it to illustrate the κ dependence of the widths of the intramolecular vibrations. This model predicts that when near thermal neutrons are scattered from a gas of vibrating molecules the scattering law at small values of κ will be:

$$S_\nu = S\, e^{-2w}\, e^{\alpha/4}\, \frac{e^{-\frac{\beta^2}{4\alpha}}}{\sqrt{4\alpha\pi}} + I_1(g_{\nu\tau})\, \frac{e^{-\frac{(\beta+\beta_\tau)^2}{4\alpha}} + e^{-\frac{(\beta-\beta_\tau)^2}{4\alpha}}}{\sqrt{4\pi\alpha}}$$

where

$$S = \sigma_{b\nu}/4\pi K_B T$$

$$\alpha = \frac{\hbar^2\kappa^2}{2MK_BT} \qquad (1)$$

$$\beta = \frac{\Delta E}{K_B T}$$

and

$$g_{\nu\tau} = \alpha M\, \frac{\bar{\bar{\delta}}_{\nu\tau}(\beta_\tau)}{\beta_\tau \sinh(\frac{\beta_\tau}{2})}$$

In these equations S_ν is the scattering law for the νth atom, $\sigma_{b\nu}$ is the total bound atom cross section for the νth atom, K_B is Boltzmann's constant, T is the absolute temperature, e^{-2w} is the Debye-Waller factor, τ represents a particular vibrational state, I_1 is a Bessel function of the second kind, M is the effective mass in units of the mass of the neutron and $\bar{\bar{\delta}}_{\nu\tau}$ is the amplitude factor for the τth vibration which has been orientation averaged.

From these equations we see that when the neutrons excite or de-excite a particular vibration of energy β_τ, the spectra of inelastically scattered neutrons will show peaks centered near energies $E_o \pm \beta_\tau$. A quasi-elastic peak centered at E_o will also be present. In most molecules there is not just one vibration of β_τ but there are many vibrations, each with a β_τ. The spectra of inelastically scattered neutrons should then show the elastic peak at E_o and the many inelastic peaks at $E_o \pm \beta_\tau$. Whether the spectra do show these peaks or only bands of overlapping peaks depends upon the energy resolution and the inherent width of the peaks.

Equation 1 shows that the inherent width at half maximum of each peak is

$$\rho \propto \kappa \sqrt{\frac{T}{M}} \qquad (2)$$

Here ρ is the full width at half height. This inherent width arises from the recoil motion imparted to the molecules and might be considered as the "recoil resolution" inherent in the scattering process in constrast to the energy resolution ϵ arising from the limits of the experimental equipment. To distinguish between two adjacent peaks in the spectra which are separated by an energy $\Delta\beta = \beta_1 - \beta_2$, requires that $\Delta\beta > \sqrt{\rho^2 + \epsilon^2}/K_B T$. Thus to observe separated peaks, the experiment must be arranged so that both adequate energy resolution and recoil resolution are achieved. In many experiments the energy resolution is good but the recoil resolution is not fine enough.

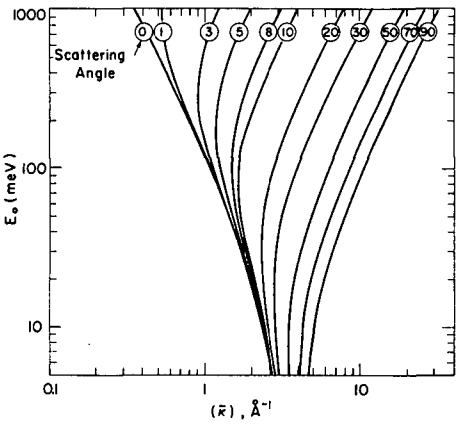

FIG.1. κ versus E_0 for a β corresponding to an energy exchange, ΔE, of 0.033 eV.

Equation 2 shows that smaller recoil resolution can be achieved by adjusting several conditions of the experiment. The temperature of the sample can be lowered or the effective mass of the sample can be increased. However, any but moderate decreases in temperature usually change the phase of the sample while the effective mass of the sample can only be increased by changing the phase or composition of the sample. Thus both of these adjustments change the nature of the experiment. The only parameter that remains to be adjusted is the momentum exchange. So in the "small κ" method the experiment is arranged to make κ small enough so that the peaks will not overlap in the neutron scattering spectra.

The relation of κ to the experimental parameters is:

$$\kappa^2 = \frac{2m}{\hbar^2}\left(2E_o + \beta K_B T - 2\sqrt{E_o(E_o + \beta K_B T)}\cos\theta\right)$$

For a fixed small scattering angle θ, there is an incident energy E_o which gives minimum κ for the desired β_T. To get to smaller κ values, one needs smaller scattering angles and warmer incident neutrons. This is displayed graphically in Fig. 1 where β was selected to correspond to an energy exchange of 33 meV, one of the β_T's of the neopentane experiment [2].

3. FITTING

A program has been written for the PDP-8 computer so that spectra can be generated from Equation 1. In this program

$$e^{-2W} = \exp\left(- \frac{\hbar^2\kappa^2}{2MK_BT} \frac{M\,\bar{\bar{\delta}}_{\nu\tau}\cosh\left(\frac{\beta_I}{2}\right)}{\beta_\tau \sinh\left(\frac{\beta_\tau}{2}\right)} \right)$$

Multiphonon terms are ignored. To demonstrate how the small κ method allows individual states to be observed, we used this program to generate spectra for several typical sets of experimental conditions. These spectra are shown in Fig. 2 as reduced partial cross sections [5] which are proportional to scattering law. The parameters were selected to represent neopentane in the gaseous phase. Here T = 300°K, M = 29.5 and $K_B T\,\beta_\tau$ = ΔE = 26, 33, 41 and 51 meV. The 41 and 51 meV transitions are bending modes observed in infrared and Raman spectra [6], while the 26 and 33 meV transitions are methyl librational transitions recently observed with the small κ method [2]. The $\bar{\bar{\delta}}$ values are ones selected to fit the neopentane data.

In Fig. 2 we note that with cold incident neutrons at a typical scattering angle of 60° only a broad band containing all four transitions is expected in neutron energy gain. A similar band is present when cold neutrons are scattered at 1°. Thus one cannot improve upon a cold neutron experiment by going to smaller angles. At an incident energy of 50 meV and a scattering angle of 7.9°, the two librational transitions are just separated in neutron energy gain but not in energy loss. The spectra at E_o = 100 meV and θ = 1° have improved the recoil resolution so that all four peaks are well resolved in energy gain and the librational peaks in energy loss. The final example in Fig. 2 is an extreme case in which E_o = 1000 meV and θ = 1°. Here all peaks are well resolved in gain and loss.

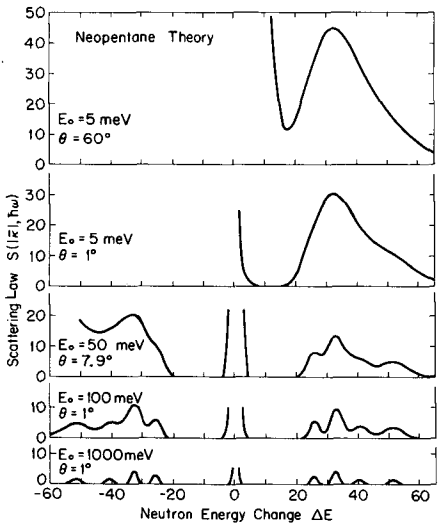

FIG. 2. Theoretical $S(|\vec{\kappa}|, \hbar\omega)$ versus E_f showing improved recoil resolution with higher incident neutron energy and small scattering angle.

In Fig. 2 and also from Equation 1 we note that while the recoil resolution improves as κ decreases, the absolute peak intensity of each peak decreases. The lower peak intensity is one of the losses that must be accepted to resolve the peaks.

4. EXPERIMENTAL CONSIDERATIONS

While the recoil resolution improves with decreasing κ, most of the other conditions of the experiment deteriorate. Absolute energy resolution is more difficult to achieve as the incident energy is increased. The intensity of inelastic scattering diminishes as κ decreases making statistical accuracy more difficult to achieve. While the inelastic scattering decreases, the elastic scattering increases making the experiment more sensitive to multiple scattering and to air scattering.

Air scattering is relatively more troublesome in these small angle scattering experiments than in experiments at larger angles because to place shielding so that the detectors see only the sample and not the beam path before and after the sample is more difficult. Neutrons in the incident beam which scatter from air in the path tend to broaden the quasi-elastic peak and produce a continuous background of inelastic scattering. The most effective way to eliminate this background is to have an evacuated path [7] for both the incident and the scattered beams.

Multiple scattering in the sample causes another background of inelastically scattered neutrons which tend to mask the peaks. The multiple scattering can be suppressed by using thin samples or by placing neutron absorbing spacers [7,8] in the sample. Since the desired scattering is at small angles, an "egg crate" type grid of spacers in the sample should be most effective while not seriously shading the counters from the sample.

The compromise as to the best energy resolution, recoil resolution and counting rate must be decided for each sample and each experimental instrument.

5. EXAMPLE OF DATA

The small κ method of neutron molecular spectroscopy has evolved out of a decade of scattering neutrons from molecules at the MTR. The experiment presently employs the MTR phased chopper velocity selector [9] which delivers bursts of monoenergetic neutrons adjustable between 15 and 150 meV. A small angle evacuated flight path [7] has been built which spans angles of 3° to 10°. Small angle flight paths filled with helium [7] were tried and found to be an improvement over air but still unsatisfactory.

Sample containers for both molecular gases and molecular liquids have been made. The gas containers [7] are cylinders 5 cm in diameter and 12 cm long; the aluminum walls of these containers are 0.025 cm thick. The pressure of the gas in the container is adjusted so that the samples have a transmission near 0.9. To suppress multiple scattering, 0.05 cm thick cadmium spacers are placed in the container perpendicular to the axis 2.5 cm distance apart.

The liquid containers [2,10] are arrays of thin walled aluminum tubes, about 0.05 cm ID. These tubes run horizontally and are stacked one above

another. The tubes are sealed to a common manifold at each end. Between each pair of tubes is a 0.007 cm space in which is placed a 0.005 cm thick sheet of gadolinium metal. This gadolinium absorbs neutrons initially scattered vertically and therefore helps to suppress multiple scattering.

Using the small κ method, data for ethane [7], propane, liquid neopentane [2] and tetramethyl silane have been obtained. Fig. 3 shows a set of data for liquid neopentane at room temperature. The incident energy was 51 meV and the scattering angle was 7.9°.

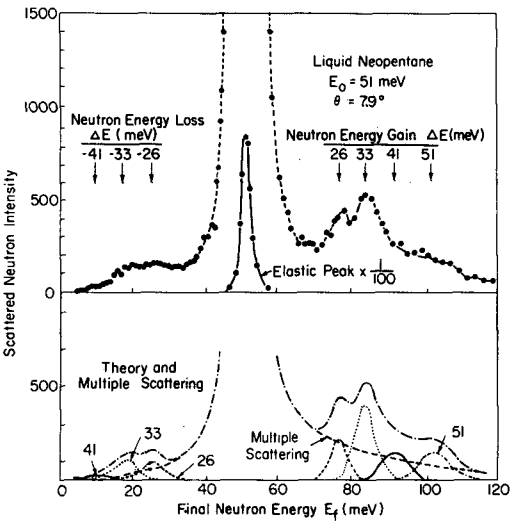

FIG.3. Scattered neutron intensity versus final neutron energy compared to a theoretical intensity plus an assumed multiple scattering contribution. Data points to the left of the elastic peak are averaged over equal energy increments of 1 meV.

Transition energies are extracted from these data by fitting spectra generated from Equation 1. However, to include the effect of energy resolution a computer program convolutes this spectrum with an energy resolution spectrum. A resolution broadened theoretical calculation which has been converted from S_υ to "intensity" is shown in the lower part of Fig. 3. The first step in fitting the data is to adjust the effective mass and S values in Equation 1 to give a good fit to the experimental elastic peak. Then this effective mass and S are held constant while the β_T's and $\overline{\delta}(\beta_T)$'s are adjusted to give the best fit to the inelastic scattering. In fitting Equation 1 to the elastic peak of the liquid neopentane data, it was found that an effective mass of 45 was required for a good fit, while in gaseous neopentane data, which has been obtained but is not presented here, a value of 29.5 was required. Note that the librational modes are separated in both energy gain and energy loss. This separation has not been achieved in previous experiments [3].

For the given incident neutron energy of 51 meV, the difference in κ resolution between the angle of 7.9°, at which the data of Fig. 3 was taken, and 4.8°, which is the lowest obtainable with the present apparatus, is quite small. Therefore, although data were obtained at an angle of

4.8° for neopentane, the 7.9° data is presented because it is statistically better. The other experimental parameters were selected as a compromise between adequate recoil resolution, adequate energy resolution, and reasonable count rates. The small κ conditions attained, coupled with the large effective mass of neopentane, were just adequate to observe the two principle methyl group librational transitions. Data at even smaller κ's would be necessary to provide better separation of the four observed states.

6. CONCLUSIONS

The previous sections have outlined the small κ method of neutron molecular spectroscopy and demonstrated with data its ability to observe discrete vibrational transitions unobservable by other methods. The samples so far studied are the more favorable ones in which only a few relatively widely spaced transitions are present. While these data were obtained with a phased chopper velocity selector, the small κ method is not limited to this instrument. Recent tests have shown that a triple axis spectrometer can also be employed. Rotating crystal spectrometers and LINAC chopper systems should also be good.

As more complicated spectra are studied, data at even lower values of κ will be required. These κ's can only be reached at very small scattering angles with hot neutrons. Since very good energy resolution will be needed while the inelastic scattering will be weak, the most intense source of neutrons will be needed.

REFERENCES

[1] EGELSTAFF, P. A., Thermal Neutron Scattering, Academic Press (1965) Chapter 10.
[2] GRANT, D. M., STRONG, K. A., BRUGGER, R. M., Observations of methyl librations in neopentane, submitted to Phys. Rev. Letters.
[3] RUSH, J. J., J. Chem. Phys. 46, No. 6 (March 1967) 2285.
[4] McMURRY, H. L., RUSSELL, G. J., BRUGGER, R. M., Nucl. Sci. and Engrg., 25 (1966) 248-260.
[5] RANDOLPH, P. D., Phys. Rev. 134 (1964) A1238.
[6] RANK, D. H., SAKSENA, B. D., SHULL, E. K., Discussion, Faraday Society (1950) 187.
[7] STRONG, K. A., BRUGGER, R. M., J. Chem. Phys. 47 (1967) 421-429.
[8] SLAGGIE, E. L., Trans. Am. Nucl. Soc. 9, (1966) 494.
[9] BRUGGER, R. M., EVANS, J. E., Nucl. Instr. 12 (1961) 75.
[10] BRUGGER, R. M., Slow neutron scattering from water, accepted for publication in Nucl. Sci. and Engrg.

THE PROPERTIES AND PERFORMANCE OF THE HOT NEUTRON SOURCE AT THE FR2 REACTOR

O. ABELN, W. DREXEL, W. GLÄSER,
F. GOMPF, W. REICHARDT AND H. RIPFEL
INSTITUT FÜR ANGEWANDTE KERNPHYSIK,
KERNFORSCHUNGSZENTRUM KARLSRUHE,
FEDERAL REPUBLIC OF GERMANY

Abstract

THE PROPERTIES AND PERFORMANCE OF THE HOT NEUTRON SOURCE AT THE FR2 REACTOR. For certain classes of neutron scattering experiments it is desirable to increase the neutron intensity at energies above the Maxwellian peak of a reactor spectrum considerably. This can be done by installing a piece of moderator having a high temperature, a so-called hot source, at the tip of the beam tube. In our experiments we used graphite as material for the hot source. The possible gain in neutron intensity attainable with a hot source was studied in a mock-up experiment for various sizes and temperatures of the graphite block using the pulsed neutron technique. The agreement of the measurements with calculations of the rethermalization properties of the graphite block based on transport theory was quite satisfactory.

A plug carrying a graphite cylinder, 18 cm in diameter and 18 cm in height, was installed at the FR2 reactor. With proper thermal isolation a graphite temperature of about 1700° K was reached by nuclear heating only. Spectrum measurements at this temperature and systematic studies of the properties of the hot source are under way. An increase in neutron intensity of about a factor of 7 is expected at a neutron energy of 0.3 eV. The source will be first used for phonon dispersion measurements.

1. INTRODUCTION

While in general the scattering of slow neutrons has proved to be a valuable method for studying the structure and dynamics of condensed matter, it is only recently that careful studies of an optimalized use of given neutron sources were started. By building 'cold' sources into research reactors, e.g., considerable gains in the useful neutron flux below 5 meV were obtained.

For a great range of problems it is of advantage or even necessary to work also with higher incident energies (up to 0.5 eV) than hitherto available with sufficient intensity. Such problems are, e.g., neutron diffraction for larger momentum transfers, the study of high excitation energies of molecular systems, solids and especially magnetic systems by inelastic neutron scattering and the determination of space-time correlation functions from the double-differential scattering cross-section, to mention only a few examples.

Higher fluxes at the energies of interest can be reached by shifting the Maxwellian spectrum of a reactor to a higher temperature. This can be achieved by inserting a hot moderator block into the normal reactor moderator. Thermal neutrons are 'rethermalized' in the 'hot source' and can be extracted by a beam tube.

It is the aim of the present paper to describe the work done to develop and test a hot source for the FR2 research reactor at Karlsruhe. In

section 2 the general concept and preparatory studies are summarized shortly. In section 3 the general layout of the hot source is described. Furthermore the choice of appropriate materials and the problem of nuclear heating and nuclear heating experiments are discussed. Finally the safety problems are mentioned. In section 4 measurements of rethermalized spectra and the resulting gain in useful neutron flux are discussed.

2. STUDIES ON RETHERMALIZATION IN A HOT MODERATOR

There are essentially four parameters which determine the neutron gain of a hot neutron source: the thermalization properties of the hot moderator material, the geometry of the source block, the temperature of the hot moderator and the position in the reactor where the hot neutron source is to be installed.

To understand the dependence of the neutron gain of a hot source on these parameters more quantitatively both experimental and theoretical studies have been carried out.

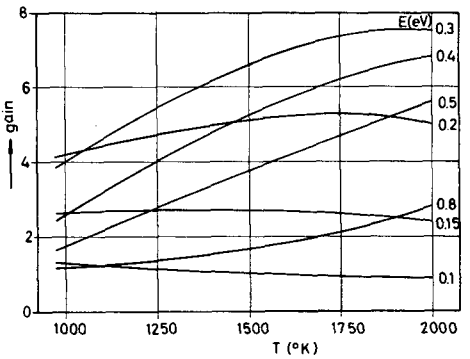

FIG.1. Calculated temperature dependence of the gain (for a graphite sphere of 10 cm radius).

Only a few materials like graphite, beryllium, beryllium oxide and perhaps some metal hydrides can be used as high-temperature moderators. The properties of metal hydrides have to be studied in more detail before such an application can be envisaged. Although simple arguments show that Be and BeO have slightly better moderating properties than graphite, the technological problems in handling these materials are greater than for graphite. Because of the excellent thermal shock resistance, the graphite block used for the hot source will not be thermally destroyed by temperature changes during reactor start-up and shut-down. Also the behaviour of graphite in high radiation fields at high temperatures is well known. Calculations result only in a gain of about 30% for beryllium compared to graphite. For these reasons graphite was chosen as hot source material.

The possible arrangement of a hot source in a reactor was simulated and rethermalized spectra were studied in a systematic manner for a range of diameters of the graphite block (d = 11-20 cm) and a range of temperatures (T = 910 - 1560°K).

Calculations of the spectra were done with a special version of the program THERMOS [1] and the code TRAKAS written for the rethermali-

zation problem in spherical geometry which calculated the directed flux using realistic scattering kernels. The agreement between experimental and theoretical results was quite satisfactory. This fact was taken as justification for using the calculational methods mentioned for optimalizing the parameters of a hot source. The following results were obtained:

Increasing the radius of a cylindrical hot source (20 cm high) from 5.5 to 10 cm leads only to an increase in the experimentally determined gain of about 15%. This means that the dimensions of a hot source can be fixed by other aspects like the radiating area required or the space which is available in the reactor.

As shown in Fig. 1, the temperature dependence of the gain is weak for energies below 0.2 eV. For higher energies the gain increases with increasing temperature.

Above 0.2 eV the intensity gain has been found to be nearly porportional to the ratio of the thermal to the epithermal flux (ϕ_{th}/ϕ_{epi}), while below this energy it is nearly independent of this ratio.

The neutron intensity of a hot source is determined practically only by the height of the thermal flux. Therefore the highest neutron intensity can be reached if the hot source is installed at the position of maximum thermal flux.

3. TECHNICAL LAYOUT OF THE HOT SOURCE AT THE FR2

3.1. Experimental set-up

Starting from the conclusions of the studies mentioned above, a concept of a hot source for the given conditions at the reactor FR2 was developed. A simple construction was sought, based on the idea of heating the source block by nuclear heating rather than a complex electrical heating system in a high radiation flux.

(a) Hot source plug

A horizontal beam tube (R6) ending 30 cm inside the outer reflector wall was available. The thermal flux at the tip of the beam tube is 5×10^{13} n cm^{-2} sec^{-1}. The inner diameter of this tube is 35.4 cm. It is reduced near the reflector by necessary installations to 27 cm, but offers the possibility of inserting a fairly large moderator block. Figure 2 shows a schematic view of the design of the whole hot source plug with auxiliary equipment.

The hot source plug consists essentially of two separate parts: The shielding part is a conventional construction made from stainless steel filled with heavy concrete and occupies only the outer part of the beam hole in the biological shield. A space of 31 cm in length between this part and the beam shutter of the R6 channel in front of the plug is reserved for the withdrawn source chamber. The hot source chamber, of 0.4-cm wall thickness (Fig. 3), is manufactured from a compact ingot of AlMg3. The chamber is tightly flanged to a 9-cm diameter aluminium tube of 300-cm length which serves two purposes, carrying the source chamber and allowing the extraction of the neutron beam. Collimators of different cross-sections can be inserted into this tube. The outer end has

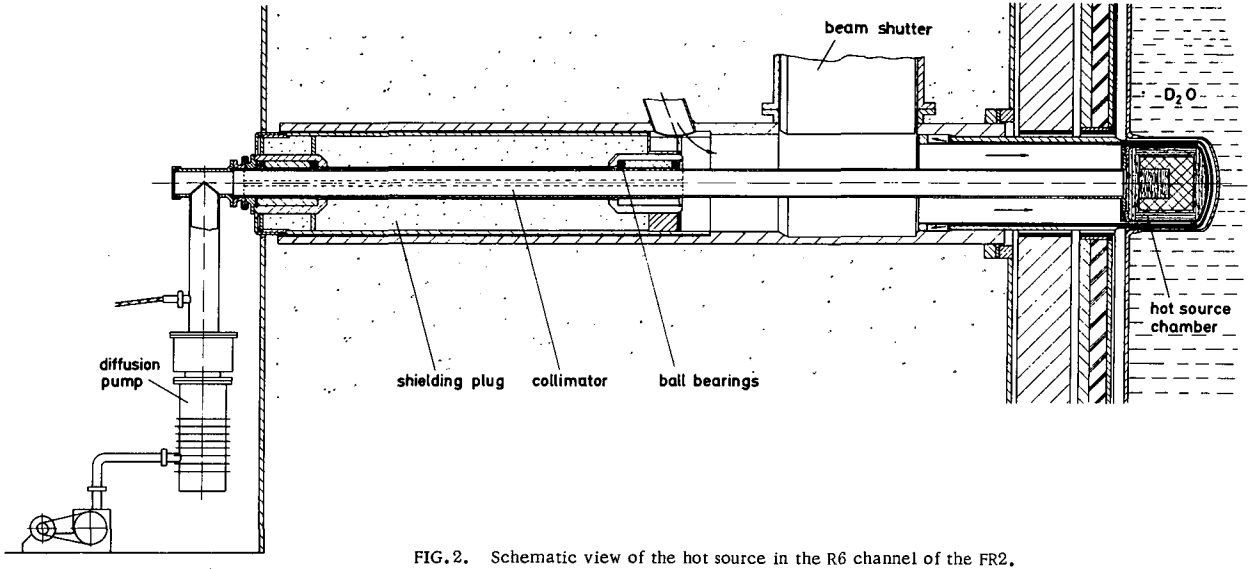

FIG. 2. Schematic view of the hot source in the R6 channel of the FR2.

proper sealings, connections for the vacuum system and grommets for the temperature control devices. The aluminium tube is supported by ball bearings in the shielding plug. This construction allows the hot source container to be easily drawn back behind the beam shutter during normal reactor operation if desired, e.g. for safety requirements.

Heat removal from the outer parts of the hot source container is achieved by an air circuit available in the beam tube. The air flow can be varied up to 400 m^3/h.

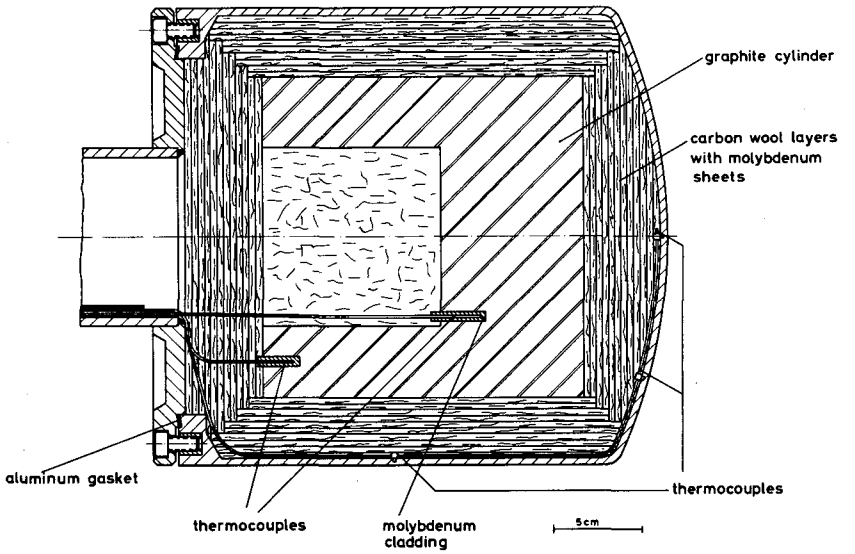

FIG.3. Hot source chamber.

(b) Hot source

Because of the low improvement compared with other moderator materials mentioned in section 2, we decided to use nuclear-grade graphite for the source material.

A cylinder 18 cm in diameter and 18 cm high with a re-entry hole (10 cm diameter, 10 cm depth) was chosen as a reasonable geometry for the available conditions at the reactor. Although the dimensions of the hole may not be optimal, this geometry increases the gain compared to a plane geometry. The block was machined from one piece of reactor-grade graphite with a density of 1.73 g/cm^3.

3.2. Nuclear heating

From the available neutron flux and γ-flux data for the source position a specific heating rate for graphite of about 0.05 to 0.1 W/cm^3 has been estimated; this means a total heating rate of about 200 to 400 W for the whole graphite block. To attain temperatures above 1000°K with such low heating rates requires a careful thermal isolation. A preliminary design using as much as 10 molybdenum heat shields around the source has been

replaced by an arrangement using carbon wool as the main isolator. Carbon wool of low density (~0.1 g/cm^3) has been found to be an excellent thermal isolator [2]. Besides the advantage in neutron economy, this technique is much more flexible and poses fewer mechanical and constructional problems than the multiple molybdenum sheet design.

The graphite cylinder was surrounded by 15 carbon wool layers each about 2 mm thick. The wool layers serve simultaneously as a support for the graphite block in the source chamber. A schematic cut showing the graphite block, the thermal isolation and the container is given in Fig. 3.

With this arrangement a graphite temperature of 1050-1300°K was reached, depending slightly on the occupation of nearby fuel element positions. In a further set-up molybdenum foils (0.25 μm) were packed between the wool layers, leading to graphite temperatures of 1500-1650°K. The temperature rise near the graphite centre during a typical heating experiment can be seen from the following table.

t(h)	0	1	2	3	4	5	...	26
T(°C)	-	220	340	430	520	610		1270

In this experiment the hot source had been pushed into its position during normal reactor operation, i.e. the reactor power at t = 0 was 44 MW. Inspection of the hot source chamber after several nuclear heating runs showed no visible changes of the graphite block and the carbon wool.

3.3. Safety aspects

The temperatures of the container and the graphite block are continuously controlled and recorded by several thermocouples. Because the heat fluxes to be removed from the outer surface of the container are relatively small (about 0.2 W/cm^2), the wall temperature can be held at 80°C by the air cooling system (350 m^3/h). Conventional chromel-alumel thermocouples are used for these temperature measurements. The graphite temperature is measured by PtRh-Pt elements which are protected against possible chemical reactions with graphite by molybdenum claddings. The vacuum (10^{-5} Torr) of the total system is continuously controlled. Two rotating pumps are available, of which normally only one is operating. Failure of this pump automatically connects the second one to the system.

Sudden mechanical damage is believed to be avoided by high safety factors in the mechanical layout. Long-time effects are detectable early enough by the control system. A nitrogen flooding system is available to decrease the temperature of the hot parts of the source to a tolerable limit in the case of an accident rapidly.

4. EXPERIMENTS

4.1. Spectrum measurements

For the practical application of the hot source the ratio of the intensity $I_s(E, T)$ of the neutron beam extracted from the source to the intensity $I_0(E)$

of the beam extracted from the same beam tube without source is of interest. This ratio may be defined as the 'gain' g(E, T):

$$g(E, T) = \frac{I_s(E, T)}{I_0(E)}$$

where E is the energy and T is the temperature.

Clearly g depends not only on the Maxwellian part of the spectrum but also, especially at higher energies, on the 1/E part. For the source arrangement described above $g(E, T_0)$ may be less than one if T_0 is the normal temperature of the reactor moderator. Although the scattering experiments to be installed at the source will use crystal monochromators, we preferred to use the time-of-flight technique with a mechanical chopper to study the energy dependence of the source intensity. This avoids otherwise necessary corrections for crystal reflectivity and higher orders.

The chopper used for the measurement is a conventional system having a rotor of 25-cm diameter running at 7350 rev/min. The slit system of the rotor is exchangeable. For the present measurements a special slit system was constructed which has an energy independent transmission in the range from 0.01 to 5 eV. The effective slit width was 1 mm giving a pulse width $\Delta t = 7.64$ μsec. A flight path 550 cm in length with a 1-in. diameter BF_3 -counter bank was used. The energy-dependent intensity of the neutron beam was determined from the time-of-flight spectra by a standard computer program, making the necessary corrections for resolution, detector efficiency and so on.

4.2. Discussion of results

Figure 4 shows the converted time-of-flight spectra of the extracted neutron beam. The curve labelled T = 330°K represents the spectrum of

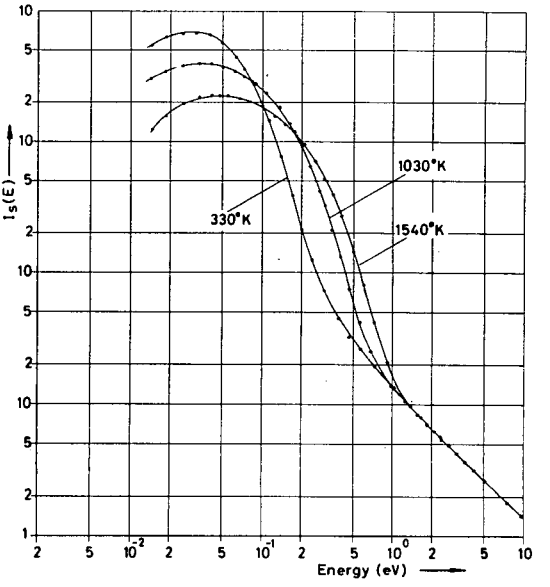

FIG. 4. Experimental spectra.

the beam from the channel without the hot source. From this measurement the ratio of ϕ_{th}/ϕ_{epi} was determined to be 32. The two other curves were obtained from the measurements at graphite temperatures of 1030 and 1540°K respectively.

It can be seen from these curves that the maxima of the spectra are not shifted to the Maxwell peak energies corresponding to these temperatures and that the shape of the hot spectra in the low energy range is not Maxwellian. This is because the graphite block is too small for the neutrons to come into thermal equilibrium at the graphite's temperatures. Figure 5 presents the gain factors g(E, T) for the two temperatures of the hot source according to the definition stated above for the case of negligibly

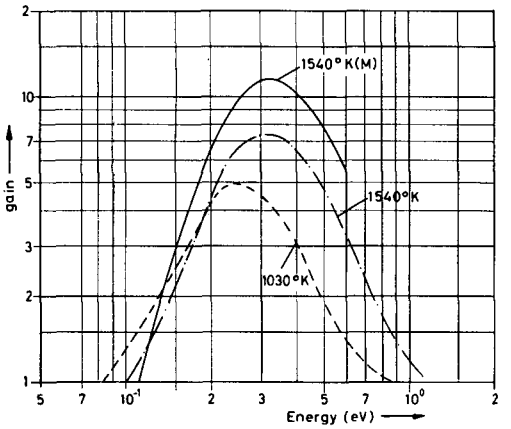

FIG. 5. Gain for various temperatures.

small flux gradients at the source position. The curve labelled 1500°K (M) shows the theoretical gain if complete rethermalization at 1540°K had been accomplished. Up to about 200 meV the gain for the temperature of 1030°K is slightly higher than that for 1540°K. The gain reaches its maximum value of 5 for 1030°K at an energy of 240 meV and of 7.3 for 1540°K at an energy of 330 meV respectively.

The agreement of these results with our theoretical calculations is quite good (Fig. 1). From the calculations it can be concluded that using temperatures of the graphite moderator below 1000°K does not yield an improvement in gain at any energy. A temperature of 1000°K is a reasonable low temperature limit for a graphite source. Much higher temperatures are only of interest for amplifying the neutron intensity at energies above 0.3 eV.

For the present installation of the hot source in the FR2 the overall reduction of the gain has been estimated from measured flux gradients to be about 1.5.

5. CONCLUSIONS

The experiments described show that a relative simple hot source construction using a small graphite moderator can improve the neutron

intensity above 0.1 eV available in a reactor beam considerably. Although the gains can be up to a factor of 7 or even more, depending on the ratio ϕ_{th}/ϕ_{epi} and the source temperature, it should be remembered that the absolute flux per unit energy is still low compared to fluxes available below 0.1 eV in a Maxwellian of room temperature. Scattering experiments with mono-energetic neutrons above 0.1 eV become feasible with the hot source described. Depending on the required energy resolution the useful energy range extends practically up to 0.3 eV.

ACKNOWLEDGEMENT

The authors thank Mr. K. Weber for invaluable technical assistance.

REFERENCES

[1] HONECK, H.C., A thermalization transport code for reactor lattice calculations, Rep. BNL-5826 (1961).

[2] REISS, F., RIPFEL, H., SCHRETZMANN, K., Der Wärmedurchgang durch Kohlefilze, Rep. KFK 638 (1967).

THE DESIGN AND PERFORMANCE OF THE HERALD COLD SOURCE

F. DAVIES, A.L. RODGERS AND M.C.J. TODD
ATOMIC WEAPONS RESEARCH ESTABLISHMENT,
ALDERMASTON, READING, BERKS.,
D.K. ROSS, Y. SANALAN AND J. WALKER
UNIVERSITY OF BIRMINGHAM,
J. BELSON, C.D. CLARK AND E.W.J. MITCHELL
UNIVERSITY OF READING,
AND
G.S.G. TUCKEY
SCIENCE RESEARCH COUNCIL,
LONDON, UNITED KINGDOM

Abstract

THE DESIGN AND PERFORMANCE OF THE HERALD COLD SOURCE. A liquid hydrogen/deuterium cold source has been installed in one of the tangential beam tubes of the reactor HERALD at AWRE, Aldermaston. The design and construction of the refrigerator and cold source assembly are described and the operating experience is outlined. Measurements have been made of the neutron spectra from ambient sources and from cold sources using apparatus installed at both ends of the beam tube. On the long-wavelength apparatus for defect studies (Reading University team) the neutron spectra were measured in the range 6-15 Å using a mechanical velocity selector. At the other end of the tube the inelastic neutron scattering apparatus (Birmingham University team) was used to measure the neutron spectra between 4 and 8 Å using high resolution time-of-flight equipment. The total cold neutron intensity transmitted by the cold beryllium filter was also recorded on the latter apparatus. Initially measurements were made on a series of ambient temperature sources to establish a reference point from which to estimate the overall gain and the gain as a function of wavelength. Measurements were also made on a number of mixtures ranging from 100% liquid hydrogen to 100% liquid deuterium.

An optimum mixture has been found. The fluxes obtained from the cold source are 20 - 30 times greater than from ambient sources. The gain is independent of wavelength in the range 6 - 15 Å. By referring measurements on all mixtures to the flux from liquid hydrogen, comparisons are made with the results obtained by other groups.

1. INTRODUCTION

The ratio (R) of neutron flux from equilibrium distributions at T_1, and at a wavelength λ, to that at T_2 is given by

$$R = \left(\frac{T_2}{T_1}\right)^2 \exp\left[\frac{h^2}{2m\lambda^2 k}\left(\frac{1}{T_2} - \frac{1}{T_1}\right)\right] \qquad (1)$$

If T_1 = 20°K and T_2 = 320°K, the values of R at 5, 10 and 15 Å are respectively R(5) = 43, R(10) = 164 and R(15) = 209. The achievement of gains of this order in research reactors would provide relatively intense sources of long-wavelength neutrons for neutron beam work.

The first use of liquid hydrogen as a cold moderator was by Butterworth et al. [1] in BEPO and subsequently by the same group [2] in

DIDO. Jacrot [3] has made measurements on several liquid hydrogen/deuterium mixtures in a moderator chamber in the EL3 reactor at Saclay. A liquid deuterium source and two hydrogen/deuterium mixtures have also been studied by Cocking and Webb [2].

In providing a cold source in HERALD for long-wavelength neutron work, it was decided to make a flexible system to allow a simultaneous study of the cold moderator to be made. The first phase of this study has been completed and is described in this paper.

The system, described in section II, has a 4.9-litre chamber in a tangential tube, as opposed to the radial tube arrangements in DIDO and EL3. A major advantage of this system is that source modifications can be made without disturbing the neutron beam instruments. The HERALD source is viewed by two instruments - a time-of-flight chopper and a multislit, multidisc velocity selector - and measurements have been made of a number of hydrogen/deuterium mixtures.

2. THE HERALD COLD SOURCE

HERALD is a 5-MW pool reactor reflected on two sides by 7.5 cm of beryllium. The cold source is inserted into a tangential beam tube (see Fig. 1). To achieve this, the centre section of the original straight-through tangential tube was cut out and plates welded over the end of the beam tube stubs. The source is suspended within the reactor tank in this centre section. Water is expelled from the gap G between the cradle and the beam tube stub by a flexible aluminium diaphragm when the cradle is pressurized to 15 lb/in^2 with helium gas. About 0.020 in. of water remains at the interface I between the source block and the cradle. This arrangement allows the shapes and sizes of cold chambers to be changed without disturbing the measuring equipment at either end of the beam tube.

Because of the tangential geometry, it was possible to use a large source chamber and to examine the moderation by liquid deuterium under more favourable conditions than with the smaller chambers used in earlier experiments. The refrigeration power available limited the source volume to about 5 litres. This volume, although still smaller than desirable, was considered acceptable since it was the intention to examine not only pure deuterium but also deuterium/hydrogen mixtures. To limit the gamma-heating, 7 cm of lead shielding was interposed between the source assembly and the beryllium reflector.

The source chamber was made of aluminium in the form illustrated in Fig. 1. There are two re-entrant tubes let into the chamber on the axis of each neutron beam tube.

The need to vary the composition of the mixture in the source chamber made it necessary for the source to be cooled indirectly. Thus heat is transferred from the independent source system to the main refrigerator circuit via a heat exchanger. The heat exchanger is situated just below the water surface in the reactor tank and is connected to the source chamber by two pipes 1.9 cm in diameter. Circulation and removal of the heat load of about 300 W is achieved by natural convection arising from the large variation of density of liquid hydrogen with temperature.

The aluminium source is connected to the stainless steel heat exchanger using friction-welded transition pieces. During operation of the source the vacuum jacket is isolated, the vacuum being maintained by a charcoal ad-

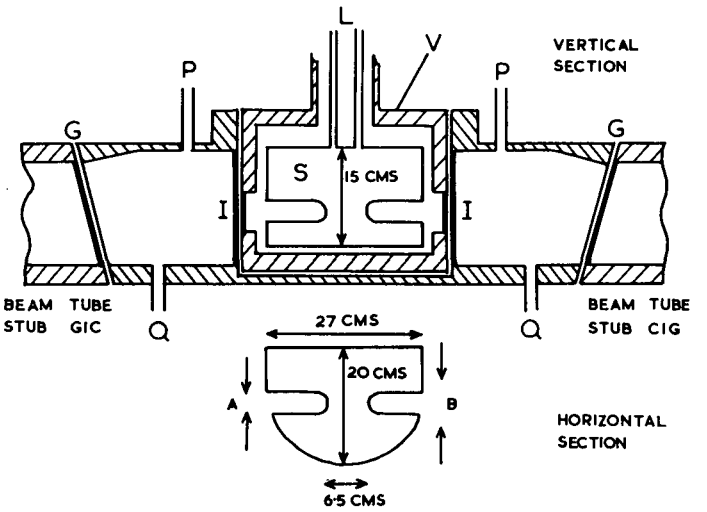

FIG.1. Sections of the cold source on HERALD. The Fermi chopper is mounted on C1G and views that part of the cold source S indicated by the arrows B. The neutron velocity selector views the area indicated by the arrows A. The overall dimensions of the cold source are quoted, the source chamber itself having aluminium walls about 0.7 cm thick. Tubes L link the cold source with the heat exchanger. V is vacuum jacket. P and Q are inlet and outlet for the He gas etc.

sorber attached to the heat exchanger. It is found that 1 litre of charcoal will maintain a satisfactory vacuum for several weeks. The source system is connected to a 2-m^3 ballast volume so that the gas charge can be conserved. The pressure in the ballast decreases from 5 to 2 atm as the source fills with liquid. Gas samples from the ballast were analysed by mass spectrometry to determine the hydrogen/deuterium content and the results for mixtures used in the series of experiments are given in Table I.

TABLE I. CONCENTRATIONS OF COLD-SOURCE MIXTURES

H_2	D_2	HD	H	D
0.87	97.82	1.24	1.49	98.44
8.03	87.23	4.52	10.29	89.49
25.87	67.77	5.67	29.70	70.60 [a]
29.94	60.03	9.26	34.57	64.66
27.69	43.21	29.00	42.19	57.77
33.65	39.52	26.76	47.03	52.90
54.75	18.92	26.16	67.83	32.00
100	0	0	100	0

[a] Studied only by incident beam monitor - integrated counts.

The refrigerator was designed and manufactured by Elliott Automation Ltd and is a liquid nitrogen pre-cooled Joule-Thomson cascade system of the Linde-Hampson type with a capacity of 600 W. It operates at a pressure of 60 atm using modified oil lubricated compressors. Alumina and liquid nitrogen charcoal beds are used to purify the gas. The whole of the gas flow through the refrigerator is passed to the heat exchanger where heat is removed from the secondary (source) system by the boiling of hydrogen on the refrigerator side of the exchanger.

3. THE TIME-OF-FLIGHT CHOPPER APPARATUS

The apparatus set up on the C1G hole is designed for cold neutron scattering experiments. It was convenient to use this instrument for assessment of the performance of the cold source. The neutron beam passes through a steel collimator 1 m long and 6.25 cm in diameter. This is embedded in iron shot concrete and can be flooded to shut off the beam. Beyond the collimator is a 30-cm length of polycrystalline beryllium cooled with liquid nitrogen which serves to scatter out of the beam all neutrons with wavelengths less than 4 Å. The filtered beam is then further collimated by a 6.25 cm × 2.75 cm aperture in a 30-cm block of barytes concrete. Over the exit of this is mounted a ^{235}U fission chamber which is referred to as the incident beam monitor and which has a sensitive layer of 10 mg/cm^2. Beyond the monitor the beam is monochromated and pulsed by a high-speed Fermi chopper. A second fission chamber (referred to as the chopped beam monitor) measures the residual beam which then passes along a 2.92-m flight path to a 5-cm diameter BF_3 counter. The time-of-flight spectra have a wavelength resolution of 7%.

4. THE MECHANICAL NEUTRON VELOCITY SELECTOR

From the G1C end of the tangential beam tube the cold source is viewed by a mechanical velocity selector which transmits neutrons with selected wavelengths between 6 and 15 Å depending on the speed of rotation. The apparatus is mainly as described by Clark et al. [4]. The wavelength resolution is 5%. The effective solid angle subtended by the source at the detector is 10^{-4} steradians. With this collimation the area of the cold source viewed is within the re-entrant tube referred to in section 2 above.

5. RESULTS AND DISCUSSION

The two neutron instruments used in the present work have different acceptance angles and are designed to work in different wavelength ranges. The Fermi chopper views a large area of the source, whereas the neutron velocity selector accepts only neutrons emerging from a re-entrant tube.

Figure 2(a) shows the spectra measured with the Fermi chopper between 4 - 7 Å for a number of different sources. The structure observed in the spectra is attributed to the Bragg edges arising from neutron scattering in the aluminium used in the cold source construction. This was confirmed by

restricting the collimation to view only the re-entrant hole in the source, as a result of which the structure disappeared.

Figure 2(b) shows spectra measured with the neutron velocity selector. Between 6 - 15 Å the wavelength dependence empirically is found to be $I(\lambda) = 4.44 \times 10^4 \exp(-0.69\lambda)$. This shape is due in part to selective transmission of neutrons by materials used in the construction of the source and beam tube.

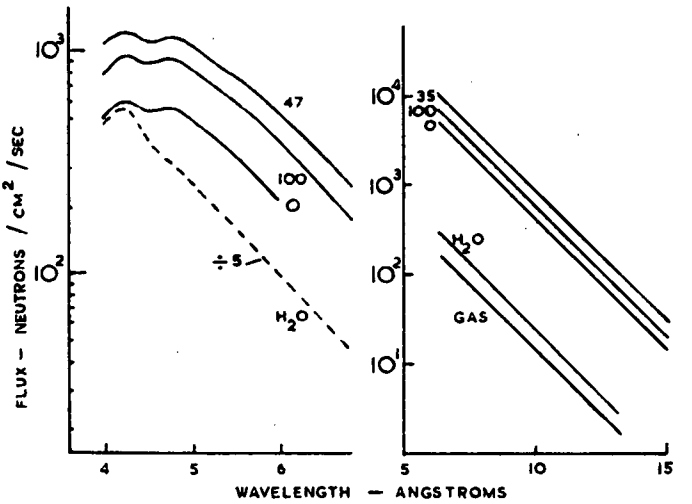

FIG. 2. (a) Neutron flux spectra recorded on C1G. The H_2O source is the 2.5-cm slab of ambient water. The numbers on the other curves give the hydrogen composition in atomic % for the cold sources. (b) Neutron flux spectra on G1C. The gas source was the source chamber S filled with hydrogen gas at 68 lb/in² and ambient temperature. Fluxes quoted in (a) and (b) are for the beams emerging from the monochromators.

The results on a number of liquid H_2:D_2: HD mixtures are presented in two ways in Figs 3 and 4. To compare with the work of previous authors, the geometries of the various ambient sources are eliminated by plotting gains with respect to a sub-cooled source of 100 at.% liquid hydrogen. The mixtures in the figures are specified as at.% hydrogen, the actual molecular contents being given in Table I. Figure 3 shows a marked difference between the results obtained on C1G and G1C for atomic H concentrations less than 40%. It is thought that this difference is due to the individual parts of the source being viewed. In G1C the neutrons originate from a small volume at the centre of the source, where one would expect the neutrons to be more fully moderated than for any other region. However, if there is insufficient hydrogen in this region, the chance of scattering neutrons into the beam tube will be relatively small. Too high a concentration of hydrogen on the other hand will lead to a depression of the total neutron density through absorption by hydrogen. The neutrons accepted by C1G are due in large part to leakage from the surface of the cold source. Because the leakage spectrum arises from neutrons having suffered fewer collisions in the source, a greater proportion of hydrogen is needed to obtain the optimum mixture.

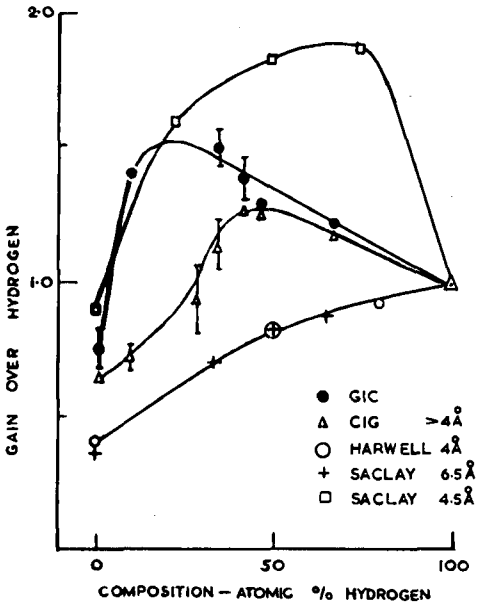

FIG.3. Flux gains relative to 100% liquid hydrogen sources as a function of composition. Closed circles are results on G1C, the error bars giving the spread of results at 7, 10 and 13 Å. Open triangles are results on C1G obtained with the incident beam monitor (integrated counts), the error bars giving the spread of results over an extended period. Crosses and open squares represent Saclay results at 6.5 and 4.5 Å respectively. The open circles are the Harwell results at 4 Å.

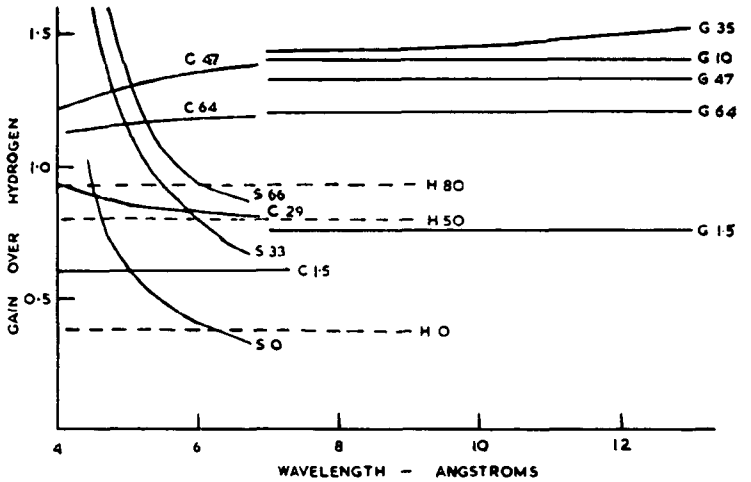

FIG.4. Flux gains relative to 100% liquid hydrogen, as a function of wavelength. The curves labelled C, G, H and S represent results obtained on C1G, G1C, at Harwell and at Saclay respectively. The numbers following the letters give the composition of the sources in at.% hydrogen.

Figure 4 shows that the flux gains over liquid hydrogen for the H/D mixtures are not very wavelength dependent between 4 - 15 Å. This is what one expects since the mean diffusion length for absorption to occur is much larger at all wavelengths between 4 - 5 Å than the mean diffusion length between scattering events. The discrepancies in the values of the gains observed on C1G and G1C, close to 7 Å and for hydrogen concentrations less than 40%, are related to the effects already seen in Fig. 3.

The present results are compared with previously reported work at Harwell [2] and at Saclay [3] in Figs 3 and 4. In the smaller volume of the DIDO source liquid hydrogen produces better thermalization than liquid deuterium because of the higher scattering cross-section, whereas hydrogen absorption is not significant in such small volumes. Similar results would

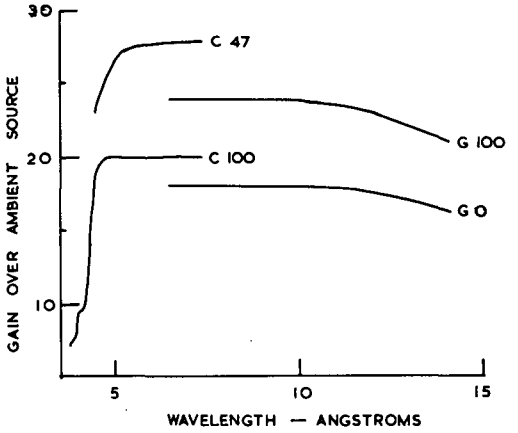

FIG. 5. Flux gains over an ambient H_2O source, measured on C1G and G1C (labelled C and G respectively). The numbers quoted give the compositions of the cold sources in at.% hydrogen.

be expected from the Saclay source because the volume is only slightly bigger than that of the DIDO source. Indeed this is observed at 6 Å where the results fall on the same curve as the DIDO values. At shorter wavelengths, however, the Saclay results differ in a remarkable way from what is observed here, and there is no obvious explanation for this.

One of the difficulties in comparing cold-source performance and theory is the specification of the gain. Simple theory refers to gain factors between two temperatures of completely thermalized sources. Experimentally not only is the extent of thermalization of the cold source unknown, but so is the thermalization of the ambient sources to which one wishes to refer a measured gain factor. Measurements have been made upon the neutron spectra scattered in C1G and G1C by a 2.5-cm thick slab of water positioned perpendicular to the beam tubes. Various gains over this ambient H_2O source are plotted in Fig. 5, and it is seen that the gain is independent of wavelength between 6 - 10 Å. The gain for the liquid hydrogen over the ambient source is 20 - 25. Assuming that the ambient source is properly moderated at 313°K, this gain factor suggests that the effective temperature of the liquid hydrogen source is about 50°K. The absence of a wavelength dependence in the 6-8 Å region is roughly in agreement with this conclusion.

ACKNOWLEDGEMENTS

This project began under the auspices of the former National Institute for Research in Nuclear Science and is now part of the neutron beam work sponsored by the Science Research Council. We are grateful for the interest shown by a number of colleagues and the support of Mr. J.J. McEnhill of AWRE, and in the initial stages Dr. J. Valentine of The Rutherford Laboratory. We should also like to acknowledge useful discussions with members of the AERE, particularly Dr. P.A. Egelstaff. Those authors from AWRE are grateful to the Director for permission to take part in this publication.

REFERENCES

[1] BUTTERWORTH, I., EGELSTAFF, P.A., LONDON, H., WEBB, F.J., Phil.Mag. 2 (1957) 917.
[2] COCKING, S.J., WEBB, F.J., AERE Rep. R5168 (1967).
[3] JACROT, B., Pile Neutron Research in Physics (Proc. Symp. Vienna, 1960), IAEA, Vienna, (1962) 393.
[4] CLARK, C.D., MITCHELL, E.W.J., PALMER, D.W., WILSON, I.H., J. sci. Instrum. 43 (1966) 1.

DISCUSSION

W. C. HAMILTON: In his presentation, Professor Brockhouse enquired as to the nature and cost of the Brookhaven Multi-spectrometer Control System. The total system – including computer, interfacing and personnel costs for much of the system programming – required about $500 000. We are at present operating nine independent experiments, so that the cost of each one is about $50 000. We use an SDS 920 computer with 16 000 words of 8-μsec core memory and a 32 000-word drum. There are a CRT display unit, two magnetic tape drives and individual input-output typewriters. I might add that this computer is quite obsolete, and a similar system could now be built for less – or, alternatively, a much more sophisticated and convenient system could be obtained for the same cost.

J. M. CARPENTER: May I address a question to Mr. Hamilton? Has the use of a single computer to serve all the instruments been found disadvantageous? What happens when the computer is out of action for reasons such as reprogramming or servicing?

W. C. HAMILTON: We do not feel that the drawbacks outweigh the great advantages in our particular experimental environment. There is very little downtime for reprogramming or servicing; and the few hours per month that are required for this are always arranged to coincide with a reactor shut-down. Users' programs are assembled on another computer and can usually be run immediately. Systems changes, when they are necessary, are made during the shut-down; we are indeed making some extensive changes in the system at the present time, and this is not leading to any major difficulties. We usually have about one failure of the system per month due to a user's error. Of course we have to be careful and we are careful, but the memory-protection hardware now available on many computers would allow us to be somewhat less so.

J. J. RUSH: I also should like to put a question to Mr. Hamilton, and perhaps also ask Mr. Mozer to comment. Is it not true that with the SDS system, which, by the way, we are also using at the National Bureau of Standards, the cost per instrument decreases as the number of instruments controlled rises?

W. C. HAMILTON: We can add an additional experiment for the cost of an additional interface - i.e. about $10 000. For example, when I needed an automatic X-ray diffractometer, I added it to the existing system for this sum. Each experiment of course requires some additional computer memory, but owing to the structure of our software this is not a serious limitation.

B. MOZER: When you buy a large computer the basic price per station is determined by the cost of the computer itself. Adding stations is relatively inexpensive. If you have numerous control operations at one station, e.g. several angle controls, sample temperature control or time-of-flight sequencing, then I think the small computer system would be preferable.

J. ALS-NIELSEN: The triple-axis spectrometers at Risø are going to be controlled by PDP 8S computers. The cost of a PDP 8S is now about $10 000. The cost of the auxiliary electronic equipment (digitizers, amplifiers, interface) is about $15 000, and so the total cost per instrument seems to be appreciably lower than at Brookhaven. However, expenditure on manpower for programming the computer is not included in these figures.

O.K. HARLING: I am going to comment on a method of achieving very highly monochromatic neutrons which has recently been published by Dr. Kottwitz of our laboratory. By using double Bragg diffraction ("Umweganregung") he has demonstrated, for example, that for rather perfect germanium crystals double Bragg monochromatization can be used to simulate normally forbidden reflections. He finds that there are at least 100 useful operating points in the energy range 3-50 meV which are relatively free from interference. Wavelength resolutions of $\Delta\lambda/\lambda \approx 10^{-4}$ are achievable in good crystals, but this resolution can be decreased by use of crystals with mosaic structure. It seems that this method, which gives precisely calculable energies and does not require very sophisticated goniometers and angle variation, may be useful both for precise determinations of crystal structure and eventually for very precise inelastic scattering work.

I also have a question for the authors of paper SM-104/131: What is the intensity on the sample at $E_0 = 0.1$ or 0.2 eV and what is the energy spread $\Delta E_0/E_0$?

J. SOSNOWSKI: The intensity of the pulsed monochromatic beam incident upon the sample, under conditions of 'direct' geometry and at a mean pulsed reactor power of 3 kW, was 10^4 n/s, with a neutron wavelength λ_0 of 2 Å. The half-width of this peak $\Delta\lambda/\lambda$ was 0.06 Å.

G. CAGLIOTI: Paper SM-104/52 by the McMaster group brings out a point of general interest: it shows the gain in reflectivity which can be obtained by mechanical treatment of the single crystals used in this work. The provision of this treatment is in fact equivalent to increasing the flux of whatever reactor is being used, and it would be very helpful if firms involved in crystal production could look into the matter.

B.N. BROCKHOUSE: Beryllium crystals are potentially better than any others for our purposes, and I think it would indeed be a good idea if a number of leading firms would get together and launch quite a substantial program with a view to providing us with the most perfect Be crystals that can be produced.

J.J. RUSH: My comment concerns the use of a fitter to cut out high-energy neutrons in the rotating crystal spectrometer. Neutron transmission measurements on single crystals of MgO by the Mol group some time ago and by Holmryd at Argonne show that this material is an excellent filter for use between about 1 and 2.5 Å, which is an important region for this technique. If one is going to use a filter rather than shielding, I feel that MgO would be a good material.

A.R. MACKINTOSH: Most people would now agree that triple-axis spectrometers are most suitable for studying solid single crystals, but I should like to ask about their performance relative to rotating crystal spectrometers when liquids are being investigated. Specifically, I should like to ask Mr. Cowley, who has up-to-date experience with both types of apparatus, whether he feels that his recent experiments on liquid helium would have been performed more or less easily and efficiently with a triple-axis spectrometer, located of course at the same beam port at which his rotating crystal spectrometer is placed.

R.A. COWLEY: I personally should have preferred to perform the whole experiment on a triple-axis spectrometer. This is largely because the raw data would have been much closer to what we required and would have needed far less processing than was called for in the case of data from the rotating crystal spectrometer.

O.K. HARLING: I quite appreciate the reasons for Mr. Cowley's choice, but all they really prove is that he and Mr. Woods have a triple-axis spectrometer which is better than their rotating crystal spectrometer. At Battelle Northwest we are also doing the same ^{4}He experiment and have a choice between a very good rotating crystal spectrometer and a good triple-axis instrument located at comparable beam holes. In our case it is clear that we will try this experiment first with our hybrid rotating crystal system. We expect to be able to go to about 25 $Å^{-1}$ as compared with about 91 $Å^{-1}$, which was the figure reached in the Chalk River work.

R.D. LOWDE: Just in case Mr. Cowley might be thought to be disparaging the rotating crystal spectrometer generally, I also should like to speak in favour of that instrument. It is without the principal weakness of multichopper machines, which is that the latter are in-line instruments and have background problems resulting from leakage of the main beam to the specimen area; it is also without the principal weakness of the triple-axis spectrometer, which is that it is difficult to make the analyser resolution low when low resolution is required. On the other hand, as Mr. Harling has shown, by the use of large monochromating crystals the continuously-variable incident energy can be extended without difficulty up to values approaching 0.5 eV, while a large number of scattering angles can be measured simultaneously. Moreover, a rotating crystal spectrometer can easily be integrated into a series of successive instruments fed by the same neutron beam.

J.J. VAN LOEF: Mr. Harling, did you use the mechanically deformed crystals as a monochromator crystal in the rotating crystal spectrometer, and did this give you the time resolution of about 10 μsec which you indicated in paper SM-104/81?

O.K. HARLING: Let me take this opportunity of emphasizing that the material we used was copper, which we prefer to beryllium for this purpose. We normally take a number of thin slabs of copper for use as deformed crystals in our rotating crystal spectrometer. This system works well and we do get time resolutions of the kind mentioned. However, the actual data shown in this paper were obtained with a single thick slab of copper.

J.J. VAN LOEF: Does a crystal consisting of several thin slabs of copper possess mechanical strength adequate to withstand rotation at 10 000 rpm?

O.K. HARLING: Yes. We embed the slabs in a low-melting Zn-SN alloy and put this inside an aluminium alloy sleeve. One can also deform single slabs as described in the paper, and the crystal is then strong enough for rotation speeds in excess of 10 000 rpm.

H. MAIER-LEIBNITZ (Chairman): I personally am convinced that there is a great future for composite or laminated crystal systems.

B.N. BROCKHOUSE: It should be pointed out that Mr. Harling is comparing 'improved' copper crystals with what one might term 'unimproved' or 'as received' beryllium crystals. Now, work can be done to improve beryllium crystals on the same lines as copper ones with the difference that, while we are a factor of about 2 or less away from the ultimate as far as copper is concerned, we are still a factor of 8 or 10 away in the case of beryllium – meaning that the latter has in fact much the greater potential.

F. WEBB: I am going to report a few results on beryllium filters which are, I think, of interest in connection with paper SM-104/117 by

Messrs Beg and Ross. Beryllium filter transmissions have been calculated using a simple Monte Carlo program, assuming isotropic elastic scattering with constant cross-section. Results for rectangular slabs, as used in filter detector methods, show that for dimensions around $10 \times 5 \times 0.8$ cm the transmission due to multiple scattering is comparable with the direct transmission. For the slabs used by Beg and Ross, which were 2.5 cm thick, the total transmission would be three or four times as large as that calculated from the cross-section. Results have also been obtained for cylindrical geometries.

M. G. ZEMLYANOV: At our Institute we are using deformed single crystals of iron silicide as crystal monochromators. For neutrons with a wavelength in the region of 1.1 Å, deformation of the single crystals results in a three- or fourfold increase in the monochromatic neutron intensity by comparison with a single crystal of lead.

I should also like to say a few words about ^{3}He neutron detectors. These instruments cannot be used in all circumstances. If the energy of the scattered neutrons is very low the counting efficiency for these neutrons will be less strongly dependent on pressure than that for fast neutrons (background being proportional to pressure). In such cases it may well be better to use BF_3 detectors.

B. N. BROCKHOUSE: Frankly, I don't see how there can be conditions under which a ^{3}He counter will not work.

Regarding crystal reflectivity measurements in general, there is, I think, an unfortunate tendency to represent these in terms of a comparison with something else. What we need are quotations of absolute reflectivities, always accompanied by a statement of the wavelength at which the reflectivity measurement was made.

H. MAIER-LEIBNITZ (Chairman): I quite agree with this latter remark.

B. DORNER: It seems to me that ^{3}He counters may not be the most suitable for use with triple-axis spectrometers. With these instruments the thickness of the counters is not of great importance. To reduce the background registered by such a spectrometer, the discriminator level must be raised for the ^{3}He counter, owing to its sensitivity to gamma radiation. But increasing the discriminator level lowers the neutron counting efficiency. I wonder if that is why Mr. Stedman and his team at Studsvik, where they had a background of only 7 counts per hour, used BF_3 counters.

D. K. ROSS: In his presentation of our paper on the Herald Cold Source (SM-104/117), Mr. Brockhouse appeared to be in some doubt concerning the variation of the gain with hydrogen/deuterium mixture. The general behaviour can be explained qualitatively in terms of the volume of moderator. To take advantage of the low absorption of deuterium, a large volume must be used. Thus, the small sources give the best gain at 100% H_2, while the very large sources constructed at Grenoble give the highest gains yet measured. The Herald source of 5 litres is in an intermediate position and gives a maximum gain for an H_2/D_2 mixture. The difference between the spectra at the two ends of the Herald beam tube indicates the importance of a probe tube for a D_2 source.

DESCRIPTION ET CARACTERISTIQUES NEUTRONIQUES DU TUBE CONDUCTEUR DE NEUTRONS INSTALLE PRES DU REACTEUR EL3

B. FARNOUX, B. HENNION ET J. FAGOT
CEA, CENTRE D'ETUDES NUCLEAIRES DE SACLAY,
FRANCE

Abstract — Résumé

DESCRIPTION AND NEUTRON CHARACTERISTICS OF A NEUTRON GUIDING TUBE AT THE EL3 REACTOR. A neutron guiding tube can provide a more intense and better filtered beam of slow neutrons than could be obtained by classical method (crystal filters). Such a device is under construction at the exit of a channel of the EL3 reactor in CEN Saclay.

A short summary of the operating principles of a guiding tube is followed by the description of the mechanical and technical characteristics of the Saclay apparatus. This is a bent rectangular (20 mm x 50 mm) tube constructed from nickel mirrors. The radius of the curvature is 835 m, the total length of the tube is 30 m. The biological protection consists of a water pool 17 m long and 2 m x 2 m in cross-section. The measurements have shown that the background at the experimental post is due to neutrons escaping through the imperfect reflecting surface of the tube. It could easily be eliminated by light shielding (Cd or Li). The neutron energy spectrum measured by the time-of-flight method at the exit of the tube confirmed the theoretical prediction: it contains only thermal and cold neutrons. The intensity distribution in a horizontal plane is homogeneous for cold neutrons (E < 5 meV) and asymmetric for thermal neutrons (filter effect). The average neutron flux in the beam is 2.3×10^7 n cm^{-2} sec^{-1}. For cold neutrons, the transmission of the device is 95%.

DESCRIPTION ET CARACTERISTIQUES NEUTRONIQUES DU TUBE CONDUCTEUR DE NEUTRONS INSTALLE PRES DU REACTEUR EL3. Un tube conducteur de neutrons a pour but de fournir un faisceau de neutrons lents intense et mieux filtré que ceux obtenus par les méthodes classiques (filtres cristallins). Un tel appareil vient d'être construit à la sortie d'un canal du réacteur EL3 au centre d'études nucléaires de Saclay.

Après un bref rappel des principes du tube conducteur de neutrons, le mémoire décrit les caractéristiques mécaniques et techniques de l'appareil du CEN de Saclay. C'est un tube courbe, de section rectangulaire (20 x 50 mm) formé par l'assemblage étanche de miroirs nickelés. Le rayon de courbure est de 835 m, et sa longueur totale de 30 m. La protection biologique est assurée par une piscine d'eau légère de 2 m^2 de section et de 17 m de long. Les mesures ont montré que le bruit de fond dans le local expérimental provient uniquement des neutrons diffusés par les imperfections des surfaces réfléchissantes du tube conducteur de neutrons. Il peut être facilement éliminé par des protections légères (cadmium ou lithium). Le spectre en énergie mesuré par la méthode du temps de vol à la sortie du guide est conforme à celui prévu théoriquement: il n'est composé que de neutrons thermiques et froids. La distribution en intensité dans un plan horizontal est homogène pour les neutrons froids (E < 5 meV) et dissymétrique pour les neutrons thermiques (effet filtre). Le flux moyen du faisceau est de $2,3 \times 10^7$ n/$cm^2 \cdot s$. La transmission pour les neutrons froids est de 95%.

INTRODUCTION

Une technique nouvelle permettant d'obtenir un faisceau pur et intense de neutrons lents a été récemment décrite [1-3]. L'idée, fondée sur le phénomène de réflexion totale mis en évidence par Fermi [4, 5] est de construire des tubes conducteurs de neutrons (notés TCN dans ce qui suit) analogues dans leur principe aux guides de lumière. Plusieurs appareils de ce type ont déjà été réalisés [6-8].

Le TCN de Saclay a été construit comme un prototype: il permet de disposer d'une maquette en grandeur réelle utilisable pour des contrôles expérimentaux sur les conditions matérielles optimales de réalisation d'un TCN. Par la suite, il fournira un faisceau de neutrons froids plus intense et mieux filtré que celui obtenu par les méthodes classiques (filtres cristallins ou mécaniques) utilisées jusqu'alors.

Dans la première partie de cet exposé nous rappellerons brièvement la théorie du tube conducteur de neutrons, et ce qui en fait son originalité par rapport aux procédés classiques. Les caractéristiques physiques et mécaniques sont décrites dans la deuxième partie. Enfin les premiers résultats expérimentaux sur le fonctionnement de l'appareil sont exposés dans la dernière partie.

1. PRINCIPES DU TUBE CONDUCTEUR DE NEUTRONS

1.1. Rappel d'optique neutronique

Il est possible de définir pour les neutrons une optique analogue à l'optique géométrique (réfraction et réflexion) utilisée dans le cas de la lumière [9]. Il faut pour cela définir l'indice de réfraction pour les neutrons. La théorie de la réfraction et de la réflexion des neutrons lents de longueur d'onde λ à la surface d'une substance établit l'expression de l'indice de réfraction sous la forme [10-12]

$$n = 1 - \lambda^2 \frac{N a_{coh}}{2\pi} \qquad (1)$$

N est la densité des atomes constituant le milieu réfractant et a_{coh} leur amplitude de diffusion cohérente. Les phénomènes d'absorption peuvent être négligés dans la majorité des cas. Pour la plupart des substances a_{coh} est positif et, par suite, l'indice de réfraction n est inférieur à l'unité de l'ordre de quelques 10^{-6}. Le phénomène de réflexion totale peut alors prendre naissance, d'une manière analogue à ce qui se produit dans le cas de la lumière, ou plus exactement des rayons X (compte tenu de l'ordre de grandeur de l'indice de réfraction).

Soit θ l'angle entre la direction des neutrons incidents de longueur d'onde λ et la surface du milieu réfléchissant, l'angle limite de réflexion totale est alors

$$\theta_c = \sqrt{2(1-n)} = \alpha\lambda \qquad (2)$$

où $\alpha = \sqrt{N a_{coh}/2\pi}$ est un coefficient caractéristique du réflecteur. Sa valeur pour quelques matériaux est donnée dans le tableau I. La valeur de θ_c étant toujours très faible, la réflexion totale se produit sous incidence rasante. Elle est donc très sensible à l'état de surface du réflecteur.

Dans le cas d'un réflecteur idéal, la valeur du facteur de réflectivité R varie en fonction de l'angle d'incidence θ suivant la formule

$$R = \left| \frac{1 - \sqrt{1 - \left(\frac{\theta_c}{\theta}\right)^2}}{1 + \sqrt{1 - \left(\frac{\theta_c}{\theta}\right)^2}} \right|^2 \qquad (3)$$

TABLEAU I. VALEURS DE (1-n) ET DE α POUR QUELQUES MATERIAUX POUVANT SERVIR DE REFLECTEUR

Réflecteur	$(1-n) \times 10^5$	$\alpha \times 10^3$ (rad/Å)	α (min/Å)
Al	3	0,82	2,82
Verre	6	1,09	3,78
Cu	10	1,41	4,87
Ni	15	1,73	5,96
^{58}Ni	21	2,05	7,07

Il est égal à l'unité pour $\theta < \theta_c$. Il a été établi expérimentalement [13] que la profondeur de pénétration du faisceau de neutrons dans le milieu réfléchissant était de l'ordre de

$$d = 100\ \lambda \tag{4}$$

1.2. Tube conducteur de neutrons idéal

Les réflecteurs peuvent être assemblés pour former un tube à parois réfléchissantes. L'utilisation du phénomène de réflexion totale permet alors de « guider» un faisceau de neutrons lents. Plusieurs types de tubes peuvent être conçus.

1.2.1. Tube conducteur droit

La disposition la plus simple est un tube réfléchissant droit. Il permet alors d'éloigner les expériences de la source de bruit de fond (réacteur) tout en conservant une intensité importante: en effet, le faisceau se propageant dans le tube par réflexion totale, il conserve tout le long du trajet le même angle solide $\Omega = 4\ \theta_c^2$.

L'intensité transmise par un tube conducteur droit d'ouverture a et de longueur L peut être calculée de la façon suivante:

Le nombre de neutrons par seconde et par électron-volt à la sortie du tube conducteur peut s'écrire sous la forme

$$\frac{dJ}{dE} = I(E)\ T(K) \tag{5}$$

I(E) est la densité de flux par stéradian à l'entrée du tube. Dans le cas où la répartition du flux $\Phi(E)$ peut être considérée comme isotrope et maxwellienne avec une température d'équilibre T, I(E) s'écrit

$$I(E) = \frac{\Phi(E)}{4\pi} = I_0 \frac{E}{(k_B T)^2} e^{-E/k_B T} \tag{6}$$

T(K) est le facteur de transmission du tube. Sa valeur dépend du rapport

$$K = \frac{\theta_c(E)}{\theta^*} \tag{7}$$

$\theta_c(E)$ est l'angle limite de réflexion totale pour les neutrons d'énergie E.

$$\theta^* = \frac{a}{L} \tag{8}$$

est l'angle caractéristique du tube.

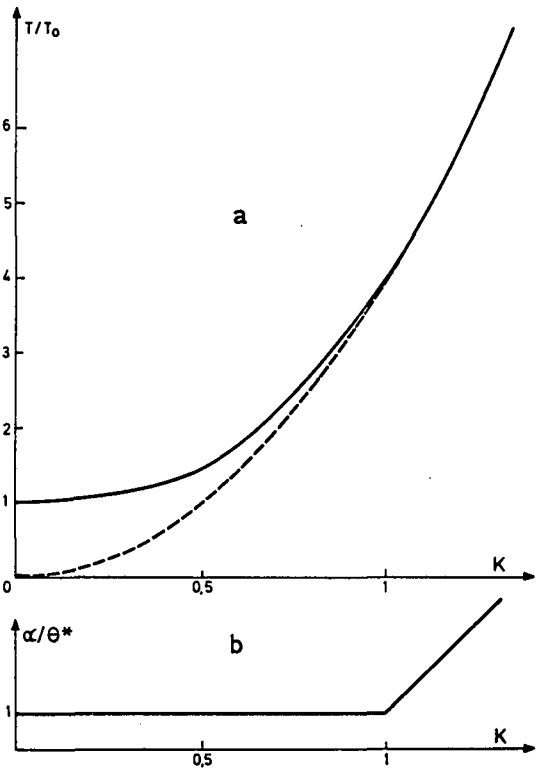

FIG.1. Variation: a - du facteur de transmission $T(K)/T_0$; b - de la divergence angulaire α/θ^* pour un tube conducteur droit, en fonction de K.

La variation du facteur de transmission T(K) en fonction de K est donnée sur la figure 1. Les remarques suivantes peuvent être faites:

Dans le cas limite où le tube est un collimateur non réfléchissant (K = 0) le facteur de transmission devient

$$T(0) = S\Omega = T_0 \tag{9}$$

Ω est l'angle solide du collimateur.

Pour les valeurs $0 < K < 1$, le calcul montre que T(K) varie de la valeur T_0 à la valeur $4T_0$. Lorsque $K \geq 1$ le facteur de transmission varie suivant la forme

$$T(K) = 4\ K^2\ T_0 \tag{10}$$

et l'intensité transmise par le tube conducteur devient

$$\frac{dJ}{dE} = I(E)\ 4K^2\ T_0 \tag{11}$$

Le gain par rapport à un collimateur non réfléchissant de même géométrie est

$$G = 4K^2 \tag{12}$$

Pour un tube en nickel de 10 m de long et de 10 cm^2 de section, le gain théorique est de 20 pour une longueur d'onde de 5 Å. La divergence angulaire du faisceau α varie aussi avec la valeur de K (fig. 1b). Pour $K < 1$ elle est simplement $\alpha = \theta^*$ et pour $K \geq 1$ elle vaut $\alpha = \theta_c(E)$.

1.2.2. Tube conducteur courbe

L'utilisation d'un TCN droit permet donc d'éloigner les spectromètres neutroniques du cœur du réacteur. Le bruit de fond (neutrons rapides, rayons γ) décroît ainsi en fonction de la distance. En plus, si le TCN est courbé il «filtre» le faisceau:

En effet, si le tube conducteur a un rayon de courbure et une longueur tels qu'aucun neutron ne puisse sortir sans avoir subi au moins une réflexion totale, les neutrons rapides et le rayonnement γ émis par le cœur du réacteur sont alors complètement diffusés par les parois du tube et absorbés dans la protection qui l'entoure. Le faisceau transmis par le guide courbe est uniquement composé de neutrons lents; le tube conducteur courbe joue ainsi un rôle de filtre.

Le faisceau étant transmis par réflexion totale, la propagation ne pourra se faire que si certaines conditions de réflexion sont remplies. Ces conditions sont exprimées par l'équation angulaire du tube conducteur courbe. Elle peut se calculer de la façon suivante:

Soit un tube réfléchissant, de section rectangulaire (largeur a, hauteur b avec $b > a$) courbé dans le plan horizontal avec un rayon de courbure ρ (fig. 2). Un neutron passant par un point P de la face d'entrée et dont la direction de propagation fait un angle θ avec l'axe du tube dans le plan horizontal tombe sur la face concave avec un angle θ_a. Un raisonnement géométrique simple établit la formule

$$\frac{\rho - x}{\cos \theta_a} = \frac{\rho}{\cos \theta} \tag{13}$$

Les angles limites de réflexion totale des neutrons étant toujours très petits dans le domaine d'énergie considéré ici (10^{-1} à 10^{-4} eV) l'équation (13) peut s'écrire

$$\theta_a^2 = \theta^2 + \frac{2x}{\rho} \tag{14}$$

L'équation (14) entraîne les remarques suivantes:

a) quand x=a, l'angle d'entrée θ est égal à l'angle d'incidence θ_i sur la face convexe et (14) montre que $\theta_a > \theta_i$.

b) Quand x = a et $\theta = 0$, l'angle d'incidence θ_a prend la valeur particulière θ^*. C'est l'angle caractéristique du tube conducteur courbe:

$$\theta^{*2} = \frac{2a}{\rho} \tag{15}$$

L'équation (14) peut alors s'écrire

$$\theta_a^2 = \theta^2 + \frac{x}{a}\theta^{*2} \tag{16}$$

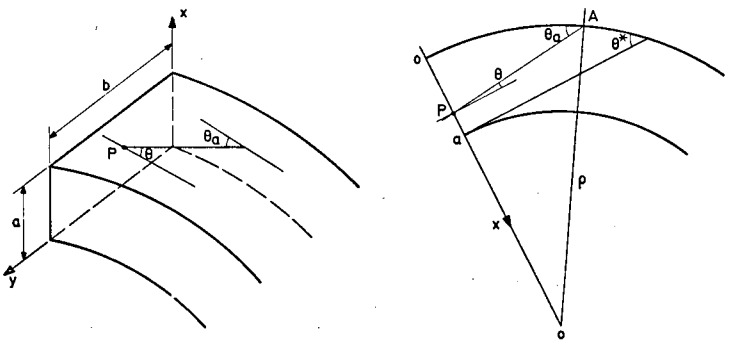

FIG.2. Géométrie du tube courbe montrant les relations entre les paramètres du tube.

C'est l'équation angulaire du tube conducteur courbe. La condition de propagation est

$$0 \leq \theta_a \leq \theta_c(\lambda) \tag{17}$$

Le tube étant courbé dans un plan horizontal un écart X est créé entre l'axe du faisceau direct et la sortie du guide de longueur L, donné par

$$X = \frac{L^2}{2\rho} \tag{18}$$

La longueur L pour laquelle aucun neutron ne peut sortir du tube sans être réfléchi ou diffusé au moins une fois est appelée longueur de vision directe et notée L_1:

$$L_1 = 2\rho\theta^* \tag{19}$$

Pour cette longueur l'écart X vaut 4a.

Dans le cas d'un tube conducteur courbe idéal (géométrie parfaite des surfaces réfléchissantes, réflectivité nulle pour $\theta_a > \theta_c$ et égale à l'unité

pour $\theta_a < \theta_c$), on peut montrer que l'intensité transmise s'écrit sous la forme

$$\frac{dJ}{dE} = I(E)\ 4K^2\ T_0\ T(K) \qquad \text{avec } T_0 = S\theta^{*2} \tag{20}$$

Cette expression diffère de celle obtenue dans le cas du tube réfléchissant droit (§ 1.2.1 (11)) par le terme T(K), dont la valeur dépend du rapport $K = \theta_c(E)/\theta^*$.

Le calcul montre que T(K) peut se mettre sous la forme suivante:

$$\begin{aligned} &\text{a) Si } K \leq 1 \qquad T(K) = \frac{2}{3} K^2 \\ &\text{b) Si } K > 1 \qquad T(K) = \frac{2}{3} K^2 \left[1 - \left(1 - \frac{1}{K^2}\right)^{3/2}\right] \end{aligned} \tag{21}$$

La figure 3 montre la variation du facteur T(K) en fonction de K. Pour des valeurs de K élevées, la transmission du tube courbe est équivalente à celle d'un tube droit. Pour K = 1 elle est égale aux deux tiers de celle du guide droit de même dimension. La transmission diminue ensuite rapidement. La variation de cette transmission avec la longueur d'onde fait que le TCN courbe est un «filtre passe-bas» en énergie.

1.2.3. Tube conducteur bicourbe

L'effet de ce filtre peut être encore accentué en utilisant un TCN composé de deux parties à courbure opposée. Dans ce cas on peut montrer que le facteur de transmission T(K) prend les valeurs suivantes:

$$\begin{aligned} &\text{a) Si } K \leq 0,707 \qquad T(K) = 0 \\ &\text{b) Si } 0,707 < K \leq 1 \qquad T(K) = \frac{2}{3} K^2 \left(2 - \frac{1}{K^2}\right)^{3/2} \\ &\text{c) Si } K > 1 \qquad T(K) = \frac{2}{3} K^2 \left[1 - \left(1 - \frac{1}{K^2}\right)^{3/2}\right] \end{aligned} \tag{22}$$

La variation de ce facteur de transmission est portée sur la figure 3. Les neutrons de longueur d'onde λ telle que $K \leq 0,707$ sont éliminés du faisceau. Cet effet permet d'obtenir un faisceau de neutrons de longueur d'onde λ telle que $K = 1$ sans harmonique $\lambda/2$. Pour les neutrons de grande longueur d'onde ($K > 1$) la transmission est la même que dans le cas d'un TCN à courbure simple (21b et 22c).

1.3. Effets des imperfections sur la transmission

Dans le cas d'un TCN réel, les imperfections des parois réfléchissantes, inévitables à l'échelle du phénomène considéré, entraînent que la réflectivité (éq. (3)) est inférieure à l'unité pour des angles $\theta_a \leq \theta_c(E)$. L'évaluation quantitative de l'effet de ces défauts sur l'intensité transmise est délicate.

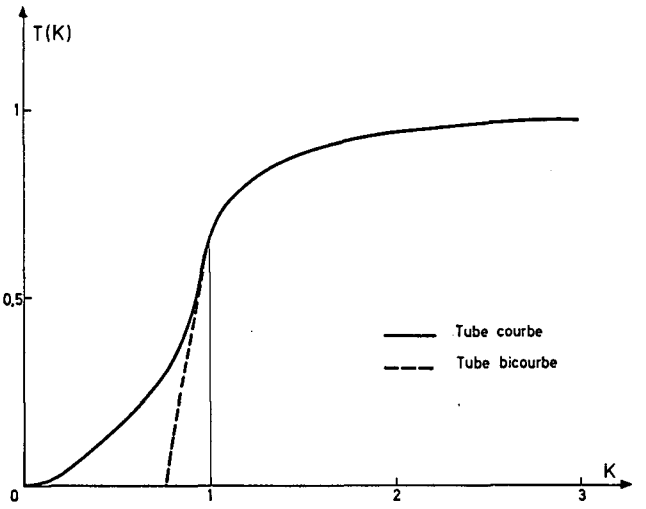

FIG.3. Variation du facteur T(K) pour un tube courbe et un tube bicourbe.

Qualitativement les défauts qui affectent la transmission d'un TCN sont de deux sortes:

a) Les imperfections microscopiques de la surface (microgéométrie), dont l'effet est proportionnel au rapport de leur taille à la longueur d'onde des neutrons. Cet effet varie comme $1/\lambda$. (La section efficace de capture des atomes constituant le miroir, qui varie comme $1/v = \lambda$, est un effet négligeable pour la majorité des substances.)

b) Les «effets géométriques»(macrogéométrie). Les neutrons étant réfléchis sous incidence rasante, l'intensité réfléchie est très sensible aux défauts de géométrie du réflecteur: ondulation de la surface, défaut d'alignement des miroirs, approximation de la courbure par une ligne brisée.

En première approximation les pertes dues à ces défauts peuvent être prises en compte en attribuant un coefficient de réflectivité global $R < 1$ aux parois du tube. Si un neutron entre dans le guide sous un angle tel qu'il fasse n réflexions sur les parois avant de sortir, alors la transmission pour ce neutron est R^n.

Pour un tube réfléchissant droit, le nombre de réflexions pour un angle d'incidence θ est donné par

$$n = k \qquad \text{avec } k = \frac{\theta}{\theta^*} \tag{23}$$

Pour un tube courbe il faut distinguer entre deux types de réflexions suivant la valeur de K (fig. 4).

Si $K \leq 1$ les neutrons ne peuvent subir des réflexions que sur la paroi concave du guide. Le nombre de réflexions de ce type (réflexions en guirlande) est alors dans le cas d'un tube de longueur égale à L_1

$$n_G = \frac{1}{\sqrt{k^2 + \frac{x}{a}}} \tag{24}$$

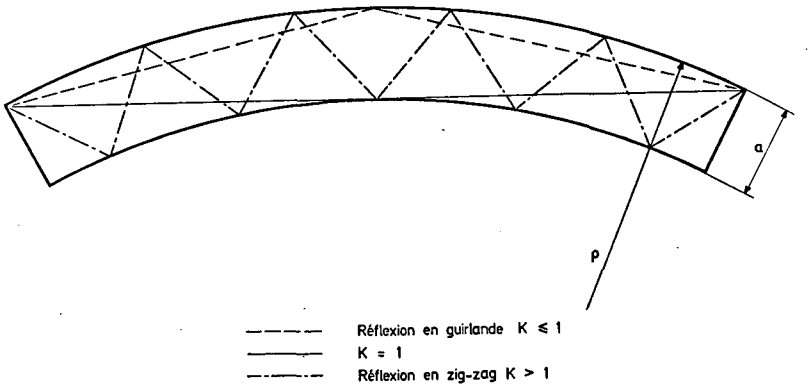

FIG.4. Les différents types de réflexions dans un tube conducteur de neutrons.

Si K > 1 les neutrons peuvent subir en plus un autre type de réflexion selon la valeur de leur angle d'incidence: ils peuvent être réfléchis alternativement sur la paroi concave et sur la paroi convexe (réflexions en zigzag). Le nombre de réflexions est donné dans ce cas par

$$n_{ZZ} = \frac{2}{\sqrt{k^2 + \frac{x}{a}} - \sqrt{k^2 + \frac{x}{a} - 1}} \qquad (25)$$

La variation du nombre de réflexions (24 et 25) en fonction de la valeur de k est portée sur la figure 5, pour trois valeurs du paramètre x/a. Lors du passage des réflexions en guirlande aux réflexions en zigzag, le nombre de réflexions passe brusquement de la valeur 1 à la valeur 2 (pour une longueur de vision directe).

1.4. Avantages du tube conducteur de neutrons

L'originalité d'un tube conducteur de neutrons par rapport aux procédés classiques (collimateurs non réfléchissants, filtres) est liée à l'utilisation du phénomène de réflexion totale et à la courbure.

1.4.1. Utilisation du phénomène de réflexion totale

Dans le cas d'un tube réfléchissant idéal, tout neutron d'énergie E entrant à l'abscisse x avec un angle θ tel que la relation $\theta_a \leq \theta_c(E)$ soit satisfaite est «guidé» jusqu'à la sortie, indépendamment de la longueur du tube. Cet effet permet d'éloigner la zone expérimentale de la source de bruit de fond (réacteur et hall du réacteur). De plus, grâce au gain de place lié à cet éloignement, le nombre d'appareils peut être augmenté autour d'un réacteur.

A cause de l'augmentation de l'angle solide par réflexion totale ($\Omega = 4\theta_c^2$) l'intensité transmise par un tube conducteur de neutrons est plus élevée que dans le cas d'un collimateur non réfléchissant. Cet effet, relativement faible pour les neutrons thermiques, devient important pour les neutrons froids.

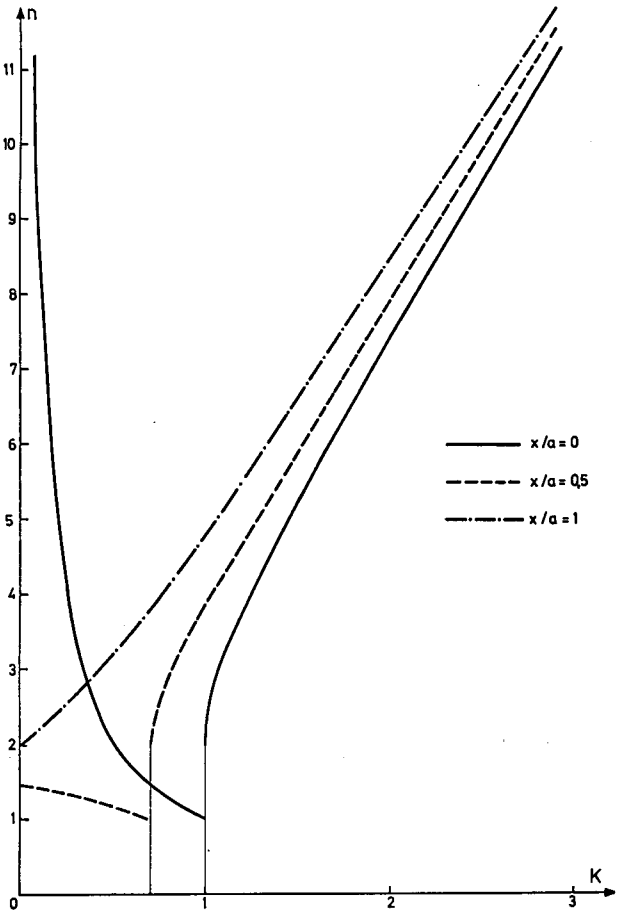

FIG. 5. Nombre de réflexions en fonction de $K = \theta/\theta^*$ pour différentes valeurs de x/a, pour un tube conducteur de longueur L_1.

1.4.2. Avantages liés au rayon de courbure

Pour un tube réfléchissant courbe de longueur égale à L_1, aucun neutron ne peut sortir sans avoir subi au moins une réflexion. Ceci entraîne une diminution du bruit de fond, les neutrons rapides et le rayonnement γ du cœur étant diffusés par les parois du tube et absorbés dans la protection. Cet effet est amélioré si le tube conducteur a une longueur égale à $2L_1$, car toute la première partie du tube est une source de bruit fond.

La courbure introduit donc un effet filtre passe-bas en énergie qui peut être caractérisé par le rapport K:

Les neutrons d'énergie E tels que $K > 1$ se propagent dans le guide en subissant les deux types de réflexions: zigzag si $\theta_a > \theta^*$ et guirlande si $\theta_a < \theta^*$. La répartition de ces neutrons à la sortie du tube conducteur est homogène en fonction de x/a (fig. 6).

Pour les neutrons d'énergie plus grande tels que $K \leq 1$ la propagation se fait uniquement par réflexion en guirlande sur la paroi concave. A la sortie du tube la répartition de ces neutrons est dissymétrique en fonction de x/a (fig. 6).

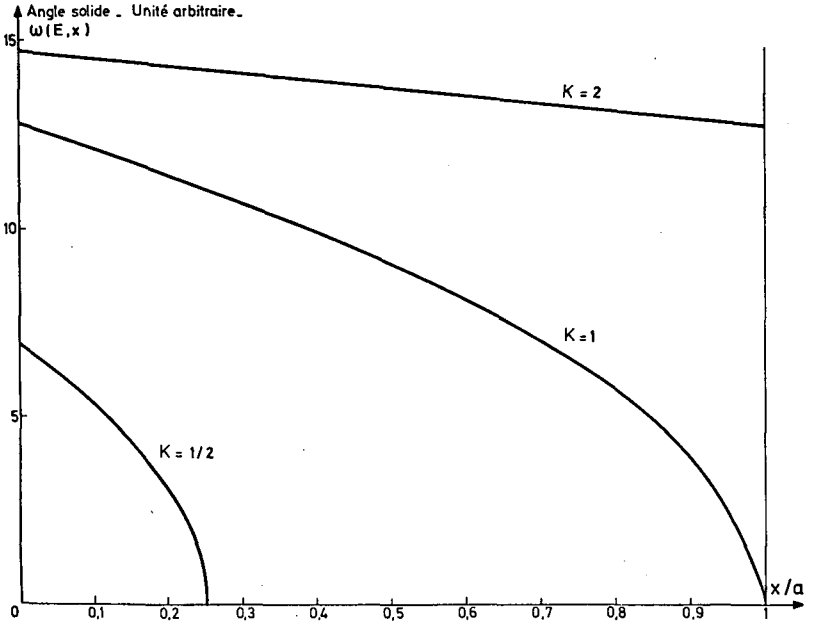

FIG. 6. Distribution théorique de l'intensité en fonction de l'abscisse de sortie. Elle est proportionnelle à l'angle solide permis $\omega(E,x)$.

2. CARACTERISTIQUES DU TUBE CONDUCTEUR DE NEUTRONS DE SACLAY

2.1. Implantation

Le TCN de Saclay est courbe. Il est implanté à la sortie du canal H_5 de la pile EL3. Le collimateur placé dans le canal définit deux faisceaux. L'axe de chacun des faisceaux fait un angle de 1° dans le plan horizontal avec l'axe théorique du canal. La divergence angulaire verticale est la même dans les deux cas: $2,9 \times 10^{-2}$ rad (1° 40'). Dans le plan horizontal elle est de 2×10^{-2} rad (1° 10') pour le premier faisceau et de $1,6 \times 10^{-2}$ rad (55') pour le second. Celui-ci est réservé pour la construction ultérieure d'un autre guide qui doit en principe transmettre un faisceau de neutrons thermiques ($\lambda \sim 1$ à 2 Å).

Le premier tube conducteur a été calculé pour transmettre un faisceau de neutrons froids ($E < 5 \times 10^{-3}$ eV). Pour en augmenter le flux une source froide sera placée dans le canal H_5. Ce sera une boucle à hydrogène liquide [14].

L'obturateur de deux faisceaux est constitué par un barillet en fonte de 80 cm d'épaisseur, percé de deux canaux. Il tourne dans un bâti métallique rempli de béton de forte densité, qui occupe entièrement la niche du canal.

2.2. Caractéristiques physiques

La section du tube conducteur est rectangulaire: largeur 20 mm, hauteur 50 mm. Cette section a été déterminée par la taille des échantillons étudiés par les physiciens. Le nickel a été choisi comme réflecteur. C'est en effet le matériau courant pour lequel l'angle limite de réflexion totale est le plus grand:

$$\underset{\text{rad}}{\theta_c(\lambda)} = 1{,}73 \times 10^{-3} \times \underset{\text{Å}}{\lambda} \qquad \text{soit } 6' \text{ par Å} \tag{26}$$

Le rayon de courbure $\rho = 835$ m a été fixé pour que $K = 1$ (éq. 21) pour $\lambda = 4$ Å ($E = 5{,}11 \times 10^{-3}$ eV) et donc $K > 1$ pour les neutrons froids. Ceci fixe la valeur de l'angle caractéristique

$$\theta^* = 6{,}92 \times 10^{-3} \text{ rad}$$

et la longueur de vision directe $L_1 = 11{,}6$ m.

La longueur totale du tube conducteur est $L = 30$ m. Elle est telle qu'aucun neutron ne peut sortir du guide sans avoir subi au moins deux réflexions totales ($L = 2{,}5\ L_1$). Elle a été imposée par la nécessité d'avoir une bonne accessibilité sur une longueur assez grande (au moins une fois L_1) pour effectuer les mesures technologiques.

Pour cela le TCN est composé de deux parties: la première a une longueur de 17 m et traverse l'enceinte étanche du hall du réacteur. Cette partie est rendue peu accessible par la protection biologique (fig. 7). La deuxième partie du tube conducteur a une longueur de 13 m. Elle est abritée dans un local extérieur au hall du réacteur (fig. 8). Aucune protection n'étant nécessaire pour la partie extérieure, elle est très accessible. Ceci permet d'effectuer des modifications techniques sur le guide pour en étudier les influences sur la transmission du TCN.

La protection biologique de la première partie est assurée par une piscine d'eau légère. Sa section moyenne est de 2 m × 2 m et elle entoure entièrement le guide. La protection est renforcée près du réacteur par un tunnel constitué par des blocs de béton de forte densité de 20 cm d'épaisseur. La piscine constitue une protection efficace contre les neutrons diffusés par les parois du guide, et forme un écran protecteur pour les expériences placées à l'extrémité du guide contre le bruit de fond venant du faisceau direct.

2.3. Caractéristiques mécaniques

La réflexion totale se produisant sous incidence rasante, l'état de surface microscopique (rugosité) et macroscopique (ondulation) de la couche réfléchissante a une importance qu'il est difficile de chiffrer. Aussi un soin tout particulier a-t-il été apporté à la réalisation de la couche réfléchissante, de son support et de la mécanique de soutien.

2.3.1. Tube réfléchissant

Le tube conducteur de neutrons froids est formé par la juxtaposition d'éléments réfléchissants rectilignes. Ils sont constitués par quatre dalles

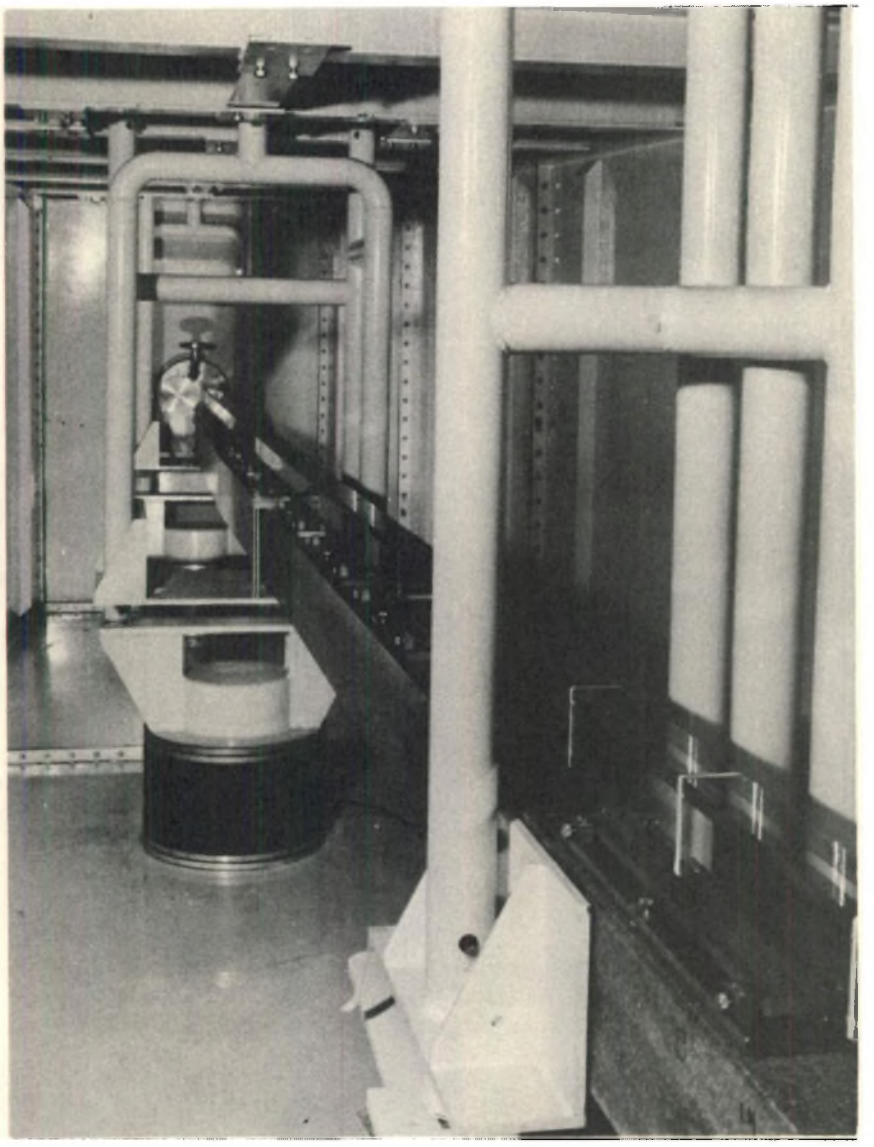

FIG. 7. Partie du TCN intérieure au hall du réacteur. Cette partie est placée dans un bac métallique qui peut être rempli d'eau pour assurer la protection biologique. Les poutres en granit sont reliées entre elles par des flasques métalliques solidaires des vérins de réglage. Ceux-ci, placés dans des tubes, dépassent le niveau de l'eau. Au fond, la bride d'étanchéité, côté réacteur, porte le tube de pompage du TCN.

de verre métallisé de 20 mm d'épaisseur et de 340 mm de longueur qui sont assemblées par collage pour former un parallélépipède creux de 20 mm × 50 mm de section intérieure (fig. 9). Avant le montage ces dalles de verre subissent un traitement optique pour assurer une parfaite

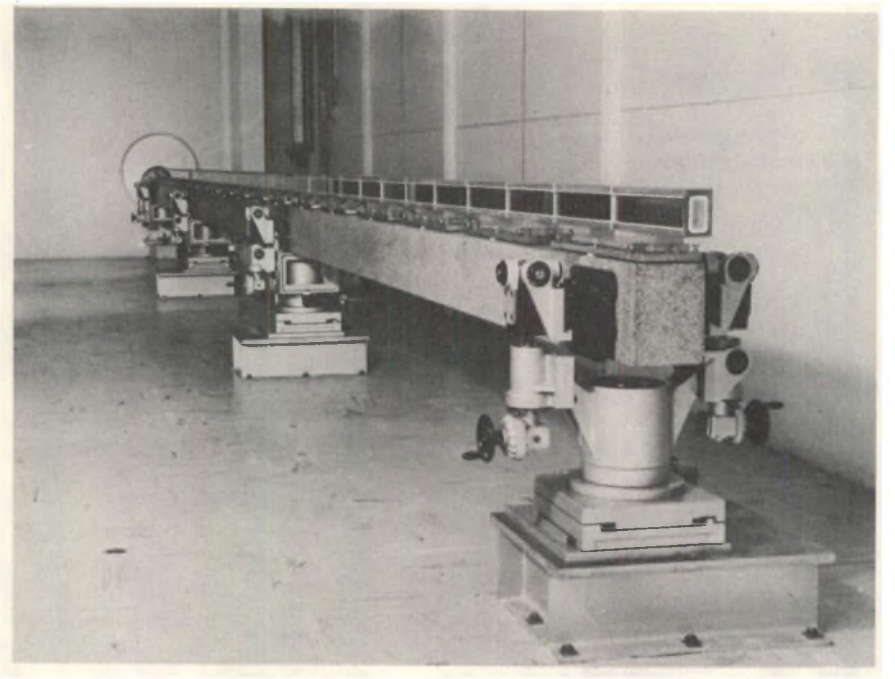

FIG. 8. Partie du TCN extérieure au hall du réacteur. La paroi du hall du réacteur sert de fond pour la piscine de protection. L'extrémité de l'élément réfléchissant qui traverse la paroi du hall se trouve à 1,5 fois la longueur de vision directe de la face d'entrée du TCN. Aucune protection biologique n'est nécessaire pour cette partie. Les poutres de soutien sont reliées entre elles par des méchanismes de précision qui permettent des déformations contrôlées de l'ensemble. On distingue au premier plan les deux vérins verticaux pour le réglage de l'assiette et du niveau. Le vérin de réglage transversal est placé derrière le support.

planéité de la surface (ondulation moyenne inférieure à deux franges sur 100 mm et rugosité moyenne inférieure à 5×10^{-3} μm). Elles sont ensuite revêtues par évaporation sous vide d'un dépôt de nickel pur (99,99%) de 0,15 μm d'épaisseur.

Pour assurer la courbure dans le plan horizontal l'angle entre chaque élément de 340 mm de longueur est de 4×10^{-4} rad (84''). Les éléments sont réglés deux par deux en laboratoire. Le couple ainsi formé est collé sur une dalle de verre. Celle-ci est fixée sur une platine métallique qui porte les paramètres de réglage. L'ajustage en translation est de $\pm$ 0,01 mm, l'écart entre chaque élément est inférieur à 0,04 mm et la précision sur l'angle $\pm 0{,}25 \times 10^{-4}$ rad ($\pm$ 5'').

Après la mise en place et le réglage, la platine métallique est scellée sur la poutre de soutien, assurant ainsi une parfaite tenue mécanique de l'ensemble. Les éléments réfléchissants sont collés entre eux par une colle souple, ce qui rend le tube conducteur parfaitement étanche. Ceci (et l'épaisseur des dalles de verre) permet de faire le vide à l'intérieur du tube pour éviter l'absorption par l'air des neutrons lents.

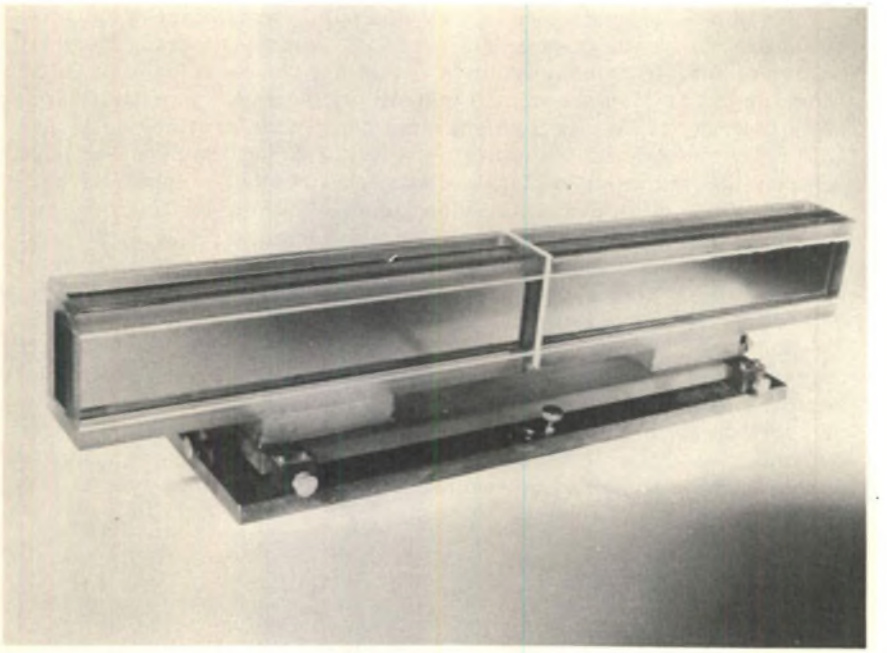

FIG.9. Elément réfléchissant double. L'angle entre les deux éléments est de 4×10^{-4} rad. Après réglage ces deux éléments sont collés sur une dalle de verre. Celle-ci est fixée sur une platine métallique qui porte les vis micrométriques de réglage.

2.3.2. Support des éléments réfléchissants

Le maintien dans le temps des réglages de précision des éléments réfléchissants (§ 2.3.1) est étroitement lié à la qualité du support. Pour cela la poutre de soutien est formée d'un matériau particulièrement inerte: le granit. Il présente une dureté uniforme, il est exempt de tensions internes et indéformable une fois mis en place. Son coefficient de dilatation thermique est faible. De plus son excellente planéité simplifie le réglage des éléments réfléchissants. Par contre c'est un matériau fragile et de dimensions limitées, comparé à d'autres types de support (béton, acier, alliage léger). Les caractéristiques physiques du granit choisi sont indiquées dans le tableau II.

TABLEAU II. CARACTERISTIQUES PHYSIQUES DU GRANIT CHOISI POUR LA POUTRE DE SOUTIEN DES ELEMENTS REFLECHISSANTS

Dureté (échelle de Mohs)	7
Coefficient de dilatation thermique	$6,7 \times 10^{-6}$
Densité	2,71
Module d'Young	6545 kg/mm^2
Planéité	± 0,5 mm/m

La poutre de soutien est constituée par l'assemblage d'éléments de 3 m à 4 m de longueur et de 200 mm × 200 mm de section. Deux types de liaison ont été retenus: pour la partie qui se trouve dans le hall du réacteur six éléments sont liés rigidement entre eux par des flasques métalliques (fig. 7). Ils forment ainsi une poutre continue de 17 m de long. Elle repose sur des fûts scellés dans le sol du hall du réacteur par l'intermédiaire de vérins de réglage. Ces vérins restent accessibles après la mise en place de la protection biologique. Pour la partie extérieure c'est une solution de poutre déformable qui a été choisie (fig. 8). Elle est formée par trois éléments de 4 m de longueur reliés entre eux par des rotules. Elles sont supportées par une mécanique de précision composée de deux vérins verticaux portés par une table à mouvements croisés. Le mouvement longitudinal est libre pour permettre le jeu de la dilatation thermique; le mouvement transversal est lié à un vérin. Les déplacements relatifs de chaque poutre sont repérés par des comparateurs mécaniques au centième de millimètre. L'ensemble de cette mécanique de précision permet de modifier le réglage de l'ensemble des éléments réfléchissants portés par une poutre et de revenir à la position initiale avec la précision requise.

3. MESURES SUR LE TCN

Les mesures neutroniques effectuées sur le TCN ont eu pour but la détermination du spectre total transmis, et la vérification de l'effet de filtre passe-bas en énergie. La construction en deux étapes a permis d'effectuer ces mesures en deux points du TCN: au bout de 1,5 et de 2,5 longueurs de vision directe. L'accessibilité de la partie extérieure au hall du réacteur et la conception du montage des éléments réfléchissants ont permis d'apporter des modifications techniques sur cette partie du TCN et d'en mesurer les effets.

3.1. Mesure du flux moyen

Le flux neutronique moyen (intégré sur toutes les énergies) transmis par le TCN a été mesuré par détecteurs à activation. Ce sont des feuilles d'or de 50 μm d'épaisseur et de 20 × 50 mm placées à la sortie du guide. Les résultats sont les suivants, pour une pile à 14 MW:

Mesure au bout de	1,5 L_1	2,5 L_1
Flux moyen ($n/cm^2 \cdot s$)	$2{,}63 \times 10^7$	$2{,}32 \times 10^7$

La transmission moyenne pour une longueur de vision directe est de 88%. Elle est de 75% pour tout le guide (30 m). Le résultat de la mesure à l'aide de détecteurs d'or de 5 mm × 5 mm et de 50 μm d'épaisseur disposés sur toute la surface de sortie du TCN (tableau III) montre la dissymétrie du faisceau en intensité entre le côté des réflexions en guirlande (position horizontale de 0 à 5 mm) et le côté des réflexions en zigzag (position horizontale de 15 à 20 mm). Cette mesure est confirmée par les résultats obtenus par temps de vol (fig. 10).

TABLEAU III. ACTIVITE (μCi/g) DES DETECTEURS D'OR EN FONCTION DE LEUR POSITION

	Position horizontale	0 à 5 mm	5 à 10 mm	10 à 15 mm	15 à 20 mm
Position verticale	0 à 5 mm	41,64	27,06	17,25	10,80
	20 à 25 mm	44,74	30,10	19,13	11,84
	45 à 50 mm	43,55	29,69	18,79	11,90

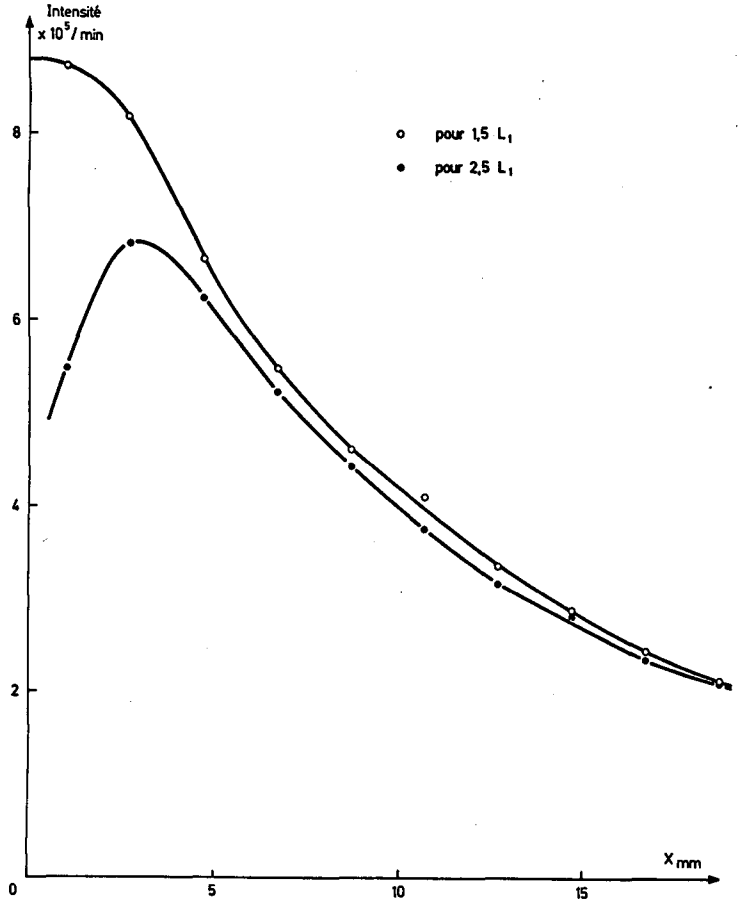

FIG.10. Répartition de l'intensité totale en fonction de l'abscisse de sortie.

3.2. Etude de la distribution de l'intensité en fonction de la longueur d'onde

Cette étude a été faite par temps de vol. Le disque de chopper a un diamètre de 350 mm. Il porte deux fentes de 2 mm de large et de 20 mm de haut, sur un rayon moyen de 140 mm. La base de temps de vol a une

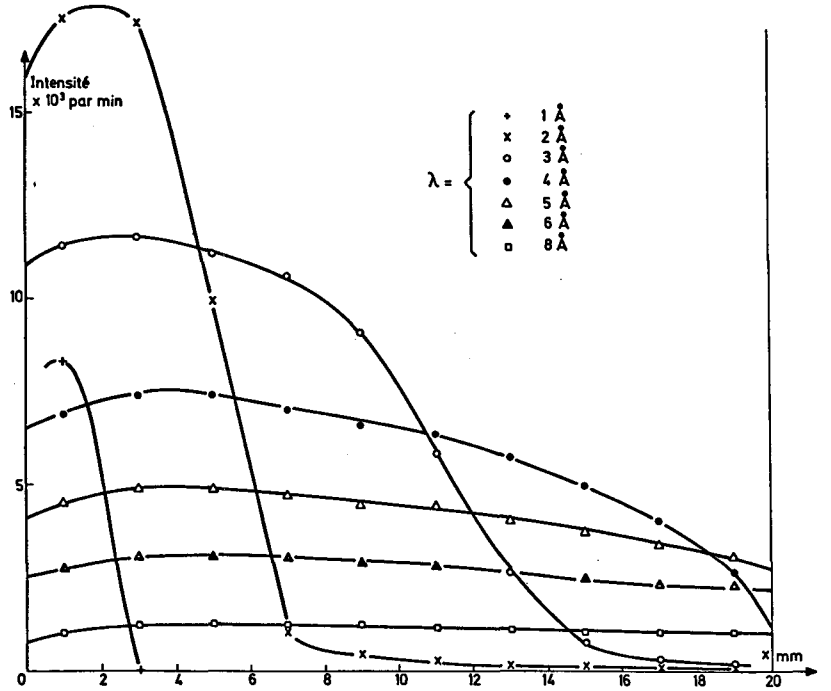

FIG.11a. Distribution $I(\lambda, x)$ au bout de $1,5L_1$.

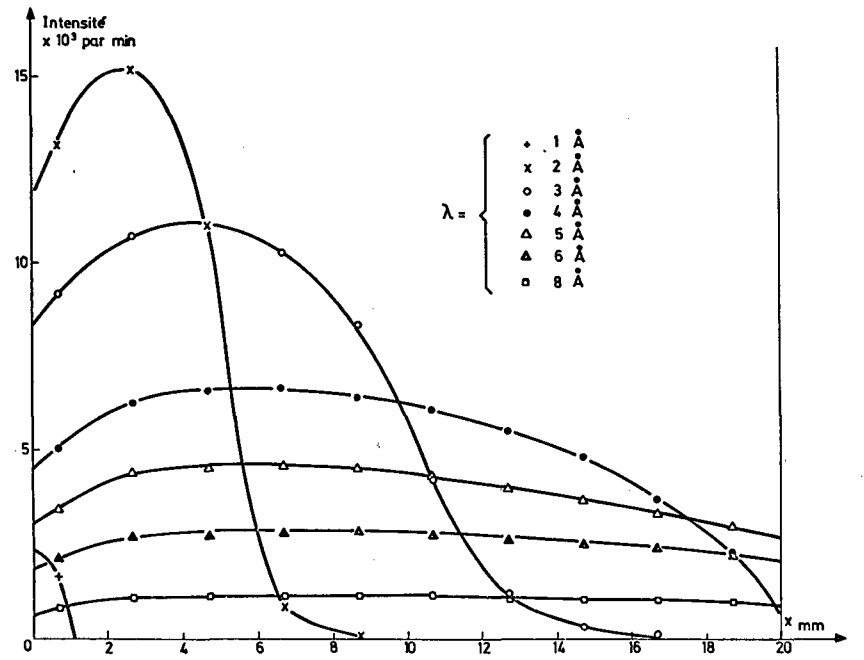

FIG.11b. Distribution $I(\lambda, x)$ au bout de $2,5L_1$.

longueur de 2,50 m. Le détecteur est constitué par une batterie de neuf compteurs à BF_3 de 240 × 125 mm de surface utile.

La mesure par activation montre que l'intensité est constante dans une bande verticale (tableau III), ce qui a été confirmé par des mesures préliminaires par temps de vol. La répartition de l'intensité en fonction de la longueur d'onde a donc été étudiée seulement dans une bande horizontale de 20 mm de haut, centrée sur la fenêtre de sortie du guide, en déplaçant le chopper de 2 mm en 2 mm.

3.2.1. Mesures sur le TCN à simple courbure

La répartition de l'intensité totale, bruit de fond soustrait, en fonction de l'abscisse de sortie x est indiquée sur la figure 10 pour les deux longueurs du TCN. Pour le TCN de longueur égale à 1,5 longueur de vision directe L_1, la variation de l'intensité totale est de 76% entre le côté guirlande et le côté zigzag. Pour le TCN de longueur égale à 2,5 L_1, une perte importante apparaît du côté guirlande, due au fait que les neutrons sortant à cet endroit subissent un nombre de réflexions plus élevé.

L'analyse du faisceau par temps de vol montre que l'effet de filtre est très net. La distribution de l'intensité en fonction de la longueur d'onde et de l'abscisse de sortie, $I(\lambda, x)$, est présentée sur les figures 11a et 11b en tenant compte du bruit de fond et de l'efficacité des compteurs. Elle est conforme aux calculs théoriques (fig. 12a, 12b et 12c) en ce qui

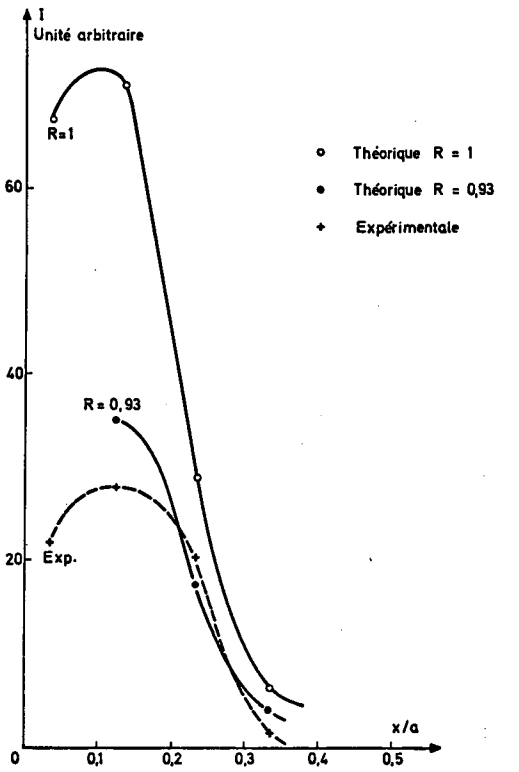

FIG.12a. Distribution $I(\lambda = 2\text{Å}, x/a)$.

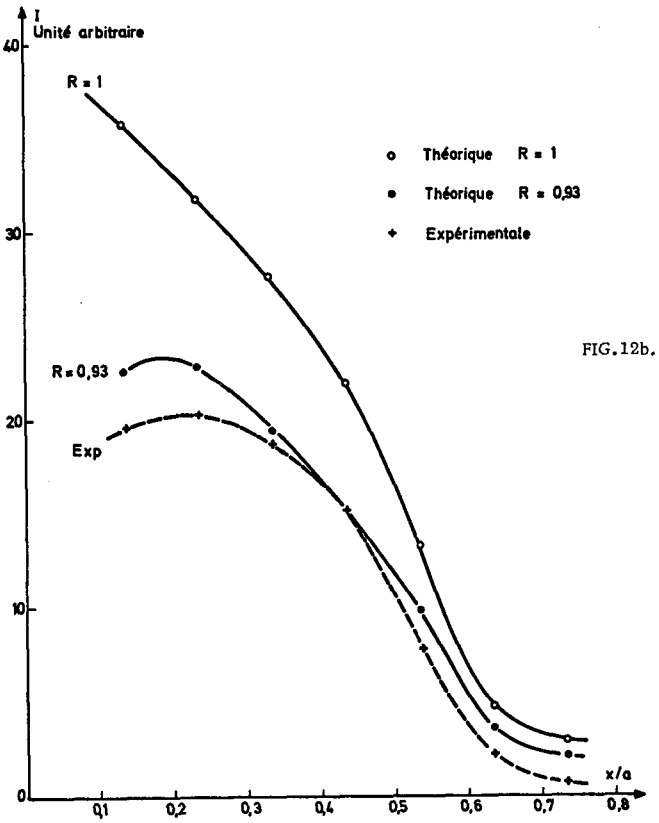

FIG.12b. Distribution I(λ = 3Å, x/a).

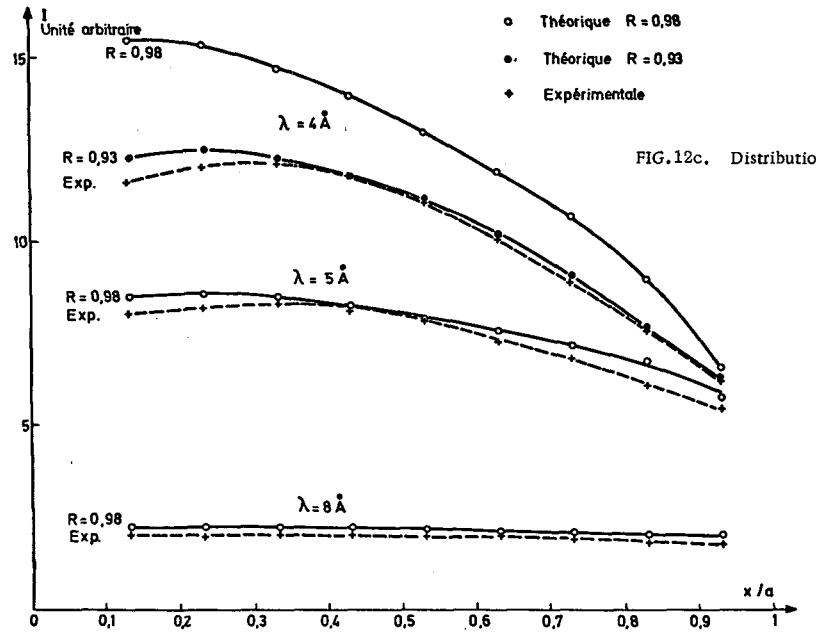

FIG.12c. Distribution I(λ, x/a).

concerne l'effet de coupure en fonction de l'abscisse de sortie. La distribution $I(\lambda, x)$ obtenue au bout de 1,5 L_1 pour $\lambda = 2$Å et $\lambda = 3$Å (fig. 11a) montre que pour cette longueur des neutrons diffusés dans la première partie du tube peuvent encore atteindre la fenêtre de sortie.

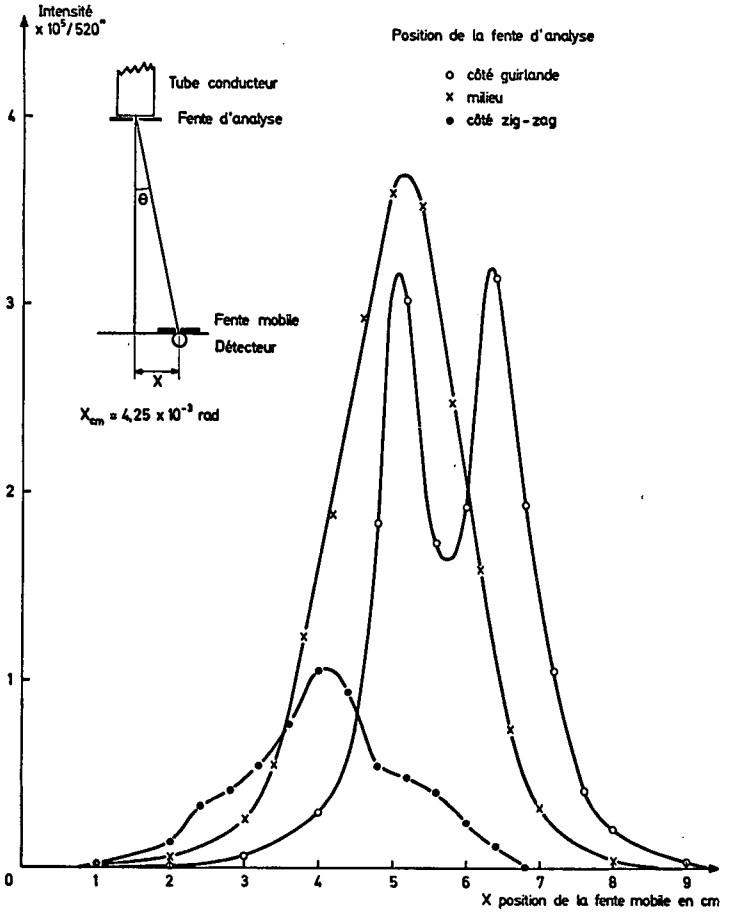

FIG. 13. Distribution de l'intensité dans le plan horizontal.

La répartition de l'intensité pour une abscisse de sortie x donnée, mesurée dans un plan horizontal, en fonction de l'angle de sortie θ est indiquée sur la figure 13 pour trois positions de la fente du chopper: x = 0 à 2 mm (côté guirlande), x = 8 à 10 mm (milieu) et x = 18 à 20 mm (côté zigzag). La distribution obtenue du côté guirlande présente une anomalie pour les angles de sortie $\theta < 2{,}5 \times 10^{-3}$ rad. L'analyse en fonction de la longueur d'onde montre que la perte existe pour toutes les longueurs d'onde. Elle est due au grand nombre de réflexions subies par les neutrons sortant du côté guirlande sous de très petits angles et à l'importance relative des défauts d'alignement des éléments réfléchissants.

Le nombre de neutrons transmis par cm^2, par s et par eV est porté sur la figure 14 pour les deux longueurs du TCN. Le spectre présente un maximum pour l'énergie $E = 1,67 \times 10^{-3}$ eV. La décroissance pour les énergies inférieures est une conséquence de la limitation angulaire apportée par le collimateur en pile (§ 2.1). Cet effet devient important dans le plan horizontal à partir de $E = 1,67 \times 10^{-3}$ eV, comme le montre le spectre théorique (fig. 15) calculé pour un coefficient de réflexion R = 1.

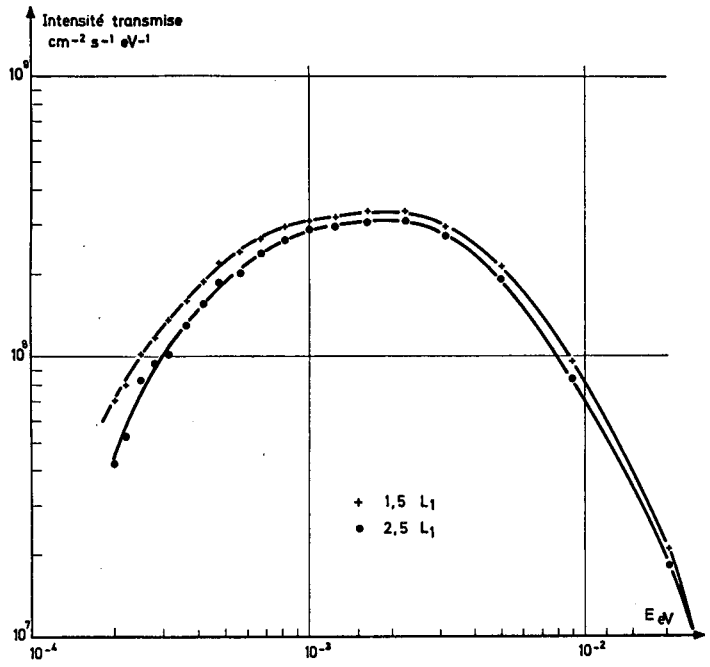

FIG. 14. Intensité transmise par le TCN de longueur égale à $1,5L_1$ et $2,5L_1$.

La comparaison des spectres obtenus au bout des deux longueurs ($1,5\ L_1$ et $2,5\ L_1$) donne la transmission en fonction de la longueur d'onde pour un TCN de longueur égale à $1\ L_1$ (Fig. 16). Elle décroît régulièrement à partir de $\lambda = 5$ Å. Le nombre moyen de réflexions, qui passe par un maximum pour $\lambda = 4$ Å, augmente en effet avec la longueur d'onde pour $\lambda > 4$ Å. Pour $\lambda < 5$ Å la transmission présente une irrégularité. Un essai d'interprétation des courbes $I(\lambda, x)$ obtenues pour un TCN de longueur $2,5\ L_1$ conduit à prendre deux valeurs pour le coefficient de réflexion global: $R = 0,93$ pour $\lambda < 5$ Å et $R = 0,98$ pour $\lambda \geq 5$ Å (fig. 12a, 12b et 12c). Le coefficient de réflexion obtenu lors d'une étude préliminaire sur la réflectivité de miroirs de nickel est de $R = 0,99 \pm 1\%$ pour des mesures faites avec cinq réflexions. L'interprétation théorique plus détaillée de cette transmission est en cours.

L'accessibilité de la partie du TCN extérieure au hall du réacteur (fig. 8) et la mécanique de précision qui lui est associée (§ 2.2) a permis de contrôler l'effet de certains défauts de réglage sur l'intensité transmise: le défaut d'alignement a été créé en déplaçant transversalement un élément

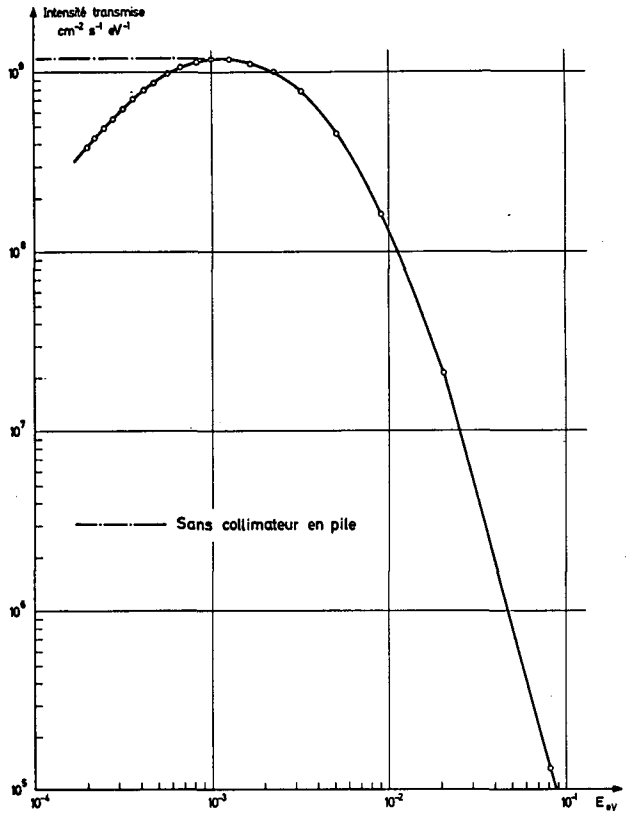

FIG.15. Intensité transmise théorique pour un coefficient de réflexion R = 1.

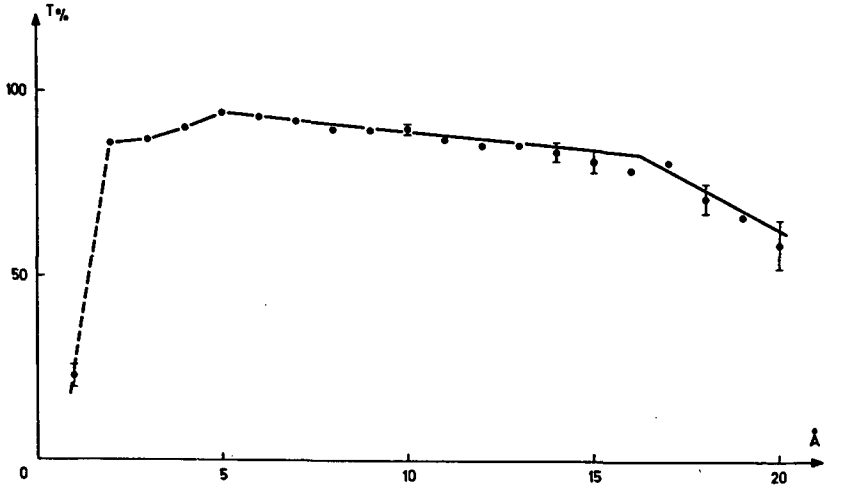

FIG.16. Transmission du tube conducteur pour une longueur de vision directe.

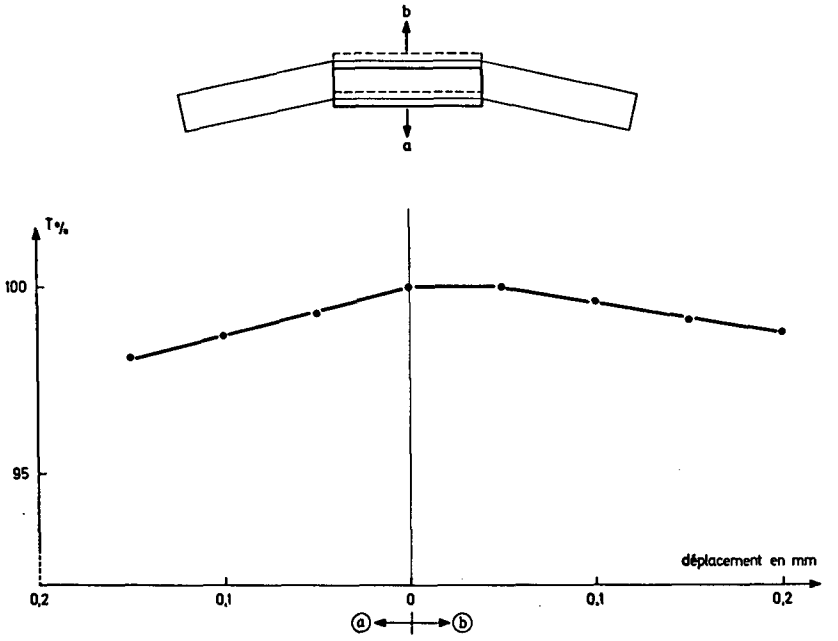

FIG.17. Défaut d'alignement sur 1 élément. Variation de l'intensité transmise.

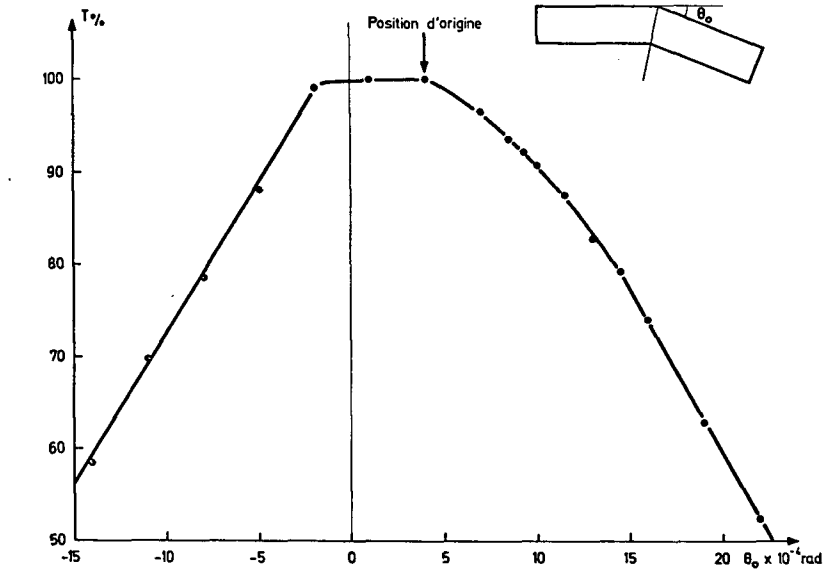

FIG.18. Défaut angulaire macroscopique. Variation de l'intensité transmise en fonction de l'angle θ_0 entre deux éléments réfléchissants.

double. La transmission (fig. 17) varie de 1% environ pour un déplacement de 0,15 mm vers l'extérieur de la courbure et de 2% pour un déplacement de 0,15 mm vers l'intérieur de la courbure.

En déplaçant transversalement la rotule de liaison de deux poutres en granit, les éléments réfléchissants restent en place sur la poutre. Seul l'angle entre les éléments situés à l'extrémité de chaque poutre varie. La courbure idéale de la surface réfléchissante (donnée par l'angle $\theta_0 = 4{,}07 \times 10^{-4}$ rad entre les éléments réfléchissants droits de 340 mm de longueur) est déformée. Un défaut par ondulation macroscopique est ainsi créé. La variation de la transmission en fonction de l'angle entre les éléments réfléchissants situés à l'extrémité des poutres est portée sur la figure 18. La transmission est constante pour $0 \leq \theta \leq 4{,}07 \times 10^{-4}$ rad et varie de 10% pour $\theta = -4{,}07 \times 10^{-4}$ rad.

3.2.2. TCN à double courbure

La partie du TCN extérieure au hall du réacteur a été réglée ensuite en courbure opposée à la partie intérieure par simple retournement des éléments réfléchissants doubles (fig. 9). L'ensemble constitue un TCN bicourbe dont la première partie a une longueur de 1,5 L_1 et la deuxième partie une longueur de 1 L_1.

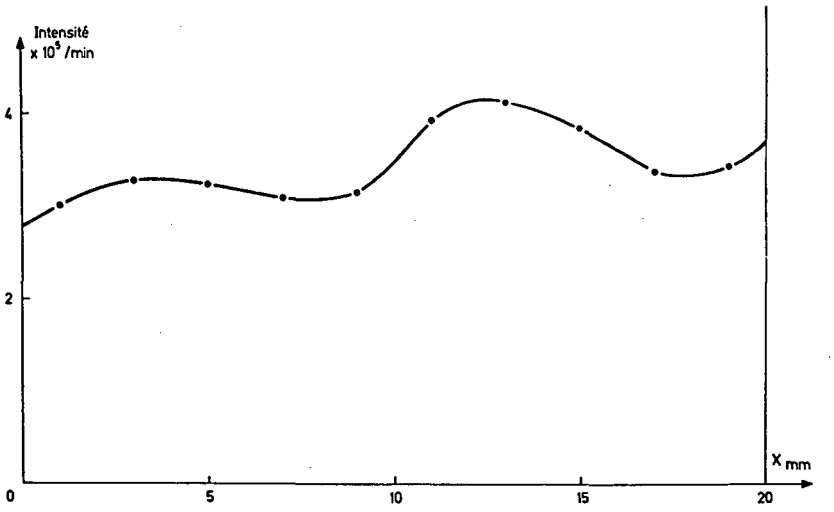

FIG.19. Distribution en intensité totale à la sortie du TCN bicourbe.

La mesure montre que la répartition de l'intensité totale à la sortie du guide (fig. 19) est plus homogène que dans le cas du TCN à simple courbure. L'analyse de l'intensité en fonction de la longueur d'onde et de l'abscisse de sortie (fig. 20) montre que les neutrons de longueur d'onde $\lambda = 2$ Å ne sont plus transmis. La répartition des neutrons de 3 et 4 Å de longueur d'onde semble en désaccord avec la théorie. Cependant une analyse détaillée des conditions de réflexion dans le TCN bicourbe montre que la répartition $I(\lambda, x)$ pour les longueurs d'onde proches de la longueur d'onde de coupure telle que $K = 1$ (éq. 21a) dépend de la longueur de la partie en courbure opposée (fig. 21).

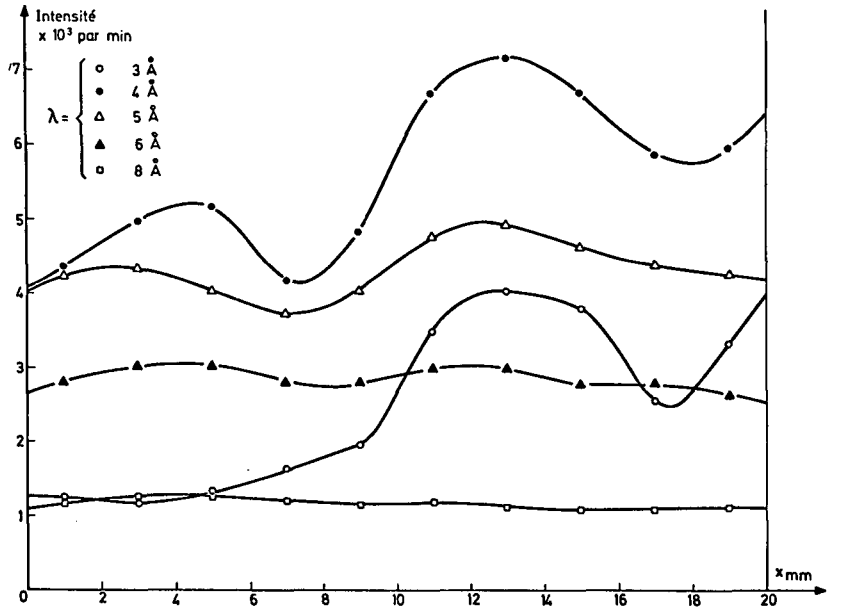

FIG. 20. Distribution de l'intensité I(λ, x) à la sortie du tube conducteur bicourbe.

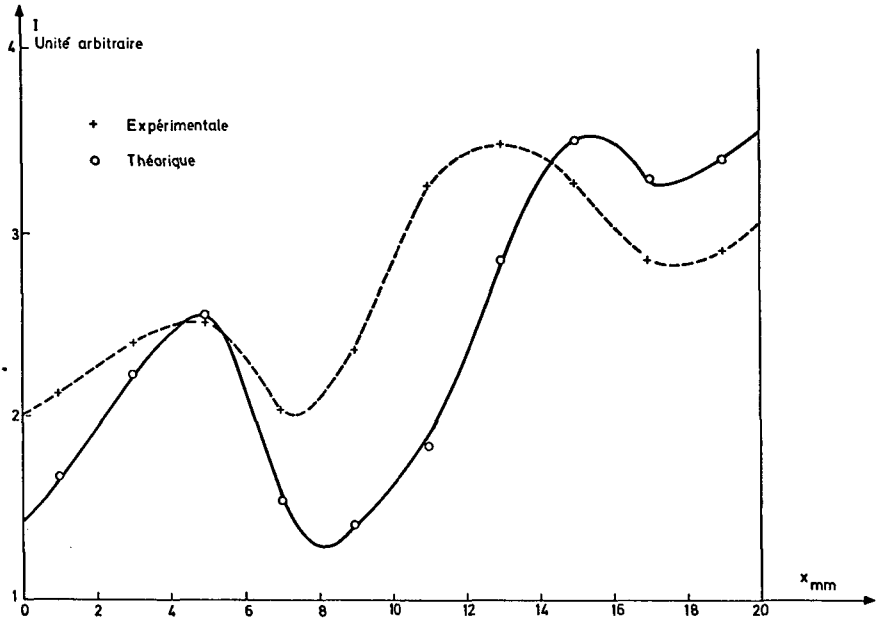

FIG. 21. Distribution de l'intensité à la sortie du TCN bicourbe pour λ = 4Å.

3.2.3. Bruit de fond

La mesure a montré que le bruit de fond dans le laboratoire était dû uniquement à des neutrons thermiques. Il disparaît totalement lorsque les compteurs sont recouverts d'une feuille de cadmium de 0,8 mm d'épaisseur. Ce bruit de fond provient des neutrons diffusés par les imperfections de la surface réfléchissante pour le TCN à simple courbure. Les mesures de radioprotection [15] ont déterminé une valeur moyenne de $3,5 \times 10^3$ n/cm^2·s en neutrons thermiques au contact des éléments réfléchissants dans le laboratoire. La dose gamma au contact, près de la sortie du guide, est de 2 mrem/h et provient essentiellement de la capture dans le verre de neutrons diffusés. Le bruit de fond est deux fois plus élevé dans le cas du TCN bicourbe et une protection contre les neutrons thermiques est alors nécessaire tout le long du guide.

CONCLUSION

Les mesures ont montré que le TCN constituait un filtre passe-bas en énergie efficace tout en conservant une bonne transmission. Elles indiquent qu'il n'est pas utile de construire un guide courbe trop long pour obtenir cet effet: 1,5 fois la longueur de vision directe semble constituer une bonne dimension. L'utilisation d'un TCN bicourbe conduit à l'élimination totale de l'harmonique de longueur d'onde de coupure telle que K = 1. Mais la répartition en intensité à la sortie de ce TCN est alors fonction de la longueur de la partie en courbure opposée. Une interprétation théorique plus poussée des résultats et de l'influence des défauts sur la transmission est en cours.

Des mesures de transmission vont être effectuées sur un TCN de section circulaire (diamètre 30 mm) constitué par des tubes en nickel (longueur 340 mm) obtenus par électro-formage.

Le TCN constitue un filtre passe-bas en énergie efficace et nouveau: sa coupure ne dépend que de ses paramètres géométriques. Il donne ainsi naissance à un nouveau type de faisceau de neutrons lents, dont les caractéristiques peuvent être adaptées au mieux à l'utilisation. Les avantages particuliers liés à l'emploi de ce faisceau vont transformer, en les améliorant considérablement, les conditions de travail autour du réacteur.

Lorsque la boucle froide entrera en fonctionnement, le TCN de Saclay constituera ainsi une source intense de neutrons froids. Elle sera utilisée pour étudier la dynamique des milieux condensés et en particulier celle des substances magnétiques. Son emploi est aussi envisagé pour étudier la diffusion des neutrons thermiques par les macromolécules.

REFERENCES

[1] CHRIST, J., SPRINGER, T., Nukleonik 4 (1962) 23.
[2] MAIER-LEIBNITZ, H., SPRINGER, T., Reactor Sci. Technol. (J. nucl. Energy, A/B) 17 (1963) 217.
[3] MAIER-LEIBNITZ, H., Nukleonik 8 (1966) 61.
[4] FERMI, E., ZINN, W.H., Phys. Rev. 70 (1946) 103.
[5] FERMI, E., MARSHALL, L., Phys. Rev. 71 (1947) 10.

[6] MILLER, P.D., ORNL-TM-1149 (1965).
[7] FIALA, W., RAUCH, H., Nucl. Instrum. Meth. 52 (1967) 15.
[8] ALEFELD, B., CHRIST, J., KUKLA, D., SHERM, R., SCHMATZ, W., JUL-294-NP (1965).
[9] HUGHES, D.J., Neutron Optics, Interscience Publ., New York (1954).
[10] FERMI, E., Nuclear Physics, Univ. of Chicago Press (1950) 201.
[12] HALPERN, O., Phys. Rev. 88 (1952) 1003.
[13] BAILLY, D., et al., Rev. scient. Instrum. 33 9 (1962) 916.
[14] JACROT, B., Pile Neutron Research in Physics (C.r. Colloque Vienne, 1960), AIEA, Vienne (1962) 393.
[15] BEAUCOURT, Ph., de, DEVILLERS, C., MANGIN, J.P., Mesures de protection autour du guide à neutrons de la pile EL3, DEP/SEPP-652, CEN Fontenay-aux-Roses (1967).

A NEUTRON CRYSTAL SPECTROMETER WITH EXTREMELY HIGH ENERGY RESOLUTION

B. ALEFELD, M. BIRR AND A. HEIDEMANN
PHYSIK-DEPARTMENT DER TECHNISCHEN HOCHSCHULE MÜNCHEN, MUNICH, FEDERAL REPUBLIC OF GERMANY

Abstract

A NEUTRON CRYSTAL SPECTROMETER WITH EXTREMELY HIGH ENERGY RESOLUTION. In the following the spectrometer proposed by Maier-Leibnitz is described. At the end of a neutron guide tube with a total length of 35 m the white neutron beam falls vertically on the (111) planes of a silicon single crystal. One half of the backscattered monochromatic neutrons enters a total-reflecting conical tube of nickelled glass plates and is focused on the sample. The scattered neutrons fall veritcally on the (111) planes of the silicon analyser crystal. This analyser is built up of about 2000 small slices of silicon which are adjusted to the inner surface of a sphere. The solid angle from the sample to the analyser is about 1/15 of 4π. Due to the finite size of the sample and the inaccurate adjustment of the silicon analysers, the neutrons are not ideally focused on the sample by the analyser. A large amount of them pass beside the sample and enter a counter. The window of the counter is about 4 times larger than the sample. By Doppler-shifting or by changing the temperature of the monochromator the energy of the monochromatic neutrons can be varied. In this way a change of neutron energy of the order of 10^{-6} to 10^{-1} eV can be measured. It is intended to measure hyperfine splitting in solids. Two thirds of the spin-incoherent cross-section is connected with nuclear spin-flip scattering of neutrons. Changes of energy of the nuclear spin are compensated by the neutron.

1. INTRODUCTION

A neutron spectrometer with extremely high energy resolution has recently been built at Munich. It is to be used for research in the fields of solid state and liquid state physics. The spectrometer is based on the fact that the energy resolution of a single crystal is very good when θ, the Bragg angle, is near or equal to 90°. A small change in the neutron energy can easily be detected by moving the crystal in the direction of the neutron beam or by changing its temperature. In this communication a description is given of the instrument together with some experiments performed to test the energy resolution of single crystals when θ is near or equal to 90°.

2. THE ENERGY RESOLUTION OF SINGLE CRYSTALS NEAR 90°

The energy resolution of a single crystal is given by the logarithmic derivative of the Bragg equation

$$\tau = 2k \sin\theta \tag{1}$$

where $\tau = n2\pi/a$; $k = 2\pi/\lambda$; n is the order of reflection; a is the distance of reflecting planes; and λ is the wavelength of the neutrons. Hence,

$$\frac{dk}{k} = \frac{1}{2} dE/E = \operatorname{ctan}\theta \, d\theta + \frac{d\tau}{\tau} \tag{2}$$

When θ is replaced by the angle α between the $\vec{\tau}$ and $\vec{k}$ vector

$$\alpha = 90° - \theta$$

and we get

$$dk/k = \tan \alpha d\alpha + (d\tau/\tau) \tag{3}$$

or for small values of α

$$dk/k = \alpha d\alpha + (d\tau/\tau) \qquad 5° > \alpha > d\alpha \tag{4}$$

or

$$dk/k = (d\alpha^2/8) + (d\tau/\tau) \qquad \alpha = 0 \quad d\alpha < 5° \tag{5}$$

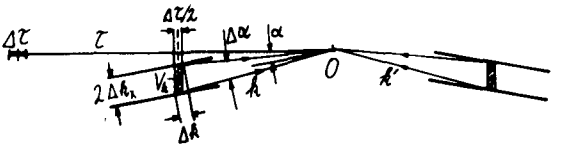

FIG.1. Backscattering in k space, $\alpha \neq 0$, perfect crystal.

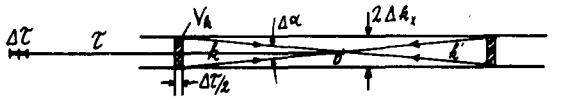

FIG.2. Backscattering in k space, $\alpha = 0$, perfect crystal.

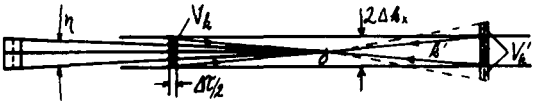

FIG.3. Backscattering in k space, $\alpha = 0$, mosaic crystal with mosaic spread η. O = origin of k space; k = in-going neutrons; k' = out-going neutrons; V_k = Bragg-reflected volume of k space; $2\Delta k_x$ = collimation of neutron guide tube; V_k' = volume lost if backscattered into neutron guide tube.

The representation of Eqs (4) and (5) in the reciprocal lattice is shown in Figs 1 and 2 for a perfect crystal. Figure 3 shows the backscattering for a mosaic crystal. It is clearly seen that a mosaic crystal does not give any intensity advantage when $\alpha = 0$ and $d\alpha \approx 10^{-2}$ rad. In Figs 1, 2 and 3 the collimation is given by a neutron guide tube.

Each reciprocal lattice point is surrounded by a finite volume within which Bragg scattering is possible. The width of this volume in the direction of the corresponding $\vec{\tau}$ vector is called $d\tau$. $d\tau$ depends on primary extinction, particle size, and variations in the lattice parameter. For a perfect lattice $d\tau$ is two times the half width of the well-known Darwin curve [1] in the k representation when $\theta = 90°$.

$$\frac{d\tau}{\tau} = \frac{16\ \pi\ N_c F}{\tau^2} \tag{6}$$

where F is the structure factor; and N_c is the number of unit cells per cm^3. Values of $d\tau/\tau$ are of the order of 10^{-4} to 10^{-5}.

3. EXPERIMENTAL RESOLUTION OF LEAD AND SILICON SINGLE CRYSTALS

Figure 4 shows an experimental device to test Eq.(4)[2], α and $d\alpha$ have the same magnitude and are 1.7×10^{-2} rad. Figure 5 shows the intensity of two silicon crystals as a function of the difference in temperature. Figure 6 shows the same experiment with lead crystals. The shift of the curves is due to the acceleration of the neutrons in the gravitational field of the earth. The energy gain between the two crystals is about 3.8×10^{-7} eV. The half width of the silicon curve is mainly due to the first term in Eq.(4). In the case of lead, the half width is mainly due to large irregularities of the crystals.

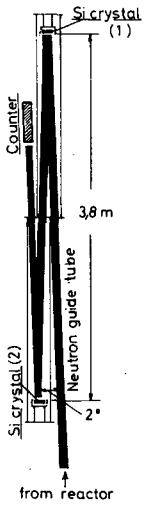

FIG.4. Backscatterer.

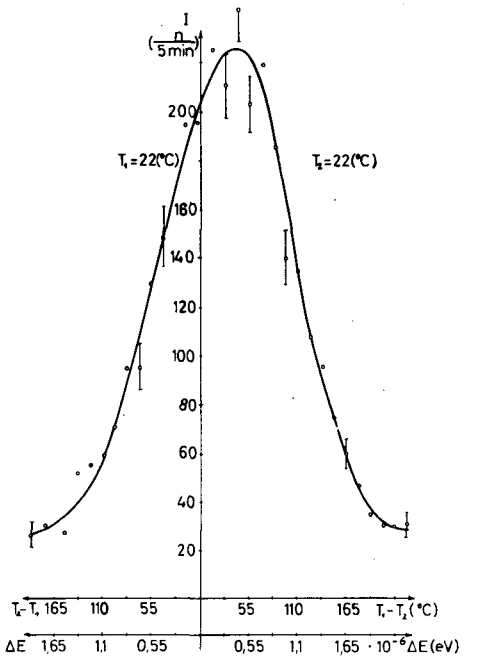

FIG.5. Backscattering from silicon single crystals.

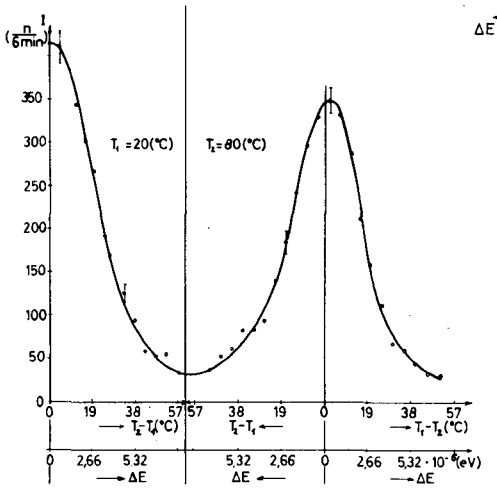

FIG.6. Backscattering from lead single crystals.

Equation (5) was tested with the experimental set-up shown in Fig. 7. A white neutron beam, emerging from a bent neutron guide tube (section 4), penetrates a silicon crystal perpendicularly to its (111) planes (α = 0). In the transmitted spectrum there are dips at the position $k_{hkl} = \tau_{hkl}/2$. A rotating counter device, which at the same time acts as a coarse chopper, is placed behind the crystal. In the open position the primary beam again enters a guide tube. At the end of this tube a second silicon crystal is adjusted. The neutrons which are backscattered from this crystal are detected by a counter which rotates into the direct beam and is shielded with cadmium from the primary beam. The time between the open position of the chopper and the counting position of the counter is proportional to twice the

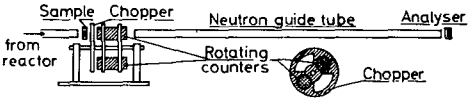

FIG. 7. Backscattering apparatus.

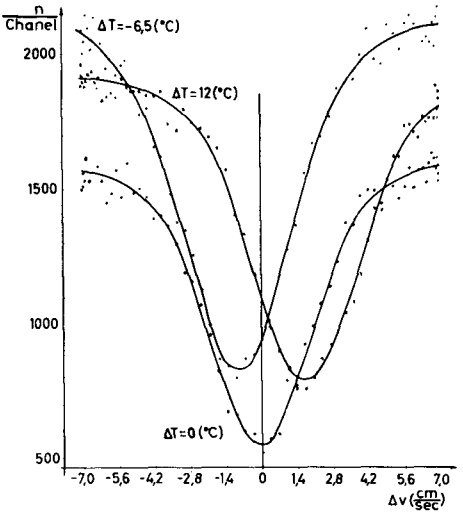

FIG. 8. Transmission curve of a silicon single crystal.

length of the flight path. In the case of two identical crystals, there are no neutrons backscattered from the second crystal. When changing the lattice parameter of one of the crystals, neutrons can be reflected from the second crystal.

Figure 8 shows the intensity versus the velocity of the second crystal, which was moved by a conventional loudspeaker used in Mössbauer experiments. Two curves are shifted due to a small difference of temperature of the crystals. The half width of the curves (folding of two curves) is 4.5 cm/sec or $E = 2.9 \times 10^{-7}$ eV ($E = 2 \times 10^{-3}$ eV).

4. THE NEUTRON GUIDE TUBE

In low-intensity experiments a small background is desirable. For this reason a bent neutron guide tube was built at the Munich Research Reactor.

The reflectivity of a neutron mirror depends crucially on its surface smoothness. Since our investigations showed that the reflectivity of ground and polished mirror glass is excellent, we used this glass as wall material. Plane glass plates 270 mm × 900 mm and 25 mm × 900 mm were glued together to make rectangular tubes with an open area of 25 × 250 (± 0.01)mm. These glass tubes were placed in a vacuum tube. They were adjusted to a bent tube with a total length of 35 m and a radius of curvature of 2860 m. The distance for direct sight from the reactor core is 24 m. Great care was taken to remove dislocations between the glass tubes. Since no filter was employed at the entrance of the tube, this tube is a strong source of background radiation along the length of direct sight. For this reason a large shield was built up around the tube. The intensity and background measurements showed that a bent neutron guide tube is an excellent device to get a high-intensity neutron beam far from the reactor (outside of the reactor hall) with practically no background of fast neutrons and γ-rays in the direct beam. The cadmium ratio, measured with a 12-cm long enriched-boron counter, is difficult to measure and is certainly better than 10^8. A direct measurement of the loss in intensity is not possible. In a large energy interval the measured spectrum agrees with the calculated one to within an error of about 15%. This large error in the calculation is due to the unknown anisotropy of the thermal flux at the entrance of the neutron guide tube. The emerging neutron beam is divided in three parts. Therefore, three distinct experiments are possible at the same time. One of these beams is used for the new backscattering spectrometer.

5. THE BACKSCATTERING SPECTROMETER (Fig. 9)

The experimental build-up of the spectrometer was finished only some weeks before the Symposium. Therefore we can report here only measurements of background and primary monochromatic intensity. We shall give here no more than a rough description of the spectrometer. More details will be reported in a later paper.

The resolution of a single crystal, caused by the divergence of the neutron beam, is four times better for exact backscattering (Eq. (5)) than for backscattering with a finite angle α of the order of $d\alpha/2$. Furthermore, the intensity in the $\alpha = 0$ position is the same as in the $\alpha \neq 0$ position. For this reason, the monochromator and the analyser crystals are adjusted in the $\alpha = 0$ position. The problem of obtaining nearly exact backscattering of the monochromatic neutrons without interfering with the direct beam is solved with the help of a 'neutron switch'. A small neutron guide tube, made of glass plates and with an open area of 20 mm × 20 mm is adjusted to the exit of the large neutron guide tube described in section 4. The neutrons emerging from this tube enter a second total reflecting tube with an open area of 20 mm × 40 mm. The latter tube is adjusted asymetrically to the former tube. A silicon single crystal is mounted on a velocity drive (loudspeaker) and adjusted with the (111) planes perpendicularly to the primary beam at the end of this tube. One half of the backscattered neutrons leave this tube at the switch. They enter a converging tube with nickelled glass walls, which enlarges the neutron flux per cm^2, and strike the scattering sample. The scattered neutrons fall perpendicularly on the (111) planes of the silicon analyser. This analyser is built up of about 2000 slices of silicon, each 20 mm in diameter and 0.5 mm thick. The (111) planes are parallel to the surface to an accuracy of about 1.5×10^{-3} rad. They are

glued to the inner surface of a sphere which has a radius of 1.3 m and extends about 1/15 of the whole solid angle. The centre of the sphere coincides with the scattering sample. The neutrons backscattered from the analyser are not ideally focused on the sample because of the finite size of the scattering sample and the inaccurate adjustment of the silicon crystals. So even in the case of a large total cross-section of the sample, enough neutrons by-pass the sample and are detected by a counter behind it. The background registered by the counter, a 95% enriched end-window boron counter (pressure 700 Torr, diameter 2.5 cm, active length 12 cm), is

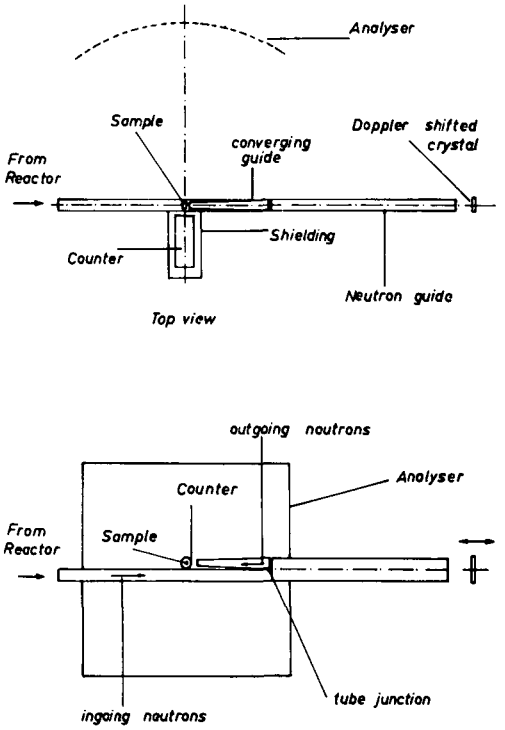

FIG. 9. Backscattering spectrometer.

about 1.5 counts per minute. This is excellent in view of the fact that the primary beam with a total flux of about 10^7 n/sec passes the counter at a distance of about 1 cm. The monochromatic intensity is about 2500 n/min. We hope that in special cases a count rate of between one and ten neutrons per minute will be obtained.

ACKNOWLEDGEMENT

The authors wish to thank Professor H. Maier-Leibnitz for the suggestion of this work and for many valuable discussions.

REFERENCES

[1] ZACHARIASEN, W.H., Theory of X-Ray Diffraction in Crystals, Wiley, New York (1946) 128.

[2] ALEFELD, B., Bayerische Akad. Wissenschaften, Math.-Nat. Klasse, Sonderdruck 11 a.d. Sitzungsber. (1966).

A NEUTRON SPIN-FLIP CHOPPER FOR TIME-OF-FLIGHT MEASUREMENTS

H. RAUCH, J. HARMS AND H. MOLDASCHL
ATOMINSTITUT DER ÖSTERREICHISCHEN HOCHSCHULEN,
VIENNA, AUSTRIA

Abstract

A NEUTRON SPIN-FLIP CHOPPER FOR TIME-OF-FLIGHT MEASUREMENTS. It is possible to change the direction of neutron polarization with high efficiency by means of a resonance spin-flip device, when Co-Fe single crystals are used as polarizer and analyser in a polarized neutron spectrometer. The neutron intensity reflected by the analyser goes to a value close to zero when the spin-flip device is on. Switching the spin-flip device on and off periodically, one obtains a chopped, monochromatic and polarized neutron beam behind the analyser. The duty cycle and the repetition rate of the neutron bursts can be determined electronically over a wide range. Therefore considerably higher repetition rates are possible than with mechanical choppers. This is of special interest for measurements of small neutron energy changes as in the case of quasi-elastic and critical magnetic scattering. Repetition rates up to 20 kc were used, however, this value can be further increased. The duty cycle can be adjusted electronically to any value < 1. For high repetition rates and favourable duty cycles the above-mentioned device yields a higher peak intensity and the same or an even better resolution than expensive two-chopper systems. The energy resolution is determined by the double crystal reflection, in our case $\Delta\lambda/\lambda = 1.3\%$. Other factors (e.g. length of the resonance coil, thickness of the detector, disturbances due to the switching process, channel width of the multichannel analyser etc.), which influence the time resolution decrease with $\Delta t_2/T$ as the time-of-flight (T) increases. For our apparatus Δt_2 had the value of 52 μsec. The neutron energy can be varied from about 60 meV to 5 meV by changing the Bragg position (and the resonance parameters). The background turned out to be favourably low as the sample was not directly in line with the reactor beam tube.

1. INTRODUCTION

Over the last few years we have been developing a method for the production of chopped, monochromatic and polarized neutron bursts by means of a neutron spin-flip chopper [1, 2]. The repetition rate and the duration of the bursts can be electronically determined over a wide range. Therefore it is possible to use very high repetition rates and optimal burst widths, which is of great advantage compared to the usual two-chopper systems, especially when measuring small changes of neutron energy (quasi-elastic, critical scattering). The advantages are higher peak intensity and higher resolution.

The available resolution and the chopper transmission for mechanical choppers (see Ref. [3]) is essentially limited by the increasing stress imposed on material at high rotation speeds. The experimental set-up for mechanical multichopper systems is much more intensive than the spin-flip chopper described, which does not require any moving parts.

2. THE NEW METHOD

For the performance of this method a resonance spin-flip device [4] located between the polarizer and analyser of a spectrometer for polarized neutrons is switched on and off periodically, a procedure intended to produce the required neutron bursts.

The neutron intensity behind the analyser is given by [5]

$$I \propto \left[1 + (1 - 2P_{12})\, P_P\, P_A\right] \tag{1}$$

where P_P, P_A are the polarization efficiency of the polarizer and analyser and P_{12} is the flipping probability of the spin-flip device.

P_P and P_A are near 1 if magnetized Co(92%) - Fe(8%) single crystals ((111) or (200) reflection) are used as polarizer and analyser. P_{12} also approaches 1, if the resonant coil is operated with the resonance frequency of the neutrons within the guide field $\omega_L = 2\mu H_0/\hbar$ (μ is the magnetic moment of the neutron, H_0 is the magnetic field strength of the guide field) and, simultaneously, the amplitude H_1 of the oscillating field (H_1 perpendicular to H_0 and $H_1 \ll H_0$) fulfils the condition $H_1 = hv/\mu l$ (v is the neutron velocity, l is the length of the coil) [4]. From Eq. (1) it can be seen that, for the ideal case ($P_P = P_A = P_{12} = 1$), the intensity behind the analyser drops to zero when the spin-flip is on, whereas for the switched-off spin-flip the whole intensity (I_0) behind the analyser exists, being only determined by the crystal reflectivities [6], the beam collimation [7] and the incident intensity.

The intensity behind the analyser averaged over many cycles is given by the product of I_0 and the modulation ratio

$$T_{SF} = t_1/t_0 \tag{2}$$

where t_1 is the time of one period, when the spin-flip is switched off, and t_0 is the time of period ($t_0 > t_1$); $1/t_0 = \nu_{SF}$ is the repetition rate. This equation is valid for $t_1 > \Delta t$ (Δt is the resolution of the whole apparatus). The modulation ratio determines the form of the bursts. For T_{SF} every value <1 can be electronically adjusted. T_{SF} can be chosen much higher than the corresponding value (T_{Ch}) for mechanical choppers ($T_{Ch} \simeq Nd/2\pi r \leq 0.02$; where d is the width of the chopper slits, N is the number of slits, and $2\pi r$ is the chopper periphery).

The peak intensity (I_m) behind the analyser, being essential for time-of-flight measurements, is given as:

$$I_m = I_0 \tau/t_0 = I_0 \nu_{SF} \tau \tag{3}$$

where τ is the channel width of the multichannel analyser.

Compared with mechanical devices, this has the advantage that ν_{SF} can be chosen much higher than the repetition rates of mechanical choppers ($\nu_{Ch} \leq 1000$ c). The repetition rate of the spin-flip chopper is limited by the resolution $\nu_{SF} < 1/\Delta t$ and in the case of inelastic scattering by the superposition of the scattered neutrons coming from different neutron bursts ($\nu_{SF} < v_0^2/L\Delta v$; where L is the flight path target-detector, Δv is the velocity change of the neutrons, and v_0 is the velocity of the elastic scattered neutrons). It can be recognized that for an optimal layout of the apparatus and for certain measurements repetition rates of 50 000 cycles and higher are possible.

The time resolution of the device is influenced by the energy resolution, some uncertainties for the place of the neutron spin-flip and those for the neutron path.

The energy resolution influenced by the double crystal reflection and the beam collimation is approximately given as:

$$\Delta t_K = C\Delta\vartheta \frac{L}{v} \cot g\, \vartheta \qquad (4)$$

where ϑ is the Bragg angle, $\Delta\vartheta$ is the divergence caused by the first collimator and C is the factor describing the improvement of the resolution by double reflection (for our apparatus C = 0.8).

If the spin-flip device is switched off, part of the neutrons is already within the coil. This effect causes an uncertainty of the slope of the neutron burst given by [1]

$$\Delta t_{SF1} = 1/2v \qquad (5)$$

This contribution can be reduced by using a shorter coil (this requires a higher H_1 and therefore a more expensive electronic set-up. A suitable excess of the first oscillations of the chopped sine burst decreases $\Delta t_{SF1} (\Delta t_{SF1} \rightarrow \Delta t_{SF'1}$; see Figs 2 and 4) [1].

The first and last oscillations of the sine burst do not fulfil the resonance conditions which causes a further uncertainty. For our apparatus

$$\Delta t_{SF2} \simeq 2.1/f_L \quad (f_L = \omega_L/2\pi) \qquad (6)$$

This contribution can also be reduced by using a more difficult electronic system and a larger flight path.

During the reduction of the two last-mentioned factors no loss of intensity occurs, on the contrary higher repetition rates (and therefore higher peak intensity) are possible. A loss of intensity only occurs on reducing Δt_K further.

Other contributions to the resolution – the uncertainty given by the neutron detector ($\Delta t_D = b/v$; where b is the effective detector thickness) and the channel width (Δt_v) of the multichannel analyser – are the same as for mechanical choppers.

3. EXPERIMENTAL SET-UP

The measurements were executed at the tangential beam hole of the TRIGA Mark II reactor on the existing polarized-neutron spectrometer [8] at a reactor power of 250 kW. Figure 1 shows the experimental set-up. For the first experiments arrangement A was used. The usual two-axis spectrometer was varied only by setting the BF_3 counter vertical to the neutron flight-path in order to decrease the detector uncertainty. This arrangement was mainly used for an exact study of the chopped beam. For further studies a longer flight path was built up with a much larger BF_3-detector battery and a more efficient neutron shielding (arrangement B), which can also be used for scattering experiments.

The most essential parameters for the equipment are: divergence of the beam-hole collimator $\Delta\vartheta = 27.5'$; Bragg-angle $\vartheta = 25°\ 20'$ ($\lambda = 1.5$ Å);

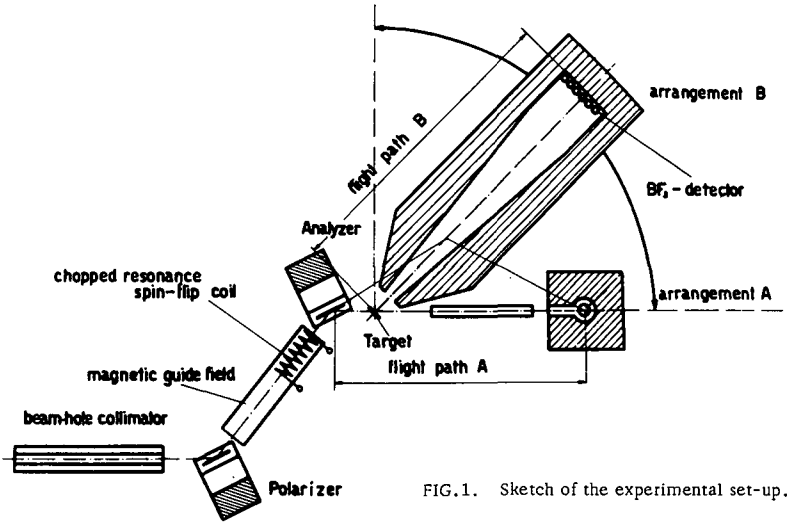

FIG.1. Sketch of the experimental set-up.

polarizer and analyser: Co-Fe single crystals (80 × 20 × 3 mm) in the reflecting position ((200) plane); mosaic spread $\beta = 12'$; distance between polarizer and analyser, 150 cm; magnetic guide field: $H_0 = 71$ Oe; resonance coil: resonance frequency, 207.0 kc; length $l = 15$ cm; cross-section, 6×3.8 cm; inductance, 3.7×10^{-3} H; amplitude of the oscillating field $H_1 = 5.32$ Oe (215 mA_{eff}); flight path: arrangement A: flight path L = 215 cm; detector, RSN-108S (perpendicular to the beam); detector area, 5 cm^2; effective detector thickness b = 4 cm; efficiency, 22%; arrangement B: flight path, 320 cm; detector, 19 units FHZ 8; detector area, 300 cm^2; effective thickness b = 2 cm; efficiency, 16%.

The neutron polarization for the stationary operation was $P = 98 \pm 1\%$, the flipping probability $P_{12} = 97 \pm 1\%$.

The resonance coil was operated in connection with a series-resonance circuit. The electronic gate, chopping the sinus signal for the coil, is described in detail in Ref. [1]. The repetition rate can be varied between 0 and 20 kc (50 kc), the modulation ratio between 0 and 1. Figure 2 shows the chopped sine signal before (a) and behind the power stage (b) for two repetition rates and switching ratios.

4. EXPERIMENTAL RESULTS

Figure 2(c) shows the measured neutron bursts corresponding to the sine bursts as shown above (a and b). The increase in the intensity for increasing repetition rates is clearly seen. The time-of-flight noted (analyser – detector) is related to the beginning of the burst. For neutrons arriving within a burst the distance to the left slope must be subtracted.

Figure 3 shows the measured peak intensity as a function of the repetition rate. The measurements are made with a channel width of 2 μsec and a modulation ratio of 0.5. The existence of a saturation value is caused by the resolution. If higher values of the modulations ratio are chosen, the satu-

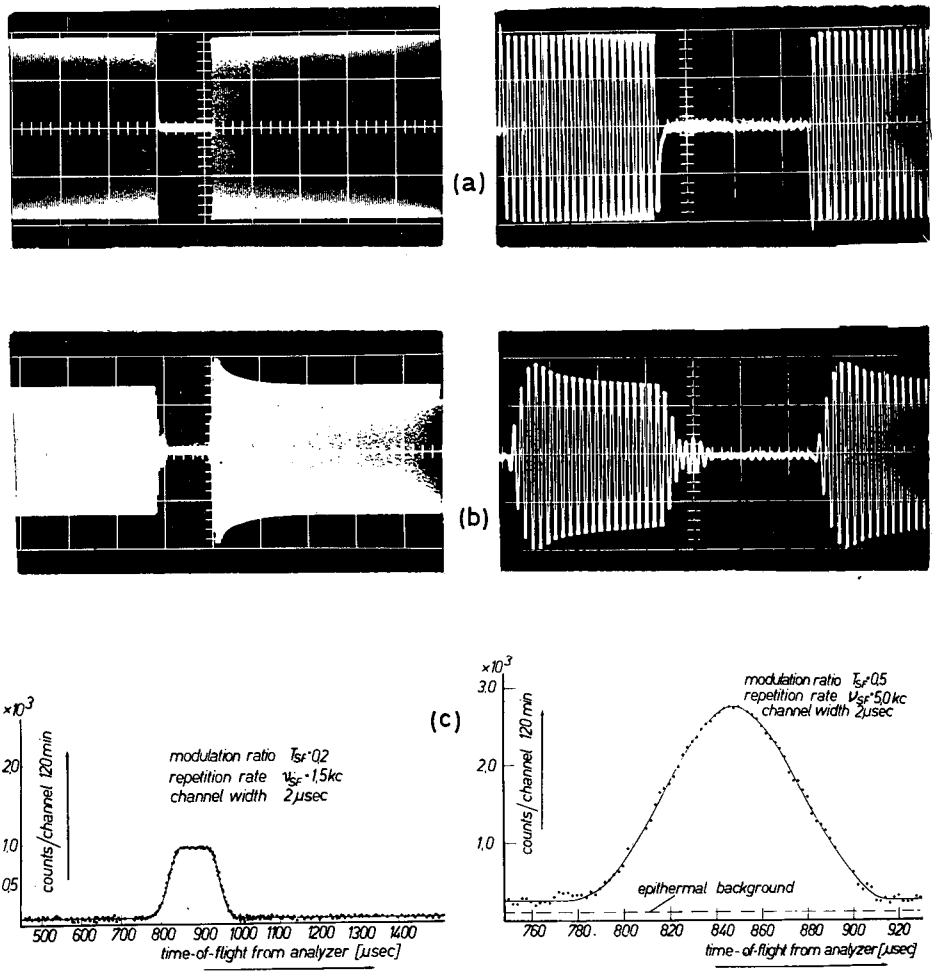

FIG. 2. Sine bursts at the input (a) and output (b) of the power stage and resulting neutron bursts (c) for two repetition rates (1.5, 5.0 kc) and two modulation ratios (0.2, 0.5) (note the different scales of the abscissa).

ration value increases, in this case the intensity between the bursts does not decrease to the background value. On the right-hand scale the absolute intensity, normed to an incident flux $\phi_0 = 1 \times \bar{v} = 2.58 \times 10^5 \, n \, cm^{-2} \, sec^{-1}$ is shown. This allows a comparison to the intensity of a comparable two-chopper apparatus (MTR chopper [9, 10]).

Figure 4 shows the result of the measurements at a cycle of 8.3 kc and a modulation ratio 0.5 by using arrangement B. From these measurements the time resolution is found by optimal Gauss approximation. In our arrangement $\Delta t / T = 4.3\%$ ($T = L/v$), which agrees very well with the theoretical value (4%). The wavelength resolution is determined by the double-crystal reflection and is $\Delta \lambda / \lambda = 1.3\%$, being also an improvement compared

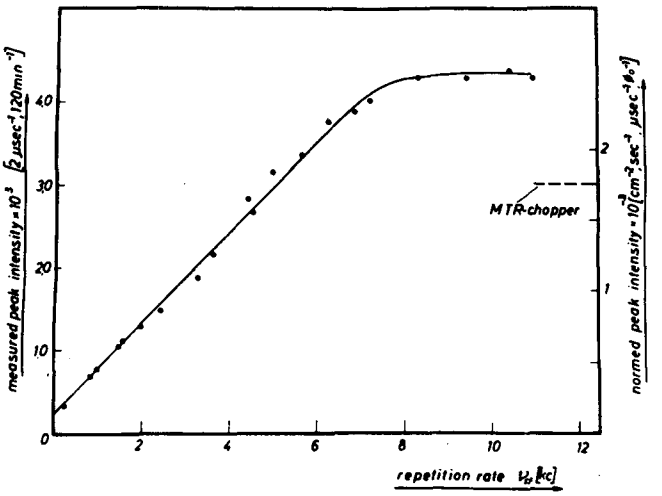

FIG. 3. Measured peak intensity (arrangement A) as a function of the repetition rate.

with the MTR chopper. The unsymmetric peak is caused by the unsymmetric sine burst within the coil (see (Fig. 2(b)).

The flux at the place of the target was also measured as 50 n cm^{-2} sec^{-1} (the measurements were made at a modulation ratio of 0.5). In relation to the same incident flux this means an increase of a factor of 2 compared with the MTR chopper [10].

5. DISCUSSION OF THE RESULTS

It has been shown that it is possible to produce neutron bursts of various modulation ratios and extremely high repetition rates by means of the spin-

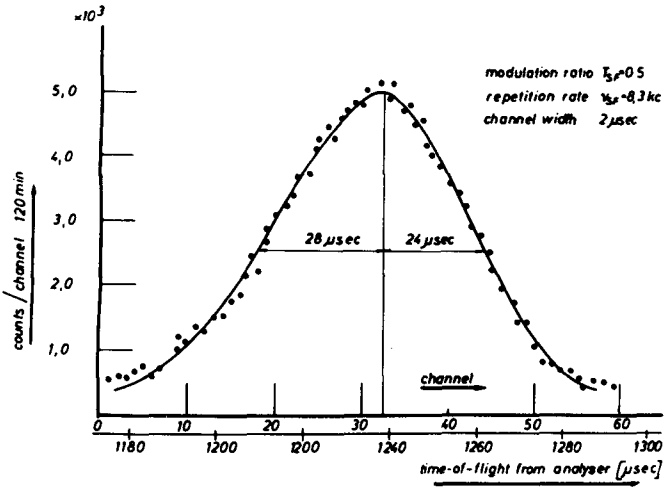

FIG. 4. Measured neutron burst for arrangement B and determination of the resolution by means of a least-squares fit.

flip chopper developed. The integral intensity, the peak intensity and the resolution are better than with mechanical choppers. Also the experimental set-up is much smaller. The use of the spin-flip chopper is of particular advantage when measuring small neutron energy changes. The fact that chopped, monochromatic neutrons are nearly polarized in total is very useful for various experiments.

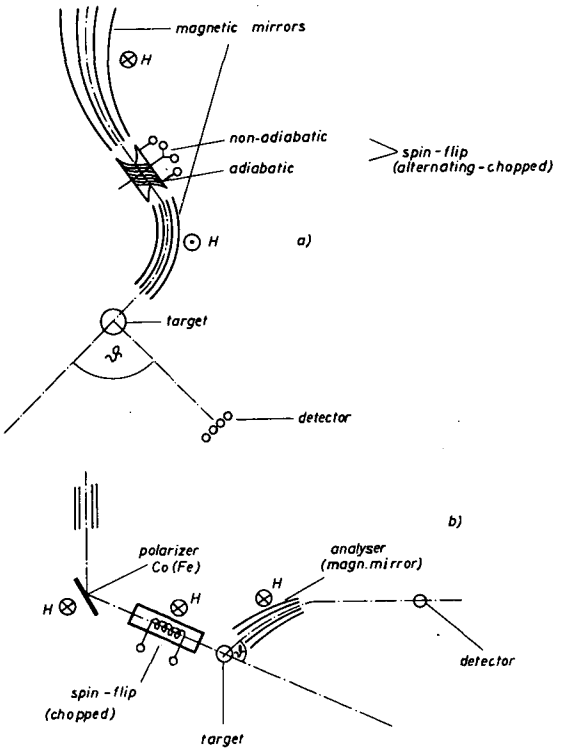

FIG. 5. Further possibilities for the use of spin-flip choppers.

For optimal adjustment the background is small, especially as the target does not stay in direction to the beam hole collimator. Further improvements (still higher intensity and better resolution) on the device described are possible by fitting a shorter coil, by shortening the distance between the polarizer and the analyser, or by using a stronger guide field, a more expensive electronic set-up and the more suitable Gd neutron detector [11, 12]. This permits a further increase in intensity at the rate of a factor of 2.

By varying the Bragg angle (H_1 must also be varied equally) and possibly also by using magnetite single crystals the energy of the monochromatic neutrons can be varied to a great extent. Further possibilities to increase the scattered intensity in a similar way are shown in Fig. 5.

In Fig. 5(b) the target is placed into the neutron beam coming from the polarizer. The inelastic scattered neutron intensity is reflected into the

detector by a curved magnetic mirror-system used as an analyser. In the set-up shown in Fig. 5(a) two magnetic mirrors are used as the polarizer, as well as the analyser. The spin-flipping is performed by chopping alternately adiabatically and non-adiabatically. This case produces a very high neutron-intensity, although the energy resolution is not very good.

ACKNOWLEDGEMENTS

The authors wish to thank Professor Dr. Gustav Ortner for many helpful discussions and to express their gratitude to the reactor crew for their extremely kind collaboration.

REFERENCES

[1] RAUCH, H., HARMS, J., MOLDASCHL, H., Austrian Physikertagung, Innsbruck, Oct.1967.
[2] RAUCH, H., HARMS, J., MOLDASCHL, H., Nucl.Instrum.Meth. 58 (1968) 261.
[3] BRUGGER, R.M., "Mechanical and time-of-flight techniques" Ch. 2, Thermal Neutron Scattering (EGELSTAFF, P.A., Ed.), Academic Press, London, New York (1965).
[4] ALVAREZ, L.W., BLOCH, F., Phys.Rev. 57 (1940) 111.
[5] STEINSVOLL, O., ABRAHAMS, K., RISTE, T., Kjeller Rep. KR-37 (1962).
[6] BACON, G.E., Neutron Diffraction, Clarendon Press, Oxford (1962).
[7] CAGLIOTI, G., PAOLETTI, A., RICCI, F.P., Nucl. Instrum.3 (1958) 223.
[8] RAUCH, H., Z. Phys. 197 (1966) 373.
[9] TOLK, N.H., BRUGGER, R.M., Nucl. Instrum.Meth. 8 (1960) 203.
[10] BRUGGER, R.M., EVANS, J.E., Nucl. Instrum.Meth. 12 (1961) 75.
[11] RAUCH, H., GRASS, F., FEIGL, B., Nucl. Instrum.Meth. 46 (1967) 157.
[12] FEIGL, B., RAUCH, H., Nucl. Instrum.Meth. (in press).

TIME-OF-FLIGHT SPECTROMETER USING AN ELECTRONIC CHOPPER FOR POLARIZED SLOW NEUTRONS

O. STEINSVOLL AND A. VIRJO*
INSTITUTT FOR ATOMENERGI,
KJELLER, NORWAY

Abstract

TIME-OF-FLIGHT SPECTROMETER USING AN ELECTRONIC CHOPPER FOR POLARIZED SLOW NEUTRONS. In a diffractometer for polarized slow neutrons the neutron spin resonance method is ordinarily used for flipping the neutron polarization. By varying the magnetic field across the flipper coil, it is possible to pulse the flipping device into or out of resonance at short intervals. One then obtains a continuous beam but with short periods of reversed neutron polarization. When this beam is reflected from a crystal by a polarization dependent scattering process (elastic or inelastic) one obtains short periods of increased neutron intensity which can be used for time-of-flight measurements of the scattered neutron energies. A time-of-flight spectrometer utilizing this principle has been built and tested on spin-wave and magneto-vibrational scattering from a single crystal of bcc iron.

1. INTRODUCTION

In a diffractometer for polarized slow neutrons the neutron spin resonance method is ordinarily used for reversing the polarization vector with respect to the magnetic field [1]. The polarized beam is passed through a solenoid situated in a homogeneous static magnetic field. The solenoid carries an R.F. current with frequency equal to the Larmor precession frequency of the neutrons in the field. At optimum current the polarization vector is flipped.

The action of the flipping device may be interrupted in a number of ways. For instance, the flipping device may be brought out of resonance by superposing an extra magnetic field on the static field across the flipper coil. We have introduced such an extra field by passing an electric current through an extra coil wound around the flipper coil. The current in this chopper coil is pulsed and adjusted so that the flipping device is tuned out of resonance for short periods of time. In this way we obtain periods of reversed neutron polarization in a polarized beam of constant intensity.

Utilizing a beam with chopped polarization for the studies of polarization dependent scattering processes (elastic or inelastic) has been suggested [2]. By such scattering one obtains short periods of increased (or decreased) neutron intensity which by suitable electronic arrangements can be used for time-of-flight analysis of the scattered neutron energies.

It has been shown [3, 4] that spin-wave and magneto-vibrational scattering from magnetic materials depend upon the polarization of the incident neutron beam. By a suitable choice of the sample magnetization parallel or normal to the scattering vector, it is possible to separate the two scattering processes. A similar separation procedure is also applicable in the case of scattering experiments with a beam of chopped polarization.

We have built a time-of-flight spectrometer utilizing the flipper-chopper principle outlined above and tested it on inelastic scattering from a crystal of bcc iron.

The main advantage of our set-up is that by using an electronic means for chopping the neutron beam, the repetition rate may be made several orders of magnitude higher than for mechanical choppers. In some of the experiments to be described below the duty cycle of the spectrometer actually approaches the theoretical limit for simple time-of-flight measurements where the correlation technique is not applied. The limit is, of course, the repetition frequency at which one gets overlap at the counter position between neutrons belonging to different bursts.

2. THEORY

The theory of the flipper-chopper and our results of preliminary tests on elastic scattering have been extensively discussed elsewhere [5-8], but a few remarks should be made about the physical parameters involved.

Let us assume that a polarized beam passes a flipper device. Having passed the flipper, the polarization has been changed to P'

$$P' = (1 - 2k_{12})P \tag{1}$$

where k_{12} is the flipping efficiency of the device. To get complete reversal of the polarization, k_{12} must equal one. This takes place for a certain combination of the values of the R. F. frequency ω and the magnetic field strength H_1.

It may be shown [5] that changing the magnetic field by a certain amount ΔH while the R. F. frequency and the current are kept constant at their optimum values will detune the flipping device. The polarized beam then passes unaffected through the solenoid. For a coil about 10 cm long and a neutron wavelength of 1 Å the value of ΔH is about 10 Oe.

Let us assume that the neutron flight time through the coil is T. Changing the field ΔH in steps from zero at time t = 0 and back again after time t = T has the effect that the polarization of the outgoing beam changes according to the following formula

$$P' = \tfrac{1}{2}(\cos^3 \Psi - 3 \cos \Psi)P \qquad (0 \leq \Psi \leq 2\pi) \tag{2}$$

where $\Psi = \pi t/T$.

The width at half maximum, $t_{\frac{1}{2}}$, of this pulse of reversed polarization is therefore $t_{\frac{1}{2}} = T$. If the field pulse does not last as long as T, the behaviour of the polarization is not as simple as in the equation above and the peak value of the reversed polarization is reduced. The transit time, T, of the neutrons through the coil is therefore a limiting value for the pulse width.

In an actual experiment it is difficult to make the extra field ΔH change like a step function. There will always be a certain rise time τ for the field, and this of course adds to the width of the pulse. The power output of the available R. F. generator sets a lower limit for the length of the

flipper coil which may be used. With unlimited R.F. power resources it may be shown, however, [7] that the physical width of the neutron beam actually is a lower physical limit for the effective length of the flipper coil.

Let us for simplicity assume a 100% polarized beam and that the flipping device works without introducing any depolarization under static conditions. Let us also assume that we are using an elastic reflection from a magnetic crystal as the analysing scattering process.

A beam with chopped polarization is converted at the sample to short periods of increased or decreased scattered intensity. The ratio between the two intensities will be equal to the flipping ratio for the scattering process under static conditions. Real background scattering from the crystal, apparatus etc. must be subtracted.

The simple theory outlined above will, of course, have to be modified when a whole series of polarization-dependent inelastic scattering processes contribute to the scattering, each process with its own set of cross-section values, σ_i^+ and σ_i^- for up and down spin. Applying a flipper-chopper, it is still possible to separate the different scattering contributions by their degree of inelasticity. The scan of an electronic time analyser may be triggered by the flipper-chopper pulse, and the flight time of the scattered neutrons from the sample may be measured after a certain flight path, L. During the intervals between the bursts we will measure a background intensity proportional to, say, $\sum_i \sigma_i^-$ which will be smeared out over the time channels and must be considered as 'background'. Each inelastic process will give rise to short periods of increased intensity proportional to σ_i^+. The peaks will therefore ride on a relatively high background.

Let us assume that the inelastically scattered neutrons from a certain magnetic crystal have a spread of energies from E_1 to E_2. After having passed the flight path, L, the neutrons will arrive with a spread in time ranging from t_1 to t_2. We may then arrange the time scan of the time analyser so that it keeps scanning for a time somewhat larger than a time $|t_1 - t_2|$. The repetition frequency of the flipper-chopper may then be increased to a value somewhat smaller than $|t_1 - t_2|^{-1}$. In this way several bursts of increased intensity may be loaded into the flight path and the duty cycle of the apparatus is very high. With this choice of parameters one does not get overlap between the slow and the fast neutrons in the different bursts at the counter position. The length of the flight path has, of course, to be chosen so that one is able to resolve the different energy groups in which one is interested.

In fact, the duty cycle of the apparatus is then close to the theoretical limit for such a set-up.

The time scan of the analyser may then actually be triggered by a chopper pulse which belongs to a neutron burst several periods behind the burst that will be registered during the scan of the time analyser. For such an arrangement it is practical to use the position of a peak of polarization-dependent elastic scattering as the reference time to which the position of the inelastic peaks are compared. Also, it is practical to have a variable delay time between the triggering pulse for the time analyser and the chopper pulse so that the inelastic spectrum may be placed at a favourable position in the time 'window'.

When the resonance flipper is working in the pulsed mode as part of a time-of-flight spectrometer, there will also be other factors influencing the burst duration as registered in the time analyser. Because of the finite

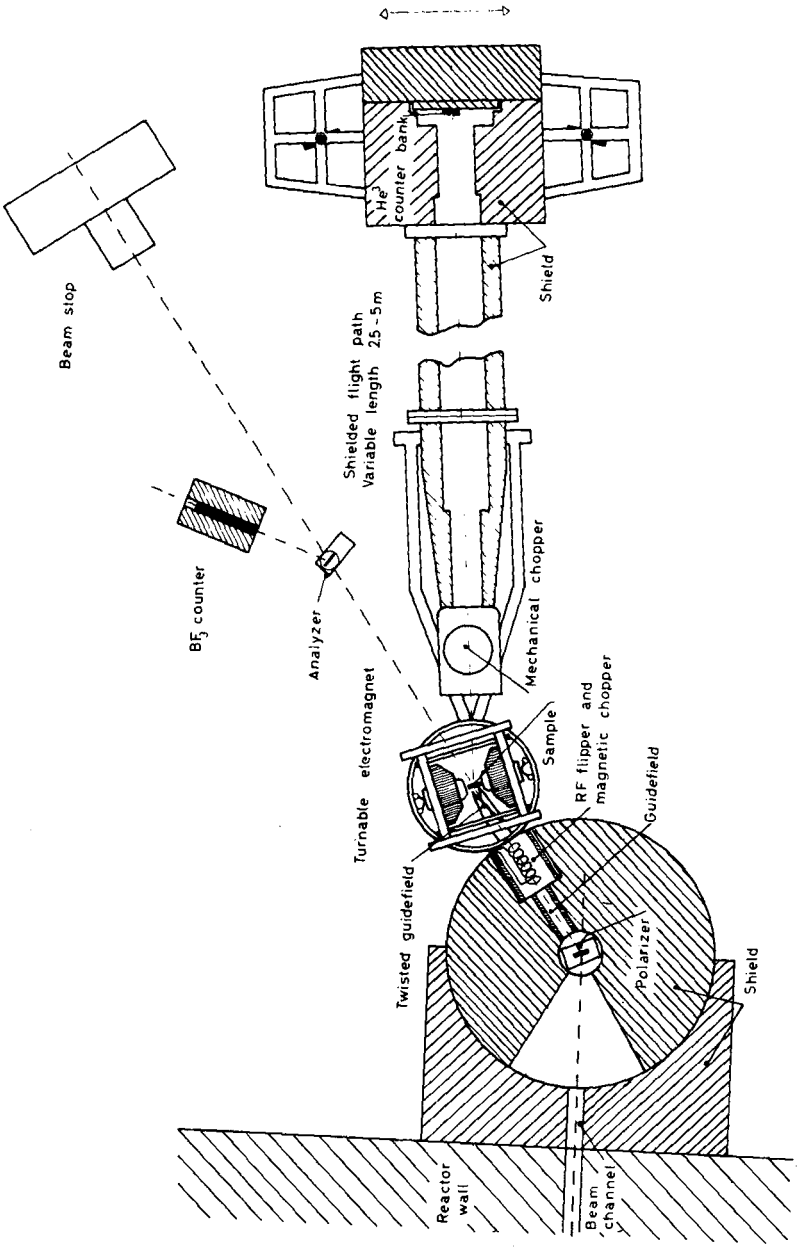

FIG. 1. Simplified view of the MISS time-of-flight spectrometer.

collimation of the beam of neutrons from the polarizer, the wavelength spread in the beam will introduce a certain spread in time, Δt_c. The width Δs of the detector also introduces an uncertainty in time, Δt_d. The uncertainty in time because of the final width of the time channels may be made negligibly small as compared to the other uncertainties in an actual case. The main contribution to the time spread of the burst will therefore come from the finite length of the flipper coil.

3. DESIGN

A multipurpose time-of-flight spectrometer, MISS, for magnetic inelastic scattering studies has recently been built and installed at the new 2-MW reactor JEEP II at IFA, Kjeller. It includes the possibility of using both a mechanical chopper and a flipper-choppper for energy analysis of the scattered neutrons from magnetic samples (see Fig. 1).

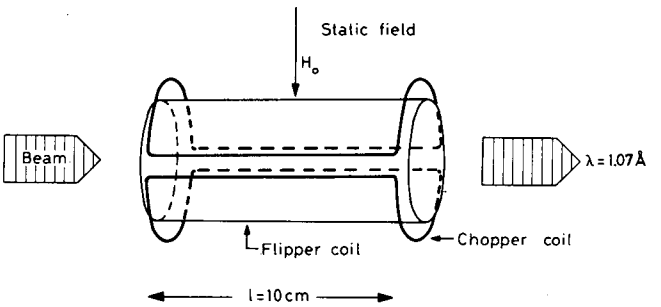

FIG. 2. The flipper coil and chopper coil geometries.

The monochromator/polarizer crystal [Co(Fe)] is situated in a shield drum which allows the choice of different wavelengths of the polarized beam. The R. F. flipper and magnetic chopper is built inside the radiation shield with magnetic shields around. The R. F. oscillator is conventional with tubes. Around the flipper coil is wound an extra saddle-shaped chopper coil (Fig. 2). Current pulses in the chopper coil sets up a small magnetic field ΔH which adds to the static field across the flipper coil. The current comes from a transistorized power supply which is excited by a conventional double-pulse generator (Fig. 3). The square pulses may have variable amplitude, duration and repetition rate so that the current pulses may be adjusted to the optimum value. There is a variable delay time between the triggering pulses for the electronic time-of-flight analyser (TMC, 4×256 channels) and the main pulses for the chopping circuit.

The sample is situated inside an electromagnet which may be rotated both around a vertical and a horizontal axis. In this way the sample may be magnetized either along the scattering vector or normal to it. With the electromagnet in the vertical position a small permanent magnet is enough to guide the polarized beam across the gap between the flipper and the magnet. In the horizontal position a twisted guide field of iron plates has to be inserted in the gap.

The shielded flight arm is connected to the magnet table and may rotate around it driven by a motor. It consists of several sections so that its length may be varied. At the end of the flight arm there is a counter bank of 3 ^{3}He counters in the vertical position whose total sensitive area is 7.5×15 cm^2.

Behind the electromagnet the polarization of the transmitted beam through the electromagnet may be monitored by a small diffractometer.

The monochromatic beam may have a cross-section up to 4 cm $\times$4 cm, but in the experiments to be reported below it was collimated down to 2 cm $\times$ 2 cm by means of B_4C-plastic.

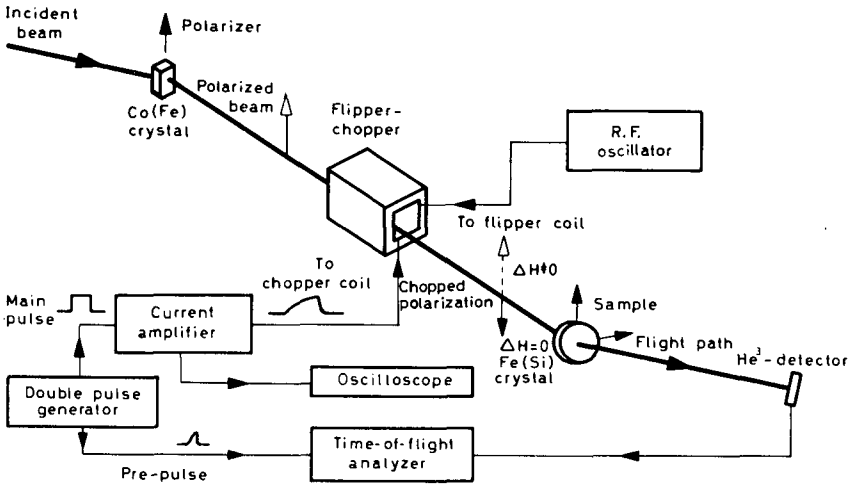

FIG. 3. Block diagram of the electronic circuit for the flipper-chopper time-of-flight spectrometer.

4. EXPERIMENTAL TESTS

The spectrometer has been tested using inelastic scattering from a single crystal of bcc iron, $Fe_{0.96}Si_{0.04}$. The crystal was disc-shaped 3 cm in diameter and 6 mm thick. The [100] direction was normal to the plane of the disc. The crystal was mounted in a holder which allowed the electromagnet to be rotated around it, magnetizing the crystal normal to or parallel to the scattering vector (i.e. along equivalent [110] directions).

It is known that the diffuse reflection around the (110) reciprocal lattice point originates both from polarization-dependent spin-wave [9] and magneto-vibrational [4] scattering. For $\vec{H} \parallel \vec{e}$ spin-wave scattering is polarization dependent, and for $\vec{H} \perp \vec{e}$ magneto-vibrational. In the latter case elastic scattering and magnetic disorder scattering will also depend on the polarization. The position of the elastic peak in the time analyser may be used as a reference.

By missetting the crystal for $\vec{H} \perp \vec{e}$ (vertical field), a certain angle $\Delta\Phi$ away from the Bragg setting, Φ, a diffuse reflection with a certain angular width, Γ, may be seen by the diffraction technique using a polarized beam. During our experiments the flight arm was always moved to the direction pointing towards the middle of the diffuse reflection for the given angle of misset.

The sense of rotation by the angle $\Delta\Phi$ of the crystal determines whether one has creation or annihilation of quasi-particles during the scattering. The energies of the scattered neutrons should accordingly be decreased or increased when compared with elastic scattering.

The sensitive area of the counter bank was about 3° in the vertical direction and 1.3° in the horizontal direction at a distance of 310 cm from the sample during the experiments. The wavelength of the incoming polarized beam was λ = 1.07 Å ($\simeq$ 270 μ sec/m). The polarization was 97%. The magnetizing field was 6 kG. 256 channels were used with either 2-μ sec or 1-μ sec channel widths. The duration of the current pulses was 35 μ sec.

In Fig. 4 we show results of the preliminary tests for the vertical field arrangement ($\vec{H} \perp \vec{e}$), i.e. vibrational scattering. The elastic peak has been corrected for dead time in the time analyser. It may be seen that

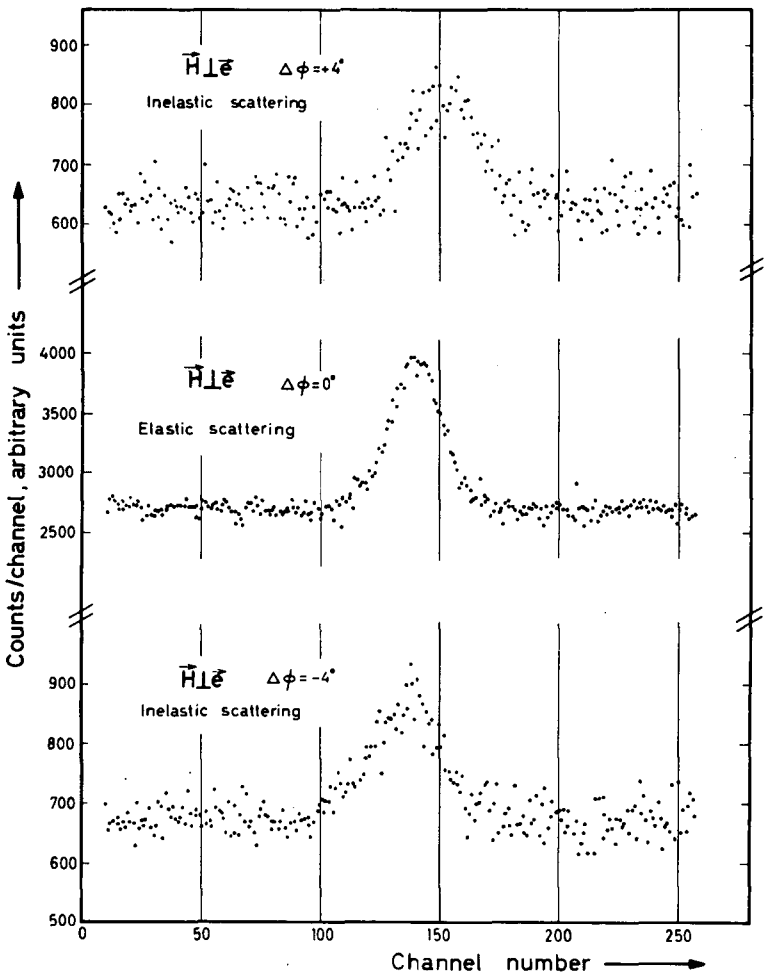

FIG. 4. Inelastic peaks caused by magneto-vibrational scattering ($\vec{H} \perp \vec{e}$) for $\Delta\Phi = \pm 4°$. In the middle insert the elastic peak is shown for comparison ($\Delta\Phi = 0°$). Channel width = 2 μsec.

the flipping ratio in the elastic (110) reflection from iron is rather small ($\simeq 1.5$) as compared to the expected value of 3.5. This is mainly due to the strong extinction effect in the rather thick crystal, but also to some depolarization of the beam during the transit. The neutron scattering cross-sections for inelastic scattering are, however, so small that there will be no extinction in that case. The results are in qualitative agreement with the fact that for $\Delta\Phi = +4°$ there is creation and for $\Delta\Phi = -4°$ annihilation of vibrational quanta in the crystal. For the positive misset the scattered neutrons are slowed down and for the negative misset the neutrons are speeded up.

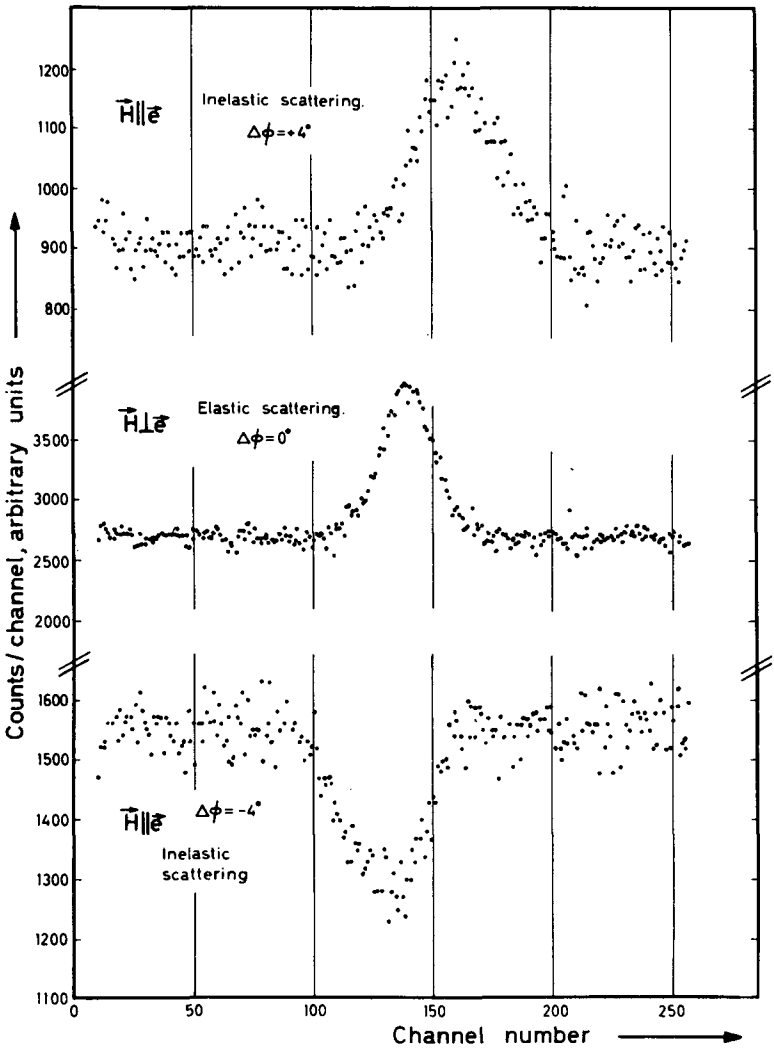

FIG. 5. Inelastic peaks caused by spin-wave scattering ($\vec{H} \parallel \vec{e}$) for $\Delta\Phi = \pm 4°$. In the middle insert the elastic peak (i.e. $\vec{H} \perp \vec{e}$) is shown for comparison. Channel width = 2 μsec.

Figure 5 shows the experimental results for the horizontal field arrangement ($\vec{H} \parallel \vec{e}$), i.e. magnon scattering. The positions of the inelastic peaks show that the scattered neutrons have suffered changes in velocity for positive and negative missetting angles in the same directions as observed above. The only difference is that for the negative angle of misset (magnon annihilation) there is a drop in intensity; the peak is negative. This is, however, a well-known feature of magnon scattering using polarized neutrons [3] and is due to the fact that for magnon annihilation the scattering cross-section for a neutron beam with positive polarization is zero. Our preliminary results, therefore, show a good qualitative agreement with the effects to be expected for such a set-up.

Figure 6 gives a simplified view of the behaviour of the scattering cross-section during a pulse of reversed neutron polarization for spin-wave scattering.

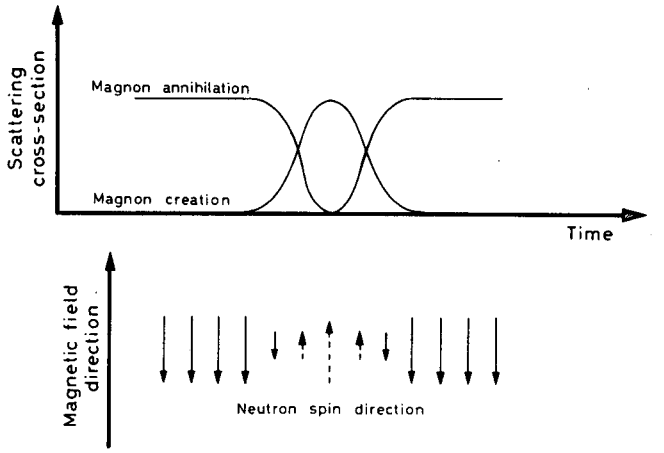

FIG. 6. Schematic picture of the polarization effects in spin-wave scattering from metallic iron.

For the small angles of misset used above the applied vertical collimation and the time resolution were too relaxed to give any direct information about the scattering surface for vibrational and spin-wave scattering. Scattering from the whole surface in reciprocal space was accepted by the counters, and the energy differences were too small. For horizontal field arrangement, i.e. spin-wave scattering, the misset was increased to $\Delta\Phi = 8°$. In this case it is known from experiments with the diffraction method on a similar crystal that the spherical scattering surface is almost 5° wide. A part of the scattering surface should therefore be 'sliced off' in our geometry, and the energy differences involved should be so large that one could expect to see some details. In fact, from Fig. 7 it is seen that the time-of-flight spectrum of the inelastically scattered neutrons for $\Delta\Phi = 8°$ seems to consist of overlapping peaks. The total width has increased relative to the elastic peak. The data from the diffraction experiments [9] for $\Delta\Phi = 8°$ leads to expected neutron flight-times of $t' = 280\ \mu\text{sec/m}$ and $t'' = 303\ \mu\text{sec/m}$ for neutron groups in this direction. For the flight path used the inelastic peak should be about 70 μsec wider than the elastic peak. This is in fair agreement with Fig. 7.

During the experimental run for $\Delta\Phi = 8°$ the spectrometer had a duty cycle close to the limiting value for this special experiment. It is seen from Fig. 7 that the inelastic spectrum almost fills the time window of width 256 μ sec; only enough time channels are left on both sides to allow the determination of the background. The spectrometer was then pulsed at 260-μsec intervals. A delay time of 60 μsec had to be introduced between

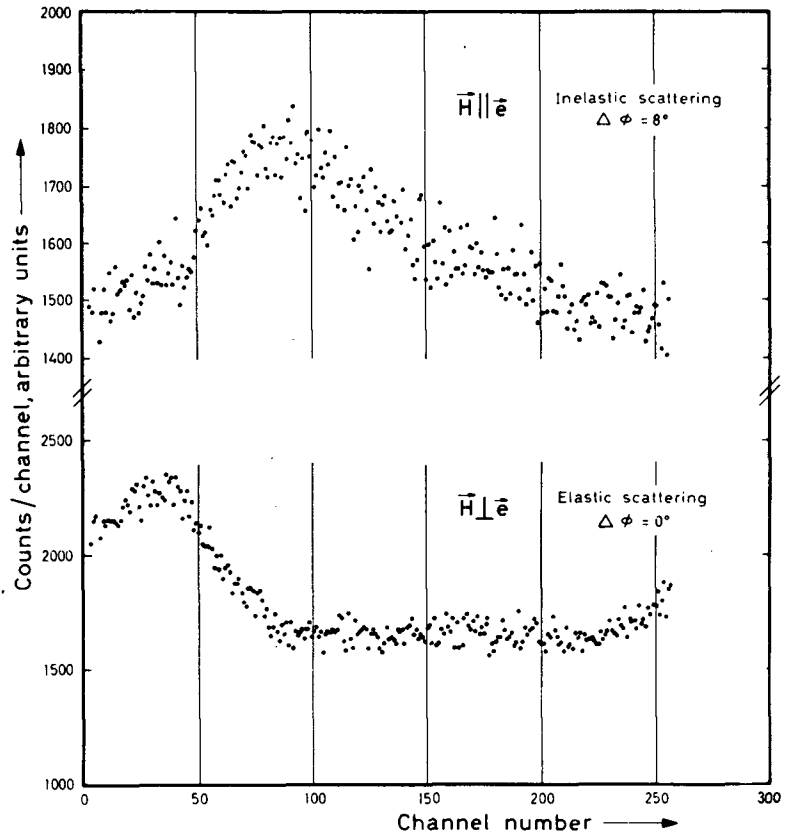

FIG. 7. Time-of-flight spectrum of neutrons scattered with creation of spin waves for $\Delta\Phi = +8°$. The elastic peak is shown for comparison. The channel width was 1 μsec and the time between chopper pulses 260 μsec.

the trigger pulse and the chopper pulse in order to place the spectrum in the middle of the time window. The data shown in Fig. 7 was collected over 37 hours. The nuclear vibrational scattering which is still present for horizontal field arrangement is partly responsible for the high background.

5. DISCUSSION

During the preliminary tests the resolution of the apparatus chosen was rather low. The width at half maximum of the elastic peak was $\Gamma \simeq 50\,\mu$sec, although the current pulse was only 35 μsec wide. The larger

value of the burst duration has its origin in the factors mentioned in the section above. With the neutron wavelength applied and the chosen length of the flight path the time resolution is therefore 6%. With the possible further increase in the flight path and a shorter current pulse duration the resolution may be increased, but at the expense of the absolute intensity and the size of the inelastic peaks (above the background). A more accurate calculation of all the factors involved in the resolution for this type of apparatus has been initiated.

Using polarized neutrons the intensities obtained from the ususal polarizer crystal, Co(Fe), is low compared with the ordinary monochromator crystals such as copper and zinc. In this apparatus we gain, however, because of the very high duty cycle of the flipper-chopper. On the other hand, we rely on a polarization effect so that the amplitude of the registered peaks above the 'background' will in the first place depend on the relative cross-sections of scattering for neutrons of up and down spin, on the polarization of the beam and on the flipping efficiency.

Similar experiments are planned at the same apparatus using the mechanical chopper. A direct comparison of the results is then possible.

6. CONCLUSION

Our experiments have shown that a flipper-chopper time-of-flight spectrometer is feasible, and that it gives results consistent with other measurements when applied to polarization dependent inelastic scattering processes. The results may be taken as the most direct proof for the fact that the polarization dependent diffuse reflections are connected with inelastic scattering phenomena.

ACKNOWLEDGEMENTS

The authors wish to express their gratitude to the staff of the Neutron Physics Division at IFA, especially fil. lic. K. Otnes whose knowledge about the practical aspects of time-of-flight spectrometers has been of extreme value.

REFERENCES

[1] NATHANS, R., SHULL, C.G., SHIRANE, G., ANDRESEN, A.F., J. Phys. Chem. Solids 10 (1959) 138.
[2] NATHANS, R., private communication (1965).
[3] SAMUELSEN, E.J., RISTE, T., STEINSVOLL, O., Phys. Lett. 6 (1963) 47.
[4] STEINSVOLL, O., these Proceedings, SM-104/64.
[5] STEINSVOLL, O., VIRJO, A., IFA Internal Work Rep. NF-5 (May 1967).
[6] VIRJO, A., STEINSVOLL, O., Physica Norvegica 2 4 (1967) 314.
[7] VIRJO, A., STEINSVOLL, O., Kjeller Rep. KR-125 (Feb. 1968).
[8] STEINSVOLL, O., VIRJO, A., Phys. Lett. 26A (1968) 469.
[9] SHIRANE, G., NATHANS, R., STEINSVOLL, O., ALPERIN, H.A., PICKART, S.J., Phys. Rev. Lett. 15 (1965) 146.

CORRELATION-TYPE TIME-OF-FLIGHT SPECTROMETER WITH MAGNETICALLY CHOPPED POLARIZED NEUTRON BEAM

L. PÁL, N. KROÓ, P. PELLIONISZ, F. SZLÁVIK AND I. VIZI
CENTRAL RESEARCH INSTITUTE FOR PHYSICS,
HUNGARIAN ACADEMY OF SCIENCES,
BUDAPEST, HUNGARY

Abstract

CORRELATION-TYPE TIME-OF-FLIGHT SPECTROMETER WITH MAGNETICALLY CHOPPED POLARIZED NEUTRON BEAM. The transfer function of a system which is the conventional time-of-flight distribution function, is proportional to the cross-correlation function involving a random signal and the response of the system to it. An experiment using this technique is described. The chopped monoenergetic, polarized neutron beam is produced by a polarizer-analyser Co(Fe) single-crystal system with a spin-flipper between the crystals. The flipper is switched off and on, following a binary pseudo-random sequence. Pulses from the detector are stored in the first half of the memory of a conventional multichannel analyser. At the end of the measurement the cross-correlation function is computed in a few seconds with the use of a special plug-in unit of the analyser and stored in the form of discrete values in the second half of the memory. The neutron economy, the resolution and the effect to background ratio of the correlation spectrometer are much better than in the conventional time-of-flight method.

1. INTRODUCTION

Neutron spectrometry initiated a new era in the study of the microdynamics of condensed systems. One of its well-known methods, the time-of-flight technique, is particularly suitable for cold neutron scattering experiments which yield information on small energy excitations in solids and liquids which is otherwise almost unobtainable. This technique requires periodic chopping of the continuous neutron beam. In the moderate energy resolution case the transmission efficiency of the chopper is usually of the order of 10^{-3}, thus the conventional time-of-flight technique offers very poor neutron economy which gets even poorer if one tries to improve the energy resolution. In many cases one does not get any valuable information because of the small effect to background ratio.

Application of the correlation technique in time-of-flight spectrometry [1-3] results in a substantial improvement in neutron economy and energy resolution. In section 2 the essential features of the method are described and the conventional time-of-flight technique is compared with the correlation method. In section 3 the experimental set-up and the results of some experimental tests of the method are reported.

2. PRINCIPLE OF THE METHOD

The principle of correlation type time-of-flight spectrometry (CTFS) is very simple. The monoenergetic neutron beam incident on the sample is randomly modulated and the neutrons are counted at a given scattering angle by a suitable detector placed at a given distance from the sample. The time

dependence of the counts is registered and its cross-correlation with the modulating random function is calculated. The cross-correlation function is proportional to the time-of-flight density function.

Let s(t) be the registered intensity of the scattered neutrons without modulation and x(t) the modulating random function. The state of the neutron modulator can be characterized by the random function

$$x^M(t) = \frac{1}{2}\left[1 + x(t)\right] \tag{1}$$

When $x(t) = 1$ or -1, the modulator is open or closed, respectively.

Denote by $h(t)\,dt$ the probability that a neutron scattered by the sample will be counted in the time interval $(t, t+dt)$ if it crosses the modulator at time $t = 0$. The density function $h(t)$ is directly related to the scattering function and it has to satisfy the conditions

$$h(t) = 0 \tag{2}$$

if $t < 0$ and

$$\int_0^\infty h(t)\,dt = 1 \tag{3}$$

The intensity of the neutron counts at any time t can be expressed in the form

$$y(t) = \int_{-\infty}^{+\infty} s(t')\,x^M(t')h(t-t')\,dt' + s^B(t) \tag{4}$$

where $s^B(t)$ is the background intensity. If one assumes that

$$E\left\{x(t)\right\} = 0 \tag{5}$$

then the cross-correlation between $y(t)$ and $x(t)$, written as

$$E\left\{y(t)\,x(t-\tau)\right\} = R_{yx}(\tau) \tag{6}$$

has a very simple form

$$R_{yx}(\tau) = \frac{1}{2}\,i_0 \int_{-\infty}^{+\infty} R_{xx}(\tau - t)\,h(t)\,dt \tag{7}$$

where $i_0 = E\{s(t)\}$ is the averaged intensity and $R_{xx}(\tau) = E\{x(t)\,x(t-\tau)\}$ is the auto-correlation function of $x(t)$. The background, fortunately, cancels out

since there is no correlation between x(t) and $s^B(t)$. If x(t) is a random process with auto-correlation of the form

$$R_{xx}(\tau) = \delta\left(\frac{\tau}{\alpha}\right) = \alpha\delta(\tau)$$

where α is a constant with time dimension, then

$$R_{yx}(\tau) = \frac{1}{2} i_0 \alpha h(\tau) \tag{8}$$

and it is apparent that the cross-correlation function $R_{yx}(\tau)$ is exactly proportional to the time-of-flight density function.

Ideal random modulation corresponding exactly to white noise, however, can be never achieved, but it may be well approximated by a suitable binary random modulation. In this case the state of the modulator does not change in a time interval shorter than a given elementary interval, say θ, and thus the auto-correlation function of x(t) has the form

$$R_{xx}(\tau) = \begin{cases} 1 - \dfrac{|\tau|}{\theta} & |\tau| \leq \theta \\ 0 & |\tau| > \theta \end{cases} \tag{9}$$

Inserting Eq.(9) into Eq.(7) and neglecting the small variation of h(t) within the time interval θ, one gets again

$$R_{yx}(\tau) \sim \frac{1}{2} i_0 \theta h(\tau) \tag{10}$$

In practice the neutron counts are stored in the channels of a memory block controlled by a clock generator. Let θ be the time interval between the consecutive clock pulses. The q^{th} channel of the memory is opened and the $(q-1)^{th}$ is closed by the q^{th} clock pulse. Each pulse generates simultaneously a random binary number (0 or 1) which determines whether the neutron modulator will be in the closed or open state during the time interval θ following the clock pulse.

In this mode of operation the number of counts in the q^{th} channel can be expressed by the equation

$$z_q = \theta \sum_{i=0}^{q} h_i \nu_{q-i} x^M_{q-i} + \nu^B_q \tag{11}$$

where

$$h_i\theta = \int_{i\theta}^{(i+1)\theta} h(t)\,dt \sim \theta h\left[\left(i + \frac{1}{2}\right)\theta\right]$$

and

$$\nu_q = \int_{(q-1)\theta}^{q\theta} s(t)\,dt, \quad \nu_q^B = \int_{(q-1)\theta}^{q\theta} s^B(t)\,dt$$

The random binary number x_q^M can be written in the form

$$x_q^M = \frac{1}{2}(1 + x_q) \tag{12}$$

where the random numbers $\ldots, x_q, x_{q+1}, \ldots$ have the following properties:

$$E\{x_q\} = 0, \qquad E\{x_p x_q\} = \delta_{pq}$$

The cross-correlation function

$$E\{z_q x_{q-j}\} = R_{zx}(j)$$

is seen again to be proportional to the time-of-flight density function h_i, i.e.

$$R_{zx}(j) = \frac{1}{2} i_0 \theta^2 h_j \qquad (j = 0, 1, \ldots, q-1) \tag{13}$$

In practice, however, an ideal random series of the numbers 0 and 1 cannot be produced because of the obvious fact that the length of the series is limited by the finite number of the channels available in the memory. It is possible, however, to use, instead of the ideal random series of infinite length, a pseudo-random sequence of finite length. Pseudo-random binary sequences can be easily generated by a multistage shift register driven by clock pulses [4]. If one uses a suitable logical feedback, a d-stage shift register produces a periodic binary sequence with period length $n = 2^d - 1$. Let us denote the binary numbers of this period by

$$V_k^M = \frac{1}{2}(1 + V_k) \qquad (k = 1, 2, \ldots, n) \tag{14}$$

where the numbers $V_k = \pm 1$ $(k = 1, 2, \ldots, n)$ have the 'pseudo-randomness' properties given by

$$\frac{1}{n}\sum_{k=1}^{n} V_k = \frac{1}{n} \tag{15}$$

$$\frac{1}{n}\sum_{k=1}^{n} V_k V_{k-j} = \begin{cases} 1, & \text{if } j = pn, \quad p = 0, \pm 1, \ldots \\ \frac{1}{n}, & \text{if } j \neq pn, \quad p = 0, \pm 1, \ldots \end{cases} \tag{16}$$

and satisfy the periodicity requirement

$$V_{k+pn} = V_k \qquad (p = 0, \pm 1, \ldots) \tag{17}$$

In actual measurements each channel of the memory is opened periodically and if the number of channels is $n = 2^d - 1$, then the time interval between two successive operations of the same channel will be simply $n\theta$. The number of counts accumulated in the k^{th} channel after N operations is given by

$$Nu_k = \sum_{p=1}^{N} z_{k+(p-1)n} \tag{18}$$

where

$$z_q = \theta \sum_{i=0}^{n-1} h_i \nu_{q-i} V_{q-i}^M + \nu_q^B$$

if

$$h_i = 0 \qquad \text{for} \qquad i \geq n$$

This last condition can be almost always satisfied by the appropriate choice of the channel number n. Introducing the notation

$$\mu_k = \frac{1}{N} \sum_{p=1}^{N} \nu_{k+(p-1)n} \tag{19}$$

and making use of the periodicity of V_q, one finds that

$$u_k = \theta \sum_{i=1}^{n-1} h_i \mu_{k-i} V_{k-i}^M + \mu_k^B \tag{20}$$

The estimate of the cross-correlation function $R_{zx}(j)$ can be written in the form

$$r_n(N, j) = \frac{1}{n} \sum_{k=1}^{n} u_k V_{k-j} \tag{21}$$

It is easy to show that

$$E\left\{r_n(N, j)\right\} = \frac{1}{2} i_0 \theta^2 h_j + \frac{i_0 \theta}{n} \left(1 + f - \frac{h_j \theta}{2}\right) \tag{22}$$

where f is the intensity ratio of the background to the effect, i.e.

$$f = \frac{E\{s^B(t)\}}{E\{s(t)\}} = \frac{b_0}{i_0} \tag{23}$$

It should be noted that the non-modulated part of the scattered neutrons gives an additional contribution to the background. It is apparent from Eq. (22) that the estimate (21) is distorted and the background, though highly reduced, is not averaged out completely.

Using some generalized 'pseudo-randomness' properties of the sequence $V_k (k = 1, \ldots, n)$, the variance of the estimate $r_n(N, j)$ can be calculated. The result of the calculation can be written in the form

$$D^2\left\{r_n(N, j)\right\} = \frac{1}{2}\frac{i_0\theta}{Nn}(\delta + 2f) + \frac{1}{2}\frac{i_0\theta}{Nn}\frac{2-\delta}{n} \tag{24}$$

where

$$\delta = \theta^2 \sum_{i=0}^{n-1} h_i^2 \leqq 1 \tag{25}$$

The relative root-mean-square deviation of the estimate $r_n(N, j)$ is

$$\frac{D\{r_n(N, j)\}}{E\{r_n(N, j)\}} \sim \sqrt{\frac{2(\delta+2f)}{i_0 T h_j^2 \theta^2}} \left\{1 + \frac{1}{n}\left[\frac{2(1+f)}{h_j\theta} - 1\right]\right\}^{-1} = \rho_{CORR} \tag{26}$$

where $T = Nn\theta$ is the total measuring time. This formula differs from that proposed earlier by Moguilner et al. [1]. Fortunately, the difference further increases the advantages of the correlation technique over the conventional time-of-flight method. This can be seen immediately if one compares the relative rms deviation of $r_n(N, j)$ with that of $h_j\theta$ measured by the conventional method. In the time-of-flight technique the relative rms deviation of the effective counts (total counts minus background) in the channel is given by

$$\rho_{TF} = \sqrt{\frac{(2f + h_j\theta)n}{i_0 T h_j^2 \theta^2}} \tag{27}$$

and thus the inequality

$$\frac{\rho_{TF}}{\rho_{CORR}} = \sqrt{\frac{n(2f+h_j\theta}{2(2f+\delta)}} \left\{1 + \frac{1}{n}\left[\frac{2(1+f)}{h_j\theta} - 1\right]\right\} \gg 1 \tag{28}$$

holds in almost all cases, in other words the correlation method has under the same conditions a much better resolution for the amplitudes $h_j\theta (j = 0, 1, \ldots, n-1)$ within the given energy resolution than the conventional technique. This advantage can be exploited for the analysis of fine details in the time-of-flight spectra.

3. EXPERIMENT

The scheme of the experimental arrangement can be seen in Fig. 1. For the modulation of the incident neutron beam a flipper-chopper proposed and tested successfully by several authors [5-7] was used. The flipper-chopper was placed between two Co(8% Fe) monocrystal slabs magnetized in the direction of easy magnetization. The thickness and the effective area of the crystals were 2.5 mm and 2 cm × 3 cm, respectively. For the experiments the transmitted (111) reflection of wavelength 1.2 Å was used. The degree of polarization was measured by means of a 0.3-mm thick iron foil and the shim ratio was found to be $p_1 p_2 = 0.98$.

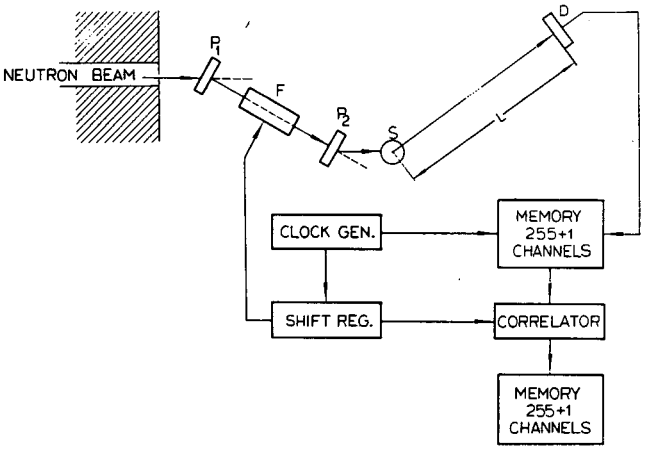

FIG. 1. Scheme of the experimental set-up: P_1 and P_2 are the monocrystal slabs, F is the flipper, S is the sample and D is the neutron detector.

The monoenergetic, polarized neutron beam, reflected by the first crystal is reflected in the same way by the second one when the spin-flipper between the crystals is switched off. When the flipper is 'on', it reverses the neutron spins and the intensity after the second crystal is expected to be practically zero.

If the oscillator of the flipper is controlled, i.e. kept in the 'on' or 'off' condition by a binary pseudo-random generator, the polarized neutron beam after the second crystal is modulated in time in a pseudo-random way. The modulation is, however, not complete since the shim ratio and the spin-flipping probability are practically always smaller than unity. The depth of the modulation can be expressed by the formula

$$M = \frac{2P_1 P_2 \eta}{1 + P_1 P_2}$$

where η is the spin-flipping probability. In our case $\eta = 0.75$ and therefore $M \sim 0.63$. The small value of η can be explained by the shortness of the flipper coil length and the inhomogeneities in the field of the permanent magnet used in the flipper. The length of the flipper coil was chosen to give

$\ell \ll \theta V_\lambda$ (V_λ is the neutron velocity) in order to obtain neutron pulse trains of nearly rectangular shape.

The block diagram of the electronic system for the pseudo-random excitation of the flipper coil is shown in Fig. 2. The rf oscillator is of the tuned L-C anode circuit type. The flipper coil is inserted into the anode circuit of the output power amplifier tube. Good power efficiency is achieved in an anti-resonant mode of operation through equalizing by the reactive component of the coil admittance.

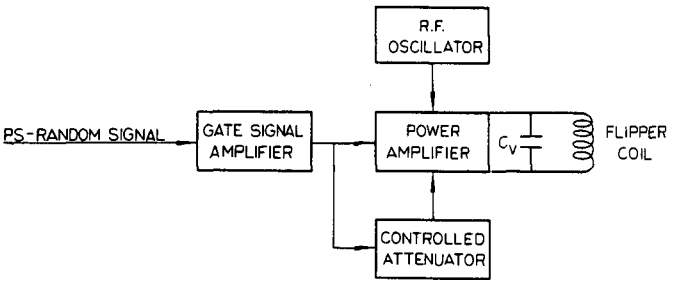

FIG. 2. Block diagram of the electronic system for the random excitation of the flipper coil.

The damping time of the rf field in the flipper coil has to be much smaller than u in order to obtain sharp neutron pulses. This can be achieved by a controlled attenuator which is an electronically switched dynamic resistance, forming a parallel circuit with the flipper coil. To obtain the maximum spin-flipping probability both the amplitude and the frequency of the rf field are continuously variable. The most important flipper data are listed in Table I.

TABLE I. FLIPPER DATA

Coil length:	4.0 cm	Static magnetic field:	345 Oe
Coil diameter:	1.8 cm	rf magnetic field:	20 - 50 Oe
Number of turns:	18	Frequency range:	0.8 - 1.2 Mc/sec
Damping and rise time: 2×10^{-6} sec			

To test the operation of the flipper as a neutron beam chopper, three intensity measurements were carried out: one (J_{off}) in the turned off state, another (J_{on}) in the turned on state and a third (J_a) with the excitation of the flipper coil controlled by a 25-kHz square-wave generator, i.e. when in every second 40-μsec period the flipper was in the on state. The good agreement of the intensity of J_a with $\frac{1}{2}(J_{off} + J_{on})$ was proof of the proper operation of the flipper.

The monoenergetic polarized modulated neutron beam is scattered by the sample to be investigated. The scattered neutrons are detected by a set of BF_3 counters at the end of the flight path of length L. The whole measuring system is controlled by intervention of the digital correlator KORALL-A [8] which is a plug-in unit of the NTA-512-type multichannel analyser.

The neutron detector counts are stored in the first section of the 512-channel ferrite core memory of the analyser. Shift pulses from the clock generator are fed into the address register of the memory, thus the channel width is equal to the time interval θ between the subsequent pulses of the clock generator. The value of θ can be chosen from the series 20, 50, 100 and 200 μsec.

When the number of counts in any channel of the memory attains a preset value, KORALL-A stops the measurement to start the computing operation in which according to Eq. (21) it computes the values

$$Nn\, r_n(N, j) = N \sum_{k=1}^{n} u_k V_{k-j}$$

$$(j = 0, 1, \ldots, n-1)$$

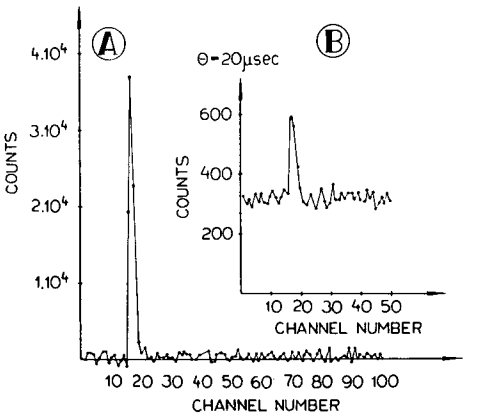

FIG. 3. Time-of-flight spectra of monoenergetic neutrons measured by (A) the correlation and (B) the conventional methods.

where Nu_k is the number of counts stored in the k^{th} channel of the first memory section and $n = 255$.

The value of $Nn\, r_n(N, j)$ is transferred into the $(j+1)^{th}$ channel of the second half of the memory. On termination of the total computing period of about 3 sec, n discrete ordinate values of the cross-correlation function are stored in the second part of the memory in a form ready for any of the conventional read-out operations. The number of counts in each channel of the first section remains unchanged during the computing operation, thus the measurement can be continued by making use of the data collected in the preceding run.

To test the operation of the correlation spectrometer, first the time-of-flight spectrum of the monoenergetic polarized beam was measured. The flight-path length L was 120 cm and two runs were carried out, one with 20 and another with 50 μsec channel width. For comparison, in Fig. 3 the cross-correlation function (A) is shown along with the time-of-flight spectrum (B) measured under the same conditions by conventional technique.

4. DISCUSSION

To show the efficiency of the correlation technique, measurements were carried out in the presence of a large background ($f \sim 0.56$). The expected advantages of the correlation technique over the conventional method are immediately seen from Fig. 3. The peak value of the cross-correlation function is about 60 times higher and, even more important, its peak to background ratio is about 16 times larger than the corresponding values of the time-of-flight spectrum measured in the conventional way.

The characteristic features of correlation type time-of-flight spectrometry, namely, the very good neutron economy and the large effect to background ratio, offer promising new perspectives in the measurements of small effects (impurity scattering etc.).

One of the most important problems in the further development of the correlation technique is to increase the transmission efficiency of the modulating system. The flipper-chopper efficiency, as estimated from the reflectivity of the monocrystal slabs and the modulation depth, is about 10^{-2}. This value is rather small, thus it seems useful to improve the modulation technique. A very promising method was proposed and tested by Mook and Wilkinson [9]. The principle of this method is very simple. The neutron beam reflected by the (111) planes of a lithium titanium ferrite monocrystal is almost completely modulated when the magnetization direction in the crystal is rapidly altered by an external magnetic field. Since, in this case, the neutron beam suffers only one reflection in the modulator, the transmission efficiency is expected to be higher by a factor of 10 than that in the flipper-chopper case.

Finally, it is of interest to note that the correlation technique may become, because of its good neutron economy and small background to effect ratio, a powerful tool in time-of-flight neutron diffraction measurements. In this case the polyenergetic neutron beam can be modulated at random by a mechanical chopper similar to that used by Moguilner et al. [1].

ACKNOWLEDGEMENT

The authors are indebted to Mr. G. Orbán for the design and building of the flipper coil electronics.

REFERENCES

[1] MOGUILNER, A.I., SALNIKOV, O.A., TIMOHIN, L.A., USSR Patent No.177112 (1964); Priborȳ Tekh. Éksp. 2 (1966) 22.

[2] COOKE-YARLOROUGH, E.H., Instrumentation Techniques in Nuclear Pulse Analysis (Proc.Conf. Monterery, Calif., 1963) National Academy of Sciences – National Research Council, Publ.1184 (1964) 207.

[3] GORDON, J., KROÓ, N., ORBÁN, G., PÁL, L., PELLIONISZ, P., SZLÁVIK, F., VIZI, I., Phys. Lett. 26A (1968) 122.

[4] KORN, G.A., Random-Process Simulation and Measurements, McGraw-Hill Book Company, New York (1966) Ch.4, 83.

[5] EGELSTAFF, P.A., Research Applications of Nuclear Pulsed Systems (Proc. Panel Dubna, 1966) IAEA, Vienna (1967) 62.

[6] RAUCH, H., HARMS, J., MOLDASCHL, H., Nucl. Instrum. Meth. 58 (1968) 261.

[7] STEINSVOLL, O., VIRJO, A., Kjeller Rep. NF-5 (1967); Phys. Lett. (to be published).

[8] PELLIONISZ, P., SZLÀVIK, F., Mérés Autom. 15 (1966) 260.

[9] MOOK, H.A., WILKINSON, M.K., Int. Conf. Magnetism and Magnetic Materials, Paper AG-4, Boston, 1967, Paper AG-4; J. appl. Phys. 39 (1968) 447.

THE USE OF A PSEUDO-STATISTICAL CHOPPER FOR TIME-OF-FLIGHT MEASUREMENTS

F. GOMPF, W. REICHARDT, W. GLÄSER AND K.H. BECKURTS
INSTITUT FÜR ANGEWANDTE KERNPHYSIK,
KERNFORSCHUNGSZENTRUM KARLSRUHE,
FEDERAL REPUBLIC OF GERMANY

Abstract

THE USE OF A PSEUDO-STATISTICAL CHOPPER FOR TIME-OF-FLIGHT MEASUREMENTS. The method of pseudo-statistical pulsing has been applied only to reactor-kinetic measurements so far. Ohanian, Perez and Uhrig proposed this method for time-of-flight measurements with pulsed accelerators. Comparative studies have shown, however, that it is not possible to give general arguments in favour of either the pseudo-statistical or the conventional time-of-flight method. Which of the two methods may be preferred depends on the kind of experiment. Pseudo-statistical pulsing may be especially advantageous for scattering experiments with thermal neutrons.

This paper is intended to give a description of a 'statistical' chopper and the method of measurement with this instrument. The different influences on the accuracy of the measurements are discussed and compared to those in a conventional time-of-flight experiment. A few examples of pseudo-statistical experiments have been simulated on a computer. It is shown that a statistical chopper is advantageous for time-of-flight spectra consisting of a number of peaks which are of main interest and have amplitudes greater than the average amplitudes of the spectra. Further, the method is advantageous in all cases where the background is very high. A preliminary experimental arrangement is described.

1. INTRODUCTION

Pseudo-statistical pulsing of a neutron source so far has been applied mainly to reactor-kinetic measurements. Recently it was proposed to use this method also for time-of-flight measurements with pulsed accelerators [1]. Detailed studies show that general arguments in favour of the pseudo-statistical pulsing compared to the conventional time-of-flight technique cannot be given. Which of the two methods is superior depends on the form of the time-of-flight distribution to be measured.

The aim of the present paper is to show that for slow neutron inelastic scattering experiments with a 'few-line' time-of-flight spectrum pseudo-statistical pulsing may offer advantages. A possible apparatus to cut the continuous neutron beam from a reactor into a sequence of pseudo-statistical pulses is a mechanical chopper with an appropriate transmission pattern.

The first part of the paper describes the principle of the method. The different influences on the accuracy of the measurements are discussed and compared to those in a conventional time-of-flight experiment. A few typical pseudo-statistical experiments have been simulated on a computer to support the theoretical investigations.

In the second part the layout and performance of a mechanical chopper built for pseudo-statistical pulsing will be described. A few preliminary measurements done with this apparatus are discussed.

2. PRINCIPLES OF PSEUDO-STATISTICAL PULSING

2.1. Properties of pseudo-statistical binary signals

A sequence of pseudo-statistical binary signals may be generated with a feedback shift-register [2]. If such a register consisting of n stages is triggered by a clock pulse with frequency $1/\Delta t$ the output can be a sequence of signals with values +1 and -1. The period of this sequence is $T = (2^n - 1)\Delta t$.

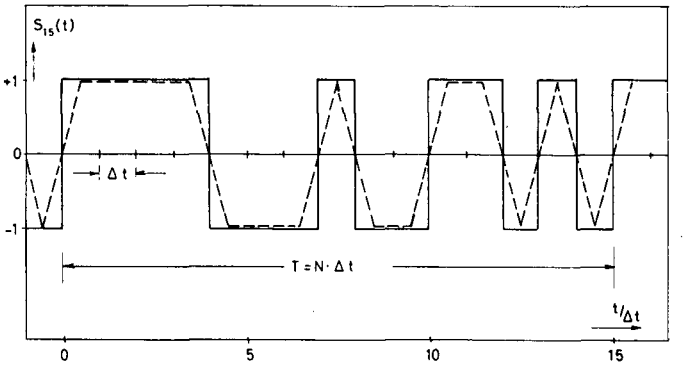

FIG.1. Pseudo-random signal functions $S_N(t)$ for N = 15.
_____ output of a shift register with four storage devices
– – – – signal function of a statistical chopper.

The switching from +1 to -1 and vice versa occurs after integral multiples of Δt. Within the period T the widths of the signals are distributed nearly statistically. A sequence of signals S(t) for a register with n = 4 is shown in Fig. 1 by the full line. The function $S_N(t)$ satisfies the condition

$$\int_0^{N\Delta t} S_N(t)\,dt = \Delta t, \qquad N = 2^n - 1 \tag{1}$$

The autocorrelation function of $S_N(t)$ is defined by

$$\phi_N(\tau) = \frac{1}{N\Delta t} \int_0^{N\Delta t} S_N(t)\, S_N(t+\tau)\,dt \tag{2}$$

From Eq. (1) follows

$$\int_0^{N\Delta t} \phi_N(\tau)\,d\tau = \frac{\Delta t}{N} \tag{3}$$

It is easy to show that the function

$$\varphi_N(\tau) = \frac{1}{N} + \phi(\tau) \tag{4}$$

is the resolution function of the pseudo-statistical pulse experiment.

2.2. Generation of a pseudo-statistical pulse sequence with a chopper

A sequence of pseudo-statistical pulses can be generated with a rotating disc of angular frequency ω and radius r made from neutron absorbing material and having an appropriate pattern of slits and bridges. The width of both are integral multiples of $r\omega\Delta t$. For an infinitely small neutron beam such a device has a transmission

$$T(t) = \frac{I_0}{2}\left(1 + S_N^R(t)\right) \tag{5}$$

where I_0 is the intensity of the continuous beam and the superscript R indicates that $S_N^R(t)$ consists of rectangular pulses.

In practice a finite beam width has to be used. A convenient choice is a width equal to the smallest slit-width. In this case $S_N^R(t)$ in Eq. (5) has to be replaced by a trapezoidal function $S_N^{Tr}(t)$ shown in Fig. 1 for n = 4 by the dashed curve. Relations (1) to (4) are valid too for $S_N^{Tr}(t)$.

2.3. Determination of the time-of-flight distribution

If the statistical pulsed beam impinging on a sample is monochromatic and the sample's scattering properties in a fixed direction are described by a time-of-flight distribution F(t') the number of neutrons arriving at the detector in the time element dt is

$$Z(t)\,dt = \frac{I_0}{2}\left\{\int_0^{N\Delta t} F(t')\,dt' + \int_0^{N\Delta t} S_N(t-t')\,F(t')\,dt'\right\} dt + u\,dt \tag{6}$$

where u is a time-independent background.

F(t) may be reconstructed by cross-correlating the count rate Z(t) with $S_N(t)$

$$\psi_N(\tau) = \frac{1}{N\Delta t}\int_0^{N\Delta t} S_N(t)Z(t+\tau)\,dt = \frac{I_0}{2}\int_0^{N\Delta t} \varphi_N(\tau - s)F(s)\,ds + \frac{u}{N} \tag{7}$$

The cross-correlation $\psi_N(t)$ is essentially the time-of-flight distribution folded with the resolution function $\varphi_N(t - s)$.

In practical applications Z(t) is counted by a multichannel analyser of width $\Delta\tau$. Neglecting resolution corrections the count rate of the k^{th} channel in a conventional chopper experiment with pulse width Δt is

$$I_0 F_k = Z(\tau_k)\,\Delta t\,\Delta\tau - U \tag{8}$$

The corresponding result of a statistical experiment is

$$I_0 F_k = \frac{2}{m(N+1)}\sum_{i=1}^{mN} S_{Ni} Z_{i+k} - \frac{2U}{N+1} \tag{9}$$

Here it is assumed that $\Delta t = m\Delta\tau$ and $U_k = U = u \cdot \Delta\tau$. From Eq.(9) follows that the influence of the background is reduced by a factor $2/(N+1)$ compared to a conventional chopper experiment. This is simply because a statistical chopper is transparent to neutrons about half of the measuring time, whereas a conventional chopper only during the fraction $1/N$ of the total time.

2.4. Time resolution

When $F(t)$ is strongly varying within the interval Δt, the resolution correction in Eq.(7) cannot be neglected. The resolution function $\varphi_N(t)$ can be calculated from Eq.(4). For a rectangular signal function $S_N^R(t)$ the result is a triangle with half-width Δt

$$\varphi_N^R(t) = \left(1+\frac{1}{N}\right)\left(1-\frac{t}{\Delta t}\right) = \left(1+\frac{1}{N}\right)\varphi_\infty^R\left(\frac{t}{\Delta t}\right) \qquad \text{for } |t| \leq \Delta t$$

$$\varphi_N^R(t) = 0 \qquad \text{for } |t| \geq \Delta t \tag{10}$$

For a trapezoidal signal $S_N^{Tr}(t)$, $\varphi_N^{Tr}(t)$ cannot be described by a simple analytical expression but the second part of Eq.(10) is valid

$$\varphi_N^{Tr}(t) = \left(1+\frac{1}{N}\right)\varphi_\infty^{Tr}\left(\frac{t}{\Delta t}\right) \qquad \text{for } |t| \leq 2\Delta t$$

$$\varphi_N^{Tr}(t) = 0 \qquad \text{for } |t| \geq 2\Delta t \tag{11}$$

From Eqs (10) and (11) follows that the time resolution of a pseudo-statistical chopper experiment with fixed Δt does not depend on the number of slits. $\varphi_\infty^R(t)$ and $\varphi_\infty^{Tr}(t)$ are compared in Fig.2. $\varphi_\infty^R(t)$ is identical to the resolution function of a chopper with one slit of width Δt. $\varphi_\infty^{Tr}(t)$ resembles a Gaussian with a half-width $t_{\varphi_{\frac{1}{2}}} \approx 1.45\ \Delta t$.

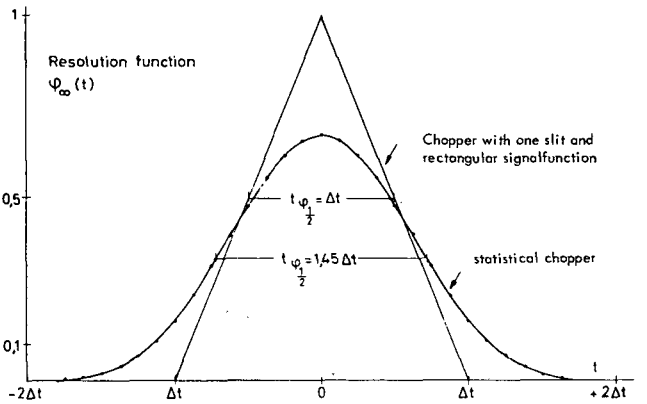

FIG.2. Resolution function for different sources.

2.5. Statistical accuracy

The statistical error of F_k can be deduced from Eq.(9)

$$\Delta F_k = \frac{2}{m(N+1)} \left\{ \sum_{i=1}^{mN} S_{Ni}^2 (Z_{i+k} + U_{i+k}) \right\}^{1/2} = \frac{2}{m(N+1)} \left\{ \overline{S^2} (Z_{tot} + mNU) \right\}^{1/2} \qquad (12)$$

where Z_{tot} is the total count rate of the experiment and I_0 was taken to be 1. If we express Z_{tot} by the average value of F_k

$$Z_{tot} = mN \left\{ \frac{(N+1)}{2} \overline{F} + U \right\}$$

where

$$\overline{F} = \frac{1}{mN} \sum_{i=1}^{mN} F_i$$

we get

$$\Delta F_k = \frac{1}{m} \left\{ \left(\frac{2}{1+1/N} \right) \overline{S^2} \left(m\overline{F} + \frac{4mU}{N+1} \right) \right\}^{1/2} \qquad (13)$$

The absolute statistical error is the same for all channels and only determined by the total of all scattering and background events at the detector.

For a rectangular signal function $\left(S_{Ni}^R\right)^2 = \overline{S^2} = 1$. For S_{Ni}^{Tr} the average $\overline{S^2}$ is 2/3. In the latter case the statistical error is smaller than for a rectangular signal function. This effect is compensated, however, by the poorer time resolution. From Eq.(2) follows a close relation between resolution and statistical accuracy:

$$\overline{S_N^2} = \left(1 + \frac{1}{N} \right) \varphi_\infty(0) - \frac{1}{N} \approx \varphi_\infty(0) \qquad (14)$$

If $t_{f_{\frac{1}{2}}}$ is the half width of $\varphi(t)$, the following approximate relations hold

$$t_{\varphi_{\frac{1}{2}}} \sim \frac{1}{\overline{S^2}} \text{ and } \Delta F_k \, t_{\varphi_{\frac{1}{2}}}^{1/2} \sim (Z_{tot} + mNU)^{1/2} \qquad (15)$$

For experiments with different S(t) but equal total count rates the product $\Delta F \cdot t_{\varphi_{\frac{1}{2}}}^{1/2}$ is constant.

For a comparison of statistical errors in statistical and conventional chopper experiments we assume for simplicity that the channel width of the time analyser is equal to the width of the smallest chopper slit (m=1). ΔF_k for a conventional chopper experiment is given by

$$\Delta F_k = (F_k + 2U)^{1/2} \qquad (16)$$

From Eqs (13) and (16)

$$g = \frac{\Delta F_{k\ statist}}{\Delta F_{k\ convent}} = \left\{ \left(\frac{N}{N+1} \right) \frac{2\overline{S^2}\left(\overline{F} + \frac{4U}{N+1} \right)}{F_k + 2U} \right\}^{1/2} \tag{17}$$

Pseudo-statistical pulsing will therefore be superior to the conventional method, if $g < 1$, or

$$F_k > \frac{2S^2N}{N+1} \left(\overline{F} + \frac{4U}{N+1} \right) - 2U \tag{18}$$

If $N \gg 1$ and $\overline{S^2} = \frac{2}{3}$, then $F_k > \frac{4}{3}\overline{F} - 2U$.

For negligible background pseudo-statistical pulsing is only advantageous for $F_k > \frac{4}{3}\overline{F}$ but it will be generally advantageous when the background is higher than $\frac{2}{3}\overline{F}$.

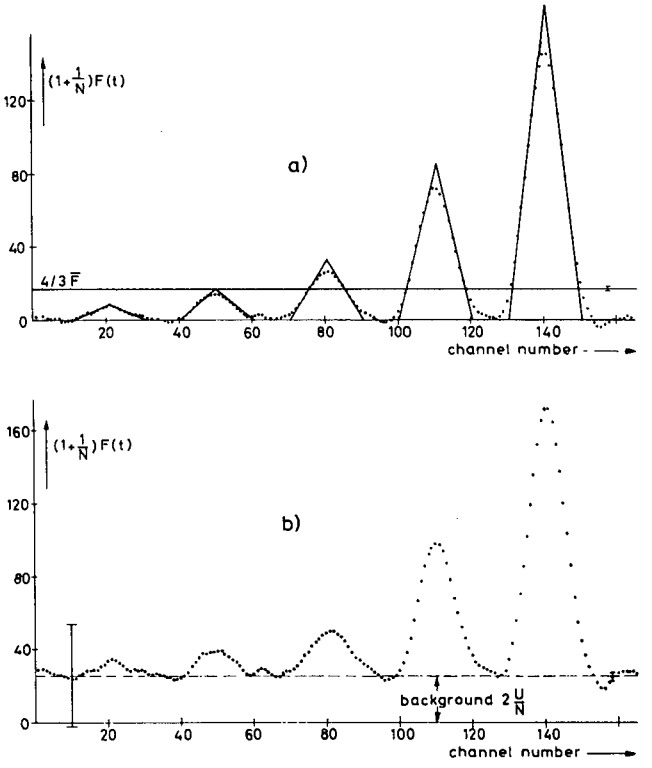

FIG.3. Determination of a time-of-flight distribution with a statistical chopper: (a) without background; (b) with a very high background $U = N\bar{F}$. The error bars to the right indicate the statistical error of the experiment. The error bar to the left in (b) indicates the error for a conventional time-of-flight experiment.

2.6. Computer simulation of scattering experiments

For the quantitative interpretation of a pseudo-statistical pulse experiment a number of questions, e.g. the influence of the finite channel width $\Delta\tau$ and of $m > 1$ on the final result, are of interest. These effects may differ from those in a conventional time-of-flight experiment because different averages are included. These questions have been investigated in the context of the present work and numerically checked by computer-simulated experiments. Briefly, the result is that using a channel width $\Delta\tau$ of the analyser equal to the pulse width Δt may cause considerable errors which are greater than in a conventional time-of-flight experiment if $F(t)$ is strongly fluctuating over a few channels. But for $\Delta\tau = \Delta t/4$ only deviations of the order of 1% from the resolution function have been found if a δ function was assumed for $F(t)$. From these calculations the conclusion can be drawn that a channel width of $\Delta t/4$ will be sufficient for all practical cases.

Figure 3 gives an example for a measurement with a statistical chopper simulated on a computer. N was chosen as 63, a time-analyser with 252 channels (m=4) was used and the average count rate was 400 counts per channel. The full line in Fig. 3(a) represents $F(t)$ for ideal resolution, the points are the result of a cross-correlated 'measurement' without background. Statistical errors have been simulated too for the count rates. Figure 3(b) shows the results when a background of 800 counts per channel is assumed. In spite of the high background all peaks are well reproduced. The indicated error on the left side of Fig. 3(b) would be obtained in a normal chopper measurement. Determination and subtraction of the background would still increase this error.

3. EXPERIMENTAL EQUIPMENT

3.1. The rotor

A pseudo-random binary sequence of reasonable length should be used to approximate a statistical distribution of slit widths and achieve a high suppression of background (Eq. (9)). N=7 was chosen, giving 127 basic steps in the pseudo-statistical pattern. In order not to weaken a neutron absorbing rotor material with such a large number of slits, an aluminium rotor (AlMg7) was chosen with attached absorber sheets. The rotor, a disc of equal radial and tangential stress, has a diameter of 51 cm and is 0.3 cm thick at the outside and 2.5 cm thick towards the centre. The disc and its shaft are manufactured out of one piece of material. With great precision two pseudo-random sequences with n=7 were milled onto one side of the disc (Fig. 4b). Because of these dimensions the basic slit has a maximum width of 0.63 cm. The absorbing material was cast into these moulds, which are 4.5 cm high, 0.05 cm thick at their outer diameter and 0.2 cm at their inner diameter, allowing the use of the statistical chopper for energies up to 100 meV by decreasing eventually the height of the window.

For both the disc and absorbing material the speed of rotation is limited due to $\omega \sim \sqrt{\sigma/\rho}$ where σ is the tensile yield strength and ρ the specific weight. Some aluminium base alloys do not only have a small neutron cross-section, but also allow high values for ω. Unfortunately cadmium as a good stopping material does not.

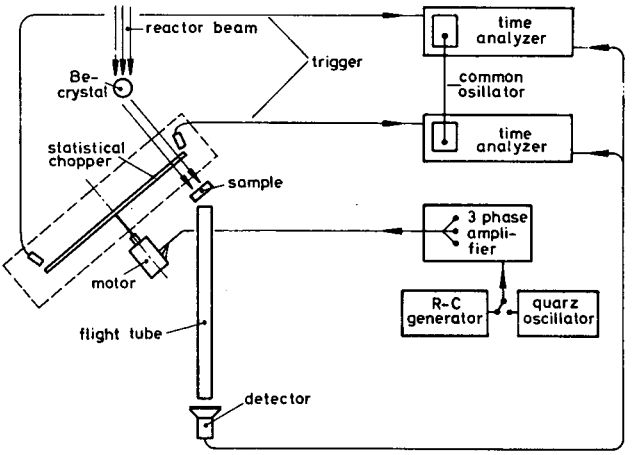

FIG. 4a. Experimental layout.

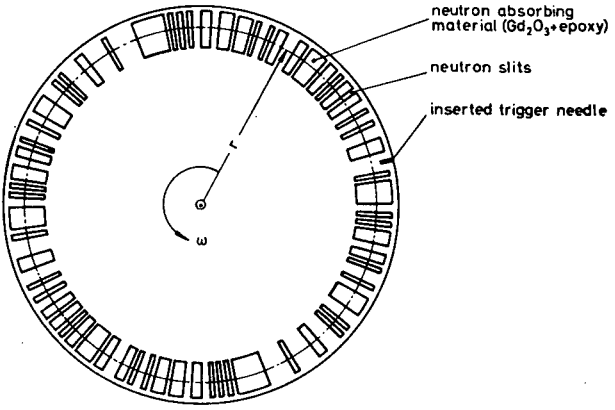

FIG. 4b. Disc with two pseudo-random binary sequences ($N = 2^n - 1 = 127$).

Much better results were achieved with a gadolinum oxide-epoxy mixture we developed. Up to 50 meV the stopping power for slow neutrons is better than that of a Cd foil of the same thickness, whereas the mechanical properties mentioned above are better by a factor of 4.

In producing the absorbing pattern a few points must be carefully taken into consideration:

(a) The mixture should contain a high percentage of homogeneously absorbed Gd_2O_3 powder, avoiding air pockets or trapped solvent. This is obtained by separately mixing both epoxy components with Gd_2O_3 powder under vacuum.

(b) The tensile yield strength of the finished absorber plate should not be reduced by the absorbed Gd_2O_3 powder. This demands an epoxy with maximum cohesion. The plates are glued onto the disc by an epoxy of maximum adhesion, which should also have a certain flexibility to reduce stress due to differences in modulus of elasticity of absorber and disc.

To reduce balancing problems, two pseudo-random sequences were chosen and the Gd_2O_3 epoxy material was mixed to have the same specific weight as aluminium. After having horizontally cast the absorbing material onto the moulds and having glued it onto the disc, the latter is brought back to its original shape with a turner's lathe.

3.2. Driving system

Ultra-precision ball bearings were used and placed as close to the disc as possible. In the direction of the axis they are kept under an initial stress by a spring system which brings their clearance to zero at all different operation temperatures. The disc with shaft and bearings is placed into vacuum and the lubrication is taken care of by a specially designed system. A flexible coupling is used to connect the motor to the disc.

The accuracy necessary for this type of neutron chopper demands a hysteresis synchronous motor and direct drive. The three-phase motor used (Elinco G1148) was placed outside the evacuated housing to avoid lubrication and heat dissipation problems. The 0.4-cm diameter connecting shaft passes through the housing wall by a self-aligning seal. The nominal speed of the rotor follows from $\omega_n = \pi/(127 \cdot \Delta t)$ and is 7382 rev/min. For acceleration a 3-phase power amplifier (200 V, 2 A) is fed by a conventional RC generator. At nominal speed the RC generator is switched to a quarz oscillator of fixed frequency. The latter system maintains the angular frequency ω_n of the disc with great accuracy. The long-time fluctuations of ω_n are less than 10^{-4}. Electronic temperature switches are attached to the ball-bearing holders to stop the chopper in case of defective bearings or lack of lubrication.

3.3. Time-of-flight spectrometer

A scheme of the scattering experiment is shown in Fig. 4a. A monoenergetic neutron beam reflected from a Be crystal is pseudo-randomly modulated by the chopper and subsequently scattered by the sample. The time-of-flight of the neutron from the sample to the detector is measured with a time-analyser triggered by the signal mentioned above.

As was shown in the theoretical discussion, it is desirable to assign at least 4 time channels to each basic slit width Δt. Δt is 32 μsec in our case. For practical reasons we used a 1024-channel analyser with 4-μsec channel width (m=8) thus supplying 1016 active channels during a period T. By triggering two time-analysers alternatively, no information is lost and the frame overlapping can be used to synchronize the two separately taken sequences.

4. EXPERIMENTAL RESULTS

Using an incident monoenergetic neutron beam of 42 ± 0.2 meV from the monochromator crystal, several measurements were made to test the generated pseudo-statistical pattern and the long-time performance of the chopper in scattering experiments.

The time-dependent transmission T(t) of the chopper was measured with a detector at the sample position directly behind the chopper (Fig. 4a).

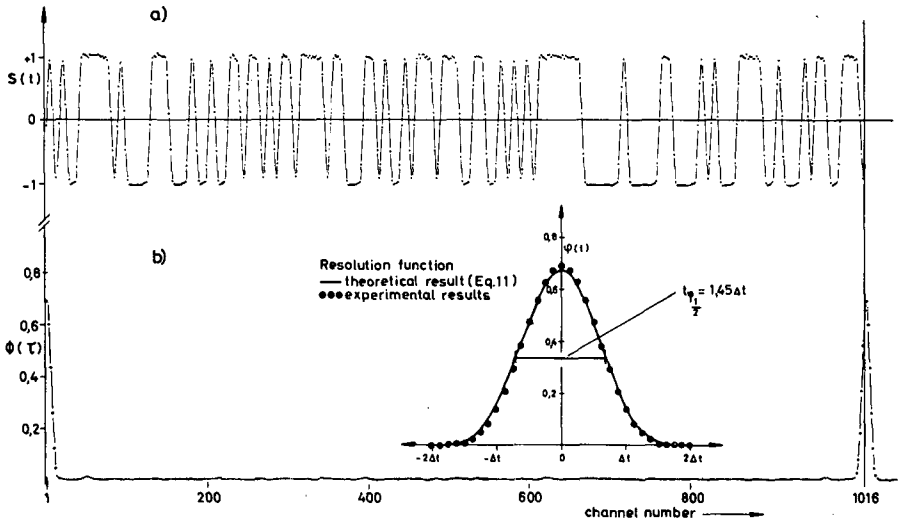

FIG. 5. (a) Signal function S(t); (b) auto-correlation function $\phi(\tau)$.

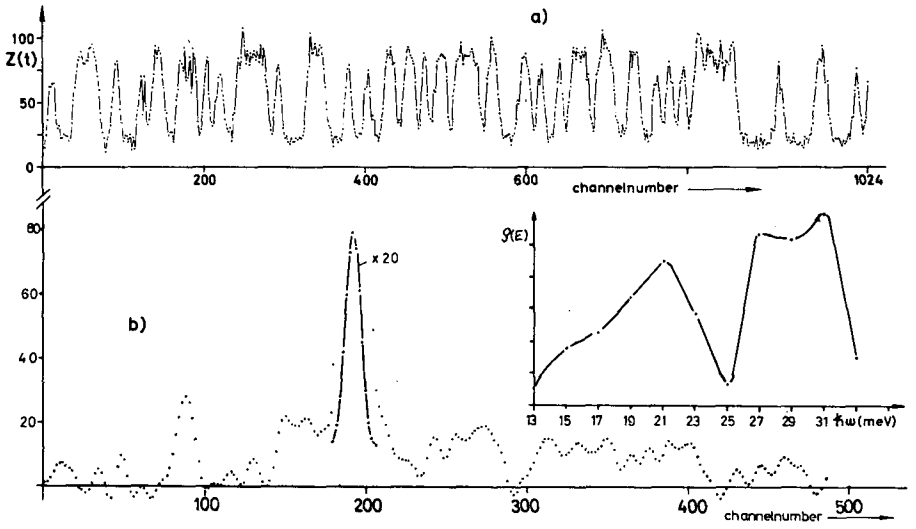

FIG. 6. Vanadium: (a) count rate Z(t); (b) cross-correlation $\psi(t)$.

The signal function S(t) evaluated from T(t) is shown in Fig. 5(a). The intended trapezoidal distribution is extremely well reproduced. The auto-correlation function $\phi(\tau)$ calculated from S(t) is given in Fig. 5(b). As an insert in Fig. 5(b) the measured resolution function $\varphi_E(t)$ is enlarged and compared to the theoretically expected function $\varphi^{Tr}(t)$. The agreement of both is excellent.

Outside the correlation peak the deviations of $\phi(\tau)$ from zero over the whole period do not exceed 1% which is the mean statistical deviation of the measured S(t). Within this limit no undesired correlations appear. From this result it is concluded that the performance of the apparatus is sufficiently perfect for scattering experiments.

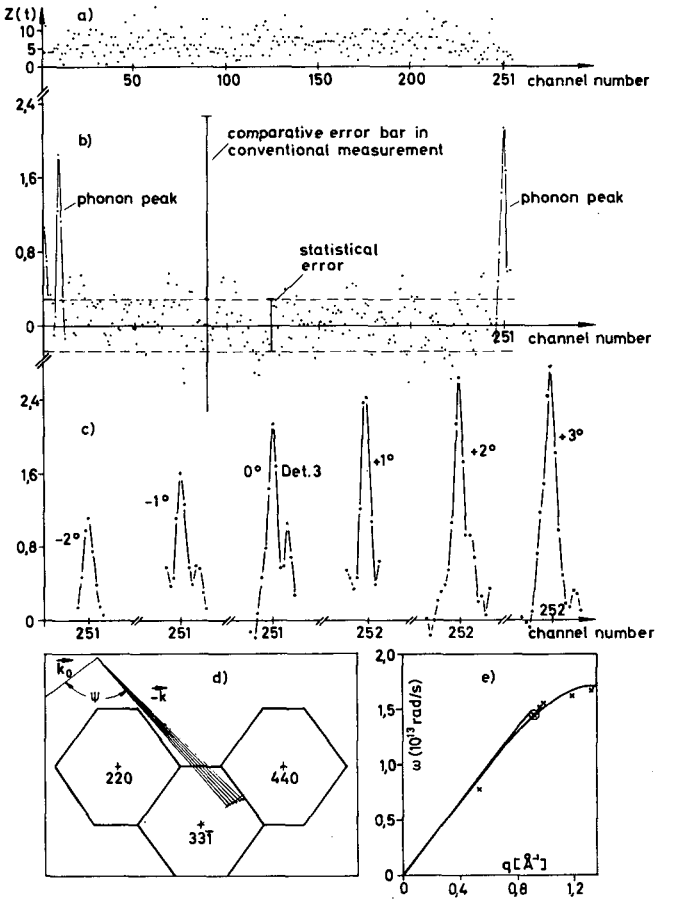

FIG. 7. Phonon measurements in platinum: (a) count rate Z(t) for detector 3 (5 h); (b) cross-correlation $\psi(t)$ of detector 3; (c) phonons at neighbouring scattering angles; (d) part of the determined scattering surface in the 111 plane of the reciprocal lattice; (e) corresponding point of the 111 transverse branch derived from (d).

Several preliminary scattering experiments from incoherent and coherent scattering samples have been conducted. The result of an 8-hour scattering run with a 2-mm thick vanadium target using a flight path of 220 cm under a scattering angle of 45° is given in Fig. 6. Figure 6(a) shows the measured distribution Z(t) which resembles a statistical noise distribution. The calculation of the cross-correlation $\psi(\tau)$ yields the distribution shown in Fig. 6(b) which shows the well-known inelastic scattering pattern of vanadium in down scattering. The statistical fluctuations of F(t) are in agreement

with the predicted ones according to Eq.(13). The detailed analysis of the measurements is in progress. A first example of measurement of phonons by coherent scattering is shown in Fig. 7. Because of the high absorption cross-section of Pt, the use of the conventional time-of-flight technique was unsuccessful in detecting the phonons shown despite much longer counting times. The advantage of the statistical chopper is here mainly due to the cancelling of the larger background.

5. CONCLUSIONS

The results presented demonstrate that a mechanical chopper with an appropriate transmission pattern can be used for pseudo-random time-of-flight scattering experiments. The theoretically predicted properties of such a device have been experimentally confirmed. There is a large number of applications in inelastic neutron scattering where pseudo-statistical pulsing will definitely offer advantages over the conventional time-of-flight technique.

ACKNOWLEDGEMENTS

The authors wish to thank Messrs. E. Albold, G. Ehret, U. Huber, H. Klann and especially the staff of the mechanical and electronic workshops of the institute for invaluable technical assistance.

REFERENCES

[1] OHANIAN, M.J., PEREZ, R.B., UHRIG, R.E., Nuclear Data for Reactors (Proc.Conf.Paris, 1966) 1, IAEA, Vienna (1967) 445.

[2] PETERSON, W.W., Error Correcting Codes, John Wiley and Sons, New York (1961).

A NEW HIGH-EFFICIENCY TIME-OF-FLIGHT SYSTEM

J.F. COLWELL, P.H. MILLER AND W.L. WHITTEMORE
GULF GENERAL ATOMIC INCORPORATED,
SAN DIEGO, CALIF., UNITED STATES OF AMERICA

Abstract

A NEW HIGH-EFFICIENCY TIME-OF-FLIGHT SYSTEM. To overcome the low efficiency with which the usual Fermi chopper time-of-flight system utilizes the available neutron source, a new system has been developed which increases the efficiency by one or more orders of magnitude in many practical cases of interest. Several experimental models have been tested successfully. The principle of the new technique is based on continuous beam modulation and depends for its success on special apparatus for the detection and manipulation of the data.

In place of the singly pulsed beam produced by a Fermi chopper, a continuous train of pulses is produced by the new system. Several methods can be employed to derive the time-of-flight distribution f(t) for the scattering data. A convenient method has been to synthesize f(t) from the Fourier amplitudes and phases determined for an appropriate number of different impressed sinusoids. In another version, a chopper with progressively increasing slit and spacing widths gave results which were successfully analysed by a standard auto-correlation technique. Traditional considerations of overlaps are no longer valid for these new modulation techniques since the overlap produced is a necessary feature of the system.

We have performed extensive analyses of the relative accuracy with which the scattering pattern f(t) can be determined with the new and conventional systems. If the scattering pattern consists of a small peak in the presence of a broad distribution, the experiment has to be examined in detail to evaluate the improvement offered by the new method. For a small bump in the valley between two enormous peaks, the conventional system may be preferred. However, for the large number of experimental cases involving a number of relatively narrow peaks, the increase in accuracy in terms of signal to noise power is proportional to the ratio of duty cycles for the two chopper systems. For almost any case connected with neutron inelastic scattering, the high-efficiency chopper system offers a substantial improvement over that with the conventional Fermi system.

INTRODUCTION

The characteristic of the Fermi chopper [1] is to provide short, isolated bursts of neutrons separated by long time intervals during which the transmitted neutrons arrive at the detector. All of the standard times-of-flight techniques have shared in common a low efficiency for utilizing the source of neutrons, using only on the order of 0.1 to 0.5% of the available neutrons. In the past, the effort to reduce the long experimental running times for high resolution experiments has been directed toward securing either larger scattering specimens and larger beam apertures (of course, organic crystal specimens are notoriously small, as are many other specimens) or more powerful neutron sources. The new Fourier approach described in this paper has been developed to use much more efficiently the existing neutron sources. From the considerations shown below, the gain in detection efficiency can in some cases be a large factor over that of present standard chopper configurations while maintaining large beam apertures and possibly increasing the time resolution.

GENERAL CONSIDERATION OF THE HIGH EFFICIENCY CHOPPER SYSTEM (HECS)

The new system is based on the notion of using a fully modulated neutron beam. Considerations of pulse overlap have traditionally dictated that the period between pulses should be at least as long as the time-of-flight of the slowest neutron. In the new system, a major amount of overlap is produced and is a necessary feature of the system. For clarity, consider a typical cold neutron scattering system which produces a time-of-flight scattering pattern f(t). To put the resulting scattering pattern in the proper perspective, one can note that this pattern represents the response of a scattering system (consisting of a neutron source, scatterer, and detector system) to an impulse signal (pulse width is $\sim \Delta t$). This response f(t) is simply the transfer function of the scattering system. The transfer function can also be obtained equally well by studying the steady-state response of the same system to a number of different, impressed sinusoidal signals. For the neutron scattering case, this is equivalent to using a phased detector to derive the Fourier amplitudes A_n and phases φ_n of the scattering response for each of the impressed sinusoidally varying signals. With these amplitudes and phases, the scattering pattern f(t) can be represented as

$$f(t) = \sum_n A_n \cos(\omega_n t + \varphi_n) . \qquad (1)$$

It will also result from the analysis that only a limited, generally small number n of individual frequencies (usually far less than 100) need be used to apply Eq. (1) even to complicated scattering patterns. In subsequent analyses, the effect of ω_{max} and $\Delta\omega = \omega_i - \omega_{i-1} \simeq \omega_{max}/n$ on the scattering pattern will be discussed. It should be noted that if the beam modulation is produced by a chopping wheel with uniformly spaced teeth together with a stationary comb having the same spacing of teeth, the beam aperture can be much wider than the tooth size. This results in a relatively small chopping wheel which can produce high chopping frequencies and a large beam aperture.

A number of variations to the above approach for deriving the scattering pattern are possible, utilizing cross correlation techniques. The cross correlation $C_{AB}(\tau)$ [2] of an impressed signal $f_A(t)$ and a response signal $f_B(t-\tau)$ where τ is a variable delay, is proportional to the transfer function and is given as

$$C_{AB}(\tau) = \lim_{T \to \infty} \frac{1}{2T} \int_0^{+T} f_A(t) f_B(t-\tau) dt . \qquad (2)$$

Application of Eq. (2) will produce the transfer function of a linear system when white noise (or its equivalent) is used as the input signal and cross correlated with the system response. LuBow [3] has shown how white noise can be applied to various research problems using commercial apparatus available for performing cross correlation. In the analogous case for neutron scattering studies, the input used is either (a) pulses occurring

"randomly" in time [4, 5], or (b) a rapid, successive application of a number of frequencies (a s has been done in this laboratory) and the output response is cross correlated with (a) or (b) to obtain f(t). If the input signal is frequency modulated, the application of cross correlation techniques is essentially a modification of (b) in which a band of frequencies is impressed on the system sequentially in an efficient manner.

In attempting to carry the technique for analysis of electrical signals over to the corresponding problem for neutron signals, one finds a fundamental difference. Neutron beam modulation is proportional to $(1+\cos\omega t)$ and the dc term cannot be eliminated by an analog filter prior to scattering whereas it can be in the electrical case. This difference leads to significant complications in the application of pulse compression techniques and the resulting considerations of signal to noise.

DETAILS OF PULSE COMPRESSED SIGNALS

It will be useful to consider first those time-of-flight signals that consist of a few narrow (delta-like) peaks. This is not as restrictive as it first might seem since (a) many time-of-flight experiments give rise directly to such signals, and (b) any reasonably behaved, arbitrary function f(t) can be represented as a sum of individual delta functions. Thus, we will consider below some useful features of a time-of-flight scattering pattern consisting of a small number of delta-like functions.

Equation (1) shows that a function f(t), which in the present example is a very narrow peak, can be represented by an equivalent set of amplitudes and phases. Figure 1 illustrates the facts that the phase φ is a

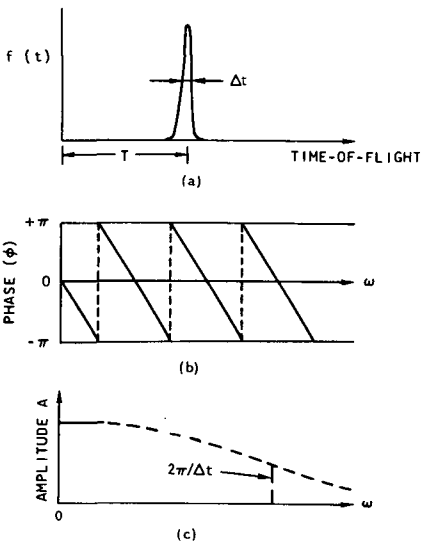

FIG. 1. Amplitude and phase for Fourier components of a narrow pulse: (a) a delta-like time-of-flight function full width Δt; (b) phase as function of frequency for a delta-like function; (c) amplitude as function of frequency for a peak of width Δt.

linear function of frequency ω and the amplitude A slowly decreases. The amplitude is constant for a delta function and, for a narrow, delta-like peak, it has a Gaussian-like dependence on frequency with a width at half maximum $\sim 1/\Delta t$ where Δt is the width of the function f(t). Of interest is the fact that the slope $d\varphi/d\omega$ is a constant equal to the time-of-flight T. Further, if Fourier components are determined for frequencies up to a maximum f_{max}, then the minimum width of the reconstructed function $f_r(t)$ cannot be less than $\sim 1/f_{max}$. The function $f_r(t)$ is approximated by $\sin \pi f_{max} t / \pi f_{max} t$, which has side lobes of decreasing amplitude and zero cross over points (when $f_{max} t$ is an integer). In addition to f_{max}, Δf also imposes a limit on the representation of f(t). If a finite number n of frequencies is included so that $\Delta f \simeq f_{max}/n$, then the representation of f(t) will be periodic with period $1/\Delta f$.

A variety of techniques is available to reduce the useless side lobes. Among these are the Wiener filter [6] or a sampling technique [7] to evaluate $f_r(t)$ in the useful central region and, in the region outside a width of $\sim 2/f_{max}$, only at the zero cross over points of $f_r(t)$ which occur periodically on both sides of the central peak separated by $\Delta t = 1/f_{max}$. It may be useful to observe that application of the Wiener filter in the frequency domain is extremely simple. As a consequence, it is easier to apply this filter to the Fourier components of f(t) than to the results obtained by cross correlation where a large matrix may be involved. Either of the two above techniques improves considerably the appearance of $f_r(t)$ and can be used regardless of whether one or more delta-like functions are involved in f(t). (It may be noted that cross correlation with a clever choice of a "random" impressed signal may give a result that automatically includes the equivalent of a Wiener filter.)

A more complicated situation arises for the case of two delta-like peaks, appearing at flight times t_1 and t_2, respectively. The Fourier transform for these two delta pulses is

$$F(j\omega) = A\exp(i\omega t_1) + B\exp(i\omega t_2) = C(\omega) + iS(\omega)$$

Writing $F(j\omega) = Fe^{i\varphi}$, we have

$$R^2 = A^2 + B^2 + 2AB \cos\omega(t_1 - t_2) \tag{3}$$

$$\tan\varphi = \frac{A \sin\omega t_1 + B \sin\omega t_2}{A \cos\omega t_1 + B \cos\omega t_2} \tag{4}$$

From Eqs (3) and (4) we see that the amplitude R now depends on frequency and that it ranges from a maximum value of (A + B) to a minimum of (A - B). The phase dependence on frequency is more complicated. For the case where $A \cong B$, the shape of φ versus ω is generally similar to that for a single delta function but with a small frequency dependent modulation which disappears for A = B.

The representation of sharp peaks in terms of their amplitudes and phases is helpful from many points of view. The generally periodic behavior of amplitude and phase may greatly reduce the number of measurements needed. Frequently it is possible to extrapolate these data to $\omega = 0$ to eliminate the negative undershoot which is proportional to f_{min}/f_{max}. Although the cross correlation technique does not permit concentration on a small frequency range, the Fourier method easily allows these measurements in regions resulting in information on the fine structure uninhibited by a large, slowly varying component in f(t). This remark applies as well to sharp, resonance absorption valleys in transmission curves. Of particular interest is the fact that the Fourier method makes available amplitude and phase data for the higher harmonic content of some forms of beam modulation. This feature can be used to extend the effective f_{max} without increased chopper speeds provided that the modulated beam is appropriately rich in the desired harmonic frequencies.

EFFECT OF NOISE ON PULSE COMPRESSED SIGNALS

Noise in the signal f(t) consists of: (1) neutrons that leak into the detector incoherent with the modulated signal; (2) statistical fluctuations in the signal due to finite counting statistics; and (3) special effects that result from the process of Fourier synthesizing the signal. Extensive analysis of this noise has been based on both theoretical developments and a computer program that applies noise to typical experimental cases.

The results of the noise calculations can be summarized in the following statements of the relative error (R.E.):

$$\text{R.E.(HECS)} = \frac{\sqrt{\alpha \Sigma N(t) + \Sigma B_i}}{\alpha N(t)} = \frac{\sqrt{S + B}}{S(t)} \qquad (5)$$

$$\text{R.E.(Fermi)} = \frac{\sqrt{N(t) + B_i}}{N(t)} \qquad (6)$$

$N(t)$ are the signal counts at time t in $f(t)$ for a Fermi chopper experiment;

$\Sigma N(t)$ are the corresponding total signal counts;

B_i are uncorrelated background counts on a time scale compatible with $N(t)$;

$B = \Sigma B_i$ are the total background counts;

α is the ratio of duty cycles for HECS and standard systems;

S are the total signal counts for HECS; and

$S(t)$ are the HECS counts (derived by Fourier synthesis and corresponding to $N(t)$) at time t in $f(t)$ where

$$S = \Sigma S(t).$$

It should be noted that the relative statistical errors for HECS are dependent only on the total number of neutrons counted and not on the number of individual frequencies used provided a sufficiently large number is used. A computer program has shown that usually 50-100 frequencies are sufficient to reproduce f(t) to an accuracy of $\sim 0.1\%$ at all times of interest. If this number of Fourier components is used, then the accuracy of the Fourier reproduction of f(t) will be governed mainly by the statistical precision of the data and will depend only on the total number of neutrons counted. Considerable freedom is thus available in performing the experimental measurements.

EXPERIMENTAL VERIFICATION OF THE HIGH EFFICIENCY SYSTEM

Several experimental verifications of the HECS have been made at Gulf General Atomic. In one system, a chopper having a series of varying width teeth and gaps was used to frequency modulate a beam of neutrons.

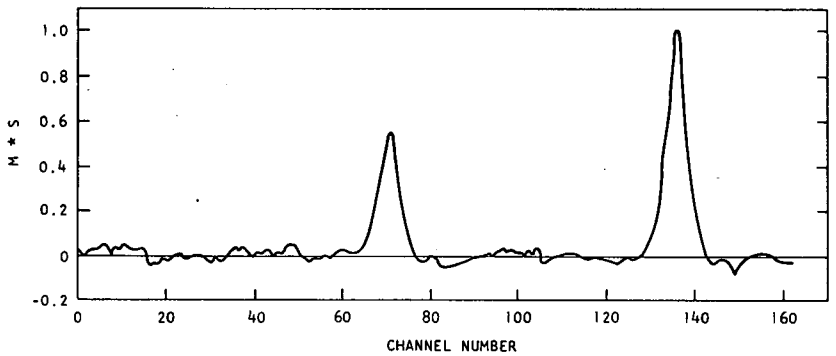

FIG. 2. Bragg reflections for two neutron energies obtained by cross-correlation.

In one manifestation of this, a beam of neutrons was selected by a copper crystal and analyzed by this chopper. Figure 2 shows the signal obtained by cross correlation (Eq. 2) of the detected signal and the monitor signal, both signals accumulated in a time-of-flight analyzer. Since the crystal was set to give roughly equal components of first and second order scattering, two peaks are observed, as is expected. This same technique has been applied to the measurement of the Maxwellian distribution of the neutron beam emerging from the TRIGA reactor. The resulting cross correlation has given a spectrum like that obtained using a Fermi chopper [8].

In another manifestation of the HECS, a chopping wheel with uniform spacing of 120 teeth was rotated at a number of different frequencies. The data were collected in four time sequenced and phased counting channels. For each frequency, these four bits of data have been analyzed to provide the amplitude and phase information. Using a copper crystal to select a single monoenergetic beam, results have been obtained for the phase and amplitude which are precisely as predicted in Fig. 1. The exactly linear dependence of the phase on applied frequency gives as its slope a value of 0.523×10^{-3} sec, exactly as expected for the Bragg angle used. In another experiment, the Bragg angle was set to give roughly equal quantities of

first and second order scattering (at energies of ~0.02 and 0.08 eV). Using the same experimental system and analysis, one obtains the results shown in Fig. 3. Here one sees the expected variation of amplitude due to interference of the two pulse trains. The phase data depends on frequency about as shown in Fig. 3 except for a small interference discussed earlier.

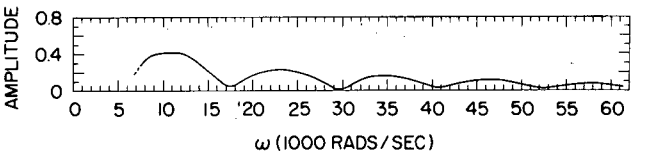

FIG.3. Amplitude versus frequency for an experimental case of two monoenergetic beams of neutrons.

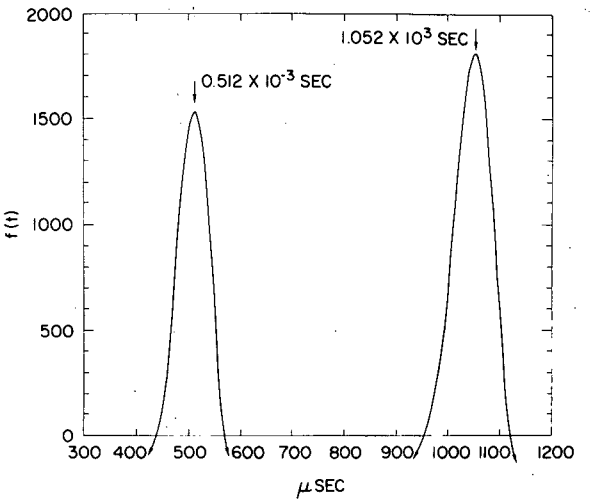

FIG.4. Time-of-flight spectrum f(t) for two monoenergetic beams of neutrons synthesized from the amplitude and phase data.

If one uses Eq. (1) to transform the data, the two peaks shown in Fig. 4 occur at flight times 0.520×10^{-3} and 1.05×10^{-3} sec, as expected, for the flight path of ≅ 2 meters and consistent with the phase and amplitude data. The width of the peaks corresponds to the minimum opening time of the shutter as in all time-of-flight experiments. Since f_{min} was not zero and thus the small frequency terms in Eq. (1) were not used, a large negative undershoot occurs for large regions of the time domain. The undershoot disappears as this ratio is made zero, a condition made possible in this case by a suitable extrapolation to $f \sim 0$ of the measured data for amplitude and phase. This facility in manipulating the data in the frequency domain is a significant advantage of the Fourier method.

SUMMARY

Pulse compression techniques notably in the form of Fourier synthesis applied to time-of-flight studies result in improved utilization of the available neutron fluxes for many applications. Important features of the system are listed here, where points 5 through 8 may represent particular advantages of the Fourier synthesis compared to cross correlation.

1. The effect of unmodulated background noise is significantly reduced compared to the Fermi system.

2. Noise from a single point of f(t) spills over to all other times but is relatively small.

3. Well developed filtering techniques are available for significantly reducing the side lobe structure present when $1/f_{max}$ is comparable to the peak widths investigated.

4. The pulse compressed system is usually preferable to the standard one although the improvement may not be large in every case; for some spectra, the new system improves the signal-to-noise ratio nearly as much as the ratio of chopper duty cycles. At Gulf General Atomic, this ratio was 120 in some examples

5. By selecting the frequency domain carefully, one can investigate the fine structure in the desired f(t) independent of (a) any slowly varying components present, and (b) whether the fine structure is positive or negative

6. A limited number of Fourier components (and hence measurements) are needed for a suitable determination of f(t).

7. Determination of a few well chosen Fourier components will allow evaluation of a natural line width provided f_{max} is suitably large.

8. Large values of f_{max} are obtainable without sacrifice in available aperture.

REFERENCES

[1] BRILL, T., LICHTENBERGER, H., Phys. Rev. 72 (1947) 585; or HUGHES, D. S., Pile Neutron Research, Addision Wesley (1953) 244.

[2] LEE, Y. W., Statistical Theory of Communication, John Wiley and Sons, New York (1960).

[3] LUBOW, B., Correlation entering new fields with real-time signal analysis, Electronics 39 (1966) 75.

[4] GORDON, J., KROÓ, N., ORBAN, G., PÁL, L., PELLIONISZ, P., SZLÁVIK, F., VIZI, I., Physics Letters, 26A 3 (1968) 122.

[5] SKÖLD, K., Use of correlation techniques in slow neutron spectroscopy, Bull. Am. Phys. Soc., II 13 3 (1968) 468.

[6] WOZENCRAFT, J. M., JACOBS, I. M., Principles of Communications Engineering, Wiley, New York (1965) 683.

[7] WAINSTEIN, L. A., ZUBAVOK, V. D., Extraction of Signals from Noise, Prentice-Hall, Inc., New Jersey (1962) Section 19.

[8] WHITTEMORE, W. L., Small neutron beam chopper, Phys. Rev. 37 (1966) 742.

DISCUSSION

H. MAIER-LEIBNITZ (Chairman): Let me say a few words comparing the ordinary time-of-flight method, pseudo-statistical pulsing and the Fourier method proposed by Whittemore. I have discussed the matter with some of the authors of the papers and I hope they agree with me.

First, consider a regular sequence of short pulses (Fig. A(a)), with a time-of-flight spectrum totally contained between two subsequent pulses (Fig. A(b)). By the pseudo-statistical method, in order to make better use of the neutron beam, one introduces many more neutron pulses in a random sequence (Fig. A(c)). A count at time t (Fig. A(d)) may be given by any of the earlier pulses as shown in the figure. We now plot, for each count, all the time differences so obtained, and from the wrong answers we get a continuous background, constant except for statistical fluctuations. Superimposed on this, the correct count pulse assignments will show the desired time-of-flight spectra (Fig. A(e)). Our description shows clearly the source of the fluctuations. In the normal evaluation procedure the background is automatically subtracted but the fluctuations remain.

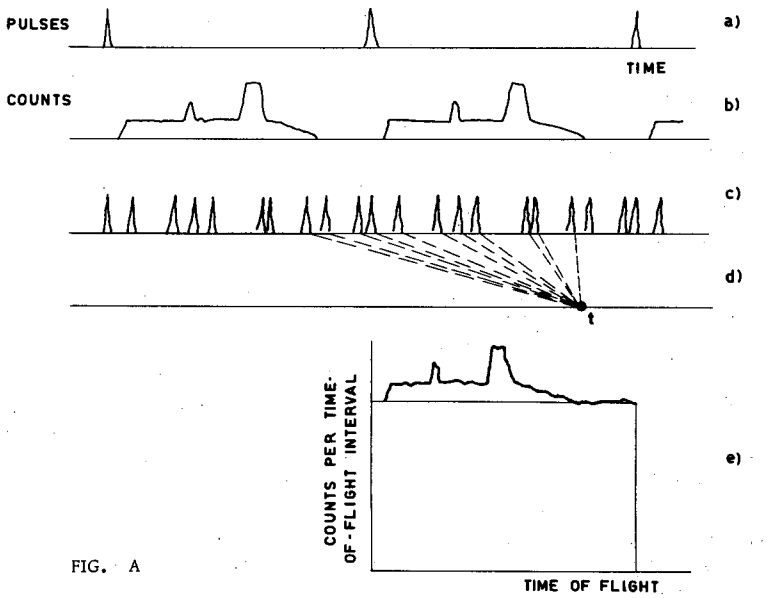

FIG. A

It is evident that the method will be good for measuring the position and the shape of relatively high peaks, especially if the total area of the time-of-flight curve is not large in comparison with the area under the peaks. The method is also very good, as has been shown by Sköld, when the distribution contains a large background which is not due to the pulsed neutron beam itself. A background of this kind becomes much less important if the number of pulses is increased.

From our description it also appears that the time-of-flight curve, on the basis of the assumptions we have made so far, is quite free from distortions that might be caused by the method of evaluation. For instance,

the position, width and intensity of the peaks will be as well defined as in a normal time-of-flight experiment with the same pulse shape.

However, in the ordinary time-of-flight technique pulse widths are also made variable up to rather long durations. For narrow peaks, this introduces effects of integration, and the evaluation implies some unfolding; thus there will probably be no overall gain in accuracy for such peaks, and there may indeed be uncertainties introduced by the evaluation. Nevertheless, for a broad distribution, as represented by the shape of a Maxwell-like spectrum, there will be an advantage because the neutron intensity is higher with long pulses.

We now come to the paper by Whittemore. I shall try to expose the essential points of the method described in the paper, without worrying about the loss of generality.

The neutron pulse spectrum is sinusoidal or triangular (Fig. B(b)), and measurements are carried out one by one at frequencies differing each time (Fig. B(b)-(d)). Each measurement is performed in, say, four channels for one pulse period. This yields the average count rate (integral of the time-of-flight curve)- which is the same for all frequencies- and, for each frequency, the amplitude and phase angle of a sine or quasi-sine component (Fig. B(f)). From a large number of such components (say 50), Fourier synthesis or something similar can be applied to reconstruct the time-of-flight curve (Fig. B(a)), with fluctuations due to the counting statistics and some uncertainties due to the synthesis, the nature of these being well known from other work.

The overall accuracy of the method should be comparable to that of the statistical pulsing method. It will have to be tried out, of course, in order to see whether there are any hidden difficulties. In some cases it may be a drawback that measurements must be carried out one after the other and not simultaneously, but this is what happens in most work on crystal structure for instance.

There may be advantages if the amount of information is limited to, say, the position and width of peaks. A suitable choice of frequencies can then be made, and time can be saved by not measuring the others.

In my opinion the main advantage of the method – and this is especially important when relatively fast neutrons are used – lies in the fact that frequencies may be reached which correspond to pulse widths of only a few microseconds. The fact that the 'pulses' are regularly spaced makes it possible to define them by a static and a moving cam, each having many slits of equal width (about 1 mm).

N. KROÓ: I have with me some figures which I calculated by way of a comparison between classical time-of-flight methods and our statistical correlation time-of-flight method.

If you have a very sharp peak in your spectrum (i.e. the preferred case) and your effect-to-background ratio is 1, then the integral number of counts in the effect is 50% of the total, with the other 50% representing the background. In such a case the relative efficiency of the new method, compared to the classical time-of-flight procedure, can be described by a factor of 12.

With the effect-to-background ratio 1 as before, but with a very broad distribution, the relative efficiency of the new method is given by a factor of 56.

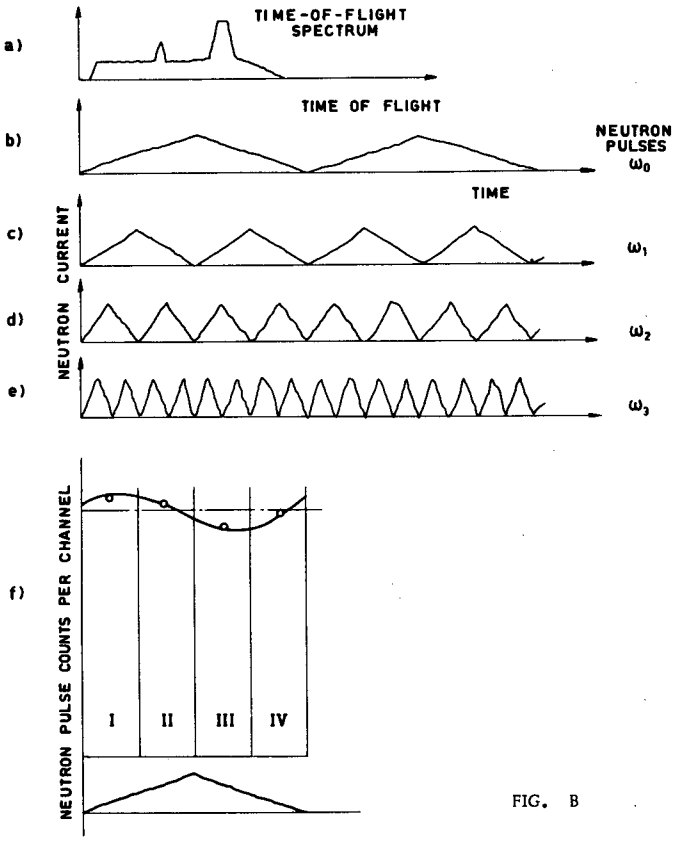

FIG. B

Assuming a large maximum, representing about 90% of the counts, and a small maximum beside it accounting for the other 10%, the relative efficiency of the new method is 9.4.

Finally, if you have a really small peak – amounting to only 2% of the total counts – and your integral effect-to-background ratio is 0.05, then you will get an efficiency factor of 3.5.

We therefore have no doubt that in all practical cases the new method is superior to the classical one.

Another point of importance is the series of pseudorandom numbers in one sequence. The more pseudorandom numbers there are per sequence, the better the results will be from the statistical point of view. The figures I have been quoting were associated with a 255-term pseudorandom sequence. If the number of terms is increased the figures become better still.

We were, incidentally, using a 255-term pseudorandom sequence for the simple reason that we had a 256-channel analyser, which could easily be converted into a 255-channel instrument. To be more exact, we had a 512-channel analyser which we divided into two parts, using the second one, with appropriate modifications, as a computer to calculate the cross-correlation function. When the measurement was stopped, the cross-correlation function appeared immediately on the oscilloscope screen.

W. GLÄSER: I find that Mr. Kroó's estimate of the statistical errors is very similar to the one we have given in our paper (SM-104/67). I cannot judge, however, whether the figures he has just given are in agreement with our conclusions. The formulas we quote have been verified by several scattering experiments.

I think I should comment again on the question of background, which may have raised some difficulties. The pseudo-statistical method is better than the conventional time-of-flight method in respect of the signal-to-background ratio simply because of the availability of useful neutrons for half of the measuring time, whereas in the conventional technique they are available for only a small fraction of the time (assuming the same background per unit time).

In principle the statistical method cannot be better than a stationary method such as that involving a triple-axis spectrometer in cases where neutrons of one energy only, scattered in one direction (one-time channel), have to be measured. But as soon as the advantages of the time-of-flight technique are fully exploited, namely by measuring several energies and several momentum transfers simultaneously, the statistical method is superior to the stationary method, also in respect of the signal-to-background ratio.

A. V. VIRJO: According to my calculations[1], the estimate of the statistical error of a cross-correlation measurement given in paper SM-104/6 is too optimistic. The reason for this, I believe, is that the statistical nature of the scattering process itself is not accounted for in the estimate. I also have doubts regarding Mr. Kroó's proposition that it is possible, by increasing the length N of the pseudorandom sequence, to improve the accuracy (where background is involved). It is true that when N is increased the cross-correlated background will be suppressed, but at the same time the measuring time is increased too. An analysis with a fixed measuring time shows, in fact, that the relative accuracy with which the time-of-flight spectrum is obtained (with background subtracted) does not depend significantly on N for $N \gg 1$. N determines only the amount of frame overlapping.

B. DORNER: I would point out to Mr. Virjo that the measuring time is quite independent of the time of one pseudorandom sequence. If you increase the length of that sequence you only improve your measurement to the extent that the background mentioned by Mr. Maier-Leibnitz, which is caused by the cross-correlation method itself, is flattened out. The measuring time will remain the same.

Commenting now on the cam wheel which is run for a certain time at one speed and then for a further period of time at a different speed, it seems to me that if there is a background varying slowly with time (and we are discussing experiments with high background), some Fourier components will be enhanced and others reduced. I believe, therefore, that the wheel can be used only under conditions of constant background.

W. L. WHITTEMORE: I should like to emphasize that Mr. Steinsvoll's system, described in paper SM-104/65, represents the best example I have seen of an optimized Fermi-type chopping system. It makes almost the best possible use of the time available.

---

[1] VIRJO, A., Statistical analysis of a cross-correlation chopper for time-of-flight measurements, Nucl. Instrum. Meth. (in press).

O. STEINSVOLL: Our most recent measurements, shown in the last figure of the paper, illustrate this point regarding optimum use of time. The inelastic spectrum fills the time window of width 256 μsec, and the chopper gives pulses at intervals of 260 μsec. This is equivalent to a mechanical chopper operating at 240 000 rpm.

W. L. WHITTEMORE: Several points can profitably be made in comparing the Fourier synthesis technique with the cross-correlation and standard techniques.

1. In the high-efficiency systems the usual incoherent background noise is reduced to nearly zero, but the statistical fluctuation in this background as well as the signal becomes the new noise in these new systems.

2. The Fourier method permits the mechanical chopper to be constructed with uniform spacing of teeth. This, in turn, allows one to use a beam much wider than the tooth size. Consequently, the Fourier method makes it possible to achieve short pulses ($\simeq$ 1 μsec) and wide beams with a relatively small-diameter chopping wheel, compared to what would be required in the cross-correlation system.

3. Modulation of the beam with a pattern rich in higher harmonics and analysis of the scattered beam for Fourier components at these harmonics reveal a significant advantage of the Fourier system over the cross-correlation system.

4. The Fourier system will be advantageous for the modulation with a crystal chopper because the crystal modulator can be made a part of a resonant circuit with significant simplifications in its switching.

SYMPOSIUM ON
NEUTRON INELASTIC SCATTERING

HELD AT COPENHAGEN, 20 - 25 MAY 1968

CHAIRMEN OF SESSIONS

Session A	W. HÄLG	Switzerland
	J. ALS-NIELSEN	Denmark
	Yu.M. KAGAN	Union of Soviet Socialist Republics
Session B	P.K. IYENGAR	India
	J.L. YARNELL	United States of America
Session C	A.G. SJÖLANDER	Sweden
	R.D. LOWDE	United Kingdom
Session D	D. JOVIĆ	Yugoslavia
	T. RISTE	Norway
Special Session	H. MAIER-LEIBNITZ	Federal Republic of Germany

SECRETARIAT OF THE SYMPOSIUM

Scientific Secretary	J. DOLNIČAR	Division of Research and Laboratories, IAEA
Administrative Secretary	H.H. STORHAUG	Division of Scientific and Technical Information, IAEA
Editor	C.N. WELSH	Division of Publications, IAEA
Records Officer	N.W.A. JONES	Division of Languages, IAEA

LIST OF PARTICIPANTS

AUSTRALIA

Paul, G.L.	Unitersity of Edinburgh, Edinburgh 8, Scotland

AUSTRIA

Eder, O.J.	Österreichische Studiengesellschaft für Atomenergie GmbH, Lenaugasse 10, 1080 Vienna
Quittner, G.	Österreichische Studiengesellschaft für Atomenergie GmbH, Lenaugasse 10, 1080 Vienna
Rauch, H.	Atominstitut der österreichischen Hochschulen, Schüttelstrasse 115, 1020 Vienna

BELGIUM

Hautecler, S.J.S.	C.E.N., 200 Boerentang, Mol-Donk
Neve de Mevergnies, M.J.B.	C.E.N., 200 Boerentang, Mol-Donk

BRAZIL

Herdade, S.B.	Instituto de Energia Atomica, Caixa Postal 11049, Pinheiros, São Paulo

CANADA

Brockhouse, B.N.	McMaster University, Hamilton, Ont.
Cowley, R.A.	Atomic Energy of Canada Ltd., Chalk River, Ont.
Ng, S.C.	McMaster University, Hamilton, Ont.
Pope, N.K.	Royal Military College, Kingston, Ont.
Powell, B.M.	Atomic Energy of Canada Ltd., Chalk River, Ont.

DENMARK

Als-Nielsen, J.	Risø Research Establishment, Roskilde
Bjerrum Møller, H.	Risø Research Establishment, Roskilde
Dietrich, O.W.	Risø Research Establishment, Roskilde
Gylden Houmann, J.C.	Risø Research Establishment, Roskilde
Jensen Højgaard, H.	University of Copenhagen Universitetsparken 5, Copenhagen Ø

Kjems, J.K.	Risø Research Establishment, Roskilde
Lebech, Bente	Risø Research Establishment, Roskilde
Lingård, P.-A.	Risø Research Establishment, Roskilde
Mackintosh, A.R.	Technical University, Lyngby
Nielsen, M.	Risø Research Establishment, Roskilde
Radhakrishna, P.R.	Risø Research Establishment, Roskilde
Warming, Elisabeth	Risø Research Establishment, Roskilde

FINLAND

Kuoppamäki, R.J.	Technical University of Helsinki, Otaniemi
Palmgren, A.	Technical University of Helsinki, Otaniemi
Sefidvash, F.F.	Technical University of Helsinki, Otaniemi
Tunkelo, E.H.	Technical University of Helsinki, Otaniemi
Virjo, A.V.	Technical University of Helsinki, Otaniemi

FRANCE

Dreyfus, B.	Institut Max von Laue-Paul Langevin, B.P. 508, 38-Grenoble
Jannink, G.	C.E.N. de Saclay, B.P. No.2, 91-Gif-sur-Yvette
Maynard, R.	C.E.N. de Grenoble, B.P. No. 269, 38-Grenoble
Pick, R.M.	C.E.N. de Saclay, B.P. No.2, 91-Gif-sur-Yvette

GERMANY, FED. REP. OF

Alefeld, B.	Technische Hochschule Arcisstrasse 21, 8 Munich
Axmann, A.	Kernforschungsanlage Jülich des Landes Nordrhein-Westfalen e.V., Postfach 365, 517 Jülich
Dorner, B.	Kernforschungsanlage Jülich des Landes Nordrhein-Westfalen e.V., Postfach 365, 517 Jülich
Drexel, W.J.	Gesellschaft für Kernforschungs mbH, Weberstrasse 5, 75 Karlsruhe
Gissler, W.	Kernforschungsanlage Jülich des Landes Nordrhein-Westfalen e.V., Postfach 365, 517 Jülich
Gläser, W.	Kernforschungszentrum Karlsruhe, Postfach 3640, 75 Karlsruhe
Jex, H.W.P.	J.W. Goethe Universität, Robert Mayer-Strasse 6-8, 6 Frankfurt/M.

Kofink, W.	University of Karlsruhe, Kaiserstrasse 12, 75 Karlsruhe
Kress, W.A.	J. W. Goethe Universität, Robert Mayer-Strasse 8, 6 Frankfurt/M.
Maier-Leibnitz, H.H.,	Institut Max von Laue-Paul Langevin, B.P. 508, 38-Grenoble, France
Mika, K.	Kernforschungsanlage Jülich des Landes Nordrhein-Westfalen e.V., Postfach 365, 517 Jülich
Springer, T.	Kernforschungsanlage Jülich des Landes Nordrhein-Westfalen e.V., Postfach 365, 517 Jülich
Steichele, E.	Technische Hochschule, Arcisstrasse 21, 8 Munich
Stiller, H.H.	Kernforschungsanlage Jülich des Landes Nordrhein-Westfalen e.V., Postfach 365, 517 Jülich
Stockmeyer, R.	Kernforschungsanlage Jülich des Landes Nordrhein-Westfalen e.V., Postfach 365, 517 Jülich

HUNGARY

Gordon, J.	Central Research Institute for Physics, Hungarian Academy of Sciences, P.O. Box 49, Budapest 114
Kroó, N.	Central Research Institute for Physics, Hungarian Academy of Sciences, P.O. Box 49, Budapest 114

INDIA

Iyengar, P.K.	Bhabha Atomic Research Centre, Bombay 74
Vijayaraghavan, P.R.	Bhabha Atomic Research Centre, Bombay 74

ISRAEL

Pelah, I.	Israel Atomic Energy Commission, Soreq Nuclear Research Centre, Yavne

ITALY

Caglioti, G.	C.N.E.N., Ispra, Varese
Menzinger, F.	C.N.E.N., Centro di Studi Nucleari di Casaccia, Via Anguillarese, Rome
Paoletti, A.	C.N.E.N., Centro di Studi Nucleari di Casaccia, Via Anguillarese, Rome
Rizzi, G.	C.N.E.N., c/o CCR Euratom, Ispra, Varese

Salvi, P.	Ministero Industria e Commercio, Rome

JAPAN

Sakamoto, M.	Japan Atomic Energy Research Institute, Tokai-Mura, Naka-gun, Ibaraki-ken

NETHERLANDS

Bergsma, J.	Reactor Centrum Nederland, Petten (N.H.)
Bleeker, E.	Institutt for Atomenergie, Kjeller, Norway
van Dijk, C.	Reactor Centrum Nederland, Petten (N.H.)
Ferziger, J.	Rijksuniversiteit, Reitdiepskade 4, Groningen
Frikkee, E.	Reactor Centrum Nederland, Petten (N.H.)
Hasman, A.	Reactor Instituut Delft, Berlageweg 15, Delft
van Loef, J.J.	Reactor Instituut Delft, Berlageweg 15, Delft
de Mul, F.F.M.	Reactor Instituut Delft, Berlageweg 15, Delft
Nijboer, B.R.A.	University of Utrecht, Maliesingel 23, Utrecht
van Tricht, J.B.	Reactor Instituut Delft, Berlageweg 15, Delft

NORWAY

Møglestue, K.T.	Reactor Centrum Nederland, Petten (N.H.)
Otnes, K.	Institutt for Atomenergie, Kjeller
Riste, T.	Institutt for Atomenergie, Kjeller
Steinsvoll, O.	Institutt for Atomenergie, Kjeller

POLAND

Sosnowski, J.	Institute of Nuclear Research, Świerk

PORTUGAL

Gama Carjalho, F.	Laboratório de Física e Engenharia Nucleares da Junta de Energia Nuclear, Sacavém

ROMANIA

Bally, D.	Institute for Atomic Physics, Bucharest
Mateescu, N.	Institute for Atomic Physics, Bucharest

SOUTH AFRICA

Raubenheimer, L.J.	South African Atomic Energy Board, Private Bag 256, Pretoria

SWEDEN

Almqvist, L.E.	AB Atomenergi, Studsvik, Nyköping
Burgman, J.O.	Royal Institute of Technology, Teknikringen 30, Stockholm
Dahlborg, U.C.A.	Royal Institute of Technology, Drottnig Kristinas Väg 47, Stockholm Ö
Friberg, B.E.N.	Royal Institute of Technology, Drottning Kristinas Väg 47, Stockholm Ö
Gräslund, C.L.	Royal institute of Technology, Drottning Kristinas Väg 47, Stockholm Ö
Grimvall, N.G.	Chalmers University of Technology, Sven Hultins gata, Göteborg
Holmryd, S.G.	AB Atomenergi, Studsvik, Nyköping
Larsson, K.-E.	Royal Institute of Technology, Drottning Kristinas Väg 47, Stockholm Ö
Nelin, G.	AB Atomenergi, Studsvik, Nyköping
Nilsson, S.G.T.	AB Atomenergi, Studsvik, Nyköping
Pauli, R.T.	AB Atomenergi, Liljeholmsvägen 32, Stockholm
Raunio, G.	Chalmers University of Technology, Göteborg and AB Atomenergi, Studsvik, Nyköping
Rolandson, S.E.R.	AB Atomenergi, Studsvik, Nyköping
Sandström, R.V.J.	Royal Institute of Technology, Stockholm 70
Sjölander, A.G.	Institute of Theoretical Physics, Göteborg
Stedman, R.S.	AB Atomenergi, Studsvik, Nyköping
Waller, I.	University of Uppsala and AB Atomenergi, Studsvik, Nyköping
Weymouth, J.W.	AB Atomenergi, Studsvik, Nyköping

SWITZERLAND

Baltensperber, W.	Eidgenössische Technische Hochschule, Hochstrasse 60, 8044 Zurich
Furrer, A.	Eidgenössisches Institut für Reaktorforschung, 5303 Würenlingen

Hälg, W.	Eidgenössisches Institut für Reaktorforschung, 5303 Würenlingen
Schneider, T.	Eidgenössisches Institut für Reaktorforschung, 5303 Würenlingen

TURKEY

Sanalan, Y.	Turkish Atomic Energy Commission Rumeli Han No. 12, Kizilav, Ankara

UNION OF SOVIET SOCIALIST REPUBLICS

Kagan, Yu. M.	Kurchatov Institute of Atomic Energy, Moscow
Zemlyanov, M. G.	Kurchatov Institute of Atomic Energy, Moscow

UNITED KINGDOM

Cochran, W.	University of Edinburgh, Edinburgh 8, Scotland
Cocking, S. J.	UKAEA, AERE, Harwell, Didcot, Berks
Evans, M. T.	Cavendish Laboratory, Free School Lane, Cambridge
Howells, W. S.	Cavendish Laboratory, Free School Lane, Cambridge
Hutchinson, P.	UKAEA, AERE, Harwell, Didcot, Berks
Lorch, E.	University of Birmingham, P. O. Box 363, Birmingham 15
Lowde, R. D.	UKAEA, AERE, Harwell, Didcot, Berks
Millington, A. J.	Cavendish Laboratory, Free School Lane, Cambridge
Page, D. I.	UKAEA, AERE, Harwell, Didcot, Berks
Pawley, G. S.	University of Edinburgh, Edinburgh 8, Scotland
Pindor, A.	Cavendish Laboratory, Free School Lane, Cambridge
Powles, J. G.	University of Kent, Canterbury
Pynn, R.	Cavendish Laboratory, Free School Lane, Cambridge
Ross, D. K.	University of Birmingham, P. O. Box 363, Birmingham 15
Sândor, E. E.	Queen Mary College, London University, Mile End Road, London, E. 1
Schofield, P.	UKAEA, AERE, Harwell, Didcot, Berks
Sharp, R. I.	Cavendish Laboratory, Free School Lane, Cambridge
Squires, G. L.	Cavendish Laboratory, Free School Lane, Cambridge
Stirling, G. C.	Physical Chemistry Laboratory, South Parks Raod, Oxford

Webb, F.	UKAEA, AERE, Harwell, Didcot, Berks
White, J.W.	Physical Chemistry Laboratory, South Parks Road, Oxford
Windsor, C.G.	UKAEA, AERE, Harwell, Didcot, Berks

UNITED STATES OF AMERICA

Carpenter, J.M.	University of Michigan, Ann Arbor, Mich. 48105
Carr, H.Y.	Rutgers University, New Brunswick, N.J.
Feldkamp, L.A.	University of Michigan, Ann Arbor, Mich. 48105
Hamilton, W.C.	Brookhaven National Laboratory, Upton, Long Island, N.Y. 11973
Harling, O.K.	Pacific Northwest Laboratory, Battelle Memorial Institute, Richland, Wash. 99352
Litovitz, T.	Catholic University of America, Washington, D.C. 20017
Lurie, N.A.	University of Michigan, Ann Arbor, Mich. 48105
Lynch, J.	Ohio State University, Columbus, Ohio 43221
Mook, H.	Oak Ridge National Laboratory, Oak Ridge, Tenn.
Mozer, B.	National Bureau of Standards, Washington, D.C. 20234
Muether, H.R.	State University of New York at Stony Brook, Stony Brook, N.Y., and Brookhaven National Laboratory, Upton, Long Island, N.Y.11973
Muhlestein, L.	University of Missouri, Columbia, Miss. 65201
Nelkin, M.S.	Cornell University, Ithaca, N.Y. 14850
Nicklow, R.M.	Oak Ridge National Laboratory, Oak Ridge Tenn.
Prask, H.	Picatinny Arsenal (US Army), Dover, N.J.
Rahman, A.	Argonne National Laboratory, Argonne, Ill. 60439
Randolph, P.D.	Idaho Nuclear Corporation, Idaho Falls, Idaho
Rowe, J.M.	Argonne National Laboratory, Argonne, Ill. 60440
Rush, J.J.	National Bureau of Standards, Washington, D.C. 20234
Sinha, S.K.	Iowa State University, Ames, Iowa 50010
Slutsky, L.J.	University of Washington, Seattle, Wash. 98105
Summerfield, G.C.	University of Michigan, Ann Arbor, Mich. 48105

Yarnell, J.L.	Los Alamos Scientific Laboratory of the University of California, Los Alamos, N.M. 87544
Yip, S.	Massachusetts Institute of Technology, Cambridge, Mass. 02139
Young, J.A.	Gulf General Atomic, San Diego, Calif. 92112
Whittemore, W.L.	Gulf General Atomic, San Diego, Calif. 92112

YUGOSLAVIA

Brajović, V.	Boris Kidrič Institute of Nuclear Sciences, Vinča, Belgrade
Dimić, V.	Josef Stefan Nuclear Institute, Ljubljana
Jović, D.	Boris Kidrič Institute of Nuclear Sciences, Vinča, Belgrade
Konstantinović, J.	Boris Kidrič Institute of Nuclear Sciences, Vinča, Belgrade
Pirkmajer, E.	Jozef Stefan Nuclear Institute, Ljubljana
Zivanović, M.	Boris Kidrič Institute of Nuclear Sciences, Vinča, Belgrade

INTERNATIONAL ORGANIZATIONS

EURATOM

Ardente, V.	Euratom, C.C.R., Ispra, Varese, Italy
Bock, E.	Euratom, 51-53, rue Belliard, Brussels, Belgium
Krebs, K.H.	Euratom, C.C.R., Ispra, Varese, Italy
Rubin, R.	Euratom, C.C.R., Ispra, Varese, Italy
Verdan, G.A.	Euratom, C.C.R., Ispra, Varese, Italy

JINR

Golikov, V.	Joint Institute for Nuclear Research, Dubna, USSR
Holas, A.	Joint Institute for Nuclear Research, Dubna, USSR
Maliszewski, E.	Joint Institute for Nuclear Research, Dubna, USSR

IAEA

Grünberg, B.	Division of Research and Laboratories, IAEA, Kärtner Ring 11, 1010 Vienna
Morgan, W.	Division of Research and Laboratories, IAEA, Kärtner Ring 11, 1010 Vienna
Sanatani, S.	Division of Nuclear Power and Reactors, IAEA, Kärtner Ring 11, 1010 Vienna

AUTHOR INDEX

Roman numerals are volume numbers.
Arabic numerals underlined refer to the first page of a paper.
Other Arabic numerals refer to a contribution to the discussions.

IAEA SALES AGENTS

Orders for Agency publications can be placed with your bookseller or any of our sales agents listed below:

ARGENTINA
Comisión Nacional de
Energía Atómica
Avenida del Libertador
General San Martin 8250
Buenos Aires - Suc. 29

AUSTRALIA
Hunter Publications,
23 McKillop Street
Melbourne, C.1

AUSTRIA
Georg Fromme & Co.
Spengergasse 39
A-1050, Vienna V

BELGIUM
Office international de librairie
30, avenue Marnix
Brussels 5

BRAZIL
Livraria Kosmos Editora
Rua do Rosario, 135-137
Rio de Janeiro

Agencia Expoente Oscar M. Silva
Rua Xavier de Toledo, 140-1° Andar
(Caixa Postal No. 5.614)
São Paulo

BYELORUSSIAN SOVIET SOCIALIST REPUBLIC
See under USSR

CANADA
The Queen's Printer
Ottawa, Ontario

CHINA (Taiwan)
Books and Scientific Supplies
Service, Ltd.,
P.O. Box 83
Taipei

CZECHOSLOVAK SOCIALIST REPUBLIC
S.N.T.L.
Spolena 51
Nové Město
Prague 1

DENMARK
Ejnar Munksgaard Ltd.
6 Nörregade
Copenhagen K

FINLAND
Akateeminen Kirjakauppa
Keskuskatu 2
Helsinki

FRANCE
Office international de
documentation et librairie
48, rue Gay-Lussac
F-75, Paris 5e

GERMANY, Federal Republic of
R. Oldenbourg
Rosenheimer Strasse 145
8 Munich 8

HUNGARY
Kultura
Hungarian Trading Co. for Books
and Newspapers
P.O.B. 149
Budapest 62

ISRAEL
Heiliger and Co.
3 Nathan Strauss Street
Jerusalem

ITALY
Agenzia Editoriale Internazionale
Organizzazioni Universali (A.E.I.O.U.)
Via Meravigli 16
Milan

JAPAN
Maruzen Company Ltd.
6, Tori Nichome
Nihonbashi
(P.O. Box 605)
Tokyo Central

MEXICO
Librería Internacional
Av. Sonora 206
Mexico 11, D.F.

NETHERLANDS
N.V. Martinus Nijhoff
Lange Voorhout 9
The Hague

NEW ZEALAND
Whitcombe & Tombs, Ltd.
G.P.O. Box 1894
Wellington, C.1

NORWAY
Johan Grundt Tanum
Karl Johans gate 43
Oslo

PAKISTAN
Karachi Education Society
Haroon Chambers
South Napier Road
(P.O. Box No. 4866)
Karachi 2

POLAND
Ośrodek Rozpowszechniana
Wydawnictw Naukowych
Polska Akademia Nauk
Pałac Kultury i Nauki
Warsaw

ROMANIA
Cartimex
Rue A. Briand 14-18
Bucarest

SOUTH AFRICA
Van Schaik's Bookstore (Pty) Ltd.
Libri Building
Church Street
(P.O. Box 724)
Pretoria

SPAIN
Librería Bosch
Ronda de la Universidad 11
Barcelona

SWEDEN
C.E. Fritzes Kungl. Hovbokhandel
Fredsgatan 2
Stockholm 16

SWITZERLAND
Librairie Payot
Rue Grenus 6
1211 Geneva 11

TURKEY
Librairie Hachette
469, Istiklâl Caddesi
Beyoğlu, Istanbul

UKRAINIAN SOVIET SOCIALIST REPUBLIC
See under USSR

UNION OF SOVIET SOCIALIST REPUBLICS
Mezhdunarodnaya Kniga
Smolenskaya-Sennaya 32-34
Moscow G-200

UNITED KINGDOM OF GREAT BRITAIN AND NORTHERN IRELAND
Her Majesty's Stationery Office
P.O. Box 569
London, S.E.1

UNITED STATES OF AMERICA
National Agency for
International Publications, Inc.
317 East 34th Street
New York, N.Y. 10016

VENEZUELA
Sr. Braulio Gabriel Chacares
Gobernador a Candilito 37
Santa Rosalía
(Apartado Postal 8092)
Caracas D.F.

YUGOSLAVIA
Jugoslovenska Knjiga
Terazije 27
Belgrade

IAEA publications can also be purchased retail at the United Nations Bookshop at United Nations Headquarters, New York, at the news-stand at the Agency's Headquarters, Vienna, and at most conferences, symposia and seminars organized by the Agency.

In order to facilitate the distribution of its publications, the Agency is prepared to accept payment in UNESCO coupons or in local currencies.

Orders and inquiries from countries where sales agents have not yet been appointed may be sent to:

Distribution and Sales Group, International Atomic Energy Agency,
Kärntner Ring 11, A-1010, Vienna I, Austria

INTERNATIONAL
ATOMIC ENERGY AGENCY
VIENNA, 1968

PRICE: US $11.-
Austrian Schillings 285.-
(£4.11.8; F.Fr. 53,90; DM 44,-)